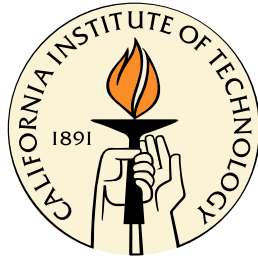


# Topics in Black Hole Perturbation Theory and the Visualization of Curved Spacetime

Thesis by  
Aaron Zimmerman

In Partial Fulfillment of the Requirements  
for the Degree of  
Doctor of Philosophy



California Institute of Technology  
Pasadena, California

2013  
(Submitted May 15, 2013)

© 2013

Aaron Zimmerman  
All Rights Reserved

To my parents, in gratitude for their love and support.

# Acknowledgments

There is no way I can give proper thanks to all the people who have helped me in myriad ways during my five years of graduate study at Caltech. I offer a partial accounting below, and ask the forgiveness of anyone left out.

I must first thank my adviser Yanbei Chen. He has supported all of my research endeavors with enthusiasm, and provided expert advice anytime I came to him for help. His good humor, kindness, excitement, and endless curiosity will always be an example to me of how to best approach physics. His technical excellence in a vast array of topics has and will always provide me with something to aspire to.

I would also like to thank Kip Thorne, who I was fortunate to work closely with on some of the research presented in this thesis. Kip's warmth, enthusiasm, drive, and expertise have all served as an inspiration for me. I am grateful for his generous advice and support during my time at Caltech.

Of course, I would be nowhere without the wealth of collaborators I have worked with on the projects presented here. In addition to Yanbei Chen and Kip Thorne, they are Emanuele Berti, Jeandrew Brink, Jeffrey D. Kaplan, Geoffrey Lovelace, Keith D. Matthews, David A. Nichols, Rob Owen, Mark Scheel, Huan Yang, Fan Zhang, and Zhongyang Zhang. Everything I have learned, I have learned with the help and encouragement of these people. I would also like to acknowledge the entire TAPIR group, for fostering a supportive and collaborative environment.

I owe a great deal to those people whose friendship and support outside of research helped keep me sane, and made graduate school enjoyable and fulfilling. I have shared a home with such luminaries as Jonathan Arnold, Jennifer Driggers, Nick Heinz, Andrew Jennings, and Matthew Abernathy; they were my family in California. Kimberly Boddy, Timothy Hill, Marisa Geyer, Erin Sanchez, and Erika Tuffli all provided regular advice and encouragement at one point or another. My office mates Fan Zhang and John Wendell, among others, kept the days bright. To my many other friends in TAPIR, you have my thanks.

Finally, I want to thank David and Barbara Groce, whose generous financial support allowed more time for research and the freedom to travel. It made a great deal of difference.

# Abstract

This thesis presents recent research into analytic topics in the classical theory of General Relativity. It is a thesis in two parts. The first part features investigations into the spectrum of perturbed, rotating black holes. These include the study of near horizon perturbations, leading to a new generic frequency mode for black hole ringdown; an treatment of high frequency waves using WKB methods for Kerr black holes; and the discovery of a bifurcation of the quasinormal mode spectrum of rapidly rotating black holes. These results represent new discoveries in the field of black hole perturbation theory, and rely on additional approximations to the linearized field equations around the background black hole. The second part of this thesis presents a recently developed method for the visualization of curved spacetimes, using field lines called the tendex and vortex lines of the spacetime. The works presented here both introduce these visualization techniques, and explore them in simple situations. These include the visualization of asymptotic gravitational radiation; weak gravity situations with and without radiation; stationary black hole spacetimes; and some preliminary study into numerically simulated black hole mergers. The second part of thesis culminates in the investigation of perturbed black holes using these field line methods, which have uncovered new insights into the dynamics of curved spacetime around black holes.

# Contents

<b>Acknowledgments</b>	<b>iv</b>
<b>Abstract</b>	<b>v</b>
<b>1 Overview and Summary</b>	<b>1</b>
1.1 Introduction . . . . .	1
1.2 Black Hole Perturbation Theory . . . . .	2
1.2.1 Review of Black Hole Perturbation Theory . . . . .	4
1.3 The Extremes of Black Hole Perturbation Theory . . . . .	6
1.3.1 The Horizon Mode . . . . .	6
1.3.2 The High Frequency Approximation and WKB Methods . . . . .	8
1.3.3 The Nearly Extreme Kerr Black Hole and the Bifurcation of the QNM Spectrum . . . . .	9
1.4 The Visualization of Curved Spacetime . . . . .	10
1.4.1 Tendex and Vortex Lines . . . . .	12
1.4.2 Gravitational Radiation and the Topology of Vortex and Tendex Lines . . . . .	15
1.4.3 Weak Gravity . . . . .	16
1.4.4 Stationary Black Holes . . . . .	18
1.4.5 Perturbed black holes . . . . .	20
1.5 Outlook . . . . .	22
<b>I Topics in Black Hole Perturbation Theory</b>	<b>25</b>
<b>2 New Generic Ringdown Frequencies at the Birth of a Kerr Black Hole</b>	<b>26</b>
2.1 Introduction . . . . .	26
2.2 The Near Horizon Approximation . . . . .	29
2.2.1 Simple Argument for a Horizon Mode . . . . .	29
2.2.2 The Near Horizon Limit: The $\Sigma$ Boundary Model . . . . .	32
2.2.3 The Characteristic Boundary Model . . . . .	35
2.3 Reconciliation with the Mino-Brink Mode . . . . .	37

2.3.1	Point Particle Radiation in Newman-Penrose Formalism . . . . .	37
2.3.2	Eliminating the Leading Order Frequency Mode of Mino and Brink . . . . .	40
2.4	Numerical Study . . . . .	41
2.4.1	Comparison of Overlaps . . . . .	43
2.4.2	Extraction of Mass and Black Hole Spin . . . . .	46
2.5	Discussion . . . . .	47
2.A	Green's Function Formalism For the Teukolsky Equation . . . . .	51
2.B	The Teukolsky Equation in the Newman-Penrose Formalism . . . . .	54
2.C	Mode Corrections to the Wavefunction . . . . .	55
<b>3</b>	<b>Quasinormal-Mode Spectrum of Kerr Black Holes and Its Geometric Interpretation</b>	<b>59</b>
3.1	Introduction . . . . .	60
3.1.1	Overview of Quasinormal Modes and Their Geometric Interpretation . . . . .	60
3.1.2	Methods and Results of this Article . . . . .	62
3.1.3	Organization of the Paper . . . . .	64
3.2	WKB Approximation for the Quasinormal-Mode Spectrum of Kerr Black Holes . . . . .	65
3.2.1	The Teukolsky Equations . . . . .	65
3.2.2	The Angular Eigenvalue Problem . . . . .	66
3.2.2.1	Real Part of $A_{lm}$ for a Real-Valued $\omega$ . . . . .	67
3.2.2.2	Complex $A_{lm}$ for a Complex $\omega$ . . . . .	70
3.2.3	The Radial Eigenvalue Problem . . . . .	71
3.2.3.1	Computing $\omega_R$ . . . . .	71
3.2.3.2	Computing $\omega_I$ . . . . .	73
3.2.4	Accuracy of the WKB Approximation . . . . .	75
3.3	Geometric Optics in the Kerr Spacetime . . . . .	78
3.3.1	Geometric Optics: General Theory . . . . .	78
3.3.2	Null Geodesics in the Kerr Spacetime . . . . .	80
3.3.3	Correspondence with Quasinormal Modes . . . . .	81
3.3.3.1	Leading Order: Conserved Quantities of Rays and the Real parts P of Quasinormal-Mode Parameters . . . . .	81
3.3.3.2	Next-to-Leading Order: Radial Amplitude Corrections and the Imag- inary Part of the Frequency . . . . .	83
3.3.3.3	Next-to-Leading Order: Angular Amplitude Corrections and the Imaginary Part of Carter's Constant . . . . .	89
3.4	Features of the Spectra of Kerr Black Holes . . . . .	91

3.4.1	Spherical Photon Orbits and Extremal Kerr Black Holes . . . . .	91
3.4.2	A Mode's Orbital and Precessional Frequencies . . . . .	93
3.4.3	Degenerate Quasinormal Modes and Closed Spherical Photon Orbits . . . . .	97
3.4.3.1	Slowly Spinning Black Holes . . . . .	98
3.4.3.2	Generic Black Holes . . . . .	98
3.5	Conclusions and Discussion . . . . .	99
3.A	The Taylor Expanded Bohr-Sommerfeld Condition . . . . .	100
<b>4</b>	<b>Branching of Quasinormal Modes for Nearly Extremal Kerr Black Holes</b>	<b>105</b>
4.1	Introduction . . . . .	105
4.2	Matched Expansion . . . . .	107
4.3	WKB Analysis . . . . .	109
4.4	Phase Boundary . . . . .	110
4.5	Bifurcation . . . . .	111
4.6	Conclusions . . . . .	113
<b>II</b>	<b>Visualization of Curved Spacetime</b>	<b>115</b>
<b>5</b>	<b>Frame-Dragging Vortexes and Tidal Tendexes Attached to Colliding Black Holes: Visualizing the Curvature of Spacetime</b>	<b>116</b>
5.1	Introduction . . . . .	116
5.2	Vortexes and Tendexes in Black-Hole Horizons . . . . .	117
5.3	3D Vortex and Tendex Lines . . . . .	118
5.4	Vortex and Tendex Evolutions in Binary Black Holes (BBHs) . . . . .	120
5.5	Conclusions . . . . .	123
<b>6</b>	<b>Classifying the Isolated Zeros of Asymptotic Gravitational Radiation by Tendex and Vortex Lines</b>	<b>125</b>
6.1	Introduction . . . . .	125
6.2	Gravitational Waves Near Null Infinity . . . . .	128
6.3	The Topology of Tendex Patterns Near Null Infinity . . . . .	129
6.4	Examples from Linearized Gravity . . . . .	133
6.4.1	Rotating Mass Quadrupole . . . . .	134
6.4.2	Rotating Mass and Current Quadrupoles in Phase . . . . .	135
6.4.3	Higher Multipoles of Rotating Point Masses . . . . .	138
6.5	Conclusions . . . . .	140

## 7 Visualizing Spacetime Curvature via Frame-Drag Vortexes and Tidal Tendexes

<b>I. General Theory and Weak-Gravity Applications</b>	<b>145</b>
7.1 Motivation and Overview . . . . .	146
7.2 The Tidal Field $\mathcal{E}_{ij}$ and Frame-Drag Field $\mathcal{B}_{ij}$ . . . . .	150
7.2.1 3+1 Split of Weyl Curvature Tensor into $\mathcal{E}_{ij}$ and $\mathcal{B}_{ij}$ . . . . .	150
7.2.2 Evolution of $\mathcal{E}_{ij}$ and $\mathcal{B}_{ij}$ . . . . .	151
7.2.2.1 General Foliation and Coordinate System in the Language of Numerical Relativity . . . . .	151
7.2.2.2 Local-Lorentz Frame of a Freely Falling Observer . . . . .	153
7.2.2.3 Weak-Gravity, Nearly Minkowski Spacetimes . . . . .	154
7.3 Physical Interpretations of $\mathcal{E}_{ij}$ and $\mathcal{B}_{ij}$ . . . . .	155
7.3.1 Physical Setup . . . . .	156
7.3.2 Interpretation of $\mathcal{E}_{ij}$ as the Tidal Field . . . . .	156
7.3.3 Interpretation of $\mathcal{B}_{ij}$ as the Frame-Drag Field . . . . .	157
7.4 Our New Tools: Tendex and Vortex Lines; Their Tendicities and Vorticities; Tendexes and Vortexes . . . . .	159
7.4.1 Tendex Lines and Their Tendicities; Vortex Lines and Their Vorticities . . . . .	159
7.4.2 Vortexes and Tendexes . . . . .	161
7.5 Weak-gravity, Stationary Systems . . . . .	162
7.5.1 One Stationary, Weakly Gravitating, Spinning Body . . . . .	162
7.5.2 Two Stationary, Weakly Gravitating, Spinning Point Particles with Opposite Spins . . . . .	165
7.5.3 The Two Spinning Particles Viewed from Afar: Stationary, Quadrupolar Frame-Drag Field . . . . .	167
7.5.4 Static, Quadrupolar Tidal Field and its Tendex Lines and Tendexes . . . . .	168
7.6 Gravitational Waves and their Generation . . . . .	169
7.6.1 Plane Gravitational Wave . . . . .	169
7.6.2 Gravitational Waves from a Head-On Collision of Two Black Holes . . . . .	172
7.6.3 Wave Generation by a Time-Varying Current Quadrupole . . . . .	173
7.6.4 Rotating Current Quadrupole . . . . .	174
7.6.4.1 Vortex and Tendex Lines in the Plane of Reflection Symmetry . . . . .	176
7.6.4.2 Vortex Lines Outside the Plane of Reflection Symmetry: Transition from Near Zone to Wave Zone . . . . .	177
7.6.4.3 Vortex Lines in the Far Wave Zone . . . . .	179
7.6.5 Oscillating Current Quadrupole . . . . .	180
7.6.6 Wave Generation by a Time-Varying Mass Quadrupole . . . . .	183

7.6.7	Slow-Motion Binary System Made of Identical, Nonspinning Point Particles . . . . .	184
7.7	Conclusions . . . . .	187
7.A	The Newman-Penrose Formalism . . . . .	189
<b>8</b>	<b>Visualizing Spacetime Curvature via Frame-Drag Vortexes and Tidal Tendexes</b>	
	<b>II. Stationary Black Holes</b>	<b>194</b>
8.1	Motivation and Overview . . . . .	195
8.2	Tendex and Vortex Lines . . . . .	197
8.3	Black-Hole Horizons; The Horizon Tendicity $\mathcal{E}_{NN}$ and Vorticity $\mathcal{B}_{NN}$ . . . . .	199
8.4	Schwarzschild Black Hole . . . . .	202
8.5	Slowly Rotating Black Hole . . . . .	203
	8.5.1 Slicing and Coordinates . . . . .	203
	8.5.2 Frame-drag Field and Deformed Tendex Lines . . . . .	205
	8.5.3 Robustness of Frame-Drag Field and Tendex-Line Spiral . . . . .	206
8.6	Rapidly Rotating (Kerr) Black Hole . . . . .	207
	8.6.1 Kerr Metric in Boyer-Lindquist Coordinates . . . . .	207
	8.6.2 Horizon-Penetrating Slices . . . . .	207
	8.6.3 Horizon-Penetrating Coordinate Systems . . . . .	209
	8.6.4 Computation of Tendex and Vortex Lines, and their Tendicities and Vorticities	211
	8.6.5 Kerr-Schild Slicing: Tendex and Vortex Lines in Several Spatial Coordinate Systems . . . . .	211
	8.6.6 Slicing-Dependence of Tendex and Vortex Lines . . . . .	214
8.7	Conclusion . . . . .	216
8.A	Kerr Black Hole in Boyer-Lindquist Slicing and Coordinates . . . . .	218
8.B	Kerr Black Hole in Kerr-Schild Slicing and Ingoing-Kerr Coordinates . . . . .	221
8.C	Spiraling Axial Vortex and Tendex Lines for Kerr Black Holes in Horizon-Penetrating Slices . . . . .	222
<b>9</b>	<b>Visualizing Spacetime Curvature via Frame-Drag Vortexes and Tidal Tendexes</b>	
	<b>III. Quasinormal Pulsations of Schwarzschild and Kerr Black Holes</b>	<b>228</b>
9.1	Motivations, Foundations and Overview . . . . .	229
	9.1.1 Motivations . . . . .	229
	9.1.2 Our New Tools, In Brief . . . . .	230
	9.1.3 Overview of This Paper's Results . . . . .	232
	9.1.3.1 Slicing, Coordinates and Gauges . . . . .	232
	9.1.3.2 Classification of Quasinormal Modes . . . . .	233
	9.1.3.3 The Duality of Magnetic-Parity and Electric-Parity Modes . . . . .	233

9.1.3.4	Digression: Electromagnetic Perturbations of a Schwarzschild Black Hole . . . . .	234
9.1.3.5	The Physical Character of Magnetic-Parity and Electric-Parity Modes	237
9.1.3.6	The (2, 2) Magnetic-Parity Mode of a Schwarzschild Hole . . . . .	238
9.1.3.7	The (2, 1) Magnetic-Parity Mode of a Schwarzschild Hole . . . . .	243
9.1.3.8	The (2, 0) Magnetic-Parity Mode of a Schwarzschild Hole . . . . .	245
9.1.3.9	The Superposed (2, 2) and (2, -2) Magnetic-Parity Mode of a Schwarzschild Hole . . . . .	248
9.1.4	This Paper's Organization . . . . .	249
9.2	Slicings, Gauges and Computational Methods . . . . .	250
9.2.1	Slicing, Spatial Coordinates, and Gauge . . . . .	250
9.2.2	Sketch of Computational Methods . . . . .	252
9.2.3	Gauge Changes: Their Influence on Tidal and Frame-Drag Fields and Field Lines . . . . .	254
9.2.3.1	Influence of a Perturbative Slicing Change . . . . .	255
9.2.3.2	Example: Perturbative Slicing Change for Schwarzschild Black Hole	255
9.2.3.3	Influence of a Perturbative Change of Spatial Coordinates . . . . .	256
9.2.3.4	Example: Perturbative Spatial Coordinate Change for a Schwarzschild Black Hole . . . . .	256
9.3	(2, 2) Quasinormal Modes of Schwarzschild and Kerr Black Holes . . . . .	258
9.3.1	Horizon Vorticity and Tendicity . . . . .	259
9.3.2	Equatorial-Plane Vortex and Tendex Lines, and Vortexes and Tendexes . . .	260
9.3.2.1	Magnetic-Parity Perturbations of Schwarzschild Black Holes . . . . .	260
9.3.2.2	Gauge Dependence of Electric-Parity Tendexes for a Schwarzschild Black Hole . . . . .	262
9.3.2.3	Duality and Influence of Spin in the Equatorial Plane . . . . .	264
9.3.2.4	Vortexes of Electric-Parity Mode, and Perturbative Tendexes of Magnetic-Parity Mode for a Schwarzschild Black Hole . . . . .	265
9.3.3	Three-Dimensional Vortexes and Tendexes . . . . .	266
9.3.3.1	Physical Description of Gravitational-Wave Generation . . . . .	266
9.3.3.2	Approximate Duality . . . . .	269
9.3.4	Comparing Vortex Lines of a Perturbed Kerr Black Hole and a Binary-Black-Hole-Merger Remnant . . . . .	269
9.4	Superposed (2, 2) and (2, -2) Quasinormal Modes of Schwarzschild . . . . .	270
9.4.1	Magnetic-Parity Superposed Modes . . . . .	270

9.4.2	Electric-Parity Superposed Mode . . . . .	272
9.4.3	Dynamics of the Magnetic-Parity Superposed Mode . . . . .	273
9.5	(2, 1) and (2, 0) Quasinormal Modes of Schwarzschild . . . . .	278
9.5.1	Vortexes of (2, 1) Magnetic-Parity Mode and Perturbative Tendexes of (2, 1) Electric-Parity Mode . . . . .	278
9.5.2	Vortexes of (2, 1) Electric-Parity Mode and Perturbative Tendexes of (2, 1) Magnetic-Parity Mode . . . . .	279
9.5.3	Vortexes of (2, 0) Magnetic-Parity Mode and Perturbative Tendexes of (2, 0) Electric-Parity Mode . . . . .	281
9.5.4	Vortex Lines of (2, 0) Electric-Parity Mode and Perturbative Tendex Lines of (2, 0) Magnetic-Parity Mode . . . . .	284
9.6	Conclusions . . . . .	286
9.A	Quasinormal Modes of a Schwarzschild Black Hole in Regge-Wheeler Gauge . . . . .	288
9.A.1	Regge-Wheeler-Zerilli Formalism . . . . .	288
9.A.2	Magnetic-Parity (2, $m$ ) Mode: Frame-Drag Field . . . . .	290
9.A.3	Electric-Parity (2, $m$ ) Modes: Frame-Drag Field . . . . .	291
9.A.4	Electric-Parity (2, 2) Mode: Tidal Field . . . . .	293
9.A.5	Perturbed Horizon and Horizon Tendicity for Electric-Parity Modes . . . . .	294
9.A.6	Magnetic-Parity, Superposed (2, 2) and (2, -2) Modes: Tidal Field . . . . .	297
9.B	Teukolsky's Equation and Black-Hole Perturbations in the Newman-Penrose Formalism	297
9.C	The Chrzanowski-Cohen-Kegeles Procedure and the Ingoing-Radiation-Gauge Metric	299
9.C.1	The CCK Procedure . . . . .	300
9.C.2	Definite-Parity Harmonics and Chrzanowski's Calculation . . . . .	303
9.C.3	Definite-Parity CCK Metric Perturbations and Tidal and Frame-Drag Fields for Schwarzschild Black Holes . . . . .	305
9.C.3.1	Electric-Parity Metric Perturbations . . . . .	305
9.C.3.2	Magnetic-Parity Metric Perturbations . . . . .	307
9.C.3.3	Tidal and Frame-Drag Fields of the (2, 2) Mode . . . . .	308
9.C.4	Analytical and Numerical Methods for Computing Metric Perturbations and Tidal and Frame-Drag Fields in IR Gauge . . . . .	310
9.D	Relationship Between Regge-Wheeler-Zerilli and Ingoing-Radiation Gauges . . . . .	311
9.D.1	Magnetic-Parity Gauge Transformation . . . . .	311
9.D.2	Electric-Parity Gauge Transformation . . . . .	313
9.E	Horizon Tendicity and Vorticity Calculated from the Weyl Scalar $\Psi_0$ . . . . .	314
9.E.1	Constructing a Hypersurface-Orthogonal Tetrad on the Horizon . . . . .	315
9.E.2	Computing the Horizon Tendicity and Vorticity from $\Psi_0$ . . . . .	316

9.E.3	Relationship Between $\Psi_2$ and the Complex Curvature . . . . .	318
9.F	Vortex and Tendex Lines of (2, 2) Perturbations of Schwarzschild and Kerr Black Holes with the Background Frame-Drag and Tidal Fields	319

# Chapter 1

## Overview and Summary

### 1.1 Introduction

This thesis details research I have completed during my time as a graduate student at Caltech. My focus has been on the analytic treatment of problems in General Relativity. My research roughly divides into two broad topics, and so I have split this thesis into two parts. The first part, Part I, deals exclusively with investigations of perturbed black holes. Part II details a new program for the visualization of curved spacetime; the intended application for this program is to interface with numerical relativity and provide a means for drawing physical insights from the dynamics of simulated spacetimes. In the papers I include in the second part of this thesis, the visualization technique is introduced, developed, and applied to various simple, analytically tractable situations in relativity. The most interesting and intricate application is to the study of perturbed black holes, and in this sense the study of perturbed black holes forms a unifying theme for my work. As such, in this summary chapter, I will first introduce the theory of linearized perturbations of the exact spacetimes which represent black holes. This is done in Section 1.2. Afterward, I will briefly summarize the work presented in this thesis, discussing each of the two parts in turn. Section 1.3 deals with studies of the spectra of perturbed black holes given in Part I, Chapters 2, 3, and 4. Section 1.4 discusses the research I have participated in which develops and applies the new visualization methods, which make up Part II, Chapters 5, 6, 7, 8, and 9. Finally, in Section 1.5, I conclude this introductory chapter with some remarks on future work which may grow out of the topics detailed here.

It is important to keep in mind that the overarching motivation for the topics of study presented in this thesis, and indeed the motivation for nearly all contemporary work in the classical theory of General Relativity, is the quest for the direct detection of gravitational waves by experiments such as LIGO [1]. These gravitational wave detectors are essentially Michelson interferometers, built with such an extreme sensitivity that they hope to measure the tiny strains which gravitational waves arriving at Earth will produce in the detector. The strongest sources for such waves, at least in the frequency band ground-based detectors are sensitive to, are binary systems of compact objects

in close orbit, and the merger of these systems. Accurate theoretical predictions of the emitted radiation is needed for data analysis in these experiments, both to serve as noise filters and to allow for interpretation of the signals. This demand for accurate theory has driven the science of relativity and compact binary mergers, and the development of analytic approximations to treat them. The need for information beyond what is available from approximations in turn has pushed the field of numerical relativity to simulate the gravitational wave signal from the merger of compact binaries. It is almost assured that direct detection of gravitational waves will occur within the next decade, an event which will fundamentally change the science of astronomy, providing a unique view into the most violent processes in the Universe. It is possible that advanced ground- and space-based gravitational wave detectors will eventually open a new window into cosmology, allowing us to probe the earliest moments of cosmic history. The promise that gravitational wave astronomy will allow us to test our physical models inspires all of the work I will present here.

## 1.2 Black Hole Perturbation Theory

A good question to ask at the outset is why we study perturbations of black holes. The first part of the answer lies in the importance of the background objects themselves, the exact solutions to the Einstein field equations which we know as black holes. Black holes, once thought of merely as mathematical artifacts, now play a central role in our understanding of the Universe. We observe them in binary systems, accreting gas from companion stars into hot disks which shine brightly in the X-ray sky. We predict their production in the violent deaths of massive stars. Most spectacularly, we have come to realize that truly enormous black holes lie at the centers of most galaxies, with masses millions to billions of times greater than our Sun. These supermassive black holes also accrete material, and the light of these active galactic nuclei is visible to us from the far reaches of space and time, giving us a probe into the history of our Universe.

Of course, no realistic physical system involving a black hole is described by the pristine, exact solutions of the Einstein field equations. Such solutions represent isolated, unchanging bodies far removed from other influences. Instead, the astrophysical black holes of our Universe are the sites of the most energetic events known to occur. As such we must consider perturbations to the exact solutions, whether it be by matter orbiting or accreting onto the hole, or the gravitational influence of distant objects. This leads us to the second part of the answer to our question, which is the large array of problems that can be treated using black hole perturbation theory (BHPT). Whenever the influence of external processes near black holes are small compared to the curvature produced by the black hole, we can linearize the Einstein field equations around the exact black hole solution; these linearized equations are the heart of BHPT.

Black hole perturbation theory governs the generation and propagation of all kinds of waves in

a black hole spacetime, whether they be electromagnetic, gravitational, or scalar in nature. If we are interested in the light that is emitted by a charge falling into a black hole, we must use black hole perturbation theory. If we wish to describe the rate at which a satellite orbiting a black hole slowly spirals inward due to the loss of orbital energy to gravitational radiation, then BHPT is the tool we must reach for. Even the description of how light is bent by the spacetime curvature of the host black hole is governed by these wave equations, since in the limit where the waves have short wavelength compared to the size of the black hole, the wave equations reduce to the equations of geometric optics in a black hole spacetime.

The pioneering paper by Regge and Wheeler [2] birthed the study of perturbations of the non-rotating Schwarzschild black hole, even before the exact solution for the rotating black hole was found by Kerr [3]. It would be another decade after Kerr's discovery before Teukolsky would give a full treatment of the perturbations of a rotating black hole [4]. The linearized Einstein equations describing waves in these spacetimes are second order partial differential equations, which can be separated into coupled ordinary differential equations. These wave equations are sourced by masses and charges associated with the matter which perturbs the hole. Alternatively, the equations can be cast in the form of an initial value problem, which allows for the evolution of arbitrary wave content in the spacetime. Finally, the linearized equations also describe fundamental excitations of the black hole spacetime. These eigenmodes of the equations represent natural, decaying oscillations of the spacetime itself, and are known as the quasinormal modes (QNMs) of the black hole. Gravitational, electromagnetic, and scalar QNMs all exist, and have been extensively studied (two standard and comprehensive reviews are [5] and [6]).

It is no surprise then that BHPT has a central role in modern research in General Relativity and in astrophysics. Perturbations of black holes and black hole-like objects also make an appearance in a variety of quantum gravity models, especially string-theory inspired models. What is surprising is that new discoveries are still being made in BHPT, after more than half a century of continuous investigation.

I have participated in a few of these discoveries during my graduate studies at Caltech. Of course, in order to break new ground in a such well-trod subject, we must look to the extremes, and so many of the topics I will present deal with regimes where additional approximations are applied to the linearized equations. These topics, where BHPT is supplemented by additional approximations, will be treated in the first part of this thesis. They include a discussion of physics near the perturbed black hole's horizon, where a new fundamental frequency of quasinormal oscillation is revealed; the specialization to the high frequency limit around spinning black holes, where connections to geometric optics are described, along with approximate QNM equations of practical value; and a treatment of rapidly rotating black holes, where a novel feature of the QNM frequency spectrum is found.

In addition to looking at the extremes, new understanding of an old problem can be found by bringing to bear new tools. The second half of this thesis details one such tool, a visualization technique for curved spacetimes, and its application to the QNM oscillations of black holes. These visualizations show that the QNM oscillations of a black hole can be thought of as being made up of near-zone, source components which generate far-zone waves that propagate away from the hole. This division is in analogy to the familiar case of electromagnetic radiation generated by time-varying sources, and hints at previously unknown spacetime dynamics, where the tidal curvature interacts with frame-dragging effects in order to produce gravitational waves. In the case of QNMs, the sources are the decaying spacetime perturbations on and near the event horizon.

Before turning to a summary of the remainder of this thesis, we will briefly review some of the essentials of BHPT.

### 1.2.1 Review of Black Hole Perturbation Theory

The fundamental equations for BHPT take a simple form when the Einstein field equations are projected onto a set of four basis vectors, two null and two complex spatial vectors, which results in the Newman-Penrose equations [7, 8]. In this case, the equations can be linearized about the black hole solutions, and Teukolsky showed that scalar, electromagnetic, and gravitational perturbations all obey the same master equation [4]. In the frequency domain this equation is separable into two second order differential equations, one which describes the angular dependence of the waveform and one which describes the radial dependence. These equations give the behavior of a spin-weighted scalar quantity which we will here call  $\psi$ , from which other physical quantities can be constructed. The scalar is expanded as

$$\psi = \frac{(r^2 - 2Mr + a^2)^{-s/2}}{\sqrt{r^2 + a^2}} \sum_{lm} \int d\omega e^{-i\omega t} e^{im\phi} {}_s u_{lm}(r) {}_s S_{lm}(\theta), \quad (1.1)$$

and indexed in terms of its spin weight  $s$ , an azimuthal quantum number  $l$ , and a magnetic quantum number  $m$ . Here  $M$  is the mass of the hole, and  $a$  is the spin parameter of the hole, which ranges from  $a = 0$  for a nonspinning black hole and  $a = M$  for a maximally spinning hole. The spin-dependent radial factors have been extracted to simplify the equation that  ${}_s u_{lm}$  obeys. The angular functions  ${}_s S_{lm}$  are the spin-weighted spheroidal harmonics [9], and they obey the Sturm-Liouville eigenequation

$$\csc \theta \frac{d}{d\theta} \left( \sin \theta \frac{d {}_s S_{lm}}{d\theta} \right) + V_\theta {}_s S_{lm} = 0, \quad (1.2)$$

$$V_\theta = a^2 \omega^2 \cos^2 \theta - m^2 \csc^2 \theta - 2a\omega s \cos \theta - 2ms \cos \theta \csc^2 \theta - s^2 \cot^2 \theta + s + {}_s A_{lm}, \quad (1.3)$$

for angular eigenvalues  ${}_s A_{lm}$ . The radial function is given by a second order radial equation

$$\frac{d^2 {}_s u_{lm}}{dr_*^2} + V_r(r, \omega, {}_s A_{lm}) {}_s u_{lm} = \mathcal{T}. \quad (1.4)$$

The potential  $V_r$  depends on spin weight of the scalar under consideration, is frequency dependent, and, in the case of a spinning black hole, is complex. We will not write it out explicitly, but it is given several times in the following chapters. The source term  $\mathcal{T}$  is determined by a combination of the stress-energy of the matter  $T_{\mu\nu}$  and the background metric, followed by an expansion in frequency space. Finally,  $r_*$  is the radial ‘‘tortoise’’ coordinate, which stretches the region near the event horizon out onto an infinite domain. It also accounts for the infinite phase shift which occurs in the asymptotic waves scattered from a Coulomb-type potential. It is defined by the expression

$$\frac{dr_*}{dr} = \frac{r^2 + a^2}{r^2 - 2Mr + a^2}, \quad (1.5)$$

and note that the horizon occurs at  $r_+$ , which is the larger of the two roots in the denominator of Eq. (1.5). In this thesis, we will deal almost exclusively with vacuum perturbations, where  $\mathcal{T} = 0$ .

The radial equation must be supplemented with appropriate physical boundary conditions. The precise behavior in the limit as  $r$  approaches the horizon or  $r \rightarrow \infty$  depends on the particular field under consideration, but the general idea is the same for all perturbations. At each of the two limits, asymptotic solutions to Eq. (1.4) can be found, and of these two solutions one will correspond to waves flowing in from the boundary and one to waves flowing out through the boundary. We require for black holes that there be no waves emerging from the horizon, and at infinity we will usually require that there be no waves coming into the spacetime. The exception to this is when we are interested in the problem of reflection and transmission through the horizon of waves impinging on the black hole from far away.

As a concrete example of the radial behavior, consider the case where the scalar quantity is the spin-weight  $s = -2$  scalar  $\Psi_4$  in a Schwarzschild spacetime; this quantity is formed by contracting certain members of the Newman-Penrose null basis with the perturbed Riemann tensor  $R_{\mu\nu\rho\sigma}$ , and it is a key element of BHPT since it describes the outgoing radiation from an isolated system. In this case we solve the radial Teukolsky equation to get  $\Psi_4$ ,

$$\psi = r^4 \Psi_4 = \frac{(r^2 - 2Mr + a^2)}{\sqrt{r^2 + a^2}} \sum_{lm} \int d\omega e^{-i\omega t} e^{im\phi} {}_{-2}u_{lm}(r) {}_{-2}S_{lm}(\theta) \quad (1.6)$$

and the asymptotic limits are given by

$${}_{-2}u_{lm} \rightarrow \begin{cases} B^{\text{trans}} (r^2 - 2Mr)^2 e^{-i\omega(t+r_*)} & r \rightarrow r_+ \\ B^{\text{out}} r^2 e^{-i\omega(t-r_*)} + B^{\text{in}} r^{-2} e^{-i\omega(t+r_*)} & r \rightarrow \infty \end{cases}. \quad (1.7)$$

We see by comparing Eq. (1.6) to the  $r \rightarrow \infty$  limit that the asymptotic behavior for outgoing radiation (at a particular frequency) is

$$\Psi_4 \sim r^{-1} e^{-i\omega(t-r_*)}, \quad (1.8)$$

just as we would expect. The generalization to spinning black holes is detailed several times in the studies included in this thesis, especially Chapters 2–4, and 9.

A final concept, central to the work discussed here, is the quasinormal mode solutions of BHPT. When there are no source terms, and no incoming waves into the spacetime, we can solve Eq. (1.4) for the eigenmodes of  ${}_{s}u_{lm}$  and the corresponding eigenvalues, the complex frequencies  $\omega$ . As mentioned above, these solutions have the physical interpretation of the natural oscillation modes of a black hole spacetime. The frequencies  $\omega$  are always found to have negative imaginary parts, which means that these eigenmodes decay in time. The QNMs have been studied in great detail in a variety of circumstances. They are excited to some degree by any perturbation of the black hole (except the special but important case of a monochromatic source) and play an important role in the gravitational wave signal from the end of a black hole binary merger. Once the two holes have merged to produce a final black hole this hole emits gravitational waves with the QNM frequency spectrum. The analysis of [10] includes a detailed example of the study of the manner in which numerically simulated merger waveforms transition into a QNM ringdown.

All of the studies in the first half of this thesis are concerned with the QNM spectrum, as is the final chapter of the second part of this thesis, Chapter 9, where the QNM oscillations of spacetime are investigated using the visualization techniques of tendex and vortex lines (Section 1.4 of this chapter).

## 1.3 The Extremes of Black Hole Perturbation Theory

The first part of this thesis is concerned with extensions to and new results concerning the QNM spectrum of perturbed Kerr black holes. These topics are covered in Chapters 2, 3, and 4, which were originally published as [11], [12], and [13], respectively. In this section, we will briefly discuss each chapter and its main results.

### 1.3.1 The Horizon Mode

The first approximation we will use to better understand BHPT is the near horizon approximation. The essential idea is that near the horizon of the black hole, the wave equations of BHPT become simple. In the near horizon region we can perform an expansion in distance from the horizon, using a parameter  $\epsilon_{NH} = (r - r_+)/r_+ \ll 1$ . We find that, in a frame which co-rotates with the black

hole, the oscillatory dependence of the waves on  $(t, r)$  is  $\psi \sim e^{-ik(t \pm r_*)}$ . In addition, particle orbits become universal in Boyer-Linquist coordinates in the near horizon region. All particles slow their radial infall as they approach the black hole and begin to co-rotate with the horizon, asymptotically freezing into place on the horizon. Mino and Brink [14] used this behavior and the near horizon expansion in order to compute the radiation produced by a point particle as it falls onto the horizon. Their results pointed to a universal frequency for radiation emitted during this final stage of a plunge. The frequency is equal to the angular frequency of the horizon  $\Omega_H$ , and decays exponentially in time due to redshifting at some rate proportional to the surface gravity of the black hole. Since every particle plunge emits at the same frequency, with an exponential decay just like a QNM, this hints at an interpretation of this final emission as a component of the natural frequency spectrum of the black hole. This “horizon mode” is not formally a QNM, but it behaves identically to one and should be considered as part of the ringdown spectrum following any event that perturbs the black hole.

In [11], Yanbei Chen and I showed that this interpretation of the horizon mode held by considering situations in which the black hole perturbations are sourced in an initial data setup, rather than by a point particle plunge. There is a subtlety in the near horizon region when prescribing this data, since the initial perturbations must have a radial dependence which ensures that infalling observers do not see diverging quantities. Taking this detail into account, we can show that a family of horizon mode frequencies exists for generic initial data with the form

$$\omega_H = m\Omega_H - 2in g_H, \quad n \geq 1, \quad (1.9)$$

where  $g_H$  is the surface gravity,  $m$  is the magnetic quantum number of the perturbation, and  $n$  is an integer which controls the decay rate. The smallest value  $n$  can take is 1, and which particular value of  $n$  is excited by the near horizon data depends on how the data decays as it approaches the horizon. From these considerations, we were also able to identify that the value for  $n$  quoted by Mino and Brink for the sourced radiation is actually smaller than is allowed by the considerations discussed above (in fact they have  $n = 1/2$ ). In our study we were able to show that their original work contained a critical error, and that a correction of this error should result in our lowest value of  $n = 1$ .

Whether the horizon mode is more than a mathematical curiosity in the case of a generic ringdown is an important question. It is possible that, like the vast array of high order frequency modes, this mode has no important role in the radiation from a strongly deformed black hole. In order to investigate this question further, in our study we searched for the presence of the horizon mode in a pragmatic fashion: we tested whether the use of this mode offered an improvement in the analysis of the gravitational waves emitted during the ringdown phase of a numerical simulation of a binary black hole merger. We found no evidence of the horizon mode in this waveform, in the sense that its

use gave no improvement over the use of the standard QNM frequencies. The waveform analyzed was from an equal-mass merger, but we expect based on our analysis that the horizon mode will be most important for events with large mass ratios, since these events can generate strong perturbations concentrated near the final black hole horizon. Our work opens up the possibility for many future studies, in particular a complete analysis of the radiation from the plunging particle (correcting and extending the work of [14]) and a search for the horizon mode in waveforms from higher mass ratio mergers.

### 1.3.2 The High Frequency Approximation and WKB Methods

The high frequency regime offers another avenue for new discoveries in BHPT. In this case, the Teukolsky equation is expanded in the limit where the frequency is large,  $M\Re[\omega] \gg 1$ , in order to arrive at simple expressions for the solutions to the QNM eigenvalue problem. This is equivalent to the requirement that the azimuthal quantum number  $l$  is large,  $l \gg 1$ . It is known that at leading order in this eikonal expansion, the waves propagate along null geodesics of the spacetime [15]. Higher order corrections determine the dispersion of the waves. For the case of QNMs, this geometric-optics correspondence demands that the waves be partially bound to the black hole, so that the signal can oscillate. For nonrotating black holes, these QNMs correspond to the unstable bound orbit of the black hole (the “light ring” of the hole) [16–19], their frequency corresponds to the orbital frequency on the light ring, and their decay rate to the rate at which a perturbed bundle of geodesics will diverge away from the unstable orbit (the Lyapunov exponent of the orbit).

One important technique for finding these modes is the WKB method familiar from nonrelativistic quantum mechanics. The WKB technique was first suggested by Schutz and Will [20], and extended to higher orders and applied to various black hole spacetimes by many authors (see [6]). However, the WKB method cannot be easily used in the case of Kerr black holes with generic spins, since in this case the angular eigenvalue problem is coupled to the radial eigenvalue problem. Dolan gave a partial solution, using a WKB method to find results for the cases where the unstable orbits are equatorial (with equal angular and azimuthal quantum numbers,  $l = m$ ) and polar ( $m = 0$ ) [21]; in these cases the angular problem can be solved or simplified, and these special cases cannot be used to understand the case of a generic mode.

In Reference [12], collaborators and I detailed a joint-WKB solution to both the radial and angular problems, which is presented in Chapter 3. This study completes the study of high frequency QNMs in Kerr; in it we provide simple analytic methods for finding the QNM frequencies and wave functions, and we also discuss the geometric correspondence of these modes with unstable null orbits in Kerr. Previous work in slow Kerr showed that the frequency of these modes could be separated into orbital and precession frequency contributions, and we gave a natural extension of this result to the case of generic spins. Perhaps of greatest interest, we examined the accuracy of our WKB

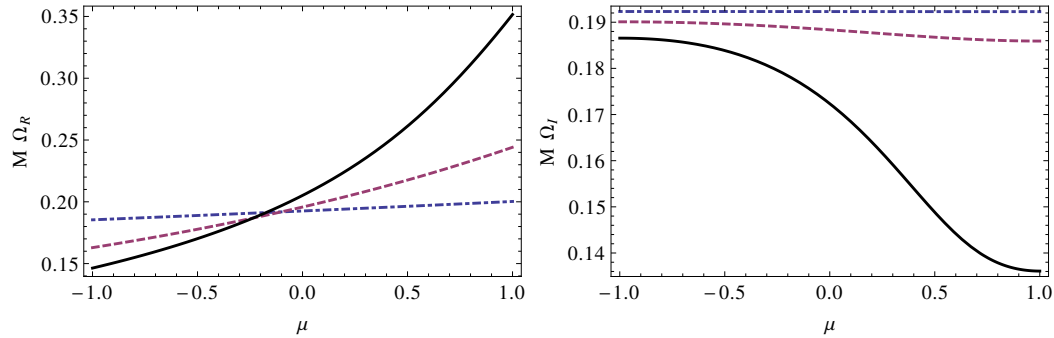


Figure 1.1: QNM frequency values in the high frequency limit, computed using WKB methods. The real part is normalized by plotting  $\Omega_R = \omega_R/(l+1/2)$  (left panel), and the imaginary part by plotting  $\Omega_I = \omega_I/(n+1/2)$  (right panel). The frequencies are plotted as a function of  $\mu = m/(l+1/2)$ . The curves indicate  $a = 0.1M$  (Blue, dot-dashed),  $a = 0.5M$  (Purple, dashed), and  $a = 0.9M$  (Black, solid).

approximations and found that they were quite accurate even for the low-frequency QNMs which are excited to the highest amplitudes during the merger of two black holes [22], or when a particle falls into a black hole [23]. This means that these approximations may be helpful in a variety of analytical and astrophysical situations in the future.

The WKB mode frequencies are plotted as a function of  $\mu = m/(l+1/2)$  are plotted in Figure 1.1 for a variety of spin values. The real part of the frequency is plotted using  $\Omega_R = \Re\{\omega\}/(l+1/2)$ , and the imaginary part using  $\Omega_I = -\Im\{\omega\}/(n+1/2)$ , where  $n$  is the overtone number; we see that in the eikonal case, the decay rate of the QNM is one order lower in  $l$  than the real part of the frequency.

My contributions to this work included reproducing and correcting computations throughout the paper and in helping to build the interpretation of the splitting of the eikonal frequencies into precession and orbital frequencies. I also aided in the writing and editing throughout the paper, especially in the introductory and concluding sections, and the geometric optics section.

### 1.3.3 The Nearly Extreme Kerr Black Hole and the Bifurcation of the QNM Spectrum

Growing out of our work on the WKB method in BHPT, I present a final approximation method used to make recent discoveries. This is the near extremal approximation, in which the Kerr black hole is assumed to be rotating almost as fast as is physically allowable. At the limit of extreme rotation, the Kerr spacetime simplifies, and analytic solutions to the radial Teukolsky equation can be found. By expanding in a small parameter  $\epsilon = 1 - a/M \ll 1$ , where  $a = M$  is the extreme spin, we can find analytic solutions for the radial equation when the spacetime is only nearly extremal. This line of investigation has been pursued in the past by many authors [24–30], but in the past

incorrect assumptions were made regarding how the frequencies would behave in the nearly extremal limit. The correct analytic formula for the QNM frequencies in this limit was found only recently by Hod [30], but even then the domain in which these expressions are applicable was not clear.

Using the WKB results discussed above, we discovered that there were two distinct regimes of mode behavior in the nearly extremal case [13]. For modes which are nearly equatorial, there is only one family of QNMs, all of which are localized near the horizon and have decay rates that limit to zero as the spin of the black hole becomes extremal. We call these the zero-damping modes, because of their limiting behavior. Meanwhile, for modes which are nearly polar, the spectrum divides into two sets of modes. The majority of the modes are also zero-damping modes localized near the horizon, but a few modes exist which are localized away from the horizon and which always have nonzero decay. We call these latter modes the damped modes. This splitting of the modes into sets localized in two regions is analogous to the wavefunctions in a double-well potential in quantum mechanics. Meanwhile, for holes which are not rapidly spinning, no such splitting has been observed. Instead, QNMs with fixed angular quantum numbers can be arranged in a tower of increasing decay rate, indexed with a single overtone number  $n$ . Our results indicate that at some high spin below the extreme case,  $a = M$ , the spectrum undergoes a transition, where the tower of overtones actually divides into two families and which can no longer be said to be indexed with a single number.

This transition in the spectrum is illustrated in Figure 1.2, which is taken from [13]. Depicted is the QNM frequencies in the complex frequency plane, with the convention  $\omega = \omega_R - i\omega_I$ . At a spin  $a = 0.999M$ , the spectrum is made up of a series of overtones with strictly increasing  $\omega_I$ , but at spin  $a = 0.9999$  the spectrum has distinctly divided into two branches. At the moment, it is not clear if this transition has astrophysical relevance. However, observational evidence hints that real black holes may in fact have large spins [31], and so these intricate features of the spectrum may have observable consequences.

My contributions to this paper included checking the results throughout, performing a numerical investigation of the bifurcation of the spectrum, and generating a numerical fit for the critical spin parameter above which the zero-damping modes become more important than the damping modes. I also contributed to the writing and editing.

## 1.4 The Visualization of Curved Spacetime

Perhaps the most important advance in GR in the past several decades the development of numerical relativity. Initially plagued by instabilities, in the past ten years the fully nonlinear evolution of the Einstein field equations on computers has become routine. These simulations primarily focus on the merger of compact binaries. Astrophysically relevant binary black hole simulations feature two black holes which orbit on quasi-circular paths, and which gradually spiral inward due to the loss

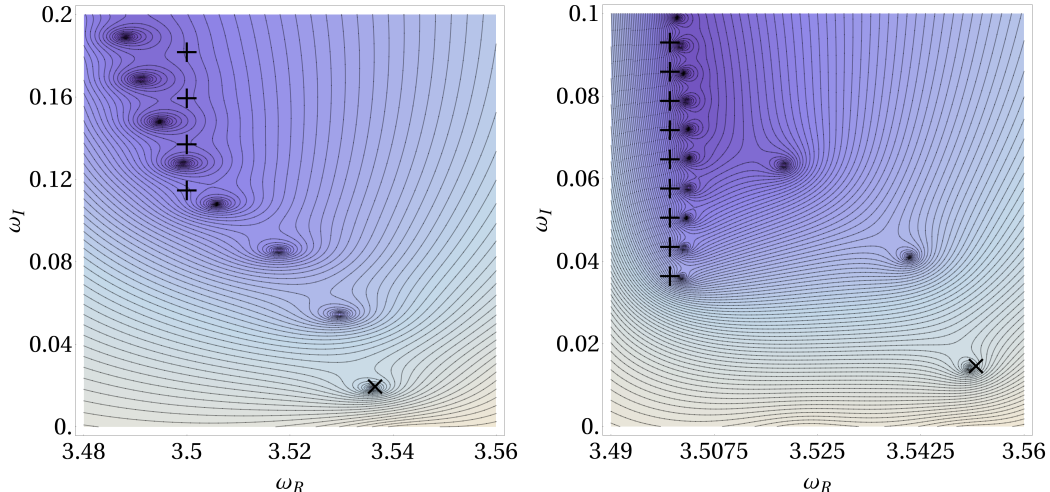


Figure 1.2: Splitting of the spectrum into two branches for the mode  $l = 10$ ,  $m = 7$ , as the spin  $a$  increases from  $a = 0.999M$  (left panel) to  $a = 0.9999M$  (right panel), so that  $\epsilon = 1 - a$  decreases from  $\epsilon = 10^{-3}$  to  $\epsilon = 10^{-4}$ . The plot gives contours of constant value of a complex series expansion whose roots are the QNM frequencies; darker values indicate values closer to zero, and they cluster around the QNM frequencies. The  $+$  markers indicate analytic predictions of the zero damped modes, and the  $\times$  marker indicates the WKB prediction for the least damped mode. In the left panel the modes form a single family of increasing decay rate, and the right panel shows how this family splits into two at a larger spin. There are three damped modes in this case.

of orbital energy and angular momentum to gravitational radiation. Eventually these holes reach the binary analogue of a last stable circular orbit, exit the adiabatic inspiral regime, and rapidly plunge towards each other. The two holes merge into a common, deformed black hole, which then rings down in accordance with Price's theorem [32–34], which states that the hole must shed all of its multipole moments and settle into a final Kerr state.

As mentioned in Section 1.1, the practical importance of carrying out these simulations in the fully nonlinear regime lies in the science of gravitational wave detection. The strongest gravitational wave signals emerge from systems where compact masses experience rapid accelerations, and this is exactly what occurs in a binary merger. While the understanding of gravitational wave signals and the eventual generation of signal templates served as a driving motivation for the development of numerical relativity, we have not fully explored the insights available to us now that we can study dynamic gravitational systems.

Even in the cases of the black hole binary mergers so far simulated, a full understanding of the gravitational dynamics has not been established. The data extracted from these simulations always includes the asymptotic gravitational wave signal, but often the only other information extracted about the bulk spacetime are the trajectories of the black holes (especially with regards to the measurement of the final black hole kick), and sometimes the evolution of the apparent and even horizons. These simulations generally do not record the evolution of the curvature in the bulk of

the spacetime, which is not surprising considering the fact that the curvature is described by a rank four tensor. It is not at all clear what quantities to record the values of during the evolution, and what any such quantities might mean. There is a need for physically meaningful quantities which can be computed and used by relativists to understand simulated spacetimes.

To this end, the second part of this thesis details studies which develop and apply novel techniques for the visualization of curved spacetimes. The essence of the method is to recast the Riemann curvature tensor into a form that can then be described entirely in terms of vector fields with associated scalar field strengths; these quantities can be visualized at a given instant of time by plotting the integral curves of the vector fields in the usual way. The letter in which we introduced this method [35] is reproduced in Chapter 5. These techniques are intended for use in numerical simulations, but the remaining papers included in this thesis deal almost exclusively with analytic explorations. In order to develop and understand these visualization techniques before applying them to simulations, I and collaborators at Caltech and Cornell applied these methods to familiar situations. These included asymptotic radiation, discussed in Chapter 6, weak gravity situations, which are discussed in Chapter 7, and also in black hole spacetimes. This last topic is split into two parts. First, in Chapter 8 we investigate exact black hole solutions, and then in Chapter 9 we apply our visualization techniques to perturbed black holes.

### 1.4.1 Tendex and Vortex Lines

We express the curvature of spacetime in terms of what we call tendex and vortex lines. The tendex lines describe tidal effects, giving at each point the preferred directions and strengths of tidal forces. The vortex line describe frame-dragging, in terms of differential gyroscopic precession at each point in spacetime. The manner in which we compute and draw these lines is a multiple part process, and is well suited for application to numerical simulations of spacetime. Let us briefly review the elements of this process, so as to make this summary relatively self-contained. The first step is to choose a way in which to divide four dimensional spacetime into three dimensional, spatial slices. These slices are moments of simultaneity according to some family of observers, and the only constraint on these observers is that they move with timelike four velocities  $u^\mu$  which are normal to a set of spatial surfaces. Their four velocities are then used to project the curvature information of spacetime onto the spatial slices, by defining first the spatial metric  $h_{\mu\nu}$  by

$$h_{\mu\nu} = g_{\mu\nu} + u_\mu u_\nu. \quad (1.10)$$

The spatial metric with one index raised,  $h_\mu{}^\nu$ , acts as projection operator onto the spatial slices. With a combination of the spatial metric and the observers' four velocities, we can project the Riemann curvature tensor onto the spatial slices. This naturally breaks the curvature tensor into

two parts, a tidal tensor  $\mathcal{E}_{ij}$  and a frame-drag tensor  $\mathcal{B}_{ij}$ . They are defined by the relations

$$\mathcal{E}_{\mu\nu} = h_\mu^\alpha h_\nu^\beta R_{\alpha\rho\beta\sigma} u^\rho u^\sigma, \quad \mathcal{B}_{\mu\nu} = \frac{1}{2} h_\mu^\alpha h_\nu^\beta \epsilon_{\mu\alpha\nu\rho} R^{\nu\rho}{}_{\beta\sigma} u^\sigma. \quad (1.11)$$

Since all free indexes have been contracted with  $h_\mu^\alpha$ , we can transition to using spatial indexes  $j, k, \dots$  for  $h$  and for any quantity completely projected onto spatial slices. In spatial coordinates, the tidal and frame drag fields are

$$\mathcal{E}_{\mu\nu} \rightarrow \mathcal{E}_{jk} = R_{j\hat{0}k\hat{0}}, \quad \mathcal{B}_{\mu\nu} \rightarrow \mathcal{B}_{jk} = \frac{1}{2} \epsilon_{jmp} R^{mp}{}_{k\hat{0}}, \quad (1.12)$$

where we have denoted with a  $\hat{0}$  indexes that are contracted with the four velocity  $u^\mu$  and where we have defined the spatial Levi-Civita tensor  $\epsilon_{ijk} = \epsilon_{\hat{0}ijk}$ . These two tensors are symmetric and traceless, and so they carry all of the curvature information of vacuum spacetimes in their ten independent components. The fact that they are tensors on spatial slices is essential for interfacing with numerical simulations, where three dimensional curvature quantities are evolved from slice to slice.

The next step is to compute the eigenvectors and eigenvalues of  $\mathcal{E}_{jk}$  and  $\mathcal{B}_{jk}$ . In order to find the eigenvectors and eigenvalues we must solve the generalized eigenvalue problem,

$$\mathcal{E}_j{}^k V_k = \lambda V_j. \quad (1.13)$$

Frequently, we find it useful to choose an orthonormal basis, a set of four vectors  $u^\mu$  and  $e_a^\mu$ , and to project  $\mathcal{E}_{jk}$  into this basis,  $\mathcal{E}_{\hat{a}\hat{b}} = \mathcal{E}_{\mu\nu} e_a^\mu e_b^\nu$ , and then solve the usual eigenvalue problem

$$\mathcal{E}_{\hat{a}\hat{b}} V_{\hat{b}} = \lambda V_{\hat{a}} \quad (1.14)$$

in this basis. The result of this procedure is a set of three eigenvector fields for the tidal field, and three more for the frame drag field. These eigenvector fields do not have a direction associated with them, in contrast to typical vector fields. Associated with each vector field is its eigenvalue. Locally, the three eigenvectors associated with each of the tidal and frame-drag fields are orthogonal, and the three eigenvalues of each field must sum to zero at a point, since  $\mathcal{E}_{jk}$  and  $\mathcal{B}_{jk}$  are traceless.

The final step in the visualization procedure is to integrate the eigenvector fields to produce field lines. These are what we call the tendex and vortex lines. We call the eigenvalues associated with the three families of tendex lines those lines tendicities, and similarly the eigenvalues of the frame-drag field the vorticities of the vortex lines. The field lines are in many ways analogous to electric and magnetic field lines, but they do not have some of the essential features which make the study of electromagnetism so intuitive. An example is that the tendex and vortex lines have

nonvanishing divergence in vacuum. As such, it is not useful to illustrate tendicity and vorticity by the density of field lines at a given point.

The tendex lines provide the preferred axes for tidal distortions at a point, and their tendicities the amounts of tidal stretch or strain, in the following way. If we consider two points separated by an infinitesimal spatial vector  $\xi^j$ , then they experience a differential acceleration  $\Delta a^j$  according to the equation

$$\Delta a^j = -\mathcal{E}^j_k \xi^k. \quad (1.15)$$

Similarly, two gyroscopes separated by  $\xi^j$  will experience differential precession. Each will measure the other to precess about its own preferred direction with a precession velocity  $\Delta \Omega^j$  given by

$$\Delta \Omega^j = \mathcal{B}^j_k \xi^k. \quad (1.16)$$

What we have in the end is a complicated set of field lines, with properties both familiar and alien, but which completely embody the spacetime curvature as measured by the family of observers who move with velocity  $u^\mu$ . We must see if their use can yield physical intuition into what can otherwise be opaque numerical results. In the papers which I participated in and which I reproduce in this thesis, I and my collaborators have begun to answer these questions, and we have begun to formulate a new understanding of the generation of gravitational radiation in curved spacetimes. Along the way, we detail and partially address a variety of challenges, perhaps the most difficult of which is the question of how to deal with the gauge ambiguities inherent in the use of tendex and vortex lines. As we will see, in fact the gauge dependence of these lines is mild in practice. Specifically, slicings used in simulations pass smoothly through event horizons without coordinate singularities. Such slicings are horizon penetrating, and black holes cannot be simulated unless the time slicing is horizon penetrating. The studies I present in this thesis indicate that, in the case of horizon penetrating slicings, the physical understanding available from the use of tendex and vortex lines is robust.

In Chapter 5, I reproduce the study in which collaborators and I introduced the idea of tendex and vortex lines, and applied them to visualize two numerical spacetimes [35]. The most interesting application of the lines was to gain a better understanding of the superkick merger of two spinning black holes. This is a merger where the spins of the black holes lie in the orbital plane, and features strongly beamed radiation and a corresponding black hole recoil, which varies sinusoidally with the initial orientations of the spins. Investigation of the tendex and vortex structures in such a simulation led to an explanation of the superkick in terms of mass- and current-multipole moments, whose relative phasing determines the strength of the kick.

My contributions to this initial study were limited in comparison to my role in later work. I

participated in discussions during the conception of the paper, helped to determine some of the underlying conventions, and helped to check the results and edit the paper.

### 1.4.2 Gravitational Radiation and the Topology of Vortex and Tendex Lines

One of the simplest situations in which we can begin to explore the use of vortex and tendex lines is the case of gravitational plane waves. Since plane waves stretch and squeeze objects orthogonal to their direction of propagation, it is not surprising that the tensor and frame-drag fields have no components in the direction of propagation. The result is that one tendex and one vortex line at each point is aligned with the propagation direction but has vanishing strength, and we can ignore these lines. The other two tendex and two vortex lines are simply related to each other; locally the two tendex lines passing through each point are orthogonal to each other, lie in the transverse plane, and have equal and opposite strength. The same is true of the vortex lines, and further the two sets are constrained such that they are rotated by  $\pi/4$  relative to each other.

For a true plane wave, these local features determine the tendex and vortex line patterns everywhere. Of greater physical interest is the asymptotic regime far from an isolated source of gravitational waves. In this case the gravitational waves are effectively spherical waves propagating radially, and locally all of the properties of plane waves hold. What is interesting is the manner in which the tendex and vortex lines link up globally. Like the famous case of a vector field on a sphere, globally the requirement that only two lines pass through each point must fail somewhere; these points are the singular points of the eigenvector fields, and at these points the radiation must have vanishing strength. The number and character of these singular points are controlled by topological considerations, just as in the case of vector fields, although there is a greater number of possible types of singular points for tendex and vortex lines, since they do not have an orientation.

I led a group of collaborators at Caltech in a short study of the topological patterns of the tendex and vortex lines of generic, asymptotic radiation [36], which is reproduced in Chapter 6. Our results indicate that, while a great variety of possible patterns and singular points are possible, for physically realistic systems where the quadrupolar component of gravitational radiation is dominant, the pattern is relatively universal.

The study includes the visualization of a simple model for a black hole merger which experiences a strong kick. The method was to compute the asymptotic multipole moments of a simple, weak gravity arrangement of point particles with spin; these moments reflect the possible asymptotic gravitational fields of spinning black holes. When there is no spin, the gravitational radiation is dominated by the time-changing mass quadrupole moment. The left hand panel of Figure 1.3 illustrates the tendex and vortex lines produced by a time-varying pure mass quadrupole. There are

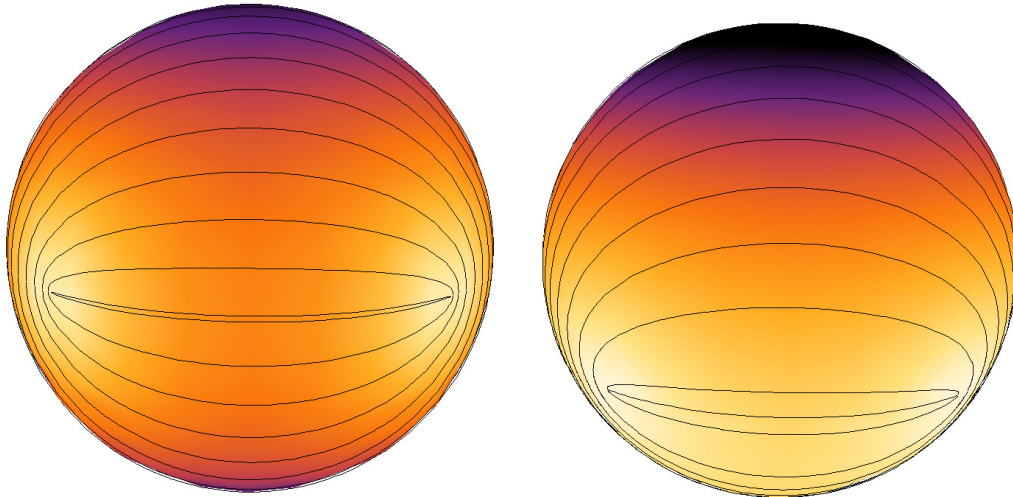


Figure 1.3: Asymptotic tendex line patterns of radiation from two sources. The coloring indicates the tendicity, where darker indicates stronger tidal effects; the lightest spots are where the radiation vanishes. Left: Mass quadrupole source, with equal radiation above and below the equator. There are two singular points in the field line pattern visible on the equator, where the radiation vanishes; two more are hidden from view. Right: Superkick model which incorporates both a mass quadrupole and a current-quadrupole. The radiation is stronger above the equator, and the singular points of vanishing radiation have moved below the equator.

four singular points, which lie in the orbital plane, and the radiation above and below the equatorial plane is equal. Adding spins gives an additional current-quadrupole contribution, and this deforms the pattern of lines far from the system in a manner that depends on the orientation of the spins. In [35], we postulated that a strong black hole kick could result from the beating of mass and a current multipole against each other, in an orientation which gave constructive interference above and destructive interference below the orbital plane. We illustrate this model in [36] by arranging the spins in the orbital plane and adjusting their direction; for constructive interference, the singular points are pushed below the orbital plane, and the relative strength of the radiation above the plane is increased compared to that below. This is shown in the right hand panel of Figure 1.3. The result is a recoil of the black hole away from the beamed radiation. We also note that the most extreme topological deformation would push all of the singular points onto the south pole of the sphere, but this does not appear possible for black holes with reasonable spins.

### 1.4.3 Weak Gravity

Chapter 7 details the first extensive analytic study of tendex and vortex lines, presented in [37]. In this paper, we explore situations where gravity is weak, and can therefore be treated by Newtonian and nearly-Newtonian equations. Our purpose was to fully introduce the formalism of tendex and vortex lines, investigate them in the simplest static situations, and then to investigate the generation

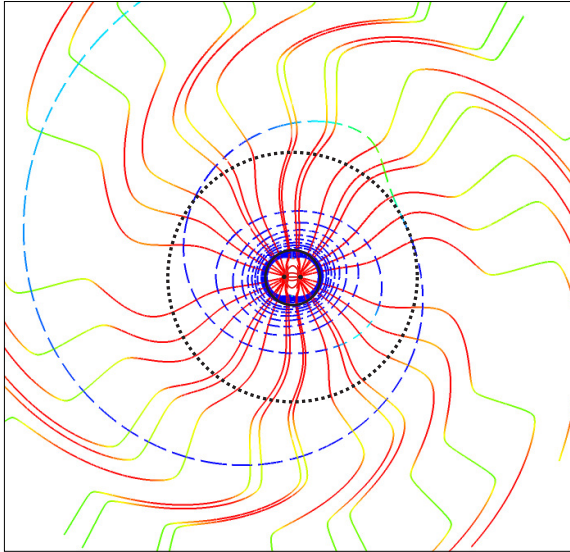


Figure 1.4: Tendex lines in the orbital plane of an equal mass binary, with separation  $a = 20M$  (where  $M$  is the total mass of the binary), produced using a multipolar approximation. The solid black circle has radius  $\lambda = 2.24a$ . The colors are fixed by the tendicity weighted by  $\omega r$  so as to scale out the  $1/r$  falloff in the wave zone (with dark blue strongly positive, dark red strongly negative, and light green near zero). Inside the dotted black curve ( $r = \frac{1}{2}a^2/M = 10a$ ), the binary's (nonradiative) monopole moment dominates,  $\mathcal{E} \simeq M/r^3$ , and the red (stretching) tendex lines are nearly radial. Outside the dotted black curve, the (radiative) quadrupole moment dominates,  $\mathcal{E} \simeq 4M^3/a^4r$ , and the tendex lines are strong only where they are approximately transverse to the radial direction.

of gravitational radiation in simple systems using the lines.

One of the most interesting insights to emerge from this study, and one which strongly influences our followup work, is the description of the generation of gravitational waves by a Newtonian binary. We focus on the appearance of the tendex lines, which are the dominant structures in this nonspinning binary pair. The leading contributions in a  $v/c$ , Post-Newtonian type expansion of the metric give a tendex line pattern near the binary system which is the same as in purely Newtonian gravity: the lines describe the near-field tidal effects which adjust almost instantaneously to the motion of the binary pair. Outside of the orbit of the binary, the system is amenable to a multipolar expansion, and retardation effects become important. It is here that the tendex lines give new insights. In Figure 1.4 (taken from [37]), we can see that as we move further from the near-zone, the radial tendex lines begin to pick up wavelike behavior. They grow weak when nearly radial, reflecting the fact that in the wave zone, the radial tendexes have zero tendicity. Meanwhile, when the tendex lines move along the approximately transverse direction, they grow in strength again. In Figure 1.4 the lines are colored by their tendicity, and in order to give a clear representation of how the strength of tidal effects vary along the lines we have scaled out the expected wave-zone radial behavior by multiplying by  $\omega r$ . This image gives a direct illustration of the manner in which near zone sources smoothly transition into asymptotic radiation.

I share first author credit with four collaborators for this study, and several other authors provided contributions to the text; Kip Thorne especially made major contributions to the writing and conceptual understanding of the text. My primary contributions were to the sections on the general formalism and to the analysis of the the Newtonian binary. I also contributed to the editing and writing throughout the rest of the paper, checked various results throughout the text, and derived a connection to the Newman-Penrose curvature quantities.

#### 1.4.4 Stationary Black Holes

In Chapter 8 I reproduce a study of tendex and vortex lines in stationary black hole spacetimes, which are the simplest spacetimes where the curvature is strong. The analytic control and familiar territory afforded by these black hole spacetimes allows for an initial investigation of the slicing-dependence of the tendex and vortex lines. We also extend our understanding of the form that the vortex lines take in weak gravity systems to situations where frame-dragging is large. The tendex lines in Schwarzschild are no different than in the Newtonian case (in fact, even the eigenvalues of the tidal tensor are the same if Schwarzschild coordinates are used). The investigation of Kerr, on the other hand, provides us with a first glimpse of how vortex lines are generated by rotations in strong gravity. We see that two families of lines emerge from the horizon, one set of negative lines from above the equator and a mirror pair from below; these lines arc around the opposite pole and return through the horizon. The third set of vortex lines form axial spirals. These lines are visualized for a slowly spinning Kerr black hole (the Kerr metric linearized in  $a/M$ ) in Figure 1.5, taken from [38].

We also expand on the idea, briefly introduced in [35], of horizon tendicity and vorticity. These are simply the projections of the tidal and frame-drag tensors onto the horizon, using the spatial horizon normals. Both our analytic explorations, and our early numerical studies such as those reported in [35], indicate that horizon tendexes and vortexes play an essential role in the physical understanding of spacetimes with black holes. An analogy can be made between these quantities and charges or currents set up on boundaries in electromagnetism. In the case of the Kerr black hole, there is a sense in which the negative horizon vorticity in the northern hemisphere sources vortex lines nearly normal to the horizon, which we call a vortex. This idea carries through to both perturbed spacetimes and numerical simulations, with the horizon vorticity sourcing near-horizon vortexes. The same can be said of the positive horizon vortex in the southern hemisphere, and also for horizon tendexes sourced by horizon tendicity. This will be discussed further below, in Section 1.4.5.

Additionally, we learned from this study that the form of the vortex and tendex lines is robust under even fairly extreme changes to the slicing, so long as the time slices are horizon penetrating. In coordinate systems where the time slices do not pass through the horizon, we found singular

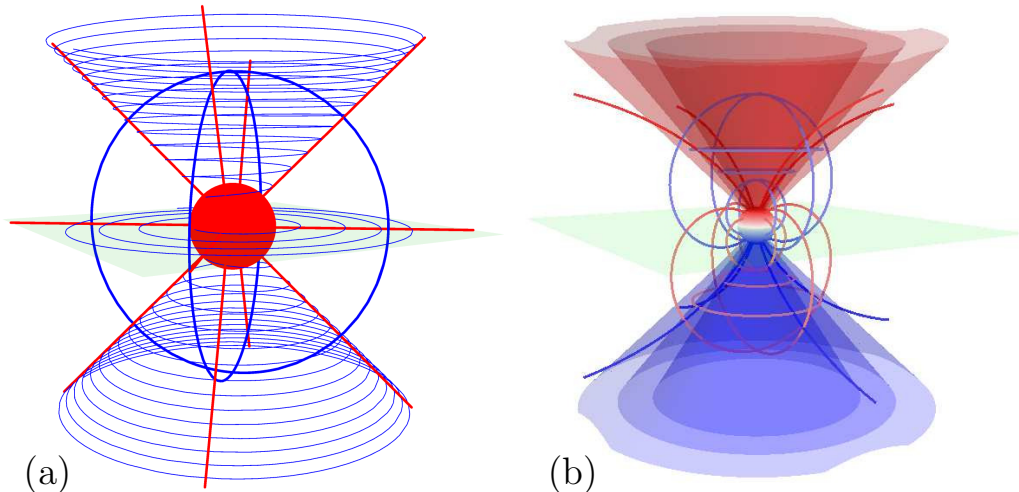


Figure 1.5: (a) Tendex lines, and (b) vortex lines for a slowly rotating Kerr black hole. Here we take  $a/M = 0.1$ . The horizon is color coded by its tendicity  $\mathcal{E}_{NN}$  in (a) (uniformly red signifying negative tendicity) and vorticity  $\mathcal{B}_{NN}$  in (b), and the field lines are color coded by the sign of their tendicity or vorticity (blue for positive, red for negative). In (a), the spiraling lines have been made to spiral more loosely by multiplying the rate of change in the  $r$  direction by five. The semi-transparent cone-like surfaces emerging from the horizon's north and south polar regions show where the magnitude of the vorticity at a given radius has fallen to 80% (outermost cones), 85%, and 90% (innermost cones) of the polar magnitude. We identify the innermost cone (the 90% contour) as the edge of the frame-drag vortex. The equatorial plane is shown for reference in both panels.

features at those horizons. In particular, in Schwarzschild coordinates around a nonrotating black hole, the lines never reach the horizon (they cannot, since the horizon is not covered by the slicing), but this fact is not obvious since the lines are either radial or degenerate on spheres. In Kerr, these lines fail to reach the horizon, and also twist around as they encounter the infinite winding implicit in the Boyer-Lindquist coordinate system. Some analytic results are given which provide an understanding of how allowing the slices to pass through the horizon tends to form generic tendex and vortex patterns in the Kerr case. These simple studies are key to future work in numerical spacetimes.

I share first author credit on this paper with Fan Zhang, and several other authors made key contributions. My contributions were in the analytical computation of the eigenvector fields for the spacetimes considered, along with the tendicities and vorticities; the treatment of the Schwarzschild, and the slowly spinning Kerr, and the checking of the Kerr visualizations; and the writing and editing. The visualization of Kerr in various coordinate systems and slicings was carried out by Fan Zhang both using analytic results I provided and using numerical tools.

### 1.4.5 Perturbed black holes

Chapter 9 presents the most intricate and involved study in our series of papers on the use of tendex and vortex methods, originally published as [39]. In this study, we use the methods introduced in previous papers to gain a deeper understanding of perturbed black holes. Along the way, we also discover a great deal about the lines themselves. For example, we develop further evidence that the lines are robust under gauge transforms, and we compare the perturbations in Schwarzschild to those in Kerr in order to gain insights into both the perturbations of Kerr and the influence which spin has on the appearance of tendex and vortex lines.

One subtlety that must be stated in advance is the almost all of the visualizations carried out in [39] are actually of the perturbation to the tidal and frame drag fields,  $\delta\mathcal{E}$  and  $\delta\mathcal{B}$ . Thus, in this study, the lines do not describe the actual tidal and frame drag effects throughout the spacetime. Rather, the goal of these visualizations is to investigate and isolate the dynamics of the curvature perturbations. It is true though that where the perturbations dominate over the background, such as in the wave zone and in regions where the background tidal and frame-drag fields have degenerate eigenvalues, the eigenvectors of the perturbations  $\delta\mathcal{E}$  and  $\delta\mathcal{B}$  do describe directly the tidal and frame-drag effects. Another important exception is in the case of the vortex lines of a perturbed Schwarzschild black hole. In this case, since there is no background frame-dragging, the lines visualize the true frame-drag field  $\mathcal{B}$ .

What is gained by visualizing only the perturbations are new insights into the dynamics of the perturbations to black holes. We find that the perturbed horizon tendicity and vorticity act as sources for these lines which extend away from the horizon and transition into gravitational radiation. In situations where the horizon tendicity and vorticity oscillate in sign over time, we will find an analogy to RLC circuits, where regions near the horizon briefly appear to store the curvature perturbations as the horizon tendicity or vorticity oscillates through zero. An example of this is given in Figure 1.6, where snapshots of the strength of the vortex lines and the strength of the (perturbative) tendex lines are plotted in the equatorial plane, over half of a wave cycle, for an oscillatory quadrupolar perturbation of the hole. In the near zone, the tendex strength lags that of the vortex by a quarter cycle, appearing to store curvature “energy” when the frame-drag field is momentarily at a minimum. In this case the analogy is promising but not exact; there is also a sense in which there are near horizon waves, propagating down into the horizon, and a study of the tendex and vortex lines themselves reveals complicated dynamics which calls for further study. Some vortex lines are illustrated in the top row of Figure 1.6. Nevertheless, these visualization techniques have revealed new aspects of black hole perturbation theory, even after more than half a century of dedicated study.

I share first author credit on this paper with David Nichols, and several other collaborators made contributions, especially Kip Thorne. My primary contribution to this study was the sections dealing

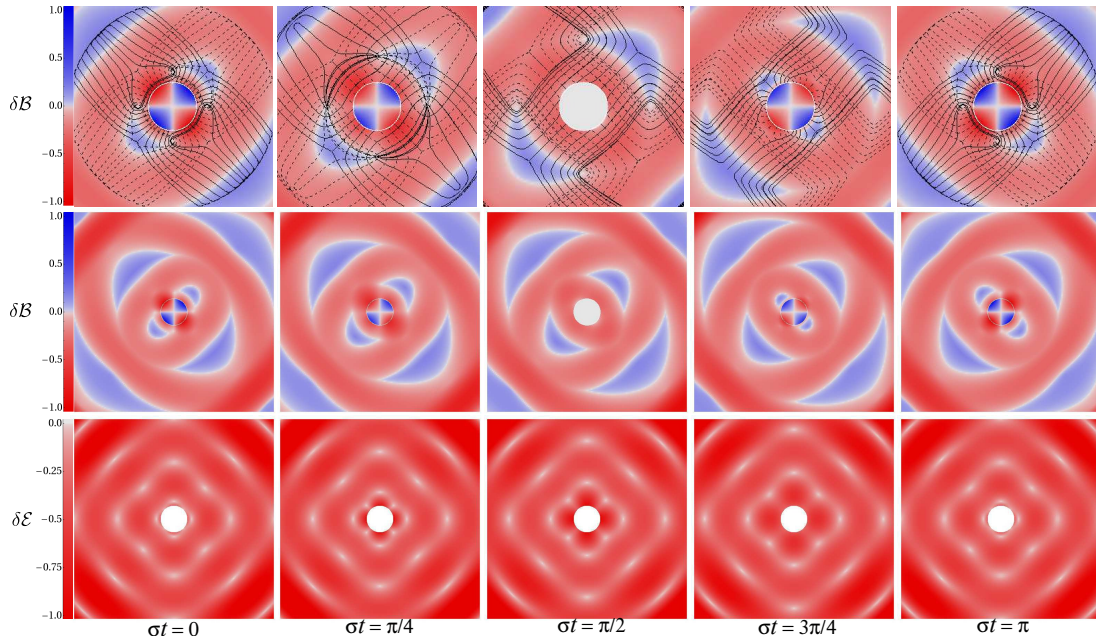


Figure 1.6: Time evolution of the equatorial vortices (top and middle rows) and equatorial perturbative tendexes (bottom row) for the superposed  $(2, 2)$  and  $(2, -2)$  magnetic-parity mode of Schwarzschild in RWZ gauge. The color scale plots  $\pm\sqrt{\text{vorticity} \times r}$ , and the gravitational-wave-induced exponential decay of the vorticity and tendicity has been removed. Top row: Equatorial vortex lines and their vorticity plotted in a region near the horizon ( $16M$  across) followed over time  $t$ . The real part of the eigenfrequency is denoted  $\sigma$ , so the successive panels, left to right cover half a cycle of the mode's oscillation. Middle row: The vorticity of the equatorial vortex lines in the near, intermediate and beginning of wave zone ( $30M$  across) at the same time steps as the top row. Bottom row: Tendicity of the negative tendex lines passing through the equatorial plane plotted at the same time steps as the top row.

with perturbed Schwarzschild black holes, analyzed using the Regge-Wheeler-Zerilli formalism. This included examining the  $l = 2$  modes for  $m = 0, 1, 2$ , and also superimposed  $m = 2$  and  $m = -2$  QNMs. These portions of the paper comprise the major investigation of the dynamics of the tidal and frame-drag fields, and also provided partial results for the gauge comparisons in our study. I also assisted partly in understanding the reconstruction of the Kerr metric from the Hertz potential, and I contributed to the writing and editing throughout the paper, as well as some limited, independent checking on the sections of the paper which dealt with the Kerr black hole, and with the Schwarzschild black hole in ingoing radiation gauge. David Nichols performed the investigation of perturbed Kerr black holes, as well as the  $l = 2, m = 2$  perturbation of Schwarzschild in ingoing radiation gauge for the gauge comparisons.

## 1.5 Outlook

The work discussed in this thesis is, in almost all cases, merely the first step in a series of larger programs. It is my hope that in the future I and other researchers will build on these topics, especially working to strengthen their application to gravitational wave science. We are entering an era in which gravitational wave theory will make contact with observations, so the computation of observable quantities is more important than ever.

For the materials in Chapters 2 – 4, contact with observations may still be far off, for these studies of the QNM spectrum of black holes will require the precise measurement of gravitational waves from black hole ringdowns. Nevertheless, the deeper understanding of BHPT that these studies offer may find application in approximations of the Green function for black holes, which in turn helps in studies of gravitational self-force and the improvement of predictions for extreme mass ratio inspirals. Actual observations of extreme mass ratio systems require the launch of a space-based gravitational wave detector, which at the time of writing of this thesis seems like a far-off prospect.

Meanwhile, the materials of Chapters 5–9 can find immediate application to numerical simulations. This is in fact the next step in the development of the techniques of tendex and vortex lines, and this effort is currently underway. There is also a great deal of promise in the application of tendex and vortex lines to the numerous exact solutions to the field equations which are known but have ambiguous physical interpretation. These solutions certainly do not represent physical systems, due to their inevitably possessing singularities or negative energy content, but they may also have much to tell us about the nonlinear side of relativity.

## Bibliography

- [1] <http://www.ligo.caltech.edu>.
- [2] T. Regge and J. A. Wheeler, *Physical Review* **108**, 1063 (1957).
- [3] R. P. Kerr, *Physical Review Letters* **11**, 237 (1963).
- [4] S. A. Teukolsky, *Astrophys. J.* **185**, 635 (1973).
- [5] H.-P. Nollert, *Classical and Quantum Gravity* **16**, 159 (1999).
- [6] E. Berti, V. Cardoso, and A. O. Starinets, *Classical and Quantum Gravity* **26**, 163001 (2009), 0905.2975.
- [7] E. Newman and R. Penrose, *J. Math. Phys.* **3**, 566 (1962).

- [8] H. Stephani, D. Kramer, M. MacCallum, C. Hoenselaers, and E. Herlt, *Exact Solutions of Einstein's Field Equations* (Cambridge University Press, Cambridge, 2003).
- [9] E. D. Fackerell and R. G. Crossman, *Journal of Mathematical Physics* **18**, 1849 (1977).
- [10] E. Berti, V. Cardoso, J. A. Gonzalez, U. Sperhake, M. Hannam, S. Husa, and B. Brügmann, *Phys. Rev. D* **76**, 064034 (2007).
- [11] A. Zimmerman and Y. Chen, *Phys. Rev. D* **84**, 084012 (2011), 1106.0782.
- [12] H. Yang, D. A. Nichols, F. Zhang, A. Zimmerman, Z. Zhang, et al., *Phys.Rev.* **D86**, 104006 (2012), 1207.4253.
- [13] H. Yang, F. Zhang, A. Zimmerman, D. A. Nichols, E. Berti, and Y. Chen, *Phys. Rev. D* **87**, 041502 (2013).
- [14] Y. Mino and J. Brink, *Phys. Rev. D* **78**, 124015 (2008), 0809.2814.
- [15] R. A. Isaacson, *Physical Review* **166**, 1263 (1968).
- [16] C. J. Goebel, *Astrophys. J. Lett.* **172**, L95 (1972).
- [17] V. Ferrari and B. Mashhoon, *Phys. Rev. D* **30**, 295 (1984).
- [18] B. Mashhoon, *Phys. Rev. D* **31**, 290 (1985).
- [19] V. Cardoso, A. S. Miranda, E. Berti, H. Witek, and V. T. Zanchin, *Phys. Rev. D* **79**, 064016 (2009), 0812.1806.
- [20] B. F. Schutz and C. M. Will, *Astrophys. J. Lett.* **291**, L33 (1985).
- [21] S. R. Dolan, *Phys. Rev. D* **82**, 104003 (2010), 1007.5097.
- [22] E. Berti, V. Cardoso, J. A. González, and U. Sperhake, *Phys. Rev. D* **75**, 124017 (2007).
- [23] F. J. Zerilli, *Phys. Rev. D* **2**, 2141 (1970).
- [24] S. A. Teukolsky and W. H. Press, *Astrophys. J.* **193**, 443 (1974).
- [25] S. Detweiler, *Royal Society of London Proceedings Series A* **352**, 381 (1977).
- [26] S. Detweiler, *Astrophys. J.* **239**, 292 (1980).
- [27] N. Andersson and K. Glampedakis, *Physical Review Letters* **84**, 4537 (2000), [arXiv:gr-qc/9909050](https://arxiv.org/abs/gr-qc/9909050).
- [28] K. Glampedakis and N. Andersson, *Phys. Rev. D* **64**, 104021 (2001), [arXiv:gr-qc/0103054](https://arxiv.org/abs/gr-qc/0103054).

- [29] V. Cardoso, Phys. Rev. D **70**, 127502 (2004), [arXiv:gr-qc/0411048](#).
- [30] S. Hod, Phys. Rev. D **78**, 084035 (2008), [0811.3806](#).
- [31] L. W. Brenneman, C. S. Reynolds, M. A. Nowak, R. C. Reis, M. Trippe, A. C. Fabian, K. Iwasawa, J. C. Lee, J. M. Miller, R. F. Mushotzky, et al., *Astrophys. J.* **736**, 103 (2011), [1104.1172](#).
- [32] R. H. Price, Phys. Rev. D **5**, 2419 (1972).
- [33] R. H. Price, Phys. Rev. D **5**, 2439 (1972).
- [34] K. S. Thorne, in *Magic Without Magic- John Archibald Wheeler. A Collection of Essays In Honor of His 60th Birthday*, edited by J. Klauder (W. H. Freeman and Company, San Francisco, 1972).
- [35] R. Owen et al., Phys. Rev. Lett. **106**, 151101 (2011).
- [36] A. Zimmerman, D. A. Nichols, and F. Zhang, Phys.Rev. **D84**, 044037 (2011), [1107.2959](#).
- [37] D. A. Nichols, R. Owen, F. Zhang, A. Zimmerman, J. Brink, et al., Phys.Rev. **D84**, 124014 (2011), [1108.5486](#).
- [38] F. Zhang, A. Zimmerman, D. A. Nichols, Y. Chen, G. Lovelace, et al., Phys.Rev. **D86**, 084049 (2012), [1208.3034](#).
- [39] D. A. Nichols, A. Zimmerman, Y. Chen, G. Lovelace, K. D. Matthews, et al., Phys.Rev. **D86**, 104028 (2012), [1208.3038](#).

## Part I

# Topics in Black Hole Perturbation Theory

## Chapter 2

# New Generic Ringdown Frequencies at the Birth of a Kerr Black Hole

We discuss a new ringdown frequency mode for vacuum perturbations of the Kerr black hole. We evolve initial data for the vacuum radial Teukolsky equation using a near horizon approximation, and find a frequency mode analogous to that found in a recent study of radiation generated by a plunging particle close to the Kerr horizon. We discuss our results in the context of that study. We also explore the utility of this mode by fitting a numerical waveform with a combination of the usual quasinormal modes (QNMs) and the new oscillation frequency.

---

Originally published as A. Zimmerman, and Y. Chen, *Phys. Rev. D* **84**, 084012 (2011).  
Copyright 2011 by the American Physical Society.

### 2.1 Introduction

Black holes are born when a massive star exhausts its nuclear burning processes, leading to a runaway collapse where gravity dominates over all other interactions. They can also be produced by the merger of binary systems containing compact stellar remnants, such as neutron stars or smaller black holes. Stellar collapse and binary mergers resulting in black holes are astrophysical processes where it is expected that gravitational effects are strong, resulting in regions of high curvature. Observations of such processes would provide a strong test of General Relativity.

Gravitational wave astronomy will provide a powerful tool for investigating astrophysical processes involving highly curved regions of spacetime. In the absence of external fields and matter, black hole binary mergers are completely invisible in the electromagnetic spectrum, and no light can reach observers from the interior of a massive star undergoing core collapse. In these situations

gravitational waves are expected to carry away as much as a few percent of the total mass energy of the system, and can provide direct information about these otherwise unobservable events (see e.g [1]).

In this study, we focus on the gravitational wave signal produced in the final stages of the birth of a black hole, when the gravitational waves can be described using linear perturbation theory on the Kerr spacetime. Measurement of such waves could provide a key test of the so called “No-Hair Theorem” of General Relativity. The No-Hair Theorem is the statement that stationary black hole spacetimes are described completely using only a few parameters, namely mass, spin, and electric charge. This theorem has been proved for the case of Einstein-Maxwell black hole solutions, through the uniqueness theorem for the Kerr-Newman black holes [2]. Thus, when a black hole is born in a merger or stellar collapse, the resulting object must radiate away all of its multipole moments  $\ell \geq 2$  over the course of a ringdown phase. This phase involves emission of gravitational waves in a well known spectrum of exponentially decaying frequency modes, called the quasinormal modes (QNMs) [3–5], and also late time “tails” which have a power-law fall-off in time. Observed deviation from QNM oscillation in the ringdown phase would be indicative that the spacetime is not represented by perturbations on a Kerr spacetime, and so would be a violation of the No-Hair Theorem [6–9].

In addition to this test, detailed study of QNM ringdown is a key component in detection of gravitational waves in the first place. Accurate theoretical and numerical gravitational waveforms are necessary for the success of the method of matched filtering, which will be used to extract the faint signal from the noise in these experiments. Matched filtering uses a gravitational wave template to filter the noise and determine if the wave is present. Accurate modeling of the ringdown phase is then necessary to build useful theoretical templates.

In this study we focus on black hole mergers, which provide a cleaner system with definite numerical predictions, and for which the possibility of detection is higher. The recent strides in numerical relativity [10] have allowed several groups to solve the problem of binary inspiral and merger completely for the first time (see [11, 12] for recent reviews). Such simulations have provided enormous insight into binary mergers, and indeed they can serve as a test bed for the theory of black hole perturbations, in addition to providing complete theoretical gravitational wave templates. However, the computational expense of such simulations prohibits their use in generating a large bank of templates for use in matched filtering. As such, a three stage, semianalytic approximation scheme has been developed to treat binary inspirals. This method has the advantage of reducing the computational expense for template generation. Also, analytic methods help to build intuition into the physical processes of the merger.

The first stage is the long, quasistatic decay of the orbit of the binary, which is treated using the Post Newtonian approximation to General Relativity. The next phase is the rapid merger of the binary, requiring full numerical treatment (though various methods have been employed to

approximate the entire merger, e.g. [13, 14]). Finally, once the two compact objects are surrounded by a common horizon, the system can be approximated by the evolution of perturbations of the final Kerr spacetime. The radiation generated in this phase is governed by the Teukolsky equation [15]. The QNM frequencies are given by the allowed spectrum of the Teukolsky equation, when physically appropriate boundary conditions are imposed. The QNMs are located at the poles in the Green’s function of the radial Teukolsky equation, and are found using a variety of methods (see e.g. [5] for a recent review).

Generally, it has been assumed that the QNMs make up the entire spectrum of oscillations during the ringdown phase after merger. Here we seek a new frequency, characterized by the properties of the Kerr horizon. We are inspired by a study by Mino and Brink [16], which investigated the radiation of a point particle falling into a Kerr black hole, using a near horizon expansion to find the radiation analytically. As the infalling particle approaches the horizon, its trajectory in Boyer-Lindquist coordinates asymptotes to pure angular motion around the black hole with frequency  $\Omega_H$ ,

$$\Omega_H = \frac{a}{2Mr_+} , \quad r_+ = M + \sqrt{M^2 - a^2} . \quad (2.1)$$

Here  $a$  is the spin parameter,  $M$  is the mass, and  $r_+$  is the Boyer-Lindquist radius of the outer horizon. From the viewpoint of an observer at infinity, the particle is frozen at the horizon, corotating with it and sourcing radiation at its rotation frequency. Calculations by Mino and Brink show that the radiation arrives at future null infinity with an exponential decay,

$$\Psi_4 \sim e^{-im\Omega_H t - g_H t} . \quad (2.2)$$

Here  $\Psi_4$  encodes the outgoing radiation, as discussed fully in Section 2.2, and  $m$  is the azimuthal quantum number of the radiation. The decay rate  $g_H$  is the surface gravity, given by

$$g_H = \frac{\sqrt{M^2 - a^2}}{2Mr_+} . \quad (2.3)$$

The frequency here does not depend on details of the particle’s energy and momentum, because the particle’s late-plunge trajectory is essentially universal in the Boyer-Lindquist coordinate system. This suggests that this oscillation mode, the “horizon mode,” may be more general than this single case considered by Mino and Brink. If we take the naive point of view that the late stages of the merger can be approximated by gravitational perturbations falling onto a final black hole, then we have a situation where the infalling perturbations will source outgoing waves like point particles. Though this viewpoint is crude, it does suggest a search for this new frequency mode in post-merger ringdowns.

In this paper we will argue for the existence of a horizon mode (HM) with a frequency of  $m\Omega_H$

and a decay constant which we find to be an integer multiple of  $g_H$ . We find that the particular decay rate depends on our model for how the spacetime transitions from the nonlinear merger into the regime of first order perturbations on the Kerr spacetime.

This paper is organized as follows: Section 2.2.1 provides a simple argument for the presence of this frequency. In Section 2.2.2 we derive this mode through a direct construction, using a simple model for the transition from merger to ringdown. In Section 2.2.3, we explore the consequences of a different model for the transition. In Section 2.3.1, we reconcile our results with those of Mino and Brink. In order to test the utility of this new HM, in Section 2.4 we use the HM in combination with the QNMs to fit a waveform generated by full numerical general relativity, and compare fits that include the HM to fits with the QNMs alone.

## 2.2 The Near Horizon Approximation

We first present a heuristic argument for the presence of an HM analogous to that of Eq. (2.2) in the solutions to the Teukolsky equation. We then derive the HM by evolving initial data for the Teukolsky equation in a near horizon approximation. Finally, we investigate the consequences of a different model for the transition of the spacetime into the regime of linear perturbation theory.

### 2.2.1 Simple Argument for a Horizon Mode

In the Boyer-Lindquist (BL) coordinate system, the components of the Weyl tensor which represent outgoing perturbations of the Kerr spacetime are represented compactly by the Newman-Penrose curvature scalar,

$$\Psi_4 = C_{\alpha\beta\gamma\delta} n^\alpha \bar{m}^\beta n^\gamma \bar{m}^\delta. \quad (2.4)$$

Note that we use a metric signature of  $(-+++)$ , and use the appropriate conventions of [17] for Newman-Penrose (NP) quantities such as  $\Psi_4$ . We use the Kinnersley null tetrad [18],

$$l_K^\mu = \left( \frac{r^2 + a^2}{\Delta}, 1, 0, \frac{a}{\Delta} \right), \quad n_K^\mu = \frac{1}{2\Sigma} \left( r^2 + a^2, -\Delta, 0, a \right), \quad m_K^\mu = \frac{-\bar{\rho}}{\sqrt{2}} \left( ia \sin \theta, 0, 1, \frac{i}{\sin \theta} \right), \quad (2.5)$$

where

$$\Delta = r^2 - 2Mr + a^2, \quad \rho = -\frac{1}{r - ia \cos \theta}, \quad \Sigma = r^2 + a^2 \cos^2 \theta, \quad (2.6)$$

and the overbar represents complex conjugation.

With these choices,  $\Psi_4$  satisfies a separable linear wave equation [15], and can be written as

$$\Psi_4(t, r, \theta, \phi) = \rho^4 \int d\omega \sum_{\ell m} e^{-i\omega t + im\phi} R_{\ell m \omega}(r) S_{\ell m \omega}(\theta). \quad (2.7)$$

Here,  $S_{\ell m \omega}(\theta)$  are the spin-weighted spheroidal harmonics [19, 20], with the appropriate spin weight for  $\Psi_4$ ,  $s = -2$ . In the limit  $\omega \rightarrow 0$ , they reduce to the spin-weighted spherical harmonics  ${}_{-2}Y_{\ell m}(\theta, \phi)$ . The radial function  $R_{\ell m \omega}(r)$  is the solution to the radial Teukolsky equation [15]. Note that  $\Psi_4$  vanishes in the background Kerr spacetime, and its perturbed value is independent of tetrad perturbations and gauge transformations.

We can see the relationship between the scalar  $\Psi_4$  and the outgoing gravitational waveform via its asymptotic form near future null infinity. In this limit, for asymptotically flat spacetimes (see, e.g. [21]),

$$\Psi_4(r \rightarrow \infty) = -\partial_t^2 (h_+ - ih_\times). \quad (2.8)$$

Here the  $+$  and  $\times$  indicate the polarization of the gravitational waves.

In the BL coordinates, using the Kinnersley tetrad, the asymptotic behavior near the horizon of the two homogeneous radial solutions are

$$R_{\ell m \omega}(r) \sim \begin{cases} e^{ikr^*} & \text{outgoing} \\ \Delta^2 e^{-ikr^*} & \text{ingoing} \end{cases}, \quad (2.9)$$

with  $k = \omega - m\Omega_H$ . Together with the separation of  $\Psi_4$ , Eq (2.7), these solutions are associated with outgoing and ingoing radiation at the horizon. The tortoise coordinate  $r^*$  is defined by  $dr^*/dr = (r^2 + a^2)/\Delta$ . Note that  $r^* \rightarrow -\infty$  as  $r \rightarrow r_+$ .

One of these two solutions is selected out as unphysical, based on its behavior near the event horizon. Here we repeat an argument first presented by Teukolsky [15]. We demand that fields neither vanish exactly nor diverge at the horizon when measured by a physical observer. Near the horizon, the trajectory of any freely falling observer will approximately match that of an ingoing null geodesic (see e.g. [16, 22]), independent of the observer's energy or angular momentum, with

$$t + r^* = \text{const}, \quad \theta = \text{const}, \quad \phi = \Omega_H t. \quad (2.10)$$

This means that for distant observers, the infalling trajectory does not appear to enter the horizon, but instead asymptotes to it while circulating around the horizon with a constant frequency. A more natural set of coordinates is ingoing Kerr coordinates,  $(v, r, \theta, \tilde{\phi})$ , where  $dv = dt + dr^*$ , and  $d\tilde{\phi} = d\phi + a dr^*/(r^2 + a^2)$ . Ingoing null geodesics lie on lines of constant  $v$  and  $\tilde{\phi}$ .

In this ingoing coordinate system, the metric does not become singular at the horizon. However,

even in these coordinates, the Kinnersley tetrad used to define  $\Psi_4$  becomes singular at the horizon. This can be repaired by using a Lorentz transform to boost into the reference frame of an infalling observer who carries a nonsingular tetrad, namely

$$\mathbf{l}_{\text{in}} = \frac{\Delta}{2(r^2 + a^2)} \mathbf{l}_K, \quad \mathbf{n}_{\text{in}} = \frac{2(r^2 + a^2)}{\Delta} \mathbf{n}_K. \quad (2.11)$$

Here the subscript ‘‘in’’ indicates the regular ingoing tetrad. The tetrad, written in the ingoing Kerr components, is

$$l_{\text{in}}^\mu = \left( 1, \frac{\Delta}{2(r^2 + a^2)}, 0, \frac{a}{r^2 + a^2} \right), \quad n_{\text{in}}^\mu = \left( 0, -\frac{r^2 + a^2}{\Sigma}, 0, 0 \right), \quad m_{\text{in}}^\mu = \frac{-\bar{\rho}}{\sqrt{2}} \left( ia \sin \theta, 0, 1, \frac{i}{\sin \theta} \right). \quad (2.12)$$

With this tetrad, the physical observer measures a curvature scalar of

$$\Psi_4^{\text{in}} = \left[ \frac{2(r^2 + a^2)}{\Delta} \right]^2 \Psi_4. \quad (2.13)$$

As a consequence, the two radial solutions in Eq. (2.9) correspond to  $\Psi_4^{\text{in}} \sim e^{-i\omega v} e^{im\tilde{\phi}}$  and  $\Psi_4^{\text{in}} \sim \Delta^{-2} e^{-i\omega v} e^{im\tilde{\phi}} e^{2ikr^*}$ . The second diverges at the horizon, and so is selected as unphysical. In other words, if waves emerge from the horizon, then the ingoing observers will see a diverging curvature due to blueshift effects. Note that while it is a particular observer that carries the tetrad of Eq. (2.12) near the horizon, these general results hold for all physical observers. This is because the tetrad that another physical observer carries can be related to that in Eq. (2.12) through nonsingular Lorentz transformations.

However, if the frequency  $\omega$  is complex, this divergence can be removed. To see this, we let  $\omega = m\Omega_H - i\gamma$ , and seek an appropriate  $\gamma$  (the real part of the frequency is chosen so that the observer does not measure increasingly rapid oscillations when approaching the horizon). We note that near the horizon,  $\Delta \sim e^{2g_H r^*}$ . For the physical observer, then,

$$\Psi_4^{\text{in}} \sim \exp\left(-i\omega v + im\tilde{\phi} - 4g_H r^* + 2\gamma r^*\right). \quad (2.14)$$

We see from this that if

$$\gamma = 2g_H, \quad (2.15)$$

this solution remains regular at the horizon, and the solution decays along the observer’s worldline in just such a way that the growth is compensated for. This particular frequency is selected out by a physically allowed solution of the Teukolsky equation, and so we must consider its place in the usual QNM spectrum. Modes with  $\gamma > 2g_H$  decay exponentially for the physical observer. In this sense, the decay rate of Eq. (2.15) gives the least damped, physically reasonable mode in this simple

argument.

### 2.2.2 The Near Horizon Limit: The $\Sigma$ Boundary Model

With our heuristic argument in hand, we now derive the HM using a specific ansatz. In order to keep our results relevant to the problem of compact binary inspiral, we consider the following model. We imagine that to the future of some spacelike hypersurface  $\Sigma$ , the spacetime can be described with linear perturbation theory on the Kerr spacetime, while to the past of  $\Sigma$  the spacetime may be nonlinear. We denote  $\Sigma$  by setting the Boyer-Lindquist time coordinate  $t = 0$ . The past of  $\Sigma$  represents the inspiral and merger phases of binary coalescence. To the future of  $\Sigma$  we can use the Teukolsky equation to evolve initial perturbations on  $\Sigma$  forward. A similar ansatz has been used in the Close Limit approach [23], and Lazarus project [24] which used numerical integration of the Teukolsky equation to evolve initial data on an initial time slice [24, 25]. We refer to our model as the  $\Sigma$  boundary model.

Given this ansatz, we evolve initial data  $\psi|_{t=0} \equiv \rho^{-4}\Psi_4|_{t=0}$  and  $\partial_t\psi|_{t=0}$ , using the Green's function. The full details of the analysis are presented in Appendix 2.A. A near horizon expansion allows us to obtain part of the evolution analytically. Physically, we postulate that just after the merger of the binary, the perturbations are concentrated in a small region near the horizon, so that the initial data used in the Green's function evolution only has support in a small region near the horizon. This expansion allows us to use the asymptotic form for the Green's function, and to keep terms only to first order in  $\epsilon \equiv (r - r_+)/r_+ \ll 1$ . While we focus on the physical picture where the perturbations are concentrated near the horizon, our results hold for the evolution of the initial data which is near the horizon even if the data on the initial surface extends to large  $r$ . In addition, due to redshift effects, this finite region near the horizon produces (decaying) radiation over an infinite region of null infinity.

Specifically, let  $\psi|_{t=0}$  and  $\partial_t\psi|_{t=0}$  be nonzero only between  $r_+$  and  $(1 + \xi)r_+$ , with  $\xi \ll 1$ . We truncate the integrals of the Green's function over the initial perturbation to this small region. To first order in distance from the horizon,  $\Delta \approx 2Mr_+\kappa\epsilon$ , with  $\kappa \equiv \sqrt{1 - a^2/M^2}$ . From Appendix 2.A, equation (2.76), we have that  $\Psi_4$  takes the form of equation (2.7) with the radial function  $R_{\ell m \omega}(r)$  given to leading order in  $\epsilon$  by equation (2.77),

$$R_{\ell m \omega}(r) \approx - \int_{r_+}^{(1+\xi)r_+} dr' \left[ \frac{\beta_{\ell m \omega}(r') + i\omega\alpha_{\ell m \omega}(r')}{2Mr_+(\kappa\epsilon)^3} + \frac{(2M\kappa + ima)\alpha_{\ell m \omega}(r')}{2(Mr_+)^2(\kappa\epsilon)^3} \right] \tilde{G}_{\ell m \omega}(r, r'), \quad (2.16)$$

where the functions  $\alpha_{\ell m \omega}(r)$  and  $\beta_{\ell m \omega}(r)$  can be found from the initial data, using equations (2.68), (2.69), (2.74), and (2.75). The function  $\tilde{G}_{\ell m \omega}(r, r')$  is the frequency domain radial Green's function.

In order to evaluate this expression, we insert the explicit form of the radial Green's function,

$$\tilde{G}_{\ell m \omega}(r, r') = \frac{1}{W_{\ell m \omega}} \begin{cases} R_{\ell m \omega}^{\text{up}}(r) R_{\ell m \omega}^{\text{in}}(r') & r' < r \\ R_{\ell m \omega}^{\text{in}}(r) R_{\ell m \omega}^{\text{up}}(r') & r' > r \end{cases}. \quad (2.17)$$

The functions  $R_{\ell m \omega}^{\text{up}}$  and  $R_{\ell m \omega}^{\text{in}}$  are two homogeneous solutions to the radial Teukolsky equation, with the up-mode (no radiation from past null infinity) and in-mode (no radiation from the past horizon) boundary conditions, respectively. They have the asymptotic forms

$$R_{\ell m \omega}^{\text{in}}(r) \rightarrow \begin{cases} B_{\ell m \omega}^{\text{trans}} \Delta^2 e^{-ikr^*} & r \rightarrow r_+ \\ B_{\ell m \omega}^{\text{ref}} r^3 e^{i\omega r^*} + B_{\ell m \omega}^{\text{in}} r^{-1} e^{-i\omega r^*} & r \rightarrow \infty \end{cases}, \quad (2.18)$$

$$R_{\ell m \omega}^{\text{up}}(r) \rightarrow \begin{cases} C_{\ell m \omega}^{\text{up}} e^{ikr^*} + C_{\ell m \omega}^{\text{ref}} \Delta^2 e^{-ikr^*} & r \rightarrow r_+, \\ C_{\ell m \omega}^{\text{trans}} r^3 e^{i\omega r^*} & r \rightarrow \infty \end{cases}, \quad (2.19)$$

where the Wronskian  $W_{\ell m \omega}$  is given by  $W_{\ell m \omega} = 2i\omega B_{\ell m \omega}^{\text{in}} C_{\ell m \omega}^{\text{trans}}$ .

Since we are interested in the waves at infinity,  $r \rightarrow \infty$ , we insert the appropriate asymptotic expression for  $R_{\ell m \omega}^{\text{in}}$ . Also, since the integral extends only over the near horizon region, we insert the asymptotic expression of  $R_{\ell m \omega}^{\text{in}} \rightarrow B_{\ell m \omega}^{\text{trans}} \Delta^2 e^{-ikr^*} \approx B_{\ell m \omega}^{\text{trans}} (2Mr_+ \kappa \epsilon)^2 e^{-ikr^*}$ . Thus,

$$R_{\ell m \omega}(r \rightarrow \infty) \approx \frac{B_{\ell m \omega}^{\text{trans}}}{2i\omega B_{\ell m \omega}^{\text{in}}} r^3 e^{i\omega r^*} Z_{\ell m \omega}, \quad (2.20)$$

$$Z_{\ell m \omega} = -\frac{2}{\kappa} \int_{r_+}^{(1+\xi)r_+} dr \epsilon^{-1} e^{-ikr^*} \left[ Mr_+ \beta_{\ell m \omega}(r) + (iM\omega r_+ + 2M\kappa + ima) \alpha_{\ell m \omega}(r) \right]. \quad (2.21)$$

In order to complete the integration, we need to know how the initial data behaves to leading order in  $\epsilon$ . We can write to leading order  $\alpha_{\ell m \omega}(r) \approx \alpha_{\ell m \omega}^0 \epsilon^n$  and  $\beta_{\ell m \omega}(r) \approx \beta_{\ell m \omega}^0 \epsilon^p$ . We find the leading order powers  $n$  and  $p$  by essentially repeating the argument given in Section 2.2.1, with some additional care.

Here we cannot follow a single observer who falls past the horizon, since we wish to know the behavior of  $\Psi_4$  on the initial slice  $\Sigma$ . We consider instead a family of accelerated observers who cross the surface  $t = 0$  at a variety of radii, extending all the way to the horizon but not penetrating it. We choose the four-velocities of these observers at this initial surface to vary with  $r$ ,  $\mathbf{u}(r)$ , such that all members of this family carry the regular tetrad (2.12). These observers measure an initial perturbation in their own frames, and for an observer at some  $r$  the measured perturbation is related to that expressed in the Kinnersley tetrad by  $\Psi_4^{\text{in}} = [2(r^2 + a^2)/\Delta]^2 \Psi_4 \sim \epsilon^{-2} \Psi_4$ . Since all the observers are physical, we expect that the perturbation they measure does not diverge as we take the limit  $r \rightarrow r_+$ , moving along the family of observers. However, this requires that  $\Psi_4 \sim \epsilon^2$ .

Thus, we require  $n = 2$ ,  $p = 2$  on this interval.

Inserting this into (2.21) we have

$$\begin{aligned} Z_{\ell m \omega} &= - \left[ M r_+ \beta_{\ell m \omega}^0 + (i M \omega r_+ + 2 M \kappa + i m a) \alpha_{\ell m \omega}^0 \right] \frac{2}{\kappa} \int_{r_+}^{r_+(1+\xi)} dr \epsilon^{-i k r^*} \\ &= \left[ M r_+ \beta_{\ell m \omega}^0 + (i M \omega r_+ + 2 M \kappa + i m a) \alpha_{\ell m \omega}^0 \right] \frac{2}{\kappa} \int_{r_+}^{r_+(1+\xi)} dr \epsilon^{1 - i k r_+ / \kappa}. \end{aligned} \quad (2.22)$$

Focusing on the integral, which we denote  $I$ , we have

$$I = \frac{i \kappa}{\omega - (m \Omega_H - 4 i g_H)} e^{(2 - i k / 2 g_H) \ln \xi}. \quad (2.23)$$

Here, there is a pole in the denominator which will select out the frequency

$$\omega_H = m \Omega_H - 4 i g_H, \quad (\Sigma \text{ Model}) \quad (2.24)$$

when Eq. (2.7) is integrated over  $\omega$ .

Combining Eqs. (2.7), (2.20), (2.22), and (2.23), we integrate over  $\omega$ . We close the contour in the lower half plane, selecting out the poles of Eq. (2.20) by the residue theorem. The zeros of  $B_{\ell m \omega}^{\text{in}}$  comprise one set of poles in the lower half plane, and these poles give the usual QNM frequencies. We wish to focus on the contribution from the additional pole at  $\omega_H$ , and so from here we ignore the poles coming from  $B_{\ell m \omega}^{\text{in}}$ . Similarly, we will not consider here the influence of the pole at  $\omega = 0$  (actually part of a branch cut along the negative imaginary axis, which generates the late-time power-law tails). Also, we will not consider the possible poles in the terms  $\alpha_{\ell m \omega}^0$  and  $\beta_{\ell m \omega}^0$ , which receive their frequency dependence from the projection of the initial data onto the spheroidal harmonics.

This integral converges for  $t - r^* + \ln \xi / 2 g_H > 0$ ; otherwise, we must close the contour in the upper half plane and the integral vanishes. Noting that as  $r \rightarrow \infty$ ,  $\rho \rightarrow -r^{-1}$ , we have

$$\Psi_4 = \frac{1}{r} \sum_{\ell m} \tilde{Z}_{\ell m \omega} e^{-i \omega_H (t - r^*) + i m \phi} S_{\ell m \omega}(\theta) H \left( t - r^* + \frac{\ln \xi}{2 g_H} \right), \quad (2.25)$$

$$\tilde{Z}_{\ell m \omega} = \frac{2 \pi B_{\ell m \omega}^{\text{trans}}}{\omega_H B_{\ell m \omega}^{\text{in}}} \left[ (M \omega_H r_+ + m a - 2 i M \kappa) \alpha_{\ell m \omega}^0 - i M r_+ \beta_{\ell m \omega}^0 \right], \quad (2.26)$$

where  $H$  is the unit step function. In the above, all frequencies are to be evaluated at  $\omega_H$  from (2.24). As  $\xi \ll 1$ , the waves at infinity appear at late retarded times. This sharp turn-on of the wave is an artifact of our truncation of the integral at  $(1 + \xi)r_+$ . A smoother falloff of the initial data with increasing radii would result in a smoother turn on of the wave at infinity. These waves at early times are sourced by initial data on  $\Sigma$  which cannot be evolved using the near horizon approximation. We see also that the waves continue to reach infinity for all retarded times after the

turn on. As mentioned previously, this is due to redshift effects near the horizon, which stretch the radiation from the finite near horizon region out over an infinite region of null infinity.

### 2.2.3 The Characteristic Boundary Model

While the frequency of the radiation in Eq. (2.23) matches the result of our heuristic argument, the decay rate does not. The decay rate is determined by the radial behavior of the initial data, as we can see in Eqs. (2.22) and (2.23). In order that  $\omega_H = m\Omega_H - 2ig_H$ , the initial data would need to behave as  $\Psi_4|_{t=0} \sim \epsilon$ , which we have argued against based on our requirement that physical observers near the horizon measure nonsingular initial data. However, a change of our ansatz shows that the initial data can be proportional to  $\epsilon$  and still represent physical perturbations. In this case the surface bounding the regime of linear perturbation theory is an ingoing null surface, instead of a surface of constant  $t$ . This differs from the  $\Sigma$  boundary model, and so differs from the Close Limit Approach. We will refer to this second model as the characteristic boundary model.

As the spacetime transitions into the linear regime, the nonlinear perturbations radiate away towards infinity or down into the black hole. We imagine that the regions of nonlinear evolution are bounded by characteristics of the linear wave equation. This is a more physically motivated assumption than a transition in spacetime properties along the entire surface  $\Sigma$ . The ingoing characteristics have a trajectory  $r(t) = r_+(1 + e^{-2g_H(t-t_0)})$  [16], where  $t - t_0 \gg 1$ . The comparison of these two models in both BL  $(t, r)$  coordinates and the tortoise  $(t, r^*)$  coordinates is given in Figure 2.1. In the  $(t, r^*)$  coordinates, we see that the horizon is pushed to  $r^* \rightarrow -\infty$ , and that the initial data of the  $\Sigma$  model is stretched out onto an infinite interval in  $r^*$ . We see in both figures that the horizon is hidden behind the boundary characteristics, and our previous argument for the radial dependence of the initial data on  $\Sigma$  no longer holds. We must find a new way to determine the  $r$  dependence of initial data in this model.

We will again evolve initial data on the constant time slice  $\Sigma$ , this time with support only on a small interval outside the boundary characteristics. At time  $t = 0$ , we set the inner boundary of the initial data set to be at  $r_+(1 + \xi_1)$ , and the outer boundary at  $r_+(1 + \xi_2)$ . We will use the same physical observers as before. To first order their trajectories are lines of constant  $v$  and  $\tilde{\phi}$ , just like the ingoing boundary characteristics. The physical observer who passes  $r_+(1 + \xi_2)$  at  $t = 0$  has a trajectory  $r_{\text{obs}}(t) = r_+(1 + e^{-2g_H(t-t_{\text{obs}})})$ . At  $t = 0$  the observer measures an initial perturbation  $\Psi_4^{\text{in}} \sim \xi_2^{-2}\Psi_4(r_{\text{obs}}(0))$ . At a later time  $t$ , the observer measures  $\Psi_4^{\text{in}} \sim \xi_2^{-2}e^{4g_H t}\Psi_4(r_{\text{obs}}(t))$ , and so the measured perturbation grows exponentially in time. However, the perturbation will also decay in time due to its evolution. We insist then that the decay be such that this observer (and similarly, all of the physical observers near the horizon) do not experience an exponentially growing perturbation. This will set the behavior of  $\Psi_4$  on the initial surface.

We examine then the perturbation as measured by the observer along his trajectory. Given

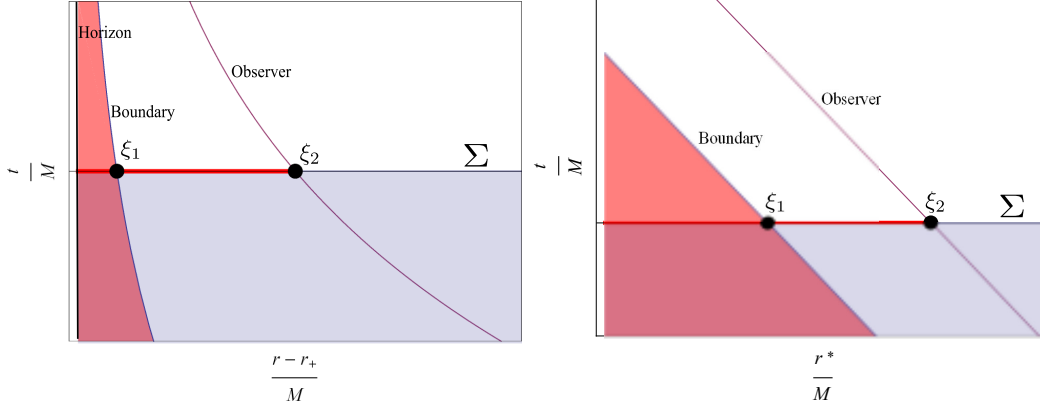


Figure 2.1: Comparison of the  $\Sigma$  and characteristic models. In both figures, the trajectory of the observer discussed and the characteristic boundary surface are plotted, with  $(\theta, \phi)$  suppressed. The thick line is the interval where the initial data is nonzero, and the two points are  $\xi_1$  and  $\xi_2$ , respectively. The shaded regions correspond to the nonlinear regime of each model. Left: Comparison in BL coordinates of the two models, with the event horizon illustrated. Right: Comparison in  $(t, r^*)$  coordinates, where the horizon is pushed to  $r^* \rightarrow \infty$ .

data that behaves as  $\alpha_{\ell m \omega} = \alpha_{\ell m \omega}^0 \epsilon^n$  and  $\beta_{\ell m \omega} = \beta_{\ell m \omega}^0 \epsilon^n$  on the initial surface, we again combine Eqs. (2.16)- (2.19), this time taking the asymptotic limits as  $r' \rightarrow r_+$  and  $r \rightarrow r_+$ . We focus on the outgoing solution only, since the observer will not measure the ingoing waves. We find that

$$R_{\ell m \omega}(r) \sim \frac{e^{ikr^*}}{\omega - (m\Omega_H - 2nig_H)} \left( e^{-2g_H(t-t_{\text{obs}})(n-ikr_+/\kappa)} - e^{\ln \xi_1(n-ikr_+/\kappa)} \right). \quad (2.27)$$

Integrating Eq. (2.7) with this radial function, and noting again that for the observer  $v_{\text{obs}} = t + r^*$  is constant, so that  $t = v_{\text{obs}} - r^*$ , we have

$$\Psi_4(r_{\text{obs}}) \sim e^{-im\Omega_H t - 4ng_H t} \left[ H(t + t_{\text{obs}}) - H\left(2t + \frac{\ln \xi_1}{2g_H}\right) \right]. \quad (2.28)$$

For  $n = 1$ , the decay of the perturbation along the worldline of the observer is just enough to cancel the exponential growth. The initial data on  $\Sigma$  can be taken to be proportional to  $\epsilon$ .

With the initial data, we can return our attention to the perturbations measured at infinity. Repeating the analysis of Section 2.2.2 with this initial data, we have for  $r \rightarrow \infty$

$$\Psi_4 = \frac{1}{r} \sum_{\ell m} \tilde{Z}_{\ell m \omega} e^{-i\omega_H(t-r^*) + im\phi} S_{\ell m \omega}(\theta) \left[ H\left(t - r^* + \frac{\ln \xi_2}{2g_H}\right) - H\left(t - r^* + \frac{\ln \xi_1}{2g_H}\right) \right], \quad (2.29)$$

with  $\tilde{Z}_{\ell m \omega}$  as in Eq. (2.26) but with  $\omega_H$  given by

$$\omega_H = m\Omega_H - 2ig_H. \quad (\text{Boundary Model}) \quad (2.30)$$

We have recovered the decay rate indicated by the heuristic argument of Section 2.2.1. The difference

of step functions here and in Eq. (2.28) is again due to the sharp truncation of the integral at each end of the interval on  $\Sigma$ . Now the radiation turns off due to the truncation of the initial data at the boundary characteristic  $\xi_1$ . At this retarded time the gravitational radiation would give way to radiation sourced by the perturbations in the nonlinear region of spacetime on  $\Sigma$ . For this second model it seems that a method for evolving data along characteristics would be better suited than an evolution from a constant time slice. Such a characteristic evolution has been presented for the Schwarzschild black hole, for example in [26]. Others [27] have presented numerical evolution of characteristics, again for the Schwarzschild black hole. Another possible formulation which would be natural in this context would be the use of an asymptotically hyperboloidal spacelike surface in place of  $\Sigma$ , as discussed in [28].

## 2.3 Reconciliation with the Mino-Brink Mode

In Section 2.2.2 and 2.2.3, we saw that the condition that physical observers measure regular curvature near the horizon determines the decay rate for the gravitational radiation at infinity. In fact, the mode of Mino and Brink, with frequency  $\omega = m\Omega_H - ig_H$ , has a decay rate which violates the regularity conditions discussed in both sections. Its decay rate is too small, for example, compared to Eqs. (2.24) and (2.30) with decay rates  $\gamma \geq 2g_H$ . Thus, although the mode found in [16] motivates our study, the two results are in disagreement. In this section, we first provide a simple alternative estimate for the expected decay rate of radiation from a point particle, using the notation of Newman and Penrose for convenience [29]. With this estimate as motivation, we then find that correction of an error in [16] unexpectedly leads to the vanishing of the first order mode discussed there. We conclude that the actual leading order radiation from an infalling point particle has a decay rate which matches our characteristic boundary model in Section 2.2.3.

### 2.3.1 Point Particle Radiation in Newman-Penrose Formalism

We wish to calculate the radiation generated by a point particle at the last stages of its plunge into a Kerr black hole. Once again, the radiation is described by the Teukolsky formalism, this time with the appropriate source term for the matter content. However, it will turn out to be convenient to make the near horizon expansion in the Newman-Penrose formalism, in order to obtain an estimate for the behavior of the radiation. As we show in Appendix 2.B, we can write to leading order in  $\Delta$  ( $\epsilon$ ) near the horizon, using the Kinnersley tetrad,

$$(\hat{D}\hat{\Delta} + 4\gamma\hat{D})\Psi_4 \approx 4\pi T_4, \quad (2.31)$$

where

$$\hat{D} = l_K^\mu \nabla_\mu, \quad \hat{\Delta} = n_K^\mu \nabla_\mu, \quad \gamma = \frac{r-M}{2\Sigma}, \quad (2.32)$$

and where the source term  $T_4$  is given by (2.79).

In addition, we can approximate

$$\hat{D} \approx \frac{r_+^2 + a^2}{2\Delta} (\partial_t + \partial_{r^*} + \Omega_H \partial_\phi) \equiv \frac{r_+^2 + a^2}{2\Delta} L_+, \quad (2.33)$$

$$\hat{\Delta} \approx \frac{r_+^2 + a^2}{2\Sigma} (\partial_t - \partial_{r^*} + \Omega_H \partial_\phi) \equiv \frac{r_+^2 + a^2}{2\Sigma} L_-, \quad (2.34)$$

and write

$$M^2 r_+^2 (L_+ L_- + 4g_H L_+) \Psi_4 \approx 4\pi \Sigma \Delta T_4. \quad (2.35)$$

In absence of  $T_4$ , this directly gives the asymptotic ingoing and outgoing waves of Eq. (2.9). Let us specialize  $\Psi_4$  to a particular azimuthal quantum number,  $m$ , and we have

$$L_\pm = \partial_t \pm \partial_{r^*} + im\Omega_H. \quad (2.36)$$

We turn now to  $T_4$ . We expand the stress-energy tensor of a point particle in terms of the azimuthal quantum number  $m$  to match the expansion of  $\Psi_4$  implicit in (2.36), which gives

$$T^{\mu\nu} = \mu \frac{u^\mu u^\nu}{\sqrt{-g}} \frac{1}{u^t} \delta(r - r(t)) \delta(\theta - \theta(t)) e^{im(\phi - \phi(t))} \quad (2.37)$$

$$= \mu \frac{u^\mu u^\nu}{u^t \Sigma} \frac{dr^*}{dr} \delta(r^* - r^*(t)) \delta(\chi - \chi(t)) e^{im(\phi - \phi(t))}. \quad (2.38)$$

Here we have defined  $\chi \equiv \cos \theta$ , and used the properties of the delta function. The mass of the particle is given by  $\mu$ . If we define  $v = t + r^*$  and  $u = t - r^*$ , and once again use the properties of the delta function, we can write

$$\delta(r^* - r^*(t)) = \delta\left(\frac{u-v}{2} - r^*\left(\frac{u-v}{2}\right)\right) = 2 \frac{\delta(v - v_0(t))}{du/dt}, \quad (2.39)$$

where  $v_0(t)$  is the value at which the argument of the delta function in (2.39) vanishes, which is at first order simply the value  $v_0 = \text{const}$  to which the trajectory asymptotes. Also, to leading order the trajectory will have  $t = -r^*$ , so  $du/dt = 2$  to leading order.

We have then that

$$T^{\mu\nu} = \mu \frac{2u^\mu u^\nu}{u^t \Sigma} \frac{dr^*/dr}{du/dt} \delta(v - v_0(t)) \delta(\chi - \chi(t)) e^{im(\phi - \Omega_H t)}. \quad (2.40)$$

We must now project  $T^{\mu\nu}$  onto the null Kinnersley basis in order to find  $T_4$ , see (2.79). This will result in a projection of the four velocity onto the Kinnersley basis, for example with  $u_n = u_\mu n^\mu$ , and in this basis some of the components are vanishing or divergent as  $r \rightarrow r_+$  (as seen in Section 2.2.1). In order to examine the leading order behavior near the horizon, it is then best to express the four velocity components in terms of the regular, ingoing basis, related to the Kinnersley tetrad by (2.11). In the ingoing basis, we have

$$\mathbf{u} = u_{\text{in}}^l \mathbf{l}_{\text{in}} + u_{\text{in}}^n \mathbf{n}_{\text{in}} + u_{\text{in}}^m \mathbf{m}_{\text{in}} + u_{\text{in}}^{\bar{m}} \bar{\mathbf{m}}_{\text{in}} , \quad (2.41)$$

with  $u_{\text{in}}^{l,n,m,\bar{m}}$  all smooth and finite throughout the trajectory — including on and within the future horizon. The four velocity in the Kinnersley basis can be expressed as

$$\mathbf{u} = u^l \mathbf{l}_K + u^n \mathbf{n}_K + u^m \mathbf{m}_K + u^{\bar{m}} \bar{\mathbf{m}}_K \quad (2.42)$$

$$= \frac{\Delta u_{\text{in}}^l}{2(r^2 + a^2)} \mathbf{l}_K + \frac{2(r^2 + a^2) u_{\text{in}}^n}{\Delta} \mathbf{n}_K + u_{\text{in}}^m \mathbf{m}_K + u_{\text{in}}^{\bar{m}} \bar{\mathbf{m}}_K . \quad (2.43)$$

Finally, we lower the tetrad indexes on the components of the four velocity using the null metric

$$\hat{\eta}_{ab} = \begin{pmatrix} 0 & -1 & 0 & 0 \\ -1 & 0 & 0 & 0 \\ 0 & 0 & 0 & 1 \\ 0 & 0 & 1 & 0 \end{pmatrix} . \quad (2.44)$$

This gives us

$$u_n u_n = \Delta^2 (u_{\text{in}}^l)^2 , \quad u_n u_{\bar{m}} = -\Delta u_{\text{in}}^l u_{\text{in}}^{\bar{m}} , \quad u_{\bar{m}} u_{\bar{m}} = (u_{\text{in}}^{\bar{m}})^2 . \quad (2.45)$$

Let us first consider  $T_{\bar{m}\bar{m}}$ , which gives the dominant contribution  $T_{4\bar{m}\bar{m}}$  to  $T_4$ ,

$$T_{4\bar{m}\bar{m}} \approx -(\hat{\Delta} + 2\gamma) \hat{\Delta} T_{\bar{m}\bar{m}} . \quad (2.46)$$

It turns out that to first order  $\hat{\Delta} T_{\bar{m}\bar{m}} = 0$ . We can see this by noting that at first order

$$\Sigma u^t \approx \frac{(r^2 + a^2)^2}{\Delta} (E - \Omega_H L_z) \quad (2.47)$$

$$T_{\bar{m}\bar{m}} \approx \mu \frac{(u_{\text{in}}^{\bar{m}})^2 e^{im(\phi - \Omega_H t)}}{2Mr_+(E - \Omega_H L_z)} \delta(v - v_0) \delta(\chi - \chi_0) , \quad (2.48)$$

with  $\chi_0 = \cos \theta_0$  the value of  $\chi$  to which the particle asymptotes to at the horizon. Acting on this

with  $\hat{\Delta}$  from (2.34), we get

$$\hat{\Delta}T_{\bar{m}\bar{m}} \sim \frac{r_+^2 + a^2}{2\Sigma} (-im\Omega_H T_{\bar{m}\bar{m}} + im\Omega_H T_{\bar{m}\bar{m}}) = 0. \quad (2.49)$$

So we see that

$$\hat{\Delta}T_{\bar{m}\bar{m}} \sim \Delta. \quad (2.50)$$

Physically, this is because  $\hat{\Delta}$  takes its derivative almost along the direction of motion, along which  $T_{\bar{m}\bar{m}}$  does not change to first order. This means that the exact contribution of  $T_{\bar{m}\bar{m}}$  to  $T_4$  must be reexamined with other terms included, and its contribution is in fact at the order of  $T_{\bar{m}n}$ . Thus, we expect

$$(L_+L_- + 4g_H L_+) \Psi_4 \sim \Delta^2 \delta(v - v_0). \quad (2.51)$$

We have a simple scenario: if we integrate across the  $v = v_0$  surface, removing the derivatives  $\partial_v = (\partial_t + \partial_{r^*})/2$  from the left-hand side, we will have a  $u$ -dependent  $\Psi_4$ , which obeys

$$\Psi_4 \sim \Delta^2 \sim e^{4g_H r^*} \sim e^{-4g_H t}. \quad (2.52)$$

Here we have recovered the decay rate near the horizon discussed in Section 2.2.3. This indicates that the corresponding decay rate of the waves as  $r \rightarrow \infty$  is that of Eqs. (2.29)-(2.30). However, this argument lacks the detailed calculations of Mino and Brink, who found a mode with a slower decay rate. Under examination, however, it is an error in [16] which leads to a mode with a spuriously low decay rate. We discuss this in the next section.

### 2.3.2 Eliminating the Leading Order Frequency Mode of Mino and Brink

We turn now to the study by Mino and Brink, which we abbreviate as MB. In this study, the source term is evolved using the Green's function method much as Section 2.2 of our study, resulting in an integrand for the integral (2.17) which has a pole at  $\omega = m\Omega_H - ig_H$ , i.e. equation (MB 3.7). The pole then selects out this oscillation frequency for the outgoing radiation at infinity. However, it turns out that this pole is canceled out by terms in the amplitude  $\tilde{Z}_{\ell m \omega}$ , when an error in MB is corrected for. We find this error in going from (MB A14) to (MB B4). The first equation gives a piece of the Fourier decomposition of the source term  $T_4$ , and is drawn from [30], equations (2.21) and (2.25) therein.

Taking the leading order contribution of (MB A14), we find that (MB B4) should read at leading order

$$A_{\bar{m}\bar{m}0} \rightarrow \frac{\kappa a^2 E_{\text{ISCO}}}{4\sqrt{2\pi} M r_+^3} \left[ -i \frac{kr_+}{\kappa} + \left( \frac{kr_+}{\kappa} \right)^2 \right]$$

$$\times \frac{r_+ - ia \cos \theta_0}{r_+ + ia \cos \theta_0} \sin^2 \theta_0 S_{\ell m \omega} \epsilon^{-1}, \quad (2.53)$$

where  $\theta_0$  is the value of  $\theta$  that the point particle asymptotes to on the horizon, and  $E_{\text{ISCO}}$  contains information on the particle's constants of motion. This equation differs from MB by the factor of  $-1$  in front of the term  $ikr_+/\kappa$ . When this difference is accounted for, we have for (MB 3.6)

$$\tilde{Z}_{\ell m \omega} \propto (\omega - m\Omega_H + ig_H)(\omega - m\Omega_H + 2ig_H). \quad (2.54)$$

The first root of  $\tilde{Z}_{\ell m \omega}$  then cancels the pole in the denominator of (MB 3.7). It also appears that the second root removes the frequency mode our rough argument in Section 2.3.1 suggests. However, (2.54) holds only to first order, and at second order there are additional terms not proportional to these roots. While a second surprising cancellation can only be ruled out by a careful study of the MB analysis at second order (or an equivalent formulation), it would seem unlikely that the next order of frequency mode would vanish as well. Such a careful study goes beyond the scope of this paper. However, investigation does indeed show that at second order there is an HM with a decay rate of  $2g_H$  [31].

## 2.4 Numerical Study

In the previous sections we argued for the presence of an HM in the ringdown spectrum. In this section we test a numerical waveform for evidence of this mode. For this study we use the publicly available waveform generated by Scheel *et. al.* [32] by the evolution of an equal mass black hole binary through merger and ringdown. First we compute the overlap between the final portion of the numerical waveform and either a combination of QNM oscillations, or a combination of QNM oscillations and the HM, in order to see if the given combination is a good fit to the waveform. Next, we use a best-fit of the overlap to extract the mass and spin of the black hole from the waveform. Again, we compare the extraction using just the QNMs with an extraction which includes the HM.

For our HM, we focus on the less damped of the two frequencies discussed in Section 2.2,  $\omega_H = m\Omega_H - 2ig_H$ . This mode agrees with the frequency mode from the point particle plunge discussed in Section 2.3.1, and also from the more physically motivated model of the perturbed black hole's transition into the linear perturbation regime, discussed in Section 2.2.3. Throughout this section we will discuss only the dominant  $\ell = 2, m = 2$  mode in the spherical harmonic decomposition of the waveform. Note that, because of the rotation of the Kerr black hole, there is a Zeeman-like splitting of the QNMs into modes which corotate with the black hole and modes which counter-rotate with the hole. The counterrotating mode frequencies are equivalent to the  $\ell = 2, m = -2$  QNM frequencies, but with a negative real part of the frequency,  $\omega_{n\ell m}^{\text{CR}} = -\bar{\omega}_{n\ell -m}$  (see [7] for a detailed discussion).

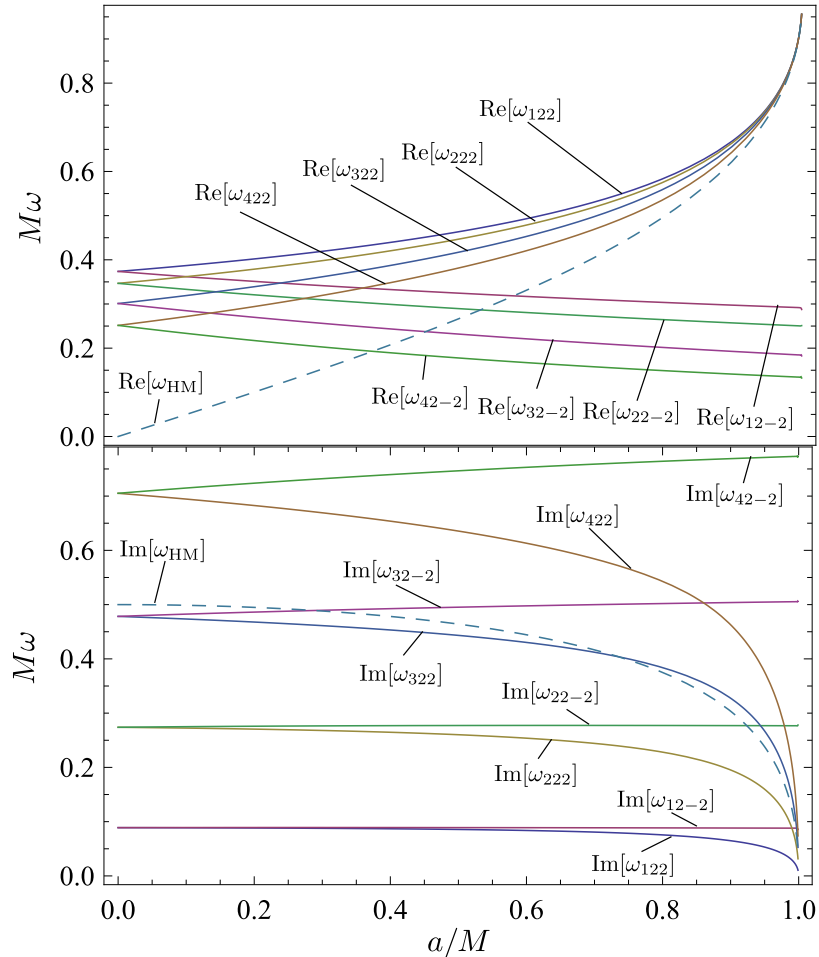


Figure 2.2: A comparison of the real and imaginary parts of  $\omega_H$  (dashed) and the first four QNMs, with  $\ell = 2, m = \pm 2$  (solid).

Each additional overtone we consider in the numerical analysis in the following sections thus adds two distinct modes.

Figure 2.2 compares the real and imaginary parts of  $\omega_H$  with those of the first four QNM for  $\ell = 2, m = 2$  (corotating modes) and  $\ell = 2, m = -2$  (counterrotating modes), as a function of  $a/M$ . These QNM frequency values are drawn from [33] and calculated using the methods discussed in [5], whose values are used throughout this study. Note also that while many studies refer to  $n = 0$  as the slowest decaying QNM, here we count overtones from  $n = 1$ . The corotating QNMs generally have a higher frequency than the HM, and the first two QNMs have slower decay rates. The third corotating QNM has a comparable decay rate, and the fourth decays faster than the HM. Meanwhile, the counterrotating QNMs decrease in frequency with increasing  $a/M$ , until they oscillate more slowly than the HM. The decay rates of the counterrotating QNMs also remain nearly constant over the whole range of  $a/M$ , and so in this case the third and fourth QNMs both decay more quickly than the HM over a large range of  $a/M$ . As  $a/M$  goes to zero,  $\omega_H$  ceases to drive

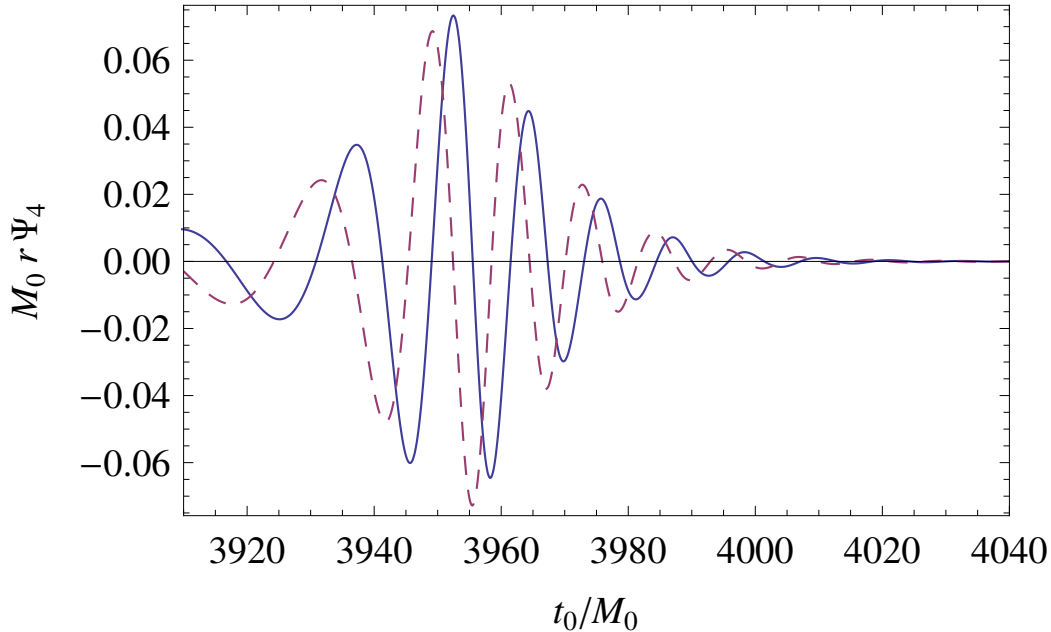


Figure 2.3: The section of the numerical waveform given in Scheel *et. al.* over which  $t_0$  ranges in the overlap integral. Here we give both the real (solid) and imaginary (dashed) portions of  $M_0 r \Psi_4$ .

oscillations, and the HM simply decays exponentially. Also, we see that as  $a/M$  goes to zero, the degeneracy between co- and counterrotating modes is restored. Finally, in Table 2.1 we give numerical values for the QNMs, evaluated at  $a_f/M_f$  for the final, merged black hole whose spectrum we study [32] (in units of the initial ADM mass of the binary), as well as the value of the HM at this spin parameter.

### 2.4.1 Comparison of Overlaps

Consider the final portion of the numerical waveform,  $\psi(t)H(t - t_0)$ , with  $H(t)$  the unit step function, and  $t_0$  a constant which we consider to be the time where the ringdown phase begins. We wish to see how well a waveform made from a linear combination of damped sinusoids,  $\psi_k = e^{(-i\omega_k - \gamma_k)(t - t_0)}H(t - t_0)$ , can be made to fit  $\psi$ . Since we do not know *a priori* at what point in the numerical waveform the ringdown phase begins, we vary  $t_0$  as a free parameter in our study. This allows us to see where in the waveform our combination of sinusoids fails to be a good fit; at sufficiently early  $t_0$  we do not expect a particular combination of  $\psi_k$  to model the chosen section of the waveform accurately. However, a combination of  $\psi_k$  that fits the waveform well over a range of  $t_0$  that includes the early parts of the ringdown more accurately represents the frequency spectrum of the ringdown than another set of damped sinusoids that first fails at a larger value of  $t_0$ .

$(n, \ell, m)$	$M\omega_{\text{QNM}}$
(1,2,2)	0.52670 + 0.08129 <i>i</i>
(2,2,2)	0.51486 + <i>i</i> 0.24581
(3,2,2)	0.49296 + 0.41513 <i>i</i>
(4,2,2)	0.46387 + 0.58873 <i>i</i>
(5,2,2)	0.43291 + 0.76035 <i>i</i>
(1,2,-2)	0.31072 + 0.08874 <i>i</i>
(2,2,-2)	0.27312 + 0.27733 <i>i</i>
(3,2,-2)	0.21198 + 0.49963 <i>i</i>
(4,2,-2)	0.15865 + 0.75811 <i>i</i>
(5,2,-2)	0.12707 + 1.03031 <i>i</i>
$m$	$M\omega_{\text{HM}}$
2	0.37177 + 0.43089 <i>i</i>

Table 2.1: Values of the QNMs and HM evaluated at the spin parameter  $a_f/M_f = 0.68646$  appropriate for the final black hole of [32].

For two waveforms  $s_1(t)$  and  $s_2(t)$  cut off at  $t_0$ , we first define the inner product

$$\langle s_1 | s_2 \rangle \equiv \int_{t_0}^{+\infty} \bar{s}_1(t) s_2(t) dt . \quad (2.55)$$

The overlap,  $\rho$ , of two waveforms is given by the magnitude of the normalized inner product of the waveforms. Our goal then is to maximize the overlap of  $\psi(t_r)$  and the combination  $\sum_k \alpha_k \psi_k$ ,

$$\rho^2 = \frac{|\langle \sum_k \alpha_k \psi_k | \psi \rangle|^2}{\langle \sum_k \alpha_k \psi_k | \sum_k \alpha_k \psi_k \rangle} = \frac{\sum_{k,j} \bar{\alpha}_k A_k \bar{A}_j \alpha_j}{\sum_{l,m} \bar{\alpha}_l B_{lm} \alpha_m} , \quad (2.56)$$

where  $A_k \equiv \langle \psi_k | \psi \rangle$ ,  $B_{lm} \equiv \langle \psi_l | \psi_m \rangle$ . This maximum overlap characterizes how well the  $\psi_k$  can be made to approximate  $\psi$ , given the optimum choice of  $\alpha_k$ . The maximization yields<sup>1</sup>

$$\rho_{\text{max}}^2[\psi; \{\omega_k, \gamma_k\}] = \frac{\bar{A}_k B_{kj}^{-1} A_j}{\langle \psi | \psi \rangle} . \quad (2.57)$$

Using this equation to compute  $\rho_{\text{max}}$ , we take the first  $n$  QNMs (recall that each overtone includes two frequency modes, both the co- and counterrotating modes) and compute the maximum overlap with the numerical waveform as a function of the starting time  $t_0$ . We then find the maximum overlap using the first  $(n - 1)$  QNMs and the HM. Here, and throughout this section, we normalize our units by  $M_0$ , the sum of the initial ADM masses for the two black holes that merge [32]. In these units, the mass  $M_f$  of the final black hole is given as  $M_f/M_0 = 0.95162 \pm 0.00002$ , and its spin  $a_f$  by  $a_f/M_0 = 0.65325 \pm 0.00004$ . For large values of  $t_0$ , only the least damped mode contributes to the waveform, and so any  $\psi_k$  that includes the first QNM will provide  $\rho_{\text{max}} \approx 1$ . Therefore it is useful

<sup>1</sup>The Lagrange multiplier method yields  $\bar{A} \bar{A}^\dagger \bar{\alpha} = \lambda \mathbf{B} \bar{\alpha}$ , with  $\lambda$  already the extremum. This means  $\lambda$  should be the maximum eigenvalue of  $\mathbf{M} = \mathbf{B}^{-1} \bar{A} \bar{A}^\dagger$ . However, since  $\mathbf{M}$  only has one non-zero eigenvalue, we have  $\lambda = \text{tr} \mathbf{M} = \bar{A}^\dagger \mathbf{B}^{-1} \bar{A}$ .

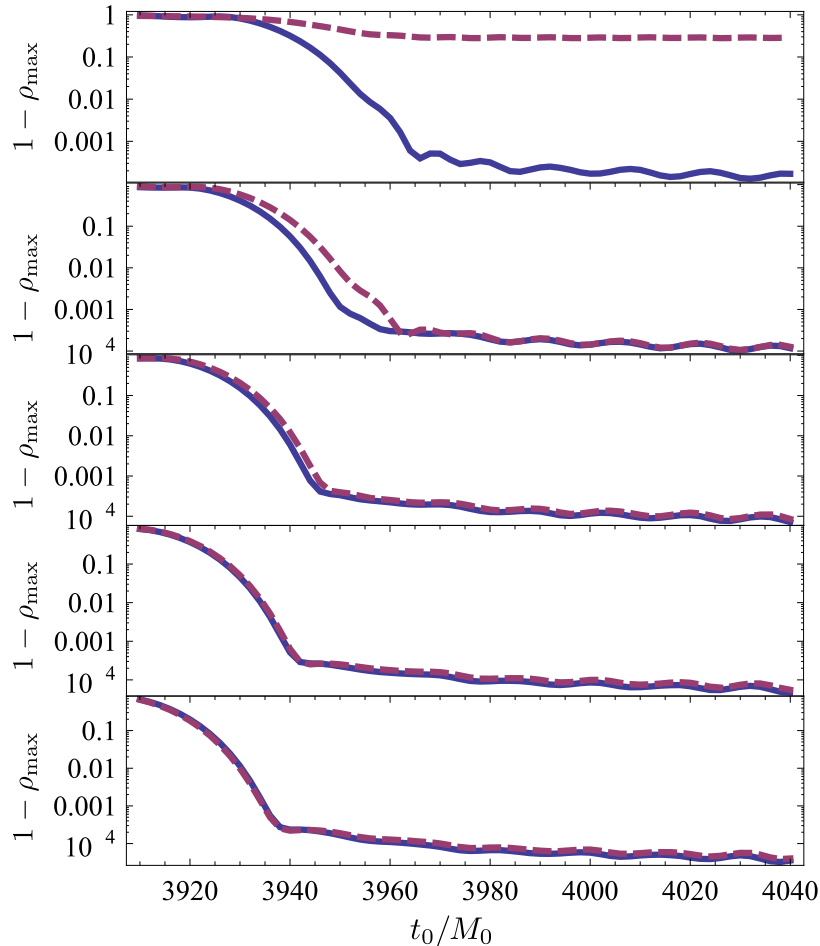


Figure 2.4: Comparisons of  $1 - \rho_{\max}$  for overlaps using just the QNMs (solid) and those which replace one QNM pair with the HM (dashed). The top panel compares the first QNM pair (both co and counterrotating) with the HM alone. The second panel compares the first two QNM pairs with the first QNM pair and the HM. Subsequent panels compare the first  $n$  ( $n = 3, 4, 5$ ) QNM pairs with the first  $n - 1$  pairs and the HM.

to investigate  $1 - \rho_{\max}$ . Figure 2.3 plots the segment of the waveform over which we range  $t_0$  for the overlap calculations. Figure 2.4 compares  $1 - \rho_{\max}$  on a log scale for overlaps using the QNMs alone to those including the HM. In the context of gravitational wave signals, it is preferable to have a good overlap for  $t_0$  close to the peak of the signal. This is when the gravitational wave signal is strongest, and also the point in the waveform when the number of QNMs that make a significant contribution to the waveform is the greatest, before the most-damped QNMs become negligible.

We see that the horizon mode alone provides a poor fit for the waveform for all values of  $t_0$ , and that the first two QNMs provide a better fit at earlier  $t_0$  than the first QNM and the horizon mode. Replacing the  $n^{\text{th}}$  QNM with the HM gives comparable results at  $n = 4$ , and provides a (very slight) improvement at early  $t_0$  for  $n \geq 5$ . We note that this improvement becomes apparent at a  $t_0$  earlier than the peak value of  $|\psi|$ , which occurs at  $t_{\max} = 3953.8M_0$ . This means even for  $n \geq 5$ , the HM

makes an improvement only when portions of the waveform which should not be well modeled by a set of damped sinusoids are included in the overlap. In fact, we find empirically that adding modes with low decay rates always tends to improve overlap calculations at early values of  $t_0$ . This is due to the fact that less damped modes will better fit the region near the peak of the waveform. In this case we would expect comparable results from the  $n = 3$  mode addition and the HM mode addition, and for the HM to improve the overlap compared to  $n = 4$ ; however, the single HM must compete with the pair of co- and counterrotating modes that make up the next overtone. For these reasons, we find that overlap comparisons do not provide a compelling case for the presence of the HM in the waveform, nor do they rule the mode out.

As a second test, we would like to investigate the use of the HM in performing parameter extraction from a ringdown waveform. This practical test of the utility of the HM is more physically motivated than overlap comparisons, and can provide better evidence for the presence of the HM in the waveforms.

### 2.4.2 Extraction of Mass and Black Hole Spin

As a second test, we will extract the mass  $M$  and the spin parameter  $a$  from the waveform. We extract the mass first. To do this, we set  $a/M_0$  to the value given in [32] for the final black hole, but allow  $M$  to vary (note that the QNMs and the HM are function of  $a/M$ , not  $a/M_0$ ). We then calculate  $\rho_{\max}$  as a function of  $M$ , using equation (2.57), and find the value of  $M$  which maximizes  $\rho_{\max}$ . When doing so, there is a distinct residual oscillation in the extracted value of  $M/M_0$ . Investigation reveals that the residual oscillation is compensated for by including the first  $\ell = 4$ ,  $m = 4$  corotating QNM in the fit. Appendix 2.C gives a brief discussion of the possible sources of this mode mixing in the numerical waveform.

The top panel of Figure 2.5 gives the extracted  $M$  as a function of  $t_0$ , for two sets of frequency modes. The first set is composed of the first three  $\ell = 2$ ,  $m = 2$  QNM pairs (co- and counterrotating), plus the first corotating  $\ell = 4$ ,  $m = 4$  QNM. The second set replaces the third  $\ell = 2$ ,  $m = 2$  QNM pair with the HM. We expect the extraction to fail at early values of  $t_0$ , where the sinusoids are a poor fit to the waveform, and at late values of  $t_0$ , where the waveform has decayed significantly. Indeed, one can see in the top panel of Figure 2.5 that the extraction begins to diverge as portions of the waveform preceding the peak of  $|\psi|$  at  $t_{\max} = 3953.8M_0$  (shown with a solid vertical line) are included in the extraction, corresponding to values of  $t_0$  earlier than the peak. The middle and bottom panels of Figure 2.5 show the results of the same extraction, using the first four and five  $\ell = 2$ ,  $m = 2$  QNM pairs, respectively, and comparing to extractions which replace the QNM pair with the largest decay with the HM. We see in these figures that the extraction can be carried out to even earlier values of  $t_0$  than the peak of  $\psi$ , but since these extractions include portions of the waveform which do not correspond to ringdown, we do not expect these early time extractions to

$n$ QNMs	$\Delta M_{\text{QNM}}$ ( $M_0 \times 10^{-3}$ )	$\Delta a_{\text{QNM}}$ ( $M_0 \times 10^{-3}$ )
3	$1.23 \pm 1.66$	$0.20 \pm 3.36$
4	$1.70 \pm 1.96$	$1.23 \pm 4.95$
5	$0.84 \pm 8.14$	$2.55 \pm 8.74$
$n$ QNMs	$\Delta M_{\text{HM}}$ ( $M_0 \times 10^{-3}$ )	$\Delta a_{\text{HM}}$ ( $M_0 \times 10^{-3}$ )
2	$0.53 \pm 1.37$	$0.42 \pm 2.95$
3	$1.15 \pm 1.73$	$1.57 \pm 5.07$
4	$0.40 \pm 8.03$	$3.00 \pm 8.93$

Table 2.2: Extracted masses and spin parameters, for extractions using the first  $n$  QNMs, and extractions using the first  $n$  QNMs plus the HM.

be accurate.

In all cases, Figure 2.5 shows that the substitution of the HM does not improve the extraction over the next most-damped QNM. We find the mean and RMS deviation of the extraction over an interval  $t_0/M_0 = [3954, 4074]$  for all three extractions. This interval covers a region of  $t_0$  that begins just outside the peak and continues until the extractions begin to diverge rapidly. We compare to the mass given in [32] giving a difference in extracted mass of  $\Delta M_{\text{QNM}} = M_f - M_{\text{QNM}}$  for the fits that use only QNMs and  $\Delta M_{\text{HM}} = M_f - M_{\text{HM}}$  for those that include the HM. We present the values of  $\Delta M$  in Table I. We see that in all cases, the HM gives a comparable extraction. For the extractions that use a larger number of QNMs, we see that the RMS deviation grows. This appears to be due to the fact that the extractions with a larger number of modes diverge slightly earlier than those with  $n = 3$  and  $n = 2$  QNMs shown in the top panel of Figure 2.5.

We carry out the same test for the spin of the black hole  $a/M_0$ , by fixing the mass  $M$  at its final value and allowing  $a/M_0$  to vary. The results are given in Figure 2.6. The situation is the same as in the case of the mass extractions. We calculate the mean and RMS deviation from the mean on the interval  $t_0/M_0 = [3954, 4074]$ , and compare the extracted spin parameters to that given in [32], and give the results for  $\Delta a$  in Table 2.4.2. Once more, extractions with just QNMs are essentially the same as those with the HM replacing the most rapidly decaying QNM of a given set. From these extraction tests, we cannot conclude that the HM is present in the numerical waveforms.

## 2.5 Discussion

Using two methods, we have found an additional ringdown mode for the Kerr black hole. This HM depends only on the fundamental properties of the black hole: it oscillates at the horizon frequency of the black hole, and decays at a rate proportional to the surface gravity of the black hole. It will arise when generic initial perturbations source linear gravitational radiation, a situation that would occur as the spacetime transitions from a regime of stronger, nonlinear perturbations into

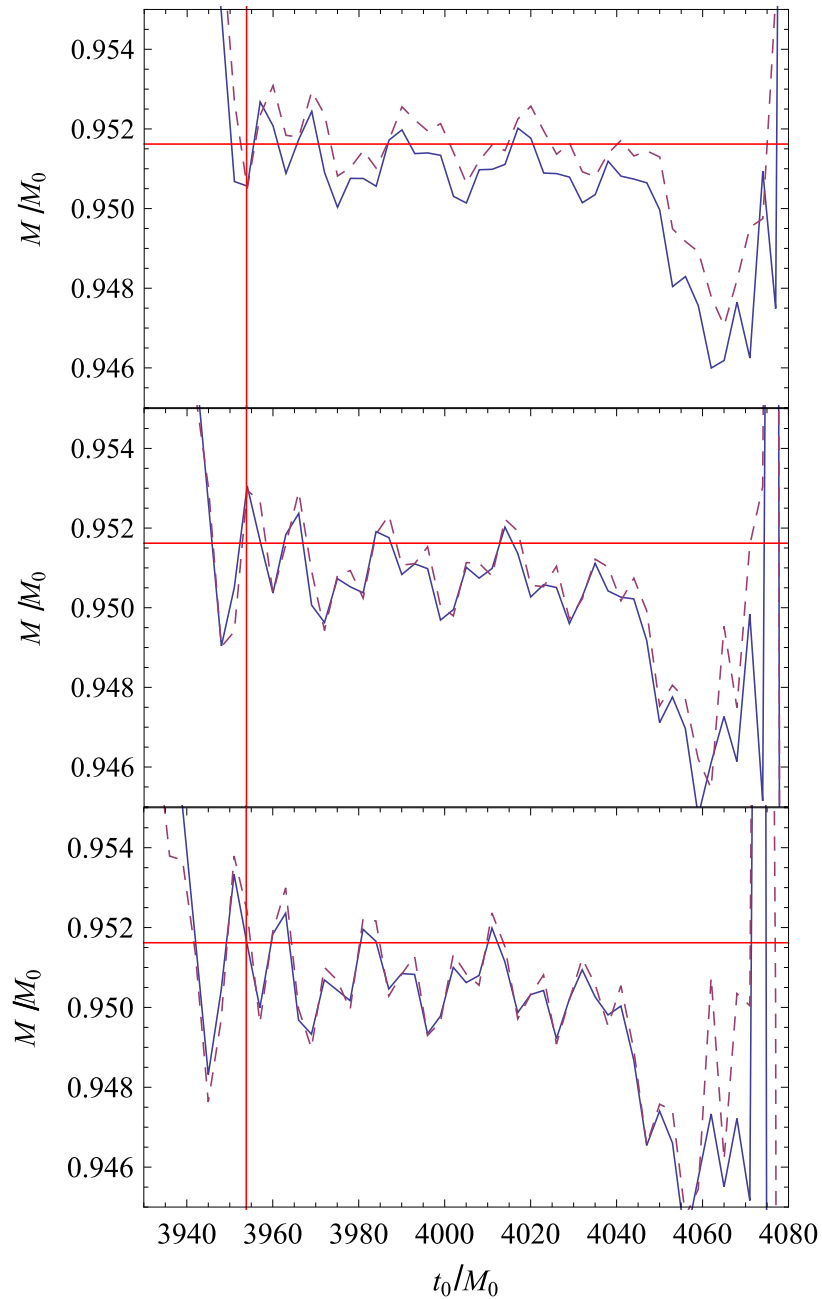


Figure 2.5: Values for the extracted masses  $M_{\text{QNM}}$  (solid) and  $M_{\text{HM}}$  (dashed) as functions of  $t_0$ , for three extractions. The top panel compares the first three QNM pairs with the first two and the HM. The middle panel compares the first four QNM pairs with the first three and the HM. The bottom panel compares the first five QNM pairs with the first four and the HM. The solid horizontal line is at  $M/M_0 = 0.95162$ , the mass of the final black hole as given in [32]. The solid vertical line gives the peak of  $|\psi|$ .

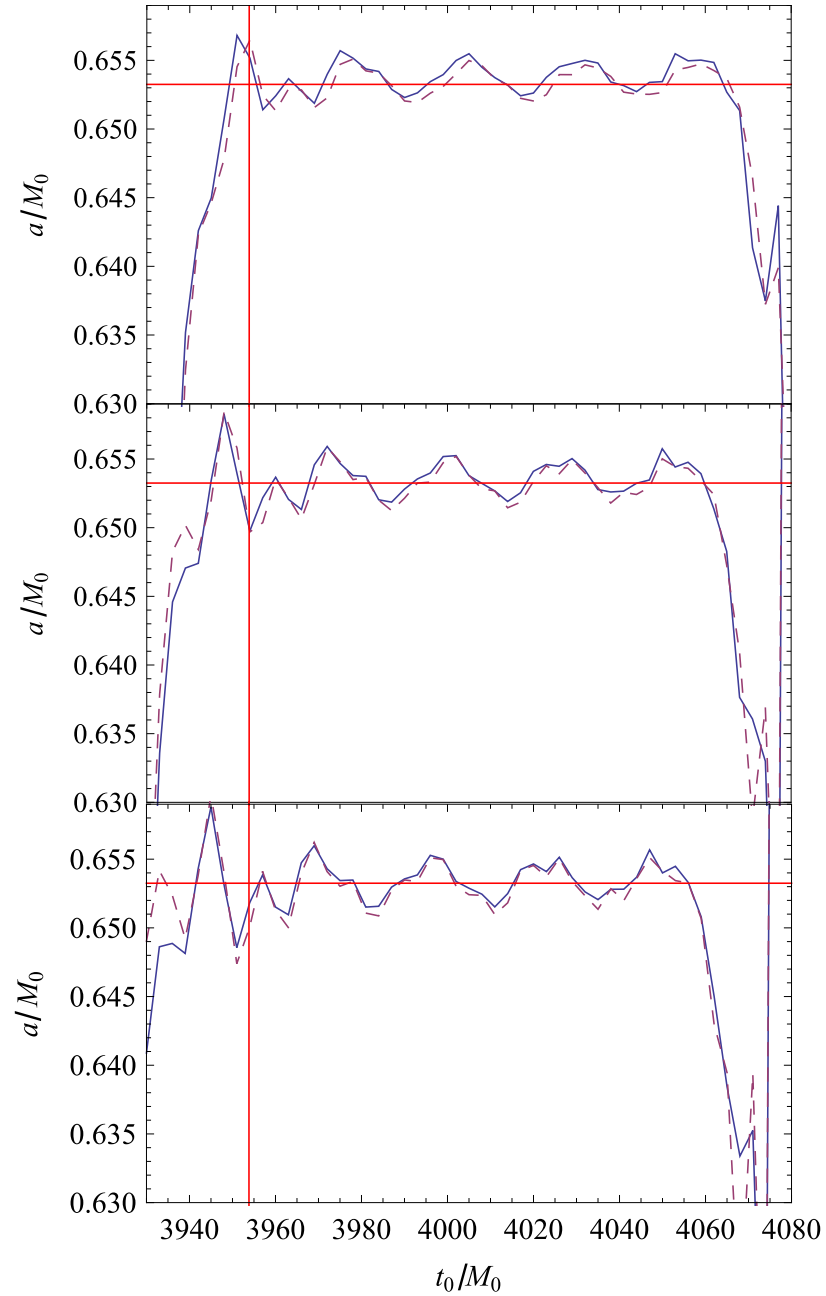


Figure 2.6: Values for the extracted spins  $a_{\text{QNM}}$  and  $a_{\text{HM}}$  as functions of  $t_0$ , for three extractions. The top panel compares the first three QNM pairs with the first two and the HM. The middle panel compares the first four QNM pairs with the first three and the HM. The bottom panel compares the first five QNM pairs with the first four and the HM. The solid horizontal line is at  $a/M_0 = 0.65325$ , the spin of the final black hole as given in [32]. The solid vertical line gives the peak of  $|\psi|$ .

a final ringdown phase. This occurs at the last stage of a compact binary merger, or stellar core collapse resulting in a black hole. We emphasize that this mode is not in the QNM spectrum which is generally taken as the complete spectrum for the ringdown of a black hole. At the same time, this oscillation mode is part of what is normally considered the “ringdown” phase of an event that results in a final black hole, since it arises in linearized perturbation theory about the final black hole.

In fact we have discussed two possible decay rates for the HM, each dependent on our model of how the spacetime transitions from nonlinear evolution into the linear regime. One mode, found using a naive model of transition at a set time slice, decays rapidly. The second was found by noting that nonperturbative regions of the spacetime should be bounded by ingoing and outgoing characteristics, and is physically better motivated. It has a decay rate  $\gamma = 2g_H$ , approximately the same decay rate as the  $n = 3, \ell = 2, m = 2$  QNM. We find that this mode has the same influence on overlap calculations as the  $n = 4$  pair of QNMs, though it does not appear to improve parameter extraction over the use of an additional QNM pair with  $n \geq 4$ . Due to its comparable decay rate to the  $n = 3$  QNMs, it should be considered in the construction of waveform templates that use  $n \geq 3$  QNMs. The HM should also be included as part of the ringdown spectrum when considering the potential use of an observed ringdown signal as a test of the No-Hair Theorem. Otherwise, the presence of this non-QNM oscillation in the spectrum might lead one to conclude that the signal was emitted from an object other than a Kerr black hole.

The analytic approach presented here also builds some intuition into the origin of various frequency modes of linear perturbations of the Kerr spacetime. The HM studied here arises when the influence of perturbations near the horizon are considered. Integration of these initial perturbations using the Green’s function approach results in the presence of a pole in the frequency integral of Eq. (2.7). This mode depends only on the properties of the black hole which govern its near horizon geometry. Meanwhile, the usual QNMs arise because of the poles in the Wronskian of the radial Green’s function, Eqs. (2.18)-(2.19). In our model, these modes arise due to the interaction of the initial perturbations with the complicated potential of the wave equation present further from the event horizon, a situation analogous to that explored for Schwarzschild black holes by Price [26]. In this work, decaying perturbations on the surface of a collapsing star are associated with outgoing radiation; comparison of our results with [26] indicates that our HM is associated with the decaying mode at the stellar surface, but that the rotation of the Kerr black hole in our case guarantees that this mode oscillates with the horizon frequency in addition to its simple decay.

We have also reviewed the problem of gravitational radiation from a point particle infalling near the horizon. Previous work [16] both motivated this study and guided our investigation. However, our results conflict with those of the motivating study. In investigating this discrepancy, we have found an error in the original calculation of [16], the correction of which cancels the first order results

for the radiation at infinity. We have also argued that the form of the next order correction agrees with our results for vacuum perturbations. We leave the detailed calculation of the correct second order terms to a future study [31].

Future study using a variety of numerical waveforms will be key in determining the importance of the HM in template generation and gravitational wave detection. In a simulation where the excitation of slowly decaying QNMs is suppressed, we would expect the HM to be a clear component of the ringdown. Future study of how one might suppress this QNM excitation would be valuable, and such simulations would provide the best testing ground for the presence of the HM in numerical simulations. In addition, the properties of the near horizon region, the HM itself, and the regularity conditions on the initial data discussed here may be of interest in the mathematical study of the stability of the Kerr black hole (see e.g. [34] and the references therein).

## Acknowledgments

We gratefully thank E. Berti for providing tables of QNM values, and also for valuable discussions about the counterrotating QNMs of the Kerr black hole. We thank Jeandrew Brink, Jim Isenberg, David Nichols, and Kip Thorne for useful discussions. A. Z. would also like to thank the National Institute for Theoretical Physics of South Africa for hosting him during the completion of this work. This work was supported by NSF Grants No. PHY-0601459, No. PHY-0653653, No. PHY-1068881, CAREER Grant No. PHY-0956189, the David and Barbara Groce Startup Fund at Caltech, and the Brinson Foundation.

## 2.A Green's Function Formalism For the Teukolsky Equation

The Teukolsky equation, for spin  $s = -2$ , can be written in Boyer-Lindquist coordinates using the Kinnersley tetrad as [15]

$$L[\psi] = \Delta^{-2}T, \quad (2.58)$$

with  $L$  the linear Teukolsky operator described below;  $\psi = \Psi_4/\rho^4$ ; and the source term  $T$  a complicated function of the stress-energy tensor  $T^{\mu\nu}$ , the Kinnersley tetrad, and the Kerr rotation coefficients. The Teukolsky operator is

$$L = L_r + L_\theta + A_1\partial_t^2 + A_2\partial_t + A_3\partial_t\partial_\phi + A_4\partial_\phi^2 + A_5\partial_\phi + A_6, \quad (2.59)$$

$$L_r = -\partial_r(\Delta^{-1}\partial_r), \quad L_\theta = -\frac{1}{\Delta^2\sin\theta}\partial_\theta(\sin\theta\partial_\theta), \quad (2.60)$$

$$A_1 = \frac{(r^2 + a^2)^2}{\Delta^3} - \frac{a^2\sin^2\theta}{\Delta^2}, \quad A_2 = \frac{4M(r^2 - a^2)}{\Delta^3} - \frac{4(r + ia\cos\theta)}{\Delta^2}, \quad (2.61)$$

$$A_3 = \frac{4Mar}{\Delta^3}, \quad A_4 = \frac{a^2}{\Delta^3} - \frac{1}{\Delta^2\sin^2\theta}, \quad (2.62)$$

$$A_5 = \frac{4a(r-M)}{\Delta^3} + \frac{i \cos \theta}{\Delta^2 \sin^2 \theta}, \quad A_6 = \frac{4 \cot^2 \theta + 2}{\Delta^2}. \quad (2.63)$$

We introduce the adjoint operator  $L^*$ , which is the Teukolsky operator with the substitutions  $(\partial_t \rightarrow -\partial_t, \partial_\phi \rightarrow -\partial_\phi)$ , and the Green's function  $G(x'^\mu; x^\mu)$  for  $L$ , which obeys  $L[G(x'^\mu; x^\mu)] = L^*[G(x'^\mu; x^\mu)] = \delta(t' - t)\delta(r' - r)\delta(\theta' - \theta)\delta(\phi' - \phi) \equiv \delta^4(x'^\mu - x^\mu)$ . Now, note that given a pair of functions  $u$  and  $v$  we have

$$\begin{aligned} uL^*[v] - vL[u] = & \partial_r[\Delta^{-1}(v\partial_r u - u\partial_r v)] + \frac{1}{\sin \theta}\partial_\theta[v \sin \theta \partial_\theta u - u \sin \theta \partial_\theta v] + A_1 \partial_t[u\partial_t v - v\partial_t u] \\ & - A_2 \partial_t[uv] + A_3[\partial_t(u\partial_\phi v) - \partial_\phi(v\partial_t u)] + A_4 \partial_\phi[u\partial_\phi v - v\partial_\phi u] - A_5 \partial_\phi[uv]. \end{aligned} \quad (2.64)$$

Now, we let  $u = \psi(x^\mu)$ ,  $v = G(x'^\mu; x^\mu)$ , and we integrate the entire expression over the domain of interest for our situation,  $t \in [0, \infty)$ ,  $r \in (r_+, \infty)$ ,  $\theta \in [0, \pi]$ ,  $\phi \in [0, 2\pi]$ , using spherical polar coordinates and a Euclidean volume element  $d^4x \equiv dt d^3x = r^2 \sin \theta dt dr d\theta d\phi$ . To evaluate the left side of equation (2.64) we note

$$\int d^4x \psi(x^\mu) L^*[G(x'^\mu; x^\mu)] = \int d^4x \psi(x^\mu) \delta^4(x'^\mu - x^\mu) = \psi(x'^\mu). \quad (2.65)$$

Also, we have

$$\int d^4x G(x'^\mu; x^\mu) L[\psi(x^\mu)] = \int d^4x G(x'^\mu; x^\mu) \Delta^{-2} T. \quad (2.66)$$

On the right hand side of Eq. (2.64), we note that the terms involving  $A_4$  and  $A_5$  vanish when integrated over  $\phi$ , due to the periodicity of  $\phi$ . The term  $-A_3 \partial_\phi(v\partial_t u)$  vanishes for the same reason. The first term becomes a boundary term when integrated over  $r$ . In order to have only ingoing waves at the horizon, and only outgoing waves at infinity, we must impose homogeneous boundary conditions on  $\psi(x^\mu)$  and  $G(x'^\mu; x^\mu)$ , and so this term also vanishes. The term involving derivatives of  $\theta$  vanishes when integrated over  $\theta$ , since we require that the initial data and the Green's function be regular on the boundary of  $[0, \pi]$ . The terms involving  $A_1$  and  $A_2$  are total derivatives in time, and so when we integrate over  $t$  we remove the time derivatives and evaluate the terms on the boundary at  $t = 0$ . Since our physical source is transient, the terms vanish at the bound of  $t \rightarrow \infty$ . We have

$$\begin{aligned} \psi(x'^\mu) = & \int d^4x G(x'^\mu; x^\mu) \Delta^{-2} T + \left[ \int d^3x A_1 \partial_t G(x'^\mu; x^\mu) \psi(x^\mu) - \int d^3x A_1 G(x'^\mu; x^\mu) \partial_t \psi(x^\mu) \right. \\ & \left. - \int d^3x A_2 G(x'^\mu; x^\mu) \psi(x^\mu) + \int d^3x A_3 \partial_\phi G(x'^\mu; x^\mu) \psi(x^\mu) \right]_{t=0} \end{aligned} \quad (2.67)$$

Thus far we have kept the source term  $T$  in place for comparison with other studies of the evolution of the Teukolsky equation. In this study we are interested in the vacuum case, and so we set  $T = 0$  here and throughout Section 2.2.

We can further simplify this expression for  $\psi(x^\mu)$  by performing the angular integrations. Let us expand the initial perturbation in terms of spherical harmonics,

$$\psi(t, r, \theta, \phi) \Big|_{t=0} = \sum_{\ell', m'} a_{\ell' m'}(r) Y_{\ell' m'}(\theta, \phi), \quad (2.68)$$

$$\partial_t \psi(t, r, \theta, \phi) \Big|_{t=0} = \sum_{\ell', m'} b_{\ell' m'}(r) Y_{\ell' m'}(\theta, \phi). \quad (2.69)$$

In addition, we expand the Green's function in the frequency domain, where it can be written down explicitly in terms of the spin-weighted spheroidal harmonics and the Green's function for the radial Teukolsky equation [15, 17],

$$G(x'^\mu; x^\mu) \Big|_{t=0} = \int \frac{d\omega}{(2\pi)^2} e^{-i\omega t'} \sum_{\ell, m} \tilde{G}_{\ell m \omega}(r', r) S_{\ell m \omega}(\theta') \bar{S}_{\ell m \omega}(\theta) e^{im(\phi' - \phi)}. \quad (2.70)$$

So, we have  $\partial_\phi G(x'^\mu; x^\mu) = -imG(x'^\mu; x^\mu)$ . With this, we can now perform the integration over  $\phi$ , using the identity

$$\int_0^{2\pi} \frac{d\phi}{2\pi} e^{i(m-m')\phi} = \delta_{mm'}, \quad (2.71)$$

which allows us to resolve the summation over  $m'$  contained in Eq. (2.68)-(2.69). From here, it is convenient to impose the near horizon approximation, for which the motivation is discussed in Section 2.2.2. We keep terms only to the leading order in  $\epsilon = (r - r_+)/r_+ \ll 1$ . In this approximation, we have that  $\Delta \approx 2Mr_+ \kappa \epsilon$ , with  $\kappa \equiv \sqrt{1 - a^2/M^2}$ . To first order in  $\epsilon$ ,

$$A_1 \approx (2Mr_+)^{-1} (\kappa \epsilon)^{-3}, \quad (2.72)$$

$$-imA_3 - A_2 \approx -\frac{2M\kappa + ima}{2(Mr_+)^2 (\kappa \epsilon)^3}. \quad (2.73)$$

We note that all  $\theta$  dependence for these functions enters in at second order in the near horizon expansion. We define

$$\alpha_{\ell m \omega}(r) \equiv \sum_{\ell'} a_{\ell' m}(r) \sqrt{\frac{(2\ell' + 1)(\ell' - m)!}{4\pi(\ell' + m)!}} \int_0^\pi \sin \theta d\theta P_{\ell' m}(\cos \theta) \bar{S}_{\ell m \omega}(\theta), \quad (2.74)$$

$$\beta_{\ell m \omega}(r) \equiv \sum_{\ell'} b_{\ell' m}(r) \sqrt{\frac{(2\ell' + 1)(\ell' - m)!}{4\pi(\ell' + m)!}} \int_0^\pi \sin \theta d\theta P_{\ell' m}(\cos \theta) \bar{S}_{\ell m \omega}(\theta), \quad (2.75)$$

where  $P_{\ell m}(x)$  are the associated Legendre polynomials. The functions  $\alpha_{\ell m \omega}(r)$  and  $\beta_{\ell m \omega}(r)$  are nonzero only on the interval  $r \in [r_+, (1 + \xi)r_+]$ , which allows us to truncate the radial integrals in Eq. (2.67). In fact, we only desire the leading order behavior in  $\epsilon$  of these functions, and this is discussed in Section 2.2.2.

Inserting Eqs. (2.68) - (2.74) into (2.67), and exchanging primed and unprimed labels, we have

finally

$$\psi(x^\mu) = \int \frac{d\omega}{2\pi} \sum_{\ell m} e^{-i\omega t + im\phi} R_{\ell m \omega}(r) S_{\ell m \omega}(\theta), \quad (2.76)$$

$$R_{\ell m \omega}(r) = - \int_{r_+}^{(1+\xi)r_+} dr' \left[ \frac{\beta_{\ell m \omega}(r') + i\omega \alpha_{\ell m \omega}(r')}{2Mr_+(\kappa\epsilon)^3} + \frac{(2M\kappa + ima)\alpha_{\ell m \omega}(r')}{2(Mr_+)^2(\kappa\epsilon)^3} \right] \tilde{G}_{\ell m \omega}(r, r'). \quad (2.77)$$

We resolve this expression in Section 2.2.2.

## 2.B The Teukolsky Equation in the Newman-Penrose Formalism

We refer the reader to [17, 29] for the full formalism. Here we simply collect some of the longer expressions used for Section 2.3.1.

From (2.14) of [15] we have

$$\left[ (\hat{\Delta} + 3\gamma - \bar{\gamma} + 4\mu + \bar{\mu})(\hat{D} + 4\epsilon - \rho) - (\bar{\delta} - \bar{\tau} + \bar{\beta} + 3\alpha + 4\pi)(\delta - \tau + 4\beta) - 3\Psi_2 \right] \Psi_4^B = 4\pi T_4. \quad (2.78)$$

Here  $\Psi_2$  refers to the background value of the NP scalar,  $\Psi_2 = M\rho^3$  for Kerr. The scalar  $\Psi_4^B$  is the perturbative value of  $\Psi_4$ , which is zero at leading order for Kerr. Here,  $\hat{D}$ ,  $\hat{\Delta}$ ,  $\delta$  are all derivative operators along the directions of the null basis, and the Greek characters represent combinations of the spin coefficients. Also note the unfortunate but standard use of  $\pi$  on the left-hand side to refer to one of the spin coefficients in the null tetrad, while on the right side it refers to the numerical  $\pi$  from the Einstein field equations. It is generally clear which is which, and in any case the NP coefficient enters at subleading order here. The source term  $T_4$  is given by

$$T_4 = (\hat{\Delta} + 3\gamma - \bar{\gamma} + 4\mu + \bar{\mu}) \left[ (\bar{\delta} - 2\bar{\tau} + 2\alpha)T_{n\bar{m}} - (\hat{\Delta} + 2\gamma - 2\bar{\gamma} + \bar{\mu})T_{\bar{m}\bar{m}} \right] + (\bar{\delta} - \bar{\tau} + \bar{\beta} + 3\alpha + 4\pi) \left[ (\hat{\Delta} + 2\gamma + 2\bar{\mu})T_{n\bar{m}} - (\bar{\delta} - \bar{\tau} + 2\bar{\beta} + 2\alpha)T_{nn} \right]. \quad (2.79)$$

Here, the terms  $T_{ab}$  are the components of the stress-energy tensor in the tetrad basis,  $T_{nn} = T_{\mu\nu}n^\mu n^\nu$ ,  $T_{n\bar{m}} = T_{\mu\nu}n^\mu \bar{m}^\nu$ , etc.

To specialize to the near horizon approximation, we note that  $\hat{D}$  contains  $\Delta^{-1}$ , and therefore dominates over all the other terms. In addition, we have  $\gamma = \bar{\gamma} = \rho\bar{\rho}(r - M)/2$  and  $\mu = 0$ , to first order.

Using the commutation relation between  $D$  and  $\hat{\Delta}$  (NP4.4), we have, near the horizon

$$\hat{\Delta}\hat{D} - \hat{D}\hat{\Delta} = 2\gamma\hat{D} + (\text{lower order terms}) \quad (2.80)$$

which subsequently gives the  $O(\Delta^{-1})$  term on the left-hand side of the equation

$$(\hat{D}\Delta + 4\gamma\hat{D})\Psi_4. \quad (2.81)$$

We investigate this expression more fully in Section 2.3.1.

## 2.C Mode Corrections to the Wavefunction

The presence of oscillation at the  $n = 1$ ,  $\ell = 4$ ,  $m = 4$  corotating QNM merits some brief discussion. Figures 2.7 and 2.8 give the extraction of  $M$  and  $a$  using the first three QNM pairs (and comparing the the first two QNM pairs with the HM), without the  $\ell = 4$ ,  $m = 4$  mode included. Comparison with the topmost panels of Figures 2.5 and 2.6 shows that the distinct oscillation is successfully removed by including this mode.

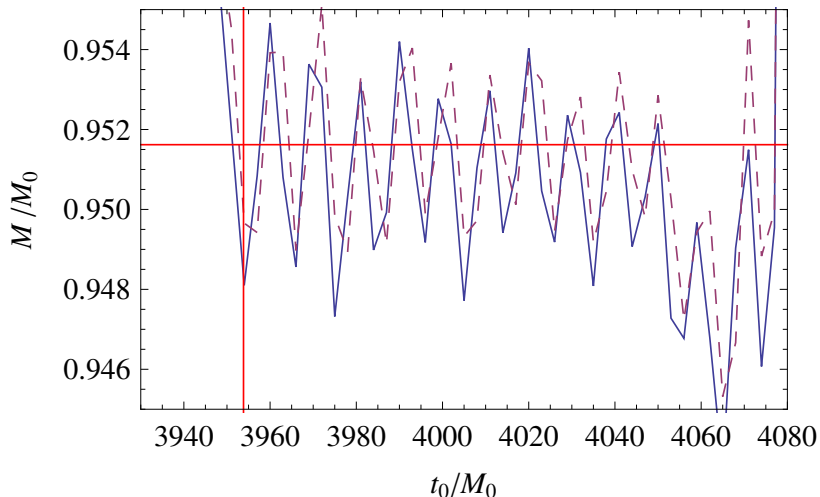


Figure 2.7: Extraction of the mass  $M/M_0$  as a function of  $t_0$ , using only first three QNM pairs (solid) or the first two QNM pairs and the HM (dashed). Here we do not include the corotating  $n = 1$ ,  $\ell = 4$ ,  $m = 4$  mode.

A certain amount of mode mixing between the QNMs is expected due to the fact that the waveform is decomposed into spin-weighted spherical harmonics during the extraction of the waveform. In fact, the angular eigenfunctions of the Teukolsky equation are the spin-weighted spheroidal harmonics. These functions become the usual spherical harmonics when  $a\omega = 0$ . Using this fact, the spheroidal harmonics can be expanded in terms of spin-weighted spherical harmonics and powers of  $a\omega$ , as first discussed in [20]. Only spherical harmonics with the same  $s$  and  $m$  contribute in the expansion. As such, we see immediately that the mixing with the  $\ell = 4$ ,  $m = 4$  QNM frequency cannot arise from the decomposition into spherical harmonics. The portions of the waveforms that can mix into the  $\ell = 2$ ,  $m = 2$  waveform arise from the expansions of  $S_{32}, S_{42}$ , etc. Explicitly, the

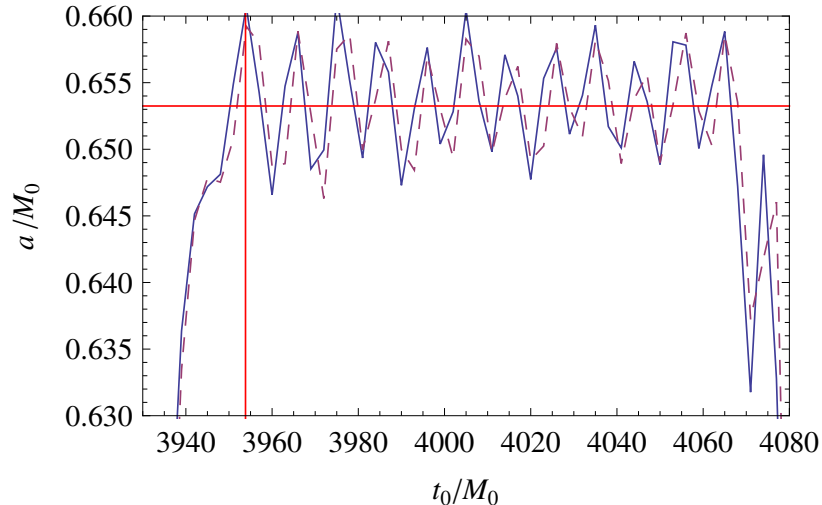


Figure 2.8: Extraction of the spin  $a/M_0$  as a function of  $t_0$ , using only first three pairs QNMs (solid) or the first two QNM pairs and the HM (dashed). We do not include the corotating  $n = 1$ ,  $\ell = 4$ ,  $m = 4$  mode.

expansion of the spheroidal harmonic for  $s = -2$ , is

$$S_{\ell m = -2} Y_{\ell m} + 4a\omega \sum_{\ell' \neq \ell} \sqrt{\frac{2\ell+1}{2\ell'+1}} \frac{C_{\ell 1 m 0}^{\ell' m} C_{\ell 1 2 0}^{\ell' m} - 2Y_{\ell m}}{[\ell(\ell+1) - \ell'(\ell'+1)]} + O(a^2\omega^2), \quad (2.82)$$

where  $C_{b\beta c\gamma}^{a\alpha}$  are the usual Clebsch-Gordan coefficients. For both the horizon mode and the lowest order QNMs,  $a\omega < 1$  is true for all  $a/M$ , and so the expansion is not obviously divergent, although it is only good when  $a/M \ll 1$ . The inclusion of additional QNM frequencies with  $m = 2$  does not remove the residual oscillation in the extraction of  $M$  and  $a$  seen in Figures 2.7 and 2.8 (though a corotating  $\ell = 3$ ,  $m = 2$  reduces the amplitude of the oscillation somewhat). In fact, extractions using a large number of modes generally have sharp features, in addition to systematic deviations from the values of  $M$  and  $a$  given in [32].

The presence of the  $\ell = 4$ ,  $m = 4$  mode in the  $\ell = 2$ ,  $m = 2$  waveform is unexpected, and we attribute it to errors arising from the numerical generation and extraction of the waveform. The spectral code used in [32] generates its gauge dynamically, and while the waveform extraction method attempts remove gauge effects, studies find that these gauge effects still generate errors [35]. We suspect such gauge errors are the source of mode-mode mixing.

## Bibliography

- [1] K. S. Thorne, in *300 Years of Gravitation*, edited by S. W. Hawking and W. Israel (Cambridge University Press, Cambridge, 1987), pp.330-458.

- [2] P. Mazur, *J. Phys. A: Math. Gen.* **15**, 3173 (1982).
- [3] H.-P. Nollert, *Classical Quantum Gravity* **16**, R159 (1999).
- [4] K. D. Kokkotas, B. G. Schmidt, *Living Rev. Rel.* **2**, 2 (1999).
- [5] E. Berti, V. Cardoso, and A. Starinets, *Classical Quantum Gravity* **26**, 163001 (2009).
- [6] O. Dreyer, B. Kelly, B. Krishnan, L. S. Finn, D. Garrison, and R. Lopez-Aleman, *Classical Quantum Gravity* **21** 787, (2004).
- [7] E. Berti, V. Cardoso, C. M. Will, *Phys. Rev. D* **73**, 064030 (2006).
- [8] E. Berti, J. Cardoso, V. Cardoso, M. Cavaglià, *Phys. Rev. D* **76** 104044 (2007).
- [9] N. Yunes, F. Pretorius, *Phys. Rev. D* **80**, 122003 (2009).
- [10] F. Pretorius, *Phys. Rev. Lett.* **95**, 121101 (2005).
- [11] I. Hinder, *Classical Quantum Gravity* **27**, 114004 (2010).
- [12] J. Centrella, J. G. Baker, B. J. Kelly, J. R. van Meter, *Rev. Mod. Phys.* **82** 3069 (2010).
- [13] Y. Pan *et. al.* *Phys. Rev. D* **81**, 084041 (2010).
- [14] D. A. Nichols, Y. Chen, *Phys. Rev. D.* **82**, 104020 (2010).
- [15] S. A. Teukolsky, *Ap. J.* **185**, 635 (1973).
- [16] Y. Mino and J. Brink, *Phys. Rev. D* **78**, 124015 (2008).
- [17] V. P. Frolov and I. D. Novikov, *Black Hole Physics* (Kulwer Academic Publishers Dordrecht/Boston/London, 1998).
- [18] W. Kinnersley, *J. Math. Phys.* **10**, 1195 (1969).
- [19] E. D. Fackerell and R. G. Crossman, *J. Math. Phys.* **18**, 1849 (1977).
- [20] W. H. Press and S. Teukolsky, *Ap. J.* **185**, 649 (1973).
- [21] J. D. Schnittman *et al.*, *Phys. Rev. D* **77**, 044031 (2008).
- [22] C. W. Misner, K. S. Thorne, and J. A. Wheeler, *Gravitation* (Freeman, New York, New York, 1973).
- [23] R. H. Price and J. Pullin, *Phys. Rev. Lett.* **72**, 3297 (1994).
- [24] J. Baker, B. Brüggmann, M. Campanelli, and C. O. Lousto, *Class. Quant. Grav.* **17**, L149 (2000).  
J. Baker, M. Campanelli, C.O. Lousto, *Phys. Rev. D*, **65** 044001 (2002).

- [25] G. Khanna, R. Gleiser, R. Price, and J. Pullin, *New J. Phys.* **2**, 3 (2000).
- [26] R. Price, *Phys. Rev. D* **5**, 2419 (1972). R. Price, *Phys. Rev. D* **5**, 2439 (1972).
- [27] M. Campanelli, R. Gomez, S. Husa, J. Winicour, and Y. Zlochower, *Phys. Rev. D* **63**, 124013 (2001).
- [28] A. Zenginoğlu, *Phys. Rev. D* **83**, 127502 (2011), [arXiv:gr-qc/1102.2451](#).
- [29] E. Newman and R. Penrose, *J. Math. Phys.* **3**, 566 (1962).
- [30] S. Mino *et. al.*, *Prog. of Th. Phys. Supp.* **128**, 1 (1997).
- [31] Y. Chen and A. Zimmerman, in preparation.
- [32] M. A. Scheel *et. al.*, *Phys. Rev. D* **79**, 024003 (2009).
- [33] E. Berti, private communication.
- [34] F. Finster, N. Kamran, J. Smoller, and S.T. Yau, *Bull. Am. Math. Soc.* **46**, 635 (2009).
- [35] F. Zhang, J. Brink, B. Szilágyi, and G. Lovelace, in preparation.

## Chapter 3

# Quasinormal-Mode Spectrum of Kerr Black Holes and Its Geometric Interpretation

There is a well-known, intuitive geometric correspondence between high-frequency quasinormal modes of Schwarzschild black holes and null geodesics that reside on the light-ring (often called spherical photon orbits): the real part of the mode's frequency relates to the geodesic's orbital frequency, and the imaginary part of the frequency corresponds to the Lyapunov exponent of the orbit. For slowly rotating black holes, the quasinormal-mode's real frequency is a linear combination of the orbit's precessional and orbital frequencies, but the correspondence is otherwise unchanged. In this paper, we find a relationship between the quasinormal-mode frequencies of Kerr black holes of arbitrary (astrophysical) spins and general spherical photon orbits, which is analogous to the relationship for slowly rotating holes. To derive this result, we first use the WKB approximation to compute accurate algebraic expressions for large- $l$  quasinormal-mode frequencies. Comparing our WKB calculation to the leading-order, geometric-optics approximation to scalar-wave propagation in the Kerr spacetime, we then draw a correspondence between the real parts of the parameters of a quasinormal mode and the conserved quantities of spherical photon orbits. At next-to-leading order in this comparison, we relate the imaginary parts of the quasinormal-mode parameters to coefficients that modify the amplitude of the scalar wave. With this correspondence, we find a geometric interpretation of two features of the quasinormal-mode spectrum of Kerr black holes: First, for Kerr holes rotating near the maximal rate, a large number of modes have nearly zero damping; we connect this characteristic to the fact that a large number of spherical photon orbits approach the horizon in this limit. Second, for black holes of any spins, the frequencies of specific sets of modes are degenerate; we find that this feature arises when the spher-

ical photon orbits corresponding to these modes form closed (as opposed to ergodically winding) curves.

---

Originally published as H. Yang, D. A. Nichols, F. Zhang, A. Zimmerman, Z. Zhang, and Y. Chen, *Phys. Rev. D* **86**, 104006 (2012). Copyright 2012 by the American Physical Society.

## 3.1 Introduction

Quasinormal modes (QNMs) of black-hole spacetimes are the characteristic modes of linear perturbations of black holes that satisfy an outgoing boundary condition at infinity and an ingoing boundary condition at the horizon (they are the natural, resonant modes of black-hole perturbations). These oscillatory and decaying modes are represented by complex characteristic frequencies  $\omega = \omega_R - i\omega_I$ , which are typically indexed by three numbers,  $n$ ,  $l$ , and  $m$ . The decay rate of the perturbation increases with the overtone number  $n$ , and  $l$  and  $m$  are multipolar indexes of the angular eigenfunctions of the QNM.

### 3.1.1 Overview of Quasinormal Modes and Their Geometric Interpretation

Since their discovery, numerically, in the scattering of gravitational waves in the Schwarzschild spacetime by Vishveshwara [1], QNMs have been thoroughly studied in a wide range of spacetimes, and they have found many applications. There are several reviews [2–6] that summarize the many discoveries about QNMs. They describe how QNMs are defined, the many methods used to calculate QNMs (e.g., estimating them from time-domain solutions [7], using shooting methods in frequency-domain calculations [8], approximating them with inverse-potential approaches [9] and WKB methods [10, 11], numerically solving for them with continued-fraction techniques [12, 13], and calculating them with confluent Huen functions [14, 15]), and the ways to quantify the excitation of QNMs (see, e.g., [16, 17]). They also discuss the prospects for detecting them in gravitational waves using interferometric gravitational-wave detectors, such as LIGO [18] and VIRGO [19], and for inferring astrophysical information from them (see, e.g., [20, 21] for finding the mass and spin of black holes using QNMs, [22, 23] for quantifying the excitation of QNMs in numerical-relativity simulations binary-black-hole mergers, and [24, 25] for testing the no-hair theorem with QNMs). There have also been several other recent applications of QNMs. For example, Zimmerman and Chen [26] (based on work by Mino and Brink [27]) study extensions to the usual spectrum of modes generated in generic ringdowns. Dolan and Ottewill use eikonal methods to approximate the modal wave function, and they use these functions to study the Green’s function and to help understand

wave propagation in the Schwarzschild spacetime [28–30].

Although QNMs are well understood and can be calculated quite precisely, it remains useful to develop intuitive and analytical descriptions of these modes. Analytical insights into QNMs have come largely from two limits: the high-overtone limit ( $n \gg 1$ ) and the eikonal limit ( $l \gg 1$ ). In the high-overtone limit, the frequencies of a QNM are related to the surface gravity of the horizon (see e.g., [31, 32] for the numerical discovery for Schwarzschild black holes, [33] for an analytical proof for Schwarzschild holes, and [34, 35] for proofs for other spherically symmetric black-hole spacetimes). In this paper, we focus on the eikonal limit.

An important calculation in the eikonal limit ( $l \gg 1$ ) was performed by Ferrari and Mashhoon [9], who showed that for a Schwarzschild black hole, the QNM’s frequency (which depends only on a multipolar index  $l$  and an overtone index  $n$ ) can be written as

$$\omega \approx (l + 1/2)\Omega - i\gamma_L(n + 1/2). \quad (3.1)$$

The quantities  $\Omega$  and  $\gamma_L$  are, respectively, the Keplerian frequency of the circular photon orbit and the Lyapunov exponent of the orbit, the latter of which characterizes how quickly a congruence of null geodesics on the circular photon orbit increases its cross section under infinitesimal radial perturbations [30, 36]. Equation (3.1) hints at an intriguing physical description of QNMs, first suggested by Goebel [37]: for modes with wavelengths much shorter than the background curvature, the mode behaves as if it were sourced by a perturbation that orbits on and diffuses away from the light ring on the time scale of the Lyapunov exponent. Thus, photon surfaces [38] play an important role in the structure of a spacetime’s QNMs.

Ferrari and Mashhoon [9] also derived an analogous result to Eq. (3.1) for slowly rotating black holes. They showed for  $l \gtrsim m \gg 1$ , the real part of the frequency is given by

$$\Omega \approx \omega_{\text{orb}} + \frac{m}{l + 1/2}\omega_{\text{prec}}, \quad (3.2)$$

where  $\omega_{\text{orb}}$  is now the Keplerian orbital frequency for the spherical photon orbit <sup>1</sup> and  $\omega_{\text{prec}}$  is the Lense-Thirring-precession frequency of the orbit (which arises because of the slow rotation of the black hole). The term proportional to  $\omega_{\text{prec}}$  also has a simple geometric-optics interpretation. Inertial frames near the high-frequency wave at the light ring are dragged with respect to inertial frames at infinity, and this frame dragging causes the perturbation’s orbit to precess about the spin axis of the black hole with a frequency,  $\omega_{\text{prec}}$ . If the orbit is inclined at an angle of  $\sin^2 \theta = m^2/l(l+1)$  (the ratio of angular momenta  $L_z^2/L^2$  for quantized waves in flat space), then the projection of the precessional velocity onto the orbital plane scales the precessional frequency by a factor of  $\sim m/(l + 1/2)$ .

---

<sup>1</sup>By “spherical photon orbits”, we mean those orbits that remain on a sphere of constant radius, but do not necessarily close or explore the whole sphere.

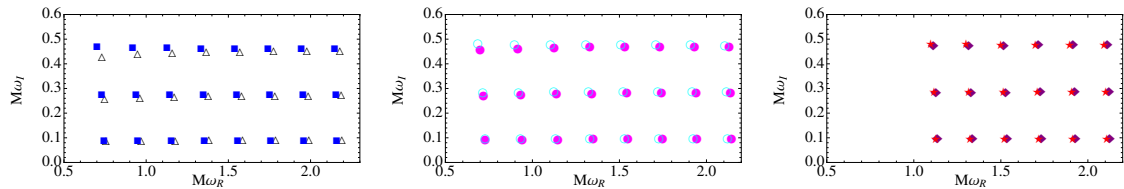


Figure 3.1: Low-overtone QNM spectrum of three Kerr black holes of different spins with approximate degeneracies in their spectra. From left to right, we plot the three lowest-overtone QNM excitations for (i)  $a/M = 0.69$  in which  $(l, m) = (j, 2)$  are black triangles and  $(l', m') = (j + 1, -2)$  are blue squares, where  $j = 3, \dots, 9$ ; (ii)  $a/M = 0.47$  in which  $(l, m) = (j, 3)$  are magenta dots and  $(l', m') = (j + 1, -3)$  are cyan circles, where  $j = 3, \dots, 9$ ; (iii)  $a/M = 0.35$  in which  $(l, m) = (j, 4)$  are red diamonds and  $(l', m') = (j + 1, -4)$  are purple stars, where  $j = 5, \dots, 10$ . For these spin parameters, the mode with positive values of  $m$  and  $\omega_R$  (a corotating mode) of index  $l$  is approximately degenerate with the mode with  $m' = -m$ , and  $\omega_R$  (a counterrotating mode) of index  $l' = l + 1$ .

Why the QNM frequency is multiplied by  $(l + 1/2)$  is a feature that we will explain in greater detail in this paper. Intuitively, this term arises because in the high-frequency limit, any wavefront traveling on null orbits will have an integral number of oscillations in the  $\theta$  and  $\phi$  directions. For the wave to be periodic and single-valued, there must be  $m$  oscillations in the  $\phi$  direction. For the  $\theta$  direction, it is a Bohr-Sommerfeld quantization condition that requires  $l - |m| + 1/2$  oscillations in this direction, which implies that there should be a net spatial frequency of roughly  $(l + 1/2)$ . This increases the frequency of the radiation seen far from the hole by the same factor.

From this intuitive argument, we expect that the real part of the mode should be

$$\omega_R = L \left( \omega_{\text{orb}} + \frac{m}{L} \omega_{\text{prec}} \right), \quad (3.3)$$

where we define  $L = l + 1/2$ . In this paper, we will show that an equation of the form of Eq. (3.3) does, in fact, describe the QNM frequencies of Kerr black holes of arbitrary astrophysical spins (and it recovers the result of Ferrari and Mashhoon for slowly spinning black holes). As we mention in the next part of this section, the exact details of the correspondence between QNMs and photon orbits is richer for rapidly rotating black holes than for slowly rotating or static black holes.

### 3.1.2 Methods and Results of this Article

To derive Eq. (3.3) requires that we develop a geometric-optics interpretation of the QNMs of Kerr black holes with arbitrary astrophysical spins. Finding the correspondence requires two steps: first, we need to calculate the approximate frequencies using the WKB method; next, we must articulate a connection between the mathematics of waves propagating in the Kerr spacetime in the geometric-optics approximation and those of the WKB approximation (the first step). Finally, with the geometric-optics description of QNMs, we can make a physical interpretation of the spectrum

(for example, the degeneracy or the lack of damping in the extremal limit).

In Section 3.2, we describe how we solve the eigenvalue problem that arises from separating the Teukolsky equation [39] (a linear partial differential equation that describes the evolution of scalar, vector, and gravitational perturbations of Kerr black holes) into two nontrivial linear ordinary differential equations. The two differential equations, the radial and angular Teukolsky equations, share two unknown constants—the frequency,  $\omega$ , and the angular separation constant,  $A_{lm}$ —that are fixed by the boundary conditions that the ordinary differential equations must satisfy (ingoing at the horizon and outgoing at infinity for the radial equation, and well-behaved at the poles for the angular equation). The goal of the WKB method is to compute the frequency and separation constant approximately.

Although there has been work by Kokkotas [40] and Iyer and Seidel [41] using WKB methods to compute QNM frequencies of rotating black holes, their results were limited to slowly rotating black holes, because they performed an expansion of the angular separation constant,  $A_{lm}$ , for small, dimensionless spin parameters,  $a/M$ , and only applied the WKB method to the radial Teukolsky equation to solve for the frequency. In a different approach, Dolan developed a matched-expansion formalism for Kerr black holes of arbitrary spins that can be applied to compute the frequency of QNMs, but only for modes with  $l = |m|$  and  $m = 0$  [29].

Therefore, it remains an outstanding problem to compute a WKB approximation to the quasi-normal modes of Kerr black holes of large spins and for any multipolar index  $m$ . In Section 3.2, we solve the joint eigenvalue problem of the radial and angular Teukolsky equations by applying a change of variables to the angular equation that brings it into the form of a bound-state problem in quantum mechanics. Applying the WKB method to the angular equation, we arrive at a Bohr-Sommerfeld condition that constrains the angular constant in terms of the frequency (and the indexes  $l$  and  $m$ ). Simultaneously, we can analyze the radial equation in the WKB approximation, and the two equations together define an system of integral equations, which can be solved for the eigenvalues. When we expand the Bohr-Sommerfeld condition in a Taylor series in terms of the numerically small parameter,  $a\omega/l$ , the system of integral equations reduces to an algebraic system (which, in turn, leads to a simpler expression for the frequency). The approximate frequency agrees very well with the result that includes all powers of  $a\omega/l$ , and, in the eikonal limit, it is accurate to order  $1/l$  for Kerr black holes of arbitrary spins, for modes with any value of  $m$ , and for both the real and the imaginary parts of the frequency.

To interpret the WKB calculation of Section 3.2 in the language of propagating waves in the geometric-optics limit within the Kerr spacetime, we analyze waves around a Kerr black hole in Section 3.3 using the geometric-optics approximation and the Hamilton-Jacobi formalism. We confirm that the leading-order pieces of the WKB frequencies and angular constants correspond to the conserved quantities of the leading-order, geodesic behavior of the geometric-optics approximation

(specifically, the real part of  $\omega$ , the index  $m$ , and the real part of  $A_{lm}$  are equivalent to the energy  $\mathcal{E}$ , the z-component of the specific angular momentum  $L_z$ , and Carter's constant  $\mathcal{Q}$  plus  $L_z^2$ , respectively). The specific geodesics corresponding to a QNM are, in fact, spherical photon orbits. The next-to-leading-order WKB quantities (the imaginary parts of  $\omega$  and  $A_{lm}$ ) correspond to dispersive, wavelike corrections to the geodesic motion (they are the Lyapunov exponent and the product of this exponent with the change in Carter's constant with respect to the energy). Table 3.1 in Section 3.3 summarizes this geometric-optics correspondence.

In Section 3.4, we make several observations about features of the QNM spectrum of Kerr black holes that have simple geometric interpretations. First, we find that for extremal Kerr black holes, a significant fraction of the QNMs have a real frequency proportional to the angular frequency of the horizon and a decay rate that rapidly falls to zero; we explain this in terms of a large number of spherical photon orbits that collect on the horizon for extremal Kerr holes. Second, we expand the WKB expression for the real part of the frequency as in Eq. (3.3), and we interpret these terms as an orbital and a precessional frequency of the corresponding spherical photon orbit. These two frequencies depend on the spin of the black hole and the value of  $m/L$  very weakly for slowly-rotating black holes, though quite strongly when the spin of the black hole is nearly extremal. Finally, we use the geometric-optics interpretation given by Eq. (3.3) to explain a degeneracy in the QNM spectrum of Kerr black holes, in the eikonal limit, which also manifests itself, approximately, for small  $l$  (see Figure 3.1). The degeneracy occurs when the orbital and precession frequencies,  $\omega_{\text{orb}}$  and  $\omega_{\text{prec}}$  are rationally related (i.e.,  $\omega_{\text{orb}}/\omega_{\text{prec}} = p/q$  for integers  $p$  and  $q$ ) for a hole of a specific spin parameter, and when the corresponding spherical photon orbits close. By substituting this result into Eq. (3.3) one can easily see that modes with multipolar indexes  $l$  and  $m$  become degenerate with those of indexes  $l' = l + kq$  and  $m' = m - kp$  for any non-negative integer  $k$ , in the eikonal limit (note that in Figure 3.1, we show an approximate degeneracy for  $k = 1$  and for three spin parameters, such that  $q/p = 1/4, 1/6$ , and  $1/8$ , respectively.)

### 3.1.3 Organization of the Paper

To conclude this introduction, we briefly summarize the organization of this paper: In Section 3.2, we review the Teukolsky equations, and we then describe the WKB formalism that we use to calculate an accurate approximation to the angular eigenvalues  $A_{lm} = A_{lm}^R + iA_{lm}^I$  and QNM frequencies  $\omega = \omega_R - i\omega_I$ , in the eikonal limit  $L \gg 1$  and for holes of arbitrary spins. We verify the accuracy of our expressions in Section 3.2.4 by comparing the WKB frequencies to exact, numerically calculated frequencies. In Section 3.3, we develop a correspondence between the WKB calculation and mathematics of wave propagation within the Kerr spacetime in the geometric-optics limit, using the geometric-optics approximation and the Hamilton-Jacobi formalism. At leading-order, the QNM frequencies and angular eigenvalues correspond to the conserved quantities of motion in the Kerr

spacetime for spherical photon orbits; at next-to-leading order in the geometric-optics approximation, we connect the the decaying behavior of the QNMs to dispersive behaviors of the waves. Finally, in Section 3.4, we interpret aspects of the QNM spectrum geometrically, such as the vanishing of the damping rate for many modes of extremal black holes, the decomposition of the frequency into orbital and precessional parts, and the degeneracies in the QNM frequency spectrum. Finally, in Section 9.6, we conclude. We use geometrized units in which  $G = c = 1$  and the Einstein summation convention throughout this paper.

## 3.2 WKB Approximation for the Quasinormal-Mode Spectrum of Kerr Black Holes

In this section, we will derive expressions for the frequencies of quasinormal modes of Kerr black holes using the WKB approximation. We will need to compute the real and imaginary parts to an accuracy of  $O(1)$  in terms of  $l \gg 1$ , which implies that we must calculate  $\omega_R$  to leading and next-to-leading order and  $\omega_I$  to leading order. Here, we will focus on obtaining an analytic approximation to the frequency spectrum, and we will leave the geometrical interpretation of our results until the next section.

Before specializing our results to the angular and radial Teukolsky equations, we will review a basic result about the WKB expansion that we will use frequently throughout this paper; a more complete discussion of WKB methods can be found in [11]. Given a wave equation for  $\psi(x)$

$$\epsilon^2 \frac{d^2 \psi}{dx^2} + U(x)\psi = 0, \quad (3.4)$$

we will expand the solution as  $\psi = e^{S_0/\epsilon + S_1 + \epsilon S_2 + \dots}$ , where the leading and next-to-leading action variables are given by

$$S_0 = \pm i \int^x \sqrt{U(x)} dx, \quad (3.5a)$$

$$S_1 = -\frac{1}{4} \log U(x). \quad (3.5b)$$

The formulas above will be the basis for our analysis of the radial and angular Teukolsky equations in the next sections.

### 3.2.1 The Teukolsky Equations

Teukolsky showed that scalar, vector, and tensor perturbations of the Kerr spacetime all satisfy a single master equation for scalar variables of spin weight  $s$ ; moreover, the master equation can be solved by separation of variables [39]. We will use  $u$  to denote our scalar variable, and we will

separate this scalar wave as

$$u(t, r, \theta, \phi) = e^{-i\omega t} e^{im\phi} \mathcal{R}(r) u_\theta(\theta). \quad (3.6)$$

Then, at the relevant order in  $l \gg 1$ , the angular equation for  $u_\theta(\theta)$  can be written as

$$\frac{1}{\sin \theta} \frac{d}{d\theta} \left[ \sin \theta \frac{du_\theta}{d\theta} \right] + \left[ a^2 \omega^2 \cos^2 \theta - \frac{m^2}{\sin^2 \theta} + A_{lm} \right] u_\theta = 0, \quad (3.7)$$

where  $A_{lm}$  is the angular eigenvalue of this equation. Following the definition in [42], we use the renormalized radial function given by  $u_r = \Delta^{s/2} \sqrt{r^2 + a^2} \mathcal{R}$ . The equation obeyed by the radial function  $u_r(r)$  is

$$\frac{d^2 u_r}{dr_*^2} + \frac{K^2 - \Delta \lambda_{lm}^0}{(r^2 + a^2)^2} u_r = 0, \quad \frac{d}{dr_*} \equiv \frac{\Delta}{r^2 + a^2} \frac{d}{dr} \quad (3.8a)$$

with

$$K = -\omega(r^2 + a^2) + am, \quad \lambda_{lm}^0 = A_{lm} + a^2 \omega^2 - 2am\omega, \quad \Delta = r^2 - 2Mr + a^2. \quad (3.8b)$$

Here we have used the facts that  $\omega_R \sim O(l)$ ,  $\omega_I \sim O(1)$ ,  $m \sim O(l)$  to drop terms that are of higher orders in the expansion than those that we treat. Note that the spin  $s$  of the perturbation no longer enters into these equations after neglecting the higher-order terms. The only subtlety here is that the  $s$ -dependent terms  $2ms \cos \theta / \sin^2 \theta$  and  $s^2 \cot^2 \theta$  diverge at the poles,  $\theta = 0, \pi$ . For non-polar modes it will be shown in the following section that the wave function asymptotes to zero near the poles, and therefore these  $s$  dependent corrections are not important. For polar modes  $m = 0$ , the angular wave functions do not vanish at the pole, and so it is not as clear that these terms can be neglected as small. However, numerical evidence presented in Section 3.2.4 also shows that neglecting the  $s$  dependent terms in the angular Teukolsky equation only contributes a relative error proportional to  $1/L^2$ .

### 3.2.2 The Angular Eigenvalue Problem

We will first find an expression for  $A_{lm}$  in terms of  $\omega$ ,  $l$ , and  $m$ , by analyzing the angular equation in the WKB approximation. By defining

$$x = \log \left( \tan \frac{\theta}{2} \right) \quad (3.9)$$

and  $dx = d\theta / \sin \theta$ , we can write the angular equation as

$$\frac{d^2 u_\theta}{dx^2} + V^\theta u_\theta = 0, \quad (3.10a)$$

where

$$V^\theta = a^2\omega^2 \cos^2\theta \sin^2\theta - m^2 + A_{lm} \sin^2\theta. \quad (3.10b)$$

When written in this form, it is clear that, aside from polar modes where  $m = 0$ ,  $u_\theta$  must satisfy a boundary condition that it be 0 as  $x \rightarrow \pm\infty$  (which corresponds to  $\theta \rightarrow 0, \pi$ ). In the special case when  $m = 0$ ,  $u_\theta$  approaches a constant instead. Furthermore, the angular equation is now in a form that is amenable to a WKB analysis (which will be the subject of the next part).

First, however, we outline how we will perform the calculation. Because the frequency  $\omega = \omega_R - i\omega_I$  is complex, the angular eigenvalue  $A_{lm}$ , a function of  $\omega$ , must also be complex. We will write

$$A_{lm} = A_{lm}^R + iA_{lm}^I, \quad (3.11)$$

to indicate the split between real and imaginary parts. We will treat a real-valued  $\omega = \omega_R$  in the first part of this section, and, therefore, a real-valued  $A_{lm}^R(\omega_R)$ ; we shall account for  $-i\omega_I$  by including it as an additional perturbation in the next part of this section.

### 3.2.2.1 Real Part of $A_{lm}$ for a Real-Valued $\omega$

For  $\omega_R \in \mathbb{R}$ , we will compute the eigenvalues  $A_{lm}^R(\omega_R)$ , of Eq. (3.10a) for standing-wave solutions that satisfy physical boundary conditions. At the boundary,  $\theta = 0, \pi$  (or  $x = \mp\infty$ ) the potential satisfies  $V^\theta = -m^2$  independent of the value of  $A_{lm}^R$ ; this implies that the solutions to Eq. (3.10a) behave like decaying exponential functions at these points (i.e., the wave does not propagate). For there to be a region where the solutions oscillate (i.e., where the wave would propagate),  $A_{lm}$  must be sufficiently large to make  $V^\theta > 0$  in some region. Depending on the relative amplitudes of  $A_{lm}$  and  $a^2\omega^2$ ,  $V^\theta$  either has one maximum at  $\theta = \pi/2$  (when  $A_{lm} \geq a^2\omega^2$ ), or two identical maxima at two locations symmetrically situated around  $\theta = \pi/2$  (when  $A_{lm} < a^2\omega^2$ ). It turns out that the region where the maximum of  $V^\theta > m^2$  is centered around  $\pi/2$ ; therefore, all solutions fall into the former category rather than the latter.

The length scale over which the function  $u_\theta$  varies is  $1/\sqrt{V^\theta}$ , and the WKB approximation is valid only if the potential  $V^\theta$  does not vary much at this scale. Therefore, to use the WKB approximation, we require that

$$\left| \frac{1}{\sqrt{V^\theta}} \frac{dV^\theta}{d\theta} \right| \ll |V^\theta|. \quad (3.12)$$

This condition applies regardless of the sign of  $V^\theta$ . Empirically, we find this condition to hold for  $V^\theta$  in Eq. (3.10a), except around points at which  $V^\theta = 0$ . We will refer to these as *turning points*, and they can be found by solving for the zeros of the potential,

$$a^2\omega_R^2 \cos^2\theta \sin^2\theta - m^2 + A_{lm}^R \sin^2\theta = 0, \quad (3.13)$$

which are given by

$$\sin^2 \theta_{\pm} = \frac{2m^2}{A_{lm} + a^2 \omega_{lm}^2 + \sqrt{(A_{lm} + a^2 \omega_{lm}^2)^2 + 4m^2}}, \quad (3.14)$$

where we only keep the physical solution and assume  $0 < \theta_- < \pi/2$ . It is obvious that  $\theta_+ = \pi - \theta_-$ . Using the leading and next-to-leading WKB approximation, we can write the solution to the wave equation in the propagative region,  $x_- < x < x_+$ , as

$$u_{\theta}(x) = \frac{a_+ e^{i \int_0^x dx' \sqrt{V^{\theta}(x')}} + a_- e^{-i \int_0^x dx' \sqrt{V^{\theta}(x')}}}{[V^{\theta}(x)]^{1/4}}, \quad (3.15)$$

where  $a_{\pm}$  are constants that must be fixed by the boundary conditions that the solution approaches zero at  $\theta = 0, \pi$ . For  $x > x_+$ , we find

$$u_{\theta}(x) = \frac{c_+ e^{-\int_{x_+}^x dx' \sqrt{-V^{\theta}(x')}}}{[V^{\theta}(x)]^{1/4}}, \quad (3.16a)$$

and  $x < x_-$ ,

$$u_{\theta}(x) = \frac{c_- e^{-\int_x^{x_-} dx' \sqrt{-V^{\theta}(x')}}}{[V^{\theta}(x)]^{1/4}}, \quad (3.16b)$$

with  $c_{\pm}$  also being constants set by the boundary conditions. Note that outside of the turning points, we have only allowed the solution that decays towards  $x \rightarrow \pm\infty$ .

Around the turning points  $x_{\pm}$ , the WKB approximation breaks down, but  $u_{\theta}$  can be solved separately by using the fact that  $V_{\theta}(x \sim x_{\pm}) \propto x - x_{\pm}$ . Solutions obtained in these regions can be matched to Eqs. (3.15)–(3.16b); the matching condition leads to the Bohr-Sommerfeld quantization condition [43]

$$\int_{\theta_-}^{\theta_+} d\theta \sqrt{a^2 \omega_R^2 \cos^2 \theta - \frac{m^2}{\sin^2 \theta} + A_{lm}^R} = (L - |m|) \pi. \quad (3.17)$$

Here we have defined

$$L \equiv l + \frac{1}{2}, \quad (3.18)$$

which will be used frequently throughout this paper. The limits of the integration are the values of  $\theta$  where the integrand vanishes [the turning points of Eq. (3.14)].

If we define

$$\mu \equiv \frac{m}{L}, \quad \alpha_R(a, \mu) \equiv \frac{A_{lm}^R}{L^2}, \quad \Omega_R(a, \mu) \equiv \frac{\omega_R}{L}, \quad (3.19)$$

then all three of these quantities are  $O(1)$  in our expansion in  $L$ . From these definitions, we can re-express the limits of integration as

$$\sin^2 \theta_{\pm} = \frac{2\mu^2}{\alpha + a^2 \Omega^2 + \sqrt{(\alpha + a^2 \Omega_R^2)^2 + 4\mu^2}}, \quad (3.20)$$

and the integral as

$$\int_{\theta_-}^{\theta_+} d\theta \sqrt{\alpha_R - \frac{\mu^2}{\sin^2 \theta} + a^2 \Omega^2 \cos^2 \theta} = (1 - |\mu|)\pi. \quad (3.21)$$

For each set of quantities  $(\alpha_R, \mu, \Omega_R)$ , we can express  $\alpha_R$  as an implicit function involving elliptic integrals; however, if we treat  $a\Omega_R$  as a small parameter, then the first two terms in the expansion are

$$\alpha_R \approx 1 - \frac{a^2 \Omega_R^2}{2} (1 - \mu^2). \quad (3.22)$$

We derive and discuss this approximation in greater detail in Appendix 3.A. Higher order corrections are on the order of  $(a\Omega_R)^4$ . For  $a = 0$ , we note that this is accurate with a relative error of  $O(1/L^2)$ , because for a Schwarzschild black hole

$$A_{lm}^{\text{Schw}} = l(l+1) - s(s+1). \quad (3.23)$$

As we will confirm later in Figure 3.2, Eq. (3.22) is an excellent approximation even for highly spinning black holes.

To understand intuitively why the approximation works so well, we will focus on corotating modes (i.e., those with positive and large  $m$ , or  $\mu$  near unity), which have the highest frequencies and, therefore, the largest possible values for  $a\Omega_R$ . For a fixed value of  $(l, m)$ ,  $\omega_R$  is a monotonically increasing function of  $a$ , and

$$\omega_R^{lm}(a) \leq \omega_R^{lm}(a = M) = m\Omega_H^{a=1} = \frac{m}{2M}. \quad (3.24)$$

In setting this upper bound, we have used the result that the low-overtone QNM frequencies approach  $m\Omega_H$  for  $m > 0$  and for extremal black holes (first discussed by Detweiler [44], and discussed further by, e.g. [45, 46]); we have also used  $\Omega_H$  to denote the horizon frequency of the Kerr black hole,

$$\Omega_H = \frac{a}{2Mr_+}, \quad (3.25)$$

and  $r_+$  to indicate the position of the horizon [note that  $r_+(a = M) = M$ ]. Normalizing Eq. (3.24) by  $L$ , we find

$$a\Omega_R \leq (\mu/2)(a/M) \leq 1/2. \quad (3.26)$$

Even for the upper bound  $a\Omega_R = 1/2$ , as can be checked numerically against Eq. (3.21), the relative accuracy of Eq. (3.22) is still better than 0.2%.

### 3.2.2.2 Complex $A_{lm}$ for a Complex $\omega$

To solve for the next-to-leading-order corrections to  $A_{lm}$ , we must compute the imaginary part  $A_{lm}^I$ . Because  $\omega_I \ll \omega_R$ , when we allow  $\omega = \omega_R - i\omega_I$  to be a complex number in the angular eigenvalue problem (3.7), we can treat the term linear in  $\omega_I$  as a perturbation to the angular equation. Using the perturbation theory of eigenvalue equations, we find that

$$A_{lm}^I = -2a^2\omega_R\omega_I\langle\cos^2\theta\rangle, \quad (3.27)$$

where

$$\langle\cos^2\theta\rangle = \frac{\int \cos^2\theta|u_\theta|^2 \sin\theta d\theta}{\int |u_\theta|^2 \sin\theta d\theta} = \frac{\int_{\theta_-}^{\theta_+} \frac{\cos^2\theta}{\sqrt{a^2\omega_R^2 \cos^2\theta - \frac{m^2}{\sin^2\theta} + A_{lm}^R}} d\theta}{\int_{\theta_-}^{\theta_+} \frac{1}{\sqrt{a^2\omega_R^2 \cos^2\theta - \frac{m^2}{\sin^2\theta} + A_{lm}^R}} d\theta}. \quad (3.28)$$

By taking the derivative of both sides of the Bohr-Sommerfeld condition (3.17) with respect to the variable  $z = a\omega_R$  and by treating  $A_{lm}$  as a function of  $z$ , we can rewrite the above expression as

$$\langle\cos^2\theta\rangle = -\frac{1}{2z} \left. \frac{\partial A_{lm}^R(z)}{\partial z} \right|_{z=a\omega_R}. \quad (3.29)$$

Substituting this expectation value into Eq. (3.27), we find

$$A_{lm}^I = a\omega_I \left[ \frac{\partial A_{lm}^R(z)}{\partial z} \right]_{z=a\omega_R}. \quad (3.30)$$

Equation (3.30) defines a numerical prescription for computing  $A_{lm} = A_{lm}^R + iA_{lm}^I$ . This approach is quite natural: as  $\omega$  becomes complex,  $A_{lm}$  is the analytic function whose value on the real axis is given by  $A_{lm}^R$ . The approximate formula (3.22), therefore, becomes

$$A_{lm} \approx L^2 - \frac{a^2\omega^2}{2} \left[ 1 - \frac{m^2}{L^2} \right], \quad (3.31a)$$

or

$$\alpha \approx 1 - \frac{a^2\Omega^2}{2} (1 - \mu^2), \quad (3.31b)$$

for a complex frequency  $\omega$ , where we have defined  $\Omega$  to be  $\omega/L$ .

### 3.2.3 The Radial Eigenvalue Problem

Now that we have solved for the angular eigenvalues  $A_{lm}$  in terms of  $\omega$ , we turn to the radial Teukolsky equation. From Eq. (4.4a), we see that the radial equation is already in the form

$$\frac{d^2 u_r}{dr_*^2} + V^r u_r = 0, \quad (3.32a)$$

if we define

$$V^r(r, \omega) = \frac{[\omega(r^2 + a^2) - ma]^2 - \Delta [A_{lm}(a\omega) + a^2\omega^2 - 2ma\omega]}{(r^2 + a^2)^2}. \quad (3.32b)$$

Note here that  $V^r$  is an analytic function of  $\omega$ , and that it is real-valued when  $\omega$  is real.

In general, the WKB approximant for  $u_r$  is given at leading order by

$$u_r = b_+ e^{i \int^{r_*} \sqrt{V^r(r'_*)} dr'_*} + b_- e^{-i \int^{r_*} \sqrt{V^r(r'_*)} dr'_*}, \quad (3.33)$$

although in order to obtain a mode which is outgoing at  $r_* \rightarrow +\infty$  (the same as  $r \rightarrow \infty$ ) and ingoing at  $r_* \rightarrow -\infty$  ( $r \rightarrow r_+$ ), we must have

$$u_r = b_+ e^{i \int^{r_*} \sqrt{V^r(r'_*)} dr'_*}, \quad (3.34a)$$

for the region containing  $r \rightarrow +\infty$ , and

$$u_r = b_- e^{-i \int^{r_*} \sqrt{V^r(r'_*)} dr'_*}, \quad (3.34b)$$

for the region containing  $r_* \rightarrow -\infty$ . Intuitively speaking, a solution to Eq. (3.32a) will satisfy the asymptotic behavior above if  $V^r \approx 0$  around a point  $r = r_0$ , and  $V_r > 0$  on both sides. Then, the WKB expansion (3.33) is valid in the two regions on both sides of  $r = r_0$ , and the solution in the vicinity of  $r_0$  must be obtained separately by matching to the WKB approximation. The matching will constrain the frequency, thereby giving a method to determine  $\omega$ . A detailed calculation of this procedure has been carried out by Iyer and Will [11] to high orders in the WKB approximation; the only difference between our calculation and their result at lower orders comes from the more complex dependence of  $V^r$  on  $\omega$  in our case (particularly because  $A_{lm}$  depends on  $\omega$  in a more involved way).

#### 3.2.3.1 Computing $\omega_R$

From Iyer and Will [11], the conditions at the leading and next-to-leading order that must be solved to find  $\omega_R$  are

$$V^r(r_0, \omega_R) = \left. \frac{\partial V^r}{\partial r} \right|_{(r_0, \omega_R)} = 0. \quad (3.35)$$

After a short calculation, these conditions can be expressed as

$$\Omega_R = \frac{\mu a}{r_0^2 + a^2} \pm \frac{\sqrt{\Delta(r_0)}}{r_0^2 + a^2} \beta(a\Omega_R), \quad (3.36a)$$

$$0 = \frac{\partial}{\partial r} \left[ \frac{\Omega_R(r^2 + a^2) - \mu a}{\sqrt{\Delta(r)}} \right]_{r=r_0}, \quad (3.36b)$$

where we have defined

$$\beta(z) = \sqrt{\alpha(z) + z^2 - 2\mu z} \approx \sqrt{1 + \frac{z^2}{2} - 2\mu z + \frac{\mu^2 z^2}{2}}. \quad (3.37a)$$

In deriving Eq. (3.36b), we have used the fact that at  $r > r_+$ ,  $(r^2 + a^2)^2/\Delta$  is a monotonically increasing function, and, therefore the extrema of  $V^r$  are the same as those of  $V^r(r^2 + a^2)^2/\Delta$ ; we then also used the fact that the quantity within the square brackets in Eq. (3.36b) is always nonzero at points at which  $V^r = 0$ .

One method of jointly solving Eqs. (3.36a) and (3.36b) would be to use Eq. (3.36b) to express  $\Omega_R$  in terms of  $r_0$

$$\Omega_R = \frac{(M - r_0)\mu a}{(r_0 - 3M)r_0^2 + (r_0 + M)a^2}, \quad (3.38)$$

and then insert this into Eq. (3.36a) to obtain  $r_0$ ; finally  $\Omega_R$  can be obtained by substituting this  $r_0$  back into Eq. (3.38). If we use the approximate formula (3.37a) in this process, the equation for  $r_0$  becomes a sixth-order polynomial in  $x = r_0/M$ , the roots of which can be found efficiently. For convenience, we write this polynomial here

$$\begin{aligned} & 2x^4(x - 3)^2 + 4x^2[(1 - \mu^2)x^2 - 2x - 3(1 - \mu^2)](a/M)^2 \\ & + (1 - \mu^2)[(2 - \mu^2)x^2 + 2(2 + \mu^2)x + (2 - \mu^2)](a/M)^4. \end{aligned} \quad (3.39)$$

For each pair  $(\mu, a/M)$ , there are in general two real roots for  $x$ , which correspond to the two possible values of  $r_0/M$  (and the two real frequencies with opposite signs).

Note that the procedure above will not work when  $m = 0$  (when both the numerator and denominator of Eq. (3.38) vanish). In this case, we can directly require that

$$(r_p - 3M)r_p^2 + (r_p + M)a^2 = 0. \quad (3.40)$$

The solution,  $r_p$ , can be found in closed form [29, 47]. Inserting it into Eq. (3.36a), the result can be expressed in terms of elliptic integrals

$$\Omega_R(a, \mu = 0) = \pm \frac{1}{2} \frac{\pi \sqrt{\Delta(r_p)}}{(r_p^2 + a^2) \text{EllipE} \left[ \frac{a^2 \Delta(r_p)}{(r_p^2 + a^2)^2} \right]}, \quad (3.41)$$

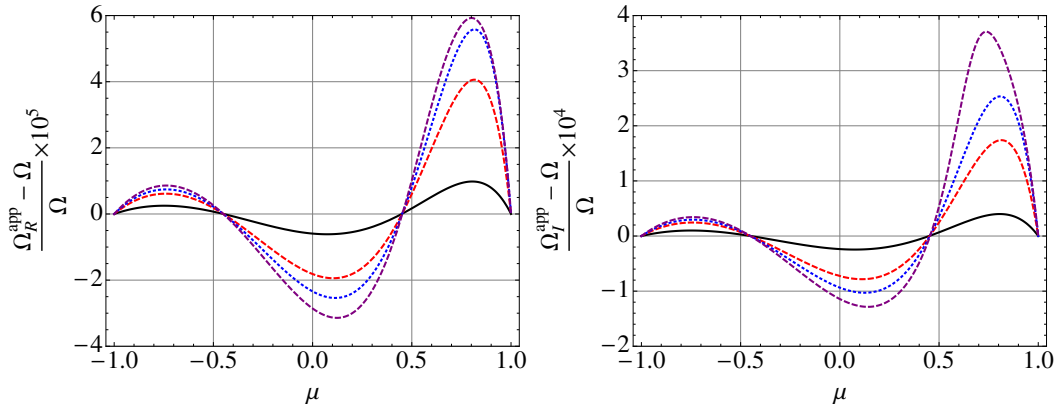


Figure 3.2: Left: Difference in  $\Omega_R(a, \mu)$  [Eq. (3.38)] that arises from using the approximate formula for  $A_{lm}$  [Eq. (3.31a)] as opposed to the exact formula. Here  $a/M = 0.7, 0.9, 0.95,$  and  $0.99$  correspond to black solid, red dashed, blue dotted, and purple long-dashed curves, respectively. The quantity plotted on the vertical axis has been scaled by  $10^5$ . Right: Difference in  $\Omega_I(a, \mu)$  [Eq. (3.42)] from using the approximate formula for  $A_{lm}$  [Eq. (3.31a)] rather than the exact formula. The same spins and conventions are used as in the right panel. We scale the quantity plotted along the vertical axis by  $10^4$  in this figure.

where  $\text{EllipE}$  denotes an elliptic integral of the second kind. Here we have used the subscript  $p$  for this special case, because this mode will turn out to correspond to polar orbits. Note this formula agrees with the one derived in [29].

We plot in Figure 3.2 the relative error in  $\Omega_R$  that comes from using the approximate expression for  $A_{lm}$  [Eq. (3.31a)] rather than the exact Bohr-Sommerfeld condition. The error is always less than  $\sim 10^{-4}$  (we scale the quantity plotted on the vertical axis by  $10^5$ ), and therefore, we will use the approximate expression for  $A_{lm}$  for the remaining calculations involving  $\Omega_R$  throughout this paper. In Figure 3.3, we plot  $\Omega_R$  for  $a/M = 0, 0.3, 0.5, 0.9, 0.99,$  and  $1$  (the flat curve corresponds to  $a/M = 0$ , and those with increasing slopes are the increasing values of  $a/M$ ). While for low values of  $a/M$  below  $\sim 0.5$ ,  $\Omega_R$  depends roughly linearly upon  $\mu$ , for higher values of  $a/M$  (and for  $\mu > 0$ ),  $\Omega_R$  grows more rapidly than linearly. For  $a/M = 1$ ,  $\Omega_R \rightarrow 1/2$  when  $\mu \rightarrow 1$ , as anticipated.

### 3.2.3.2 Computing $\omega_I$

At leading order, the imaginary part  $\omega_I$  can be calculated using the same procedure set forth by Iyer and Will [11]. They find that

$$\begin{aligned} \omega_I &= -(n+1/2) \frac{\sqrt{2 \left( \frac{d^2 V^r}{dr_*^2} \right)_{r_0, \omega_R}}}{\left( \frac{\partial V^r}{\partial \omega} \right)_{r_0, \omega_R}}, \\ &= -(n+1/2) \Omega_I(a, \mu). \end{aligned} \tag{3.42}$$

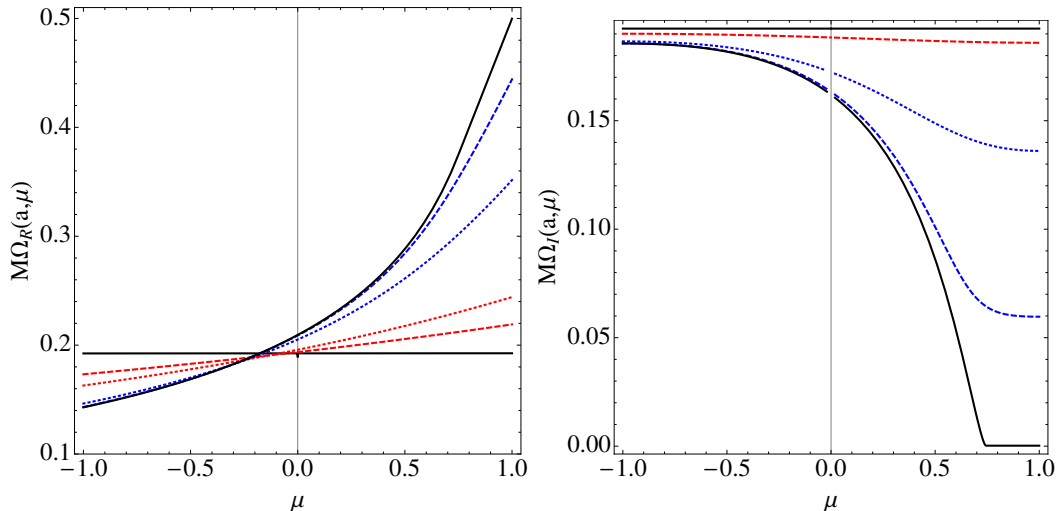


Figure 3.3: Real and imaginary parts of the QNM spectra from the WKB approximation. Left: Black solid curves show  $\Omega_R$  for  $a/M = 0$  (the flat curve) and  $a/M = 1$  (the curve that increases towards 0.5); red (light gray) dashed and dotted curves show  $a/M = 0.3$  and  $0.5$ , while blue (dark gray) dotted and dashed curves show  $a/M = 0.9$  and  $0.99$ . Right: Black solid curves show  $\Omega_I$  for  $a/M = 0$  (again the flat curve) and  $a/M = 1$  the curve that decreases and heads to zero. The red dashed curve shows  $a/M = 0.5$ , while blue dotted and dashed curves show  $a/M = 0.9$  and  $0.99$ , respectively. For  $a/M = 1$ , modes with  $\mu \gtrsim 0.74$  approach zero (modes that do not decay), while others still decay.

In our calculation, we must also take into account that  $V^r$  also depends on  $\omega$  through the angular eigenvalue's dependence on  $\omega$ . If we use the approximate formula for  $\alpha$ , we obtain a reasonably compact expression for  $\Omega_I$ :

$$\Omega_I = \Delta(r_0) \frac{\sqrt{4(6r_0^2\Omega_R^2 - 1) + 2a^2\Omega_R^2(3 - \mu^2)}}{2r_0^4\Omega_R - 4aMr_0\mu + a^2r_0\Omega_R[r_0(3 - \mu^2) + 2M(1 + \mu^2)] + a^4\Omega_R(1 - \mu^2)}. \quad (3.43)$$

In Figure 3.2, we plot the relative error in  $\Omega_I$  from using the approximate formula for  $A_{lm}$  identically to the way in which it is used in Figure 3.2 (although here we scale the quantity plotted on the vertical axis by  $10^4$ ). Because the error is always less than  $\sim 10^{-3}$ , we will use the approximate expression for  $A_{lm}$  for computing  $\Omega_I$  in the remainder of this paper. In [29], an alternate expression for  $\omega_I$  (for  $m = 0$ ) was computed by finding an analytic expression for the *Lyapunov exponent* (see Section 3.3.3.2, where we discuss the exponent's connection to the QNM's decay rate); this expression gives the same result as (3.43) for  $\mu = 0$  to a high accuracy. In Figure 3.3, we plot  $\Omega_I(a, \mu)$  for several values of  $a/M$  (the same as those in Figure 3.3, though not  $a/M = 0.3$ ). The curve for  $a/M = 0$  is flat, and those with larger spins have more rapidly decreasing slopes for increasing values of  $a/M$ . It is interesting to note that in the limit  $a \rightarrow 1$ ,  $\Omega_I$  becomes zero for values of  $\mu$  in a finite interval  $0.74 \lesssim \mu \leq 1$  (not only for  $\mu = 1$  does  $\Omega_I$  vanish). We will put forward an explanation for this phenomenon in Section 3.4, after we make connections between QNMs and wave propagation in

the Kerr spacetime.

The vanishing of the QNM's decay rate for extremal black holes has been discussed by many authors in the past. Detweiler [44] first showed that modes with  $l = m$  had vanishing decay. Mashhoon [48] extended the work of Goebel [37] to Kerr-Newman black holes when he calculated the frequency and Lyapunov exponent of equatorial unstable photon orbits. He found that for extremal Kerr-Newman holes (which have  $M^2 = a^2 + Q^2$ , with  $Q$  the charge of the hole) when  $a \geq M/2$ , the Lyapunov exponent vanished, by analogy with the vanishing decay for  $\mu \gtrsim 0.74$  discussed above. For QNMs of a massive scalar field around an extremal Kerr black hole, Hod [49] found that the modes have vanishing damping when the mass of the scalar field is smaller than a critical value. Berti and Kokkotas [50] numerically calculated QNM frequencies for Kerr-Newman black holes using continued fractions, and found good agreement with Mashhoon's result for  $l = m = 2$ ,  $s = 2$  modes (i.e., for extremal holes there was zero decay). Cardoso [45] explored Detweiler's calculation of the decay of extremal modes, and could show that some but not all modes with  $m \neq l$  and  $m > 0$  have vanishing decay rates. Hod also extended Detweiler's calculation to  $m \geq 0$  and found that all such modes have zero decay in the extremal Kerr case [46], in contrast to our findings. Hod also computed QNM frequencies and decays for eikonal QNMs in the extremal Kerr limit [51] and found agreement with Mashhoon's result. In the end, the particular value of  $m$  at which the QNM mode decay rate for an extremal black hole vanishes is not a settled issue; our results here indicate that for  $L \gg 1$ , only some subset of the  $m > 0$  modes have vanishing decay rates.

### 3.2.4 Accuracy of the WKB Approximation

Because we calculated the leading and next-to-leading orders in the WKB approximation to  $\omega_R$ , we expect that the relative error for increasing  $L$  should scale as  $O(1/L^2)$ . For the imaginary part, we computed only the leading-order expression, and we would expect that the relative error might scale as  $O(1/L)$ . In addition, because at this order of approximation we do not account for the spin of the wave, we anticipate that the error for the gravitational modes may be larger than those for scalar modes. In Figures 3.4–3.7, we confirm most of these expectations, but we find the somewhat unexpected result that the relative error for the imaginary part also scales as  $O(1/L^2)$ . In fact, this finding is consistent with Eqs. (52) and (53) of [29], where the next order contributions are calculated for the special cases of  $m = l$  and  $m = -l$  respectively.

In Figure 3.4, we compare the WKB approximation to  $\omega_R$  with numerical computations of the  $s = 2$ , gravitational-wave, quasinormal-mode spectra; specifically, we plot the fractional error against  $\mu = m/L$ , for  $l = 2, 3, \dots, 14$ , and for black holes of spins  $a/M = 0.3, 0.5, 0.9$ , and  $0.95$ . The relative error clearly converges to  $O(L^2)$ . Even for  $l = 2$ , the relative error tends to be  $\lesssim 30\%$ , and at  $l \geq 3$  the relative error stays below  $\sim 1.5L^{-2}$  (this means error is  $\lesssim 10\%$  for  $l = 3$  and higher).

In Figure 3.5, we compare the WKB spectra with  $s = 0$  scalar quasinormal-mode spectra, for

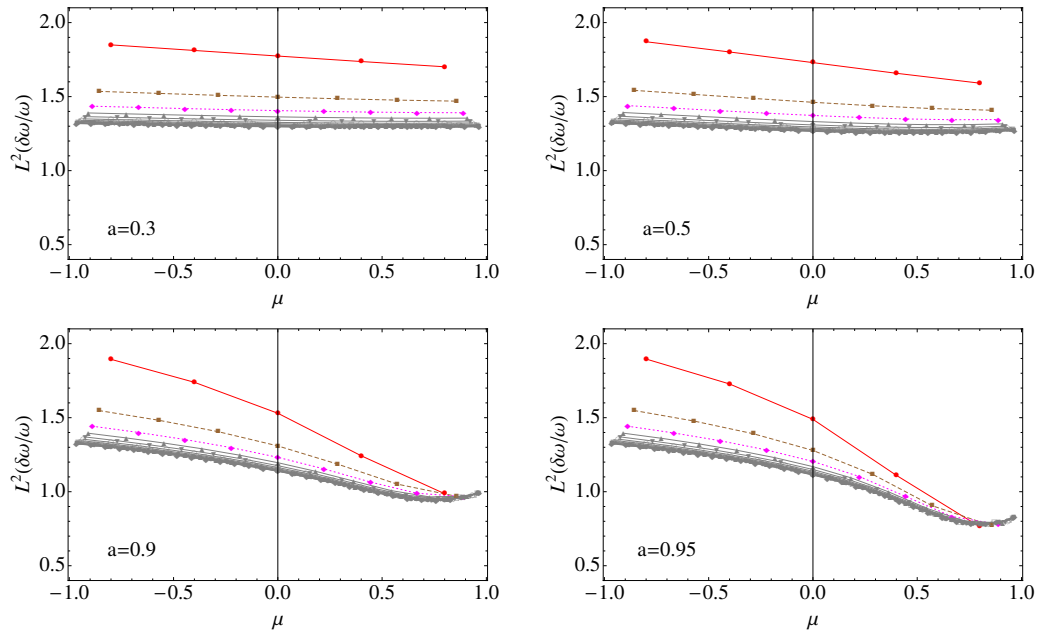


Figure 3.4: Fractional error,  $\delta\omega_R/\omega_R$ , of the WKB approximation to the  $s = 2$ , gravitational-wave, quasinormal-mode spectrum, multiplied by  $L^2$ . The four panels correspond to four different spins which (going clockwise from the top left) are  $a/M = 0.3, 0.5, 0.95$ , and  $0.9$ . Errors for  $l = 2, 3, 4$  are highlighted as red solid, brown dashed, and pink dotted lines, while the rest ( $l = 5, \dots, 14$ ) are shown in gray. This shows that the relative error approaches the  $O(1/L^2)$  scaling quite quickly.

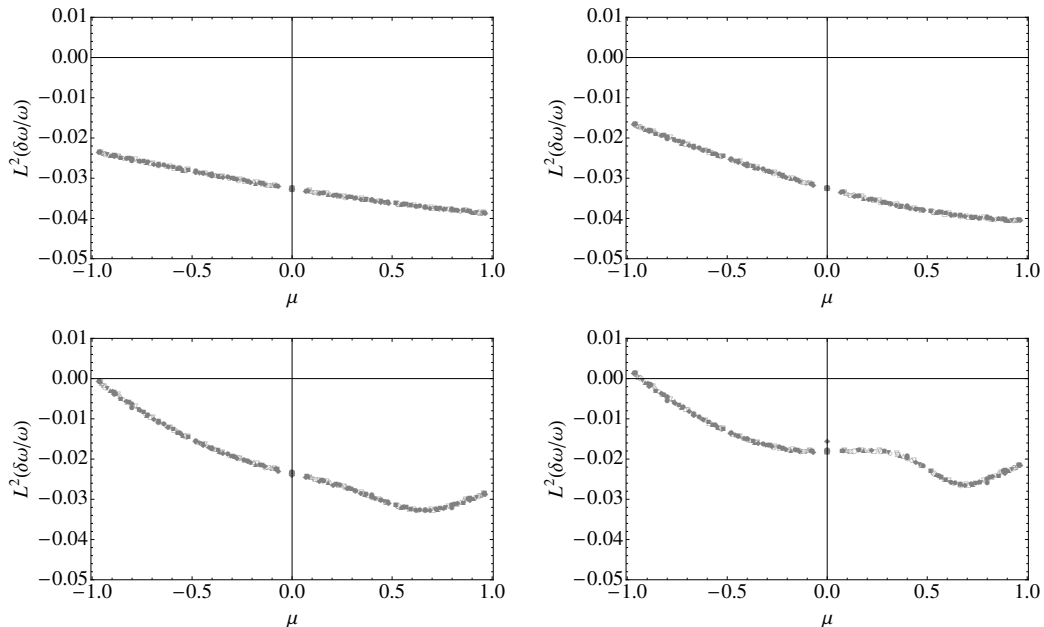


Figure 3.5: Fractional error,  $\delta\omega_R/\omega_R$ , of the WKB approximation to the  $s = 0$ , scalar-wave, quasinormal-mode spectrum, again scaled by  $L^2$ . The four panels correspond to the same four spins in Figure 3.4. The points shown in the four panels are for values of  $l$  in the range  $l = 2, 3, \dots, 14$ . Because all values of  $l$  nearly lie on the same curve, the relative error has converged at an order  $O(1/L^2)$  even for very low  $l$ . The overall error is also significantly lower than that for the  $s = 2$  modes.

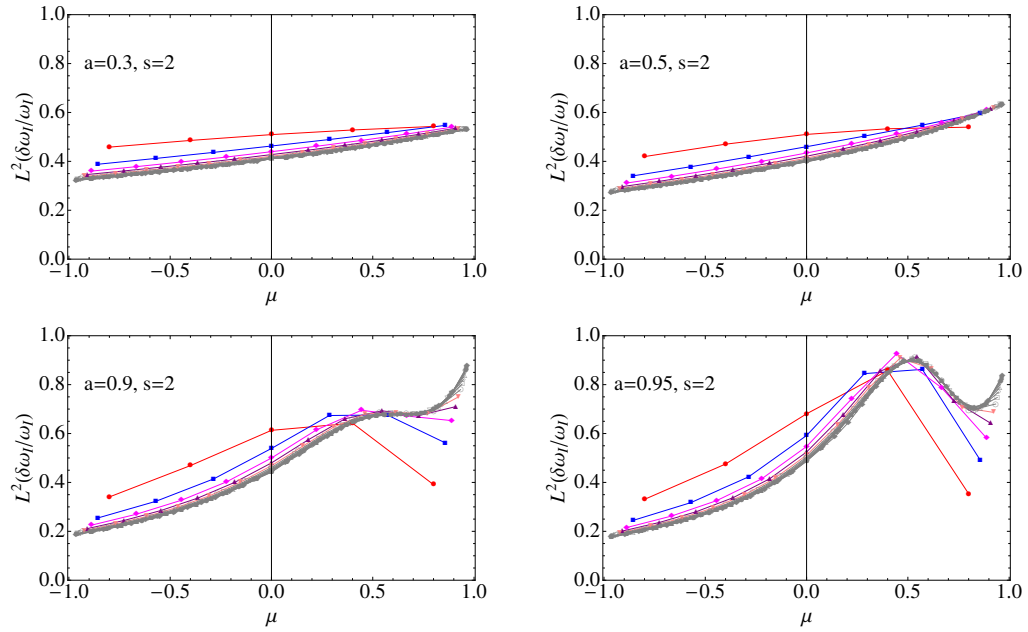


Figure 3.6: Fractional error,  $\delta\omega_I/\omega_I$ , of the WKB approximation to the  $s = 2$ , gravitational-wave, quasinormal-mode spectrum, also scaled by  $L^2$ . The panels and the curves are plotted in the same way as in Figure 3.4, and the error scales similarly.

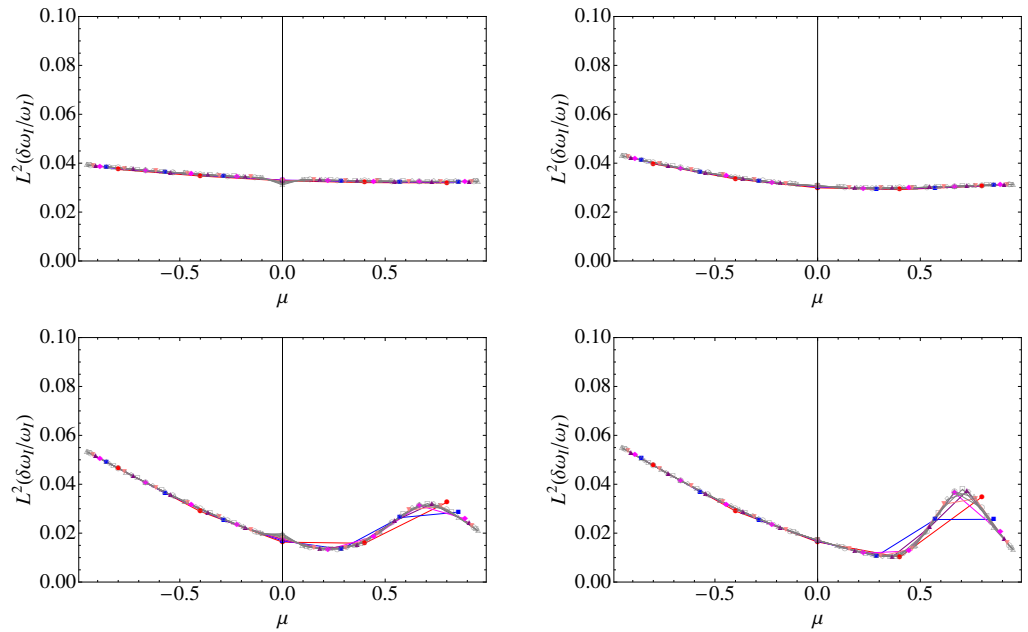


Figure 3.7: Fractional error,  $\delta\omega_I/\omega_I$ , of the WKB approximation to the  $s = 0$ , scalar-wave, quasinormal-mode spectrum, again multiplied by  $L^2$ . The four panels and the points are shown in the same way as in Figure 3.5, and there is a similar rapid convergence of the error.

the same values of  $l$  and the same black-hole spins. We find a much better agreement. For all  $l \geq 2$  modes, the relative error stays below  $4 \times 10^{-2} L^{-2}$ . This suggests that coupling between the spin of the wave (i.e., its tensor polarization) and the background curvature of the Kerr black hole is the main source of error in our WKB approximation.

In Figures 3.6 and 3.7, we perform the same comparisons as in Figures 3.4 and 3.5 for the imaginary part of frequency. Surprisingly, we find that for both  $s = 0$  and 2, the relative error in  $\omega_I$  is  $O(L^{-2})$ . For  $s = 0$ , the relative error is  $\lesssim 6 \times 10^{-2} L^{-2}$ , while for  $s = 2$ , the error is  $\lesssim L^{-2}$ .

With this comparison, we conclude our direct calculation of the QNM spectrum by WKB techniques. We will discuss additional features of the QNM spectrum in Section 3.4, but before doing so, we will develop a geometric interpretation of our WKB results. Doing so will help us to develop more intuition about our WKB expressions.

### 3.3 Geometric Optics in the Kerr Spacetime

In this section, we first briefly review the formalism of geometric optics, which describes the propagation of waves with reduced wavelengths  $\lambda$  that are much shorter than the spacetime radius of curvature,  $R$ , and the size of the phase front,  $\mathcal{L}$ . In the geometric-optics approximation, the phase of the waves remains constant along null geodesics (rays), while the amplitude can be expressed in terms of the expansion and contraction of the cross-sectional area of bundles of null rays. We will then specialize the geometric-optics formalism to the Kerr spacetime, and we will write down the most general form of propagating waves in the geometric-optics approximation. Using the Hamilton-Jacobi method, we see that the waves' motion can be related to the null geodesics in the spacetime. By applying boundary conditions to the approximate wave, we obtain expressions for the quasinormal-mode waveforms and their corresponding complex frequency spectra and angular separation constants, in the eikonal limit.

#### 3.3.1 Geometric Optics: General Theory

Here we briefly review the geometric-optics approximation to scalar-wave propagation (see, e.g., Section 22.5 of Reference [52] for details). A massless scalar wave  $u$  propagating in curved spacetime satisfies the wave equation

$$g^{\mu\nu} \nabla_\mu \nabla_\nu u = 0. \quad (3.44)$$

If we write

$$u = A e^{i\Phi}, \quad (3.45)$$

then at leading order in  $\lambda/\mathcal{L}$ , we have

$$g^{\mu\nu}k_\mu k_\nu = 0, \quad k_\mu \equiv \partial_\mu \Phi, \quad (3.46)$$

while at next-to-leading order,

$$2k^\mu \partial_\mu \log A + \nabla_\mu k^\mu = 0. \quad (3.47)$$

Note that Eq. (3.46) also implies that  $k^\mu$  is geodesic,

$$k^\mu \nabla_\mu k_\nu = k^\mu \nabla_\mu \nabla_\nu \Phi = k^\mu \nabla_\nu \nabla_\mu \Phi = k^\mu \nabla_\nu k_\mu = 0. \quad (3.48)$$

Equations (3.45)–(3.48) encode information about the transport of the amplitude  $A$  and phase  $\Phi$  along a null geodesic (or a *ray*). The phase should be kept constant, because Eq. (3.46) states

$$k^\mu \partial_\mu \Phi = 0, \quad (3.49)$$

while the amplitude is transported along the ray in a manner that depends upon the propagation of neighboring rays. Because the 2D area,  $\mathcal{A}$ , of a small bundle of null rays around the central ray satisfies the equation

$$\nabla_\mu k^\mu = k^\mu \partial_\mu \log \mathcal{A}, \quad (3.50)$$

it is possible to show from Eq. (3.47) that

$$k^\mu \partial_\mu (\mathcal{A}^{1/2} A) = 0, \quad (3.51)$$

which implies  $A \propto \mathcal{A}^{-1/2}$ .

The transport equations (3.49) and (3.51) provide a way to construct a wave solution from a single ray; therefore, any solution to the wave equation (3.44) in a 4D spacetime region can be found from a three-parameter family of null rays (with smoothly varying initial positions and wave vectors) by assigning smoothly varying initial values of  $(\Phi, A)$  and then transporting these values along the rays. (We use the phrase “smoothly varying” to mean that the values of  $(\Phi, A)$  must change on the scale of  $\mathcal{L} \gg \lambda$ .) We note it is often convenient to divide the three-parameter family of initial positions of the null rays into two-parameter families of rays with constant initial values of  $\Phi$ . The constant- $\Phi$  surfaces are the initial phase fronts, which, upon propagation along the rays, become 3D phase fronts of the globally defined wave. The more usual 2D phase fronts, at a given time, are obtained if we take a particular time slicing of the spacetime and find the 2D cross sections of the 3D phase fronts in this slicing.

The above formalism describes wave propagation up to next-to-leading order in  $\mathcal{L}/\lambda$ , which will

be enough for us to build a geometric correspondence for both the real frequency, the decay rate, and the angular separation constant of QNMs in the Kerr spacetime.

### 3.3.2 Null Geodesics in the Kerr Spacetime

Now let us review the description of null geodesics in the Kerr spacetime using the Hamilton-Jacobi formalism. In general, the Hamilton-Jacobi equation states

$$g^{\mu\nu}(\partial_\mu S)(\partial_\nu S) = 0, \quad (3.52)$$

where  $S(x^\mu)$  is called the *principal function*. For the Kerr spacetime, the Hamilton-Jacobi equation can be solved via separation of variables (see, e.g., [53]), through which the principal function can be expressed as

$$S(t, \theta, \phi, r) = S_\theta(\theta) + L_z \phi + S_r(r) - \mathcal{E}t, \quad (3.53)$$

where  $\mathcal{E}$  and  $L_z$  are constants that are conserved because of the the timelike and axial Killing vectors of the Kerr spacetime. Physically,  $\mathcal{E}$  and  $L_z$  represent the energy and  $z$ -directed specific angular momentum of the massless scalar particle. The functions  $S_r(r)$  and  $S_\theta(\theta)$  are given by

$$S_r(r) = \int^r \frac{\sqrt{\mathcal{R}(r')}}{\Delta(r')} dr', \quad S_\theta(\theta) = \int^\theta \sqrt{\Theta(\theta')} d\theta', \quad (3.54a)$$

where  $\mathcal{R}(r)$  and  $\Theta(\theta)$  are given by

$$\mathcal{R}(r) = [\mathcal{E}(r^2 + a^2) - L_z a]^2 - \Delta[(L_z - a\mathcal{E})^2 + \mathcal{Q}], \quad (3.54b)$$

$$\Theta(\theta) = \mathcal{Q} - \cos^2 \theta (L_z^2 / \sin^2 \theta - a^2 \mathcal{E}^2), \quad (3.54c)$$

and  $\Delta(r)$  is given in Eq. (4.4b). The constant  $\mathcal{Q}$  is the Carter constant of the trajectory, which is a third conserved quantity along geodesics in the Kerr spacetime.

The principal function  $S(x^\mu; \mathcal{E}, L_z, \mathcal{Q})$  contains information about all null geodesics; equations of motion for individual null geodesics are given by first choosing a particular set of  $(\mathcal{E}, L_z, \mathcal{Q})$ , and then imposing

$$\frac{\partial S}{\partial \mathcal{E}} = 0, \quad \frac{\partial S}{\partial L_z} = 0, \quad \frac{\partial S}{\partial \mathcal{Q}} = 0. \quad (3.55)$$

These conditions lead to a set of first-order differential equations

$$\frac{dt}{d\lambda} = \frac{r^2 + a^2}{\Delta} [\mathcal{E}(r^2 + a^2) - L_z a] - a(a\mathcal{E} \sin^2 \theta - L_z), \quad (3.56a)$$

$$\frac{d\phi}{d\lambda} = - \left( a\mathcal{E} - \frac{L_z}{\sin^2 \theta} \right) + \frac{a [\mathcal{E}(r^2 + a^2) - L_z a]}{\Delta}, \quad (3.56b)$$

Table 3.1: Geometric-optics correspondence between the parameters of a quasinormal mode, ( $\omega$ ,  $A_{lm}$ ,  $l$ , and  $m$ ), and the conserved quantities along geodesics, ( $\mathcal{E}$ ,  $L_z$ , and  $\mathcal{Q}$ ). To establish a correspondence with the next-to-leading-order, geometric-optics approximation, the geodesic quantities  $\mathcal{E}$  and  $\mathcal{Q}$  must be complex.

Wave Quantity	Ray Quantity	Interpretation
$\omega_R$	$\mathcal{E}$	Wave frequency is same as energy of null ray (determined by spherical photon orbit).
$m$	$L_z$	Azimuthal quantum number corresponds to $z$ angular momentum (quantized to get standing wave in $\phi$ direction).
$A_{lm}^R$	$\mathcal{Q} + L_z^2$	Real part of angular eigenvalue related to Carter constant (quantized to get standing wave in $\theta$ direction).
$\omega_I$	$\gamma = -\mathcal{E}_I$	Wave decay rate is proportional to Lyapunov exponent of rays neighboring the light sphere.
$A_{lm}^I$	$\mathcal{Q}_I$	Nonzero because $\omega_I \neq 0$ (see Sections 3.2.2.2 and 3.3.3.3 for further discussion).

$$\frac{dr}{d\lambda} = \sqrt{\mathcal{R}}, \quad \frac{d\theta}{d\lambda} = \sqrt{\Theta}, \quad (3.56c)$$

where we have defined

$$\frac{d}{d\lambda} \equiv \Sigma \frac{d}{d\zeta}, \quad \Sigma = r^2 + a^2 \cos^2 \theta, \quad (3.57)$$

and  $\zeta$  is an affine parameter along the null geodesics.

### 3.3.3 Correspondence with Quasinormal Modes

Here we will find connection between the general set of wave solutions in the previous section, and the particular solutions that correspond to a quasinormal modes, in the geometric-optics limit. Specifically, we will look for waves that propagate outwards at infinity and down the horizon. With this correspondence, we will be able to make a geometric interpretation of our WKB results from Section 3.2.

#### 3.3.3.1 Leading Order: Conserved Quantities of Rays and the Real parts P of Quasinormal-Mode Parameters

It is straightforward to note that the Hamilton-Jacobi equation (3.52) is identical to the leading-order geometric-optics equations, if we identify the phase,  $\Phi$ , with the principal function,  $S$ . Therefore, at leading order, we can write

$$u = e^{iS} = e^{-i\mathcal{E}t} e^{iL_z\phi} e^{\pm iS_\theta} e^{\pm iS_r}, \quad (3.58)$$

where we recall that the amplitude  $A$  differs from unity only at next-to-leading order (we will treat it in the following subsections). Here, we have a chosen set of conserved quantities, ( $\mathcal{E}$ ,  $\mathcal{Q}$ ,  $L_z$ ), to

identify the wave we wish to connect with a quasinormal-mode solution. The region in which the wave propagates is identical to the region in which geodesics with these conserved quantities can propagate. In addition, for each point in this region, there is one (and only one) geodesic passing through it; that we have  $\pm$  in front of  $S_\theta$  and  $S_r$  means only that either propagation direction could be a solution to the wave equation.

Now we note that  $u$ , a scalar wave in the Kerr spacetime, must separate as in Eq. (3.6). By comparing Eq. (3.6) and Eq. (3.58), we can immediately identify that

$$\mathcal{E} = \omega_R. \quad (3.59)$$

Because  $\mathcal{E}$  is a real quantity (the conserved energy of the null geodesic), we see that at leading order, the wave does not decay. Next, we also observe that in order for  $u$  to be consistently defined in the azimuthal direction,  $L_z$  (of the null geodesics that  $S$  describes) must be an integer. This allows us to make the second identification

$$L_z = m. \quad (3.60)$$

Comparing  $S_\theta$  from Eq. (3.54a) and  $u_\theta$  from Eqs. (3.15) and (3.10b) (focusing on one direction of  $\theta$  propagation, and ignoring next-to-leading-order terms), we can also conclude that

$$\mathcal{Q} = A_{lm}^R - m^2. \quad (3.61)$$

At this stage, given any set of  $(\mathcal{E}, \mathcal{Q}, L_z)$ , we will be able to find a wave solution that exists in the region in which the geodesics travel. Not all such sets of conserved quantities correspond to quasinormal modes, however, because they may not satisfy the correct boundary conditions of QNMs.

We will first explain the conditions on the radial motion of the geodesics that will allow these particular geodesics to correspond to a wave that satisfies outgoing and downgoing conditions at  $r_* \rightarrow \pm\infty$ , respectively. If the radial geodesics satisfy  $\mathcal{R} > 0$  everywhere, then there will be traveling waves across the entire  $r_*$  axis, which will not satisfy the boundary conditions; if there are two disconnected regions of traveling waves, however, waves will scatter off the potential on each side, and they will also fail to satisfy the boundary conditions. The only way to satisfy the boundary conditions is to have a point  $r_0$  at which  $\mathcal{R} = 0$  and  $\mathcal{R}' = 0$ , in which case there will be a family of geodesics on each side of  $r = r_0$  (with each member a *homoclinic orbit* which has  $r \rightarrow r_0$  on one end) and a *spherical orbit* with constant  $r = r_0$ . The corresponding wave has zero radial spatial frequency at  $r = r_0$ , and this frequency increases towards  $r < r_0$  and decreases towards  $r > r_0$ . Noting that

$$\mathcal{R} = V^r (r^2 + a^2)^2, \quad (3.62)$$

the condition

$$\mathcal{R} = \mathcal{R}' = 0 \tag{3.63}$$

is the same as the condition, Eq. (3.35), which determines  $\omega_R$  in terms of  $L$  and  $m$  in the WKB approximation. It is worth mentioning that although the condition of Eq. (3.63) imposed on  $(\mathcal{E}, \mathcal{Q}, L_z)$  can be interpreted most easily as the condition for a spherical photon orbit, the wave function for the quasinormal mode we are considering is *not* localized around that orbit. The wave function at leading order, in fact, has a constant magnitude at every location that homoclinic orbits reach (i.e., the entire  $r$  axis). We will derive the amplitude corrections in the next section.

The quantization of the frequency  $\omega_R$  in terms of the multipolar indices  $l$  and  $m$  arises from the quantization of the motion in the angular directions. For the azimuthal direction, it is easy to see that for the wave function to be single-valued, we need to impose  $L_z = m \in \mathbb{Z}$ . For the  $\theta$  direction, we note that

$$\Theta = V^\theta \sin^2 \theta, \tag{3.64}$$

and the  $\theta$ -quantization condition for the wave, Eq. (3.17), is

$$\int_{\theta_-}^{\theta_+} \sqrt{\Theta} d\theta = (L - |m|)\pi. \tag{3.65}$$

This corresponds to the Bohr-Sommerfeld condition for a particle moving in a potential given by  $\Theta$ . Consequently, the condition for a standing wave along the  $\theta$  direction (at leading order) is equivalent to

$$\mathcal{Q} = A_{lm}(\omega_R a) - m^2 \approx L^2 - m^2 - \frac{a^2 \omega_R^2}{2} \left[ 1 - \frac{m^2}{L^2} \right]. \tag{3.66}$$

In summary, we connected the QNM's wave function to the Hamilton-Jacobi principal function of homoclinic null geodesics (at leading order). These geodesics have the same energy, Carter constant, and  $z$ -component of its angular momentum as a spherical photon orbit; however only spherical orbits with *quantized* Carter constants and  $z$ -angular momenta correspond to quasinormal modes. In Table 3.1, we summarize our geometric-optics correspondence; so far we have identified the first three entries on the table. We can find the next two correspondences by investigating next-to-leading-order geometric optics in the next part.

### 3.3.3.2 Next-to-Leading Order: Radial Amplitude Corrections and the Imaginary Part of the Frequency

We showed in the previous part that the conserved quantities of a spherical photon orbit,  $(\mathcal{E}, \mathcal{Q}, L_z)$ , correspond simply to the real parts of the quasinormal-mode parameters,  $(\omega_R, A_{lm}^R, m)$ , which are

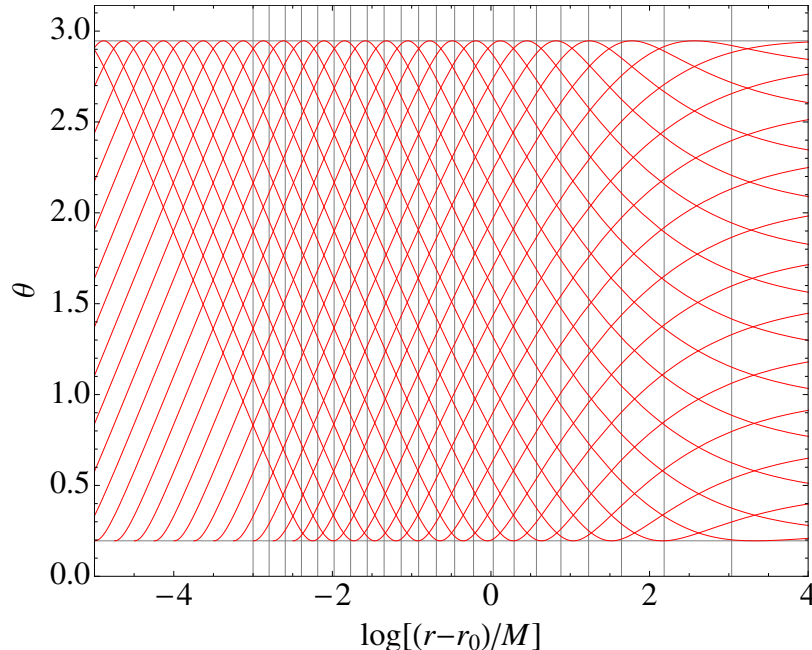


Figure 3.8: Schematic plot of trajectories in the  $r$ - $\theta$  plane of homoclinic orbits outside of the peak of the potential (specifically for a black hole with spin  $a/M = 0.7$  and a photon orbit with radius  $r_0/M = 2.584$ ). The two horizontal grid lines mark the turning points,  $\theta = \theta_{\pm}$ ; between these turning points, there are two homoclinic orbits passing through every point, while at turning points only one orbit passes through. Vertical grid lines indicate when the value of parameter  $\lambda$  has changed along the orbit by (an arbitrarily chosen value)  $\Delta\lambda = 0.046M$ . Near the spherical photon orbit, each homoclinic orbit undergoes an infinite number of periodic oscillations in  $\theta$  while  $r - r_0$  is growing exponentially as a function of  $\lambda$ .

the leading-order quantities of a quasinormal mode. Here, we will show that the behavior of the homoclinic orbits—namely, how the orbits propagate away from the spherical orbit, and how they move between  $\theta_{\pm}$ —reveals the spatiotemporal variation of the wave (i.e, the decay rate and the shape of its wave function in space). In Figure 3.8, we plot the trajectory of a particular series of homoclinic orbits on the  $r$ - $\theta$  plane, to which we will refer at several points in the discussion below.

With the appropriate values of  $(\mathcal{E}, \mathcal{Q}, L_z)$ , the function  $u$  in Eq. (3.58) solves the wave equation to leading order and satisfies the required boundary conditions. To recover the decaying behavior of quasinormal modes, however, we make corrections to the amplitude of the wave, which appear at next-to-leading order in the geometric-optics approximation. Because of symmetry, there should not be any correction to the amplitude in the  $\phi$  direction, and the correction in the  $t$  direction should be a simple decay; therefore, we write

$$u = A \exp(iS) = \underbrace{e^{-\gamma t} A_r(r) A_{\theta}(\theta)}_{A(t,r,\theta)} e^{-i\mathcal{E}t} e^{iL_z\phi} e^{\pm iS_{\theta}} e^{\pm iS_r}. \quad (3.67)$$

This general expression contains four possible directions in which the wave could be propagating:

the  $\pm\theta$  direction and the  $\pm r$  direction (depending on the signs in front of  $S_r$  and  $S_\theta$ ). Because the boundary conditions require that the waves propagate towards  $r_* \rightarrow +\infty$  for  $r > r_0$  and  $r_* \rightarrow -\infty$  for  $r < r_0$ , the sign in front of  $S_r$  should be positive for  $r > r_0$  and negative for  $r < r_0$ . For  $\theta$  motion, however, we insist that both directions (signs) be present, because a quasinormal mode is a standing wave in the  $\theta$  direction. Focusing on  $r > r_0$ , we write

$$u = e^{-\gamma t} A_r(r) [A_\theta^+ e^{iS_\theta} + A_\theta^- e^{-iS_\theta}] e^{-i\mathcal{E}t + iL_z\phi + iS_r} \equiv u_+ + u_- . \quad (3.68)$$

We will next require that both  $u_+$  and  $u_-$  satisfy the wave equation to next-to-leading order, separately. By explicitly computing Eq. (3.47) (or  $A\sqrt{\mathcal{A}} = \text{const}$ ) in the Kerr spacetime, we find the amplitude satisfies the relation

$$\Sigma \frac{d \log A}{d\zeta} = -\frac{1}{2} \left[ \partial_r (\Delta(r) \partial_r S_r) + \frac{1}{\sin \theta} \partial_\theta (\sin \theta \partial_\theta S_\theta) \right] . \quad (3.69)$$

Here  $\zeta$  is an affine parameter along the geodesic specified by  $(\mathcal{E}, \mathcal{Q}, \mathcal{L}_z)$ . If we use the parameter  $\lambda$  defined by  $d/d\lambda = \Sigma d/d\zeta$  then we can separate the left-hand side of the equation as

$$\Sigma \frac{d \log A}{d\zeta} = \frac{d}{d\lambda} \log A_r(r) + \frac{d}{d\lambda} \log A_\theta(\theta) - \gamma \frac{dt}{d\lambda} . \quad (3.70)$$

Because the right-hand side of Eq. (3.56a) for  $dt/d\lambda$ , separates into a piece that depends only upon  $r$  and one that depends only upon  $\theta$ , we will write Eq. (3.56a) schematically as

$$\frac{dt}{d\lambda} = \bar{t} + \tilde{t} , \quad (3.71)$$

where  $\bar{t}$  is only a function of  $r$  and  $\tilde{t}$  is only a function of  $\theta$ . Unlike in Eq. (3.56a), we will require that  $\tilde{t}$  average to zero when integrating over  $\lambda$  for half a period of motion in the  $\theta$  direction (i.e., from  $\theta_-$  to  $\theta_+$ ). We can ensure this condition is satisfied by subtracting an appropriate constant from  $\tilde{t}$  and adding it to  $\bar{t}$ . Combining Eqs. (3.69)–(3.71) and performing a separation of variables, we obtain

$$\sqrt{\mathcal{R}} \frac{d \log A_r}{dr} - \gamma \bar{t} = -\frac{\mathcal{R}'}{4\sqrt{\mathcal{R}}} , \quad (3.72a)$$

$$\sqrt{\Theta} \frac{d \log A_\theta^\pm}{d\theta} \mp \gamma \tilde{t} = -\frac{1}{2 \sin \theta} (\sqrt{\Theta} \sin \theta)' , \quad (3.72b)$$

where a prime denotes a derivative with respect to  $r$  for functions of  $r$  only, and a derivative with respect to  $\theta$  for functions of  $\theta$  only (whether it is a  $\theta$  or  $r$  derivative should be clear from the context). While it might at first seem possible to add a constant to the definition of  $\bar{t}$ , and subtract it from  $\tilde{t}$  and still have both  $u_+$  and  $u_-$  satisfy the next-to-leading order geometric optics, because we have

already chosen to have  $\bar{t}$  average to zero,

$$\int_{\theta_-}^{\theta_+} \gamma \bar{t} \frac{d\theta}{\sqrt{\Theta}} = \int \gamma \bar{t} d\lambda = 0, \quad (3.73)$$

this separation is the only way to guarantee that  $|A_\theta^\pm|$  match each other at both ends. We will discuss the angular wave function in greater detail in the next part of this section.

Let us now turn to the radial equation, from which we will be able to compute the decay rate. Close to  $r_0$ , we can expand  $\mathcal{R}(r)$  to leading order as

$$\mathcal{R}(r) \approx \frac{(r - r_0)^2}{2} \mathcal{R}''(r_0). \quad (3.74)$$

Substituting this result into Eq. (3.72a), we find

$$\frac{d \log A_r}{dr} = \frac{1}{r - r_0} \left[ \gamma \bar{t} \sqrt{\frac{2}{\mathcal{R}_0''}} - \frac{1}{2} \right], \quad (3.75)$$

where we used the notation  $\mathcal{R}_0'' \equiv \mathcal{R}''(r_0)$ . For  $A_r$  to be a function that scales as  $A_r \sim (r - r_0)^n$  around  $r_0$  for some integer  $n$  (namely it scales like a well-behaved function), we need to have

$$\gamma = \left( n + \frac{1}{2} \right) \frac{\sqrt{\mathcal{R}_0''/2}}{\bar{t}} = (n + 1/2) \lim_{r \rightarrow r_0} \frac{1}{r - r_0} \frac{dr/d\lambda}{\langle dt/d\lambda \rangle_\theta}. \quad (3.76)$$

To arrive at the second line, we used Eq. (3.74), the fact that  $dr/d\lambda = \sqrt{\mathcal{R}}$ , and that  $\bar{t}$  is the part of  $dt/d\lambda$  that does not vanish when averaging over one cycle of motion in the  $\theta$  direction; the limit in the expression comes from the fact that the approximation in Eq. (3.74) becomes more accurate as  $r \rightarrow r_0$ .

The physical interpretation of the rate that multiplies  $(n + 1/2)$  is somewhat subtle. Because the  $\theta$  motion is independent from  $r$  motion, a bundle of geodesics at the same  $r$  slightly larger than  $r_0$ , but at different locations in  $\theta$ , will return to their respective initial values of  $\theta$  with a slightly increased value of  $r$  after one period of motion in the  $\theta$  direction. The area of this bundle increases in the process, and by Eq. 3.51, the amplitude of the wave must decay; the rate of decay is governed by the quantity that multiplies  $(n + 1/2)$  in Eq. (3.76).

In addition, as shown in Figure 3.8, the homoclinic orbits do pass through an infinite number of such oscillations near  $r_0$ , because the radial motion is indefinitely slower than the  $\theta$  motion as  $r$  approaches  $r_0$ . It is clear from Figure 3.8 that

$$\frac{1}{r - r_0} \frac{\Delta r}{\Delta \lambda} = \frac{\Delta \log(r - r_0)}{\Delta \lambda} \quad (3.77)$$

approaches a constant as  $r \rightarrow r_0$ . By multiplying the above equation by the constant value of

$(\Delta\lambda)/(\Delta t)$  over one orbit of motion in the  $\theta$  direction,

$$\frac{1}{r-r_0} \frac{\Delta r}{\Delta t} = \frac{\Delta \log(r-r_0)}{\Delta t} \equiv \gamma_L \quad (3.78)$$

also approaches a constant. This is usually defined as the *Lyapunov exponent* of one-dimensional motion; here, however, we emphasize that it is defined only after averaging over entire cycle of  $\theta$  motion. By comparing Eq. (3.78) with the second line of Eq. (3.76), and bearing in mind that the Lyapunov exponent is defined after averaging over one period of  $\theta$  motion, one can write Eq. (3.76) as

$$\gamma = (n + \frac{1}{2})\gamma_L. \quad (3.79)$$

To put Eq. (3.76) into a form that relates more clearly to Eq. (3.42), we use the conditions on the phase function,

$$\frac{\partial S}{\partial \mathcal{E}} = 0, \quad \frac{\partial S}{\partial \mathcal{Q}} = 0, \quad (3.80)$$

which hold for any point on the trajectory of the particle. We will apply this condition to two points on the particle's trajectory: one at  $(t, r, \theta, \phi)$  and the second at  $(t + \Delta t, r + \Delta r, \theta, \phi + \Delta \phi)$ , where  $\Delta t$  is chosen such that the particle completes a cycle in  $\theta$  in this time (and it moves to a new location shifted  $\Delta r$  and  $\Delta \phi$ ). Substituting in the explicit expressions for the principal function in Eqs. (3.53) and (3.54a), we find

$$\frac{\partial}{\partial \mathcal{E}} \left[ \int_r^{r+\Delta r} \frac{\sqrt{\mathcal{R}(r')}}{\Delta(r')} dr' + \Delta S_\theta \right] = \Delta t \quad (3.81a)$$

$$\frac{\partial}{\partial \mathcal{Q}} \left[ \int_r^{r+\Delta r} \frac{\sqrt{\mathcal{R}(r')}}{\Delta(r')} dr' + \Delta S_\theta \right] = 0. \quad (3.81b)$$

where we have defined

$$\Delta S_\theta \equiv 2 \int_{\theta_-}^{\theta_+} \sqrt{\Theta(\theta')} d\theta' \equiv \oint \sqrt{\Theta(\theta')} d\theta'. \quad (3.82)$$

Because the change  $\Delta r$  is infinitesimal for  $r$  near  $r_0$ , the integrand is roughly constant, and the  $r$ -dependent part of the integral becomes the product of the integrand with  $\Delta r$ . Then, one can use Eq. (3.74) to write Eqs. (3.81a) and (3.81b) as

$$\frac{1}{\sqrt{2\mathcal{R}_0''\Delta_0}} \frac{\partial \mathcal{R}}{\partial \mathcal{E}} \frac{\Delta r}{r-r_0} + \frac{\partial \Delta S_\theta}{\partial \mathcal{E}} = \Delta t, \quad (3.83a)$$

$$\frac{1}{\sqrt{2\mathcal{R}_0''\Delta_0}} \frac{\partial \mathcal{R}}{\partial \mathcal{Q}} \frac{\Delta r}{r-r_0} + \frac{\partial \Delta S_\theta}{\partial \mathcal{Q}} = 0. \quad (3.83b)$$

Now, we also note that for a given fixed  $L_z = m$ , the angular Bohr-Sommerfeld condition in Eq. (3.65) makes  $\mathcal{Q}$  a function of  $\mathcal{E}$  through the condition that  $\Delta S_\theta = (L - |m|)\pi$ . Because  $\Delta S_\theta$  is a

function of  $\mathcal{E}$ , its total derivative with respect to  $\mathcal{E}$  must vanish,

$$\frac{\partial \Delta S_\theta}{\partial \mathcal{E}} + \frac{\partial \Delta S_\theta}{\partial \mathcal{Q}} \left( \frac{d\mathcal{Q}}{d\mathcal{E}} \right)_{\text{BS}} = 0. \quad (3.84)$$

Therefore, when we multiply Eq. (3.83b) by  $(d\mathcal{Q}/d\mathcal{E})_{\text{BS}}$  and add it to Eq. (3.83a), we obtain the condition that

$$\frac{1}{\sqrt{2\mathcal{R}_0''}\Delta_0} \left[ \frac{\partial \mathcal{R}}{\partial \mathcal{E}} + \frac{\partial \mathcal{R}}{\partial \mathcal{Q}} \left( \frac{d\mathcal{Q}}{d\mathcal{E}} \right)_{\text{BS}} \right] \frac{\Delta r}{r - r_0} = \Delta t. \quad (3.85)$$

Combining this fact with the definition of the Lyapunov exponent in Eq. (3.78) and Eq. (3.79), we find that

$$\gamma = \left( n + \frac{1}{2} \right) \frac{\sqrt{2\mathcal{R}_0''}\Delta_0}{\left[ \frac{\partial \mathcal{R}}{\partial \mathcal{E}} + \frac{\partial \mathcal{R}}{\partial \mathcal{Q}} \left( \frac{d\mathcal{Q}}{d\mathcal{E}} \right)_{\text{BS}} \right]_{r_0}}, \quad (3.86)$$

where we recall that the quantities should be evaluated at  $r_0$ . Equation (3.86) is equivalent to Eq. (3.42). Note, however, that in Eq. (3.86) we explicitly highlight the dependence of  $\mathcal{Q}$  on  $\mathcal{E}$  through the term  $(d\mathcal{Q}/d\mathcal{E})_{\text{BS}}$ . There is an analogous term in Eq. (3.42) from the dependence of  $A_{lm}$  on  $\omega$  in the expression for the potential  $V^r$ , which we must take into account when computing  $\partial V^r / \partial \omega$ ; however, we did not write it out explicitly in Eq. (3.42).

Summarizing the physical interpretation of the results in this subsection, we note that the Lyapunov exponent  $\gamma_L$  is the rate at which the cross-sectional area of a bundle of homoclinic rays expand, when averaged over one period of motion in the  $\theta$  direction in the vicinity of  $r_0$ . The spatial Killing symmetry along  $\phi$  means the extension of the ray bundle remains the same along that direction. This, therefore, allows us to write

$$\mathcal{A} \sim e^{\gamma_L t}. \quad (3.87)$$

Correspondingly, the  $A\sqrt{\mathcal{A}} = \text{const}$  law requires that

$$A \sim e^{-\gamma_L t/2}, \quad (3.88)$$

which agrees with the decay rate of the least-damped QNM. The higher decay rates given by Eq. (3.76) come from an effect related to the intrinsic expansion of the area of a phase front. More specifically, if the amplitude is already nonuniform at points with different  $r - r_0$  (but same  $\theta$ ), then shifting the spatial locations of the nonuniform distribution gives the appearance of additional decay.

### 3.3.3.3 Next-to-Leading Order: Angular Amplitude Corrections and the Imaginary Part of Carter's Constant

Having found a relation in Eq. (3.72a) between the imaginary part of the energy,  $\omega_I$ , and the rate of divergence of rays, we now turn to Eq. (3.72b) to understand the geometric meaning of the complex part of  $A_{lm}$ . We recall from Section 3.3.3.1 that  $\mathcal{Q} = A_{lm}^R - m^2$ , at leading order, for a real Carter constant  $\mathcal{Q}$ . Because  $A_{lm}$  becomes complex at next to leading order (and because  $m$  remains unchanged), if the correspondence  $\mathcal{Q} = A_{lm} - m^2$  holds for a complex  $A_{lm}$ , then the Carter constant should also be complex, and its imaginary part should be equivalent to  $A_{lm}^I$ . In this part, we argue that this relationship holds.

By integrating Eq. (3.72b), we find that

$$A_{\theta}^{\pm} = \sqrt{\frac{1}{\sin \theta \sqrt{\Theta}}} \exp \left[ \pm \int_{\theta_-}^{\theta} \frac{\gamma \tilde{t}}{\sqrt{\Theta}} d\theta' \right]. \quad (3.89)$$

To interpret this equation, we will assume that the orbit is sufficiently close to  $r_0$  that the change in  $r$  over the course of a period of motion in  $\theta$  is negligible. Under this assumption (and with the fact that  $d\lambda = d\theta/\sqrt{\Theta}$ ) we can write the integral in the exponent in Eq. (3.89) as

$$\int_{\theta_-}^{\theta} \frac{\gamma \tilde{t}}{\sqrt{\Theta}} d\theta' = \gamma \left[ [t(\theta) - t(\theta_-)] - \left( \frac{\Delta t}{\Delta \lambda} \right) [\lambda(\theta) - \lambda(\theta_-)] \right], \quad (3.90)$$

where  $\Delta t/\Delta \lambda$  is the average of  $dt/d\lambda$  over a cycle of  $\theta$  motion. We obtain this expression by using the fact that  $dt/d\lambda$  is equivalent to  $\tilde{t}$  plus a constant when  $r$  (and hence  $\tilde{t}$ ) does not change. Because  $\tilde{t}$  has zero average (by definition) over a period of  $\theta$  motion, then when written in the form above, the constant must be  $(\Delta t)/(\Delta \lambda)$ . We can write this average rate of change in a useful form by noting that, from Eq. (3.56a) and Eq. (3.54b),

$$\frac{dt}{d\lambda} = \frac{1}{2\Delta} \frac{\partial \mathcal{R}}{\partial \mathcal{E}} + a^2 \mathcal{E} \cos^2 \theta. \quad (3.91)$$

Averaging this expression over a cycle of  $\theta$  motion, noting that the first term on the right-hand side is independent of  $\theta$ , and using Eq. (3.54b) gives

$$\begin{aligned} \frac{\Delta t}{\Delta \lambda} &= \frac{1}{2\Delta} \frac{\partial \mathcal{R}}{\partial \mathcal{E}} + a^2 \mathcal{E} \left( \int_{\theta_-}^{\theta^+} \frac{\cos^2 \theta}{\sqrt{\Theta}} d\theta \right) \left( \int_{\theta_-}^{\theta^+} \frac{d\theta}{\sqrt{\Theta}} \right)^{-1} = \frac{1}{2\Delta} \frac{\partial \mathcal{R}}{\partial \mathcal{E}} + \frac{\partial \Delta S_{\theta} / \partial \mathcal{E}}{2\partial \Delta S_{\theta} / \partial \mathcal{Q}} \\ &= \frac{1}{2\Delta} \frac{\partial \mathcal{R}}{\partial \mathcal{E}} - \frac{1}{2} \left( \frac{d\mathcal{Q}}{d\mathcal{E}} \right)_{\text{BS}}. \end{aligned} \quad (3.92)$$

In the last step we have used the Bohr-Sommerfeld condition (3.84). Also according to Eq. (3.56a)

and Eq. (3.56c), we can find

$$t(\theta) - t(\theta_-) = \frac{\partial}{\partial \mathcal{E}} \int_{\theta_-}^{\theta} \sqrt{\Theta(\theta')} d\theta' + \frac{1}{2\Delta} \frac{\partial \mathcal{R}}{\partial \mathcal{E}} (\lambda(\theta) - \lambda(\theta_-)), \quad (3.93a)$$

$$\lambda(\theta) - \lambda(\theta_-) = 2 \frac{\partial}{\partial \mathcal{Q}} \int_{\theta_-}^{\theta} \sqrt{\Theta(\theta')} d\theta', \quad (3.93b)$$

where to derive these two equations, we can again use the fact that  $d\lambda = d\theta/\sqrt{\Theta}$  and the definition of  $\Theta$ ; for the first we also make use of Eq. (3.91).

Finally, we insert Eqs. (3.93a), (3.93b), and (3.92) into Eq. (3.90) to find

$$\int_{\theta_-}^{\theta} \frac{\gamma \tilde{t}}{\sqrt{\Theta}} d\theta' = (-i\gamma) \left[ \frac{\partial}{\partial \mathcal{E}} + \left( \frac{d\mathcal{Q}}{d\mathcal{E}} \right)_{\text{BS}} \frac{\partial}{\partial \mathcal{Q}} \right] [iS_{\theta}(\theta)]. \quad (3.94)$$

Substituting Eq. (3.94) into the solution for  $A_{\theta}^{\pm}$  in Eq. (3.89) gives that

$$A_{\theta}^{\pm} = \frac{\exp \left\{ (\pm i\gamma) \left[ \frac{\partial}{\partial \mathcal{E}} + \left( \frac{d\mathcal{Q}}{d\mathcal{E}} \right)_{\text{BS}} \frac{\partial}{\partial \mathcal{Q}} \right] [iS_{\theta}(\theta)] \right\}}{\sqrt{\sin \theta \sqrt{\Theta}}}. \quad (3.95)$$

The phase in this equation, however, is precisely the correction to the leading-order expression for the phase  $e^{iS_{\theta}(\theta)}$  if we allow  $\mathcal{E}$  and  $\mathcal{Q}$  to be complex, where their imaginary parts are given by

$$\text{Im} \mathcal{E} = -\gamma = -\omega_I, \quad \text{Im} \mathcal{Q} = \left( \frac{d\mathcal{Q}}{d\mathcal{E}} \right)_{\text{BS}} (-\gamma). \quad (3.96)$$

Through next-to-leading order, therefore, the  $\theta$  portion of the wave is given by

$$A_{\theta}^{+} e^{iS_{\theta}(\theta)} + A_{\theta}^{-} e^{-iS_{\theta}(\theta)} = \frac{e^{iS_{\theta}(\theta)} + e^{-iS_{\theta}(\theta)}}{\sqrt{\sin \theta \sqrt{\Theta}}}, \quad (3.97)$$

where  $\mathcal{E}$  and  $\mathcal{Q}$  used in  $S_{\theta}$  are complex.

In the geometric-optics approximation, therefore, we have shown that we can account for the amplitude corrections to the wave by allowing the conserved quantities,  $\mathcal{E}$  and  $\mathcal{Q}$ , to be complex [with their imaginary parts given in Eq. (3.96)]. Furthermore, through the geometric-optics correspondence, and the definition of  $A_{lm}^I$  in Eq. (3.30) we can confirm that  $A_{lm}^I = \mathcal{Q}_I$ ; therefore, the relationship

$$\mathcal{Q} = A_{lm} - m^2, \quad (3.98)$$

is true for a complex  $\mathcal{Q}$  and  $A_{lm}$ .

In closing, we note that at the same  $\theta$ , the magnitude of the two components of the wave in Eq. (3.95) are not equal. More specifically, the integral involving  $\tilde{t}$  makes  $A^{+}$  have a larger amplitude at  $\theta < \pi/2$  and a smaller amplitude at  $\theta > \pi/2$ ;  $A^{-}$  has the opposite profile. Therefore, the net wave function remains symmetric about  $\theta = \pi/2$ .

### 3.4 Features of the Spectra of Kerr Black Holes

In this section, we will use the WKB formula and the geometric-optics correspondence in the first two sections of this paper to explain several aspects of the quasinormal-mode spectrum of Kerr black holes. Specifically, we will explain the absence of damping for a significant fraction of modes of extremal Kerr holes. We will also decompose the frequency into orbital and precessional parts and explain a degeneracy in the spectra of Kerr holes in terms of a rational relation of these frequencies when the corresponding photon orbits close.

#### 3.4.1 Spherical Photon Orbits and Extremal Kerr Black Holes

We will first review the properties of spherical photon orbits. These orbits can be found by setting  $\mathcal{R}(r) = \mathcal{R}'(r) = 0$  (see, e.g., [53]), and their conserved quantities are fixed by the radius of the orbit  $r$  and the spin of the black hole  $a$  to be

$$\mathcal{Q}/\mathcal{E}^2 = -\frac{r^3(r^3 - 6Mr^2 + 9M^2r - 4a^2M)}{a^2(r - M)^2}, \quad (3.99a)$$

$$L_z/\mathcal{E} = -\frac{r^3 - 3Mr^2 + a^2r + a^2M}{a(r - M)}. \quad (3.99b)$$

We will next discuss additional features of these orbits.

For a given spin parameter  $a$ , there is a unique spherical photon orbit with parameters  $(\mathcal{E}, L_z, \mathcal{Q})$  for any radius between the outermost and innermost photon orbits (the retrograde and prograde equatorial photon orbits). Their radii (which we denote  $r_1$  for prograde and  $r_2$  for retrograde orbits) are given by

$$r_1 = 2M \left[ 1 + \cos \left( \frac{2}{3} \arccos \left( -\frac{|a|}{M} \right) \right) \right], \quad (3.100a)$$

$$r_2 = 2M \left[ 1 + \cos \left( \frac{2}{3} \arccos \left( \frac{|a|}{M} \right) \right) \right]. \quad (3.100b)$$

At each  $r_1 \leq r \leq r_2$ , the spherical orbit's inclination angle reaches a maximum and minimum of  $\theta_{\pm}$  (at which  $\Theta = 0$ ). These angles are given by

$$\cos^2 \theta_{\pm} = \frac{\left[ 2\sqrt{M\Delta(2r^3 - 3Mr^2 + Ma^2)} - (r^3 - 3M^2r + 2Ma^2) \right] r}{a^2(r - M)^2}, \quad (3.101)$$

which are equivalent to the turning points of the integral (3.17) (and, therefore, we use the same symbols for these angles).

Using the geometric-optics correspondence between  $(\mathcal{E}, L_z, \mathcal{Q})$  and  $(\Omega_R, \mu, \alpha_{lm}^R)$ , we see that equatorial orbits at  $r_1$  and  $r_2$  correspond to modes with  $\mu = -1$  and  $+1$ , respectively, or modes with  $m = \pm l$  and  $l \gg 1$  (strictly speaking, though,  $\mu = m/(l + 1/2)$  never precisely reaches  $\pm 1$ ). We

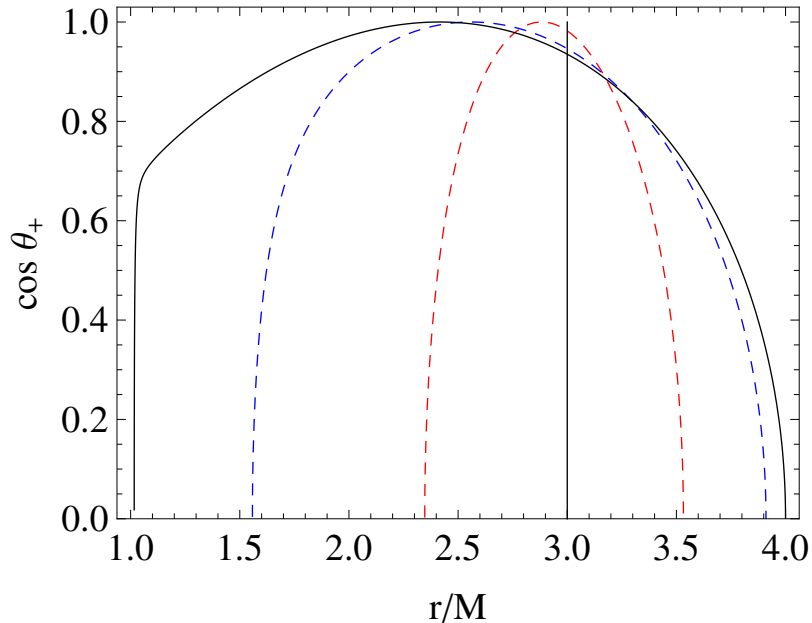


Figure 3.9: The values of  $r$  and  $\cos \theta_+$  of spherical spherical orbits, for  $a/M = 0$  (black, solid vertical line), 0.5 [red (light gray) dashed curve], 0.9 [blue (dark gray) dashed curve] and 0.99999 (black, solid curve). Note that for  $a = 0$ , all such orbits have  $r = 3M$ , while for  $a = M$ , a significant fraction reside at  $r = M$ .

can also relate  $r_p$ , the real root of Eq. (3.40), to the polar orbit and modes with  $m = 0$ . For orbits between the equatorial and polar ones, we can use Eqs. (3.36a) and (3.36b) to obtain a  $\mu$  between  $-1$  and  $+1$ . Then, only those modes that can be written as  $m/(l + 1/2)$  with the allowed integer values of  $l$  and  $m$  correspond to a QNM (though the photon orbits that correspond to QNMs are a dense subset of all photon orbits).

Note in Figure 3.9 that for  $a \sim M$ , a significant fraction of spherical photon orbits of different inclination angles all have nearly the same radius,  $r \approx M$ . Through the geometric-optics correspondence, a large fraction of modes (a finite range of values of  $\mu$ ) relate to this set of modes with  $r \approx M$ . In Figure 3.10, we explicitly show the relation between modes characterized by  $\mu$  and their corresponding spherical-photon-orbit radii (normalized by the horizon radius) for several values of  $a/M$  of slightly less than unity. The radius exhibits an interesting transition between two kinds of behaviors: for  $\mu > \mu_* \approx 0.744$ , the value of  $r$  is very close to  $M$  (the horizon radius for an extremal Kerr black hole), and for  $\mu < \mu_*$  the radii increase linearly. The orbits with  $\mu > \mu_*$  have a range of inclination angles. Their  $\sin \theta_{\pm}$  span from 0.731 (at  $\mu_*$ , the most inclined orbit) to 1 (at  $\mu = 1$ , the prograde equatorial orbit).

For the extremal black holes, therefore, a nonzero fraction of corotating spherical photon orbits appear to coincide with the horizon in the Boyer-Lindquist coordinate system. Although the proper distance between these orbits will not vanish (see [54]), this does not seem to be a coordinate effect,

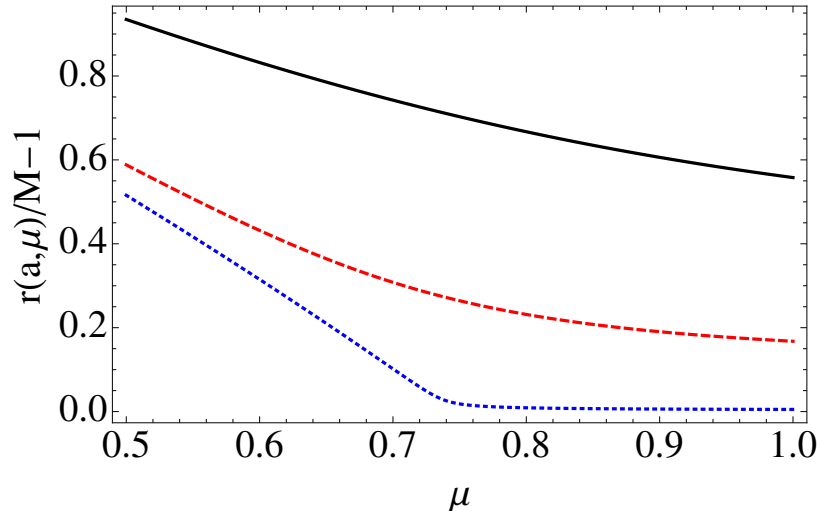


Figure 3.10: Radii of corotating spherical photon orbits as a function of  $\mu$ , for  $a/M = 0.9$  (black solid line), 0.99 (red dashed curve), 0.9999 (blue dotted line). For extremal Kerr black holes, a nonzero fraction of all spherical photon orbits are on the horizon.

because there is a definite physical change of the modes for these values of  $\mu > \mu_*$ . By comparing Figure 3.10 with Figure 3.3, we see that these orbits also have  $\Omega_I \approx 0$ . A vanishing imaginary part of the frequency corresponds to a vanishing of the radial Lyapunov exponent for this entire nonzero region of spherical photon orbits. This, therefore, would lead to a curious effect for a highly spinning black hole: for perturbations with  $\mu \geq \mu_*$ , modes do not move away from or into the horizon very quickly. If we were to solve an initial-data problem containing these modes, we would find that they live for a long time. One subtlety here is that QNMs with low damping rates are generally difficult to excite: the black hole excitation factor for a generic Kerr black hole can be proved to be proportional to  $\omega_I$  (See [30] for Schwarzschild case and [55] for Kerr; see also [56] for Kerr). In the long run the exponential factor  $e^{-i\omega t}$  over the linear factor  $\omega_I$  dominates and we would eventually see these long-lived perturbations. Moreover, as these modes are centered around the equatorial plane, we would see these perturbations escaping roughly near the equatorial direction. In fact [56] showed that a long-lived emission in the form of superposed QNMs with zero decay results from the perturbations of an extremal Kerr black hole; their work was for  $l = m$  modes only, and together with our eikonal results for generic  $m$  can provide a basis for future studies of zero-decay modes.

### 3.4.2 A Mode's Orbital and Precessional Frequencies

In this part, we will define two frequencies associated with individual spherical photon orbits (the orbital and precessional frequencies) and understand their connection to the real part of the QNM frequency. We begin by noting that because spherical photon orbits have only two independent degrees of freedom describing their motion [see, e.g., Eq. (3.99)], the orbit can be characterized

by two frequencies. The first is the  $\theta$ -frequency,  $\Omega_\theta$ , the frequency at which the particle oscillates below and above the equatorial plane. During each  $\theta$ -cycle, which takes an amount of time given by  $T_\theta = 2\pi/\Omega_\theta$ , the particle also moves in the azimuthal (or  $\phi$ ) direction. If this angle is  $2\pi$  for a corotating orbit ( $m > 0$ ) or  $-2\pi$  for a counterrotating orbit ( $m < 0$ ), then there is no precession (and these simple, closed orbits have effectively one frequency describing their motion, as the spherical photon orbits of a Schwarzschild black hole do). The difference between the  $\Delta\phi$  and  $\pm 2\pi$  (its precession-free value) we will denote as the *precession angle*,

$$\Delta\phi_{\text{prec}} \equiv \Delta\phi - 2\pi \operatorname{sgn} m, \quad (3.102)$$

where  $\operatorname{sgn} m$  is the sign of  $m$ . We can also associate the rate of change of  $\phi_{\text{prec}}$  with a frequency,

$$\Omega_{\text{prec}} \equiv \Delta\phi_{\text{prec}}/T_\theta = \Delta\phi_{\text{prec}}\Omega_\theta/(2\pi). \quad (3.103)$$

Both  $T_\theta$  and  $\Delta\phi_{\text{prec}}$  can be computed from geodesic motion [see the formulas for  $\Omega_\theta$  and  $\Delta\phi_{\text{prec}}$  in Eq. (3.106)].

It is possible to perform a split of the real part of the QNM into two analogous frequencies. To derive this split, start from a single ray, along which the phase of the wave must be constant. Also suppose that the ray originates from  $\theta_-$  and ends at  $\theta_+$  after traveling only one-half of a cycle of motion in the  $\theta$  direction. During this time, the statement that the phase is unchanged is that

$$0 = -\omega_R T_\theta/2 + (L - |m|)\pi + m\Delta\phi/2. \quad (3.104)$$

Using (half of) Eq. (3.102), the real part of the frequency is

$$\omega_R = L\Omega_\theta(m/L) + m\Omega_{\text{prec}}(m/L). \quad (3.105)$$

Note that  $\Omega_\theta$  and  $\Omega_{\text{prec}}$  both depend on  $m/L$ .

More explicitly, given the orbital parameters  $(\mathcal{E}, \mathcal{Q}, L_z)$ , the quantities  $T_\theta$  and  $\Delta\phi$  can be obtained by computing

$$T_\theta = \frac{\partial}{\partial \mathcal{E}} \oint \sqrt{\Theta} d\theta + \frac{1}{2\Delta} \frac{\partial \mathcal{R}}{\partial \mathcal{E}} \oint \frac{d\theta}{\sqrt{\Theta}}, \quad (3.106a)$$

$$\Delta\phi = -\frac{1}{L_z} \left[ 1 - \frac{\partial}{\partial \log \mathcal{E}} \right] \oint \sqrt{\Theta} d\theta + \frac{1}{2\Delta} \frac{\partial \mathcal{R}}{\partial L_z} \oint \frac{d\theta}{\sqrt{\Theta}}, \quad (3.106b)$$

(expressions that hold for any spherical photon orbit—not simply orbits that satisfy the Bohr-

Sommerfeld condition) and the two frequencies are given by

$$\Omega_\theta = 2\pi \left( \frac{\partial}{\partial \mathcal{E}} \oint \sqrt{\Theta} d\theta + \frac{1}{2\Delta} \frac{\partial \mathcal{R}}{\partial \mathcal{E}} \oint \frac{d\theta}{\sqrt{\Theta}} \right)^{-1} \quad (3.107a)$$

$$\Omega_{\text{prec}} = \Omega_\theta \frac{\Delta \phi}{2\pi} - (\text{sgn} L_z) \Omega_\theta. \quad (3.107b)$$

These can be expressed in terms of  $(\mathcal{E}, \mathcal{Q}, L_z)$  using elliptic integrals (as was done in [47]), but we will not carry this out explicitly.

For very slowly spinning black holes, a short calculation shows that

$$\Omega_\theta \approx \frac{1}{\sqrt{27M}} = \sqrt{\frac{M}{r_0^3}}, \quad (3.108a)$$

$$\Omega_{\text{prec}} \approx \frac{2a}{27M^2} = \frac{2S}{r_0^3}, \quad (3.108b)$$

where  $r_0$  is the circular-photon-orbit radius for a Schwarzschild black hole,  $r_0 = 3M$ , and  $S = aM$ . The expression for  $\Omega_\theta$  is the Keplerian frequency of the spherical photon orbit, and  $\Omega_{\text{prec}} = 2S/r_0^3$  is the Lense-Thirring precessional frequency. In the slow-rotation limit, therefore, our formula recovers Ferrari and Mashhoon's result Eq. (3.2).

For any value of  $a$ , we can normalize Eq. (3.105) by  $L$ , and write

$$\Omega_R(a, \mu) = \Omega_\theta(a, \mu) + \mu \Omega_{\text{prec}}(a, \mu). \quad (3.109)$$

In Figure 3.11, we explore the two frequencies in the decomposition of  $\Omega_R$  by separately plotting  $\Omega_\theta$  and  $\Omega_{\text{prec}}$ , for different values of  $a$ .

For small values of  $a/M$ ,  $\Omega_\theta$  and  $\Omega_{\text{prec}}$  are consistent with the constant values predicted by Eqs. (3.108a) and (3.108b). For larger values of  $a/M$ ,  $\Omega_\theta$  does not vary much as a function of  $\mu$  until  $a \sim 0.7M$ ; for spins greater than this value, it is only for larger values of  $\mu$  that  $\Omega_\theta$  changes significantly by decreasing from the equivalent values for  $a = 0$ . Finally, as  $a \rightarrow M$ ,  $\Omega_\theta$  vanishes for  $\mu \geq \mu_* \approx 0.744$ . The precessional frequency,  $\Omega_{\text{prec}}$ , on the other hand, monotonically increases as a function of  $\mu$  even for small values of  $a/M$ ; as  $a \rightarrow M$ ,  $\Omega_{\text{prec}}$  grows to  $\Omega_H$  at  $\mu \sim \mu_*$ , and stays there for all values of  $\mu > \mu_*$ . For  $a \sim M$  and  $\mu > \mu_*$ , there is one additional feature worth noting: because  $\Omega_\theta \sim 0$  and  $\Omega_\phi \sim \Omega_H$ , this gives rise to the interpretation of the mode as a ray that sticks on the horizon and corotates with the horizon at its angular frequency of  $\Omega_H$ ; moreover, there seems to be no restoring force along the  $\theta$  direction.

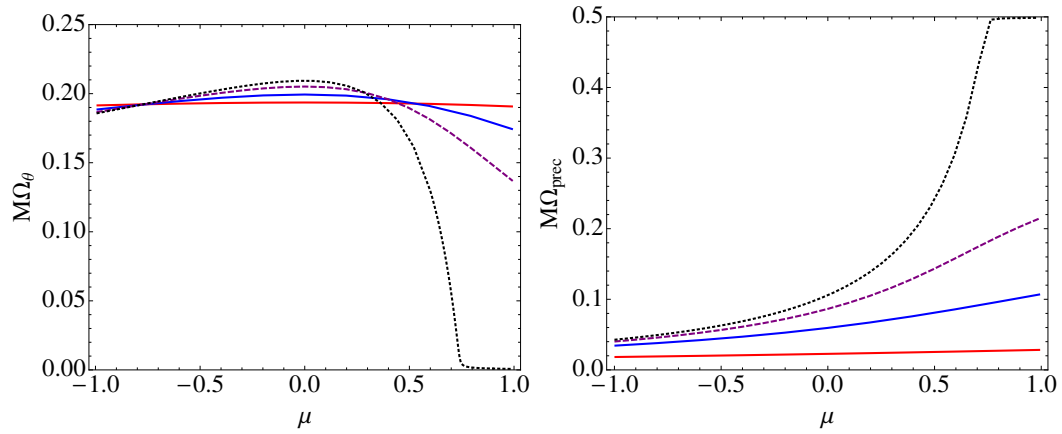


Figure 3.11: Right: Orbital frequency,  $\Omega_\theta$ , plotted against  $\mu$ , for  $a/M = 0.3$  [red (light gray) solid curve],  $0.7$  [blue (dark gray) solid curve],  $0.9$  (purple dashed line), and  $1$  (black dotted line). The orbital frequency vanishes for a significant range of  $\mu$  for extremal black holes. Left: Precessional frequency,  $\Omega_\phi$ , versus  $\mu$ , using the same conventions relating curves to spins as in the left panel. The precessional frequency approaches the horizon frequency,  $\Omega_H$ , for a range of values of  $\mu$  for extremal black holes.

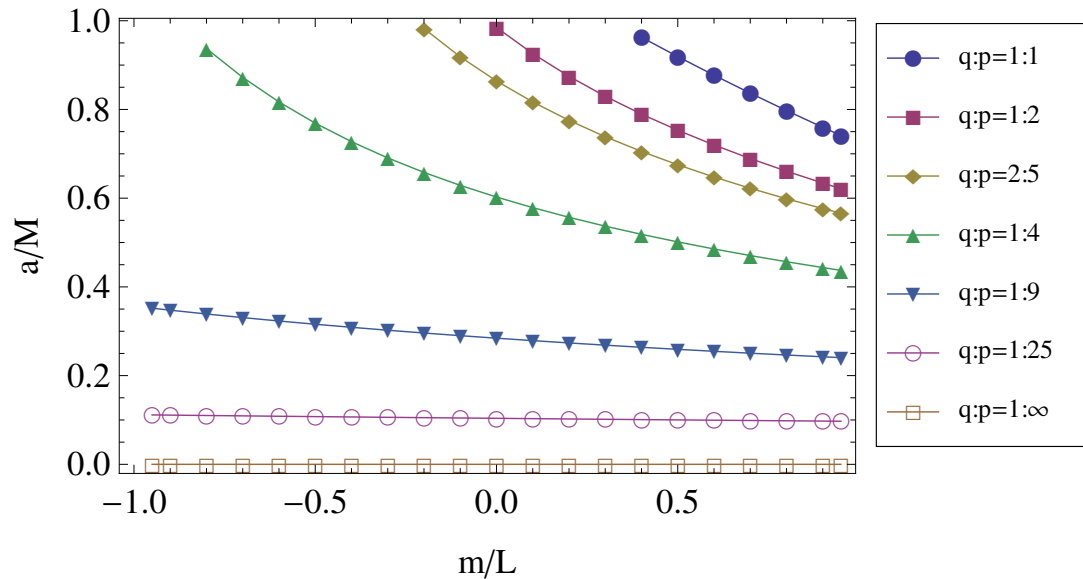


Figure 3.12: A diagram showing the spin parameters,  $a$ , and the ratios of the multipolar indexes  $m/L$ , at which the orbital and precessional frequencies have a ratio of  $p/q$ . Although we only perform our numerical calculations at a discrete set of  $m/L$  values (shown by the dots), in the eikonal limit, each set of points for a given ratio of  $p/q$  approaches a continuous curve.

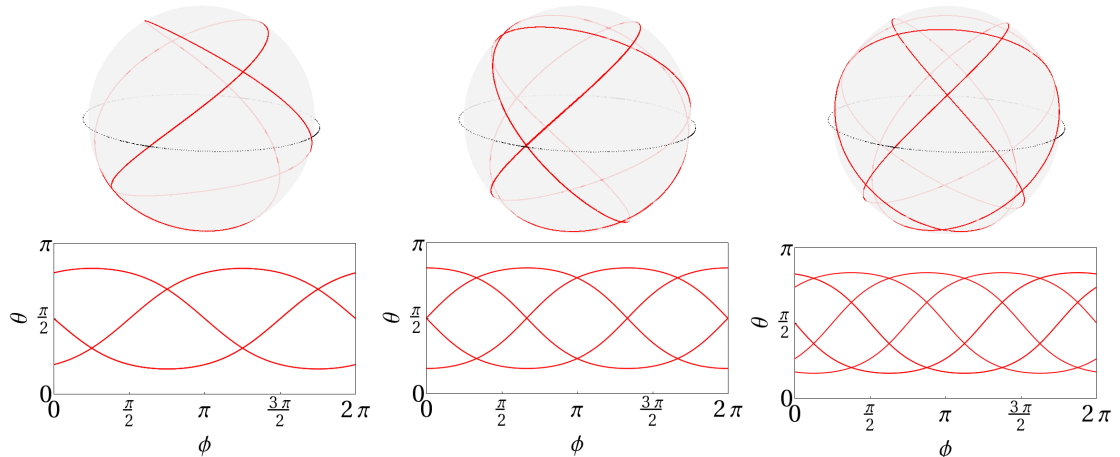


Figure 3.13: For black holes with spins  $a/M = 0.768$ ,  $0.612$ , and  $0.502$ , the spherical photon orbits with  $\omega_{\text{orb}} = 2\omega_{\text{prec}}$ , on the left,  $\omega_{\text{orb}} = 3\omega_{\text{prec}}$  in the center, and  $\omega_{\text{orb}} = 4\omega_{\text{prec}}$  on the right, respectively. These orbits correspond to quasinormal modes in the eikonal limit with  $m/L = 0.5$ . The top figures show the photon orbit, the red, solid curve, on its photon sphere (represented by a transparent sphere). The dashed black line is the equatorial ( $\theta = \pi/2$ ) plane, which was inserted for reference. The bottom figures are the same photon orbits, but plotted in the  $\phi$ - $\theta$  plane, instead.

### 3.4.3 Degenerate Quasinormal Modes and Closed Spherical Photon Orbits

Finally, in this section, we interpret the degeneracy of QNM frequencies (of which Figure 3.1 was an example). Recall that in that figure, for  $a/M \approx 0.7$ , we found pairs of modes such as  $(2, 2)$  and  $(3, -2)$ ,  $(3, 2)$  and  $(4, -2)$ ,  $(4, 2)$  and  $(5, -2)$ , and so on, all have approximately the same frequency. For another, lower spin  $a/M \approx 0.4$ , pairs like  $(3, 3)$  and  $(4, -3)$ ,  $(4, 3)$  and  $(5, -3)$ , et cetera, have approximately the same frequency.

The approximate degeneracy exists because the ratio between  $\Omega_\theta$  and  $\Omega_{\text{prec}}$  can be rational, and the photon orbits close. If for a certain mode of a black hole with spin  $a$ , with  $m$  and  $L$ , and for integers  $p$  and  $q$ ,

$$q\Omega_\theta\left(a, \frac{m}{L}\right) = p\Omega_{\text{prec}}\left(a, \frac{m}{L}\right), \quad (3.110)$$

this means that there exists a closed spherical photon orbit that satisfies the conditions necessary to correspond to a QNM. Equation (3.110) implies that

$$L\Omega_\theta\left(a, \frac{m}{L}\right) + m\Omega_{\text{prec}}\left(a, \frac{m}{L}\right) = (L + kq)\Omega_\theta\left(a, \frac{m}{L}\right) + (m - kp)\Omega_{\text{prec}}\left(a, \frac{m}{L}\right). \quad (3.111)$$

If  $\Omega_\theta$  and  $\Omega_{\text{prec}}$  do not change much from  $\mu = m/L$  to  $\mu' = (m - kp)/(L + kq)$  (either because spin is small—and therefore  $\Omega_\theta$  and  $\Omega_{\text{prec}}$  depend weakly on  $\mu$ —or because  $L \gg kq$  and  $m \gg kp$ ), then

$$\omega_R^{l,m} \approx \omega_R^{l+kq, m-kp}. \quad (3.112)$$

Because  $\Omega_I$  depends similarly on  $\mu$ , under the same conditions,

$$\omega_I^{l,m} \approx \omega_I^{l+kq, m-kp}; \quad (3.113)$$

therefore, the modes are degenerate. It is also clear from Eq. (3.110) that the degeneracy happens at the same time that the corresponding orbit is closed. The three series mentioned at the beginning of the paper correspond to  $p/q = 4, 6,$  and  $8,$  respectively (for  $k = 1$ ).

### 3.4.3.1 Slowly Spinning Black Holes

For  $a/M \ll 1$ , when Eqs. (3.108a) and (3.108b) apply, the condition for degenerate modes becomes

$$\frac{q\sqrt{27}}{2p} = \frac{a}{M} \ll 1 \quad (3.114)$$

(a statement that holds independent of  $\mu$ ). This implies that orbits of all inclinations close for these spins.

For these specific spins, the QNM spectrum is completely degenerate, by which we mean that all modes have the same decay rate, and all real parts of the frequencies are integer multiples of only one frequency (similar to those of a Schwarzschild black hole). Using this approximate formula to find  $a$  for the three instances of degeneracy in Figure 3.1, we find

$$a_{4/1} \approx 0.65M, \quad a_{6/1} \approx 0.43M, \quad a_{8/1} \approx 0.32M. \quad (3.115)$$

These are not very far away from spins we found empirically.

### 3.4.3.2 Generic Black Holes

For a generic spin parameter  $a$ , we will explain degeneracies that exist around a mode with  $L \gg 1$  and  $|m| \gg 1$ . If the condition in Eq. (3.110) holds for  $p, q \ll \min(L, |m|)$ , then there is a range of  $|k| \ll \min(L, |m|)/\max(p, q)$  in which there is a degeneracy between all  $(L+kq, m-kp)$  and  $(L, m)$ . These modes must be those close to the mode of indices  $(L, m)$ , because, strictly speaking, it is only the orbit corresponding to  $m/L$  which is precisely closed.

To find this degeneracy, we will search for spin parameters  $a$  for which Eq. (3.110) holds for any set of indexes  $(L, m)$  and integers  $(p, q)$  that satisfy  $L, |m| \gg p, q$  (we generally either find one or zero solutions). To visualize this degeneracy, for each pair  $(p, q)$ , we will mark all possible pairs of  $(m/L, a)$  in a 2D plot; the values of the spins are sufficiently dense for each value of  $m/L$  that they form a smooth curve when plotted against  $m/L$ . Some of these curves are shown in Figure 3.12. Because for a fixed  $p/q$  the degenerate spins for  $a/M \lesssim 0.3$  are nearly independent of  $m/L$ , Eq. (3.114) should be an accurate prediction for spins less than that value. As a concrete illustration of the orbits

corresponding to these degenerate modes, we plot closed orbits for  $m/L = 0.5$  and for  $a/M \approx 0.5, 0.61,$  and  $0.77$  in Figure 3.13. The values of the spins agree quite well with those predicted in Figure 3.12.

### 3.5 Conclusions and Discussion

In this paper, we extended the results of several earlier works [9, 29, 40, 41] to compute the quasinormal-mode frequencies and wave functions of a Kerr black hole of arbitrary astrophysical spins, in the eikonal limit ( $l \gg 1$ ). We focused on developing a greater intuitive understanding of their behavior, but, in the process, we calculated expressions for large- $l$  quasinormal-mode frequencies that are reasonably accurate even at low  $l$ . Specifically, we applied a WKB analysis to the system of equations defined by the angular and radial Teukolsky equations. Using a Bohr-Sommerfeld condition for the angular equation, we related the angular separation constant to the frequency; when we expanded the constraint to leading order in  $a\omega/l$ , we found an equally accurate and algebraically simpler relation between the frequency and angular eigenvalue. We then used a well-known WKB analysis on the radial Teukolsky equation to obtain expressions for the QNM frequencies and the angular separation constants. The accuracy of the approximate expressions for the QNM frequency are observed to be of order  $O(L^{-2})$  even though we had only expected a  $O(L^{-1})$  convergence for the imaginary part.

Next, we reviewed that a massless scalar wave in the leading-order, geometric-optics approximation obeys the Hamilton-Jacobi equations, which are very similar to the Teukolsky equations when  $l \gg 1$ . By identifying terms in the Hamilton-Jacobi equations and Teukolsky equations, we related the conserved quantities of the Hamilton-Jacobi equations to the eigenvalues of the separated Teukolsky equations. Specifically, we confirmed that the energy, angular momentum in the  $z$  direction, and Carter constant in the Hamilton-Jacobi equations correspond to the real frequency, the index  $m$ , and the angular eigenvalue minus  $m^2$  in the Teukolsky equations, respectively. Furthermore, we found that the conditions that define a quasinormal mode in the WKB approximation are equivalent to the conditions in the geometric-optics approximation that determine a spherical photon orbit that satisfies an identical Bohr-Sommerfeld quantization condition.

By analyzing the next-to-leading-order, geometric-optics approximation, we showed that the corrections to the amplitude of the scalar wave correspond to the imaginary parts of the WKB quantities. Specifically, we saw that the imaginary part of the frequency is equal to a positive half-integer times the Lyapunov exponent averaged over a period of motion in the  $\theta$  direction. The imaginary part of the angular eigenvalue is equal to the imaginary part of the Carter constant, which is, in turn, related to an amplitude correction to the geometric-optics approximation to the angular function for  $\theta$ .

We then applied these results to study properties of the QNM spectra of Kerr black holes. We observed that for extremal Kerr black holes a significant fraction of the QNMs have nearly zero imaginary part (vanishing damping) and their corresponding spherical photon orbits are stuck on the horizon (in Boyer-Lindquist coordinates). We plan to study this unusual feature of extremal Kerr black holes in future work. In addition, we showed that for Kerr black holes of any spin, the modes' frequencies (in the eikonal limit) are a linear combination of the orbital and precession frequencies of the corresponding spherical photon orbits. This allows us to study an intriguing feature of the QNM spectrum: namely, when the orbital and precession frequencies are rationally related—i.e, when the spherical photon orbits are closed—then the corresponding quasinormal-mode frequencies are also degenerate.

We hope that the approximate expressions for the quasinormal-mode frequencies in this paper will prove helpful for understanding wave propagation in the Kerr spacetime. This not unreasonable to suppose, because Dolan and Ottewill have shown in [28, 30] that to calculate the Green's function analytically in the Schwarzschild spacetime, one needs to know analytical expressions for the frequency of the quasinormal modes (specifically, this comes from the fact that the frequencies of the quasinormal mode are the poles of the Green's function in the frequency domain). We, therefore, think that our approximate formulas could assist with the calculation of the Green's function in the Kerr spacetime, in future work.

## Acknowledgments

We thank Emanuele Berti for discussing this work with us and pointing out several references to us. We also thank Jeandrew Brink for insightful discussions about spherical photon orbits in the Kerr spacetime. We would also like to thank the anonymous referee for carefully reviewing our manuscript and offering many helpful suggestions. We base our numerical calculation of the QNM frequencies on the Mathematica notebook provided by Emanuele Berti and Vitor Cardoso [57]. This research is funded by NSF Grants PHY-1068881, PHY-1005655, CAREER Grant PHY-0956189; NASA Grant No.NNX09AF97G; the Sherman Fairchild Foundation, the Brinson Foundation, and the David and Barbara Groce Startup Fund at Caltech.

## 3.A The Taylor Expanded Bohr-Sommerfeld Condition

The Bohr-Sommerfeld constraint (3.17) gives us a way to evaluate  $A_{lm}$  in terms of  $l$ ,  $m$ , and  $\omega$ ; the error in this approximation scales as  $1/l$ . Because it is an integral equation, it is not particularly convenient to solve, and it is beneficial to have an approximate, but algebraic expression for the frequency of a QNM. With the benefit of hindsight, one can confirm through numerical calculations

of exact QNM frequencies performed using Leaver's method that the parameter  $a\omega/l$  is numerically a small number for all black hole spins. We can then expand the angular separation constant,  $A_{lm}$ , in a series in  $a\omega/l$  as  $A_{lm} = A_{lm}^0 + \delta A_{lm}$ , where  $A_{lm}^0$  satisfies the equation

$$\int_{\theta_-^0}^{\theta_+^0} \sqrt{A_{lm}^0 - \frac{m^2}{\sin^2 \theta}} = \pi \left( l + \frac{1}{2} - |m| \right), \quad (3.116)$$

and at leading order,  $\theta_+^0, \theta_-^0 = \pm \arcsin[m/(l+1/2)]$ . One can easily verify that the solution to this equation is the angular eigenvalue of a Schwarzschild black hole,  $A_{lm}^0 = (l+1/2)^2$  (note that we are assuming  $l \gg 1$ ). Now we will compute the lowest-order perturbation in  $a\omega/l$ , which turns out to be quadratic in this parameter [i.e.,  $(a\omega/l)^2$ ] below:

$$\int_{\theta_-^0}^{\theta_+^0} \frac{\delta A_{lm} + a^2 \omega^2 \cos^2 \theta}{\sqrt{(l+1/2)^2 - m^2/\sin^2 \theta}} d\theta = 0. \quad (3.117)$$

The integration limits  $\theta_+, \theta_-$  also can be expanded in a series in  $a\omega/l$ , and the lowest-order terms of this series are given by  $\theta_+^0, \theta_-^0$ ; The perturbation in  $\theta_+, \theta_-$  would result in some quartic corrections in  $a\omega/l$  [i.e.,  $(a\omega/l)^4$ ] when we evaluate the integrals of Eqs. (3.117) and (3.116), because the integrand is of order  $(a\omega/l)^2$  and the width of the correction in  $\theta_+, \theta_-$  are also of order  $(a\omega/l)^2$ . As a result, we will not need it here. Evaluating the integral in Eq. (3.117) is straightforward, and we find

$$A_{lm} = A_{lm}^0 + \delta A_{lm} = l(l+1) - \frac{a^2 \omega^2}{2} \left[ 1 - \frac{m^2}{l(l+1)} \right] \quad (3.118)$$

Interestingly, the above expression is consistent with the expansion of  $A_{lm}$  for small  $a\omega$  given in [58], even in the eikonal limit, where  $a\omega$  is large. The reason for this fortuitous agreement is again that for QNMs of Kerr black holes of any spin,  $a\omega/l$  is small, and the expansion only involves even powers of this parameter,  $(a\omega/l)^2$ . Because the coefficients in the expansion of  $a\omega$  scale as  $1/l^k$  for even powers of  $(a\omega)^k$  and  $1/l^{k+1}$  for odd powers of  $(a\omega)^k$ , in the limit of large  $l$ , the two series actually are equivalent in the eikonal limit. In principle, one can also expand and solve Eq. (3.17) to higher orders in the parameter  $a\omega/l$  and compare with the expansion in  $a\omega$  in [58]; we expect that the two series should agree. This would be useful, because it would effectively let one use the small  $a\omega$  expansion in the eikonal limit, where the series would, ostensibly, not be valid.

## Bibliography

- [1] C. V. Vishveshwara, *Nature* **227**, 936 (1970).
- [2] K. D. Kokkotas and B. Schmidt, *Living Rev. Relativity* **2**, 2 (1999), <http://www.livingreviews.org/lrr-1999-2>.

- [3] H.-P. Nollert, *Classical Quantum Gravity* **16**, R159 (1999).
- [4] V. Ferrari and L. Gualtieri, *Gen. Relativ. Gravit.* **40**, 945 (2008).
- [5] E. Berti, V. Cardoso, A. O. Starinets, *Classical Quantum Gravity* **26**, 163001 (2009).
- [6] R. A. Konoplya and A. Zhidenko, *Rev. Mod. Phys.* **83**, 793 (2011).
- [7] M. Davis, R. Ruffini, W. H. Press, and R. H. Price, *Phys. Rev. Lett.* **27**, 1466 (1971).
- [8] S. Chandrasekhar and S. Detweiler, *Proc. R. Soc. Lond. A* **344**, 441 (1975).
- [9] V. Ferrari and B. Mashhoon, *Phys. Rev. D* **30**, 295 (1984).
- [10] B. F. Schutz and C. M. Will, *Astrophys. J.* **291**, L33 (1985).
- [11] S. Iyer and C. M. Will, *Phys. Rev. D* **35**, 3621 (1987).
- [12] E. W. Leaver, *Proc. R. Soc. Lond. A* **402**, 285 (1985).
- [13] H.-P. Nollert, *Phys. Rev. D* **47**, 5253 (1993).
- [14] P. P. Fiziev, *Classical Quantum Gravity* **27**, 135001 (2010).
- [15] D. Staicova and P. P. Fiziev, [arXiv:1112.0310](https://arxiv.org/abs/1112.0310) (2011).
- [16] E. W. Leaver, *Phys. Rev. D* **34**, 384 (1986).
- [17] Y. Sun and R. H. Price, *Phys. Rev. D* **38**, 1040 (1988).
- [18] <http://www.ligo.caltech.edu/>
- [19] <http://www.ego-gw.it/public/virgo/virgo.aspx>
- [20] F. Echeverria, *Phys. Rev. D* **40**, 3194 (1989).
- [21] E. E. Flanagan, and S. A. Hughes, *Phys. Rev. D* **57**, 4566 (1998).
- [22] A. Buonanno, G. B. Cook, and F. Pretorius, *Phys. Rev. D* **75**, 124018 (2007).
- [23] E. Berti, V. Cardoso, J. A. Gonzalez, U. Sperhake, M. Hannam, S. Husa, and B. Brügmann, *Phys. Rev. D* **76**, 064034 (2007).
- [24] O. Dreyer, B. Kelly, B. Krishnan, L. S. Finn, D. Garrison, and R. Lopez-Aleman, *Classical Quantum Gravity* **21**, 787 (2004).
- [25] E. Berti, V. Cardoso, and C. M. Will, *Phys. Rev. D* **73**, 064030 (2006).
- [26] A. Zimmerman and Y. Chen, *Phys. Rev. D* **84**, 084012 (2011).

- [27] Y. Mino and J. Brink, Phys. Rev. D **78**, 124015 (2008).
- [28] S. R. Dolan and A. C. Ottewill, Classical Quantum Gravity **26**, 225003 (2009).
- [29] S. R. Dolan, Phys. Rev. D **82**, 104003 (2010).
- [30] S. R. Dolan and A. C. Ottewill, Phys. Rev. D **84**, 104002 (2011).
- [31] H. P. Nollert, Phys. Rev. D **47**, 5253 (1993).
- [32] N. Andersson, Classical Quantum Gravity **10**, L61 (1993).
- [33] L. Motl, Adv. Theor. Math. Phys. **6**, 1135 (2003).
- [34] L. Motl and A. Neitzke, Adv. Theor. Math. Phys. **7**, 307 (2003).
- [35] T. Padmanabhan, Classical Quantum Gravity **21**, L1 (2004).
- [36] V. Cardoso, A. S. Miransa, E. Berti, H. Witek, V. T. Zanchin, Phys. Rev. D **79**, 064016 (2009).
- [37] C. J. Goebel, Astrophys. J. **172**, L95 (1972).
- [38] C.-M. Claudel, K. S. Virbhadra, and G. F. R. Ellis, J. Math. Phys. **42**, 818 (2001).
- [39] S. A. Teukolsky, Phys. Rev. Lett. **29**, 1114 (1972).
- [40] K. D. Kokkotas, Classical Quantum Gravity **8**, 2217 (1991).
- [41] E. Seidel and S. Iyer, Phys. Rev. D **41**, 374 (1990).
- [42] S. A. Teukolsky, Astrophys. J. **185**, 635 (1973).
- [43] R. Shankar, *Principles of Quantum Mechanics*, (Plenum Press, New York, 1980).
- [44] S. Detweiler, Astrophys. J. **239**, 292 (1980).
- [45] V. Cardoso Phys. Rev. D **70**, 127502 (2004).
- [46] S. Hod, Phys. Rev. D **78**, 084035 (2008).
- [47] E. Teo, Gen. Relativ. and Gravit. **35**, 1909 (2003).
- [48] B. Mashhoon, Phys. Rev. D **31**, 290 (1985).
- [49] S. Hod, Phys. Rev. D **84**, 044046 (2011).
- [50] E. Berti and K. D. Kokkotas, Phys. Rev. D **71**, 124008 (2005).
- [51] S. Hod, Phys. Rev. D **80**, 064004 (2009).

- [52] C. W. Misner, K. S. Thorne and J. A. Wheeler, *Gravitation*, (W. H. Freeman and Company, New York, 1973).
- [53] S. Chandrasekhar, *The Mathematical Theory of Black Holes* (Oxford University Press, Oxford, 1983).
- [54] J. M. Bardeen, W. H. Press, and S. A. Teukolsky, *Astrophys. J.* **178**, 347 (1972).
- [55] H. Yang, A. Zimmerman, Z. Y. Zhang and Y. Chen, unpublished
- [56] K. Glampedakis and N. Andersson, *Phys. Rev. D* **64**, 104021 (2001).
- [57] <http://www.phy.olemiss.edu/~berti/qnms.html>
- [58] E. Berti, V. Cardoso, M. Casals, *Phys. Rev. D* **73**, 024013 (2006).

## Chapter 4

# Branching of Quasinormal Modes for Nearly Extremal Kerr Black Holes

We show that nearly extremal Kerr black holes have two distinct sets of quasinormal modes, which we call zero-damping modes (ZDMs) and damped modes (DMs). The ZDMs exist for all harmonic indexes  $l$  and  $m \geq 0$ , and their frequencies cluster onto the real axis in the extremal limit. The DMs have nonzero damping for all black hole spins; they exist for all counterrotating modes ( $m < 0$ ) and for corotating modes with  $0 \leq \mu \lesssim \mu_c = 0.74$  (in the eikonal limit), where  $\mu \equiv m/(l + 1/2)$ . When the two families coexist, ZDMs and DMs merge to form a single set of quasinormal modes as the black hole spin decreases. Using the effective potential for perturbations of the Kerr spacetime, we give intuitive explanations for the absence of DMs in certain areas of the spectrum and for the branching of the spectrum into ZDMs and DMs at large spins.

---

Originally published as H. Yang, F. Zhang, A. Zimmerman, D. A. Nichols, E. Berti, and Y. Chen, *Phys. Rev. D* **87**, 041502 (R) (2013). Copyright 2013 by the American Physical Society.

### 4.1 Introduction

Nearly extremal Kerr (NEK) black holes (BHs)—i.e., BHs for which the dimensionless angular momentum  $a \approx 1$  in the geometrical units,  $G = c = M = 1$ , used in this paper—have drawn much attention recently. Besides the mounting evidence for fast-rotating BHs in astronomy [1], NEK BHs have considerable theoretical significance, e.g., in studies of weak cosmic censorship [2] and in calculations of black-hole entropy [3].

For extremal Kerr BHs ( $a = 1$ ) the near-horizon geometry reduces to  $\text{AdS}_2 \times \text{S}^2$  [4]. This

observation led to the Kerr/CFT conjecture, which states that extremal Kerr BHs are dual to the chiral limit of a two-dimensional conformal field theory [5]. In the past few years the extremal Kerr spacetime and spacetimes violating the Kerr bound were shown to be unstable [6]. The stability of BHs depends on the sign of the imaginary part of their complex free vibration modes, called quasinormal modes (QNMs) [7]. Therefore the NEK QNM frequencies studied here can shed light on the onset of extremal Kerr instabilities and prove useful in quantum field theory (for example, in the calculation of two-point functions [8]).

Detweiler first used an approximation to the radial Teukolsky equation for NEK BHs (see also [9]) to show that QNMs with angular indexes  $l = m$  have a long decay time [10]. Using Detweiler’s result, Sasaki and Nakamura [11] calculated QNM frequencies analytically and Andersson and Glampedakis proposed long-lived emission from NEK BHs [12]. However, there remains a long-standing controversy in the literature about what set of QNMs decay slowly [13], whether long-lived radiation is possible [14], and whether the imaginary part of the QNM frequencies vanishes as  $a \rightarrow 1$  (compare [11, 14] with [13]). Despite the importance of this problem, our present understanding of the QNM spectrum of NEK BHs is inconclusive.

In a recent paper [15], some of us used a WKB analysis to relate Kerr QNMs in the eikonal limit to spherical photon orbits around Kerr BHs. We pointed out that a subset of spherical photon orbits of extremal Kerr BHs reside on the horizon and that the corresponding QNMs have zero damping. This happens when the parameter  $\mu \equiv m/(l + 1/2) \gtrsim \mu_c \simeq 0.74$ . Hod [16] computed  $\mu_c$  in the eikonal limit, finding an approximate analytical result in agreement with [15].

In this work, we will show that the NEK geometry has two distinct sets of QNMs: zero-damping modes (ZDMs) and damped modes (DMs). ZDMs are associated with the near-horizon geometry of the BH, and they exist for *all* allowed values of  $l$  and  $m \geq 0$  (we classify modes using Leaver’s conventions [17], but we use units in which the BH has mass  $M = 1$ ). DMs are associated with peaks of the potential barrier; in the eikonal limit, they exist when  $\mu \leq 0.74$ . This implies that ZDMs and DMs coexist if  $0 \leq \mu \leq 0.74$ . Figure 4.1 is a “phase diagram” in QNM space, showing the regions where either the ZDMs or both the DMs and the ZDMs exist for scalar and gravitational perturbations with  $l \leq 15$ . We will discuss this phase diagram further below.

When the ZDMs and DMs coexist, and when the BH spin  $a$  is small, for each  $(l, m)$  there is only a single set of QNMs characterized by the overtone number  $n$  (where modes with larger  $n$  have stronger damping). For larger  $a$ , this set of QNMs appears to break into two branches. The DM branch originates from lower-overtone modes at smaller  $a$ , and its modes retain a finite decay rate as  $a \rightarrow 1$ . The ZDM branch originates from higher-overtone modes whose imaginary part becomes smaller than that of DMs as  $a \rightarrow 1$ , thereby forming the second branch. This is similar to the behavior of eigenmodes in quantum mechanics when we parametrically split a single potential well into two potential wells (cf. Figure 4.2 below, as well as [18] for a somewhat analogous phenomenon

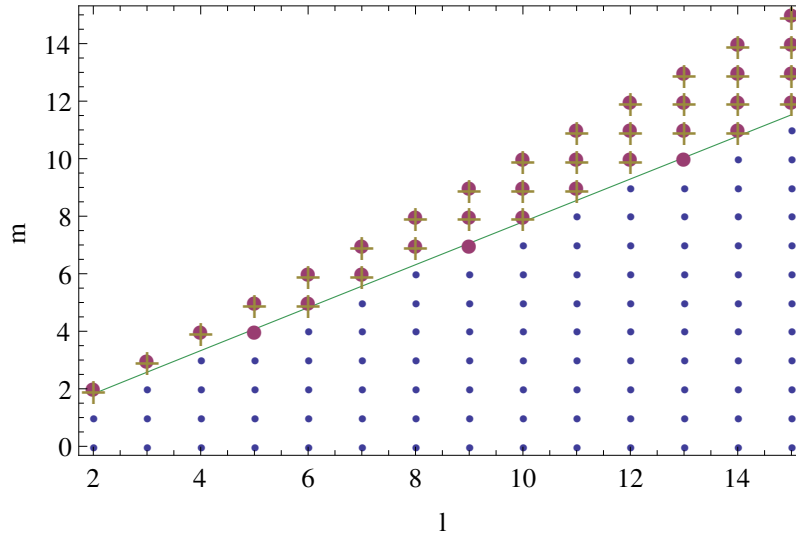


Figure 4.1: (Color online.) Phase diagram for the separation between the single- and double-branch regime for NEK BHs. Large purple dots and gold crosses correspond to  $(l, m)$  pairs with only ZDMs for perturbations with spin  $-2$  and  $0$ , respectively. Smaller blue dots correspond to  $(l, m)$  pairs with both ZDMs and DMs. The green line is the phase boundary, computed using the eikonal approximation.

in the theory of oscillations of ultracompact stars).

## 4.2 Matched Expansion

For  $\epsilon \equiv 1 - a \ll 1$  and  $\omega - m/2 \ll 1$ , the radial Teukolsky equation can be written in a self-similar form when  $(r - 1) \ll 1$  and in an asymptotic form (by setting  $a = 1$ ) when  $(r - 1) \gg \sqrt{\epsilon}$  (cf. [9, 10, 19]). The solutions of the Teukolsky equation in these regions (hypergeometric and confluent hypergeometric functions, respectively) can be matched at  $\sqrt{\epsilon} \ll (r - 1) \ll 1$  to provide the following condition for QNM frequencies:

$$e^{-\pi\delta - 2i\delta \ln(m) - i\delta \ln(8\epsilon)} \frac{\Gamma^2(2i\delta)\Gamma(1/2 + s - im - i\delta)}{\Gamma^2(-2i\delta)\Gamma(1/2 + s - im + i\delta)} \times \frac{\Gamma(1/2 - s - im - i\delta)\Gamma[1/2 + i(m - \delta - \sqrt{2}\tilde{\omega})]}{\Gamma(1/2 - s - im + i\delta)\Gamma[1/2 + i(m + \delta - \sqrt{2}\tilde{\omega})]} = 1. \quad (4.1)$$

Here we denote the eigenvalues of the angular Teukolsky equation by  ${}_sA_{lm}$ , and we define  $\delta^2 \equiv 7m^2/4 - (s + 1/2)^2 - {}_sA_{lm}$  and  $\tilde{\omega} \equiv (\omega - m\Omega_H)/\sqrt{\epsilon}$  [note that  $\Omega_H = a/(r_+^2 + a^2)$  is the horizon frequency and  $r_+ = 1 + \sqrt{1 - a^2}$  is the horizon radius]. Scalar, electromagnetic, and gravitational perturbations correspond to spin  $s = 0, -1, -2$ , respectively. If we choose the conventions that  $\mathcal{R}e(\delta) \geq 0$  and  $\mathcal{I}m(\delta) \geq 0$  when  $\delta^2$  is positive and negative, respectively, then the left-hand side of Eq. (4.1) is usually a very small number, except when it is near the poles of the  $\Gamma$ -functions in the

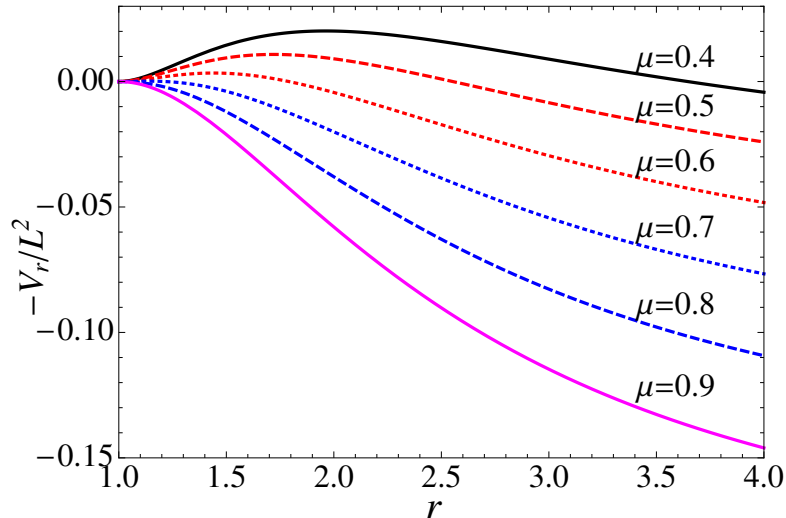


Figure 4.2: (Color online.) Plot of the potential term for  $a = 1$ , Eq. (4.6), for  $\mu = 0.4, 0.5, 0.6, 0.7, 0.8$ , and  $0.9$  (black-solid, red-dashed, red-dotted, blue-dotted, blue-dashed, and magenta-solid curves, respectively). The transition from single-branch to double-branch happens between  $\mu = 0.7$  and  $\mu = 0.8$ .

numerator. When  $m \geq 0$ , we can always find the solution near the poles at negative integers:

$$1/2 + i(m - \delta - \sqrt{2}\tilde{\omega}) \approx -n, \quad (4.2)$$

or

$$\omega \approx \frac{m}{2} - \frac{\delta\sqrt{\epsilon}}{\sqrt{2}} - i\left(n + \frac{1}{2}\right) \frac{\sqrt{\epsilon}}{\sqrt{2}}. \quad (4.3)$$

Note that the overtone index  $n$  of these ZDM frequencies need not correspond precisely to the same overtone index of Kerr QNMs at lower spins. This set of solutions was first discovered by Hod [13]. The matched-expansion derivation shows that this set of modes depends on the near-horizon region of the Kerr BH. Equation (4.3) is quite accurate when  $|\delta| \gg 1$ , but when  $|\delta| < 1$  it needs an additional correction [19]. However, the  $\sqrt{\epsilon}$  scaling of the decay rate is still correct when  $|\delta| < 1$ . The solutions to Eq. (4.3) with  $m < 0$  are those that arise from the symmetry  $\omega_{l,m} = -\omega_{l,-m}^*$ ; there are no solutions with  $m < 0$  and  $\mathcal{R}e(\omega) > 0$ , when  $\omega - m/2$  is not small. Thus, the ZDMs only exist in the *corotating* regime  $m \geq 0$ .

Another set of solutions of Eq. (4.1) may exist when  $\delta^2 < 0$  and  $2i\delta \approx -n$ , with  $n$  a positive integer. A more detailed analysis shows that, in this case, two nearly degenerate hypergeometric functions have comparable contributions to the near-horizon solution [19]. As a result, Eq. (4.1) is no longer valid when  $2i\delta \approx -n$ . As a consistency check, we looked for solutions with  $2i\delta \approx -n$  using Leaver's method and we did not find any.

### 4.3 WKB Analysis

The matched-expansion method assumes that  $\omega \approx m/2$ , but Eq. (4.1) does not hold for modes which do *not* meet this requirement (i.e., DMs). To compute these modes, we will instead use a WKB analysis in the eikonal limit  $l \gg 1$ . The radial Teukolsky equation when  $l \gg 1$  is [15]

$$\frac{d^2 u_r}{dr_*^2} + V_r u_r = \frac{d^2 u_r}{dr_*^2} + \frac{K^2 - \Delta \lambda_{lm}^0}{(r^2 + a^2)^2} u_r = 0, \quad (4.4a)$$

with

$$\begin{aligned} K &= -\omega(r^2 + a^2) + am, & \frac{d}{dr_*} &\equiv \frac{\Delta}{r^2 + a^2} \frac{d}{dr}, & \lambda_{lm}^0 &= A_{lm} + a^2 \omega^2 - 2am\omega, \\ \Delta &= r^2 - 2r + a^2. \end{aligned} \quad (4.4b)$$

We define  $\omega \equiv \omega_R - i\omega_I$ , and we note that the real and imaginary parts scale as  $\omega_R \propto l$  and  $\omega_I \propto l^0$ , while the angular constant scales as  $A_{lm} \propto l^2$ . We only keep the leading-order terms in the eikonal limit in the following discussion (therefore all  $s$ -dependent terms are neglected, and the  $A_{lm}$  are real). In Figure 4.2 and below, we will refer to  $-V_r$  as “the potential”. According to the WKB analysis and its geometric correspondence in [15], the position of the peak of the potential asymptotes the horizon as  $a \rightarrow 1$  for some of the corotating modes. For this set of QNMs, one can verify that  $V_r''$  (where primes denote derivatives with respect to  $r_*$ ) scales as  $\Delta^2$ ; thus, the peak  $r_0$  of the potential becomes broad as  $r_0$  approaches the horizon. It then follows that  $\omega_I \propto \sqrt{V_r''}/\partial_\omega V_r \rightarrow 0$ , and  $\omega_R \rightarrow m/2$  in order to satisfy  $V_r(\omega_R, r_0) = 0$  for these modes. Assuming that  $r_0 = 1 + c\sqrt{\epsilon}$  for the nearly extremal modes, where  $c$  is some constant, we can apply the eikonal equations in [15] and obtain

$$r_0 \approx 1 + \frac{m\sqrt{2\epsilon}}{\mathcal{F}_0}, \quad \omega_R \approx \frac{m}{2} - \frac{\mathcal{F}_0\sqrt{\epsilon}}{\sqrt{2}}, \quad \omega_I \approx \left(n + \frac{1}{2}\right) \frac{\sqrt{\epsilon}}{\sqrt{2}}, \quad (4.5)$$

with  $\mathcal{F}_0 = \sqrt{7m^2/4 - A_{lm}(\omega = m/2)}$ . Comparing this result with Eqs. (4.3) and (4.5), we can see the two sets of frequencies are essentially the *same* modes, although obtained in very different ways. Here  $\mathcal{F}_0^2$  and  $\delta^2$  differ by 1/4, which is reasonable because in the eikonal limit  $\mathcal{F}_0 \propto l$  and  $\delta \propto l$  (making 1/4 a higher-order correction).

To build intuition about  $\mathcal{F}_0$  and  $\delta$ , we look at  $V_r$  for extreme Kerr BHs, with  $\omega$  replaced by  $m/2$ :

$$V_r = L^2 \frac{(r-1)^2}{(r^2+1)^2} \left[ \frac{(r+1)^2}{4} \mu^2 - \alpha(\mu) + \frac{3}{4} \mu^2 \right], \quad (4.6)$$

where  $L \equiv l + 1/2$  and  $\alpha(\mu) \equiv A_{lm}/L^2$ . According to the WKB analysis of the radial Teukolsky equation [20], the QNM frequencies are determined by the peak of the potential. As shown in Figure 4.2, when  $\mu$  is large the maximum of the potential is at the horizon,  $r = 1$ , as expected for

ZDMs. As  $\mu$  decreases and falls below some critical value  $\mu_c$ , the peak moves outside the horizon, and the horizon becomes a local minimum of the potential. At the peak  $\omega_I$  is nonzero because  $d^2V_r/dr_*^2|_{r_0} \neq 0$ , so we have DMs. The criterion for having no peak outside the horizon is

$$\frac{(r+1)^2}{4}\mu^2 - \alpha(\mu) + \frac{3}{4}\mu^2 > 0 \quad \text{for } r=1, \quad (4.7)$$

i.e.,  $\mathcal{F}_0^2 > 0$  (or  $\delta^2 > 0$ ). The values at which  $\mathcal{F}_0^2$  (or  $\delta^2$ ) vanish lead to the condition for the critical  $\mu_c$ :  $\alpha(\mu_c) = \frac{7}{4}\mu_c^2$ . If we use the approximation  $\alpha(\mu) \approx 1 - a^2\omega^2(1-\mu^2)/(2L^2)$  [15], this will reproduce Hod's approximate analytical result  $\mu_c \approx [(15 - \sqrt{193})/2]^{1/2}$  [16]. We can obtain the exact  $\mu_c$  (in the eikonal limit) by inserting  $\alpha(\mu_c) = \frac{7}{4}\mu_c^2$  into the Bohr-Sommerfeld condition for  $\alpha$  derived in [15]:

$$\int_{\theta_-}^{\theta_+} \sqrt{\alpha - \frac{\mu^2}{\sin^2\theta} + \frac{\mu^2}{4} \cos^2\theta} d\theta = (1 - |\mu|)\pi, \quad (4.8)$$

where  $\theta_+ = \pi - \theta_-$  and  $\theta_- = \arcsin(\sqrt{3}-1)$  are the angles at which the integrand vanishes. Therefore we have

$$\mu_c = \frac{1}{1 + \mathcal{I}/\pi} \quad \mathcal{I} = \int_{\theta_-}^{\theta_+} d\theta \sqrt{\frac{7}{4} - \frac{1}{\sin^2\theta} + \frac{1}{4} \cos^2\theta}, \quad (4.9)$$

which yields the numerical value  $\mu_c \simeq 0.74398$ . In the eikonal limit, when  $\mu > \mu_c$  NEK BHs have only ZDMs (“single-phase regime”); when  $0 \leq \mu \leq \mu_c$ , both DMs and ZDMs exist (“double-phase regime”).

## 4.4 Phase Boundary

Although there is a clear criterion for determining the boundary between the single-phase regime and the double-phase regime in the eikonal limit (when  $\mu < \mu_c$ , the peak of the potential no longer resides on the horizon) it is not immediately clear if a similar criterion holds when  $l$  is small. For scalar perturbations, however, we can write the radial Teukolsky potential for extreme-Kerr BHs with generic  $l, m$ , under the assumption that  $\omega = m/2$  (and, therefore, the  ${}_0A_{lm}$  remain real for the ZDMs):

$$V_r = \frac{(r-1)^2}{(r^2+1)^2} \left[ \frac{(r+1)^2}{4} m^2 - {}_0A_{lm} \right] + \frac{(r-1)^2}{(r^2+1)^2} \left[ \frac{3}{4} m^2 + \frac{(r-1)(2r^2+3r-1)}{(1+r^2)^2} \right]. \quad (4.10)$$

It is not difficult to see that there is still no peak outside the horizon when  $\frac{7}{4}m^2 > {}_0A_{lm}$ , or  $\mathcal{F}_0^2 > 0$ . For electromagnetic and gravitational perturbations the potential terms  $-V_r$  are complex functions, thereby making the positions of their extrema more difficult to define. Detweiler [21], however, has shown that the radial function can be transformed so that it satisfies a differential

equation with a real potential. Using this potential, the criterion to exclude peaks outside the horizon is [19]:

$$\mathcal{F}_s^2 \equiv \frac{7}{4}m^2 - s(s+1) - {}_sA_{lm} \left( \omega = \frac{m}{2} \right) > 0. \quad (4.11)$$

Note that this expression respects the pairing symmetry  $-{}_sA_{lm} = {}_sA_{lm} + 2s$ , and that for all  $s$ ,  $\mathcal{F}_s^2$  and  $\delta^2$  differ from each other only by  $1/4$ . For  $s = 0, -2$  and  $2 \leq l \leq 100$ , we have searched all QNMs numerically and have not found any mode simultaneously satisfying  $\delta^2 < 0$  and  $\mathcal{F}_s^2 > 0$ ; therefore, the sign of  $\delta^2$  also determines whether a peak exists outside the horizon. In addition, we have used Leaver's continued-fraction algorithm to determine the phase boundary numerically. As shown in Figure 4.1, the actual phase boundary matches the criterion predicted by the eikonal limit,  $\mu = \mu_c$ . In addition, for scalar and gravitational perturbations, we find numerically that modes are in the single-phase regime when  $\mathcal{F}_s^2 > 0$  for all  $l \leq 15$ . This reinforces our physical understanding that DMs are associated with a peak of the potential outside the horizon, while ZDMs are somewhat similar in nature to the  $s$ -modes in ultracompact stars [18].

## 4.5 Bifurcation

Schwarzschild and slowly spinning Kerr BHs have a single set of QNMs for each  $l, m$  that are characterized by their overtone number  $n$ . If the ZDMs originate from modes at higher- $n$  than the DMs when the BH spin is low, then when the spin increases beyond a critical value  $a_s = 1 - \epsilon_s$ , a single set of QNMs may split into two branches.

We numerically investigate this bifurcation effect by examining the complex QNM frequency plane to search for solutions of Leaver's continued-fraction equations [17, 19]. In Figure 4.3, we plot the contours of constant value of the logarithm of the continued-fraction expansion, truncating at  $N = 800$  terms. The QNM frequencies correspond to the local minima of this sum, where the contours cluster. The shading indicates the value of the fraction, with darker values nearly zero.

When  $\mu < \mu_c$ , a single set of QNMs splits into two branches for increasing  $a$  (see the left-hand panels of Figure 4.3, where  $l = 10, m = 7$ , as the spin increases from  $a = 0.9990$  to  $a = 0.9999$  from the upper panel to the lower). The ZDM branch is quite accurately described by Eq. (4.3); the imaginary part of the ZDMs scales like  $\sqrt{\epsilon}$ , and they move towards the real axis as  $\epsilon \rightarrow 0$ . The DM branch changes relatively little with increasing spin (it is expected that the WKB peak can only support a finite number of modes [19], and there are only three DMs in the lower-left panel). In this case, the WKB formulae of [15] are in good agreement with the lowest-overtone DM (marked with a  $\times$  in the figure).

For  $\mu > \mu_c$  there is no bifurcation, and the modes are predicted fairly well by Eq. (4.3). We can

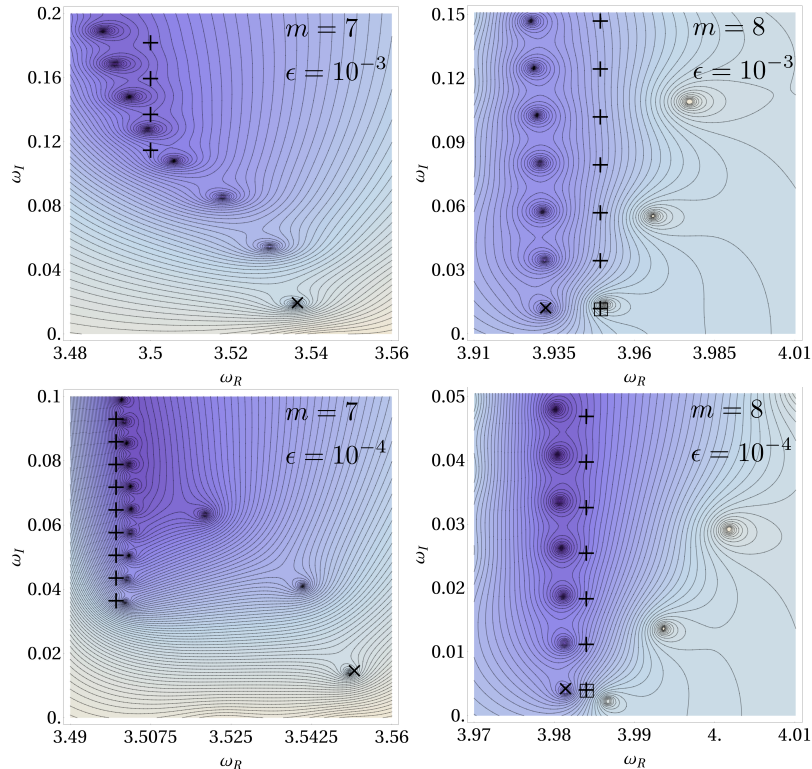


Figure 4.3: (Color online.) QNM frequencies with  $l = 10$  for NEK BHs. Contours are constant values of the logarithm of the continued fraction in the complex plane; darker shading indicates values near zero. The + symbols are the ZDM predictions, a  $\times$  is the lowest-overtone WKB prediction from [15], and the box is centered at the WKB prediction from Eq. (4.5). No branching is observed for modes with  $m = 8$ . Note that the closed contours with light shading have large values and do not correspond to any QNM. Further discussion of the figure is in the text.

see this in the right-hand panels of Figure 4.3, where  $l = 10$ ,  $m = 8$  and we again raise the spin from  $a = 0.9990$  to  $a = 0.9999$ . For the  $m = 8$  modes, we also mark the leading-order WKB prediction of Eq. (4.5) with a box. For the bifurcation effect, we can define a benchmark  $a_c = 1 - \epsilon_c$  as the BH spin at which the imaginary part of the *fundamental* ZDM is equal to that of the *fundamental* DM:

$$\frac{\sqrt{\epsilon_c}}{2\sqrt{2}}(1 + 2|\delta|) = \frac{1}{2} \left. \frac{\sqrt{2V_r''}}{\partial_\omega V_r} \right|_{r_0}. \quad (4.12)$$

The right-hand side of Eq. (4.12) can be evaluated using the approximate WKB formula in [15]. Since both sides of Eq. (4.12) depend on  $\epsilon$ , we solve for  $\epsilon_c$  iteratively; this converges quickly for a variety of initial spins. By computing  $\epsilon_c$  for  $l \leq 15$  and  $0 < m < (l + 1/2)\mu_c$ , we find that  $L^2\epsilon_c = 10^{-3}(11.6 - 3.12\mu - 18.0\mu^2)$  is a reasonable fitting formula. For the  $l = 10$ ,  $m = 7$  case, Eq. (4.12) gives  $\epsilon_c \sim 10^{-5}$ , which is in agreement with numerical results; for the  $l = 2$ ,  $m = 1$  case it gives  $\epsilon_c \sim 10^{-3}$ .

In Figure 4.3, however, it is clear that the bifurcation actually starts when the *fundamental*

ZDM's imaginary part equals the imaginary part of the *highest-overtone* DM (in Figure 4.3 it is the third overtone). This happens at a spin  $a_s < a_c$ . Because we do not have a good estimate of the number of modes in the DM branch (beyond the fact that it should be proportional to  $L$  and a function of  $\mu$  in the eikonal limit [19]) and because WKB techniques are not accurate for these high-overtone DMs, finding an analytic solution for  $a_s$  remains an open problem.

## 4.6 Conclusions

We identified two different regimes in the NEK QNM spectrum. In the double-phase regime, we found that the lowest ZDM becomes less damped than the lowest DM at some critical  $a_c$ , for which we provided an analytical estimate. For sufficiently large  $a$ , Eq. (4.3) is accurate at the least for those ZDMs with smaller decays than the point where the branches bifurcate. We estimate that the number of ZDMs below the bifurcation is  $\propto \sqrt{\epsilon_s/\epsilon}$  [19]. In the future, we would like to investigate the behavior of the ZDM branch in the high-overtone limit [22], where these approximations break down.

## Acknowledgments

We thank Sam Dolan for advice on the WKB method, and Zhongyang Zhang for discussions during the early stages of this work. This research is funded by NSF Grants PHY-1068881 and PHY-1005655, CAREER Grants PHY-0956189 and PHY-1055103, NASA Grant No.NNX09AF97G, the Sherman Fairchild Foundation, the Brinson Foundation, and the David and Barbara Groce Startup Fund at Caltech.

## Bibliography

- [1] L. W. Brenneman *et al.*, *Astrophys. J.* **736**, 103 (2011).
- [2] R. Wald, *Ann. Phys.*, **83**, 548, (1974); S. Hod, *Phys. Rev. Lett.* **100** 121101 (2008); T. Jacobson and T. P. Sotiriou, *Phys. Rev. Lett.* **103**, 141101 (2009); E. Barausse, V. Cardoso, and G. Khanna, *Phys. Rev. Lett.* **105**, 261102 (2010); P. Zimmerman, I. Vega, E. Poisson, and R. Haas (2012), [arXiv:1211.3889](https://arxiv.org/abs/1211.3889).
- [3] A. Strominger and C. Vafa, *Phys. Lett. B* **379**, 99 (1996).
- [4] J. Bardeen and G. T. Horowitz, *Phys. Rev. D* **60**, 104030 (1999).
- [5] M. Guica, T. Hartman, W. Song, and A. Strominger, *Phys. Rev. D* **80**, 124008 (2009); O. J. C. Dias, H. S. Reall, and J. E. Santos, *JHEP* **0908**, 101 (2009); I. Bredberg, C. Keeler,

- V. Lysov, and A. Strominger, Nucl. Phys. Proc. Suppl. **216**, 194 (2011); G. Compere, Living Rev. Rel. **15**, 11 (2012).
- [6] G. Dotti, R. J. Gleiser, I. F. Ranea-Sandoval, and H. Vucetich, Class. Quant. Grav. **25**, 245012 (2008); P. Pani, E. Barausse, E. Berti, and V. Cardoso, Phys. Rev. D **82**, 044009 (2010); G. Dotti, R. J. Gleiser, and I. F. Ranea-Sandoval, Class. Quant. Grav. **29**, 095017 (2012); J. Lucietti and H. S. Reall, Phys. Rev. D **86**, 104030 (2012).
- [7] E. Berti, V. Cardoso, and A. O. Starinets, Class. Quant. Grav. **26**, 163001 (2009).
- [8] I. Bredberg, T. Hartman, W. Song, and A. Strominger, JHEP **1004**, 019 (2010).
- [9] S. A. Teukolsky and W. H. Press, Ap. J. **193**, 443 (1974).
- [10] S. Detweiler, Ap. J. **239**, 292 (1980).
- [11] M. Sasaki and T. Nakamura, Gen. Rel. Grav. **22**, 1351 (1990).
- [12] N. Andersson and K. Glampedakis, Phys. Rev. Lett. **84**, 4537 (2000).
- [13] S. Hod, Phys. Rev. D **78**, 084035 (2008).
- [14] V. Cardoso, Phys. Rev. D **70**, 127502 (2004).
- [15] H. Yang, D. A. Nichols, F. Zhang, A. Zimmerman, Z. Zhang, and Y. Chen, Phys. Rev. D **86**, 104006 (2012).
- [16] S. Hod, Phys. Lett. B **715**, 348 (2012).
- [17] E. W. Leaver, Proc. R. Soc. A **402**, 285 (1985); E. W. Leaver, Phys. Rev. D **34**, 384 (1986).
- [18] S. Chandrasekhar and V. Ferrari, Proc. Roy. Soc. Lond. A **434**, 449 (1991).
- [19] H. Yang, F. Zhang, A. Zimmerman, D. A. Nichols, E. Berti, and Y. Chen, in preparation.
- [20] S. Iyer and C. M. Will, Phys. Rev. D **35**, 3621 (1987).
- [21] S. Detweiler, Proc. R. Soc. A **352**, 381, (1977).
- [22] E. Berti, V. Cardoso, and S. Yoshida, Phys. Rev. D **69**, 124018 (2004); U. Keshet and A. B. Meir (2012), [arXiv:1207:2460](https://arxiv.org/abs/1207.2460).

## Part II

# Visualization of Curved Spacetime

## Chapter 5

# Frame-Dragging Vortexes and Tidal Tendexes Attached to Colliding Black Holes: Visualizing the Curvature of Spacetime

When one splits spacetime into space plus time, the spacetime curvature (Weyl tensor) gets split into an “electric” part  $\mathcal{E}_{jk}$  that describes tidal gravity and a “magnetic” part  $\mathcal{B}_{jk}$  that describes differential dragging of inertial frames. We introduce tools for visualizing  $\mathcal{B}_{jk}$  (frame-drag vortex lines, their vorticity, and vortexes) and  $\mathcal{E}_{jk}$  (tidal tendex lines, their tendicity, and tendexes), and also visualizations of a black-hole horizon’s (scalar) vorticity and tendicity. We use these tools to elucidate the nonlinear dynamics of curved spacetime in merging black-hole binaries.

---

Originally published as R. Owen, J. Brink, Y. Chen, J. D. Kaplan, G. Lovelace, K. D. Matthews, D. A. Nichols, M. A. Scheel, F. Zhang, A. Zimmerman, and K. S. Thorne, *Phys. Rev. Lett.* **106**, 151101 (2011). Copyright 2011 by the American Physical Society.

### 5.1 Introduction

When one foliates spacetime with spacelike hypersurfaces, the Weyl curvature tensor  $C_{\alpha\beta\gamma\delta}$  (same as Riemann in vacuum) splits into “electric” and “magnetic” parts  $\mathcal{E}_{jk} = C_{\hat{0}j\hat{0}k}$  and  $\mathcal{B}_{jk} = \frac{1}{2}\epsilon_{j pq} C^{pq}{}_{k\hat{0}}$  (see e.g. [1] and references therein); both  $\mathcal{E}_{jk}$  and  $\mathcal{B}_{jk}$  are spatial, symmetric, and trace-free. Here the indexes are in the reference frame of “orthogonal observers” who move orthogonal to the space slices;  $\hat{0}$  is their time component,  $\epsilon_{j pq}$  is their spatial Levi-Civita tensor, and throughout we use

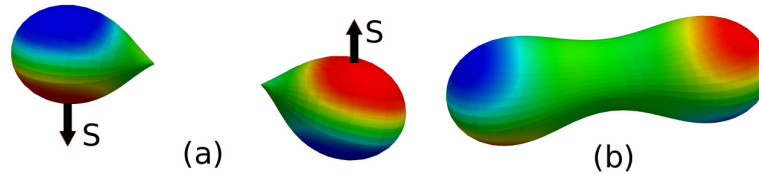


Figure 5.1: Vortices (with positive vorticity blue, negative vorticity red) on the 2D event horizons of spinning, colliding black holes, just before and just after merger. (From the simulation reported in [4].)

units with  $c = G = 1$ .

Because two orthogonal observers separated by a tiny spatial vector  $\xi$  experience a relative tidal acceleration  $\Delta a_j = -\mathcal{E}_{jk}\xi^k$ ,  $\mathcal{E}_{jk}$  is called the *tidal field*. And because a gyroscope at the tip of  $\xi$  precesses due to frame dragging with an angular velocity  $\Delta\Omega_j = \mathcal{B}_{jk}\xi^k$  relative to inertial frames at the tail of  $\xi$ , we call  $\mathcal{B}_{jk}$  the *frame-drag field*.

## 5.2 Vortexes and Tendexes in Black-Hole Horizons

For a binary black hole, our space slices intersect the 3-dimensional (3D) event horizon in a 2D horizon with inward unit normal  $\mathbf{N}$ ; so  $\mathcal{B}_{NN}$  is the rate the frame-drag angular velocity around  $\mathbf{N}$  increases as one moves inward through the horizon. Because of the connection between rotation and vorticity, we call  $\mathcal{B}_{NN}$  the horizon’s *frame-drag vorticity*, or simply its *vorticity*.

Because  $\mathcal{B}_{NN}$  is boost-invariant along  $\mathbf{N}$  [2], the horizon’s vorticity is independent of how fast the orthogonal observers fall through the horizon, and is even unchanged if the observers hover immediately above the horizon (the FIDOs of the “black-hole membrane paradigm” [3]).

Figure 5.1 shows snapshots of the horizon for two identical black holes with transverse, oppositely directed spins  $\mathbf{S}$ , colliding head on. Before the collision, each horizon has a negative-vorticity region (red) centered on  $\mathbf{S}$ , and a positive-vorticity region (blue) on the other side. We call these regions of concentrated vorticity *horizon vortexes*. Our numerical simulation [4] shows the four vortexes being transferred to the merged horizon (Figure 5.1b), then retaining their identities, but sloshing between positive and negative vorticity and gradually dying, as the hole settles into its final Schwarzschild state; see the movie in Reference [5].

Because  $\mathcal{E}_{NN}$  measures the strength of the tidal-stretching acceleration felt by orthogonal observers as they fall through (or hover above) the horizon, we call it the horizon’s *tendicity* (a word coined by David Nichols from the Latin *tendere*, “to stretch”). On the two ends of the merged horizon in Figure 5.1b there are regions of strongly enhanced tendicity, called *tendexes*; cf. Figure 5.5 below.

An orthogonal observer falling through the horizon carries an orthonormal tetrad consisting of

her 4-velocity  $\mathbf{U}$ , the horizon's inward normal  $\mathbf{N}$ , and transverse vectors  $\mathbf{e}_2$  and  $\mathbf{e}_3$ . In the null tetrad  $\mathbf{l} = (\mathbf{U} - \mathbf{N})/\sqrt{2}$  (tangent to horizon generators),  $\mathbf{n} = (\mathbf{U} + \mathbf{N})/\sqrt{2}$ ,  $\mathbf{m} = (\mathbf{e}_2 + i\mathbf{e}_3)/\sqrt{2}$ , and  $\mathbf{m}^*$ , the Newman-Penrose Weyl scalar  $\Psi_2$  [6] is  $\Psi_2 = (\mathcal{E}_{NN} + i\mathcal{B}_{NN})/2$ . Here we use sign conventions of [7], appropriate for our  $(-+++)$  signature.

Penrose and Rindler [8] define a complex scalar curvature  $\mathcal{K} = \mathcal{R}/4 + i\mathcal{X}/4$  of the 2D horizon, with  $\mathcal{R}$  its intrinsic (Ricci) scalar curvature (which characterizes the horizon's shape) and  $\mathcal{X}$  proportional to the 2D curl of its Hájíček field [9] (the space-time part of the 3D horizon's extrinsic curvature). Penrose and Rindler show that  $\mathcal{K} = -\Psi_2 + \mu\rho - \lambda\sigma$ , where  $\rho$ ,  $\sigma$ ,  $\mu$ , and  $\lambda$  are spin coefficients related to the expansion and shear of the null vectors  $\mathbf{l}$  and  $\mathbf{n}$ , respectively. In the limit of a shear- and expansion-free horizon (e.g. a quiescent black hole; Figure 5.2a,b,c),  $\mu\rho - \lambda\sigma$  vanishes, so  $\mathcal{K} = -\Psi_2$ , whence  $\mathcal{R} = -2\mathcal{E}_{NN}$  and  $\mathcal{X} = -2\mathcal{B}_{NN}$ . As the dimensionless spin parameter  $a/M$  of a quiescent (Kerr) black hole is increased, the scalar curvature  $\mathcal{R} = -2\mathcal{E}_{NN}$  at its poles decreases, becoming negative for  $a/M > \sqrt{3}/2$ ; see the blue spots on the poles in Figure 5.2b compared to solid red for the nonrotating hole in Figure 5.2a. In our binary-black-hole simulations, the contributions of the spin coefficients to  $\mathcal{K}$  on the apparent horizons are small [ $L2$ -norm  $\lesssim 1\%$ ] so  $\mathcal{R} \simeq -2\mathcal{E}_{NN}$  and  $\mathcal{X} \simeq -2\mathcal{B}_{NN}$ , except for a time interval  $\sim 5M_{\text{tot}}$  near merger. Here  $M_{\text{tot}}$  is the binary's total mass. On the event horizon, the duration of spin-coefficient contributions  $> 1\%$  is somewhat longer, but we do not yet have a good measure of it.

Because  $\mathcal{X}$  is the 2D curl of a 2D vector, its integral over the 2D horizon vanishes. Therefore, positive-vorticity regions must be balanced by negative-vorticity regions; it is impossible to have a horizon with just one vortex. By contrast, the Gauss-Bonnet theorem says the integral of  $\mathcal{R}$  over the 2D horizon is  $8\pi$  (assuming  $S_2$  topology), which implies the horizon tendicity  $\mathcal{E}_{NN}$  is predominantly negative (because  $\mathcal{E}_{NN} \simeq -\mathcal{R}/2$  and  $\mathcal{R}$  is predominantly positive). Many black holes have negative horizon tendicity everywhere (an exception is Figure 5.2b), so their horizon tendexes must be distinguished by deviations of  $\mathcal{E}_{NN}$  from a horizon-averaged value.

### 5.3 3D Vortex and Tendex Lines

The frame-drag field  $\mathcal{B}_{jk}$  is symmetric and trace free and therefore is fully characterized by its three orthonormal eigenvectors  $\mathbf{e}_{\bar{j}}$  and their eigenvalues  $\mathcal{B}_{\bar{1}\bar{1}}$ ,  $\mathcal{B}_{\bar{2}\bar{2}}$  and  $\mathcal{B}_{\bar{3}\bar{3}}$ . We call the integral curves along  $\mathbf{e}_{\bar{j}}$  *vortex lines*, and their eigenvalue  $\mathcal{B}_{\bar{j}\bar{j}}$  those lines' *vorticity*, and we call a concentration of vortex lines with large vorticity a *vortex*. For the tidal field  $\mathcal{E}_{jk}$  the analogous quantities are *tendex lines*, *tendicity* and *tendexes*. For a nonrotating (Schwarzschild) black hole, we show a few tendex lines in Figure 5.2a; and for a rapidly-spinning black hole (Kerr metric with  $a/M = 0.95$ ) we show tendex lines in Figure 5.2b and vortex lines in Figure 5.2c.

If a person's body (with length  $\ell$ ) is oriented along a positive-tendicity tendex line (blue in

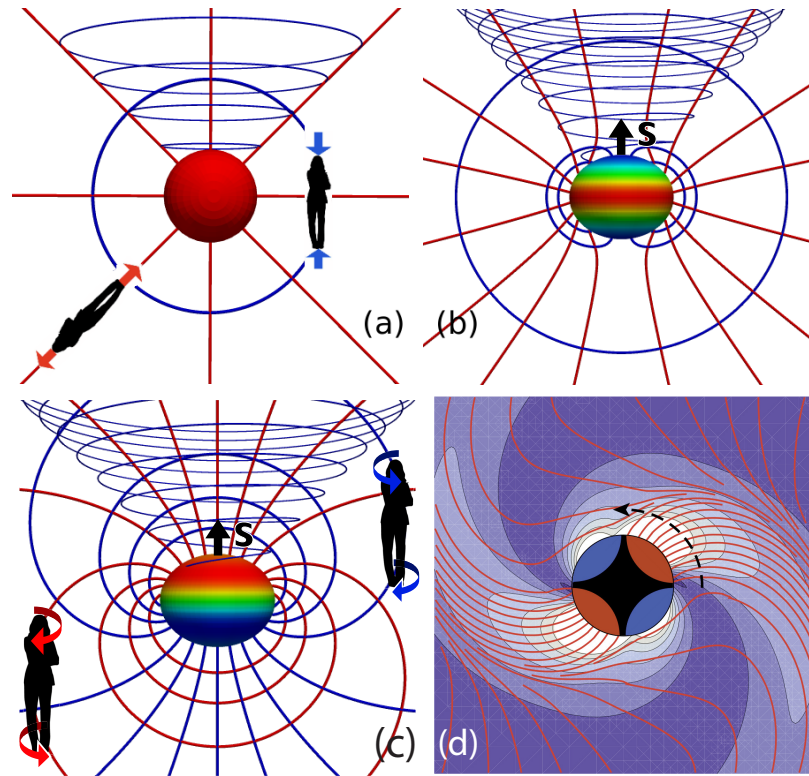


Figure 5.2: Four different black holes, with horizons colored by their tendicity (upper two panels) or vorticity (lower two panels), ranging from most negative (red) to most positive (blue); and with a Kerr-Schild horizon-penetrating foliation (Exercise 33.8 of Reference [18]). (a) A nonrotating black hole and its tendex lines; negative-tendicity lines are red, and positive blue. (b) A rapidly rotating (Kerr) black hole, with spin  $a/M = 0.95$ , and its tendex lines. (c) The same Kerr black hole and its vortex lines. (d) Equatorial plane of a nonrotating black hole that is oscillating in an odd-parity  $l = m = 2$  quasinormal mode, with negative-vorticity vortex lines emerging from red horizon vortices. The lines' vorticities are indicated by contours and colors; the contour lines, in units  $(2M)^{-2}$  and going outward from the hole, are  $-10, -8, -6, -4, -2$ .

Figure 5.2a), she feels a head-to-foot compressional acceleration  $\Delta a = |\text{tendicity}|\ell$ ; for negative tendicity (red) it is a stretch. If her body is oriented along a positive-vorticity vortex line (blue in Figure 5.2c), her head sees a gyroscope at her feet precess clockwise with angular speed  $\Delta\Omega = |\text{vorticity}|\ell$ , and her feet see a gyroscope at her head also precess clockwise at the same rate. For negative vorticity (red) the precessions are counterclockwise.

For a nonrotating black hole, the stretching tendex lines are radial, and the squeezing ones lie on spheres (Figure 5.2a). When the hole is spun up to  $a/M = 0.95$  (Figure 5.2b), its toroidal tendex lines acquire a spiral, and its poloidal tendex lines, when emerging from one polar region, return to the other polar region. For any spinning Kerr hole (e.g. Figure 5.2c), the vortex lines from each polar region reach around the hole and return to the same region. The red vortex lines from the red north polar region constitute a *counterclockwise vortex*; the blue ones from the south polar region constitute a *clockwise vortex*.

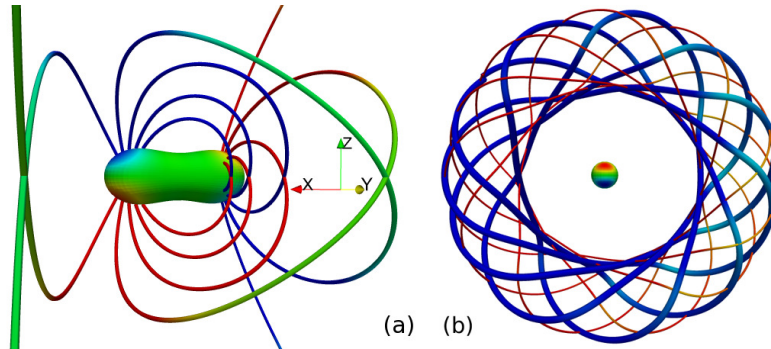


Figure 5.3: Head-on, transverse-spin simulation: (a) Shortly after merger, vortex lines link horizon vortices of same polarity (red to red; blue to blue). Lines are color coded by vorticity (different scale from horizon). (b) Sloshing of near-zone vortices generates vortex loops traveling outward as gravitational waves; thick and thin lines are orthogonal vortex lines.

As a dynamical example, consider a Schwarzschild black hole's fundamental odd-parity  $l = m = 2$  quasinormal mode of pulsation, which is governed by Regge-Wheeler perturbation theory [10] and has angular eigenfrequency  $\omega = (0.74734 - 0.17792i)/2M$ , with  $M$  the hole's mass. From the perturbation equations, we have deduced the mode's horizon vorticity:  $\mathcal{B}_{NN} = \Re\{9 \sin^2 \theta / (2i\omega M^3) \exp[2i\phi - i\omega(\tilde{t} + 2M)]\}$ . (Here  $\tilde{t}$  is the ingoing Eddington-Finkelstein time coordinate, and the mode's Regge-Wheeler radial eigenfunction  $Q(r)$  is normalized to unity near the horizon.) At time  $\tilde{t} = 0$ , this  $\mathcal{B}_{NN}$  exhibits four horizon vortices [red and blue in Figure 5.2d], centered on the equator at  $(\theta, \phi) = (\pi/2, 1.159 + k\pi/2)$  ( $k = 0, 1, 2, 3$ ), and with central vorticities  $\mathcal{B}_{NN} = -(-1)^k 39.22 / (2M)^2$ . From analytic formulae for  $\mathcal{B}_{jk}$  and a numerical  $Q(r)$ , we have deduced the equatorial-plane red vortex lines and vorticities shown in Figure 5.2d. As time  $\tilde{t}$  passes, the vortices rotate counterclockwise, so they resemble water splayed out from a turning sprinkler. The transition from near zone to wave zone is at  $r \sim 4M$  (near the outermost part of the second contour line). As one moves into the wave zone, each of the red vortices is smoothly transformed into a gravitational-wave trough and the 3D vortices that emerge from the blue horizon vortices (concentrated in the dark region of this figure) are transformed into gravitational-wave crests.

## 5.4 Vortex and Tendex Evolutions in Binary Black Holes (BBHs)

We have explored the evolution of frame-drag vortices and tidal tendexes in numerical simulations of three BBHs that differ greatly from each other.

Our first simulation (documented in Reference [4]; movies in Reference [5]) is the head-on, transverse-spin merger depicted in Figure 5.1 above, with spin magnitudes  $a/M = 0.5$ . As the holes approach each other then merge, their 3D vortex lines, which originally link a horizon vortex

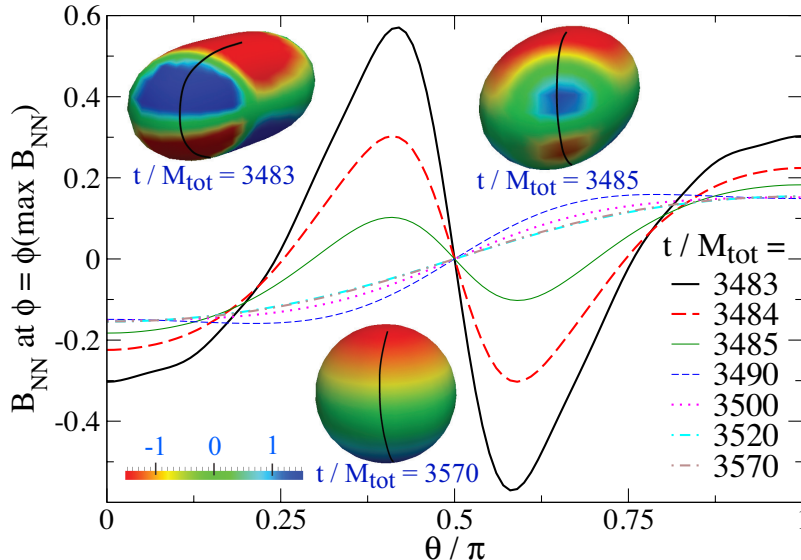


Figure 5.4: Insets: snapshots of the common apparent horizon for the  $a/M = 0.95$  anti-aligned simulation, color coded with the horizon vorticity  $B_{NN}$ . Graphs:  $B_{NN}$  as a function of polar angle  $\theta$  at the azimuthal angle  $\phi$  that bisects the four vortexes (along the black curves in snapshots).

to itself on a single hole (Figure 5.2c), reconnect so on the merged hole they link one horizon vortex to the other of the same polarity (Figure 5.3a). After merger, the near-zone 3D vortexes slosh (their vorticity oscillates between positive and negative), generating vortex loops (Figure 5.3b) that travel outward as gravitational waves.

Our second simulation (documented in Reference [11]; movies in Reference [12]) is the inspiral and merger of two identical, fast-spinning holes ( $a/M = 0.95$ ) with spins antialigned to the orbital angular momentum. Figure 5.4 shows the evolution of the vorticity  $\mathcal{B}_{NN}$  on the common apparent horizon beginning just after merger (at time  $t/M_{\text{tot}} = 3483$ ), as seen in a frame that co-rotates with the small horizon vortexes. In that frame, the small vortexes (which arise from the initial holes' spins) appear to diffuse into the two large central vortexes (which arise from the initial holes' orbital angular momentum), annihilating some of their vorticity. (This is similar to the diffusion and annihilation of magnetic field lines with opposite polarity threading a horizon [3].) Making this heuristic description quantitative, or disproving it, is an important challenge.

Our third simulation (see movies in Reference [13]) is a variant of the “extreme-kick” merger studied by Campanelli et al. [14] and others [15, 16]: two identical holes, merging from an initially circular orbit, with oppositely directed spins  $a/M = 0.5$  lying in the orbital  $(x, y)$  plane. In this case, the vortexes and tendexes in the merged hole's  $(x, y)$  plane rotate as shown in Figure 5.2d. We have tuned the initial conditions to make the final hole's kick (nearly) maximal, in the  $+z$  direction. The following considerations explain the origin of this maximized kick:

In a plane gravitational wave, all the vortex and tendex lines with nonzero eigenvalues lie in the

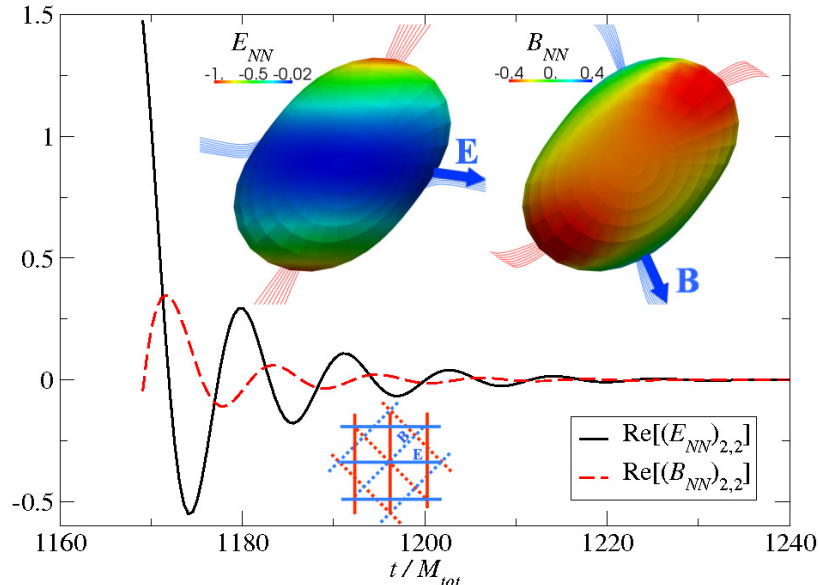


Figure 5.5: Bottom inset: tendex and vortex lines for a plane gravitational wave;  $\mathbf{E} \times \mathbf{B}$  is in the propagation direction. Upper two insets: for the “extreme-kick simulation”, as seen looking down the merged hole’s rotation axis ( $-z$  direction): the apparent horizon color coded with the horizon tendicity (left inset) and vorticity (right inset), and with 3D vortex lines and tendex lines emerging from the horizon. The tendexes with the most positive tendicity (blue;  $\mathbf{E}$ ) lead the positive-vorticity vortices (blue,  $\mathbf{B}$ ) by about  $45^\circ$  as they rotate counterclockwise. This  $45^\circ$  lead is verified in the oscillating curves, which show the rotating  $\mathcal{B}_{NN}$  and  $\mathcal{E}_{NN}$  projected onto a nonrotating  $\ell = 2, m = 2$  spherical harmonic.

wave fronts and make angles of 45 degrees to each other (bottom inset of Figure 5.5.) For vectors  $\mathbf{E}$  (parallel to solid, positive-tendicity tendex line) and  $\mathbf{B}$  (parallel to dashed, positive-vorticity vortex line),  $\mathbf{E} \times \mathbf{B}$  is in the wave’s propagation direction.

Now, during and after merger, the black hole’s near-zone rotating tendex lines (top left inset in Figure 5.5) acquire accompanying vortex lines as they travel outward into the wave zone and become gravitational waves; and the rotating near-zone vortex lines acquire accompanying tendex lines. Because of the evolution-equation duality between  $\mathcal{E}_{ij}$  and  $\mathcal{B}_{ij}$ , the details of this wave formation are essentially the same for the rotating tendex and vortex lines. Now, in the near zone, the vectors  $\mathbf{E}$  and  $\mathbf{B}$  along the tendex and vortex lines (Figure 5.5) make the same angle with respect to each other as in a gravitational wave (45 degrees) and have  $\mathbf{E} \times \mathbf{B}$  in the  $-z$  direction. This means that the gravitational waves produced by the rotating near-zone tendex lines and those produced by the rotating near-zone vortex lines will superpose constructively in the  $-z$  direction and destructively in the  $+z$  direction, leading to a maximized gravitational-wave momentum flow in the  $-z$  direction and maximized black-hole kick in the  $+z$  direction. An extension of this reasoning shows that the black-hole kick velocity is sinusoidal in twice the angle between the merged hole’s near-zone rotating vortices and tendexes, in accord with simulations.

## 5.5 Conclusions

In our BBH simulations, the nonlinear dynamics of curved spacetime appears to be dominated by (i) the transfer of spin-induced frame-drag vortexes from the initial holes to the final merged hole, (ii) the creation of two large vortexes on the merged hole associated with the orbital angular momentum, (iii) the subsequent sloshing, diffusion, and/or rotational motion of the spin-induced vortexes, (iv) the formation of strong negative  $\mathcal{E}_{NN}$  poloidal tendexes on the merged horizon at the locations of the original two holes, associated with the horizon's elongation, and a positive  $\mathcal{E}_{NN}$  tendex at the neck where merger occurs, and (v) the oscillation, diffusion, and/or circulatory motion of these tendexes.

We *conjecture* that there is no other important dynamics in the merger and ringdown of BBHs. If so, there are important consequences: (i) This could account for the surprising simplicity of the BBH gravitational waveforms predicted by simulations. (ii) A systematic study of frame-drag vortexes and tidal tendexes in BBH simulations may produce improved understanding of BBHs, including their waveforms and kicks. The new waveform insights may lead to improved functional forms for waveforms that are tuned via simulations to serve as templates in LIGO/VIRGO data analysis. (iii) Approximation techniques that aim to smoothly cover the full spacetime of BBH mergers (e.g. the combined Post-Newtonian and black-hole-perturbation theory method [17]) might be made to capture accurately the structure and dynamics of frame-drag vortexes and tidal tendexes. If so, these approximations may become powerful and accurate tools for generating BBH waveforms.

## Acknowledgements

We thank Larry Kidder and Saul Teukolsky for helpful discussions. Our simulations have been performed using the Spectral Einstein Code (SpEC) [19]. This research was supported by NSF grants PHY-0601459, PHY-0653653, PHY-0960291, PHY-0969111, PHY-1005426, and CAREER grant PHY-0956189, by NASA grants NNX09AF97G and NNX09AF96G, and by the Sherman Fairchild Foundation, the Brinson Foundation, and the David and Barbara Groce fund.

## Bibliography

- [1] R. Maartens and B. A. Bassett, *Class. Quantum Grav.* **15**, 705 (1998).
- [2] R. H. Price and K. S. Thorne, *Phys. Rev. D* **33**, 330915 (1986).
- [3] K. S. Thorne, R. H. Price, and D. A. MacDonald, *Black Holes: The Membrane Paradigm* (Yale University Press, New Haven and London, 1986).
- [4] G. Lovelace, Y. Chen, M. Cohen, J. D. Kaplan, D. Keppel, K. D. Matthews, D. A. Nichols, M. A. Scheel, and U. Sperhake, *Phys. Rev. D* **82**, 064031 (2010), [arXiv:0907.0869](https://arxiv.org/abs/0907.0869).

- [5] <http://www.black-holes.org/headon05aa.html>.
- [6] E. Newman and R. Penrose, *J. Math. Phys.* **3**, 566 (1962).
- [7] V. P. Frolov and I. D. Novikov, *Black Hole Physics: Basic Concepts and New Developments* (Kluwer, 1998).
- [8] R. Penrose and W. Rindler, *Spinors and Space-time, Volume 1* (Cambridge University Press, Cambridge, 1992).
- [9] T. Damour, in *Proceedings of the Second Marcel Grossman Meeting on General Relativity*, edited by R. Ruffini (North-Holland Publishing Company, Amsterdam, 1982), pp. 587–606.
- [10] S. Chandrasekhar and S. Detweiler, *Proc. R. Soc. A* **344**, 441 (1975).
- [11] G. Lovelace, M. Scheel, and B. Szilagy, *Phys.Rev.* **D83**, 024010 (2011), 1010.2777.
- [12] <http://www.black-holes.org/inspiral95aa.html>.
- [13] <http://www.black-holes.org/extreme-kick.html>.
- [14] M. Campanelli, C. O. Lousto, Y. Zlochower, and D. Merritt, *Phys. Rev. Lett.* **98**, 231102 (2007), [gr-qc/0702133](#).
- [15] J. A. Gonzalez, M. D. Hannam, U. Sperhake, B. Brügmann, and S. Husa, *Phys. Rev. Lett.* **98**, 231101 (2007), [gr-qc/0702052](#).
- [16] C. O. Lousto and Y. Zlochower, *Phys. Rev. D.* **83**, 024003 (2011), [arXiv:1011.0593](#).
- [17] D. A. Nichols and Y. Chen, *Phys. Rev. D* **82**, 104020 (2010), 1007.2024.
- [18] C. W. Misner, K. S. Thorne, and J. A. Wheeler, *Gravitation* (Freeman, New York, New York, 1973).
- [19] <http://www.black-holes.org/SpEC.html>.

## Chapter 6

# Classifying the Isolated Zeros of Asymptotic Gravitational Radiation by Tendex and Vortex Lines

A new method to visualize the curvature of spacetime was recently proposed. This method finds the eigenvectors of the “electric” and “magnetic” components of the Weyl tensor and, in analogy to the field lines of electromagnetism, uses the eigenvectors’ integral curves to illustrate the spacetime curvature. Here we use this approach, along with well-known topological properties of fields on closed surfaces, to show that an arbitrary, radiating, asymptotically flat spacetime must have points near null infinity where the gravitational radiation vanishes. At the zeros of the gravitational radiation, the field of integral curves develops singular features analogous to the critical points of a vector field. We can, therefore, apply the topological classification of singular points of unoriented lines as a method to describe the radiation field. We provide examples of the structure of these points using linearized gravity and discuss an application to the extreme-kick black-hole-binary merger.

---

Originally published as A. Zimmerman, D. A. Nichols, and F. Zhang, *Phys. Rev. D*, (2011). Copyright 2011 by the American Physical Society.

### 6.1 Introduction

A recent study [1] proposed a method for visualizing spacetime curvature that is well-suited for studying spacetimes evolved from initial data using numerical-relativity codes. The method first projects the Riemann curvature tensor  $R_{\mu\nu\sigma\rho}$  into a spatial slice, thereby splitting it into two sym-

metric, trace-free spatial tensors,  $\mathcal{E}$  and  $\mathcal{B}$  (see e.g. [2] and the references therein). These tensors are the spacetime-curvature analogs of the electric and magnetic fields in Maxwell’s theory. The “electric” tensor  $\mathcal{E}$  is familiar; it is the tidal field in the Newtonian limit. The frame-drag field  $\mathcal{B}$  (the “magnetic” curvature tensor) describes the differential frame dragging of spacetime. The eigenvectors of the tidal field provide the preferred directions of strain at a point in spacetime, and its eigenvalues give the magnitude of the strain along those axes. Similarly, the eigenvectors of the frame-drag field give preferred directions of differential precession of gyroscopes, and their eigenvalues give the magnitude of this precession [1, 3, 4].

The study [1] then proposed using the integral curves of these eigenvectors as a way to visualize the curvature of spacetime. Three orthogonal curves associated with  $\mathcal{E}$ , called tendex lines, pass through each point in spacetime. Along each tendex line there is a corresponding eigenvalue, which is called the tendicity of the line. For the tensor  $\mathcal{B}$ , there is a second set of three orthogonal curves, the vortex lines, and their corresponding eigenvalues, the vorticities. These six curves are analogous to the field lines of electromagnetism, and the six eigenvalues to the electric and magnetic field strengths. The tendex and vortex lines, with their corresponding vorticities and tendicities, represent very different physical phenomena from field lines of electromagnetism; they allow one to visualize the aspects of spacetime curvature associated with tidal stretching and differential frame-dragging. In addition, each set of curves satisfies the constraint that its eigenvalues sum to zero at every point, since  $\mathcal{E}$  and  $\mathcal{B}$  are trace-free.

Wherever the eigenvector fields are well-behaved, the tendex and vortex lines form extended, continuous fields of lines in a spatial slice. At points where two (or more) eigenvectors have the same eigenvalue, the eigenvectors are said to be degenerate. Any linear combination of the degenerate eigenvectors at these points is still an eigenvector with the same eigenvalue; therefore, the span of these eigenvectors forms a degenerate subspace. Singular features can appear at points of degeneracy, where many lines intersect, terminate, or turn discontinuously. The topology of unoriented fields of lines and their singular points has been studied both in the context of general relativity and elsewhere. For example, Delmarcelle and Hesselink [5] studied the theory of these systems and applied them to real, symmetric two-dimensional tensors. In the context of relativity, Penrose and Rindler [6] examined the topology of unoriented lines, or ridge systems, to characterize the principle null directions about single points in spacetime. Finally, Penrose [7] also applied the study of ridge systems to human handprint and fingerprint patterns.

In this paper, we focus on the vortex and tendex lines and their singular points far from an isolated, radiating source. In Section 6.2, we show that two of the vortex and tendex lines lie on a sphere (the third, therefore, is normal to the sphere), and that the vortex and tendex lines have the same eigenvalues. Moreover, the two eigenvalues on the sphere have opposite sign, and the eigenvalue normal to the sphere has zero eigenvalue. This implies that the only singular points in

the lines occur when all eigenvalues vanish (i.e. when the curvature is exactly zero at the point, and all three eigenvectors are degenerate).

In Section 6.3 we employ a version of the Poincaré-Hopf theorem for fields of integral curves to argue that there must be singular points where the curvature vanishes. Penrose, in a 1965 paper [8], made a similar observation. There, he notes in passing that gravitational radiation must vanish for topological reasons, although he does not discuss the point any further. Here we show that the topological classification of singular points of ridge systems can be applied to the tendex and vortex lines of gravitational radiation. This allows us to make a topological classification of the zeros of the radiation field.

In Section 6.4, we visualize the tendex and vortex lines of radiating systems in linearized gravity. We begin with radiation from a rotating mass-quadrupole moment, the dominant mode in most astrophysical gravitational radiation. We then move to an idealized model of the “extreme-kick” configuration (an equal-mass binary-black-hole merger with spins anti-aligned in the orbital plane [9]). As we vary the magnitude of the spins in the extreme-kick configuration, we can relate the positions of the singular points of the tendex and vortex patterns to the degree of beaming of gravitational waves. We also visualize the radiation fields of individual higher-order multipole moments, which serve, primarily, as examples of patterns with a large number of singularities. Astrophysically, these higher multipoles would always be accompanied by a dominant quadrupole moment; we also, therefore, look at a superposition of multipoles. Since the tendex lines depend nonlinearly upon the multipoles, it is not apparent, *a priori*, how greatly small higher multipoles will change the leading order quadrupole pattern. Nevertheless, we see that for an equal-mass black-hole binary, higher multipoles make only small changes to the tendex line patterns. Finally, we discuss our results in Section 9.6.

Throughout this paper we use Greek letters for spacetime coordinates in a coordinate basis and Latin letters from the beginning of the alphabet for spatial indexes in an orthonormal basis. We use a spacetime signature  $(-+++)$  and a corresponding normalization condition for our tetrad. We will use geometric units, in which  $G = c = 1$ .

We will also specialize to vacuum spacetimes, where the Riemann tensor is equal to the Weyl tensor  $C_{\mu\nu\rho\sigma}$ . To specify our slicing and to compute  $\mathcal{E}$  and  $\mathcal{B}$ , we use a hypersurface-orthogonal, timelike unit vector,  $e_0$ , which we choose to be part of an orthonormal tetrad,  $(e_0, e_1, e_2, e_3)$ . We then perform a 3 + 1 split of the Weyl tensor by projecting it and its Hodge dual  $*C_{\mu\nu\rho\sigma} = \frac{1}{2}\epsilon_{\mu\nu}{}^{\alpha\beta}C_{\alpha\beta\rho\sigma}$  into this basis,

$$\mathcal{E}_{ab} = C_{a\mu b\nu}e_0^\mu e_0^\nu, \quad (6.1)$$

$$\mathcal{B}_{ab} = -*C_{a\mu b\nu}e_0^\mu e_0^\nu. \quad (6.2)$$

Here our convention for the alternating tensor is that  $\epsilon_{0123} = +1$  in an orthonormal basis. Note that, while the sign convention on  $\mathcal{B}$  is not standard (see e.g. [10]), it has the advantage that  $\mathcal{E}$  and  $\mathcal{B}$  obey constraints and evolution equations under the 3 + 1 split of spacetime that are directly analogous to Maxwell's equations in electromagnetism [2, 4]. After the projection, we will solve the eigenvalue problem for the tensors  $\mathcal{E}$  and  $\mathcal{B}$  in the orthonormal basis,

$$\mathcal{E}_{ab}v^b = \lambda v_a, \quad (6.3)$$

and we will then find their streamlines in a coordinate basis via the differential equation relating a curve to its tangent vector,

$$\frac{dx^\mu}{ds} = v^a e_a{}^\mu. \quad (6.4)$$

Here  $s$  is a parameter along the streamlines.

## 6.2 Gravitational Waves Near Null Infinity

Consider a vacuum, asymptotically flat spacetime that contains gravitational radiation from an isolated source. We are specifically interested in the transverse modes of radiation on a large sphere  $S$  near future null infinity. To describe these gravitational waves, we use an orthonormal tetrad  $(e_0, e_1, e_2, e_3)$ , with  $e_0$  timelike and  $e_2, e_3$  tangent to the sphere, and we associate with this tetrad a corresponding complex null tetrad,

$$\begin{aligned} l &= \frac{1}{\sqrt{2}}(e_0 + e_1), & n &= \frac{1}{\sqrt{2}}(e_0 - e_1), \\ m &= \frac{1}{\sqrt{2}}(e_2 + ie_3), & \bar{m} &= \frac{1}{\sqrt{2}}(e_2 - ie_3). \end{aligned} \quad (6.5)$$

Here,  $l$  is tangent to outgoing null rays that pass through  $S$  and strike a sphere at null infinity. We enforce that the null tetrad is parallelly propagated along these rays, and that it is normalized such that  $l_\mu n^\mu = -m_\mu \bar{m}^\mu = -1$  (all other inner products of the null tetrad vanish). With these rays, we can associate Bondi-type coordinates (see e.g. [11, 12]) on a sphere at future null infinity with those on  $S$ . The timelike vector  $e_0$  specifies our spatial slicing in this asymptotic region. When the orthonormal and null tetrads are chosen as in Eq. (6.5),  $\mathcal{E}$  and  $\mathcal{B}$  are related to the complex Weyl scalars [13]. With the Newman-Penrose conventions appropriate to our metric signature (see, e.g., [10]), and our convention in Eq. (6.2), one can show that

$$\mathcal{E}_{ab} - i\mathcal{B}_{ab} = \begin{pmatrix} 2\Psi_2 & \Psi_3 - \Psi_1 & i(\Psi_1 + \Psi_3) \\ * & \frac{\Psi_0 + \Psi_4}{2} - \Psi_2 & \frac{i(\Psi_4 - \Psi_0)}{2} \\ * & * & -\frac{\Psi_0 + \Psi_4}{2} - \Psi_2 \end{pmatrix}, \quad (6.6)$$

where \* indicates entries that can be inferred from the symmetry of  $\mathcal{E}$  and  $\mathcal{B}$ .

In an asymptotically flat spacetime, the peeling theorem [13] ensures that  $\Psi_4 \sim r^{-1}$  (with  $r$  an affine parameter along the rays), and that the remaining Weyl scalars fall off with progressively higher powers of  $r$ ,  $\Psi_3 \sim r^{-2}$ ,  $\Psi_2 \sim r^{-3}$ ,  $\Psi_1 \sim r^{-4}$ , and  $\Psi_0 \sim r^{-5}$ . Asymptotically, only  $\Psi_4$  contributes to  $\mathcal{E}$  and  $\mathcal{B}$ ,

$$\mathcal{E}_{ab} - i\mathcal{B}_{ab} = \frac{1}{2} \begin{pmatrix} 0 & 0 & 0 \\ 0 & \Psi_4 & i\Psi_4 \\ 0 & i\Psi_4 & -\Psi_4 \end{pmatrix}. \quad (6.7)$$

We see immediately that one eigenvector of both  $\mathcal{E}$  and  $\mathcal{B}$  is the “radial” basis vector  $\mathbf{e}_1$ , with vanishing eigenvalue. The remaining  $2 \times 2$  block is transverse and traceless, and the eigenvectors in this subspace have a simple analytical solution. The eigenvalues are  $\lambda_{\pm} = \pm|\Psi_4|/2$  for both tensors, and the eigenvectors of  $\mathcal{E}$  have the explicit form

$$\mathbf{v}_{\pm} = \frac{-\mathcal{E}_{23}\mathbf{e}_2 + (\mathcal{E}_{22} - \lambda_{\pm})\mathbf{e}_3}{\sqrt{\mathcal{E}_{23}^2 + (\mathcal{E}_{22} - \lambda_{\pm})^2}} = \frac{\text{Im}\Psi_4\mathbf{e}_2 + (\text{Re}\Psi_4 \mp |\Psi_4|)\mathbf{e}_3}{\sqrt{(\text{Im}\Psi_4)^2 + (\text{Re}\Psi_4 \mp |\Psi_4|)^2}}. \quad (6.8)$$

The eigenvectors of  $\mathcal{B}$  are locally rotated by  $\pm\pi/4$  with respect to those of  $\mathcal{E}$  [4]. As a result, although the global geometric pattern of vortex and tendex lines may differ, their local pattern and their topological properties on  $S$  will be identical. Moreover, when the eigenvalues of  $\mathcal{E}$  (the tendicity of the corresponding tendex line) vanish, so must those of  $\mathcal{B}$  (the vorticity of the vortex lines). In arguing that the radiation must vanish, we can, therefore, focus on the tendex lines on  $S$  without loss of generality. Physically, however, both the vortex and the tendex lines are of interest. Similarly, since the two sets of tendex lines on  $S$  have equal and opposite eigenvalue and are orthogonal, we need only consider the properties of a single field of unoriented lines on  $S$  in order to describe the topological properties of all four tendex and vortex lines on the sphere. Note that thus far we leave the coordinates  $(x^2, x^3)$  on  $S$  unspecified. We will assume that these coordinates are everywhere nonsingular, for instance by being constructed from two smooth, overlapping charts on  $S$ .

### 6.3 The Topology of Tendex Patterns Near Null Infinity

Before investigating the properties of the tendex lines on  $S$ , we first recall a few related properties of vector fields on a 2-sphere. A well-known result regarding vector fields on a sphere is the “hairy-ball theorem.” This result states, colloquially, that if a sphere is covered with hairs at each point, the hair cannot be combed down everywhere without producing cowlicks or bald spots. The hairy-ball theorem is a specific illustration of the Poincaré-Hopf theorem, applied to a 2-sphere. On a 2-sphere, this theorem states that the sum of the indexes of the zeros of a vector field must equal the Euler characteristic,  $\chi$ , of the sphere, specifically  $\chi = 2$ . The index of a zero of a vector field

(also called a singular point) can be found intuitively by drawing a small circle around the point and traveling once around the circle counterclockwise. The number of times the local vector field rotates counterclockwise through an angle of  $2\pi$  during this transit is the index. More precisely, we can form a map from the points near a zero of the vector field to the unit circle. To do this consider a closed, oriented curve in a neighborhood of the zero, and map each point on the curve to the unit circle by associating the direction of the vector field at that point with a particular point on the unit circle. The index is the degree of the map (the number of times the map covers the circle in a positive sense). For the zero of a vector field, the index is a positive or negative integer, because we must return to the starting point on the unit circle as we finish our circuit of the curve around the zero.

The concept of an index and the formal statement of the Poincaré-Hopf theorem generalizes naturally to ridge systems, fields of unoriented lines such as the tendex lines on  $S$ . For ridge systems on the sphere, the index of a singular point can be a half-integer [5]. Intuitively, this can occur because fields of lines do not have orientation. As one traverses counterclockwise about a small circle around a singular point, the local pattern of lines can rotate through an angle of  $\pm\pi$  during the transit. We illustrate the two fundamental types of singularity in Figure 6.1, which, following [6], we call loops for index  $i = 1/2$  and triradii for  $i = -1/2$ . One can argue that the Poincaré-Hopf Theorem holds for ridge systems, by noting that we can create a singular point with integer index by bringing two half-index singularities together (see Figure 6.2 for a schematic of the creation of a singularity of index  $i = 1$  from two loop singularities). Ridge patterns near singularities with integer index  $i = \pm 1$  can be assigned orientations consistently; they must, therefore, have the same topological properties as streamlines of vector fields (which, in turn, have the same properties as the underlying vector fields themselves). By arguing that one can always deform a ridge system so that its singular points have integer index, one can see that the sum of the indexes of a ridge system on a sphere must equal the Euler characteristic of the surface,  $\chi = 2$  (see [5] and the references therein for a more formal statement and proof of this theorem). In Figure 6.3 we show several other ridge singularities with integer index for completeness. In the top row, we show three patterns with index  $i = 1$ , and in the bottom left, we sketch a saddle type singularity with index  $i = -1$ . All of these patterns can be consistently assigned an orientation and, thus, have the same topological properties as vector field singularities.

Having arrived at the result that the tendex lines on  $S$  must have singular points in a general, asymptotically flat vacuum spacetime, we now recall the fact that the singular points appear where there is a degenerate eigenvalue of the tidal tensor. From the result of Section 6.2, the only degeneracies occur where the curvature vanishes completely, and it follows therefore that there must be points of vanishing curvature on  $S$ . In general we would expect the radiation to vanish at a minimum of four points, as Penrose [8] had previously noted. In this case there would be four loop

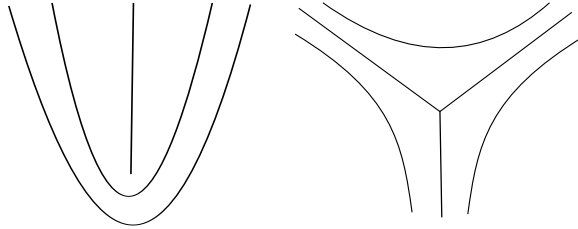


Figure 6.1: Illustrations of the two types of half-index singularities for ridge systems on a two-dimensional space. On the left is a loop singularity with index  $i = 1/2$ , and on the right is a triradius with  $i = -1/2$ .

singularities with index  $i = 1/2$ , whose index sums to  $\chi = 2$ . As we highlight in Section 6.4, where we show several examples of multipolar radiation in linearized theory, the number of singular points, the types of singularities, and the pattern of the tendex lines contains additional information.

Additional symmetry, however, can modify the structure of the singular points, as we see in the simple example of an axisymmetric, head-on collision of two non-spinning black holes. Axisymmetry guarantees that the Weyl scalar  $\Psi_4$  is purely real when we construct our tetrad, Eq. (6.5), by choosing  $\mathbf{e}_2$  and  $\mathbf{e}_3$  to be the orthonormal basis vectors of spherical polar coordinates on  $S$ ,  $\mathbf{e}_\theta$  and  $\mathbf{e}_\phi$  [14]. Using the relation  $\Psi_4 = -\ddot{h}_+ + i\ddot{h}_\times$ , we see that the waves are purely  $+$  polarized. By substituting this relationship into (6.7), we also see that  $\mathbf{e}_\theta$  and  $\mathbf{e}_\phi$  are the eigenvectors whose integral curves are the tendex lines. The tendex lines, therefore, are the lines of constant latitude and longitude, and the singular points reside on the north and south poles of  $S$ . Their index must be  $i = 1$ , and the local pattern at the singularity will resemble the pattern at the top left of Figure 6.3 for one set of lines, and the image on the top right of Figure 6.3 for the other set (see also [4]). In this special situation, axisymmetry demands that there be two singular points on the axis, rather than four (or more). Moreover, these singular points are each generated from the coincidence of two loop singularities, with one singular point at each end of the axis of symmetry. Similarly, if  $\Psi_4$  were purely imaginary, then the radiation would only contain the  $\times$  polarization. The  $\pi/4$  rotations of the unit spherical vectors would then be the eigenvectors of the tidal field, and the two singularities at the poles would resemble that illustrated at the top middle of Figure 6.3.

It is even conceivable that four loops could merge into one singular point. This singularity would have the dipole-like pattern illustrated at the bottom right of Figure 6.3, and it would have index  $i = 2$ . Though this situation seems very special, we show in the next section how a finely tuned linear combination of mass and current multipoles can give rise to this pattern. Because there is only one zero, the radiation is beamed in the direction opposite the zero, resulting in a net flux of momentum opposite the lone singular point.

Before concluding this section, we address two possible concerns. The scalar  $\Psi_4 = C_{\mu\nu\rho\sigma}n^\mu\bar{m}^\nu n^\rho\bar{m}^\sigma$  depends both on the curvature and on the chosen tetrad. We first emphasize that the singular points

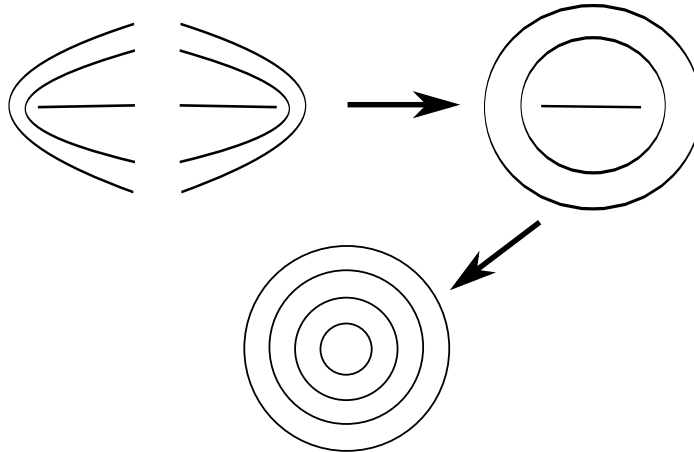


Figure 6.2: An illustration of the formation of a singularity with index  $i = 1$  from two loop singularities with index  $i = 1/2$ . The local structure of the two loops is shown in the top left, and the arrow represents, schematically, how they might join together into the extended pattern at the top right. Finally, the two loop singularities can be brought together until they coincide (which we represent by an arrow pointing to the image at the bottom). This resulting local pattern can be assigned an orientation and is equivalent to the singular point of a vector field.

we have discussed have nothing to do with tetrad considerations, in particular with the behavior of the vectors tangent to the sphere,  $\mathbf{m}$ , and  $\bar{\mathbf{m}}$ . Though these vectors will also become singular at points on the sphere, we are free to use a different tetrad on  $S$  in these regions, just as we can cover the sphere everywhere with smooth coordinates using overlapping charts. Secondly, the vanishing of radiation does not occur due to the null vector  $\mathbf{n}$  coinciding with a principle null direction of the spacetime. We note that, if  $\Psi_4$  vanishes at a point on  $S$ , then a change of basis cannot make  $\Psi_4$  (or any of the other curvature scalars) non-vanishing. For example, a rotation about  $\mathbf{l}$  by a complex parameter  $a$  induces a transformation on the other basis vectors,

$$\mathbf{l}' = \mathbf{l}, \quad \mathbf{m}' = \mathbf{m} + a\mathbf{l}, \quad \bar{\mathbf{m}}' = \bar{\mathbf{m}} + \bar{a}\mathbf{l}, \quad \mathbf{n}' = \mathbf{n} + a\bar{\mathbf{m}} + \bar{a}\mathbf{m} + a\bar{a}\mathbf{l}. \quad (6.9)$$

Under this rotation,  $\Psi_4$  transforms as

$$\Psi_4' = \Psi_4 + 4\bar{a}\Psi_3 + 6\bar{a}^2\Psi_2 + 4\bar{a}^3\Psi_1 + \bar{a}^4\Psi_0, \quad (6.10)$$

which vanishes when the Weyl scalars are zero in the original basis. The remaining scalars transform analogously, and the other independent tetrad transformations are also homogeneous in the Weyl scalars (see e.g. [10]).

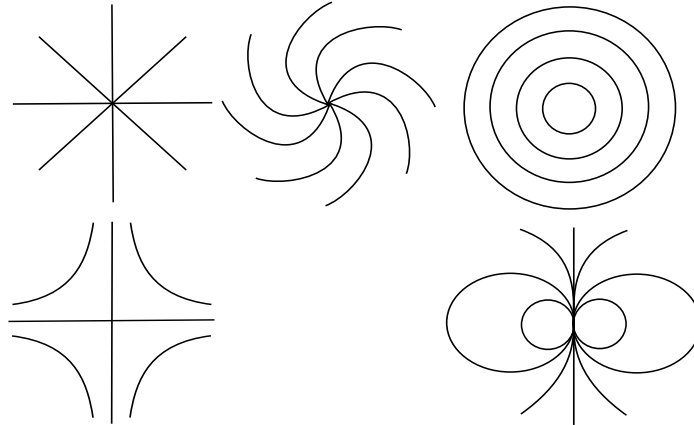


Figure 6.3: Top row: Diagrams of three orientable ridge patterns, which can be made from a combination of two loops, all with index  $i = 1$ . Bottom row: On the left is an orientable ridge pattern with index  $i = -1$  (which is identical to a saddle point of a vector field). It can be constructed by joining two triradii singularities. The figure on the right shows a dipole-like pattern with index  $i = 2$ , which can come from the coincidence of four loops.

## 6.4 Examples from Linearized Gravity

We now give several examples of the tendex and vortex patterns on  $S$  from weak-field, multipolar sources. We first investigate quadrupolar radiation, produced by a time-varying quadrupole moment. For many astrophysical sources, such as the inspiral of comparable-mass compact objects, the gravitational radiation is predominantly quadrupolar. As a result, our calculations will capture features of the radiation coming from these astrophysical systems. We will then study a combination of rotating mass- and current-quadrupole moments that are phase-locked. The locking of these moments was observed by Schnittman et al. in their multipolar analysis of the extreme-kick merger [15]. We conclude this section by discussing isolated higher multipoles. Although it is unlikely that astrophysical sources will contain only higher multipoles, it is of interest to see what kinds of tendex patterns occur. More importantly, while the tidal tensor is a linear combination of multipoles, the tendex lines will depend nonlinearly on the different moments. Actual astrophysical sources will contain a superposition of multipoles, and it is important to see how superpositions of multipoles change the leading-order quadrupole pattern.

We perform our calculations in linearized theory about flat space, and we use spherical polar coordinates and their corresponding unit vectors for our basis. One can compute from the multipolar metric in [16] that for a symmetric, trace-free (STF) quadrupole moment  $\mathcal{I}_{ab}$ , the leading-order contributions to  $\mathcal{E}$  and  $\mathcal{B}$  on  $S$  are

$$\mathcal{E}_{ab}^{(\ell=2)} = -\frac{1}{2r} \left[ {}^{(4)}\mathcal{I}_{ab}(t-r) + \epsilon_{ac} {}^{(4)}\mathcal{I}_{cd}(t-r) \epsilon_{db} \right]^{\text{TT}}, \quad (6.11)$$

$$\mathcal{B}_{ab}^{(\ell=2)} = -\frac{1}{r} \left[ \epsilon_{c(a} {}^{(4)}\mathcal{I}_{b)c}(t-r) \right]^{\text{TT}}. \quad (6.12)$$

Here, the superscript  $^{(4)}$  indicates four time derivatives, TT means to take the transverse-traceless projection of the expression, and  $\epsilon_{ac}$  is the antisymmetric tensor on a sphere. In this expression, and in what follows, the Latin indexes run only over the basis vectors  $\mathbf{e}_\theta$  and  $\mathbf{e}_\phi$ , and repeated Latin indexes are summed over even when they are both lowered.

### 6.4.1 Rotating Mass Quadrupole

As our first example, we calculate the STF quadrupole moment of two equal point masses (with mass  $M/2$ ) separated by a distance  $a$  in the equatorial plane, and rotating at an orbital frequency  $\Omega$ . We find that

$$\begin{aligned} {}^{(4)}\mathcal{I}_{\theta\theta}(t-r) &= Ma^2\Omega^4(1 + \cos^2\theta) \cos\{2[\phi - \Omega(t-r)]\}, \\ {}^{(4)}\mathcal{I}_{\theta\phi}(t-r) &= -2Ma^2\Omega^4 \cos\theta \sin\{2[\phi - \Omega(t-r)]\}, \\ {}^{(4)}\mathcal{I}_{\phi\phi}(t-r) &= -{}^{(4)}\mathcal{I}_{\theta\theta}(t-r). \end{aligned} \quad (6.13)$$

By substituting these expressions into Eqs. (6.11) and (6.8), we find the eigenvectors of the tidal field. We can then calculate the tendex lines on the sphere by solving Eq. (6.4) with a convenient normalization of the parameter along the curves,

$$\frac{d\theta}{ds} = \frac{1}{r} {}^{(4)}\mathcal{I}_{\theta\phi}, \quad (6.14)$$

$$\frac{d\phi}{ds} = \frac{1}{r \sin\theta} ({}^{(4)}\mathcal{I}_{\theta\theta} - \lambda_+). \quad (6.15)$$

Here,  $\lambda_+$  is the positive eigenvalue. The differential equation for the vortex lines [found from the corresponding frame-drag field of Eq. (6.12)], has the same form as those of the tendex lines above; however, one must replace  ${}^{(4)}\mathcal{I}_{\theta\phi}$  in the first equation by  ${}^{(4)}\mathcal{I}_{\theta\theta}$  and  ${}^{(4)}\mathcal{I}_{\theta\theta}$  by  $-{}^{(4)}\mathcal{I}_{\theta\phi}$  in the second equation.

We show the tendex and vortex lines corresponding to the positive eigenvalues in the left and right panels of Figure 6.4, respectively, at a retarded time  $t-r=0$ . We also plot the magnitude of the eigenvalue on the sphere, using a color scheme in which purple (darker) regions at the poles correspond to large eigenvalues and yellow (lighter) colors near the equator are closer to zero. Both the tendex and vortex lines have four equally spaced loop singularities on the equator at the points where the field is zero (the two on the back side of the sphere are not shown). Because the vortex and tendex lines must cross each other at an angle of  $\pi/4$ , the global geometric patterns are quite different.

We note here that these two figures also provide a visualization for the transverse-traceless (TT),

“pure-spin” tensor spherical harmonics [16]. For example, we can see that the mass-quadrupole tendex lines are the integral curves of the eigenvectors of the real part of the  $\ell = 2$ ,  $m = 2$  electric-type TT tensor harmonic. First, the tendex lines correspond to the electric-type harmonic, because the tidal tensor is even under parity. Second, the radiation pattern will not contain an  $\ell = 2$ ,  $m = 0$  harmonic, because the overall magnitude of the quadrupole moment of the source is not changing in time; also, the  $\ell = 2$ ,  $m = \pm 1$  harmonics are absent because the source is an equal-mass binary and is symmetric under a rotation of  $\pi$ . Finally, the  $\ell = 2$ ,  $m = -2$  moment is equal in magnitude to the  $m = 2$  harmonic, since the tidal tensor is real. Using similar considerations, we can identify the vortex lines of the mass quadrupole as a visualization of the real parts of the  $\ell = 2$ ,  $m = 2$  magnetic-type tensor harmonics.

In addition, the eigenvalue (the identical color patterns of both panels of Figure 6.4) is given by the magnitude of the sum of spin-weighted spherical harmonics,

$$\lambda_+ \propto |_{-2}Y_{22} + _{-2}Y_{2-2}|. \quad (6.16)$$

One can see this most easily by using the symmetries described above, the expression for the eigenvalue  $\lambda_+ = |\Psi_4|/2$ , and the spin-weighted spherical harmonic decomposition of  $\Psi_4$ . It is also possible to verify this expression using the tensor harmonics above and the standard relations between tensor spherical harmonics and spin-weighted spherical harmonics (see e.g. [16]). Radiation from numerical spacetimes is usually decomposed into spin-weighted spherical harmonics, and, as a result, the pattern of the eigenvalue is familiar. The tendex lines, however, also show the polarization pattern of the waves on  $S$  (a feature that numerical simulations rarely explicitly highlight). Figure 6.4 (and the accompanying negative-tendicity lines not shown) gives the directions of preferred strain on  $S$ , and hence the wave polarization that can be inferred from gravitational-wave-interferometer networks such as LIGO/VIRGO. Thus, visualizations such as Figure 6.4 give complete information about the gravitational waves passing through  $S$ .

### 6.4.2 Rotating Mass and Current Quadrupoles in Phase

As our second example, we will consider a source that also has a time-varying current-quadrupole moment,  $\mathcal{S}_{ab}$ . In linearized theory, one can show that the tidal tensor and frame-drag field of a current quadrupole are simply related to those of a mass quadrupole. In fact,  $\mathcal{B}_{ab}$  of the current quadrupole has exactly the same form as  $\mathcal{E}_{ab}$  of a mass quadrupole, Eq. (6.11), when one replaces  ${}^{(4)}\mathcal{I}_{ab}$  by  $(4/3){}^{(4)}\mathcal{S}_{ab}$ . Similarly,  $\mathcal{E}_{ab}$  of the current quadrupole is identical to  $\mathcal{B}_{ab}$  of a mass quadrupole, Eq. (6.12), when  ${}^{(4)}\mathcal{I}_{ab}$  is replaced by  $-(4/3){}^{(4)}\mathcal{S}_{ab}$ .

We impose that the source’s mass- and current-quadrupole moments rotate in phase, with frequency  $\Omega$ , and with the current quadrupole lagging in phase by  $\pi/2$ . This arrangement of multipoles

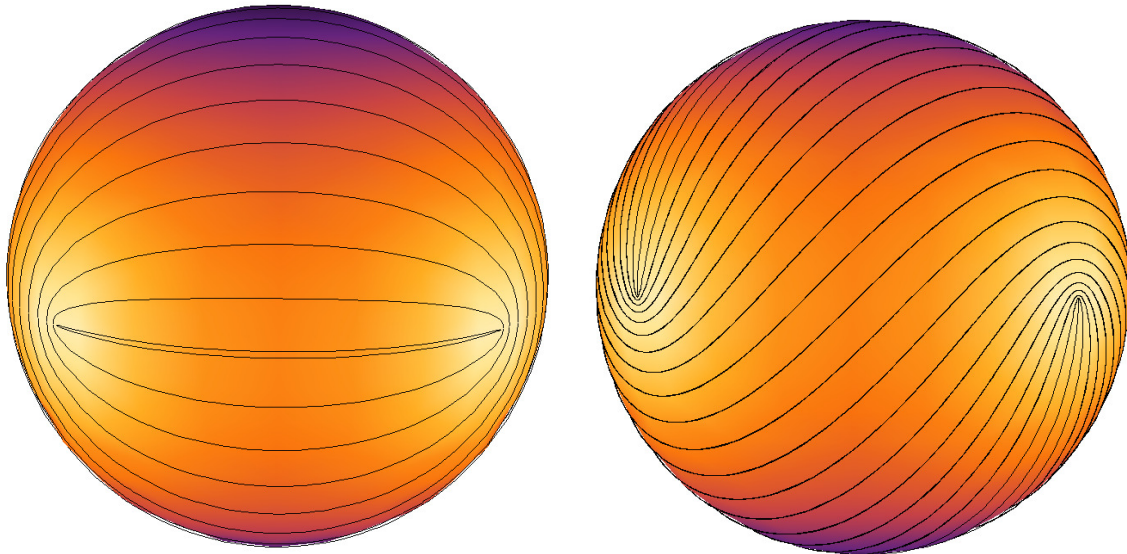


Figure 6.4: Left: The positive tendex lines on  $S$  generated by a rotating quadrupole moment in linearized gravity. The sphere is colored by the magnitude of the eigenvalue; purple (darker) areas at the poles corresponding to a large eigenvalue, and yellow (lighter) areas near the equator indicate a value closer to zero. Four loop singularities appear equally spaced on the equator at the points of vanishing tendicity. Right: As in the left panel, the positive vortex lines and their magnitude of the eigenvalue on  $S$  (using the same coloring). The loop singularities lie at the same locations as they do for the tendex lines, but they are locally rotated by  $\pi/4$ .

models the lowest multipoles during the merger and ringdown of the extreme-kick configuration (a collision of equal mass black holes in a quasi-circular orbit that have spins of equal magnitude lying in the orbital plane, but pointing in opposite directions), when the mass- and current-quadrupole moments rotate in phase [15]. The relative amplitude of the mass- and current-multipoles depends upon, among other variables, the amplitude of the black-holes' spin. We, therefore, include a free parameter  $C$  in the strength of the current quadrupole which represents the effect of changing the spin. An order-of-magnitude estimate based on two fast-spinning holes orbiting near the end of their inspiral indicates that their amplitudes could be nearly equal,  $C = O(1)$ . To determine the exact relative amplitude of the mass- and current-quadrupole moments of the radiation would require comparison with numerical relativity results.

We calculate the current-quadrupole moment by scaling the mass quadrupole by the appropriate factor of  $C$  and letting the term  $2[\phi - \Omega(t-r)]$  in the equations for  $\mathcal{I}_{ab}(t-r)$  become  $2[\phi - \Omega(t-r)] - \pi/2$  in the corresponding expressions for  $\mathcal{S}_{ab}(t-r)$ . In linearized theory, the tidal tensor and frame-drag fields of the different multipoles add directly. As a result, the equations for the tendex lines have the same form as Eqs. (6.14) and (6.15), but one must now replace the mass quadrupole  ${}^{(4)}\mathcal{I}_{\theta\phi}$  by  ${}^{(4)}\mathcal{I}_{\theta\phi} - (4/3){}^{(4)}\mathcal{S}_{\theta\theta}$  in the first expression and  ${}^{(4)}\mathcal{I}_{\theta\theta}$  by  ${}^{(4)}\mathcal{I}_{\theta\theta} + (4/3){}^{(4)}\mathcal{S}_{\theta\phi}$  in the second.

First, we allow the current quadrupole to be half as large as the mass quadrupole,  $C = 1/2$ .

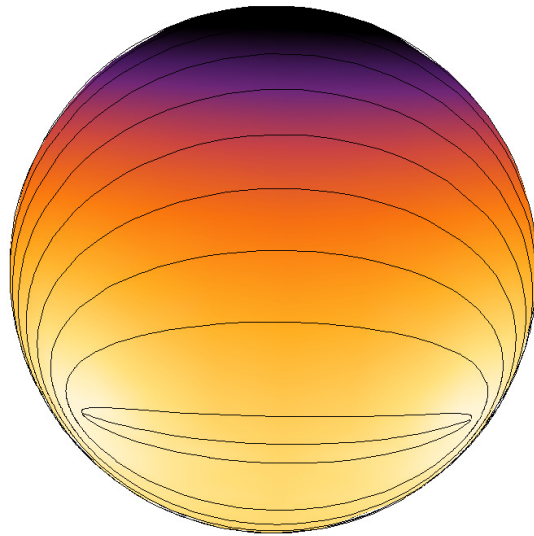


Figure 6.5: The positive tendex lines on  $S$  generated by the superposition of rotating mass- and current-quadrupole moments,  $\pi/2$  out of phase, in linearized gravity. The sphere is colored by the tendicity as in Figure 6.4. Interference between the moments leads to beaming of the radiation toward the north pole. Similarly, the singular points of the tendex lines now fall on a line of constant latitude in the southern hemisphere.

We show the positive tendex lines and positive eigenvalue in Figure 6.5. Due to the relative phase and amplitude of the two moments, the tensors add constructively in the northern hemisphere and destructively in the southern hemisphere on  $S$ . This is evident in the eigenvalue on the sphere in Figure 6.5, which, one can argue, is now given by an unequal superposition of spin-weighted spherical harmonics,

$$\lambda_+ \propto |_{-2}Y_{22} + b_{-2}Y_{2-2}|, \quad (6.17)$$

with  $b < 1$ . As in previous figures, dark colors (black and purple) represent where the eigenvalue is large, and light colors (white and yellow) show where it is nearly zero. While the singular points are still equally spaced on a line of constant latitude, they no longer reside on the equator; they now fall in the southern hemisphere. This is a direct consequence of the beaming of radiation toward the northern pole.

The case shown above has strong beaming, but it is possible to make the beaming more pronounced. To get the greatest interference of the multipoles, the mass and current quadrupoles must have equal amplitude in the tidal field. Because the tidal field of the current quadrupole is  $4/3$  as large as the tidal field of the mass quadrupole, setting  $C = 3/4$  gives the strongest constructive interference in the tidal fields. In this case, the eigenvalue vanishes at just one point, the south pole, and the eigenvalue can be shown to be proportional to just a single spin-weighted spherical harmonic,

$$\lambda_+ \propto |_{-2}Y_{22}|. \quad (6.18)$$

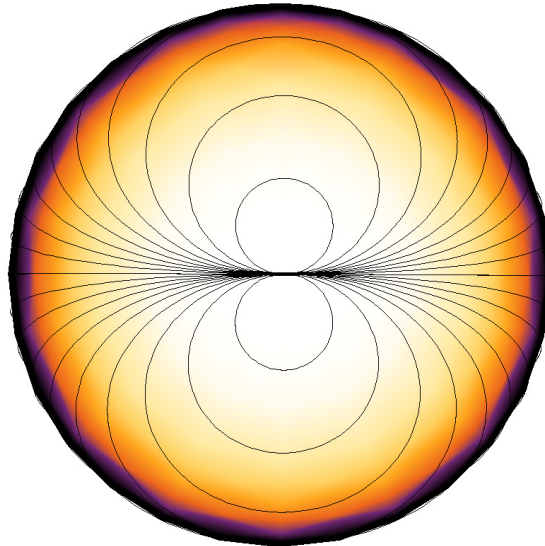


Figure 6.6: South polar region of the tendex line pattern of a gravitational wave generated by rotating mass- and current-quadrupole moments. The amplitude and phase of the moments are chosen so that the radiation vanishes only at the south pole. The purple (darker) areas indicate a positive eigenvalue, while yellow (lighter) areas are values closer to zero. The singularity at the pole has index  $i = 2$ .

As a result, the four equally spaced singular points of the tendex lines must coincide at one singular point whose index must be  $i = 2$ . This is precisely the dipole-like pattern depicted in Figure 6.3. We show the tendex lines around the south pole in Figure 6.6. The vortex lines are identical to the tendex lines, but they are globally rotated by  $\pi/4$  in this specific case.

We see that the beaming can be maximized by carefully tuning the phase and amplitude of the mass- and current-quadrupole moments. Interestingly, the maximally beamed configuration corresponds with the coincidence of all singular points at the south pole in the radiation zone. Whether this degree of beaming could occur from astrophysical sources is an open question.

### 6.4.3 Higher Multipoles of Rotating Point Masses

We also investigate the effect of including higher multipoles on the tendex lines on  $S$ . For the orbiting, non-spinning, point masses of the first example the next two lowest multipoles arise from the current octopole (the  $\ell = 3$  STF moment [16]) and the mass hexadecapole (the  $\ell = 4$  STF moment). From the multipolar metric in [16], one can show that the tidal field for these two moments are

$$\mathcal{E}_{ab}^{\ell=3} = -\frac{1}{2r} \left[ \epsilon_{c(a} {}^{(5)}\mathcal{S}_{b)cr}(t-r) \right]^{\text{TT}}, \quad (6.19)$$

$$\mathcal{E}_{ab}^{\ell=4} = -\frac{1}{24r} \left[ {}^{(6)}\mathcal{I}_{abbr}(t-r) + \epsilon_{ac}\epsilon_{db} {}^{(4)}\mathcal{I}_{cdr}(t-r) \right]^{\text{TT}}, \quad (6.20)$$

where the index  $r$  indicates contraction with the radial basis vector  $\mathbf{e}_r$ , and so repeated  $r$  indexes do not indicate summation. The STF current-octopole moment can be expressed compactly as  $\mathcal{S}_{ijk} = (L_N^i x_A^j x_A^k)^{\text{STF}}$ , where  $L_N^i$  is the Newtonian angular momentum and  $x_A^j$  is the position of one of the point masses. The superscript STF indicates that all indexes should be symmetrized, and all traces removed. In Cartesian coordinates, the vectors have the simple forms  $\mathbf{L}_N = (0, 0, Mav/4)$  and  $\mathbf{x}_A = (a/2)(\cos[\Omega t], \sin[\Omega t], 0)$ , where  $\Omega$  is the Keplerian frequency and  $v$  is the relative velocity. Similarly, one can write the STF mass-hexadecapole moment as  $\mathcal{I}_{ijkl} = M(x_A^i x_A^j x_A^k x_A^l)^{\text{STF}}$ , for the same vector  $x_A^j$  as above. Because these tensors have many components, we shall only list those that are relevant for finding the tendex lines. We will also define  $\alpha = \phi - \Omega(t - r)$  for convenience. For the current octopole the relevant components are

$$\begin{aligned} {}^{(5)}\mathcal{S}_{\theta\theta r}(t-r) &= -\frac{Ma^3v\Omega^5}{24}(5\cos\theta + 3\cos 3\theta)\sin 2\alpha, \\ {}^{(5)}\mathcal{S}_{\theta\phi r}(t-r) &= -\frac{Ma^3v\Omega^5}{3}\cos 2\theta\cos 2\alpha, \\ {}^{(5)}\mathcal{S}_{\phi\phi r}(t-r) &= -{}^{(5)}\mathcal{S}_{\theta\theta r}(t-r), \end{aligned} \tag{6.21}$$

and for the mass hexadecapole they are

$$\begin{aligned} {}^{(6)}\mathcal{I}_{\theta\theta rr}(t-r) &= \frac{Ma^4\Omega^6}{8}[(\cos^2\theta + \cos 4\theta)\cos 2\alpha - 128\sin^2\theta(1 + \cos^2\theta)\cos 4\alpha] \\ {}^{(6)}\mathcal{I}_{\theta\phi rr}(t-r) &= -\frac{Ma^4\Omega^6}{4}[\cos 3\theta\sin 2\alpha - 128\sin^2\theta\cos\theta\sin 4\alpha], \\ {}^{(6)}\mathcal{I}_{\phi\phi rr}(t-r) &= -{}^{(6)}\mathcal{I}_{\theta\theta rr}(t-r). \end{aligned} \tag{6.22}$$

The tendex lines of the current octopole can be found by solving the system of differential equations in Eqs. (6.14) and (6.15) by substituting  ${}^{(4)}\mathcal{I}_{\theta\phi}$  by  ${}^{(5)}\mathcal{S}_{\theta\theta r}/2$  and  ${}^{(4)}\mathcal{I}_{\theta\theta}$  by  $-{}^{(5)}\mathcal{S}_{\theta\phi r}/2$ . Similarly, for the mass hexadecapole, one must make the substitutions of  ${}^{(4)}\mathcal{I}_{\theta\phi}$  by  ${}^{(6)}\mathcal{I}_{\theta\phi rr}/12$  and  ${}^{(4)}\mathcal{I}_{\theta\theta}$  by  ${}^{(6)}\mathcal{I}_{\theta\theta rr}/12$  in the same equations.

In the left panel of Figure 6.7 we show the tendex line pattern for the current octopole, and in the right panel of Figure 6.7 we show the pattern for the mass hexadecapole. Together with the mass quadrupole, Figure 6.4, these are the three lowest multipole moments for the equal-mass circular binary. For the current octopole, there are eight triradius singular points and twelve loop singularities (and thus the net index is two). Four of the loop singularities remain equally spaced on the equator, at the same position of those of the quadrupole, but the remaining singularities appear at different points on  $S$ . The mass hexadecapole has eight loop singularities equally spaced on the equator, and there are integer-index saddle-point-like singularities at each pole.

Gravitational radiation from astrophysical sources will likely not be dominated by these higher multipoles. Nevertheless, these figures are of interest as examples of tendex lines with many singular

points and as visualizations of tensor harmonics. By analyzing the symmetries in a way analogous to that discussed in Section 6.4.1, we can identify the current-octopole tendex lines with the integral curves of  $\ell = 3$ ,  $m = 2$  magnetic-type harmonics, and we can associate the mass-hexadecapole lines with those of the  $\ell = 4$ ,  $m = 4$  electric-type harmonics. In the case of the mass hexadecapole, the  $m = 2$  moment is not ruled out by symmetry, but it is suppressed relative to the  $m = 4$  moment. This occurs because the  $m = 4$  moment oscillates at twice the frequency of the  $m = 2$  moment, and the tidal tensor for this higher-order moment is given by taking six time derivatives of the STF moment, Eq. (6.22). This enhances the  $m = 4$  radiation by a factor of  $2^6$  over the  $m = 2$  contribution. Similarly, we can relate the eigenvalue to the magnitude of the corresponding sum of  $s = -2$  spin-weighted spherical harmonics, and the tendex line patterns to the the polarization directions that could be inferred from networks of gravitational-wave interferometers.

Finally, we show the pattern generated from the linear combination of the three lowest multipole moments in Figure 6.8. Any astrophysical source will contain several multipoles, with the quadrupole being the largest. The tendex lines depend nonlinearly on the multipoles, and it is important, therefore, to see to what extent higher multipoles change the overall pattern. We find the total tidal tensor by linearly combining the tidal tensor of each individual moment, and we then find the eigenvectors and tendex lines of the total tidal tensor. The pattern formed from the combination of multipoles depends upon the parameters of the binary; in making this figure we assumed (in units in which  $M = 1$ ) a separation of  $a = 15$ , an orbital frequency  $\Omega = a^{-3/2}$ , and a velocity  $v = a\Omega = a^{-1/2}$ . When these higher moments are combined with the mass quadrupole, the tendex line structure resembles that of the mass quadrupole. The pattern is deformed slightly, however, by the presence of the higher multipoles. The loop singularities on the equator are no longer evenly spaced; rather, the pair illustrated (and the corresponding pair which is not visible) are pushed slightly closer together.

## 6.5 Conclusions

Tendex and vortex lines provide a new tool with which to visualize and study the curvature of spacetime. Fundamentally, they allow for the visualization of the Riemann tensor, through its decomposition into two simpler, trace-free and symmetric spatial tensors. These tensors,  $\mathcal{E}$  and  $\mathcal{B}$ , can be completely characterized by their eigenvectors and corresponding eigenvalues. The integral curves of these eigenvector fields are easily visualized, and their meaning is well understood; physically, the lines can be interpreted in terms of local tidal strains and differential frame-dragging. Here, the simple nature of these lines allows us to apply well-known topological theorems to the study of radiation passing through a sphere near null infinity.

Tendex line patterns must develop singularities (and thus have vanishing tendicity) on a closed

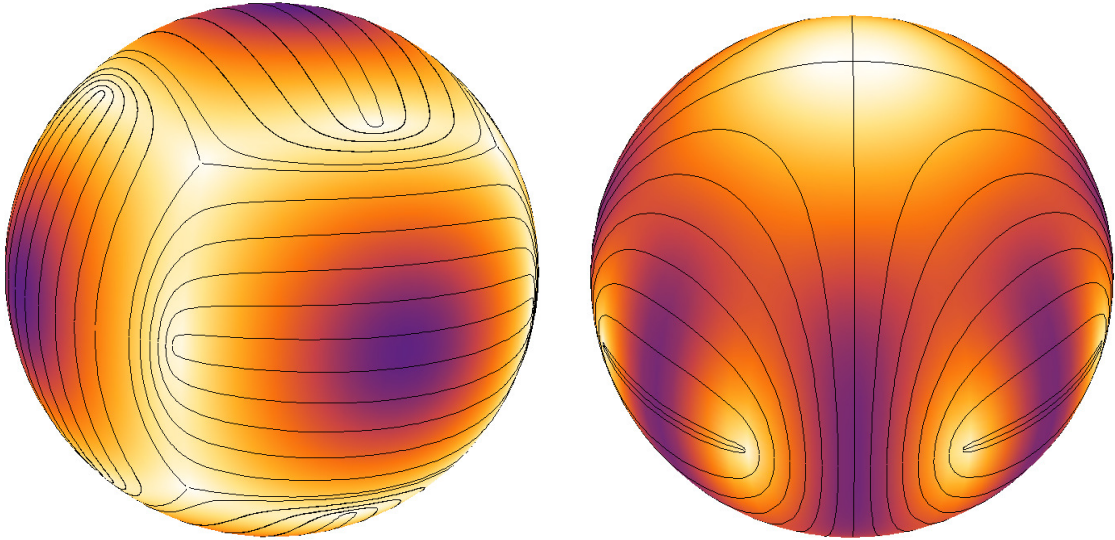


Figure 6.7: Left: The tendex lines of a current-octopole moment of an equal-mass, circular binary of point masses. The colors on the sphere represent the tendicity, with the same scale described in Figure 6.4. The current octopole also has four loop singularities on the equator (at the same position of those of the rotating quadrupole), but it has eight additional loops and eight triradius singularities off of the equator. Only half of the singular points are visible on the sphere; the other half appear on the back side. Right: The tendex lines on  $S$  of the mass hexadecapole of an equal-mass, circular binary of point masses, with the sphere colored by the tendicity as in the left panel. The hexadecapole has eight loop singularities equally spaced on the equator and two saddle-point-like singularities (from the coincidence of two triradius singularities at a point) at the poles. Again, only half are visible in the figure. Four of the singular points on the equator coincide with those of the quadrupole, but the remaining four appear at different locations.

surface. When we applied this fact to the tendex lines of gravitational radiation near null infinity from arbitrary physical systems, we could easily show that the gravitational radiation must at least vanish in isolated directions. Although this result is somewhat obvious in retrospect and has been noted before [8], the result does not appear to be well-known. We also began exploring the manner in which these singular points can provide a sort of fingerprint for radiating spacetimes. The essential elements of this fingerprint consist of the zeros of the curvature on the sphere, together with the index and the tendex line pattern around these zeros. We studied these patterns for a few specific examples, such as the four equally spaced loops of a rotating mass quadrupole. A more interesting case is that of a radiating spacetime composed of locked, rotating mass and current quadrupoles, which can be thought of as a simplified model of the late stages of the extreme-kick black-hole-binary merger. Here, the shifted positions of the singular points of the tendex pattern provide a direct illustration of gravitational beaming for this system. By seeking the most extreme topological arrangement of singular points, we also described a maximally beaming configuration of this system.

The radiation generated by higher-order STF multipole moments gives more complex examples of tendex and vortex patterns, with many singular points of varied types. Additionally, we argued

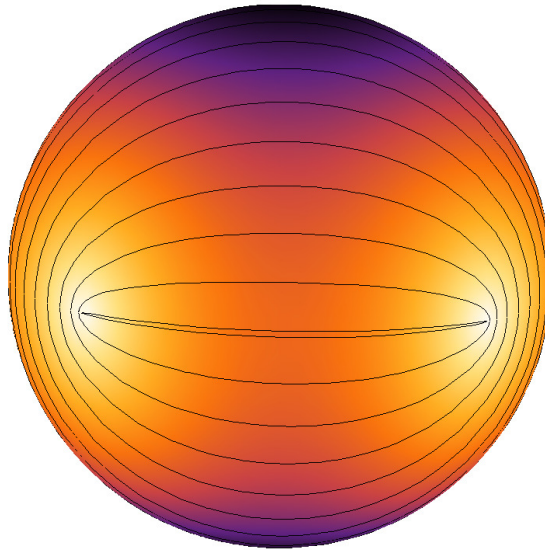


Figure 6.8: The tendex lines of a superposition of mass-quadrupole, current-octopole, and mass-hexadecapole moments of an equal-mass circular binary. It assumes a total mass  $M = 1$ , a separation  $a = 15$ , an orbital frequency  $\Omega = a^{-3/2}$  and a velocity  $v = a\Omega = a^{-1/2}$ . The sphere is colored by the tendicity in an identical way to that of Figure 6.4. When the tidal tensors of the three multipoles are combined, the net pattern is dominated by the quadrupole and contains only the four loops. The loop singularities are no longer equally spaced on the equator; the two pairs are pushed closer together due to the influence of the higher multipoles.

that their tendex and vortex patterns provide a visualization of the tensor spherical harmonics on the sphere; the eigenvalue illustrates the magnitude of these harmonics, and the lines show the tensor's polarization in an intuitive manner. The sum of the three multipoles illustrated in Figure 6.8 shows how including higher-order multipoles slightly deforms the pattern of quadrupole radiation to make a more accurate total radiation pattern of the equal-mass binary. Similar illustrations of complete radiation patterns could be readily produced from numerical spacetimes, when  $\Psi_4$  is extracted asymptotically using a tetrad with appropriate peeling properties. Such visualizations, and their evolution in time, could provide a useful method for visualizing the gravitational emission from these systems.

This study of the tendex and vortex lines (and their singular points) of asymptotic radiation fields is one of several [4] exploring and developing this new perspective on spacetime visualization. Naturally, it would be of interest to extend the two-dimensional case here to a larger study of the singular points in the full, three-dimensional tendex and vortex fields. Methods to find and visualize the singular points (and singular lines) of 3D tensors have been discussed preliminarily in [17], though there is still room for further work. We suspect that singular points will be important in visualizing and studying the properties of numerical spacetimes with these methods. Further, we expect that there is still much to be learned from the study of the vortexes and tendexes of dynamical spacetimes.

## Acknowledgments

We thank Rob Owen for inspiring our investigation of ridge topology in tendex and vortex patterns. We would also like to thank Yanbei Chen, Tanja Hinderer, Jeffrey D. Kaplan, Geoffrey Lovelace, Charles W. Misner, Ezra T. Newman, and Kip S. Thorne for valuable discussions. This research was supported by NSF Grants No. PHY-0601459, PHY-0653653, PHY-1005655, CAREER Grant PHY-0956189, NASA Grant No. NNX09AF97G, the Sherman Fairchild Foundation, the Brinson Foundation, and the David and Barbara Groce Startup Fund.

## Bibliography

- [1] R. Owen et al., *Phys. Rev. Lett.* **106**, 151101 (2011).
- [2] R. Maartens and B. A. Bassett, *Classical Quantum Gravity* **15**, 705 (1998).
- [3] F. B. Estabrook and H. D. Wahlquist, *J. Math. Phys.* **5**, 1629 (1964).
- [4] R. Owen et al., in preparation.
- [5] T. Delmarcelle and L. Hesselink, in *Proceedings of the Conference on Visualization '94*. (1994), VIS '94, pp. 140–147.
- [6] R. Penrose and W. Rindler, *Spinors and Space-time. Volume 2: Spinor and Twistor Methods in Space-time Geometry*. (Cambridge University Press, London, 1986).
- [7] R. Penrose, *Ann. Hum. Genet., Lond.* **42**, 435 (1979).
- [8] R. Penrose, *Proc. R. Soc. A* **284**, 159 (1965).
- [9] M. Campanelli, C. O. Lousto, Y. Zlochower, and D. Merritt, *Phys. Rev. Lett.* **98**, 231102 (2007).
- [10] H. Stephani, D. Kramer, M. MacCallum, C. Hoenselaers, and E. Herlt, *Exact Solutions of Einstein's Field Equations* (Cambridge University Press, London, 2003).
- [11] H. Bondi, M. G. J. van der Burg, and A. W. K. Metzner, *Proc. R. Soc. A* **269**, 21 (1962).
- [12] L. A. Tamburino and J. H. Winicour, *Phys. Rev.* **150**, 1039 (1966).
- [13] E. Newman and R. Penrose, *J. Math. Phys.* **3**, 566 (1962).
- [14] D. R. Fiske, J. G. Baker, J. R. van Meter, D.-I. Choi, and J. M. Centrella, *Phys. Rev. D* **71**, 104036 (2005).
- [15] J. D. Schnittman, A. Buonanno, J. R. van Meter, J. G. Baker, W. D. Boggs, J. Centrella, B. J. Kelly, and S. T. McWilliams, *Phys. Rev. D* **77**, 044031 (2008).

- [16] K. S. Thorne, *Rev. Mod. Phys.* **52**, 299 (1980).
- [17] J. Weickert, and H. Hagen, ed., *Visualization and Processing of Tensor Fields* (Springer Verlag, Berlin, 2006).

## Chapter 7

# Visualizing Spacetime Curvature via Frame-Drag Vortexes and Tidal Tendexes

## I. General Theory and Weak-Gravity Applications

When one splits spacetime into space plus time, the Weyl curvature tensor (vacuum Riemann tensor) gets split into two spatial, symmetric, and trace-free (STF) tensors: (i) the Weyl tensor's so-called "electric" part or *tidal field*  $\mathcal{E}_{jk}$ , which raises tides on the Earth's oceans and drives geodesic deviation (the relative acceleration of two freely falling test particles separated by a spatial vector  $\xi^k$  is  $\Delta a_j = -\mathcal{E}_{jk}\xi^k$ ); and (ii) the Weyl tensor's so-called "magnetic" part or (as we call it) *frame-drag field*  $\mathcal{B}_{jk}$ , which drives differential frame dragging (the precessional angular velocity of a gyroscope at the tip of  $\xi^k$ , as measured using a local inertial frame at the tail of  $\xi^k$ , is  $\Delta\Omega_j = \mathcal{B}_{jk}\xi^k$ ).

Being STF,  $\mathcal{E}_{jk}$  and  $\mathcal{B}_{jk}$  each have three orthogonal eigenvector fields which can be depicted by their integral curves. We call the integral curves of  $\mathcal{E}_{jk}$ 's eigenvectors *tidal tendex lines* or simply *tendex lines*, we call each tendex line's eigenvalue its *tendicity*, and we give the name *tendex* to a collection of tendex lines with large tendicity. The analogous quantities for  $\mathcal{B}_{jk}$  are *frame-drag vortex lines* or simply *vortex lines*, their *vorticities*, and *vortexes*.

These concepts are powerful tools for visualizing spacetime curvature. We build up physical intuition into them by applying them to a variety of weak-gravity phenomena: a spinning, gravitating point particle, two such particles side-by-side, a plane gravitational wave, a point particle with a dynamical current-quadrupole moment or dynamical mass-quadrupole moment, and a slow-motion binary system made of nonspinning

point particles. We show that a rotating current quadrupole has four rotating vortices that sweep outward and backward like water streams from a rotating sprinkler. As they sweep, the vortices acquire accompanying tendexes and thereby become outgoing current-quadrupole gravitational waves. We show similarly that a rotating mass quadrupole has four rotating, outward-and-backward sweeping tendexes that acquire accompanying vortices as they sweep, and become outgoing mass-quadrupole gravitational waves. We show, further, that an oscillating current quadrupole ejects sequences of vortex loops that acquire accompanying tendex loops as they travel, and become current-quadrupole gravitational waves; and similarly for an oscillating mass quadrupole. And we show how a binary's tendex lines transition, as one moves radially, from those of two static point particles in the deep near zone, to those of a single spherical body in the outer part of the near zone and inner part of the wave zone (where the binary's mass monopole moment dominates), to those of a rotating quadrupole in the far wave zone (where the quadrupolar gravitational waves dominate).

In paper II we will use these vortex and tendex concepts to gain insight into the quasi-normal modes of black holes, and in subsequent papers, by combining these concepts with numerical simulations, we will explore the nonlinear dynamics of curved spacetime around colliding black holes. We have published a brief overview of these applications in *Physical Review Letters* [1]. We expect these vortex and tendex concepts to become powerful tools for general relativity research in a variety of topics.

---

Originally published as D. A. Nichols, R. Owen, F. Zhang, A. Zimmerman, J. Brink, Y. Chen, J. D. Kaplan, G. Lovelace, K. D. Matthews, M. A. Scheel, and K. S. Thorne, *Phys. Rev. D* **84**, 124914 (2011). Copyright 2011 by the American Physical Society.

## 7.1 Motivation and Overview

In the 1950s John Archibald Wheeler coined the phrase *geometrodynamics* to epitomize his intuition that curved spacetime must have a rich range of nonlinear dynamical behaviors — behaviors that are important in our Universe and are worthy of probing deeply by both theoretical and observational means (see Reference [2] and earlier papers by Wheeler reprinted therein and also Reference [3]). It was obvious to Wheeler that analytical tools by themselves would not be sufficient to reveal the richness of geometrodynamics, so he encouraged his colleagues and students to begin developing numerical tools [4–6], and he encouraged Joseph Weber to develop technology for gravitational-wave observations [7].

Today, a half century later, numerical relativity has finally reached sufficient maturity (for a

review, see Reference [8] and the references therein) that, hand in hand with analytical relativity, it can be used to explore nonlinear geometrodynamics in generic situations; and gravitational-wave detectors are sufficiently mature [9–13] that they may soon observe nonlinear geometrodynamics in black-hole collisions.

Unfortunately, there is a serious obstacle to extracting geometrodynamical insights from numerical-relativity simulations: a paucity of good tools for visualizing the dynamics of curved spacetime. We are reasonably sure that buried in the billions of numbers produced by numerical-relativity simulations there are major discoveries to be made, but extracting those discoveries is exceedingly difficult and perhaps impossible with the tools we have had thus far.

Until now, curved spacetime has been visualized primarily via (isometric) *embedding diagrams* (Section 23.8 of Reference [14]): choosing spacelike two-dimensional surfaces in spacetime, and embedding them in flat 3-dimensional Euclidean space or 2+1-dimensional Minkowski spacetime in a manner that preserves the surfaces' intrinsic geometry. (For some examples of embedding diagrams applied to black-hole spacetimes, see, e.g., References [15–17]). Unfortunately, such embedding diagrams are of very limited value. They capture only two dimensions of spacetime, and the 2-surfaces of greatest interest often cannot be embedded globally in flat Euclidean 3-space or flat Minkowski 2+1-dimensional spacetime [15, 18–20]. Mixed Euclidean/Minkowski embeddings are often required (e.g., Figure 4 of Reference [15]), and such embeddings have not proved to be easily comprehended. Moreover, although it is always possible to perform a local embedding in a flat 3-space (in the vicinity of any point on the two-surface), when one tries to extend the embedding to cover the entire two-surface, one often encounters discontinuities analogous to shocks in fluid mechanics [18, 20].

A systematic approach to understanding the connection between nonlinear near-field dynamics in general relativity and emitted gravitational waves is being developed by Rezzolla, Jaramillo, Macedo, and Moesta [21–24]. This approach focuses on correlations between data on a surface at large radius (ideally null infinity) and data on world tubes in the source region (such as black-hole horizons). The purpose is to use such correlations to infer the dynamics of a black hole (e.g. the kick) directly from data on its horizon. While we find this approach exciting and attractive, in our own work we seek a more direct set of tools: tools that can probe the dynamics of spacetime curvature that cause such correlations in the first place, and that can be more readily and intuitively applied to a wider range of other geometrodynamical phenomena. It is our hope that eventually our tools and those of Rezzolla et. al. [21–23] will provide complementary pictures for understanding spacetime dynamics, and particularly black-hole kicks.

We have introduced our new set of tools in a recent paper in *Physical Review Letters* [1]. They are tools for visualizing spacetime curvature, called *tidal tendex lines*, *tendicities*, and *tendexes*; and *frame-drag vortex lines*, *vorticities* and *vortexes*. These tools capture the full details of the Weyl curvature tensor (vacuum Riemann tensor), which embodies spacetime curvature. They do so in

three-dimensional, dynamically evolving pictures, of which snapshots can be printed in a paper such as this one, and movies can be made available online.<sup>1</sup> Specifically, as of this writing two movies can be seen at References [26, 27]; one shows the vortex lines from a rotating current quadrupole, the other, vortex lines from two particles that collide head-on with transverse, antiparallel spins.

We have found these tools to be an extremely powerful way to visualize the output of numerical simulations. We have also used them to obtain deep new insights into old analytical spacetimes. We have applied them, thus far, to pedagogical linear-gravity problems (this paper and [28]), to stationary and perturbed black holes (Paper II in this series), and to simulations of the inspiral and mergers of spinning black holes ([1] and Paper III). We plan to apply them in the future in a variety of other geometrodynamical venues, such as black holes ripping apart neutron stars and curved spacetime near various types of singularities.

This is the first of a series of papers in which we will (i) present these tools, (ii) show how to use them, (iii) build up physical intuition into them, and (iv) employ them to extract geometrodynamical insights from numerical-relativity simulations. Specifically:

In this paper (Paper I), we introduce these vortex and tendex tools, and we then apply them to weak-gravity situations (linearized general relativity) with special focus on the roles of vortexes and tendexes in gravitational-wave generation. In a closely related paper [28], three of us have applied these tools to visualize asymptotic gravitational radiation and explore the topology of its vortex and tendex lines, and also to explore a linearized-gravity model of an extreme-kick merger. In Paper II we shall apply our new tools to quiescent black holes and quasinormal modes of black holes, with special focus once again on the roles of vortexes and tendexes in generating gravitational waves. In Paper III and subsequent papers we shall apply our tools to numerical simulations of binary black holes, focusing on nonlinear geometrodynamics in the holes’ near zone and how the near-zone vortexes and tendexes generate gravitational waves.

The remainder of this paper is organized as follows:

In Section 7.2.1 we review the well-known split of the Weyl curvature tensor into its “electric” and “magnetic” parts  $\mathcal{E}_{ij}$  and  $\mathcal{B}_{ij}$ , and in Section 7.2.2 we review the Maxwell-like evolution equations for  $\mathcal{E}_{ij}$  and  $\mathcal{B}_{ij}$  and discuss the mathematical duality between these fields. Then in Section 7.3 we review the well-known physical interpretation of  $\mathcal{E}_{ij}$  as the *tidal field* that drives geodesic deviation and the not so well-known interpretation of  $\mathcal{B}_{ij}$  [29, 30] as the *frame-drag* field that drives differential frame dragging, and we derive the equation of differential frame dragging.

In Section 9.1.2 we introduce our new set of tools for visualizing spacetime curvature. Specifically: In Section 7.4.1 we introduce tendex lines and their tendicities, and we quantify them by their

---

<sup>1</sup>Just as there is no unique method to evolve field lines in electromagnetism, so too is there no unique way to match tendex or vortex lines at one time with others at a later time. Nevertheless, animations of field lines are useful for pedagogical purposes and for building intuition [25]. While some of the authors and colleagues are investigating how to evolve tendex and vortex lines in generic situations, the animations of the lines posted online all have special symmetries that provide a natural way to connect lines at one time with lines at the next.

stretching or compressional force on a person; and we also introduce vortex lines and their vorticities and quantify them by their twisting (precessional) force on gyroscopes attached to the head and feet of a person. Then in Section 7.4.2 we introduce *vortexes* and *tendexes* (bundles of vortex and tendex lines that have large vorticity and tendicity) and give examples.

In the remainder of this paper we illustrate these new concepts by applying them to some well-known, weak-gravity, analytic examples of spacetime curvature. In Section 7.5 we focus on the spacetime curvature of stationary systems, and in Section 7.6 we focus on dynamical systems and develop physical pictures of how they generate gravitational waves.

More specifically, in Section 7.5.1, we compute  $\mathcal{E}_{ij}$  and  $\mathcal{B}_{ij}$  for a static, gravitating, spinning point particle; we explain the relationship of  $\mathcal{B}_{ij}$  to the particle’s dipolar “gravitomagnetic field,” we draw the particle’s tendex lines and vortex lines, and we identify two vortexes that emerge from the particle, a counterclockwise vortex in its “north polar” region and a clockwise vortex in its “south polar” region. In Section 7.5.2, we draw the vortex lines for two spinning point particles that sit side by side with their spins in opposite directions, and we identify their four vortexes. Far from these particles, they look like a single point particle with a current-quadrupole moment. In Section 7.5.3, we draw the vortex lines for such a current-quadrupole particle and identify their vortexes. Then in Section 7.5.4, we show that the tendex lines of a mass-quadrupole particle have precisely the same form as the vortex lines of the current-quadrupole particle, and we identify the mass quadrupole’s four tendexes.

Turning to dynamical situations, in Section 7.6.1 we compute  $\mathcal{E}_{ij}$  and  $\mathcal{B}_{ij}$  for a plane gravitational wave, we express them in terms of the Weyl scalar  $\Psi_4$ , and we draw their vortex and tendex lines. In Section 7.6.2 we explore the quadrupolar ( $l = 2, m = 0$ ) angular pattern of gravitational waves from the head-on collision of two black holes, and we draw their vortex lines and tendex lines, intensity-coded by vorticity and tendicity, on a sphere in the wave zone. In Section 7.6.3 we compute  $\mathcal{E}_{ij}$  and  $\mathcal{B}_{ij}$  for a general, time-varying current-quadrupolar particle, and then in Sections 7.6.4 and 7.6.5 we specialize to a rotating current quadrupole and an oscillating current quadrupole, and draw their vortex and tendex lines. Our drawings and the mathematics reveal that the particle’s outgoing gravitational waves are generated by its near-zone vortexes. The rotating current quadrupole has four vortexes that spiral outward and backward like four water streams from a rotating sprinkler. As it bends backward, each vortex acquires an accompanying tendex, and the vortex and tendex together become a gravitational-wave crest or gravitational-wave trough. The oscillating current quadrupole, by contrast, ejects vortex loops that travel outward, acquiring accompanying tendex loops with strong tendicity on the transverse segment of each loop and weak on the radial segment—thereby becoming outgoing gravitational waves.

In Section 7.6.6 we show that a time-varying mass quadrupole produces the same phenomena as a time-varying current quadrupole, but with vortexes and tendexes interchanged.

In Section 7.6.7 we study the vortexes and tendexes of a slow-motion binary made of nonspinning point particles. In the near zone, the tendex lines transition, as one moves radially outward, from those of two individual particles (radial and circular lines centered on each particle) toward those of a single spherical body (radial and circular lines centered on the binary and produced by the binary's mass monopole moment). In the transition zone and inner wave zone, the mass monopole continues to dominate. Then at radii  $r \sim a^2/M$  (where  $a$  is the particles' separation and  $M$  is the binary's mass), the radiative quadrupole moment begins to take over and the tendex lines gradually transition into the outward-and-backward spiraling lines of a rotating quadrupole.

We make some concluding remarks in Section 9.6.

Throughout this paper we use geometrized units with  $c = G = 1$ , and we use the sign conventions of MTW [14] for the metric signature, the Weyl curvature, and the Levi-Civita tensor. We use Greek letters for spacetime indexes (0–3) and Latin letters for spatial indexes (1–3), and we use arrows over 4-vectors and bold-face font for spatial 3-vectors and for tensors. In orthonormal bases, we use hats over all kinds of indexes.

## 7.2 The Tidal Field $\mathcal{E}_{ij}$ and Frame-Drag Field $\mathcal{B}_{ij}$

### 7.2.1 3+1 Split of Weyl Curvature Tensor into $\mathcal{E}_{ij}$ and $\mathcal{B}_{ij}$

For a given spacetime, the Weyl curvature tensor can be calculated from the Riemann tensor by subtracting Riemann's trace from itself; i.e., by subtracting from Riemann the following combinations of the Ricci curvature tensor  $R^\mu{}_\nu$ , and Ricci curvature scalar  $R$  (Eq. (13.50) of MTW [14]):

$$C^{\mu\nu}{}_{\rho\sigma} = R^{\mu\nu}{}_{\rho\sigma} - 2\delta^{[\mu}{}_{[\rho} R^{\nu]}{}_{\sigma]} + \frac{1}{3}\delta^{[\mu}{}_{[\rho} \delta^{\nu]}{}_{\sigma]} R. \quad (7.1)$$

Here  $\delta^\mu{}_\rho$  is the Kronecker delta, and the square brackets represent antisymmetrization. Note that in vacuum,  $C^{\mu\nu}{}_{\rho\sigma} = R^{\mu\nu}{}_{\rho\sigma}$ , and thus in vacuum the Weyl tensor contains all information about the spacetime curvature.

Let us pick a foliation of spacetime into a family of spacelike hypersurfaces. We shall denote by  $u^\mu$  the 4-velocity of observers who move orthogonal to the foliation's space slices, and by  $\gamma_{\mu\nu} = g_{\mu\nu} + u_\mu u_\nu$  the induced spatial three metric on these slices, so that  $\gamma_\alpha{}^\mu$  is the projection operator onto the slices. As is well-known, e.g. [31], using this projection operator, we can split the Weyl tensor covariantly into two irreducible parts, which are symmetric, trace-free (STF) tensors that lie in the foliation's hypersurfaces (i.e. that are orthogonal to  $u^\mu$ ). These pieces are

$$\mathcal{E}_{\alpha\beta} = \gamma_\alpha{}^\rho \gamma_\beta{}^\sigma C_{\rho\mu\sigma\nu} u^\mu u^\nu, \quad \text{i.e.} \quad \mathcal{E}_{ij} = C_{i\hat{0}j\hat{0}}, \quad (7.2a)$$

an even-parity field called the “electric” part of  $C^{\mu\nu}_{\rho\sigma}$ , and

$$\mathcal{B}_{\alpha\beta} = -\gamma_\alpha{}^\rho \gamma_\beta{}^\sigma {}^*C_{\rho\mu\sigma\nu} u^\mu u^\nu, \quad \text{i.e.} \quad \mathcal{B}_{ij} = \frac{1}{2} \epsilon_{ipq} C^{pq}_{j\hat{0}}, \quad (7.2b)$$

an odd-parity field known as the “magnetic” part of  $C^{\mu\nu}_{\rho\sigma}$ . Here the symbol  $*$  represents the (left) Hodge dual,  ${}^*C_{\rho\mu\sigma\nu} = \frac{1}{2} \epsilon_{\rho\mu\eta\lambda} C^{\eta\lambda}_{\sigma\nu}$ , and for each field the second expression is written in 3+1 notation: the Latin (spatial) indexes are components in the foliation’s hypersurface, and the  $\hat{0}$  is a component on the foliation’s unit time basis vector  $\vec{e}_{\hat{0}} \equiv \vec{u}$ . Our normalization for the Levi-Civita tensor is that of MTW: in a right-handed orthonormal frame,  $\epsilon_{\hat{0}\hat{1}\hat{2}\hat{3}} = +1$ , and the spatial Levi-Civita tensor is defined by  $\epsilon_{ipq} = \epsilon_{\hat{0}ipq}$ , with  $\epsilon_{\hat{1}\hat{2}\hat{3}} = 1$  in a right-handed orthonormal basis. Note that Eqs. (8.1) are a direct and intentional analogy to the decomposition of the Maxwell tensor of electromagnetism  $F_{\mu\nu}$  into the familiar electric and magnetic fields  $E_i$  and  $B_i$  [31]:

$$E_i = F_{i\hat{0}}, \quad B_i = -{}^*F_{i\hat{0}} = \frac{1}{2} \epsilon_{ipq} F^{pq}. \quad (7.3)$$

Note that our sign conventions differ from [31], where  $\epsilon_{\hat{0}\hat{1}\hat{2}\hat{3}} = -1$ , and so Eq. (8.1b) has an additional minus sign in order to maintain a strict analogy with the magnetic field  $B_i$  of electromagnetism. This results in a  $\mathcal{B}_{ij}$  defined with a different sign convention than, for example, in [32, 33].

## 7.2.2 Evolution of $\mathcal{E}_{ij}$ and $\mathcal{B}_{ij}$

The propagation equations for the Weyl tensor and its gravito-electromagnetic representation are the Bianchi identities. We shall write them down and discuss them in three contexts: a general foliation and coordinate system, the local-Lorentz frame of a freely falling observer, and the weak-gravity, nearly Minkowski spacetimes of the current paper (Paper I in this series).

### 7.2.2.1 General Foliation and Coordinate System in the Language of Numerical Relativity

Because this paper is a foundation for using  $\mathcal{E}_{ij}$  and  $\mathcal{B}_{ij}$  to interpret the results of numerical-relativity simulations, we shall write their evolution equations (the Bianchi identities) in a general coordinate system of the type used in numerical relativity, and we shall discuss these equations’ mathematical structure in the language of numerical relativity.

We denote by  $t$  a time coordinate that is constant on the foliation’s hypersurfaces, and by  $\alpha$  and  $\vec{\beta}$  the foliation’s lapse and shift functions, so the orthogonal observers’ 4-velocity is  $\vec{u} = \alpha^{-1}(\vec{\partial}_t - \vec{\beta})$ . The 3+1 split divides the Bianchi identities into evolution equations that govern the time evolution of the spatial fields, and constraint equations that are obeyed by the fields on each time slice. The

evolution equations are [34, 35]

$$\begin{aligned}\partial_t \mathcal{E}_{ij} &= \mathcal{L}_\beta \mathcal{E}_{ij} + \alpha [D_k \mathcal{B}_{l(i} \epsilon_j^{kl)} - 3\mathcal{E}^k_{(i} K_{j)k} + K^k_k \mathcal{E}_{ij} - \epsilon_i^{kl} \mathcal{E}_{km} K_{ln} \epsilon_j^{mn} + 2a_k \mathcal{B}_{l(i} \epsilon_j^{kl)}], \\ \partial_t \mathcal{B}_{ij} &= \mathcal{L}_\beta \mathcal{B}_{ij} + \alpha [-D_k \mathcal{E}_{l(i} \epsilon_j^{kl)} - 3\mathcal{B}^k_{(i} K_{j)k} + K^k_k \mathcal{B}_{ij} - \epsilon_i^{kl} \mathcal{B}_{km} K_{ln} \epsilon_j^{mn} - 2a_k \mathcal{E}_{l(i} \epsilon_j^{kl)}].\end{aligned}\quad (7.4)$$

Here the extrinsic curvature, Lie derivative on a second rank tensor, and acceleration of the slicing are respectively defined by

$$K_{ij} = -\frac{1}{2\alpha} (\partial_t \gamma_{ij} - D_i \beta_j - D_j \beta_i), \quad (7.5)$$

$$\mathcal{L}_\beta \mathcal{E}_{ij} = \beta^k D_k \mathcal{E}_{ij} + \mathcal{E}_{ik} D_j \beta^k + \mathcal{E}_{kj} D_i \beta^k, \quad (7.6)$$

$$a_k = D_k \ln \alpha. \quad (7.7)$$

The derivative  $D_i$  is the covariant derivative associated with the induced metric  $\gamma_{ij}$  on the slices. The evolution system (7.4) is closed by an additional evolution equation for the 3-metric, which is Eq. (7.5), and evolution equations for the extrinsic curvature and the 3-dimensional connection  $\Gamma_{ij}^k$ , which are

$$\begin{aligned}\partial_t K_{ij} &= \mathcal{L}_\beta K_{ij} - \alpha [\partial_k \Gamma_{ij}^k - \Gamma_{lj}^k \Gamma_{ki}^l + \partial_i \partial_j q + \partial_i \ln \alpha \partial_j \ln \alpha - \Gamma_{ij}^k \partial_k q - 2\mathcal{E}_{ij} + K^k_k K_{ij}], \\ \partial_t \Gamma_{ij}^k &= \mathcal{L}_\beta \Gamma_{ij}^k - \alpha D^k K_{ij} + K_{ij} D^k \alpha - 2K^k_{(i} D_{j)} \alpha + 2\alpha \epsilon^{kl}_{(i} \mathcal{B}_{j)l},\end{aligned}\quad (7.8)$$

where we have defined

$$q = \ln(\alpha \gamma^{-1/2}), \quad (7.9)$$

$$\mathcal{L}_\beta \Gamma_{ij}^k = \beta^l \partial_l \Gamma_{ij}^k + 2\Gamma_{l(j}^k \partial_i) \beta^l - \Gamma_{ij}^l \partial_l \beta^k + \partial_i \partial_j \beta^k. \quad (7.10)$$

The above equations are symmetric hyperbolic if  $q$  and  $\beta^i$  are specified functions of time and space.

The constraint equations on each slice are the definitions of  $\mathcal{E}_{ij}$  and  $\mathcal{B}_{ij}$ ,

$$\begin{aligned}\mathcal{E}_{ij} &= {}^{(3)}R_{ij} + K^k_k K_{ij} - K^k_i K_{jk}, \\ \mathcal{B}_{ij} &= \epsilon_j^{lk} D_k K_{li},\end{aligned}\quad (7.11)$$

from which the Einstein constraints follow from the condition that  $\mathcal{E}_{ij}$  and  $\mathcal{B}_{ij}$  are symmetric and trace-free, and the definition of  $\Gamma_{ij}^k$ ,

$$\Gamma_{ij}^k = \frac{1}{2} \gamma^{k\ell} (\partial_i \gamma_{j\ell} + \partial_j \gamma_{i\ell} - \partial_\ell \gamma_{ij}). \quad (7.12)$$

The Bianchi identities imply derivative constraints on  $\mathcal{E}_{ij}$  and  $\mathcal{B}_{ij}$ :

$$D^i \mathcal{E}_{ij} = \mathcal{B}_{ik} K^i_l \epsilon^{kl}{}_j, \quad D^i \mathcal{B}_{ij} = -\mathcal{E}_{ik} K^i_l \epsilon^{kl}{}_j. \quad (7.13)$$

These last equations are automatically satisfied if Eqs. (7.11) are satisfied. Equations. (7.13) are nonlinear, but otherwise they have the same structure as the constraints in simple electromagnetism.

Note also that the equations governing  $\mathcal{E}$  and  $\mathcal{B}$ , Eqs (7.4) and (7.13) share another similarity with the field equations of electromagnetism. Namely, just as the Maxwell equations are invariant under the duality transformation

$$\mathbf{E} \rightarrow \mathbf{B}, \quad \mathbf{B} \rightarrow -\mathbf{E}, \quad (7.14)$$

i.e. under a rotation in the complexified notation

$$\mathbf{E} - i\mathbf{B} \rightarrow e^{i\pi/2}(\mathbf{E} - i\mathbf{B}), \quad (7.15)$$

so the exact Maxwell-like Bianchi identities (7.4) are also invariant under the same duality transformation

$$\mathcal{E} \rightarrow \mathcal{B}, \quad \mathcal{B} \rightarrow -\mathcal{E}. \quad (7.16)$$

This *duality* in the structure of Eqs. (7.4) and also (7.13) does not in general enable one to construct one metric solution of Einstein's equations from another, known solution. However, as we shall see, we can utilize this duality in weakly gravitating systems to find the  $\mathcal{E}$  and  $\mathcal{B}$  generated by one set of source moments, given the expressions for  $\mathcal{E}$  and  $\mathcal{B}$  for a dual set of moments.

### 7.2.2.2 Local-Lorentz Frame of a Freely Falling Observer

When one introduces the local-Lorentz frame of a freely falling observer in curved spacetime, one necessarily specializes one's foliation: (i) The local-Lorentz foliation's space slices are flat at first order in distance from the observer's world line, so its extrinsic curvature  $K_{ij}$  vanishes along the observer's world line. (ii) Because the observer is freely falling, her acceleration  $a_k$  vanishes, which means that successive hypersurfaces in the foliation are parallel to each other along the observer's world line.

These specializations, plus the vanishing shift  $\beta_i = 0$  and unit lapse function  $\alpha = 1$  of a local-Lorentz frame, bring the constraint and evolution equations (7.13) and (7.4) into the following Maxwell-like form:

$$\nabla \cdot \mathcal{E} = 0, \quad \nabla \cdot \mathcal{B} = 0,$$

$$\frac{\partial \mathcal{E}}{\partial t} - (\nabla \times \mathcal{B})^S = 0, \quad \frac{\partial \mathcal{B}}{\partial t} + (\nabla \times \mathcal{E})^S = 0. \quad (7.17)$$

Here the superscript  $S$  means “take the symmetric part” and the remaining notation is the same as in the flat-spacetime Maxwell equations (including changing from  $\mathbf{D}$  to  $\nabla$  for the spatial gradient).

### 7.2.2.3 Weak-Gravity, Nearly Minkowski Spacetimes

In this paper’s applications (Sections 7.5 and 7.6), we shall specialize to spacetimes and coordinate systems that are weakly perturbed from Minkowski, and we shall linearize in the perturbations. In this case, the Bianchi identities (7.4) take on precisely the same Maxwell-like form as in a local-Lorentz frame in strongly curved spacetime, Eqs. (7.17). To see that this is so, note that  $\beta_k$ ,  $K_{jk}$ ,  $a_k$ ,  $\mathcal{E}_{jk}$ , and  $\mathcal{B}_{jk}$  are all first-order perturbations and that  $\alpha$  is one plus a first-order perturbation; and linearize Eqs. (7.4) in these first-order quantities.

When the weak-gravity spacetime is also characterized by slow motion, so its source regions are small compared to the wavelengths of its gravitational waves, the evolution equations control how the near-zone  $\mathcal{E}_{jk}$  and  $\mathcal{B}_{jk}$  get transformed into gravitational-wave fields. For insight into this, we specialize to harmonic gauge, in which the trace-reversed metric perturbation  $\bar{h}_{\mu\nu}$  is divergence-free,  $\partial^\mu \bar{h}_{\mu\nu} = 0$ .

Then *in the near zone*,  $\mathcal{E}_{jk}$  and  $\mathcal{B}_{jk}$  [which are divergence-free and curl-free by Eqs. (7.17)] are expressible in terms of the metric perturbation itself as

$$\mathcal{E}_{ij} = -\frac{1}{2} \partial_i \partial_j h_{00}, \quad \mathcal{B}_{ij} = \frac{1}{2} \epsilon_i^{pq} \partial_q \partial_j h_{p0}. \quad (7.18)$$

Because  $h_{00}$ , at leading order in  $r/\lambda$  (ratio of radius to reduced wavelength), contains only mass multipole moments (Eq. (8.13a) of [36]), so also  $\mathcal{E}_{jk}$  contains only mass multipole moments. And because  $h_{p0}$  at leading order in  $r/\lambda$  contains only current multipole moments, so also  $\mathcal{B}_{jk}$  contains only current multipole moments.

*In the wave zone*, by contrast, Eqs. (7.17) show that the locally plane waves are sustained by mutual induction between  $\mathcal{E}$  and  $\mathcal{B}$ , just like for electromagnetic waves, which means that these two wave-zone fields must contain the same information. This is confirmed by the wave-zone expressions for  $\mathcal{E}_{jk}$  and  $\mathcal{B}_{jk}$  in terms of the metric perturbation,

$$\mathcal{E}_{ij} = -\frac{1}{2} \partial_0^2 h_{ij}, \quad \mathcal{B}_{ij} = -\frac{1}{2} \epsilon_i^{pq} n_p \partial_0^2 h_{qj}. \quad (7.19)$$

Both fields are expressed in terms of the same quantity,  $h_{ij}$ . In addition, in the wave zone,  $\mathcal{E}$  and  $\mathcal{B}$  are related to each other through a  $\pi/4$  rotation of their polarization tensors (see Section 7.6.1 below). Correspondingly, we will see in Section 7.6 that, if a time-varying mass moment produces

+ polarized radiation in the wave zone, then the current moment that is dual to it produces  $\times$  polarized radiation of the same magnitude.

In the transition zone, the inductive coupling between  $\mathcal{E}$  and  $\mathcal{B}$ , embodied in Eqs. (7.4), enables these equations to act like a blender, mixing up the multipolar information that in the near zone is stored separately in these two fields. After an infinite amount of inductive blending, we arrive at future null infinity,  $\mathcal{I}^+$ , where the mixing has been so thorough that  $\mathcal{E}$  and  $\mathcal{B}$  contain precisely the same information, though it is distributed differently among their tensor components [Eqs. (7.19)].

The details of this transition-zone mixing, as embodied in Eqs. (7.17), are in some sense the essence of gravitational-wave generation. We shall explore those details visually in Section 7.6 by tracking the tendex and vortex lines (introduced in Sec 9.1.2) that extend from the near zone, through the transition zone, and into the far zone.

Finally, note that the duality of  $\mathcal{E}$  and  $\mathcal{B}$  becomes especially convenient for slow-motion systems, where we can relate  $\mathcal{E}$  and  $\mathcal{B}$  to source multipole moments that appear in the weak-field near zone. In particular: to obtain the  $\mathcal{E}$  and  $\mathcal{B}$  generated by a specific current moment  $\mathcal{S}_\ell$ , we can simply apply the duality transformation (7.16) to the  $\mathcal{E}$  and  $\mathcal{B}$  for its dual moment, which is the mass moment  $\mathcal{I}_\ell$ , but with one caveat: the differing normalizations used for mass moments and current moments [36] enforce the duality relation

$$\mathcal{I}_\ell \rightarrow \frac{2\ell}{\ell+1} \mathcal{S}_\ell, \quad \mathcal{S}_\ell \rightarrow -\frac{\ell+1}{2\ell} \mathcal{I}_\ell, \quad (7.20)$$

when making this duality transformation; note that both transformations, Eqs. (7.16) and (7.20), must be made at once to arrive at the correct expressions; see Section 7.6.

### 7.3 Physical Interpretations of $\mathcal{E}_{ij}$ and $\mathcal{B}_{ij}$

It is rather well-known that in vacuum<sup>2</sup> the electric part of the Weyl tensor,  $\mathcal{E}_{ij}$ , describes tidal gravitational accelerations: the relative acceleration of two freely falling particles with separation vector  $\xi^k$  is  $\Delta a^i = -\mathcal{E}^i_j \xi^j$ . For this reason  $\mathcal{E}_{ij}$  is often called the *tidal field*, a name that we shall adopt.

Not so well-known is the role of the magnetic part of the Weyl tensor  $\mathcal{B}_{jk}$  in governing differential frame dragging, i.e. the differential precession of inertial reference frames: in vacuum<sup>2</sup> a gyroscope at the tip of the separation vector  $\xi^k$ , as observed in the local-Lorentz frame of an observer at the tail of  $\xi^k$ , precesses with angular velocity  $\Delta\Omega^j = \mathcal{B}^j_k \xi^k$ . For this reason, we call  $\mathcal{B}_{jk}$  the *frame-drag*

<sup>2</sup> In a non-vacuum region of spacetime, the local stress-energy tensor also contributes to tidal accelerations via its algebraic relation to the Ricci tensor which in turn contributes to the Riemann tensor. In this case,  $\mathcal{E}_{ij}$  describes that portion of the tidal acceleration due to the “free gravitational field,” i.e., the portion that is sourced away from the location where the tidal acceleration is measured; and similarly for  $\mathcal{B}_{jk}$  and differential frame dragging. In this paper we shall ignore this subtle point and focus on tidal forces and differential frame dragging in vacuum.

field.

We deduced this frame-drag role of  $\mathcal{B}_{jk}$  during our research and then searched in vain for any reference to it in the literature, while writing our Physical Review Letter on vortexes and tendexes [1]. More recently we have learned that this role of  $\mathcal{B}_{jk}$  was known to Frank Estabrook and Hugo Wahlquist [29] 46 years ago and was rediscovered two years ago by Christoph Schmidt [30] (who states it without proof).

For completeness, in this section we shall give a precise statement and proof of the frame-drag role of  $\mathcal{B}_{jk}$ , and a corresponding precise statement of the tidal-acceleration role of  $\mathcal{E}_{jk}$ .

### 7.3.1 Physical Setup

Consider an event  $\mathcal{P}$  in spacetime and an observer labeled  $A$  whose world line passes through  $\mathcal{P}$  and has 4-velocity  $\vec{u}$  there; see Figure 7.1. Introduce an infinitesimally short 4-vector  $\vec{\xi}$  at  $\mathcal{P}$ , that is orthogonal to  $\vec{u}$  and thus is seen as spatial by observer  $A$ . Denote by  $\mathcal{P}'$  the event at the tip of  $\vec{\xi}$ . Introduce a second observer  $B$  whose world line passes through  $\mathcal{P}'$  and is parallel there to the world line of observer  $A$ , so if we denote  $B$ 's 4-velocity by the same symbol  $\vec{u}$  as that of  $A$  and imagine a vector field  $\vec{u}$  that varies smoothly between the two world lines, then  $\nabla_{\vec{\xi}}\vec{u} = 0$  at  $\mathcal{P}$ . Let  $\vec{\xi}$  be transported by observer  $A$  in such a way that it continues to reach from world line  $A$  to world line  $B$ . Then the vectors  $\vec{u}$  and  $\vec{\xi}$  satisfy the following three relations at  $\mathcal{P}$ :

$$\vec{\xi} \cdot \vec{u} = 0, \quad [\vec{u}, \vec{\xi}] = 0, \quad \nabla_{\vec{\xi}}\vec{u} = 0. \quad (7.21)$$

The first says that the separation vector is purely spatial at  $\mathcal{P}$  in the reference frame of observer  $A$ ; the second says that  $\vec{\xi}$  continues to reach between world lines  $A$  and  $B$ , so the quadrilateral formed by  $\vec{u}$  and  $\vec{\xi}$  in Figure 7.1 is closed; the third says that the two observers' world lines are parallel to each other at  $\mathcal{P}$ —i.e., these observers regard themselves as at rest with respect to each other.

### 7.3.2 Interpretation of $\mathcal{E}_{ij}$ as the Tidal Field

Let the two observers  $A$  and  $B$  fall freely, i.e. move on geodesics. Then for this physical setup, the equation of geodesic deviation states that [e.g. [14] Eq. (11.10)]

$$\nabla_{\vec{u}}\nabla_{\vec{u}}\vec{\xi} = -\mathbf{R}(\_, \vec{u}, \vec{\xi}, \vec{u}), \quad (7.22)$$

where  $\mathbf{R}$  is the Riemann tensor. In physical language, the left side is the acceleration  $\Delta\vec{a}$  of observer  $B$  at  $\mathcal{P}'$ , as measured in the local-Lorentz frame of observer  $A$  at  $\mathcal{P}$ . This relative acceleration is purely spatial as seen by observer  $A$ , and the right side of Eq. (7.22) tells us that in spatial,

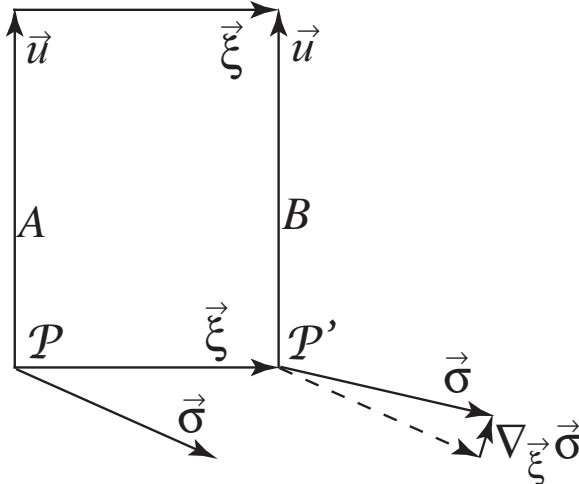


Figure 7.1: Spacetime geometry for computing the precession of a gyroscope at one location  $\mathcal{P}'$ , relative to gyroscopic standards at a nearby location  $\mathcal{P}$ .

3-dimensional vector and tensor notation (and in vacuum so  $R_{\alpha\beta\gamma\delta} = C_{\alpha\beta\gamma\delta}$ ), it is given by

$$\Delta a^j = -R^j_{\hat{0}k\hat{0}} \xi^k = -\mathcal{E}^j_k \xi^k; \quad \text{i.e.} \quad \Delta \mathbf{a} = -\mathcal{E}(\_, \boldsymbol{\xi}). \quad (7.23)$$

Since (as is well-known) this relative acceleration produces the Earth's tides when  $\mathcal{E}_{jk}$  is caused by the moon and sun,  $\mathcal{E}_{jk}$  is called the *tidal field*, and Eq. (7.23) is known as *the tidal-acceleration equation*.

### 7.3.3 Interpretation of $\mathcal{B}_{ij}$ as the Frame-Drag Field

Next let the two observers  $A$  and  $B$  in Figure 7.1 be accelerated if they wish (with the same 4-acceleration  $\vec{a}$  up to differences proportional to  $\vec{\xi}$ ), and give each of them a spatial unit vector  $\vec{\sigma}$  that is tied to an inertial-guidance gyroscope, so the following relations are satisfied:

$$\vec{\sigma} \cdot \vec{u} = 0, \quad \vec{\sigma} \cdot \vec{\sigma} = 1, \quad \nabla_{\vec{u}} \vec{\sigma} = (\vec{a} \cdot \vec{\sigma}) \vec{u}, \quad \vec{a} \equiv \nabla_{\vec{u}} \vec{u}. \quad (7.24)$$

The first of these says that  $\vec{\sigma}$  is purely spatial as seen in the observer's reference frame; the second says that  $\vec{\sigma}$  has unit length; the third is the Fermi-Walker transport law for an inertial-guidance gyroscope.

The local-frame-dragging-induced rate of change of  $\vec{\sigma}$  at  $\mathcal{P}'$ , as measured using inertial-direction standards at  $\mathcal{P}$ , is  $\nabla_{\vec{u}} \nabla_{\vec{\xi}} \vec{\sigma}$ . We can write this as

$$\nabla_{\vec{u}} \nabla_{\vec{\xi}} \vec{\sigma} = \nabla_{\vec{\xi}} \nabla_{\vec{u}} \vec{\sigma} + [\nabla_{\vec{u}}, \nabla_{\vec{\xi}}] \vec{\sigma} = \nabla_{\vec{\xi}} \nabla_{\vec{u}} \vec{\sigma} + \mathbf{R}(\_, \vec{\sigma}, \vec{u}, \vec{\xi}), \quad (7.25)$$

where  $R$  is the Riemann tensor and we have used the fact that  $[\vec{u}, \vec{\xi}] = 0$ ; cf. Eqs. (11.8) and (11.9) of MTW [14].

Evaluating the first term  $\nabla_{\vec{\xi}} \nabla_{\vec{u}} \vec{\sigma}$  using the Fermi-Walker transport law [the third of Eqs. (7.24)] and the fact that the observers are momentarily at rest with respect to each other [the third of Eqs. (7.21)], we bring Eq. (7.25) into the form

$$\nabla_{\vec{u}} \nabla_{\vec{\xi}} \vec{\sigma} = R(\_, \vec{\sigma}, \vec{u}, \vec{\xi}) + \vec{u} \nabla_{\vec{\xi}} (\vec{a} \cdot \vec{\sigma}) . \quad (7.26)$$

We are only interested in the spatial part of this rate of change, so we can ignore the second term on the right side of the equation. We switch to the three-dimensional viewpoint of the observer at  $\mathcal{P}$  (where our calculation is being done) and we denote the spatial part of  $\nabla_{\vec{u}} \nabla_{\vec{\xi}} \vec{\sigma}$  by  $\dot{\sigma}$ :

$$\dot{\sigma} \equiv \left[ \nabla_{\vec{u}} \nabla_{\vec{\xi}} \vec{\sigma} \right]_{\text{project orthogonal to } \vec{u}} . \quad (7.27)$$

Equation (7.26) tells us that this rate of change is not only orthogonal to  $\vec{u}$  (spatial) but also orthogonal to  $\sigma$ ; it therefore can be written as a rotation

$$\dot{\sigma} = \Delta \Omega \times \sigma . \quad (7.28)$$

Here  $\Delta \Omega$  is the frame-dragging angular velocity at  $\mathcal{P}'$  as measured using inertial standards at  $\mathcal{P}$ . We can solve for this angular velocity  $\Delta \Omega$  by crossing  $\sigma$  into Eq. (7.28) and using  $\sigma \cdot \sigma = 1$ :

$$\Delta \Omega = \sigma \times \dot{\sigma} . \quad (7.29)$$

Inserting expression (7.26) for  $\dot{\sigma}$  and switching to index notation, we obtain

$$\Delta \Omega_i = \epsilon_{ijk} \sigma^j R^k_{\hat{p}0q} \sigma^p \xi^q . \quad (7.30)$$

Rewriting the Riemann tensor component in terms of the gravitomagnetic part of the Weyl tensor (in vacuum),  $R^k_{\hat{p}0q} = -\epsilon^k_{ps} \mathcal{B}^s_q$ , performing some tensor manipulations, and noticing that because  $\Delta \Omega$  is crossed into  $\sigma$  when computing the precession any piece of  $\Delta \Omega$  along  $\sigma$  is irrelevant, we obtain

$$\Delta \Omega_i = \mathcal{B}_{ij} \xi^j , \quad \text{i.e.} \quad \Delta \Omega = \mathcal{B}(\_, \xi) . \quad (7.31)$$

Put in words: *in vacuum the frame-dragging angular velocity at  $\mathcal{P}'$ , as measured using inertial directions at the adjacent event  $\mathcal{P}$ , is obtained by inserting the vector  $\xi$  (which reaches from  $\mathcal{P}$  to  $\mathcal{P}'$ ) into one slot of the gravitomagnetic part of the Weyl tensor.*

Because of the role of  $\mathcal{B}_{ij}$  in this equation of differential frame dragging, we call  $\mathcal{B}_{ij}$  the frame-drag

field.

## 7.4 Our New Tools: Tendex and Vortex Lines; Their Tendicities and Vorticities; Tendexes and Vortexes

### 7.4.1 Tendex Lines and Their Tendicities; Vortex Lines and Their Vorticities

As symmetric, trace-free tensors, the tidal field  $\mathcal{E}$  and frame-drag field  $\mathcal{B}$  can each be characterized completely by their three principal axes (eigendirections) and their three associated eigenvalues.

If  $\mathbf{p}$  is a (smoothly changing) unit eigenvector of the tidal field  $\mathcal{E}$  (or of the frame-drag field  $\mathcal{B}$ ), then the integral curves of  $\mathbf{p}$  can be regarded as “field lines” associated with  $\mathcal{E}$  (or  $\mathcal{B}$ ). For  $\mathcal{E}$  we call these integral curves *tidal tendex lines*, or simply *tendex lines*<sup>3</sup>, because  $\mathcal{E}$  tidally stretches objects it encounters, and the Latin word *tendere* means “to stretch.” For  $\mathcal{B}$  we call the integral curves *frame-drag vortex lines*, or simply *vortex lines*, because  $\mathcal{B}$  rotates gyroscopes, and the Latin word *vertere* means “to rotate.” At each point  $\mathcal{P}$  in space there are three orthogonal eigendirections of  $\mathcal{E}$  (and three of  $\mathcal{B}$ ), so through each point there passes three orthogonal tendex lines and three orthogonal vortex lines.

Outside a spherically symmetric gravitating body with mass  $M$ , such as the Earth or a Schwarzschild black hole, the tidal field, in a spherical polar orthonormal basis, has components

$$\mathcal{E}_{\hat{r}\hat{r}} = -\frac{2M}{r^3}, \quad \mathcal{E}_{\hat{\theta}\hat{\theta}} = \mathcal{E}_{\hat{\phi}\hat{\phi}} = +\frac{M}{r^3} \quad (7.32)$$

(e.g. Section 1.6 and Eq. (31.4) of [14]). The tidal-acceleration equation  $\Delta a^j = -\mathcal{E}^j_k \xi^k$  tells us that this tidal field stretches objects radially and squeezes them equally strongly in all tangential directions (see the people in Figure 7.2). Correspondingly, one eigenvector of  $\mathcal{E}$  is radial, and the other two are tangential with degenerate eigenvalues. This means that one set of tendex lines is radial (the red tendex lines in Figure 7.2), and any curve lying on a sphere around the body is a tendex line. If we break the tangential degeneracy by picking our tangential unit eigenvectors to be the basis vectors  $\mathbf{e}_{\hat{\theta}}$  and  $\mathbf{e}_{\hat{\phi}}$  of a spherical polar coordinate system, then the tangential tendex lines are those vectors’ integral curves — the blue curves in Figure 7.2.

When the spherical body is weakly gravitating and is set rotating slowly, then it acquires a nonzero frame-drag field given by Eqs. (7.43) below. The corresponding vortex lines are shown in Figure 7.3. (See Section 7.5.1 below for details.)

To any tendex (or vortex) line, with unit eigenvector  $\mathbf{p}$ , there is associated an eigenvalue  $\mathcal{E}_{pp} =$

---

<sup>3</sup>The word tendex was coined by David Nichols.

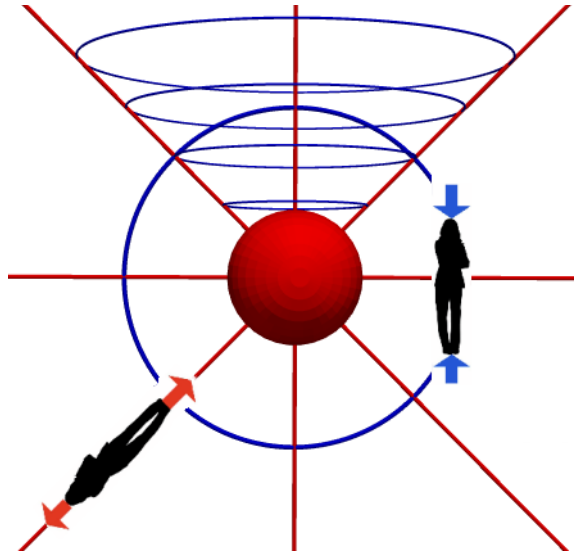


Figure 7.2: Tendex lines outside a spherically symmetric, gravitating body. The lines are colored by the sign of their tendicity: red lines have negative tendicity (they stretch a person oriented along them); blue lines have positive tendicity (they squeeze).

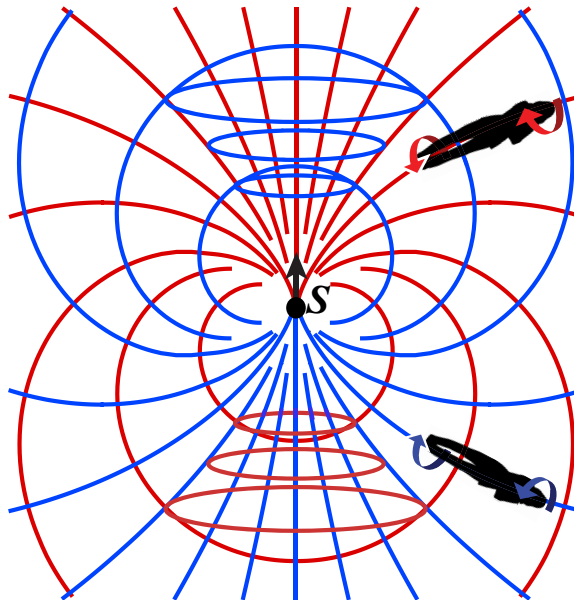


Figure 7.3: Vortex lines outside a slowly spinning, spherically symmetric, gravitating body with spin angular momentum  $\mathcal{S}$ . The lines are colored by the sign of their vorticity: red lines have negative vorticity (they produce a counterclockwise differential precession of gyroscopes); blue lines have positive vorticity (clockwise differential precession).

$\mathcal{E}_{jk}p^j p^k$  which is called the line's *tendicity* (or  $\mathcal{B}_{pp} = \mathcal{B}_{jk}p^j p^k$  which is called the line's *vorticity*). The physical meaning of this tendicity (or vorticity) can be read off the tidal-acceleration equation (7.23) [or the equation of differential frame dragging (7.31)]. Specifically, if a person's body (with length  $\ell$ ) is oriented along a tidal tendex line (Figure 7.2), she feels a head-to-foot stretching acceleration  $\Delta a = -\mathcal{E}_{pp}\ell$ . If the line's tendicity  $\mathcal{E}_{pp}$  is negative (red tendex line), her body gets stretched; if the tendicity is positive (blue tendex line), she gets compressed.

If her body is oriented along a vortex line (Figure 7.3), then a gyroscope at her feet precesses around the vortex line with an angular speed, relative to inertial frames at her head, given by  $\Delta\Omega = \mathcal{B}_{pp}\ell$ . If the line's vorticity is negative (red vortex lines in Figure 7.3), then the gyroscope at her feet precesses counterclockwise relative to inertial frames at her head, and (because  $\mathcal{B}_{pp}$  is unchanged when one reverses the direction  $\mathbf{p}$ ), a gyroscope at her head precesses counterclockwise relative to inertial frames at her feet. Correspondingly, we call the (red) vortex line a *counterclockwise vortex line*. If the line's vorticity is positive (blue vortex lines in Figure 7.3), the precessions are clockwise and the vortex line is said to be clockwise.

For any spacetime, the tendex lines color coded by their tendicities (e.g. Figure 7.2) and the vortex lines color coded by their vorticities (e.g. Figure 7.3) depict visually all details of the Weyl curvature tensor.

Since  $\mathcal{E}$  and  $\mathcal{B}$  are trace-free, at any point in space the sum of the three tendex lines' tendicities vanishes, and the sum of the three vorticities vanishes. Because  $\mathcal{E}$  and  $\mathcal{B}$  are also symmetric, each is characterized by five numbers at any point in space. The direction of one tendex line fixes two numbers and its tendicity fixes a third, leaving only two numbers to be specified. The direction of a second tendex line, in the plane orthogonal to the first, fixes a fourth number and the second line's tendicity fixes the fifth and final number — leaving the last line's direction and tendicity fully determined. Similarly, this is the case for vortex lines and their vorticities.

### 7.4.2 Vortexes and Tendexes

We give the name *frame-drag vortex*, or simply *vortex*, to a bundle of vortex lines with large vorticity. In Figure 7.3, the red vortex lines near the north polar axis, which are enclosed by blue circles, constitute a negative-vorticity (counterclockwise) vortex; the blue vortex lines near the south polar axis, which are enclosed by red circles, constitute a positive-vorticity (clockwise) vortex. These two vortexes emerge from the north and south poles of the spinning point particle.

Similarly, we give the name *tidal tendex*, or simply *tendex*, to a strong concentration of tendex lines. We shall meet our first example at the end of Section 7.5.4 below.

## 7.5 Weak-gravity, Stationary Systems

### 7.5.1 One Stationary, Weakly Gravitating, Spinning Body

When gravity is weak and slowly changing (e.g., outside a slowly precessing, spinning, weakly gravitating body such as the Earth), one can write the spacetime metric in the form

$$ds^2 = -\alpha^2 dt^2 + \delta_{jk}(dx^j + \beta^j dt)(dx^k + \beta^k dt) \quad (7.33a)$$

(e.g. Section 23.9.3 of [37]; or Chap. 10 of MTW [14] with the spatial coordinates changed slightly).

Here

$$\alpha^2 = \left(1 - \frac{2M}{r}\right), \quad \boldsymbol{\beta} = -\frac{2\mathbf{S}}{r^2} \times \mathbf{n}, \quad (7.33b)$$

are the squared lapse function and the shift function,  $M$  is the body's mass,  $\mathbf{S}$  is its spin angular momentum, and

$$r = \sqrt{x^2 + y^2 + z^2}, \quad \mathbf{n} = \mathbf{e}_r \quad (7.33c)$$

are the radius and the unit radial vector, with  $\{x^1, x^2, x^3\} = \{x, y, z\}$ . In spherical polar coordinates (associated with the Cartesian coordinates  $\{x, y, z\}$  in the usual way), the metric (7.33a) becomes

$$\begin{aligned} ds^2 &= -\alpha^2 dt^2 + dr^2 + r^2 d\theta^2 + r^2 \sin^2 \theta (d\phi - \omega dt)^2, \\ \omega &= 2S/r^3. \end{aligned} \quad (7.33d)$$

It is conventional to rewrite general relativity, in this weak-field, slow-motion situation, as a field theory in flat spacetime. In this language, the geodesic equation for a test particle takes the form

$$\frac{d^2 \mathbf{x}}{dt^2} = \mathbf{g} + \mathbf{v} \times \mathbf{H}, \quad (7.34)$$

which resembles the Lorentz force law in electromagnetic theory; see, e.g., [38] and references therein, especially [39]. Here  $\mathbf{v} = d\mathbf{x}/dt$  is the particle's velocity [Cartesian components  $(dx/dt, dy/dt, dz/dt)$ ] and

$$\begin{aligned} \mathbf{g} &= -\frac{1}{2} \nabla \alpha^2 = -\frac{M}{r^2} \mathbf{n}, \\ \mathbf{H} &= \nabla \times \boldsymbol{\beta} = 2 \left[ \frac{\mathbf{S} - 3(\mathbf{S} \cdot \mathbf{n})\mathbf{n}}{r^3} \right] \end{aligned} \quad (7.35)$$

are the body's *gravitoelectric field* (same as Newtonian gravitational acceleration) and its *gravitomagnetic field*. Note that these fields have the same monopole and dipole structures as the electric and magnetic fields of a spinning, charged particle.

In this paper we shall adopt an alternative to this “gravito-electromagnetic” viewpoint. For the

gravitational influence of the mass  $M$ , we shall return to the Newtonian viewpoint of a gravitational acceleration  $\mathbf{g}$  and its gradient, the tidal gravitational field (the electric part of the Weyl tensor)

$$\mathcal{E} = -\nabla\mathbf{g}, \quad \text{i.e., } \mathcal{E}_{ij} = -g_{i,j} = \Phi_{,ij} = \frac{1}{2}\alpha^2_{,ij}. \quad (7.36)$$

Here the comma denotes partial derivative (actually, the gradient in our Cartesian coordinate system) and  $\Phi$  is the Newtonian gravitational potential, which is related to the lapse function by  $\alpha^2 = 1 + 2\Phi$  in the Newtonian limit. The components of this tidal field in the spherical coordinates' orthonormal basis  $\mathbf{e}_{\hat{r}} = \partial/\partial r$ ,  $\mathbf{e}_{\hat{\theta}} = (1/r)\partial/\partial\theta$ ,  $\mathbf{e}_{\hat{\phi}} = (1/r \sin\theta)\partial/\partial\phi$  are easily seen to be

$$\mathcal{E}_{\hat{r}\hat{r}} = -\frac{2M}{r^3}, \quad \mathcal{E}_{\hat{\theta}\hat{\theta}} = \mathcal{E}_{\hat{\phi}\hat{\phi}} = +\frac{M}{r^3}, \quad (7.37)$$

[Eqs. (7.32) above], which are symmetric and trace-free as expected. The field lines associated with this tidal field are easily seen to be those depicted in Figure 7.2 above.

For the effects of the spin angular momentum, we shall think of the spinning body as “dragging space into motion” with a velocity and angular velocity (relative to our Cartesian coordinates) given by

$$\frac{d\mathbf{x}_{\text{space}}}{dt} \equiv \mathbf{v}_{\text{space}} = -\boldsymbol{\beta} = \frac{2\mathbf{S}}{r^2} \times \mathbf{n}, \quad \frac{d\phi_{\text{space}}}{dt} = \omega = \frac{2S}{r^3} \quad (7.38)$$

[cf. the  $\delta_{jk}(dx^j + \beta^j dt)(dx^k + \beta^k dt)$  term in the metric (7.33a) and the  $(d\phi - \omega dt)^2$  term in the metric (7.33d)]. Just as the vorticity  $\nabla \times \mathbf{v}$  of a nonrelativistic fluid with velocity field  $\mathbf{v}(\mathbf{x})$  is twice the angular velocity  $\boldsymbol{\Omega}$  of rotation of a fluid element relative to an inertial reference frame, so the vorticity associated with the “space motion,”  $\nabla \times \mathbf{v}_{\text{space}}$ , turns out to be twice the vectorial angular velocity of an inertial-guidance gyroscope relative to inertial reference frames far from the body (“at infinity”) — or equivalently, relative to our spatial Cartesian coordinates  $\{x, y, z\}$ , which are locked to inertial frames at infinity. In formulas: Let  $\boldsymbol{\sigma}$  be a unit vector along the spin angular momentum vector of an inertial-guidance gyroscope. Viewed as a vector in our Cartesian basis, it precesses

$$\frac{d\boldsymbol{\sigma}}{dt} = \boldsymbol{\Omega}_{\text{fd}} \times \boldsymbol{\sigma}, \quad (7.39)$$

with a *frame-dragging vectorial angular velocity* equal to half the vorticity of space viewed as a fluid:

$$\boldsymbol{\Omega}_{\text{fd}} = \frac{1}{2}\nabla \times \mathbf{v}_{\text{space}} = -\frac{1}{2}\nabla \times \boldsymbol{\beta} = -\frac{1}{2}\mathbf{H} = -\left[\frac{\mathbf{S} - 3(\mathbf{S}\cdot\mathbf{n})\mathbf{n}}{r^3}\right]; \quad (7.40)$$

see e.g. Eq. (25.14) of [37], or Eq. (40.37) of [14]. This dipolar frame-dragging angular velocity is shown in Figure 7.4.

For dynamical black holes and other strong-gravity, dynamical situations, it is not possible to measure gyroscopic precession with respect to inertial frames at infinity, since there is no unambigu-

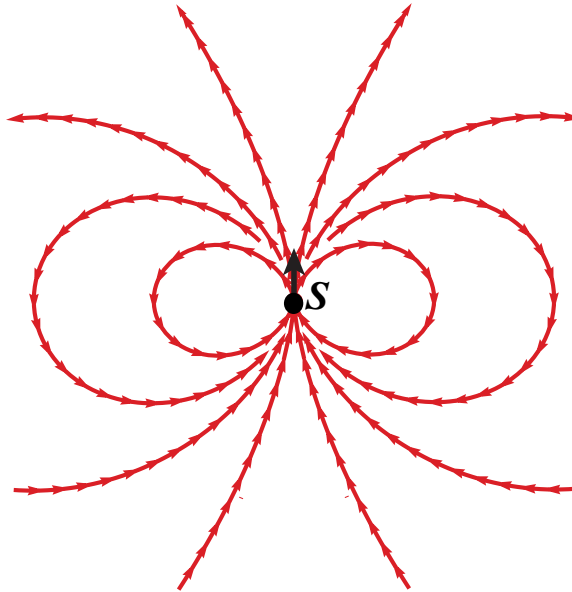


Figure 7.4: For a weakly gravitating, slowly rotating body with spin angular momentum  $\mathbf{S}$ , the dipolar frame-dragging angular velocity relative to inertial frames at infinity,  $\boldsymbol{\Omega}_{\text{fd}}$ . The arrows are all drawn with the same length rather than proportional to the magnitude of  $\boldsymbol{\Omega}_{\text{fd}}$ .

ous way to compare vectors at widely separated events.<sup>4</sup>

On the other hand, we *can*, in general, measure the precession of inertial-guidance gyroscopes at one event, with respect to inertial frames at a neighboring event — i.e., we can measure *differential frame dragging* as embodied in the frame-drag field (magnetic part of the Weyl tensor)  $\mathcal{B}_{ij}$ . In our weak-gravity, slow-motion situation, this frame-drag field is equal to the gradient of  $\boldsymbol{\Omega}_{\text{fd}}$  (Eq. (5.45b) of [42]):

$$\mathcal{B} = \nabla \boldsymbol{\Omega}_{\text{fd}}, \quad \text{i.e. } \mathcal{B}_{jk} = \Omega_{\text{fd},j,k}. \quad (7.41)$$

For our weakly gravitating, spinning body,  $\boldsymbol{\Omega}_{\text{fd}}$  has the dipolar form (7.40), so the frame-drag field is

$$\mathcal{B}_{jk} = \frac{3}{r^4} [2S_{(j}n_{k)} + (\mathbf{S} \cdot \mathbf{n})(\delta_{jk} - 5n_j n_k)]. \quad (7.42)$$

Here the parentheses on the subscripts indicate symmetrization. In spherical polar coordinates, the components of this frame-drag field are

$$\mathcal{B}_{\hat{r}\hat{r}} = -2\mathcal{B}_{\hat{\theta}\hat{\theta}} = -2\mathcal{B}_{\hat{\phi}\hat{\phi}} = -\frac{6S \cos \theta}{r^4}, \quad \mathcal{B}_{\hat{r}\hat{\theta}} = \mathcal{B}_{\hat{\theta}\hat{r}} = -\frac{3S \sin \theta}{r^4}. \quad (7.43)$$

For this (and any other axially symmetric) frame-drag field, one of the three sets of vortex lines

<sup>4</sup>There is an exception: One can introduce additional geometric structure, e.g. an auxiliary flat spacetime, that provides a way of carrying a reference frame inward from infinity to all other locations and thereby compare vectors at different events. Some of us have used this approach to localize linear momentum in the gravitational field around black holes [40, 41]. However, the auxiliary structure has great arbitrariness, and for the vortex and tendex concepts of this paper there is no need for such auxiliary structure, so we eschew it.

is along the  $\phi$  direction (i.e. the  $\mathbf{S} \times \mathbf{x}$  direction)—i.e., it is *axial*—and the other two are *poloidal*. By computing the eigenvectors of the tensor (7.42) and then drawing the curves to which they are tangent, one can show that the body’s vortex lines have the forms shown in Figure 7.3.

Notice that the poloidal, negative-vorticity vortex lines (the poloidal red curves in Figure 7.3) all emerge from the north polar region of the spinning body, encircle the body, and return back to the north polar region.

Why do these have negative rather than positive vorticity? Choose the eigendirection  $\mathbf{p}$  at the body’s north pole to point away from the body. The body drags inertial frames in a right-handed manner (counterclockwise as seen looking down on the north pole), and the frame dragging is stronger at the tail of  $\mathbf{p}$  (nearer the body) than at the tip, so the frame-dragging angular velocity decreases from tail to tip, which means it is more left-handed (clockwise) at the tip than the tail; it has negative vorticity.

The poloidal, positive-vorticity vortex lines (the poloidal blue curves in Figure 7.3) all emerge from the body’s south polar region, swing around the body, and return to the south polar region.

The azimuthal vortex lines have negative vorticity above the hole’s equatorial plane (blue azimuthal circles) and positive vorticity below the hole’s equatorial plane (red azimuthal circles).

## 7.5.2 Two Stationary, Weakly Gravitating, Spinning Point Particles with Opposite Spins

Consider, next, two weakly gravitating, spinning point particles with opposite spins, sitting side by side. Place the particles (named  $A$  and  $B$ ) on the  $x$  axis, at locations  $\{x_A, y_A, z_A\} = \{+a, 0, 0\}$ ,  $\{x_B, y_B, z_B\} = \{-a, 0, 0\}$  and give them vectorial spins  $\mathbf{S}_A = S\mathbf{e}_z$ ,  $\mathbf{S}_B = -S\mathbf{e}_z$ . Then the frame-drag angular velocity relative to inertial frames at infinity is

$$\boldsymbol{\Omega}_{\text{fd}} = -\frac{\mathbf{S}_A - 3(\mathbf{S}_A \cdot \mathbf{n}_A)\mathbf{n}_A}{r_A^3} - \frac{\mathbf{S}_B - 3(\mathbf{S}_B \cdot \mathbf{n}_B)\mathbf{n}_B}{r_B^3}, \quad (7.44)$$

where  $r_A = |\mathbf{x} - \mathbf{x}_A|$  and  $r_B = |\mathbf{x} - \mathbf{x}_B|$  are the distances to the particles and  $\mathbf{n}_A = (\mathbf{x} - \mathbf{x}_A)/r_A$  and  $\mathbf{n}_B = (\mathbf{x} - \mathbf{x}_B)/r_B$  are unit vectors pointing from the particles’ locations to the field point; cf. Eq. (7.40). This vector field is plotted in Figure 7.5(a). It has just the form one might expect from the one-spin field of Figure 7.4.

For these two spinning particles, the frame-drag field (gradient of Eq. (7.44)) is

$$\mathcal{B}_{jk} = \frac{3}{r_A^4} \left[ 2S_A^{(j} n_A^{k)} + (\mathbf{S}_A \cdot \mathbf{n}_A)(\delta^{jk} - 5n_A^j n_A^k) \right] + \frac{3}{r_B^4} \left[ 2S_B^{(j} n_B^{k)} + (\mathbf{S}_B \cdot \mathbf{n}_B)(\delta^{jk} - 5n_B^j n_B^k) \right] \quad (7.45)$$

[cf. Eq. (7.42)], where we have moved the vector and tensor indexes up for simplicity of notation.

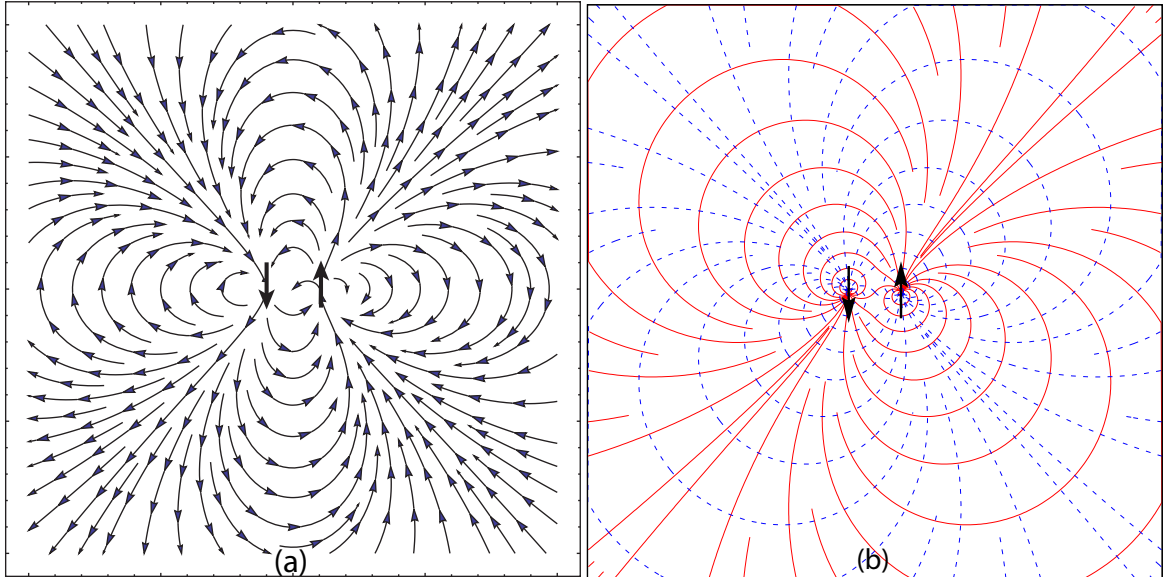


Figure 7.5: For two stationary point particles sitting side-by-side with their spins in opposite directions (thick black arrows), two types of streamlines in the plane of reflection symmetry formed by the particles' spins and their separation vector. (a) The frame-dragging angular velocity  $\mathbf{\Omega}_{\text{fd}}$  and its streamlines, with the arrows all drawn at the same length rather than proportional to the magnitude of  $\mathbf{\Omega}_{\text{fd}}$ . (b): The two sets of vortex lines of the frame-drag field  $\mathbf{B}$ . The negative-vorticity vortex lines are solid and colored red, and the positive-vorticity ones are dashed and blue. In this figure, as in preceding figures, the colors are not weighted by the lines' vorticities, but only by the signs of the vorticities.

(In our Cartesian basis, there is no difference between up and down indexes.)

The best two-dimensional surface on which to visualize vortex lines of this  $\mathbf{B}$  is the  $x$ - $z$  plane (the plane formed by the particles' spins and their separation vector). The system is reflection symmetric through this plane. On this plane, one of the principal directions of  $\mathbf{B}$  is orthogonal to it (in the  $y$  direction); the other two lie in the plane and are tangent to the in-plane vortex lines. By computing the eigendirections of  $\mathbf{B}$  [i.e., of the tensor (7.45)] and mapping out their tangent vortex lines, and checking the sign of  $\mathcal{B}_{pp}$  along their tangent directions  $\mathbf{p}$ , we obtain Figure 7.5.

Note that, as for a single spinning particle (Figure 7.3), so also here for two spins, the negative-vorticity vortex lines (solid red curves) emerge from the tips of the spins and the positive-vorticity vortex lines (dashed blue curves) emerge from their tails. For a single spin, the negative-vorticity vortex lines emerge from the tip, travel around the body, and return to the same tip. Here, the lines close to each spinning body leave and enter the same body's tip, but the majority emerge from one body's tip, travel around that body and enter the other body's tip. Similarly the positive-vorticity vortex lines (dashed and blue) emerge from one body's tail, travel around that body, and enter the other body's tail (aside from the lines near each body that exit and return to the same body's tail).

The collection of solid red vortex lines near each arrow tip in Figure 7.5(b) constitutes a negative-vorticity frame-drag vortex, and the collection of dashed blue vortex lines near each arrow tail is a

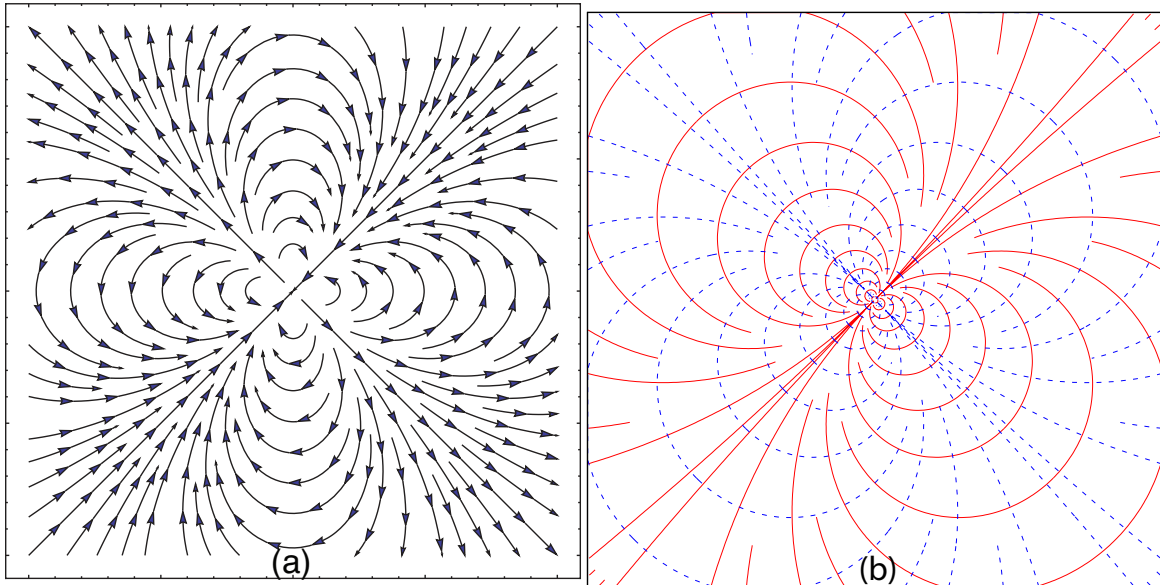


Figure 7.6: Current-quadrupolar streamlines associated with the two stationary spinning particles of Figure 7.5, for which the current-quadrupole moment has nonzero components  $\mathcal{S}_{xz} = \mathcal{S}_{zx} = Sa$ . (a) The frame-dragging angular velocity  $\boldsymbol{\Omega}_{\text{fd}}$  and its streamlines, and (b) the two sets of vortex lines, in the  $x$ - $z$  plane. Figure (b) also describes the tendex lines for a static mass-quadrupolar particle whose only nonzero quadrupole-moment components are  $\mathcal{I}_{xz} = \mathcal{I}_{zx}$ .

positive-vorticity vortex.

### 7.5.3 The Two Spinning Particles Viewed from Afar: Stationary, Quadrupolar Frame-Drag Field

When viewed from afar, the two spinning bodies produce a current-quadrupole gravitational field with quadrupole moment (e.g. Eq. (5.28b) of [36])

$$\mathcal{S}_{pq} = \left( \int j_p x_q d^3x \right)^{\text{STF}} = (S_p a_q + (-S_p)(-a_q))^{\text{STF}} = S_p a_q + S_q a_p - \frac{2}{3}(\mathbf{S} \cdot \mathbf{a})\delta_{pq}. \quad (7.46)$$

Here  $j_p = S_p \delta(\mathbf{x} - \mathbf{a}) - S_p \delta(\mathbf{x} + \mathbf{a})$  is the angular momentum density. Since the only nonzero components of  $\mathbf{S}$  and  $\mathbf{a}$  are  $S_z = S$  and  $a_x = a$ , the only nonzero components of the current-quadrupole moment are

$$\mathcal{S}_{xz} = \mathcal{S}_{zx} = Sa. \quad (7.47)$$

The frame-drag-induced velocity of space (negative of the shift function) for this current quadrupole, and the frame-drag angular velocity and frame-drag tensor field are

$$\mathbf{v}_{\text{space}} = -\boldsymbol{\beta} = \frac{4\mathbf{n} \times \mathbf{S} \cdot \mathbf{n}}{r^3}, \quad \boldsymbol{\Omega}_{\text{fd}} = \frac{1}{2}\boldsymbol{\nabla} \times \mathbf{v}_{\text{space}}, \quad \mathcal{B} = \boldsymbol{\nabla}\boldsymbol{\Omega}_{\text{fd}}, \quad (7.48)$$

[e.g. Eq. (10.6b) of [36]; also Eqs. (7.40) and (7.41) above]. Inserting Eq. (7.47) for the quadrupole moment into Eqs. (7.48), and plotting  $\mathbf{\Omega}_{\text{fd}}$  and the vortex lines of  $\mathbf{B}$  in the  $x$ - $z$  plane, we obtain the graphs shown in Figure 7.6.

Notice that the current-quadrupolar frame-drag angular velocity in Figure 7.6(a) is, indeed, the same as that for two oppositely directed spins [Figure 7.5(a)] in the limit that the spins' separation goes to zero—i.e., as seen from afar—and the current-quadrupolar vortex lines of the frame-drag tensor field [Figure 7.6(b)] is the vanishing-separation limit of that for the two oppositely directed spins (Figure 7.5b).

Here, as for finitely separated spinning particles, there are two red frame-drag vortexes, one emerging from the origin in the upper right direction, the other in the lower-left direction; and similarly, there are two blue frame-drag vortexes, one emerging in the upper left direction and the other in the lower right direction.

#### 7.5.4 Static, Quadrupolar Tidal Field and its Tendex Lines and Tendexes

For an idealized static particle with time-independent mass-quadrupole moment  $\mathcal{I}_{pq}$  and all other moments (including the mass) vanishing, the squared lapse function is  $\alpha^2 = 1 + 2\Phi = 1 - (\mathcal{I}_{pq}/r)_{,pq}$  [36], where  $\Phi$  is the Newtonian gravitational potential. Therefore, the particle's tidal field  $\mathcal{E}_{jk} = \Phi_{,jk}$  [Eq. (7.40)] is

$$\mathcal{E}_{jk} = -\frac{1}{2} \left( \frac{\mathcal{I}_{pq}}{r} \right)_{,pqjk} . \quad (7.49)$$

For comparison, for a particle with time-independent current-quadrupole moment  $\mathcal{S}_{pq}$ , the shift function is  $\beta_j = (-4/3)\epsilon_{j pq}(\mathcal{S}_{pk}/r)_{,kq}$ , which implies that the frame-drag field is [Eqs. (7.48)]

$$\mathcal{B}_{jk} = -\frac{2}{3} \left( \frac{\mathcal{S}_{pq}}{r} \right)_{,pqjk} . \quad (7.50)$$

Notice that, once the differing normalization conventions (7.20) are accounted for, Eqs. (7.49) and (7.50) are the same, as required by the duality relations (7.16) and (7.20). This means that, for a static current quadrupole whose only nonzero components are  $\mathcal{I}_{xz} = \mathcal{I}_{zx}$ , the tendex lines will have precisely the same forms as the vortex lines of the static current quadrupole (7.47); i.e., they will have the forms shown in Figure 7.6b. In this case there are two negative-tendicity (solid red) tidal tendexes, one emerging from the origin in the upper right direction, and the other in the lower-left direction; and there are two positive-tendicity (dashed blue) tidal tendexes, one emerging in the upper left direction and the other in the lower right direction.

## 7.6 Gravitational Waves and their Generation

We turn now to dynamical situations, which we describe using linearized gravity. We first discuss the tendex and vortex structure of plane gravitational waves. We then examine wave generation by time-varying multipolar fields, and the accompanying tendex and vortex structures of these systems.

### 7.6.1 Plane Gravitational Wave

In this section, we will describe the features of  $\mathcal{E}$  and  $\mathcal{B}$  for plane gravitational waves, and connect our observations to the linearized-gravity and Newman-Penrose (NP) formalisms. In Appendix 7.A we review the Newman-Penrose formalism and its connection to the spatial tensors  $\mathcal{E}$  and  $\mathcal{B}$ .

Consider gravitational-wave propagation in an asymptotically flat spacetime, in transverse-traceless (TT) gauge. Near future null infinity,  $\mathcal{I}^+$ , we can linearize around a Minkowski background and obtain

$$\mathcal{E}_{ij} = -\frac{1}{2}\partial_0^2 h_{ij}, \quad \mathcal{B}_{ij} = -\frac{1}{2}\epsilon_i^{pq} n_p \partial_0^2 h_{qj}. \quad (7.51)$$

It is convenient to expand these expressions in terms of the two gravitational-wave polarization tensors,  $e_{ij}^+$  and  $e_{ij}^\times$ ,

$$\mathcal{E}_{ij} = -\frac{1}{2}(\ddot{h}_+ e_{ij}^+ + \ddot{h}_\times e_{ij}^\times), \quad \mathcal{B}_{ij} = -\frac{1}{2}(\ddot{h}_+ e_{ij}^\times - \ddot{h}_\times e_{ij}^+), \quad (7.52)$$

where  $e_{ij}^+$  and  $e_{ij}^\times$  are symmetric, trace-free, and orthogonal to the waves' propagation direction. Letting the unit-norm vector  $\mathbf{e}_1$  denote the direction of propagation of the gravitational wave, then one can expand the polarization tensors in terms of the remaining two vectors of an orthonormal triad,  $\mathbf{e}_2$  and  $\mathbf{e}_3$ , as

$$\mathbf{e}_+ = \mathbf{e}_2 \otimes \mathbf{e}_2 - \mathbf{e}_3 \otimes \mathbf{e}_3, \quad (7.53)$$

$$\mathbf{e}_\times = \mathbf{e}_2 \otimes \mathbf{e}_3 + \mathbf{e}_3 \otimes \mathbf{e}_2. \quad (7.54)$$

Consider first a + polarized wave. We have that

$$\mathcal{E} = -\frac{1}{2}\ddot{h}_+ \mathbf{e}^+ = \frac{1}{2}[(-\ddot{h}_+) \mathbf{e}_2 \otimes \mathbf{e}_2 + \ddot{h}_+ \mathbf{e}_3 \otimes \mathbf{e}_3], \quad (7.55)$$

so we see that  $\mp \ddot{h}_+/2$  are the two eigenvalues of  $\mathcal{E}$  (the two tendicities), and  $\mathbf{e}_2$  and  $\mathbf{e}_3$  are the two corresponding eigenvectors. Now, define a second basis locally rotated at each point by  $\pi/4 = 45^\circ$ ,

$$\begin{pmatrix} \tilde{\mathbf{e}}_2 \\ \tilde{\mathbf{e}}_3 \end{pmatrix} = \begin{pmatrix} \cos \frac{\pi}{4} & \sin \frac{\pi}{4} \\ -\sin \frac{\pi}{4} & \cos \frac{\pi}{4} \end{pmatrix} \begin{pmatrix} \mathbf{e}_2 \\ \mathbf{e}_3 \end{pmatrix}. \quad (7.56)$$

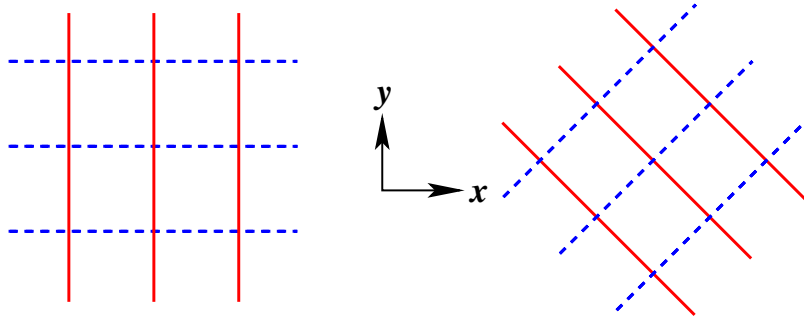


Figure 7.7: The tendex lines (left) and vortex lines (right) of a plane gravitational wave propagating in the  $z$  direction (out of the picture). The tendex lines are lines of constant  $x$  and  $y$ , and the vortex lines are rotated by  $\pi/4$  (lines of constant  $x \pm y$ ). The blue (dashed) curves correspond to positive tendicity and vorticity (squeezing and clockwise differential precession, respectively) and the red (solid) curves denote negative tendicity and vorticity (stretching and counterclockwise precession). The tendicity (vorticity) is constant along a tendex line (vortex line), and the tendicity (vorticity) of a red line is equal in magnitude but opposite in sign to that of a blue (dashed) line.

Then, a simple calculation shows that

$$\mathbf{e}_\times = \tilde{\mathbf{e}}_2 \otimes \tilde{\mathbf{e}}_2 - \tilde{\mathbf{e}}_3 \otimes \tilde{\mathbf{e}}_3, \quad (7.57)$$

and one can immediately see that  $\mathcal{B}$  is diagonal in this new basis

$$\mathcal{B} = -\frac{1}{2}\ddot{h}_+ \mathbf{e}^\times = -\frac{1}{2}[\ddot{h}_+ \tilde{\mathbf{e}}_2 \otimes \tilde{\mathbf{e}}_2 - \ddot{h}_+ \tilde{\mathbf{e}}_3 \otimes \tilde{\mathbf{e}}_3]. \quad (7.58)$$

The eigenvalues of  $\mathcal{B}$  (the vorticities), like those of  $\mathcal{E}$  (the tendicities), are  $\mp \ddot{h}_+/2$ , but  $\mathcal{B}$ 's eigenvectors,  $\tilde{\mathbf{e}}_2$  and  $\tilde{\mathbf{e}}_3$ , are locally rotated by  $\pi/4$  compared to those of  $\mathcal{E}$ . Correspondingly, the vortex lines of  $h_+$  must be locally rotated by  $\pi/4$  with respect to the tendex lines.

The local rotation of the tendex and vortex lines is most transparent for a plane gravitational wave. In Figure 7.7, we show the tendex and vortex lines of a plane gravitational wave propagating out of the page (i.e.  $\mathbf{e}_1 = \mathbf{e}_z$  is the propagation direction). Because the eigenvectors of  $\mathcal{E}$  are  $\mathbf{e}_2 = \mathbf{e}_x$  and  $\mathbf{e}_3 = \mathbf{e}_y$ , the tendex lines are the lines of constant  $x$  and  $y$ , illustrated by red (solid) lines and blue (dashed) lines, respectively, on the left of Figure 7.7. Similarly, the vortex lines are lines of constant  $x \pm y$ , again drawn as blue (dashed) lines and red (solid) lines, respectively. The tendicity (vorticity) has constant magnitude along the lines, but the two sets of tendex (vortex) lines have opposite sign; consequently, the tidal (frame-drag) field produces a stretching (counterclockwise differential precession) along the solid red direction and a squeezing (clockwise differential precession) of the same magnitude along the dashed blue direction.

More generally, gravitational waves will contain both  $+$  and  $\times$  polarizations, and to study their vortex and tendex lines, it will be useful to express the electric and magnetic tensors in the spatial

orthonormal basis  $(\mathbf{e}_1, \mathbf{e}_2, \mathbf{e}_3)$ . They can be written conveniently as matrices:

$$\mathcal{E}_{\hat{a}\hat{b}} = \frac{1}{2} \left( \begin{array}{c|cc} 0 & 0 & 0 \\ \hline 0 & -\ddot{h}_+ & -\ddot{h}_\times \\ 0 & -\ddot{h}_\times & \ddot{h}_+ \end{array} \right), \quad \mathcal{B}_{\hat{a}\hat{b}} = \frac{1}{2} \left( \begin{array}{c|cc} 0 & 0 & 0 \\ \hline 0 & \ddot{h}_\times & -\ddot{h}_+ \\ 0 & -\ddot{h}_+ & -\ddot{h}_\times \end{array} \right). \quad (7.59)$$

It is useful to introduce an associated Newman-Penrose null tetrad consisting of two real null vectors,  $\vec{l}$  (along the waves' propagation direction) and  $\vec{n}$ , and a conjugate pair of complex null vectors  $\vec{m}$  and  $\vec{m}^*$  given by

$$\vec{l} = \frac{1}{\sqrt{2}}(\vec{e}_0 + \vec{e}_1), \quad \vec{n} = \frac{1}{\sqrt{2}}(\vec{e}_0 - \vec{e}_1), \quad \vec{m} = \frac{1}{\sqrt{2}}(\vec{e}_2 + i\vec{e}_3), \quad \vec{m}^* = \frac{1}{\sqrt{2}}(\vec{e}_2 - i\vec{e}_3) \quad (7.60)$$

[Eqs. (7.74) of Appendix 7.A]. For plane waves on a Minkowski background, the NP curvature scalar that characterizes the radiation is

$$\Psi_4 = C_{\mu\nu\rho\sigma} n^\mu m^{*\nu} n^\rho m^{*\sigma} = -\ddot{h}_+ + i\ddot{h}_\times, \quad (7.61)$$

so we can compactly rewrite Eqs. (7.59) as

$$\mathcal{E}_{\hat{a}\hat{b}} + i\mathcal{B}_{\hat{a}\hat{b}} = \frac{1}{2} \left( \begin{array}{c|cc} 0 & 0 & 0 \\ \hline 0 & \Psi_4 & i\Psi_4 \\ 0 & i\Psi_4 & -\Psi_4 \end{array} \right). \quad (7.62)$$

This expression holds for any plane gravitational wave propagating in the  $\vec{e}_1$  direction.

For any outgoing gravitational wave in an asymptotically flat space, as one approaches asymptotic null infinity the general expression (7.76) for  $\mathcal{E}_{\hat{a}\hat{b}} + i\mathcal{B}_{\hat{a}\hat{b}}$  reduces to expression (7.62), because all the curvature scalars except  $\Psi_4$  vanish due to the peeling property of the Weyl scalars near null infinity. Further discussion of the tidal and frame-drag fields of radiation near null infinity and their tenses and vortex lines is given in [28].

It is helpful to draw some simple analogies between gravitational and electromagnetic plane waves. For a generic mixture of + and  $\times$  polarizations, the magnitudes of the nonvanishing eigenvalues of both  $\mathcal{E}$  and  $\mathcal{B}$  are simply

$$\frac{1}{2}\sqrt{\ddot{h}_+^2 + \ddot{h}_\times^2} = \frac{1}{2}|\Psi_4|. \quad (7.63)$$

This mirrors plane waves in electromagnetism, where  $|\vec{E}| = |\vec{B}|$  is equal to the sum in quadrature of the magnitudes of the two polarizations. The absent longitudinal components in an electromagnetic plane wave correspond to the vanishing of the eigenvalues for the eigenvectors of  $\mathcal{E}$  and  $\mathcal{B}$  along

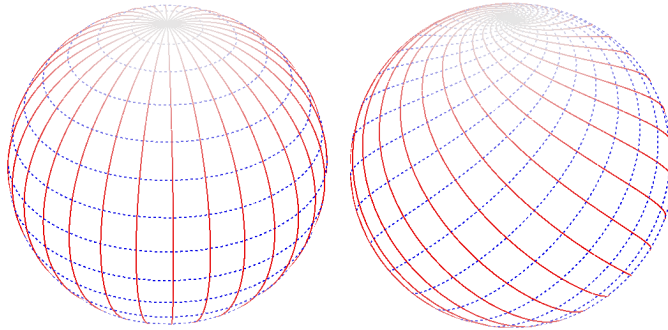


Figure 7.8: Tendex lines (left) and vortex lines (right) for the gravitational waves that would arise from the merger of equal-mass black holes falling together along the  $z$  axis. The positive tendicity and vorticity lines are shown in blue (dashed) and the negative lines are depicted in red (solid). Each line's intensity is proportional to its tendicity (or vorticity), which varies over the sphere as the dominant spin-weighted spherical harmonic,  ${}_{-2}Y_{2,0}(\theta, \phi) \propto \sin^2 \theta$ . Dark red and blue near the equator correspond to large-magnitude tendicity and vorticity, and light nearly white colors at the poles indicate that the tendicity and vorticity are small there.

the propagation direction. The orthogonality of the vectorial electromagnetic field strengths  $\vec{E} \perp \vec{B}$  becomes the  $\pi/4$  rotation between the meshes (Figure 7.7) formed by the two transverse eigenvectors of the tensorial quantities  $\mathcal{E}$  and  $\mathcal{B}$ .

### 7.6.2 Gravitational Waves from a Head-On Collision of Two Black Holes

As an example of the usefulness of this approach, we calculate the tendex and vortex lines at large radii for gravitational waves emitted by the head-on collision of two equal-mass nonspinning black holes. If the holes move along the  $z$  axis and we use as our spatial triad the unit vectors of spherical polar coordinates,  $(\mathbf{e}_1, \mathbf{e}_2, \mathbf{e}_3) = (\mathbf{e}_r, \mathbf{e}_\theta, \mathbf{e}_\phi) = (\partial_r, r^{-1}\partial_\theta, (r \sin \theta)^{-1}\partial_\phi)$ , and choose our null tetrad in the usual way (7.60), then we can apply the results described by Fiske et al. [43], namely, that  $\Re[\Psi_4]$  is axisymmetric [and, when decomposed into spin-weighted spherical harmonics, is dominated by the  $l = 2, m = 0$  harmonic,  ${}_{-2}Y_{2,0}(\theta, \phi)$ ] and that  $\Im[\Psi_4] = 0$ . Then the electric and magnetic parts of the Weyl tensor are given by

$$\mathcal{E}_{\hat{a}\hat{b}} = \frac{1}{2} \left( \begin{array}{c|cc} 0 & 0 & 0 \\ \hline 0 & \Re(\Psi_4) & 0 \\ 0 & 0 & -\Re(\Psi_4) \end{array} \right), \quad \mathcal{B}_{\hat{a}\hat{b}} = \frac{1}{2} \left( \begin{array}{c|cc} 0 & 0 & 0 \\ \hline 0 & 0 & \Re(\Psi_4) \\ 0 & \Re(\Psi_4) & 0 \end{array} \right), \quad (7.64)$$

and the eigenvalues of both  $\mathcal{E}$  and  $\mathcal{B}$  are  $\pm \Re(\Psi_4)/2$ . The eigenvectors of  $\mathcal{E}$  are the unit vectors  $\mathbf{e}_\theta$  and  $\mathbf{e}_\phi$ , and those of  $\mathcal{B}$  are  $\mathbf{e}_\theta \pm \mathbf{e}_\phi$ . Thus, the radiation is purely + polarized in this basis. The tendex lines are the lines of constant  $\theta$  and  $\phi$  on a sphere, and the vortex lines are rotated relative to the tendex lines by  $\pi/4 = 45^\circ$ .

We show these lines in Figure 7.8: the tendex lines on the left, and the vortex lines on the right.

As in Figure 7.7, the red (solid) lines correspond to negative tendicity and vorticity, and the blue (dashed) lines denote positive values. The intensity of each line is proportional to the magnitude of its tendicity (or vorticity), which varies over the sphere as  ${}_{-2}Y_{2,0}(\theta, \phi) \propto \sin^2 \theta$  (the dominant spherical harmonic). Correspondingly, the dark blue and red regions near the equator represent strong tendicity and vorticity, whereas the light off-white colors near the poles indicate that the tendicity and vorticity are small there.

We remark in passing that the duality of  $\mathcal{E}$  and  $\mathcal{B}$  implies that, if there were a source of gravitational waves which had a  $\Psi_4$  that is purely imaginary and equal to the  $i\Re[\Psi_4]$  for our colliding black holes, then those waves' vortex lines would be the same as the tendex lines of Figure 7.8, and the tendex lines would be the same as the vortex lines of the same figure (but with the sign of the lines' vorticity flipped). One can see this because (i) Eq. (7.61) shows we would have a pure  $\times$  polarized wave, and (ii) when we apply the rotation of basis (7.56) to (7.62) under the condition of  $\Re(\Psi_4) = 0$  we get once again the matrices (7.64), but with  $(\tilde{e}_2, \tilde{e}_3)$  as basis vectors and with all instances of  $\Re(\Psi_4)$  replaced by  $\Im(\Psi_4)$ . This duality does not address, however, how to construct a source with a purely imaginary  $\Psi_4$ .

### 7.6.3 Wave Generation by a Time-Varying Current Quadrupole

A dynamical current-quadrupole moment  $\mathcal{S}_{pq}(t)$  generates a metric perturbation described by the  $\mathcal{S}_{pq}(t-r)/r$  terms in Eqs. (8.13) of [36]. It is straightforward to show that the corresponding frame-drag field is

$$\mathcal{B}_{ij} = \frac{2}{3} \left[ - \left( \frac{\mathcal{S}_{pq}}{r} \right)_{,pqij} + \epsilon_{ipq} \left( \frac{{}^{(2)}\mathcal{S}_{pm}}{r} \right)_{,qn} \epsilon_{jmn} + 2 \left( \frac{{}^{(2)}\mathcal{S}_{p(i}}{r} \right)_{,j)p} - \left( \frac{{}^{(4)}\mathcal{S}_{ij}}{r} \right) \right]. \quad (7.65)$$

Here  $\mathcal{S}_{pq}$  is to be regarded as a function of retarded time,  $t-r$ , and the prefixes  ${}^{(2)}$  and  ${}^{(4)}$  mean two time derivatives and four time derivatives. This equation shows explicitly how  $\mathcal{B}_{ij}$  in the near zone transitions into  $\mathcal{B}_{ij}$  in the wave zone — or equivalently, how rotating (or otherwise time-changing) frame-drag vortexes in the near zone generate gravitational waves.

This transition from near zone to far zone can also be described by the linear approximation to the Maxwell-like equations for the frame-drag field  $\mathcal{B}$  and the tidal field  $\mathcal{E}$ , Eqs. (7.17). These equations govern the manner by which the current-quadrupole near-zone frame-drag field (7.50) acquires an accompanying tidal field as it reaches outward into and through the transition zone, to the wave zone. That accompanying tidal field is most easily deduced from the  $\mathcal{S}_{pq}(t-r)/r$  terms in

the metric perturbation, Eqs. (8.13) of [36]. The result is:

$$\mathcal{E}_{ij} = \frac{4}{3} \epsilon_{pq(i} \left[ - \left( \frac{{}^{(1)}\mathcal{S}_{pk}}{r} \right)_{,j)kq} + \left( \frac{{}^{(3)}\mathcal{S}_{j)p}}{r} \right)_{,q} \right]. \quad (7.66)$$

In the near zone, the current quadrupole’s tidal field [first term of (7.66)] behaves differently from its frame-drag field [first term of (7.65)]: it has one additional time derivative and one fewer space derivative. As a result, *the tidal field is smaller than the frame-drag field in the near zone by a factor of  $r/\lambda$* , where  $\lambda$  is the reduced wavelength of the emitted gravitational waves.

As one moves outward through the near zone to the transition zone, where  $r \sim \lambda$ , the tidal field increases in magnitude to become the same strength as the frame-drag field. The frame-drag and tidal fields behave this way, because it is the near-zone vortices that generate the gravitational waves, as discussed above.

In the wave zone, the general current-quadrupole (outgoing-wave) frame-drag field (7.65) reduces to

$$\mathcal{B}_{\hat{a}\hat{b}} = \frac{4}{3r} \left[ {}^{(4)}\mathcal{S}_{\hat{a}\hat{b}}(t-r) \right]^{\text{TT}}. \quad (7.67)$$

Here the indexes are confined to transverse directions (the surface of a sphere of constant  $r$ ) in the orthonormal basis  $\mathbf{e}_{\hat{\theta}}$ ,  $\mathbf{e}_{\hat{\phi}}$ , and “TT” means “take the transverse, traceless part”. From the third of the Maxwell-like equations (7.17), or equally well from the general current-quadrupole tidal field, Eq. (7.66), we infer the wave-zone tidal field:

$$\mathcal{E}_{\hat{a}\hat{b}} = \frac{4}{3r} \left[ \epsilon_{\hat{c}(\hat{a}} {}^{(4)}\mathcal{S}_{\hat{b})\hat{c}}(t-r) \right]^{\text{TT}}, \quad (7.68)$$

where  $\epsilon_{\hat{c}\hat{d}}$  is the 2-dimensional Levi-Civita tensor on the sphere. Since  $\mathcal{E}_{\hat{a}\hat{b}} = \mathcal{R}_{\hat{a}\hat{\theta}\hat{b}\hat{\theta}} = -\frac{1}{2} {}^{(2)}h_{\hat{a}\hat{b}}^{\text{TT}}$ , where  $h_{\hat{a}\hat{b}}^{\text{TT}}$  is the transverse, traceless gravitational-wave field, our wave-zone tidal distortion (7.68) agrees with the standard result for the wave-zone current-quadrupole gravitational-wave field (Eq. (4.8) of [36]).

## 7.6.4 Rotating Current Quadrupole

In this section, we will discuss the vortex and tendex lines of a rotating current quadrupole.

A large rotating-current-quadrupole moment arises during the merger and ringdown of the extreme-kick configuration of a binary black hole (a quasicircular binary made of identical black holes, whose spins are antialigned and lie in the orbital plane). During the merger, the four vortices associated with the initial holes’ spins get deposited onto the merged horizon’s equator, and they then rotate around the final Kerr hole’s spin axis at the same rate as their separation vector rotates, generating a large, rotating-current-quadrupole moment (paper III in this series).

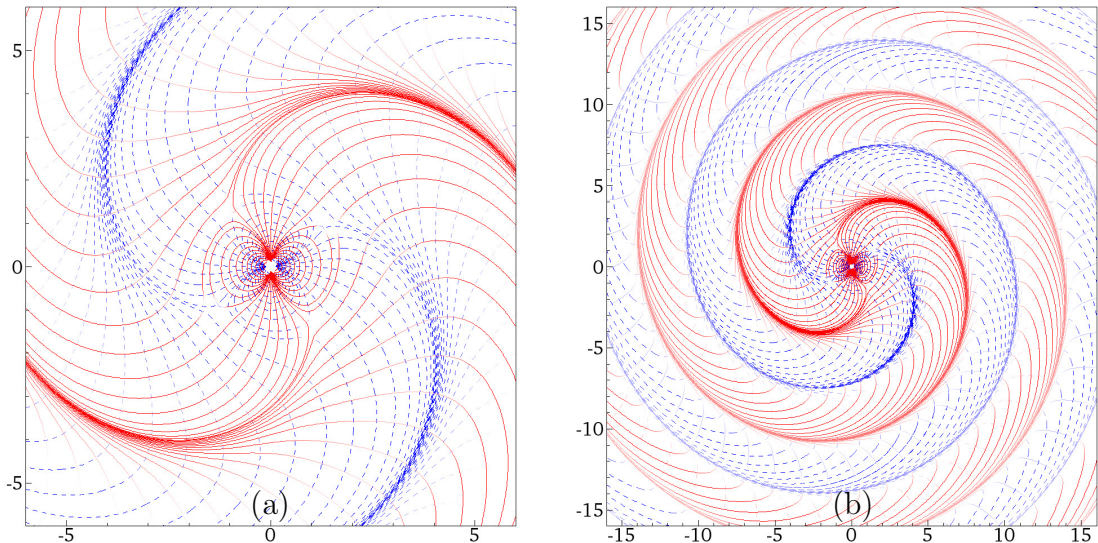


Figure 7.9: For a rotating current quadrupole in linearized theory, two families of vortex lines in the plane of reflection symmetry (the  $x-y$  plane). The red (solid) curves are lines with negative vorticity, and the blue (dashed) curves are lines of positive vorticity. The color intensity of the curves represents the strength of the vorticity, but rescaled by  $(kr)^5/[1+(kr)^4]$  (with  $k$  the wave number) to remove the vorticity’s radial decay. (a) We see the quadrupolar near-zone pattern and the transition into the induction zone. In the induction zone, the pattern carries four “triradius” singular points [44] in each family of curves, necessitated for the transition from the static quadrupole pattern to the spiraling radiation pattern. This same figure also describes the tendex lines of a rotating mass quadrupole (see the end of Section 7.6.6). (b) In the wave zone, the lines generically collect into spirals, which form the boundaries of vortexes (regions of concentrated vorticity).

As a simple linearized-gravity model of this late time behavior, imagine that at an initial time  $t = 0$ , the two vortex-generating spins, of magnitude  $S$ , are separated by a distance  $a$  along the  $x$  axis and are pointing in the  $\pm y$  direction — i.e. they have the same configuration as the static current quadrupole discussed in Section 7.5.3 above. Then at  $t = 0$ , the spins’ current-quadrupole moment has as its nonzero components  $\mathcal{S}_{xy} = \mathcal{S}_{yx} = Sa$  [Eq. (7.47) with the spin axes changed from  $z$  to  $y$ ]. As time passes, the spins’ separation vector and the spins’ directions rotate at the same angular velocity  $\omega$  so the configuration rotates rigidly. Then it is not hard to show that the current-quadrupole moment evolves as

$$\begin{aligned}\mathcal{S}_{xy} &= \mathcal{S}_{yx} = Sa \cos(2\omega t), \\ \mathcal{S}_{xx} &= -\mathcal{S}_{yy} = -Sa \sin(2\omega t).\end{aligned}\tag{7.69}$$

It is straightforward to calculate the frame-drag field produced by this quadrupole moment using Eq. (7.65), and to then compute the vortex lines and their vorticities.

The explicit expressions for these lines are somewhat lengthy, and not particularly instructive; but the shapes of the vortex lines and the values of their vorticities are quite interesting.

#### 7.6.4.1 Vortex and Tendex Lines in the Plane of Reflection Symmetry

There are two sets of vortex lines that lie in the  $x$ - $y$  plane (the plane of reflection symmetry) and one set that passes orthogonally through this plane. We show the in-plane vortex lines in Figure 7.9a and 7.9b. The two panels depict the negative-vorticity vortex lines by red (solid) curves and the positive-vorticity lines by blue (dashed) curves. The darkness of the lines is proportional to the vorticity; dark red (blue) indicates strong negative (positive) vorticity, and light red (blue) indicates weaker vorticity. To remove the effects of the radial dependence in the coloring, we have scaled the vorticity by  $(kr)^5/[1 + (kr)^4]$ , where  $k = 1/\lambda = 2\omega$  is the wave number of the radiation. Figure 7.9a shows the region of the near zone that is difficult to see in Figure 7.9b, an equivalent figure that spans a larger region of the  $x$ - $y$  plane. As one can see from the figures, the two sets of lines have the same pattern, but are rotated with respect to each other by  $\pi/2 = 90^\circ$ .

In the near zone (inner region of Figure 7.9a), the vortex-line pattern is the same as for the static current quadrupole of Figure 7.6b. At the transition to the wave zone, the vortex lines fail to curve back into the central region and instead bend outward, joining a wave-zone spiral pattern.

That spiral pattern consists of four vortexes (regions of concentrated vorticity) that spiral outward and backward as the quadrupole rotates. These four regions of alternating positive and negative vorticity are bounded by tight clusters of vortex lines, just outside of which the sign of the dominant vorticity changes.

This same rotating vortex structure occurs in the case of an  $l = 2$ ,  $m = 2$ , odd-parity (current-quadrupolar) perturbation of a Schwarzschild black hole (Paper II in this series). There the horizon vorticity pattern takes the place of the current quadrupole.

In Figure 7.10 we indicate the structure of the tendex lines on the equatorial plane. Because the symmetry properties of the system imply different constraints on the tendex field than on the vortex field, some explanation is needed. The plane in which this and the previous two figures are drawn is a plane of reflection symmetry for the problem. However, because the source is a pure current quadrupole, it must be antisymmetric under reflection across this plane (as such a reflection is a parity inversion). The vorticity, which itself has an odd-parity relationship with its source, is symmetric under this reflection, constraining the vortex lines to be either tangent or orthogonal to the plane, as noted above. The tendicity is antisymmetric under this reflection, so one family of lines can be tangent to the plane, so long as it has zero tendicity, and two other families of lines must cross the plane at equal and opposite inclinations, with equal and opposite tendicities, such that they are exchanged under the reflection. The diagram in Figure 7.10 shows the single family of tendex lines tangent to the symmetry plane. As these curves have exactly zero tendicity, they are physically relevant only in that they denote the orientation of the other two families of tendex lines, which are not tangent to the plane, but whose projection onto the plane must be orthogonal to the curves shown (because all three curves are mutually orthogonal). The shading of the lines in

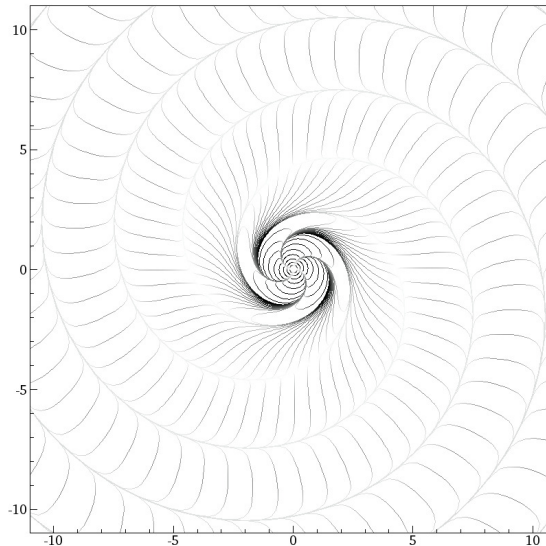


Figure 7.10: Tendex lines in the equatorial plane for a rotating current quadrupole in linearized theory. The curves shown are lines of identically zero tendicity, enforced by symmetry. The lines are shaded by the absolute value of the tendicity of the other two tendex lines that cross the lines shown, but are not tangent to the plane, and have equal and opposite tendicities.

Figure 7.10 does not represent the tendicity of the lines drawn (which is identically zero), but rather of the other two tendex lines, which intersect the lines drawn with mutually equal and opposite tendicity. Again, this shading is rescaled by  $(kr)^5/[1 + (kr)^4]$ . Though it is not apparent to the eye, the strength of the tendicity grows only as  $r^4$  near the singular point (origin), rather than  $r^5$  as for the vorticity. As argued early in Section 7.6.3, this can be interpreted intuitively as meaning that the vorticity is sourced directly from the current quadrupole, while the tendicity is sourced by induction from the time-varying vortex field.

For a rotating mass quadrupole (e.g. the quadrupole moment of an equal-mass binary), the tendex lines in the plane of reflection symmetry will have precisely the same form as the rotating-current-quadrupole vortex lines of Figures 7.9a and 7.9b; see Section 7.6.6.

#### 7.6.4.2 Vortex Lines Outside the Plane of Reflection Symmetry: Transition from Near Zone to Wave Zone

Outside the plane of reflection symmetry and in the wave zone, the extrema of the vorticity show a spiraling pattern that is the same at all polar angles. More specifically, at all polar angles  $\theta$ , the magnitude of the vorticity, as a function of azimuthal angle  $\phi$ , has four maxima, and the locations of those maxima are the same as in the equator ( $\theta = \pi/2$ ). As in the equator, the maxima at fixed time  $t$  spiral around at an angular rate  $d\phi_{\max}/dr = -\omega$  as one moves outward in radius, and as in the equator, vortex lines collect near these spiraling maxima, and those lines too undergo spiraling behavior.

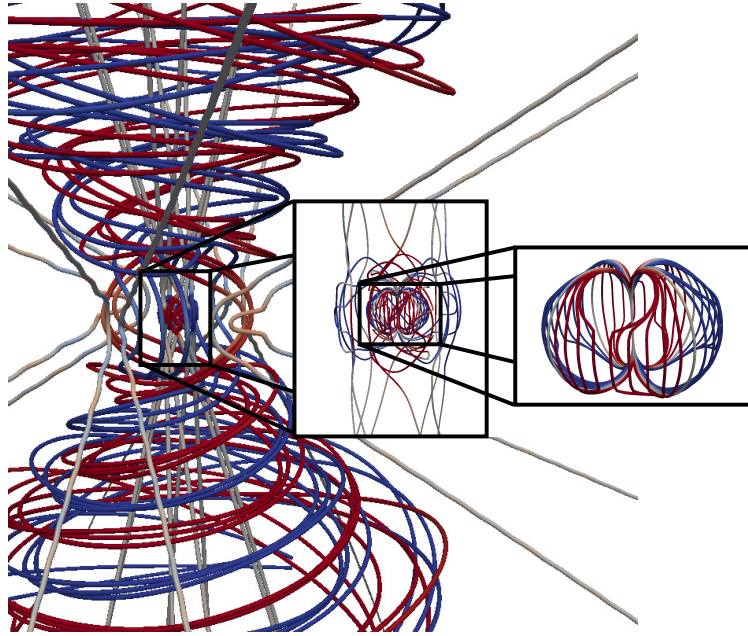


Figure 7.11: For the same rotating current quadrupole as in Figure 7.9, the family of vortex lines that pass orthogonally through the  $x$ - $y$  plane of reflection symmetry, color coded as in Figure 7.9. In the wave zone, lines with approximately zero vorticity extend away from the source nearly radially, while lines with significant vorticity are dragged into tangled spirals by the rotation of the source. In the left inset, we see the transition between the near and wave zones. Here, lines with nearly zero vorticity escape to infinity as in the wave zone, but those with significant vorticity are drawn toward the source. The right inset delves down into the near zone, where the lines are approximately those of a stationary current quadrupole. This same figure also describes the tendex lines of a rotating mass quadrupole (see the end of Section 7.6.6).

Figure 7.11 shows the development of this spiraling structure as one moves outward from the near zone (innermost inset) into the wave zone (outer region of figure). This figure focuses on the family of vortex lines that pass orthogonally through the  $x$ - $y$  plane of reflection symmetry. After entering the wave zone, the lines with nonnegligible vorticity (the blue and red lines) collect into a somewhat complicated spiral pattern, tangling among themselves a bit as they spiral. The gray lines with very low vorticity, by contrast, point radially outward. An animation of this rotating system can be seen at Reference [26].

It should be noted Figure 7.11, and the animation at Reference [26], represent somewhat incomplete descriptions of the structure of these field lines. The red and blue helical spirals shown in Figure 7.11 do not cross one another. However, at any point in space, there must be three mutually orthogonal vortex lines, with vorticities summing to zero. Since at all points in the wave zone there is a field line of nearly zero vorticity directed in a nearly radial direction, through any point along these spirals of positive or negative vorticity, field lines of opposite vorticity must lie orthogonal to the spiral and to the approximately radial lines. As shown in the following subsection, these lines form closed loops in the far-field region.

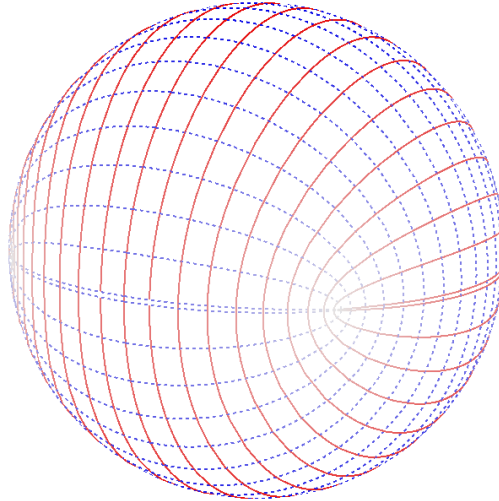


Figure 7.12: Vortex lines of a time-varying current quadrupole at very large  $r$ . The lines are colored by the vorticity scaled by  $r$ , to remove the  $1/r$  falloff, but the color coding is the same as in previous figures. At very large distances from the source, the lines are transverse and live on a sphere. The third vortex line not shown is radial and has vanishing eigenvalue.

#### 7.6.4.3 Vortex Lines in the Far Wave Zone

In the far wave zone (strictly speaking at future null infinity), the frame-drag field becomes transverse and traceless, and takes the simple form (7.67). Of its three sets of vortex lines, one is radial (with vanishing vorticity) and the other two are tangent to a sphere of constant radius  $r$  (with vorticity of equal and opposite sign). The two sets of vortex lines on the sphere have an interesting angular pattern that is shown in Figure 7.12. The vortex line that lies in the equator alternates between positive and negative vorticity, going to zero at four points (one of which is shown at the front of the sphere). This line is just the limit of the spirals where vortex lines collect in Figure 7.9b at very large  $r$ . [Further discussion of the vortex and tendex lines of radiation at large  $r$  is given in [28], where the dual figure to Figure 7.12 (tendex lines of a rotating mass quadrupole) is discussed in detail.]

How the vortex lines transition to the transverse pattern of Figure 7.12 at very large  $r$ , from the spiraling pattern of Figure 7.11 in the inner wave zone, is of considerable interest. We can explore this by examining the frame-drag field at sufficiently large radii that the  $1/r$  piece dominates over all other components, and that the  $1/r^2$  part of the frame-drag field may be thought of as a perturbation to the leading-order  $1/r$  part. In this region, the vortex lines show two kinds of qualitative behavior. Some of the vortex lines continue to form spirals that meander out and do not close, as in Figure 7.11. There also are lines that form closed loops similar to the leading-order vortex lines of Figure 7.12. We show both of these types of lines in Figure 7.13. The red, solid, spiraling lines continue to collect on the maximum-vorticity spirals in the far wave zone. These lines begin to resemble the transverse

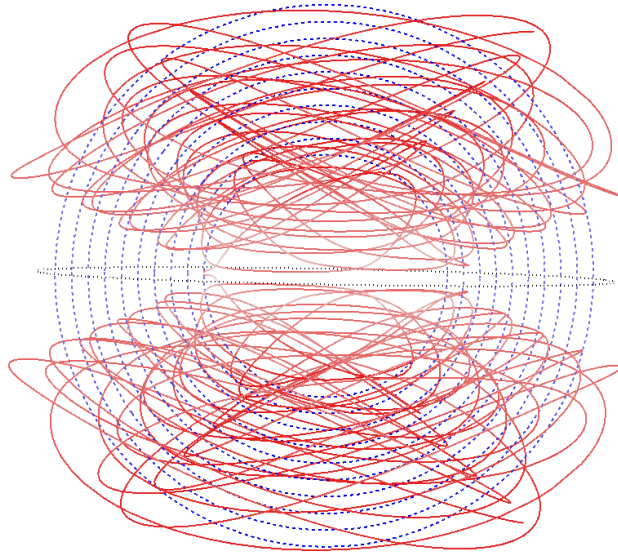


Figure 7.13: Vortex lines of a rotating current quadrupole at sufficiently large  $r$  that the  $1/r^2$  part of the frame-drag field may be thought of as a perturbation to the transverse vortex lines of Figure 7.12. The lines are colored by the vorticity as in that figure. We also show a black dotted circle in the equatorial plane to identify this plane. The red solid lines shown here continue to collect on the maximum-vorticity spiral, but they oscillate much more in polar angle than do the similar lines shown in the near wave zone in Figure 7.11. The blue dashed lines shown here form closed loops that pass from one positive-vorticity spiral to the next. This family of lines more closely resembles the transverse lines of Figure 7.12, though in the limit of infinite radius, the spiraling lines will also close to form transverse lines on the sphere. There are also spiraling positive-vorticity (blue) lines and closed-loop, negative-vorticity (red) lines, but to keep the figure from appearing muddled, we do not show them.

lines of Figure 7.12 more than the spiraling lines in the near wave zone of Figure 7.11 do, because they rise and fall in polar angle as they wind around the maximum-vorticity spiral. It is only in the limit of infinite radius that these spirals close to form loops. The blue, dashed, closed lines, on the other hand, resemble the closed lines at infinity in Figure 7.12 much more closely. The lines at finite  $r$  do have some subtle differences between the corresponding lines at infinity: At finite radii, each individual line passes from one maximum-vorticity spiral to the other; in doing so the line must slightly increase in radius and rotate in azimuthal angle. At the large radii shown in Figure 7.13, this effect is very subtle. We finally note that there are also spiraling, positive-vorticity lines and closed, negative-vorticity lines that we do not show to avoid visual clutter.

### 7.6.5 Oscillating Current Quadrupole

The vortex lines of an oscillating current quadrupole (this section) have a very different structure from those of the rotating current quadrupole (last section). This should not be surprising, because the two quadrupoles arise from very different physical scenarios, e.g., for the oscillating quadrupole, the ringdown following a head-on collision of black holes with antialigned spins, and for the rotating

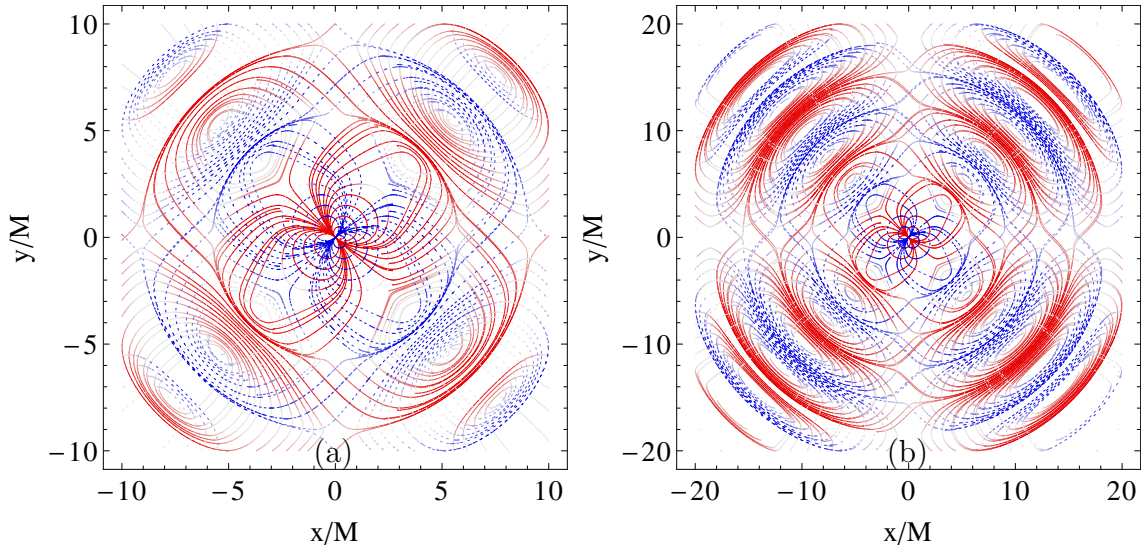


Figure 7.14: For an oscillating current quadrupole in linearized theory, two families of vortex lines in the plane of reflection symmetry (the  $x$ - $y$  plane). The color coding is the same as for the rotating current quadrupole, Figure 7.9. (a) The vortex lines begin, near the origin, like the static quadrupole pattern of Figure 7.6. The effects of time retardation cause the pattern to stretch making larger rectangular loops in the transition zone. As time passes and the quadrupole oscillates, these loops detach from the origin and propagate out into the wave zone. (b) Farther from the source, the loops take on a more regular alternating pattern of gravitational waves. The coloring shows that the vorticity is strongest at the fronts and backs of the loops, where the vortex lines are transverse to the direction of propagation. In the regions of the closed loops that extend radially, the field is weak (as one would expect for a transverse gravitational wave). This same figure also describes the tendex lines of an oscillating mass quadrupole (see the end of Section 7.6.6).

quadrupole, the ringdown following the inspiral and merger of an extreme-kick black-hole binary. See Papers II and III of this series.

In linearized theory, one can envision an oscillating current quadrupole as produced by two particles, separated by a distance  $a$  along the  $x$  axis, whose spins, antialigned and pointing in the  $\pm y$  direction, oscillate in magnitude as  $S \cos \omega t$ . The resulting quadrupole moment is [cf. Eq. (7.46)]

$$\mathcal{S}_{xy} = \mathcal{S}_{yx} = Sa \cos \omega t. \quad (7.70)$$

The frame-drag and tidal fields, and thence vortex and tendex lines, for this current quadrupole can be computed from Eqs. (7.65) and (7.66).

As for the rotating quadrupole, the  $x$ - $y$  plane of reflection symmetry contains two families of vortex lines, and a third family passes orthogonally through that plane. The in-plane vortex lines are depicted in Figure 7.14 using the same color conventions as for the rotating quadrupole (Figure 7.9). Figure 7.14a shows the region of the near zone that is difficult to see in Figure 7.14b, an equivalent image that spans a larger region of the  $x$ - $y$  plane. As one can see from the figures, the two families of vortex lines, solid red (negative vorticity) and dashed blue (positive vorticity) have the same

pattern, but are rotated by  $\pi/2 = 90^\circ$ .

The way in which the gravitational waves are generated differs greatly from the rotating current quadrupole of the previous section. In the near zone, the two sets of vortex lines form a static quadrupole pattern (identical to the near-zone rotating quadrupole of Figure 7.9a, but rotated by  $\pi/4$  due to the orientation of the spins). In the transition zone, the vortex lines form distorted loops that head away from the origin, along the lines  $y = \pm x$ , in alternating fashion. As they extend into the wave zone, the lines form two qualitatively different kinds of loops. The majority of the loops reside only in one of the four quadrants of the equatorial plane, but there are also loops that pass through all four quadrants, staying near the regions of maximum vorticity, where lines collect at the gravitational-wave crests. For both types of loops, they maintain the same wavelength, but the wave front becomes wider at larger radii, as they become gravitational waves. The portion of a loop transverse to the radial direction (the direction of propagation) has strong vorticity, as one would expect for a gravitational wave; in the radial portion of the loop, the vorticity is weak. Each cycle of the oscillating quadrupole casts off another set of vortex loops as the near-zone region passes through zero vorticity, and the loops travel outward towards infinity. This illustrates clearly the manner in which the near-zone vortex pattern generates gravitational waves in the far zone through its dynamics.

As with the rotating current quadrupole, one can envision the equatorial vortex line of Figure 7.12 as the limit of the wave fronts of the planar vortex lines in Figure 7.14b at large distances. It is again of interest to understand how the vortex lines outside the equatorial plane become the remaining vortex lines in Figure 7.12. To do so, we will make reference to Figure 7.15, which shows the vortex lines at a distance sufficiently large that the  $1/r^2$  portions of the frame-drag field can be thought of as a small perturbation to the transverse vortex lines of Figure 7.12. We show only the three-dimensional analog of the lines that pass through all four quadrants in the equatorial plane, and do not show the lines that remain in just one octant (analogous to the loops that remain in one quadrant in the equatorial plane) to keep the figure as simple as possible.

Near the poles, these vortex lines have nearly the same structure as the purely transverse lines of Figure 7.12; it is only near the equator that the lines begin to differ. As the lines approach the equator, they also increase in radius, due to the  $1/r^2$  parts of the frame-drag field. In doing so, they pass from one gravitational-wave crest to the next, and the lines sharply turn during their passage between successive crests. The portion of the line on this next crest runs nearly parallel to the equator, until it begins moving slightly inward (again due to the  $1/r^2$  parts of the frame-drag field). As it then sharply turns again, it returns to the original crest and begins heading back toward the poles. This sharp turning happens on both sides of the sphere, which causes the lines to form the closed loops that reside in either the northern or the southern hemisphere in Figure 7.15. Only in the limit that  $r$  goes to infinity do the radial perturbations vanish, and the loops in the northern

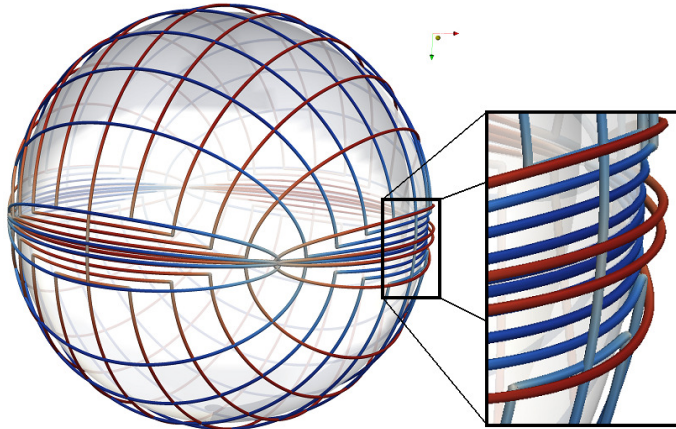


Figure 7.15: Vortex lines of an oscillating current quadrupole at sufficiently large  $r$  that the  $1/r^2$  part of the frame-drag field may be thought of as a perturbation to the transverse vortex lines of Figure 7.12. The lines are colored in the same way as that figure, and the pattern of the lines around the poles is nearly identical to the transverse lines of Figure 7.12. Near the equator, the  $1/r^2$  perturbation causes the lines to bend and form closed loops that reside in either the northern or the southern hemisphere. The blue horizontal lines in the blow-up inset should be compared with dense blue (dashed) bundles in Figure 7.14b, and red lines with the red bundles immediately outside of the blue ones.

and southern hemisphere connect to form the transverse pattern in Figure 7.12.

### 7.6.6 Wave Generation by a Time-Varying Mass Quadrupole

A time-varying mass-quadrupole moment  $\mathcal{I}_{pq}(t)$  gives rise to metric perturbations of flat space given by the terms proportional to  $\mathcal{I}_{pq}(t-r)/r$  and its derivatives in Eqs. (8.13) of [36]. It is straightforward to calculate that the frame-drag field for these metric perturbations is

$$\mathcal{B}_{ij} = \epsilon_{pq(i} \left[ \left( \frac{{}^{(1)}\mathcal{I}_{pk}}{r} \right)_{,j)kq} - \left( \frac{{}^{(3)}\mathcal{I}_{jp}}{r} \right)_{,q} \right]. \quad (7.71)$$

Notice that this mass-quadrupolar frame-drag field is the same as the current-quadrupolar tidal field (7.66), with the current-quadrupole moment  $\mathcal{S}_{pq}$  replaced by  $-\frac{3}{4}\mathcal{I}_{pq}$ ; cf. the duality relations (7.16) and (7.20). Correspondingly, the vortex lines of this mass quadrupole will be the same as the tendex lines of the equivalent current quadrupole.

The mass quadrupole's tidal field can be deduced from its frame-drag field (7.71) by using the third of the Maxwell-like equations (7.17). The result is

$$\mathcal{E}_{ij} = \frac{1}{2} \left[ - \left( \frac{\mathcal{I}_{pq}}{r} \right)_{,pqij} + \epsilon_{ipq} \left( \frac{{}^{(2)}\mathcal{I}_{pm}}{r} \right)_{,qn} \epsilon_{jmn} + 2 \left( \frac{{}^{(2)}\mathcal{I}_{p(i}}{r} \right)_{,j)p} - \left( \frac{{}^{(4)}\mathcal{I}_{ij}}{r} \right) \right]. \quad (7.72)$$

Alternatively, this mass-quadrupolar tidal field can be deduced from the current-quadrupolar frame-

drag field (7.65) by using the duality relation  $\mathcal{S}_{pq} \rightarrow +\frac{3}{4}\mathcal{I}_{pq}$  [Eqs. (7.16) and (7.20)].

As a result, the tendex lines of this mass quadrupole will be the same as the vortex lines of the current quadrupole, Figures 7.9 and 7.11 - 7.14, with the red (solid) lines describing tidal stretching, and the blue (dashed) lines, tidal squeezing.

### 7.6.7 Slow-Motion Binary System Made of Identical, Nonspinning Point Particles

As a final example of a weakly gravitating system, we investigate the tendex lines of a Newtonian, equal-mass binary made of nonspinning point particles in a circular orbit. We assume a separation  $a$  between particles that is large compared to their mass  $M$ , so the orbital velocity  $v = \frac{1}{2}\sqrt{M/a}$  is small compared to the speed of light (“slow-motion binary”).

Close to the binary, where retardation effects are negligible, the tidal field is given by the Newtonian expression  $\mathcal{E}_{jk} = \Phi_{,jk}$  [Eq. (7.36)], with  $\Phi$  the binary’s Newtonian gravitational potential

$$\Phi = -\frac{M_A}{|\mathbf{x} - \mathbf{x}_A|} - \frac{M_B}{|\mathbf{x} - \mathbf{x}_B|}. \quad (7.73)$$

Here  $M_A = M_B = M/2$  are the particles’ masses with  $M$  the total mass, and  $\mathbf{x}_A$  and  $\mathbf{x}_B$  are the locations of particles, which we take to be on the  $x$  axis, separated by a distance  $a$ .

In Figure 7.16, we show the near-zone tendex lines associated with this potential’s tidal field, color coded in the usual way (see the figure’s caption). Close to each particle, the tendex lines resemble those of a static, spherically symmetric object. Moving farther from the particle, one can see the effects of the particle’s companion, bending and compressing the lines. At radii  $r \gtrsim a$ , the Newtonian potential and tidal field can be expanded in multipole moments with the monopole and quadrupole dominating. At  $r \gg a$ , the monopole dominates and the tendex lines become those of a single spherical body.

The binary’s orbital angular velocity is  $\omega = \sqrt{M/a^3}$  (Kepler’s formula), and the binary emits gravitational waves with angular frequency  $2\omega$ , reduced wavelength  $\lambda = 1/(2\omega) = \frac{1}{2}\sqrt{a^3/M}$ , and wavelength  $\lambda = 2\pi\lambda$ . As a concrete example, we choose the particles’ separation to be  $a = 20M$ ; then  $\lambda = \sqrt{5}a \simeq 2.24a$ , and  $\lambda = 2\pi\sqrt{5}a \simeq 14a$ .

Figure 7.17 shows tendex lines in this binary’s orbital plane, focusing on the transition and wave zones  $r \gtrsim \lambda = 2.24a$  (outside the solid black circle). The shapes and colors of the tendex lines in this figure can be understood in terms of the binary’s multipole moments:

In the transition zone and wave zone,  $r \gtrsim \lambda$ , the tidal field is the sum of a nonradiative monopolar piece with magnitude  $\mathcal{E}_M \simeq M/r^3$ , and a quadrupolar piece with magnitude  $(1/r)\partial^4\mathcal{I}/\partial t^4 \simeq (2\omega)^4(\frac{1}{4}Ma^2)/r \simeq 4M^3/a^4r$ ; higher order moments are negligible. The two moments contribute about equally at radius  $r = \frac{1}{2}a^2/M = 10a$  (dotted black circle in the figure). The (nonradiative)

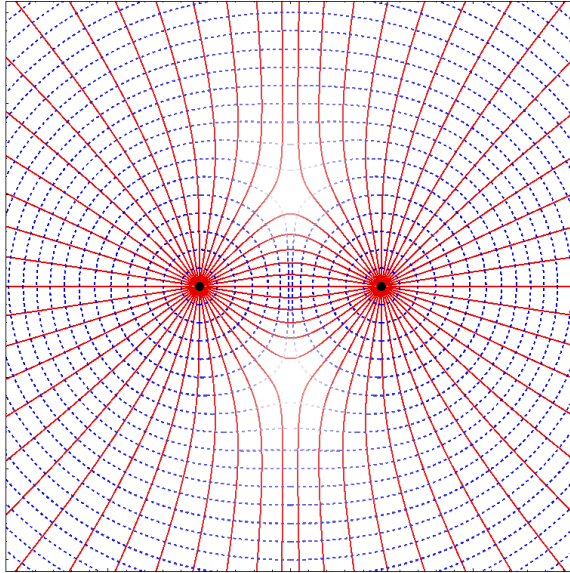


Figure 7.16: For a weak-gravity binary made of identical nonspinning point particles, in the near zone where retardation is negligible, two families of tendex lines lying in a plane that passes through the two particles (e.g. the orbital plane). The red (solid) curves are lines with negative tendicity, and the blue (dashed) curves have positive tendicity. The color intensity of the curves represents the magnitude of the tendicity, rescaled by  $r_A^3 r_B^3 / [M^3 (r_A^3 + r_B^3)]$ , where  $r_A$  and  $r_B$  are the distances to the particles, to remove the tendicity's radial falloff. Near each particle, the tendex lines resemble those of an isolated spherical body; as one moves closer to the particle's companion, the lines bend in response to its presence. At radii large compared to the particles' separation  $a$ , the binary's monopole moment comes to dominate, and the tendex lines resemble those of a single isolated spherical body.

monopole moment, with its red radial and blue circular tendex lines, dominates inside this circle. The (radiative) quadrupole moment dominates outside the circle, so there the tendicity is significant (strong red and blue) only when the tendex lines are transverse; strong red alternates, radially, with strong blue as the waves propagate radially. Ultimately, at very large radii (far outside the domain of Figure 7.17), the quadrupole moment will totally dominate, and the tendex-line pattern will become that of a rotating quadrupole, depicted in Figure 7.9b.

Figure 7.18 shows the tendex lines for this same binary, with the same parameters, in three dimensions, i.e. above and below the equatorial plane. In the inner region, the monopole moment dominates so the red (stretching) tendex lines are nearly radial, and the blue (squeezing) tendex lines are nearly circular, centered on the binary. As one moves outward, the radiative quadrupole moment begins to distort these radial and circular tendex lines, and then at large radii, the now-dominant quadrupole moment drives them into the same spiraling pattern as we have seen in Figure 7.11 for the tendex lines of a rotating, pure mass quadrupole.

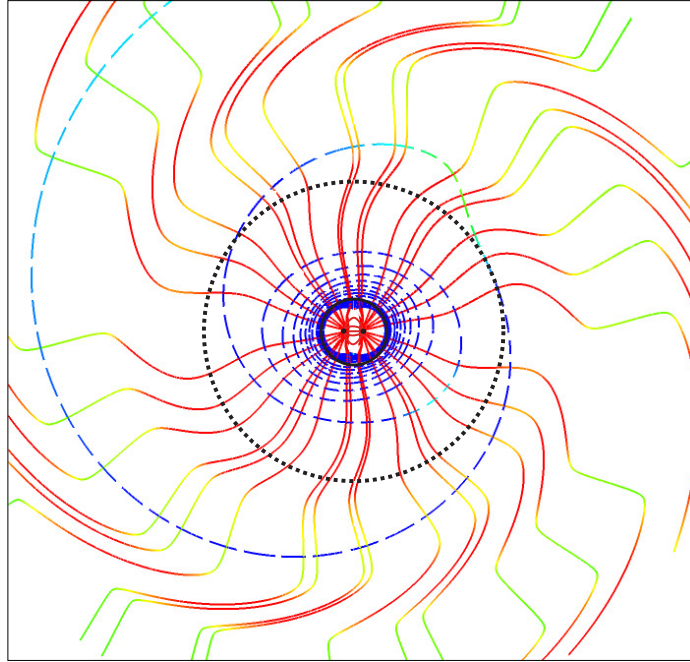


Figure 7.17: Tendex lines in the orbital plane of the same binary as Figure 7.16, with separation  $a = 20M$  (where  $M$  is the total mass), focusing on the transition and wave zones  $r \gtrsim \lambda = 2.24a$ . The solid black circle has radius  $\lambda$ . The colors are fixed by the tendicity weighted by  $\omega r$  so as to scale out the  $1/r$  falloff in the wave zone (with dark blue strongly positive, dark red strongly negative, and light green near zero). Inside the dotted black curve ( $r = \frac{1}{2}a^2/M = 10a$ ), the binary's (nonradiative) monopole moment dominates,  $\mathcal{E} \simeq M/r^3$ , and the red (stretching) tendex lines are nearly radial. Outside the dotted black curve, the (radiative) quadrupole moment dominates,  $\mathcal{E} \simeq 4M^3/a^4r$ , and the tendex lines are strong (significant tendicity) only where they are approximately transverse to the radial direction.

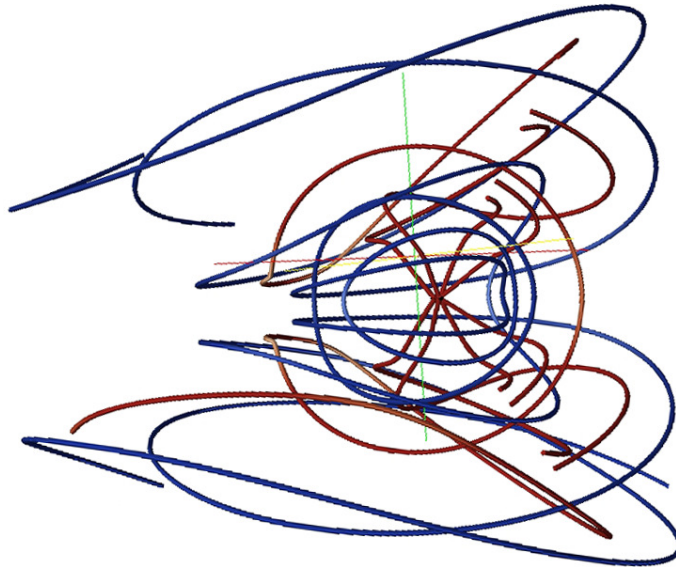


Figure 7.18: Tendex lines outside the (central, horizontal) orbital plane, for the same binary and parameters as Figure 7.17. In the inner region, the binary’s monopole moment dominates,  $\mathcal{E} \simeq M/r^3$ , so the red (stretching) tendex lines are nearly radial and the blue (squeezing) tendex lines are nearly circular. At larger radii, the (radiative) quadrupole moment begins to be significant and then dominate, so the tendex lines begin to spiral outward as for the rotating quadrupole of Figure 7.11.

## 7.7 Conclusions

In this paper, we have focused on the electric and magnetic parts of the Weyl curvature tensor,  $\mathcal{E}_{ij}$  and  $\mathcal{B}_{ij}$ , and have given them the names *tidal field* and *frame-drag field*, based on their roles in producing tidal gravitational accelerations and differential frame dragging. Being parts of the Riemann tensor, these fields are well defined (though slicing dependent) in strong-gravity situations such as the near zone of colliding black holes. For this reason, and because they embody the full vacuum Riemann tensor and are easily visualized,  $\mathcal{E}_{ij}$  and  $\mathcal{B}_{ij}$  are powerful tools for exploring the nonlinear dynamics of spacetime curvature (geometrodynamics).

As tools for visualizing  $\mathcal{E}_{ij}$  and  $\mathcal{B}_{ij}$ , we have introduced tendex and vortex lines (the integral curves of the eigenvectors of  $\mathcal{E}_{ij}$  and  $\mathcal{B}_{ij}$ ), along with their tendicities and vorticities (the eigenvectors’ eigenvalues). The tendex and vortex lines are gravitational analogs of electric and magnetic field lines. Moreover, just as the electromagnetic field tensor is fully determined by its electric and magnetic field lines, together with their field-line densities (which encode the lengths of the electric and magnetic vectors), so the vacuum Riemann curvature tensor is fully determined by its tendex and vortex lines, together with their colors (which encode the tendicities and vorticities as in Figure 7.17).

In terms of their transformation properties, the  $(\mathcal{E}_{ij}, \mathcal{B}_{ij})$  pair is strictly analogous to the pair of electric and magnetic 3-vector fields: they are components of a 4-tensor, divided into two groups in a slicing dependent manner. We are confident that this mild and transparent form of frame

dependence will not prevent our tendex and vortex concepts from becoming useful tools for studying geometrodynamics, any more than the frame dependence of electric and magnetic fields and field lines have been impeded these fields from being useful tools for studying electromagnetism in flat or curved spacetime.

Using various examples from linearized gravity, for which analytical formulas are available, we have plotted color-coded tendex and vortex lines, and thereby we have gained insight into the behaviors of the tidal and frame-drag fields. This intuition from weak-gravity examples will be of great value when studying strongly gravitating systems in asymptotically flat spacetimes, e.g. binary black holes. This is because, in the weak-gravity region of spacetime outside such strong-gravity systems, linearized gravity is a good approximation. More specifically:

For stationary, strongly gravitating systems (e.g., stationary black holes and neutron stars), the tendex and vortex lines in their asymptotic, weak-gravity regions will be well approximated by our linearized-theory results in Section 7.5 (and, perhaps in some cases, extensions to higher multipoles).

For oscillatory, strongly gravitating systems (e.g., binary black holes and oscillating neutron stars), the wave zones' tendex and vortex lines will be well approximated by those of our examples in Section 7.6, and their extensions. Whether the system has strong gravity or weak gravity, its wave-zone field lines are controlled by radiative multipole moments that are tied to the system's near-zone dynamics.

As one moves inward through the weak-gravity wave zone into the near zone and the region of strong gravity, the details of the field lines and the system's dynamics may be quite different for strong-gravity systems than for our weak-gravity examples. Nevertheless it seems likely that in *all* cases, the gravitational waves will be generated by dynamical motions of near-zone tendexes and vortexes (regions of strong tendicity and vorticity). By exploring that near-zone tendex/vortex dynamics, we can gain deep physical insight into nonlinear spacetime curvature. This will be a central theme of Papers II and III in this series.

Whatever may be a source's strong-field dynamics, it will be useful to focus on the imprints that the strong-field dynamics leaves on the tendex/vortex structures in the strong-to-weak-gravity transition region. Those transition-region tendex/vortex imprints will govern spacetime curvature throughout the asymptotic, weak-gravity region, and in particular will govern the radiative multipole moments that control the emitted gravitational waves. Moreover, the imprinted structures in the strong-to-weak-gravity transition region may turn out to have some sort of effective dynamics that can be captured by simple analytical models and can become a powerful tool for generating approximate gravitational waveforms, e.g. for use in gravitational-wave data analysis.

## Acknowledgments

We thank John Belcher, Larry Kidder, Richard Price, and Saul Teukolsky for helpful discussions. Our simulations have been performed using the Spectral Einstein Code (SpEC) [45]. This research was supported by NSF grants PHY-0601459, PHY-0653653, PHY-0960291, PHY-0969111, PHY-1005426, PHY-1068881 and CAREER grant PHY-0956189, by NASA grants NNX09AF97G and NNX09AF96G, and by the Sherman Fairchild Foundation, the Brinson Foundation, and the David and Barbara Groce fund.

## 7.A The Newman-Penrose Formalism

In this appendix we give the connection between the electric and magnetic parts of the Weyl tensor  $\mathcal{E}$  and  $\mathcal{B}$ , and the five Newman-Penrose (NP) curvature scalars [46].

The NP formalism [46] is especially useful for expressing the gravitational-wave content of a dynamical spacetime at asymptotic null infinity. It is also a crucial foundation for the study of black-hole perturbations and for the Petrov classification of vacuum spacetimes, both of which will naturally make contact with the study of vortexes and tendexes. In order to make contact with numerical simulations, we will need to understand the connection between the NP formalism and gravitational waves propagating on a flat background, as discussed in Section 7.6.1.

Because we use the opposite metric signature to that of the original Newman-Penrose paper [46] and the widely used Penrose-Rindler book [32], our sign conventions for the NP quantities and for Eqs. (7.76) and (7.81) below differ from theirs. Ours are the same as in [33].

To begin with, we define an orthonormal tetrad  $\vec{e}_{\hat{\alpha}} = (\vec{e}_{\hat{0}}, \vec{e}_{\hat{1}}, \vec{e}_{\hat{2}}, \vec{e}_{\hat{3}})$  with time basis vector  $\vec{e}_{\hat{0}} = \vec{u}$  orthogonal to our chosen foliation's spacelike hypersurfaces, and with the spatial basis vectors  $\vec{e}_{\hat{1}}, \vec{e}_{\hat{2}}, \vec{e}_{\hat{3}}$  lying in those hypersurfaces. We use this tetrad to build a complex null tetrad for use in the NP formalism:

$$\vec{l} = \frac{1}{\sqrt{2}}(\vec{e}_{\hat{0}} + \vec{e}_{\hat{1}}), \quad \vec{n} = \frac{1}{\sqrt{2}}(\vec{e}_{\hat{0}} - \vec{e}_{\hat{1}}), \quad \vec{m} = \frac{1}{\sqrt{2}}(\vec{e}_{\hat{2}} + i\vec{e}_{\hat{3}}), \quad \vec{m}^* = \frac{1}{\sqrt{2}}(\vec{e}_{\hat{2}} - i\vec{e}_{\hat{3}}). \quad (7.74)$$

By projecting the Weyl tensor onto this null basis, we construct the complex Weyl scalars,

$$\Psi_0 = C_{\mu\nu\rho\sigma} l^\mu m^\nu l^\rho m^\sigma, \quad (7.75a)$$

$$\Psi_1 = C_{\mu\nu\rho\sigma} l^\mu n^\nu l^\rho m^\sigma, \quad (7.75b)$$

$$\Psi_2 = C_{\mu\nu\rho\sigma} l^\mu m^\nu m^{*\rho} n^\sigma, \quad (7.75c)$$

$$\Psi_3 = C_{\mu\nu\rho\sigma} l^\mu n^\nu m^{*\rho} n^\sigma, \quad (7.75d)$$

$$\Psi_4 = C_{\mu\nu\rho\sigma} n^\mu m^{*\nu} n^\rho m^{*\sigma}. \quad (7.75e)$$

Using the null tetrad (7.74) built from our orthonormal tetrad, we can express the spatial orthonormal components of the electric and magnetic parts of the Weyl tensor in terms of the Weyl scalars as follows:

$$\begin{aligned} & \mathcal{E}_{\hat{a}\hat{b}} + i\mathcal{B}_{\hat{a}\hat{b}} \\ = & \begin{bmatrix} 2\Psi_2 & -(\Psi_1 - \Psi_3) & i(\Psi_1 + \Psi_3) \\ * & \frac{\Psi_0 + \Psi_4}{2} - \Psi_2 & -\frac{i}{2}(\Psi_0 - \Psi_4) \\ * & * & -\frac{\Psi_0 + \Psi_4}{2} - \Psi_2 \end{bmatrix}, \end{aligned} \quad (7.76)$$

(cf. Eq (3.65) of [33], where the differences are due to differing conventions on both  $\mathcal{B}$  and our null tetrad). In Eq. (7.76), the rows and columns are ordered as  $\hat{1}, \hat{2}, \hat{3}$  and the entries indicated by \* are given by the symmetry of the matrix.

The entries in Eq. (7.76) can be derived in a straightforward manner from the definitions of  $\mathcal{E}$  and  $\mathcal{B}$ , Eqs. (8.1a) and (8.1b), and the definitions of the Weyl scalars, Eqs. (7.75a)-(7.75e). For example, we have

$$\mathcal{E}_{\hat{1}\hat{1}} = R_{\hat{1}\hat{0}\hat{1}\hat{0}} = \frac{1}{2}(R_{\hat{r}l\hat{r}l} + 2R_{\hat{r}l\hat{r}n} + R_{\hat{r}n\hat{r}n}) = \frac{1}{4}(R_{nlnl} - 2R_{nlln} + R_{lnln}) = R_{lnln}, \quad (7.77)$$

where we have used the symmetry properties of the Riemann tensor to eliminate and combine many terms. This result is not obviously equal to any of the Weyl scalars, but note that

$$\begin{aligned} R_{lnln} &= -R^n{}_{nl}n = R^n{}_{nll} = -(R^l{}_{nll} + R^m{}_{nml} + R^{m*}{}_{nm^*l}) = -R_{m^*nml} - R_{mnm^*l} \\ &= R_{lmm^*n} + R_{lm^*mn} = \Psi_2 + \Psi_2^*, \end{aligned} \quad (7.78)$$

where we have used the fact that in the null tetrad basis  $\{\vec{l}, \vec{n}, \vec{m}, \vec{m}^*\}$ , indexes are raised and lowered with the metric components

$$g_{\alpha\beta} = g^{\alpha\beta} = \begin{pmatrix} 0 & -1 & 0 & 0 \\ -1 & 0 & 0 & 0 \\ 0 & 0 & 0 & 1 \\ 0 & 0 & 1 & 0 \end{pmatrix}, \quad (7.79)$$

and the fact that the Ricci tensor vanishes in vacuum spacetimes. Similar manipulations give

$$B_{\hat{1}\hat{1}} = \frac{1}{2}\epsilon_1^{\hat{p}\hat{q}}R_{\hat{p}\hat{q}\hat{1}\hat{0}} = R_{2\hat{3}\hat{1}\hat{0}} = -iR_{m^*mln} = i(R_{lmnm^*} + R_{lm^*mn}) = i(-\Psi_2 + \Psi_2^*), \quad (7.80)$$

so we see that  $\mathcal{E}_{\hat{1}\hat{1}} + i\mathcal{B}_{\hat{1}\hat{1}} = 2\Psi_2$ . Similar computations give all of the entries of (7.76).

We will often have reason to consider the ‘‘horizon tendicity’’ and ‘‘horizon vorticity.’’ These

are the values of  $\mathcal{E}$  and  $\mathcal{B}$  projected normal to the two-dimensional event horizon of a spacetime containing a black hole, evaluated at the horizon. If the inward normal to the horizon is denoted  $\mathbf{N}$  and we choose the vector  $\mathbf{e}_{\hat{1}}$  such that it coincides with  $-\mathbf{N}$  at the horizon, then we immediately have the useful result

$$\Psi_2 = \frac{1}{2}(\mathcal{E}_{NN} + i\mathcal{B}_{NN}) = \frac{1}{2}(\mathcal{E}_{ij} + i\mathcal{B}_{ij})N^i N^j, \quad (7.81)$$

which we will use in our studies of analytic and numerical spacetimes containing horizons (papers II and III in this series).

## Bibliography

- [1] R. Owen, J. Brink, Y. Chen, J. D. Kaplan, G. Lovelace, K. D. Matthews, D. A. Nichols, M. A. Scheel, F. Zhang, A. Zimmerman, et al., *Phys. Rev. Lett.* **106**, 151101 (2011).
- [2] J. A. Wheeler, *Geometrodynamics* (Academic Press, New York, 1963).
- [3] J.A. Wheeler, in *Relativity, Groups and Topology (Les Houches Summer School, 1963)*, edited by B. DeWitt and C. DeWitt (Gordon and Breach, New York, 1964), pp. 325–520.
- [4] C. W. Misner, *Phys. Rev.* **118**, 1110 (1960).
- [5] D. R. Brill and R. W. Lindquist, *Phys. Rev.* **131**, 471 (1963).
- [6] S. Hahn and R. Lindquist, *Ann. Phys. (NY)* **29**, 304 (1964).
- [7] J. Weber, *Phys. Rev.* **117**, 306 (1960).
- [8] J. Centrella, J. G. Baker, B. J. Kelly, and J. R. van Meter, *Rev. Mod. Phys.* **82**, 3069 (2010).
- [9] B. C. Barish and R. Weiss, *Phys. Today* **52**, 44 (1999).
- [10] D. Sigg and the LIGO Scientific Collaboration, *Classical Quantum Gravity* **25**, 114041 (2008).
- [11] F. Acernese, M. Alshourbagy, P. Amico, F. Antonucci, S. Aoudia, et al., *Classical Quantum Gravity* **25**, 184001 (2008).
- [12] K. Kuroda and the LCGT Collaboration, *Classical Quantum Gravity* **27**, 084004 (2010).
- [13] G. M. Harry (for the LIGO Scientific Collaboration), *Classical Quantum Gravity* **27**, 084006 (2010).
- [14] C. W. Misner, K. S. Thorne, and J. A. Wheeler, *Gravitation* (Freeman, New York, New York, 1973).

- [15] L. Smarr, Phys. Rev. D **7**, 289 (1973).
- [16] D. Marolf, Gen. Rel. Grav. **31**, 919 (1999).
- [17] U. Jacob and T. Piran, Classical Quantum Gravity **23**, 4035 (2006).
- [18] J. D. Romano and R. H. Price, Classical Quantum Gravity **12**, 875 (1995).
- [19] M. Bondarescu, M. Alcubierre, and E. Seidel, Classical Quantum Gravity **19**, 375 (2002).
- [20] H. Chan, Classical Quantum Gravity **23**, 225 (2006).
- [21] L. Rezzolla, R. P. Macedo, and J. L. Jaramillo, Phys. Rev. Lett. **104**, 221101 (2010), [arxiv:1003.0873](https://arxiv.org/abs/1003.0873).
- [22] J. L. Jaramillo, R. P. Macedo, P. Moesta, and L. Rezzolla (2011), [arxiv:1108.0060](https://arxiv.org/abs/1108.0060).
- [23] J. L. Jaramillo, R. P. Macedo, P. Moesta, and L. Rezzolla (2011), [arxiv:1108.0061](https://arxiv.org/abs/1108.0061).
- [24] J. L. Jaramillo (2011), [arxiv:1108.2408](https://arxiv.org/abs/1108.2408).
- [25] J. W. Belcher and S. Olbert, Am. J. Phys. **71**, 220 (2003).
- [26] <http://www.black-holes.org/curQuadVortex.html>.
- [27] <http://www.black-holes.org/antiAliPoints.html>.
- [28] A. Zimmerman, D. A. Nichols, and F. Zhang, Phys. Rev. D **84**, 044037 (2011).
- [29] F. B. Estabrook and H. D. Wahlquist, Journal of Mathematical Physics **5**, 1629 (1964).
- [30] C. Schmid, Phys. Rev. D **79**, 064007 (2009).
- [31] R. Maartens and B. A. Bassett, Classical Quantum Gravity **15**, 705 (1998).
- [32] R. Penrose and W. Rindler, *Spinors and Space-time, Volume 1* (Cambridge University Press, Cambridge, 1992).
- [33] H. Stephani, D. Kramer, M. MacCallum, C. Hoenselaers, and E. Herlt, *Exact solutions of Einstein's field equations* (Cambridge University Press, Cambridge, UK, 2003).
- [34] H. Friedrich, Classical Quantum Gravity **13**, 1451 (1996).
- [35] A. Anderson, Y. Choquet-Bruhat, and J. W. York, Jr., Topol. Meth. Nonlin. Anal. **10**, 353 (1997).
- [36] K. S. Thorne, Rev. Mod. Phys. **52**, 299 (1980).

- [37] R. D. Blandford and K. S. Thorne, *Applications of Classical Physics* (California Institute of Technology, 2008), URL <http://www.pma.caltech.edu/Courses/ph136/yr2011/>.
- [38] J. D. Kaplan, D. A. Nichols, and K. S. Thorne, *Phys. Rev. D* **80**, 124014 (2009).
- [39] R. L. Forward, *Proc. IRE* **49**, 892 (1961).
- [40] D. Keppel, D. A. Nichols, Y. Chen, and K. S. Thorne, *Phys. Rev. D* **80**, 124015 (2009), [arXiv:0902.4077](https://arxiv.org/abs/0902.4077).
- [41] G. Lovelace, Y. Chen, M. Cohen, J. D. Kaplan, D. Keppel, K. D. Matthews, D. A. Nichols, M. A. Scheel, and U. Sperhake, *Phys. Rev. D* **82**, 064031 (2010), [arXiv:0907.0869](https://arxiv.org/abs/0907.0869).
- [42] K. S. Thorne, R. H. Price, and D. A. MacDonald, *Black Holes: The Membrane Paradigm* (Yale University Press, New Haven and London, 1986).
- [43] D. R. Fiske, J. G. Baker, J. R. van Meter, D.-I. Choi, and J. M. Centrella, *Phys. Rev. D* **71**, 104036 (pages 11) (2005).
- [44] R. Penrose, *Ann. Hum. Genet., Lond.* **42**, 435 (1979).
- [45] <http://www.black-holes.org/SpEC.html>.
- [46] E. Newman and R. Penrose, *J. Math. Phys.* **3**, 566 (1962).

## Chapter 8

# Visualizing Spacetime Curvature via Frame-Drag Vortexes and Tidal Tendexes

## II. Stationary Black Holes

When one splits spacetime into space plus time, the Weyl curvature tensor (which equals the Riemann tensor in vacuum) splits into two spatial, symmetric, traceless tensors: the *tidal field*  $\mathcal{E}$ , which produces tidal forces, and the *frame-drag field*  $\mathcal{B}$ , which produces differential frame dragging. In recent papers, we and colleagues have introduced ways to visualize these two fields: *tidal tendex lines* (integral curves of the three eigenvector fields of  $\mathcal{E}$ ) and their *tendicities* (eigenvalues of these eigenvector fields); and the corresponding entities for the frame-drag field: *frame-drag vortex lines* and their *vorticities*. These entities fully characterize the vacuum Riemann tensor. In this paper, we compute and depict the tendex and vortex lines, and their tendicities and vorticities, outside the horizons of stationary (Schwarzschild and Kerr) black holes; and we introduce and depict the black holes' *horizon tendicity and vorticity* (the normal-normal components of  $\mathcal{E}$  and  $\mathcal{B}$  on the horizon). For Schwarzschild and Kerr black holes, the horizon tendicity is proportional to the horizon's intrinsic scalar curvature, and the horizon vorticity is proportional to an extrinsic scalar curvature.

We show that, for horizon-penetrating time slices, all these entities ( $\mathcal{E}$ ,  $\mathcal{B}$ , the tendex lines and vortex lines, the lines' tendicities and vorticities, and the horizon tendicities and vorticities) are affected only weakly by changes of slicing and changes of spatial coordinates, within those slicing and coordinate choices that are commonly used for black holes. We also explore how the tendex and vortex lines change as the spin of a black hole is increased, and we find, for example, that as a black hole is spun up through a dimensionless spin  $a/M = \sqrt{3}/2$ , the horizon tendicity at its poles changes sign, and

an observer hovering or falling inward there switches from being stretched radially to being squeezed. At this spin, the tendex lines that stick out from the horizon's poles switch from reaching radially outward toward infinity, to emerging from one pole, swinging poloidally around the hole and descending into the other pole.

---

Originally published as Z. Zhang, A. Zimmerman, D. A. Nichols, Y. Chen, G. Lovelace, K. D. Matthews, R. Owen, and K. S. Thorne, Phys. Rev. D **86**, 084049 (2012). Copyright 2012 by the American Physical Society.

## 8.1 Motivation and Overview

It has long been known that, when one performs a 3+1 split of spacetime into space plus time, the Weyl curvature tensor  $C_{\alpha\beta\gamma\delta}$  gets split into two spatial, symmetric, traceless tensors: the so-called “electric” part,  $\mathcal{E}$ , which we call the *tidal field* (because it is responsible for the gravitational stretching and squeezing that generates tides), and the so-called “magnetic” part  $\mathcal{B}$ , which we call the *frame-drag field* (because it generates differential frame dragging, i.e., differential precession of gyroscopes).

Recently [1, 2], we and colleagues have proposed visualizing the tidal field by means of the integral curves of its three eigenvector fields, which we call *tendex lines*, and each line's eigenvalue, which we call its *tendicity*. These are very much like electric field lines and the magnitude of the electric field. Similarly, we have proposed visualizing the frame-drag field by integral curves of its three eigenvector fields, which we call *vortex lines*, and each curve's eigenvalue, which we call its *vorticity*. These are analogous to magnetic field lines and the magnitude of the magnetic field.

In our initial presentation [1] of these new concepts and their applications, we demonstrated that they can be powerful tools for visualizing the nonlinear dynamics of curved spacetime that is triggered by the inspiral, collision, and merger of binary black holes. We expect them also to be powerful visualization tools in other venues of nonlinear spacetime dynamics (geometrodynamics).

After our initial presentation [1], we have turned to a methodical exploration of these tools, in a series of papers in this journal. We are beginning in Papers I–III by applying these tools to “analytically understood” spacetimes, in order to gain intuition into the relation between their visual pictures and the analytics. Then in Paper IV and thereafter, we shall apply them to numerical spacetimes, looking for types of features we have already found, and retrieving their analytical origin.

In [2] (henceforth Paper I), using examples of nearly flat (linearized) spacetimes, we have shown that tendex lines and vortex lines can illustrate very well the spacetime dynamics around oscillating multipole sources, and we have connected various features of the field lines to physical understanding, and to the analytics. We found that, in the near zone of an oscillating multipole, the field lines are

attached to the source; in the transition zone, retardation effects cause the field lines to change character in understandable ways; and in the wave zone, the field lines approach those of freely propagating plane waves. In a supplementary study [3], some of us have classified the tendex and vortex lines of asymptotically flat space times at future null infinity according to the lines' topological features.

Recently, Dennison and Baumgarte [4] computed the tendex and vortex fields of approximate analytical solutions of boosted, non-spinning black holes (both isolated holes and those in binaries). Specifically, they computed an analytical initial-data solution of the Einstein constraint equations (in the form of that of Bowen and York [5]) that is accurate through leading order in a boost-like parameter of the black holes. Their results are an important analytical approximation to the vortex and tendex fields of a strong-field binary, and will likely be useful for understanding aspects of numerical-relativity simulations of binary black holes.

In Paper III, we shall explore the tendex and vortex lines, and their tendicities and vorticities, for quasinormal-mode oscillations of black holes—and shall see very similar behaviors to those we found, in the linearized approximation, in Paper I [2]. In preparation for this, we must explore in depth the application of our new tools to stationary (Schwarzschild and Kerr) black holes. That is the purpose of this Paper II.

In Paper IV we shall apply our tools to numerical simulations of binary-black-hole inspiral, collision, and merger, and shall use our linearized visualizations (Paper I), our stationary-black-hole visualizations (Paper II), our quasinormal-mode visualizations (Paper III), and Dennison and Baumgarte's visualizations [4] to gain insight into the fully nonlinear spacetime dynamics that the binary black holes trigger.

This paper is organized as follows: In Section 8.2, we briefly review the underlying theory of the  $3 + 1$  split of spacetime and our definitions of the tidal field  $\mathcal{E}$  and frame-drag field  $\mathcal{B}$  in [1, 2]. In Section 8.3, we introduce the concepts of *horizon tendicity* (the normal-normal component of  $\mathcal{E}$  on a black-hole horizon) and *horizon vorticity* (the normal-normal component of  $\mathcal{B}$ ), which, for stationary black holes, can be related to the real and imaginary parts of the Newman-Penrose Weyl scalar  $\Psi_2$  and are the horizon's scalar intrinsic curvature and scalar extrinsic curvature (aside from simple multiplicative factors).

In Section 8.4, we give formulae for the eigenvector and eigenvalue fields for the tidal field around a static (Schwarzschild) black hole, we draw pictures of the black hole's corresponding tendex lines, and we discuss the connection to the tidal stretching and squeezing felt by observers near a Schwarzschild hole. (The frame-drag field vanishes for a Schwarzschild hole.)

In Section 8.5, we turn on a slow rotation of the hole, we compute the frame-drag field  $\mathcal{B}$  generated by that rotation, we visualize  $\mathcal{B}$  via color-coded pictures of the horizon vorticity and the vortex lines, and we discover a spiraling of azimuthal tendex lines that is created by the hole's rotation. In this

section, we restrict ourselves to time slices (and the fields on those time slices) that have constant ingoing Eddington-Finkelstein time, and that therefore penetrate the horizon smoothly. (For the Schwarzschild black hole of Section 8.4, the tendex lines are the same in Schwarzschild slicing as in Eddington-Finkelstein slicing; the hole's rotation destroys this.)

In Section 8.6, we turn to rapidly rotating (Kerr) black holes, and explore how the vortex and tendex lines and the horizon vorticities and tendicities change when a hole is spun up to near maximal angular velocity. In these explorations, we restrict ourselves to horizon-penetrating slices, specifically: slices of constant Kerr-Schild time  $\tilde{t}$ , and the significantly different slices of constant Cook-Scheel, harmonic time  $\bar{t}$ . By using the same spatial coordinates in the two cases, we explore how the time slicing affects the tendex and vortex lines and the horizon tendicities and vorticities. There is surprisingly little difference, for the two slicings; the field lines and horizon properties change by only modest amounts when one switches from one slicing to the other (top row of Figure 8.6 compared with bottom row). By contrast, when we use non-horizon-penetrating Boyer-Lindquist slices (Appendix 8.A), the field lines are noticeably changed. In Section 8.6 we also explore how the vortex and tendex lines (plotted on a flat computer screen or flat sheet of paper) change when we change the spatial coordinates with fixed slicing (Figure 8.5). We find only modest changes, and they are easily understood and quite obvious once one understands the relationship between the spatial coordinate systems.

In Section 8.7, we briefly summarize our results. In three appendices, we present mathematical details that underlie some of the results in the body of the paper.

Throughout this paper we use geometrized units, with  $G = c = 1$ . Greek indexes are used for 4D spacetime quantities, and run from 0 to 3. Latin indexes are used for spatial quantities, and run from 1 to 3. Hatted indexes indicate components on an orthonormal tetrad. Capital Latin indexes from the start of the alphabet are used for angular quantities defined on spheres of some constant radius, and they generally run over  $\theta, \phi$ . We use signature  $(-+++)$  for the spacetime metric, and our Newman-Penrose quantities are defined appropriately for this signature, as in [6].

## 8.2 Tendex and Vortex Lines

In this section we will briefly review the  $3+1$  split and the definition of our spatial curvature quantities. A more detailed account is given in Paper I of this series [2]. To begin with, we split the spacetime using a unit timelike vector  $\vec{u}$ , which is everywhere normal to the slice of constant time. This vector can be associated with a family of observers who travel with four-velocity  $\vec{u}$ , and will observe the corresponding time slices as moments of simultaneity. We consider only vacuum spacetimes, where the Riemann tensor  $R_{\mu\nu\rho\sigma}$  is the same as the Weyl tensor  $C_{\mu\nu\rho\sigma}$ . The Weyl tensor has ten independent degrees of freedom, and these are encoded in two symmetric, traceless

spatial tensors  $\mathcal{E}$  and  $\mathcal{B}$ . These spatial tensors are formed by projection of the Weyl tensor  $C_{\mu\nu\rho\sigma}$  and (minus) its Hodge dual  $*C_{\mu\nu\rho\sigma}$  onto the spatial slices using  $u^\mu$ , and the spatial projection operator  $\gamma_\alpha^\mu$ . The projection operator is given by raising one index on the spatial metric of the slice,  $\gamma_{\mu\nu} = g_{\mu\nu} + u_\mu u_\nu$ . The resulting spatial projection of the Weyl tensor is given by an even-parity field called the “electric” part of  $C_{\mu\nu\rho\sigma}$  and also called the “tidal field”,

$$\mathcal{E}_{\alpha\beta} = \gamma_\alpha^\rho \gamma_\beta^\sigma C_{\rho\mu\sigma\nu} u^\mu u^\nu, \quad \text{i.e. } \mathcal{E}_{ij} = C_{i\hat{0}j\hat{0}}, \quad (8.1a)$$

and an odd-parity field called the “magnetic” part of  $C_{\mu\nu\rho\sigma}$  and also called the “frame-drag field”,

$$\mathcal{B}_{\alpha\beta} = -\gamma_\alpha^\rho \gamma_\beta^\sigma *C_{\rho\mu\sigma\nu} u^\mu u^\nu, \quad \text{i.e. } \mathcal{B}_{ij} = \frac{1}{2} \epsilon_{ipq} C_{j\hat{0}}^{pq}. \quad (8.1b)$$

Here, as usual, we give spatial (Latin) indexes to quantities after projection onto the spatial slices using  $\gamma_\alpha^\mu$ . We note that our conventions on the antisymmetric tensors are, when expressed in an orthonormal basis,  $\epsilon_{\hat{0}\hat{1}\hat{2}\hat{3}} = +1$  and  $\epsilon_{\hat{1}\hat{2}\hat{3}} = +1$ , with  $\epsilon_{ijk} = \epsilon_{\hat{0}ijk}$ .

The real, symmetric matrices,  $\mathcal{E}_{ij}$  and  $\mathcal{B}_{ij}$  are completely characterized by their orthogonal eigenvectors and corresponding eigenvalues. Note that, since each tensor is traceless, the sum of its three eigenvalues must vanish. Our program for generating field lines to visualize the spacetime curvature is to find these eigenvector fields by solving the eigenvalue problem,

$$\mathcal{E}^i_j v^j = \lambda v^i. \quad (8.2)$$

This results in three eigenvector fields for each of the two tensors  $\mathcal{E}$  and  $\mathcal{B}$ . These fields are vector fields on the spatial slice, and behave as usual under transformations of the spatial coordinates (but not changes of the slicing vector  $u^\mu$ ). By integrating the streamlines of these eigenvector fields, we arrive at a set of three *tendex* lines and three *vortex* lines. These lines are associated with the corresponding eigenvalues, the *tendicity* of each tendex line and *vorticity* of each vortex line. In visualizations, we color code each tendex or vortex line by its tendicity or vorticity.

This method of visualization represents physical information about the spacetime in a very natural way. It was shown in Paper I that the tidal field  $\mathcal{E}$  describes the local tidal forces between nearby points in the spacetime, and the less-familiar frame-drag field  $\mathcal{B}$  describes the relative precession of nearby gyroscopes. In the local Lorentz frame of two freely falling observers, separated by a spatial vector  $\xi^j$ , the differential acceleration experienced by the observers is

$$\Delta a^i = -\mathcal{E}^i_j \xi^j. \quad (8.3a)$$

If these same observers carry inertial guidance gyroscopes, each will measure the gyroscope of the

other to precess (relative to her own) with a vectorial angular velocity dictated by  $\mathcal{B}$ ,

$$\Delta\Omega^i = \mathcal{B}^i_{\ j}\xi^j. \quad (8.3b)$$

In particular, note that if one observer measures a clockwise precession of the other observer's gyroscope, the second observer will also measure the precession of the first to be clockwise.

The physical meaning of the tendex and vortex lines is then clear: if two observers have a small separation along a tendex line, they experience an acceleration along that line with a magnitude (and sign, in the sense of being pushed together or pulled apart) given by the value of the tendicity of that line, as governed by Eqs. (8.3a) and (8.2). In the same way, two observers separated along a vortex line experience differential frame dragging as dictated by Eqs. (8.3b) and (8.2) (with  $\mathcal{E}_{ij} \rightarrow \mathcal{B}_{ij}$ ).

### 8.3 Black-Hole Horizons; The Horizon Tendicity $\mathcal{E}_{NN}$ and Vorticity $\mathcal{B}_{NN}$

In many problems of physical interest, such as black-hole perturbations and numerical-relativity simulations using excision (as in the SpEC code [7]), black-hole interiors are not included in the solution domain. However, we are interested in structures defined on spacelike surfaces that penetrate the horizon, and, in order to retain the information describing the dynamics of spacetime in and near the black-hole region, we must define quasilocal quantities representing the tendicity and vorticity of the excised black-hole region.

We define the horizon tendicity and vorticity as follows: For a hypersurface-normal observer with 4-velocity  $\vec{u}$ , passing through a worldtube such as an event horizon or a dynamical horizon, the worldtube has an inward pointing normal  $\vec{N}$  orthogonal to  $\vec{u}$ , and two orthonormal vectors tangent to its surface,  $\vec{e}_2$  and  $\vec{e}_3$  (together these four vectors form an orthonormal tetrad). The horizon tendicity is defined as  $\mathcal{E}_{NN} = \mathcal{E}_{ij}N^iN^j$  and the horizon vorticity is  $\mathcal{B}_{NN} = \mathcal{B}_{ij}N^iN^j$ . Physically, they represent the differential acceleration and differential precession of gyroscopes, respectively, as measured by the observer, for two points separated in the direction of  $\vec{N}$ , and projected along that direction.

The horizon tendicity and vorticity have several interesting connections with other geometric quantities of 2-surfaces. In particular, they fit nicely into the Newman-Penrose (NP) formalism [8]. Rather than describe spacetime in terms of the tetrad  $\vec{u}$ ,  $\vec{N}$ ,  $\vec{e}_2$  and  $\vec{e}_3$ , the NP approach describes spacetime in terms of a null tetrad, with two null vectors  $\vec{l}$ , and  $\vec{n}$ , together with a complex spatial vector  $\vec{m}$  and its complex conjugate  $\vec{m}^*$ . It is convenient to adapt this tetrad to the 2-surface so

that it is given by

$$\begin{aligned}\vec{l} &= \frac{1}{\sqrt{2}}(\vec{u} - \vec{N}), & \vec{n} &= \frac{1}{\sqrt{2}}(\vec{u} + \vec{N}), \\ \vec{m} &= \frac{1}{\sqrt{2}}(\vec{e}_2 + i\vec{e}_3).\end{aligned}\tag{8.4}$$

On an event horizon,  $\vec{l}$  is tangent to the generators of the horizon and  $\vec{n}$  is the ingoing null normal. It is not difficult to show that in this tetrad the complex Weyl scalar  $\Psi_2$  is given by

$$\Psi_2 = C_{lmm^*n} = (\mathcal{E}_{NN} + i\mathcal{B}_{NN})/2,\tag{8.5}$$

where  $C_{lmm^*n}$  is the Weyl tensor contracted into the four different null vectors of the tetrad in the order of the indexes.

Penrose and Rindler [9] relate the NP quantities to curvature scalars of a spacelike 2-surface in spacetime. In turn, we can then connect their results to the horizon tendicity and vorticity. More specifically: Penrose and Rindler define a complex curvature of a 2-surface that equals

$$\mathcal{K} = \frac{1}{4}(\mathcal{R} + i\mathcal{X}).\tag{8.6}$$

Here  $\mathcal{R}$  is the intrinsic Ricci curvature scalar of a the 2D horizon and  $\mathcal{X}$  is a scalar extrinsic curvature (a curvature of the bundle of vector spaces normal to the two-surface in spacetime). This extrinsic curvature  $\mathcal{X}$  is related to the Hájíček field [10]  $\Omega_A = n^\mu \nabla_A l_\mu$  (where  $\nabla_A$  denotes the covariant derivative projected into the 2D horizon) by  $\mathcal{X} = \epsilon^{AB} \nabla_A \Omega_B$ , where  $\epsilon^{AB}$  is the antisymmetric tensor of the 2D horizon. In the language of differential forms,  $\mathcal{X}$  is the dual of the exterior derivative of the Hájíček 1-form.

Penrose and Rindler [9] show that for a general, possibly dynamical black hole,

$$\mathcal{K} = -\Psi_2 + \mu\rho - \lambda\sigma,\tag{8.7}$$

where  $\rho$ ,  $\sigma$ ,  $\mu$ , and  $\lambda$  are spin coefficients related to the expansion and shear of the null vectors  $\vec{l}$  and  $\vec{n}$ , respectively. This means that the horizon tendicity and vorticity are given by

$$\mathcal{E}_{NN} = -\mathcal{R}/2 + 2\Re[\mu\rho - \lambda\sigma],\tag{8.8a}$$

$$\mathcal{B}_{NN} = -\mathcal{X}/2 + 2\Im[\mu\rho - \lambda\sigma].\tag{8.8b}$$

In the limit of a stationary black hole (this paper),  $\rho$  and  $\sigma$  vanish, so

$$\mathcal{E}_{NN} = -\mathcal{R}/2, \quad \text{and} \quad \mathcal{B}_{NN} = -\mathcal{X}/2.\tag{8.9}$$

The 2D horizon of a stationary black hole has spherical topology, and the Gauss-Bonnet theorem requires that the integral of the scalar curvature  $\mathcal{R}$  over a spherical surface is  $8\pi$ ; accounting for factors of two, the integral of the horizon tendicity  $\mathcal{E}_{NN}$  over the horizon is  $-4\pi$  (the average value of the horizon tendicity will be negative). Stokes's theorem states that the integral of an exact form such as  $\mathcal{X}$  vanishes on a surface of spherical topology, and the horizon vorticity will also have zero average. In formulae:

$$\oint \mathcal{E}_{NN} dA = -4\pi, \quad \oint B_{NN} dA = 0 \quad (8.10)$$

for the horizon of a stationary black hole.

It is worth noting a few other examples in the literature where the complex curvature quantities (and as such, horizon tendicity and vorticity) have been used. The most common use of horizon vorticity (in a disguised form) is for computing the spin angular momentum associated with a quasilocal black-hole horizon. Following References [11–13], it has become common to compute black hole spin in numerical-relativity simulations using the following integral over the horizon:

$$J = -\frac{1}{8\pi} \oint K_{ij} N^i \varphi^j dA, \quad (8.11)$$

where  $K_{ij}$  is the extrinsic curvature of the spatial slice embedded in spacetime,  $\vec{N}$  is the inward-pointing unit normal vector to the horizon in the spatial slice, and  $\vec{\varphi}$  is a rotation-generating vector field tangent to the two-dimensional horizon surface. If  $\vec{\varphi}$  is a Killing vector, then one can show that  $J$  is conserved. In Reference [14], this was applied to binary-black-hole simulations with  $\vec{\varphi}$  given as a certain kind of approximate Killing vector that can be computed even on a deformed two-surface. In Reference [15], and independently in References [16, 17], this idea was refined. The quantity  $J$  can be shown to be *boost invariant* (independent of boosts of the spatial slice in the direction of  $\vec{N}$ ) if  $\vec{\varphi}$  is divergence-free. Hence, in References [15–17],  $\vec{\varphi}$  is restricted to have the form  $\varphi^A = \epsilon^{AB} \nabla_B \zeta$ , where  $\zeta$  is some scalar quantity on the two-surface (eventually fixed by a minimization problem for other components of the Killing equation). Once this substitution has been made, an integration by parts allows  $J$  to be written as:

$$J = \frac{1}{8\pi} \oint \mathcal{X} \zeta dA. \quad (8.12)$$

The quantity  $\zeta$  is fixed by a certain eigenvalue problem on the horizon 2-surface. On a round 2-sphere, the operator in this eigenproblem reduces to the conventional Laplacian, and  $\zeta$  can be shown to reduce to an  $\ell = 1$  spherical harmonic. Thus the quasilocal black-hole spin defined in References [15–17] can be thought of as the dipole part of the horizon vorticity.

There are simpler ways in which one can distill a measure of black hole spin from the concepts of horizon vorticity and tendicity. In Reference [17], an alternative measure of spin was made by comparing the maximum and minimum values of the horizon scalar curvature to formulae for a Kerr

black hole. This method has roots in older techniques by which spin is inferred from the horizon’s intrinsic geometry through measurements of geodesic path length (see, for example, References [18–20]). The method of computing spin by comparing horizon curvature extrema to Kerr formulae could be extended to use the extrinsic scalar curvature, or the horizon vorticity or tendicity (which differ from the scalar curvatures in dynamical situations). While such methods have the benefit of relative simplicity, their practical value in numerical relativity is weakened by an empirical sensitivity of the inferred spin to effects such as “junk” radiation and black hole tides [17, 21].

In Reference [22], it was shown that higher spherical-harmonic components of these horizon quantities provide natural definitions of *source multipoles* on axisymmetric isolated horizons. In References [23] and [24], this formalism was extended to less symmetric cases for use with numerical-relativity simulations, while attempting to introduce as little gauge ambiguity as possible into the process. Related applications of this formalism can be found in References [25, 26].

## 8.4 Schwarzschild Black Hole

In this section, we examine vortex and tendex lines for a non-rotating black hole with mass  $M$ . These lines, of course, depend on our choice of time slicing. As in the numerical simulations that are the focus of Paper IV, so also here, we shall use a slicing that penetrates smoothly through the black hole’s horizon. The slices of constant Schwarzschild time  $t$  for the hole’s Schwarzschild metric

$$ds^2 = -(1 - 2M/r)dt^2 + \frac{dr^2}{1 - 2M/r} + r^2 d\theta^2 + r^2 \sin^2 \theta d\phi^2 \quad (8.13)$$

do not penetrate the horizon smoothly; rather, they become singular as they approach the horizon. (Dennison and Baumgarte [4] compute the tidal and frame-drag fields of a Schwarzschild black hole in a slice of constant Schwarzschild time and in isotropic coordinates; see their paper for comparison.)

The simplest horizon-penetrating slices are those of constant ingoing Eddington-Finkelstein (EF) time

$$\tilde{t} = t + 2M \ln |r/2M - 1| . \quad (8.14)$$

The Schwarzschild metric (8.13), rewritten using EF coordinates  $\{\tilde{t}, r, \theta, \phi\}$ , takes the form

$$ds^2 = -\left(1 - \frac{2M}{r}\right) d\tilde{t}^2 + \frac{4M}{r} d\tilde{t} dr + \left(1 + \frac{2M}{r}\right) dr^2 + r^2 d\theta^2 + r^2 \sin^2 \theta d\phi^2 . \quad (8.15)$$

The observers who measure the tidal and frame-drag fields that lie in a slice of constant  $\tilde{t}$  have 4-velocities  $\vec{u} = -\alpha_{\text{EF}} \vec{\nabla} \tilde{t}$ , where  $\alpha_{\text{EF}} = 1/\sqrt{1 + 2M/r}$  is the normalizing lapse function. These

observers can be regarded as carrying the following orthonormal tetrad for use in their measurements:

$$\begin{aligned}\vec{u} &= \frac{1}{\sqrt{1+2M/r}} \left[ \left(1 + \frac{2M}{r}\right) \partial_t - \frac{2M}{r} \partial_r \right], & \vec{e}_{\hat{r}} &= \frac{1}{\sqrt{1+2M/r}} \partial_r, \\ \vec{e}_{\hat{\theta}} &= \frac{1}{r} \partial_\theta, & \vec{e}_{\hat{\phi}} &= \frac{1}{r \sin \theta} \partial_\phi.\end{aligned}\quad (8.16)$$

The nonzero components of the tidal field that they measure using this tetrad are

$$\mathcal{E}_{\hat{r}\hat{r}} = -\frac{2M}{r^3}, \quad \mathcal{E}_{\hat{\theta}\hat{\theta}} = \mathcal{E}_{\hat{\phi}\hat{\phi}} = \frac{M}{r^3}, \quad (8.17)$$

and the frame-drag field  $\mathcal{B}_{\hat{a}\hat{b}}$  vanishes. (See, e.g., Eq. (31.4b) of [27]).

Note that the black hole's tidal field (8.17) has the same form as the Newtonian tidal tensor outside of a spherical source. Since the tidal field is diagonal in this tetrad, its eigenvalues and its unit-normed eigenvectors are

$$\begin{aligned}\vec{V}_r &= \vec{e}_{\hat{r}}, & \vec{V}_\theta &= \vec{e}_{\hat{\theta}}, & \vec{V}_\phi &= \vec{e}_{\hat{\phi}}, \\ \lambda_r &= -\frac{2M}{r^3}, & \lambda_\theta &= \lambda_\phi = \frac{M}{r^3}.\end{aligned}\quad (8.18)$$

Because the two transverse eigenvalues  $\lambda_\theta$  and  $\lambda_\phi$  are degenerate, any vector in the transverse vector space spanned by  $\vec{e}_{\hat{\theta}}$  and  $\vec{e}_{\hat{\phi}}$  is a solution to the eigenvalue problem, and correspondingly, any curve that lies in a sphere of constant  $r$  can be regarded as a tendex line. However (as we shall see in the next section), when the black hole is given an arbitrarily small rotation about its polar axis  $\theta = 0$ , the degeneracy is broken, the non-degenerate transverse eigenvectors become  $\vec{e}_{\hat{\theta}}$  and  $\vec{e}_{\hat{\phi}}$ , and the transverse tendex lines become circles of constant latitude and longitude.

In Figure 8.1, we plot a few of these transverse tendex lines (giving them a blue color corresponding to positive tendicity  $\lambda_\theta > 0$  and  $\lambda_\phi > 0$ ), and also a few of the radial tendex lines (colored red for negative tendicity  $\lambda_r < 0$ ). Also shown are two human observers, one oriented along a blue tendex line (and therefore being squeezed by the tidal field) the other oriented along a red tendex line (and therefore being stretched).

## 8.5 Slowly Rotating Black Hole

### 8.5.1 Slicing and Coordinates

When the black hole is given a slow rotation with angular momentum per unit mass  $a$ , its metric (8.13) in Schwarzschild coordinates acquires an off-diagonal  $g_{t\phi}$  term:

$$ds^2 = -(1 - 2M/r)dt^2 + \frac{dr^2}{1 - 2M/r} + r^2 d\theta^2 + r^2 \sin^2 \theta d\phi^2 - \frac{4aM}{r} \sin^2 \theta dt d\phi \quad (8.19)$$

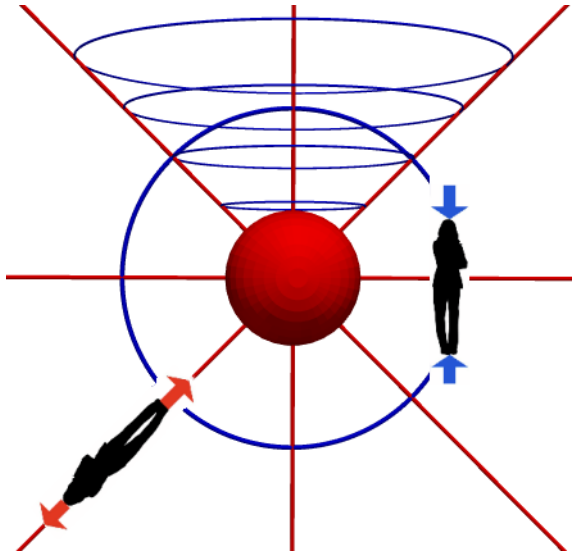


Figure 8.1: Tendex lines for a non-rotating (Schwarzschild) black hole. These lines are identical to those generated by a spherically symmetric mass distribution in the Newtonian limit. Also shown are observers who experience the tidal stretching and compression associated with the tendex lines.

[the Kerr metric in Boyer-Lindquist coordinates, Eq. (8.28) below, linearized in  $a$ ]. The slices of constant EF time  $\tilde{t} = t + 2M \ln |r/2M - 1|$  are still smoothly horizon penetrating, but the dragging of inertial frames (the off-diagonal  $g_{t\phi}$  term in the metric) causes the Schwarzschild  $\phi$  coordinate to become singular at the horizon. To fix this, we must “unwrap”  $\phi$ , e.g., by switching to

$$\tilde{\phi} = \phi + (a/2M) \ln |1 - 2M/r| , \quad (8.20)$$

thereby bringing the “slow-Kerr” metric (8.19) into the form

$$ds^2 = - \left(1 - \frac{2M}{r}\right) d\tilde{t}^2 + \frac{4M}{r} d\tilde{t}dr + \left(1 + \frac{2M}{r}\right) dr^2 + r^2 d\theta^2 + r^2 \sin^2 \theta d\tilde{\phi}^2 - \frac{4aM}{r} \sin^2 \theta d\tilde{t}d\tilde{\phi} - 2a\sqrt{1 + 2M/r} \sin^2 \theta drd\tilde{\phi} \quad (8.21)$$

[Eq. (8.45) below, linearized in  $a$ ], which is well behaved at and through the horizon. The observers who move orthogonally to the slices of constant  $\tilde{t}$  have 4-velocity  $\vec{u}$  and orthonormal basis the same as for a non-rotating black hole, Eq. (8.16), except that  $\vec{e}_{\hat{r}}$  is changed to

$$\vec{e}_{\hat{r}} = \frac{1}{\sqrt{1 + 2M/r}} \left[ \partial_r + \frac{a}{r^2} (1 + 2M/r) \partial_{\tilde{\phi}} \right] \quad (8.22)$$

[Eq. (8.46) below, linearized in  $a$ ].

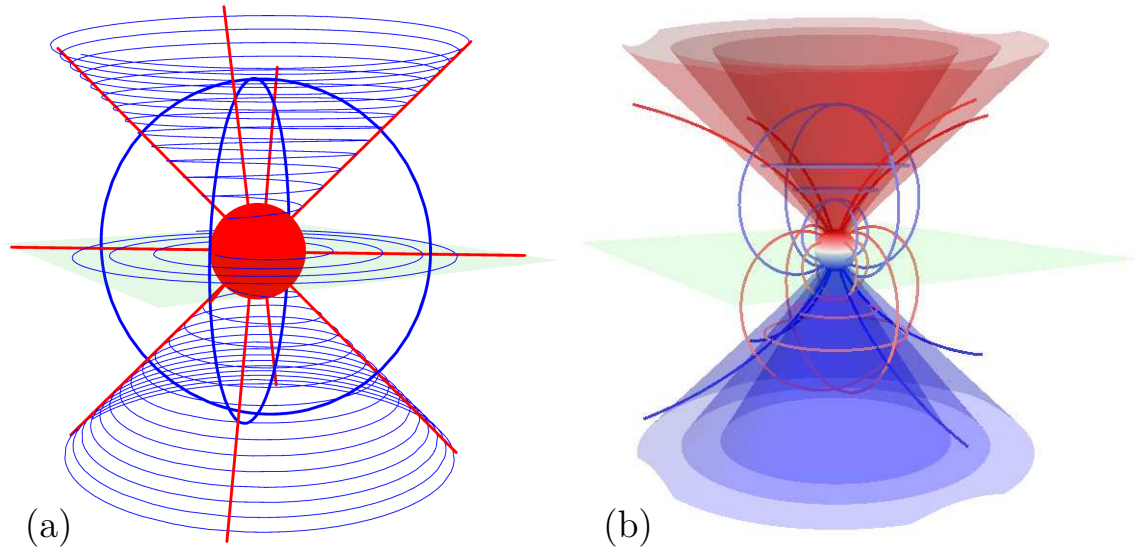


Figure 8.2: (a) Tendex lines, and (b) vortex lines for a slowly rotating (Kerr) black hole. Here we take  $a/M = 0.1$ . The horizon is color coded by its tendicity  $\mathcal{E}_{NN}$  in (a) (uniformly red signifying negative tendicity) and vorticity  $\mathcal{B}_{NN}$  in (b), and the field lines are color coded by the sign of their tendicity or vorticity (blue for positive, red for negative). That is, the radial tendex lines, the vortex lines emerging from the north pole and the azimuthal vortex lines on the bottom carry negative tendicity or vorticity, while all other lines have positive tendicity or vorticity.) In (a), the spiraling lines have been made to spiral more loosely by multiplying the rate of change in the  $r$  direction by five. The semi-transparent cone-like surfaces emerging from the horizon's north and south polar regions show where the magnitude of the vorticity at a given radius has fallen to 80% (outermost cones), 85%, and 90% (innermost cones) of the polar magnitude. We identify the innermost cone (the 90% contour) as the edge of the frame-drag vortex. The equatorial plane is shown for reference in both panels.

### 8.5.2 Frame-drag Field and Deformed Tendex Lines

The slow rotation gives rise to a frame-drag field

$$\mathcal{B}_{\hat{r}\hat{r}} = \frac{-6aM \cos \theta}{r^4}, \quad \mathcal{B}_{\hat{r}\hat{\theta}} = \mathcal{B}_{\hat{\theta}\hat{r}} = \frac{-3aM \sin \theta}{r^4 \sqrt{1 + 2M/r}}, \quad \mathcal{B}_{\hat{\theta}\hat{\theta}} = \mathcal{B}_{\hat{\phi}\hat{\phi}} = \frac{3aM \cos \theta}{r^4} \quad (8.23)$$

[Eq. (8.40b) linearized in  $a/M$ ] that lives in the slices of constant EF time  $\tilde{t}$ . This field's vortex lines, shown in Figure 8.2b, are poloidal and closely resemble those of a spinning point mass (a “current dipole”) in the linearized approximation to general relativity (Figure 3 of Paper I [2]). At radii  $r \gg M$ , the field asymptotes to that of a linearized current dipole.

The rotating hole's horizon vorticity is  $\mathcal{B}_{NN} = \mathcal{B}_{\hat{r}\hat{r}} = -6(aM/r^4) \cos \theta$ , which is negative in the north polar regions and positive in the south polar regions. Correspondingly, there is a counterclockwise frame-drag vortex sticking out of the hole's north pole, and a clockwise one sticking out of its south pole. We identify the edge of each vortex, at radius  $r$ , as the location where the vorticities of

the vortex lines that emerge from the hole at the base of the vortex, fall (as a function of  $\theta$  at fixed  $r$ ) to 90% of the on-pole vorticity. The vortex edges are shown, in Figure 8.2, as semi-transparent surfaces; for comparison we also show where the vorticity has fallen to 85% and 80% of the on-pole vorticity at a given radius  $r$ .

The hole's (small) spin not only generates a frame-drag field  $\mathcal{B}_{ij}$ ; it also modifies, slightly, the hole's tidal field  $\mathcal{E}_{ij}$  and its tendex lines. However, the spin does not modify the field's tendicities, which (to first order in  $a/M$ ) remain  $\lambda_r^\mathcal{E} = -2M/r^3$ ,  $\lambda_\theta^\mathcal{E} = \lambda_\phi^\mathcal{E} = M/r^3$  [Eq. (8.18)]. The modified unit tangent vectors to the tendex lines are

$$\vec{V}_r^\mathcal{E} = \vec{e}_{\hat{r}} - \frac{2Ma \sin \theta}{r^2 \sqrt{1 + 2M/r}} \vec{e}_{\hat{\phi}}, \quad \vec{V}_\phi^\mathcal{E} = \vec{e}_{\hat{\phi}} + \frac{2Ma \sin \theta}{r^2 \sqrt{1 + 2M/r}} \vec{e}_{\hat{r}}, \quad \vec{V}_\theta^\mathcal{E} = \vec{e}_{\hat{\theta}}. \quad (8.24)$$

Correspondingly, there is a slight (though hardly noticeable) bending of the radial tendex lines near the black hole, and—more importantly—the azimuthal tendex lines (the ones tangent to  $\vec{V}_\phi^\mathcal{E}$ ) cease to close. Instead, the azimuthal tendex lines spiral outward along cones of fixed  $\theta$ , as shown in Figure 8.2a. Since these lines have been only slightly perturbed from closed loops, they spiral quite tightly, appearing as solid cones. In order to better visualize these spiraling lines, we have increased their outward ( $r$  directed) rate of change by a factor of five as compared to the axial rate of change in Figure 8.2a.

### 8.5.3 Robustness of Frame-Drag Field and Tendex-Line Spiral

The two new features induced by the hole's small spin (the frame-drag field, and the spiraling of the azimuthal tendex lines) are, in fact, robust under changes of slicing. We elucidate the robustness of the tendex spiral in Appendix 8.C. We here elucidate the robustness of the frame-drag field and its vortex lines and vorticities:

Suppose that we change the time function  $\tilde{t}$ , which defines our time slices, by a small fractional amount of order  $a/M$ ; i.e., we introduce a new time function

$$t' = \tilde{t} + \xi(r, \theta), \quad (8.25)$$

where  $\tilde{t}$  is EF time and  $\xi$  has been chosen axisymmetric and time-independent, so it respects the symmetries of the black hole's spacetime. Then “primed” observers who move orthogonal to slices of constant  $t'$  will be seen by the EF observers (who move orthogonal to slices of constant  $\tilde{t}$ ) to have small 3-velocities that are poloidal,  $\mathbf{v} = v^{\hat{r}} \mathbf{e}_{\hat{r}} + v^{\hat{\theta}} \mathbf{e}_{\hat{\theta}}$ . The Lorentz transformation from the EF reference frame to the primed reference frame at some event in spacetime induces a change of the frame-drag field given by

$$\delta \mathcal{B} = -2(\mathbf{v} \times \mathcal{E})^S \quad (8.26)$$

[see, e.g., Eq. (B12) of [28], linearized in small  $\mathbf{v}$ ], where the  $S$  means symmetrize. Inserting the EF tidal field (8.17) and the poloidal components of  $\mathbf{v}$ , we obtain as the only nonzero components of  $\delta\mathcal{B}$

$$\delta\mathcal{B}_{\hat{r}\hat{\phi}} = \delta\mathcal{B}_{\hat{\phi}\hat{r}} = -(3M/r^3)v^{\hat{\theta}}. \quad (8.27)$$

This axisymmetric, slicing-induced change of the frame-drag field does not alter the nonzero components of the frame-drag field in Eq. (8.23); it only introduces a change in the component  $\mathcal{B}_{\hat{r}\hat{\phi}}$ . This is a sense in which we mean the frame-drag field is robust. A simple calculation can show that one vorticity is unchanged,  $\mathcal{B}_{\hat{\phi}\hat{\phi}} = 3aM \cos\theta/r^4$ , but the corresponding vortex line will no longer be a circle of constant  $(r, \theta)$ . Instead, it will wind on a sphere of constant  $r$  relative to these closed azimuthal circles with an angle whose tangent is given by  $v^{\hat{\theta}} \csc\theta \sqrt{r^2 + 2Mr}$ . The poloidal vortex lines must twist azimuthally to remain orthogonal to these spiralling azimuthal lines, as well.

Although we will not see this specific kind of spiraling vortex lines in the next section on rapidly rotating Kerr black holes, we will see a different spiraling of the azimuthal vortex lines: spiraling on cones of constant  $\theta$ . We describe the reason for this in Appendix 8.C.

## 8.6 Rapidly Rotating (Kerr) Black Hole

We shall now explore a rapidly rotating black hole described by the precise Kerr metric.

### 8.6.1 Kerr Metric in Boyer-Lindquist Coordinates

The Kerr metric is usually written in Boyer-Lindquist (BL) coordinates  $\{t, r, \theta, \phi\}$ , where it takes the form

$$ds^2 = -\left(1 - \frac{2Mr}{\Sigma}\right) dt^2 + \frac{\Sigma}{\Delta} dr^2 + \Sigma d\theta^2 + \frac{\sin^2\theta}{\Sigma} Ad\phi^2 - \frac{4Mar \sin^2\theta}{\Sigma} dt d\phi, \\ \Sigma = r^2 + a^2 \cos^2\theta, \quad \Delta = r^2 - 2Mr + a^2, \quad A = (r^2 + a^2)^2 - a^2 \Delta \sin^2\theta. \quad (8.28)$$

Because the slices of constant  $t$  are singular at the horizon (and therefore not of much interest to us), we relegate to Appendix 8.A the details of their tidal and frame-drag fields, and their vortex and tendex lines.

### 8.6.2 Horizon-Penetrating Slices

In our study of Kerr black holes, we shall employ two different slicings that penetrate the horizon smoothly: surfaces of constant Kerr-Schild time coordinate  $\tilde{t}$ , and surfaces of constant Cook-Scheel time coordinate  $\bar{t}$ . By comparing these two slicings' tendex lines with each other, and also their vortex lines with each other, we shall gain insight into the lines' slicing dependence.

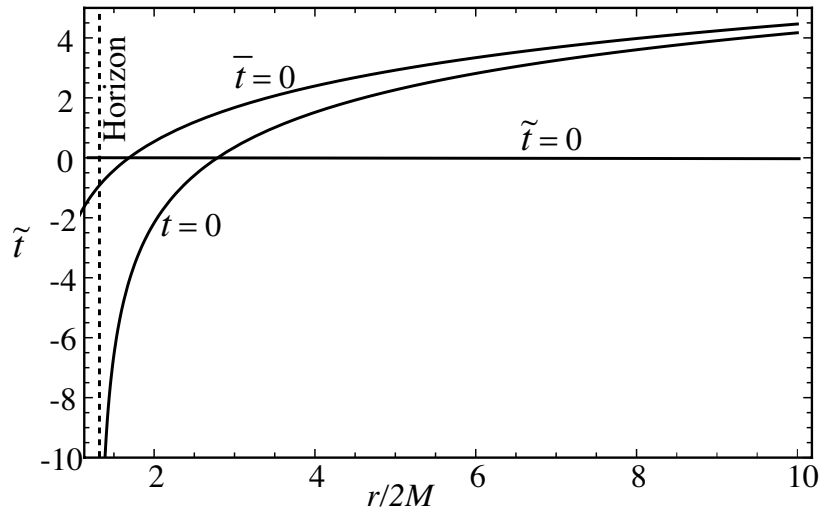


Figure 8.3: Slices of constant Boyer-Lindquist time  $t$ , Kerr-Schild time  $\tilde{t}$ , and Cook-Scheel time  $\bar{t}$ , drawn in a Kerr-Schild spacetime diagram for a black hole with  $a/M = 0.95$ .

The Kerr-Schild ([29, 30], see also, e.g., Exercise 33.8 of [27]) time coordinate (also sometimes called ingoing-Kerr time) is defined by

$$\tilde{t} = t + r_* - r, \quad \text{where} \quad \frac{dr_*}{dr} = \frac{r^2 + a^2}{\Delta}. \quad (8.29)$$

The Cook-Scheel [31] time coordinate is

$$\bar{t} = t + \frac{r_+^2 + a^2}{r_+ - r_-} \ln \left| \frac{r - r_+}{r - r_-} \right| = \tilde{t} + 2M \ln \left| \frac{2M}{r - r_-} \right|, \quad (8.30)$$

(see Eqs. (19) and (20) of [31]) where  $r_+$  is the value of the Boyer-Lindquist radial coordinate  $r$  at the event horizon, and  $r_-$  is its value at the (inner) Cauchy horizon:

$$r_{\pm} = M \pm \sqrt{M^2 - a^2}. \quad (8.31)$$

Figure 8.3 shows the relationship between these slicings for a black hole with  $a/M = 0.95$ . In this figure, horizontal lines are surfaces of constant Kerr-Schild time  $\tilde{t}$ . Since  $t$ ,  $\bar{t}$  and  $\tilde{t}$  differ solely by functions of  $r$ , the surfaces of constant Cook-Scheel time  $\bar{t}$  are all parallel to the  $\bar{t} = 0$  surface shown in the figure, and the surfaces of constant Boyer-Lindquist time  $t$  are all parallel to the  $t = 0$  surface. The Kerr-Schild and Cook-Scheel surfaces penetrate the horizon smoothly. By contrast, the Boyer-Lindquist surfaces all asymptote to the horizon in the deep physical past, never crossing it; i.e., they become physically singular at the horizon.

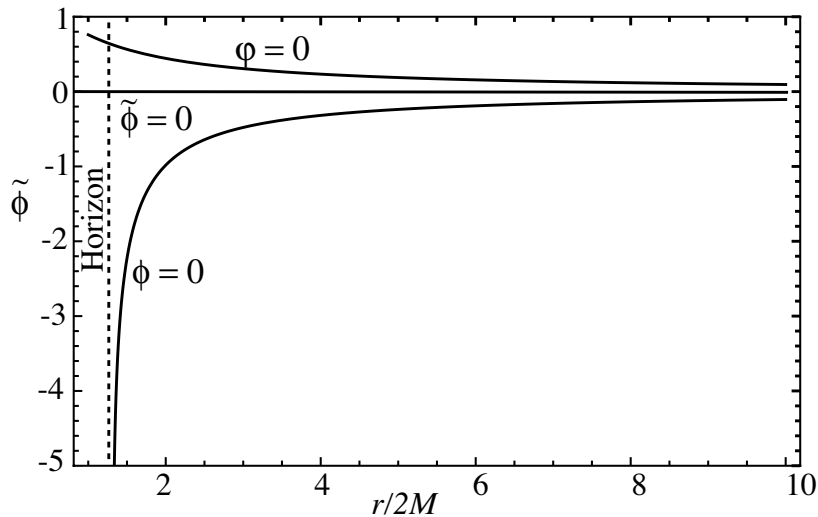


Figure 8.4: Curves of constant Boyer-Lindquist angle  $\phi$ , Kerr-Schild angle  $\varphi$ , and ingoing-Kerr angle  $\tilde{\phi}$  for a black hole with  $a/M = 0.95$ .

### 8.6.3 Horizon-Penetrating Coordinate Systems

Not only is the Boyer-Lindquist time coordinate  $t$  singular at the event horizon; so is the Boyer-Lindquist azimuthal angular coordinate  $\phi$ . It winds around an infinite number of times as it asymptotes to the horizon. We shall use two different ways to unwind it, associated with two different horizon-penetrating angular coordinates: The ingoing-Kerr coordinate

$$\tilde{\phi} = \phi + \frac{a}{r_+ - r_-} \ln \left| \frac{r - r_+}{r - r_-} \right| = \phi + \int_r^\infty \frac{a}{\Delta} dr, \quad (8.32)$$

and the Kerr-Schild coordinate

$$\varphi = \tilde{\phi} - \tan^{-1}(a/r). \quad (8.33)$$

Figure 8.4 shows the relationship of these angular coordinates for a black hole with  $a/m = 0.95$ . Notice that: (i) all three angular coordinates become asymptotically the same as  $r \rightarrow \infty$ ; (ii) the two horizon-penetrating coordinates, ingoing-Kerr  $\tilde{\phi}$  and Kerr-Schild  $\varphi$ , differ by less than a radian as one moves inward to the horizon; and (iii) the Boyer-Lindquist coordinate  $\phi$  plunges to  $-\infty$  (relative to horizon-penetrating coordinates) as one approaches the horizon, which means it wraps around the horizon an infinite number of times.

In the literature on Kerr black holes, four sets of spacetime coordinates are often used:

- **Boyer-Lindquist coordinates**,  $\{t, r, \theta, \phi\}$ . These are the coordinates in Section 8.6.1.
- **Ingoing-Kerr coordinates**,  $\{\tilde{t}, r, \theta, \tilde{\phi}\}$ . Often in this case  $\tilde{t}$  is replaced by a null coordinate,

$v = \tilde{t} + r$  (curves  $v = \text{const}$ ,  $\theta = \text{const}$ , and  $\tilde{\phi} = \text{const}$  are ingoing null geodesics).

- Quasi-Cartesian ***Kerr-Schild coordinates***,  $\{\tilde{t}, x, y, z\}$  and their cylindrical variant  $\{\tilde{t}, \varpi, z, \varphi\}$ . Here

$$\begin{aligned} x + iy &= (r + ia)e^{i\tilde{\phi}} \sin \theta, & z &= r \cos \theta, \\ \varpi &= \sqrt{x^2 + y^2} = \sqrt{r^2 + a^2} \sin^2 \theta, \\ \varphi &= \arctan(y/x) = \tilde{\phi} + \arctan(a/r). \end{aligned} \quad (8.34)$$

The Kerr-Schild spatial coordinates  $\{x, y, z\}$  resemble the coordinates typically used in numerical simulations of binary black holes at late times, when the merged hole is settling down into its final, Kerr state. These coordinate systems resemble each other in the senses that (i) both are quasi-Cartesian, and (ii) for a fast-spinning hole, the event horizon in both cases, when plotted in the coordinates being used, looks moderately oblate. For this reason, in our study of Kerr black holes, we shall focus our greatest attention on Kerr-Schild coordinates. The Kerr metric, written in Kerr-Schild coordinates, has the form

$$ds^2 = \left( \eta_{\mu\nu} + \frac{2Mr^3}{r^4 + a^2 z^2} k_\mu k_\nu \right) dx^\mu dx^\nu, \quad k_\mu = \left( 1, \frac{rx + ay}{r^2 + a^2}, \frac{ry - ax}{r^2 + a^2}, \frac{z}{r} \right), \quad (8.35)$$

where  $r$  is the Boyer-Lindquist radial coordinate, and is the larger root of

$$x^2 + y^2 + z^2 = r^2 + a^2 \left( 1 - \frac{z^2}{r^2} \right), \quad (8.36)$$

and  $\eta_{\mu\nu}$  is the usual flat Minkowski metric.

- ***Cook-Scheel harmonic coordinates*** [31],  $\{\bar{t}, \bar{x}, \bar{y}, \bar{z}\}$  where  $\bar{t}$  is given by Eq. (8.30), while the spatial coordinates are defined by

$$\bar{x} + i\bar{y} = [r - M + ia] e^{i\tilde{\phi}} \sin(\theta), \quad (8.37)$$

$$\bar{z} = [r - M] \cos(\theta). \quad (8.38)$$

These coordinates are harmonic in the sense that the scalar wave operator acting on them vanishes. In these coordinates, the event horizon of a spinning black hole is more oblate than in Kerr-Schild coordinates—and much more oblate for  $a/M$  near unity.

### 8.6.4 Computation of Tendex and Vortex Lines, and their Tendicities and Vorticities

Below we show pictures of tendex and vortex lines, color coded with their tendicities and vorticities, for our two horizon-penetrating slicings and using our three different sets of spatial coordinates. In all cases we have computed the field lines and their eigenvalues numerically, beginning with analytical formulas for the metric. More specifically, after populating a numerical grid using analytical expressions for the metric, we numerically compute  $\mathcal{E}_{ij}$  and  $\mathcal{B}_{ij}$ , as well as their eigenvalues and eigenvectors. A numerical integrator is then utilized to generate the tendex and vortex lines. Finally, we apply analytical transformations that take these lines to whatever spatial coordinate system we desire.

Although not required for the purpose of generating the figures in the following sections, it is nevertheless possible to find analytical expressions for  $\mathcal{E}_{ij}$  and  $\mathcal{B}_{ij}$ , and subsequently their eigenvalues and eigenvectors. These expressions provide valuable insights into the behavior of the tendex and vortex lines, and we present such results for the ingoing-Kerr coordinates in Appendix 8.B.

### 8.6.5 Kerr-Schild Slicing: Tendex and Vortex Lines in Several Spatial Coordinate Systems

Once the slicing is chosen, the tidal and frame-drag fields, and also the tendex and vortex lines and their tendicities and vorticities, are all fixed as geometric, coordinate-independent entities that live in a slice. If we could draw an embedding diagram showing the three-dimensional slice isometrically embedded in a higher-dimensional flat space, then we could visualize the tendex and vortex lines without the aid of a coordinate system. However, the human mind cannot comprehend embedding diagrams in such high-dimensional spaces, so we are forced to draw the tendex and vortex lines in some coordinate system for the slice, in a manner that makes the coordinate system look like it is one for flat space.

Such a coordinate-diagram plot of the lines makes them look coordinate dependent—i.e., their shapes depend on the coordinate system used. Nevertheless, the lines themselves are geometrically well-defined, independent of coordinate system, and they map appropriately between them. The visual features of these lines are also qualitatively similar in reasonable coordinate systems.

Figure 8.5 is an important example. It shows the tendex lines (left column of plots) and vortex lines (right column of plots) for a fast-spinning Kerr black hole, with  $a = 0.95M$ . We have also colored the horizon of the black hole according to its horizon tendicity and vorticity, respectively. In all cases the slicing is Kerr-Schild; i.e., the lines lie in a slice of constant  $\tilde{t}$ . The three rows of figures are drawn in three different spatial coordinate systems: ingoing-Kerr, Kerr-Schild, and Cook-Scheel.

Notice the following important features of this figure:

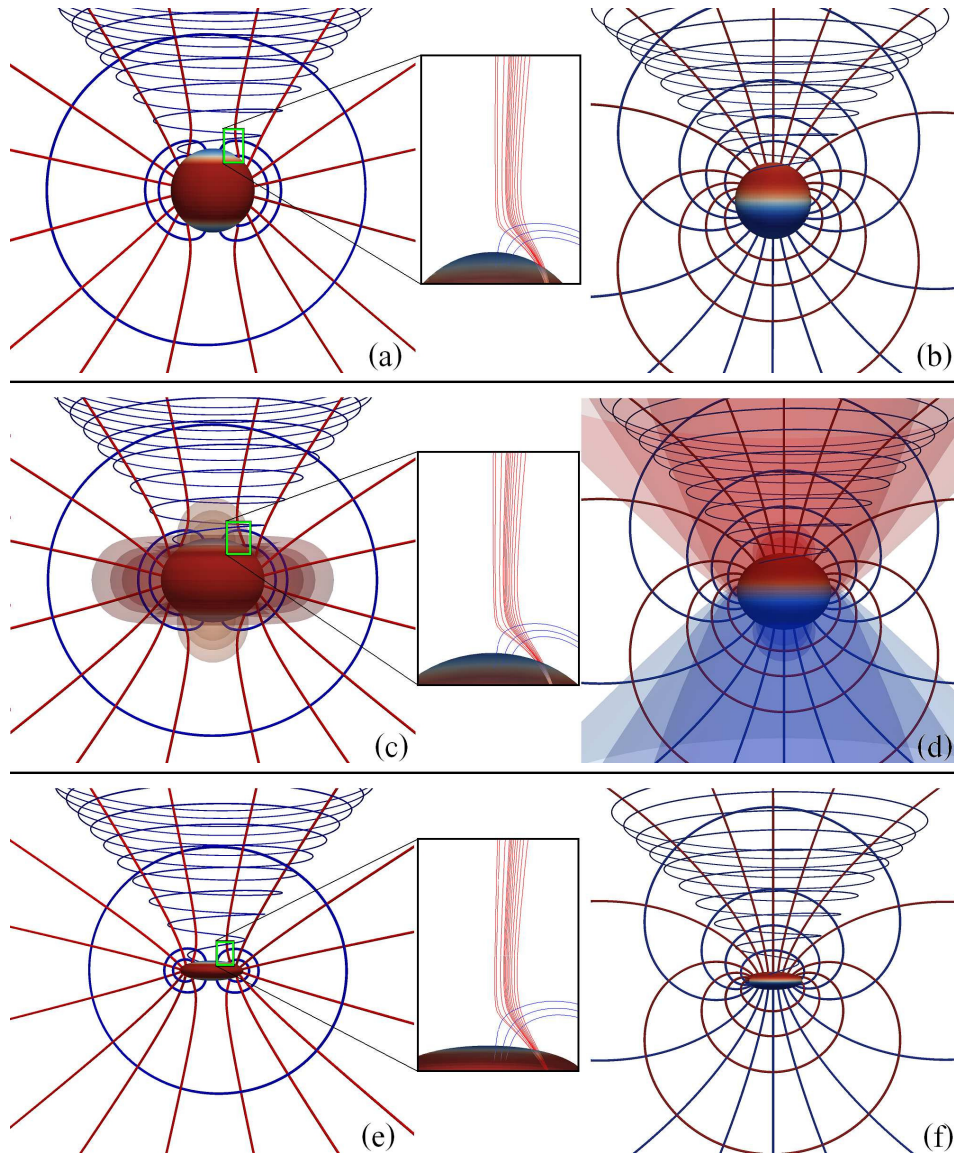


Figure 8.5: Kerr black hole with  $a/M = 0.95$  in *Kerr-Schild slicing*, drawn in three different spatial coordinate systems. The left and center columns of drawings [panels (a), (c), (e)] show tendex lines; the right column of drawings [panels (b), (d), (f)] show vortex lines. The three rows, from top downward, use ingoing-Kerr spatial coordinates  $\{r, \theta, \tilde{\phi}\}$  [panels (a) and (b)], Kerr-Schild spatial coordinates  $\{x, y, z\}$  [panels (c) and (d)], and Cook-Scheel spatial coordinates  $\{\tilde{x}, \tilde{y}, \tilde{z}\}$  [panels (e) and (f)]. In all cases, the lines with positive tendicity or vorticity are colored blue; those with negative tendicity or vorticity are colored red. The horizon is shown with its horizon tendicity (left column of drawings) and horizon vorticity (right column) color coded from dark blue for strongly positive to dark red for strongly negative. (Horizon tendicity is negative near the equator and positive near the poles. Vorticity on the other hand transitions from being negative on top to positive on the bottom.) In Kerr-Schild coordinates [panels (c) and (d)], we have also shown as semi-transparent surfaces, contours of  $\tilde{r}^3$  times tendicity and  $\tilde{r}^4$  times vorticity, where  $\tilde{r}^2 = x^2 + y^2 + z^2$  for Kerr-Schild spatial coordinates. In panel (c), the innermost equatorial contour has the most negative tendicity while the others have 90%, 80%, 30%, 20%, and 10% this value, and the innermost polar contour has the least negative tendicity. In panel (d) the contour with the most negative vorticity consists of the innermost red cone and the outermost red bubble (at the north pole), and the others are at 90% and 80% of this value. The blue contours of panel (d) (at the bottom half of that panel) are arranged similarly but with positive vorticity.

- As expected, the qualitative features of the tendex lines are independent of the spatial coordinates. The only noticeable differences from one coordinate system to another are a flattening of the strong-gravity region near the hole as one goes from ingoing-Kerr coordinates (upper row of panels) to Kerr-Schild coordinates (center row of panels) and then a further flattening for Cook-Scheel coordinates (bottom row of panels).
- The azimuthal (toroidal) tendex and vortex lines (those that point predominantly in the  $\vec{e}_{\tilde{\phi}}$  direction) spiral outward from the horizon along cones of constant  $\theta$ , as for the tendex lines of a slowly spinning black hole [cf. the form of  $\vec{V}_{\tilde{\phi}}$  in Eqs. (8.50)]. As we shall discuss in Appendix 8.C, this is a characteristic of a large class of commonly used, horizon-penetrating slicings of spinning black holes.
- All the poloidal tendex and vortex lines have (small) azimuthal ( $\tilde{\phi}$ ) components, which do not show up in this figure; see the  $\vec{e}_{\tilde{\phi}}$  components of the eigenvectors  $\vec{V}_r^{\mathcal{E}}$ ,  $\vec{V}_{\theta}^{\mathcal{E}}$ ,  $\vec{V}_-^{\mathcal{B}}$  and  $\vec{V}_+^{\mathcal{B}}$  in Eqs. (8.50) and (8.51).
- Left column of drawings: For this rapidly spinning black hole, the horizon tendicity is positive (blue) in the north and south polar regions, and negative (red) in the equatorial region, by contrast with a slowly spinning hole, where the horizon tendicity is everywhere negative (Figure 8.2). Correspondingly, a radially oriented person falling into a polar region of a fast-spinning hole gets *squeezed* from head to foot, rather than stretched, as conventional wisdom demands. The relationship  $\mathcal{E}_{NN} = -\mathcal{R}/2$  between the horizon's tendicity and its scalar curvature tells us that this peculiar polar feature results from the well-known fact that, when the spin exceeds  $a/M = \sqrt{3}/2 \approx 0.8660$ , the scalar curvature goes negative near the poles, at angles  $\theta$  satisfying  $2(a/M)^2 \cos^2 \theta > 1 + \sqrt{1 - (a/M)^2}$ . This negative scalar curvature is also responsible for the fact that it is impossible to embed the horizon's 2-geometry in a 3-dimensional Euclidean space when the spin exceeds  $a/M = \sqrt{3}/2$  [32].
- Left column of drawings: The blue (positive tendicity) tendex lines that emerge from the north polar region sweep around the hole, just above the horizon, and descend into the south polar region. In order to stay orthogonal to these blue (squeezing) tendex lines, the red (stretching) lines descending from radial infinity get deflected away from the horizon's polar region until they reach a location with negative tendicity (positive scalar curvature), where they can attach to the horizon; see the central panels, which are enlargements of the north polar region for the left panels.
- Right column of drawings: The vortex-line structure for this fast-spinning black hole is very similar to that for the slow-spinning hole of Figure 8.2, and similar to that for a spinning point mass in the linear approximation to general relativity (Figure 3 of Paper I [2]). The

principal obvious change is that the azimuthal vortex lines are not closed; instead, they spiral away from the black hole, like the azimuthal tendex lines.

- Right column of drawings: Most importantly, as for a slow-spinning black hole, there are two vortices (regions of strong vorticity): as a counterclockwise vortex emerging from the north polar region, and a clockwise vortex emerging from the south polar region. As we shall see in Paper IV, when two spinning black holes collide and merge, these vortices sweep around, emitting gravitational waves. In Figure 8.5(d), these vortices are indicated by contours of  $\tilde{r}^4$  times vorticity, where  $\tilde{r}^2 = x^2 + y^2 + z^2$  for Kerr-Schild coordinates  $\{x, y, z\}$ . Notice in particular that each contour consists of one cone together with one bubble attached to the horizon, with the bubbles enclosing the polar regions excluding them from the vortices. This is a feature not seen for the slow-spinning case.

### 8.6.6 Slicing-Dependence of Tendex and Vortex Lines

To explore how a Kerr black hole's vortex and tendex lines depend on the choice of slicing, we focus in Figure 8.6 on a black hole with  $a/M = 0.875$ , viewed in a slice of constant Kerr-Schild time,  $\tilde{t} = \text{constant}$ , and in a slice of constant Cook-Scheel harmonic time,  $\bar{t} = \text{constant}$ . In the two slices, we use the same spatial coordinates: Kerr-Schild. (We chose  $a/M = 0.875$ , rather than the 0.95 that we used for exploring spatial coordinate dependence, because it is simpler to handle numerically in the Cook-Scheel slicing.)

The most striking aspect of Figure 8.6 is the close similarity of the tendex lines (left column of drawings) in the two slicings (upper and lower drawings), and also the close similarity of the vortex lines (right column of drawings) in the two slicings (upper and lower). There appears to be very little slicing dependence when we restrict ourselves to horizon-penetrating slicings.

By contrast, if we switch from a horizon-penetrating to a horizon-avoiding slice, there are noticeable changes in the field lines: Compare the top row of Figure 8.6 ( $a/M = 0.875$  for a Kerr-Schild, horizon-penetrating slice) with Figure 8.7 (the same hole,  $a/M = 0.875$ , for a Boyer-Lindquist, horizon-avoiding slice), concentrating for now on panels (a) and (b) depicting tendex and vortex lines in Boyer-Lindquist spatial coordinates. The most striking differences are (i) the radial tendex lines' failure to reach the horizon for horizon-avoiding slices, contrasted with their plunging through the horizon for horizon-penetrating slices, and (ii) the closed azimuthal tendex and vortex lines for Boyer-Lindquist horizon-avoiding slices, contrasted with the outward spiraling azimuthal lines for horizon-penetrating slices. In Appendix 8.C we show that this outward spiral is common to a class of horizon-penetrating slices. Lastly, we note that Figure 8.7 (a) and (b) are plotted using Boyer-Lindquist spatial coordinates in order to compare with analytical expressions given in that appendix. When we use Kerr-Schild spatial coordinates, as is done in Figure 8.6, in order to fa-

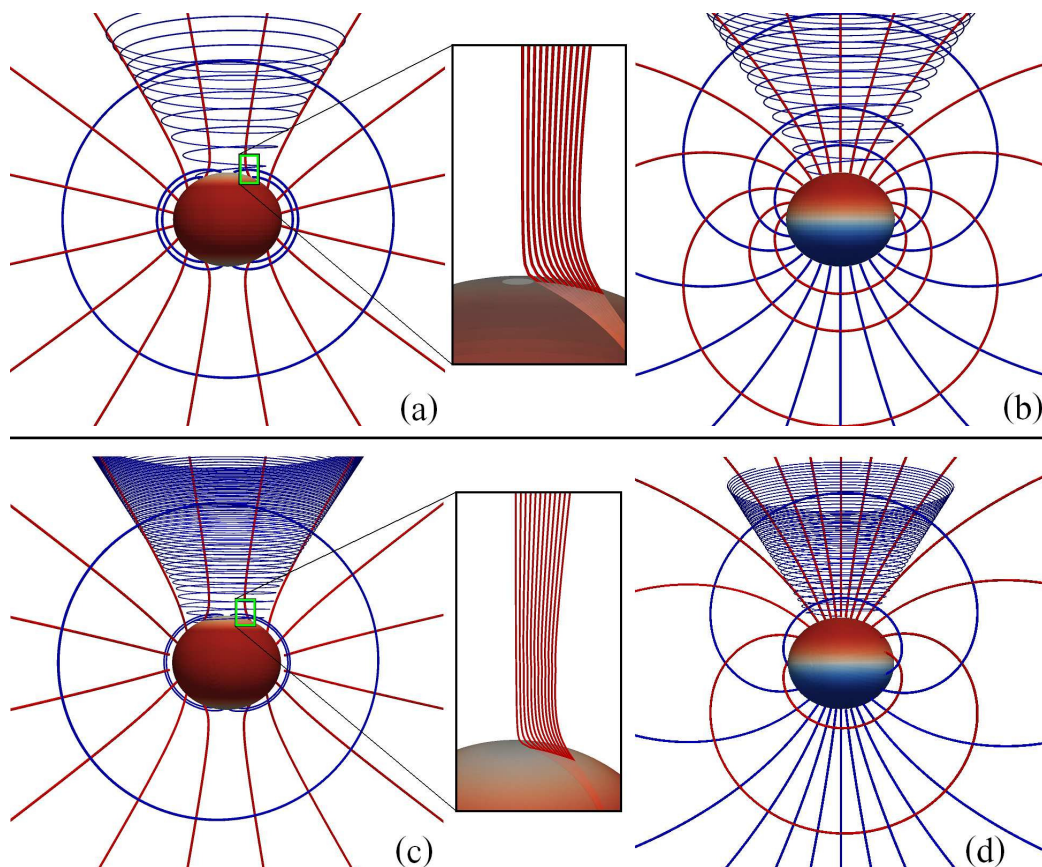


Figure 8.6: Tendex lines and vortex lines for a Kerr black hole with  $a/M = 0.875$  in *Kerr-Schild spatial coordinates*, for two different slicings: *Kerr-Schild*  $\tilde{t} = \text{constant}$ , and *Cook-Scheel*  $\tilde{t} = \text{constant}$ . The left and center columns of drawings [panels (a) and (c)] show tendex lines; the right column of drawings [panels (b) and (d)] show vortex lines. The top row of drawings [panels (a) and (b)] is for Kerr-Schild slicing; the bottom row [panels (c) and (d)] is for Cook-Scheel slicing. Since the slicings are different, it is not possible to focus on the same sets of field lines in the Kerr-Schild (upper panels) and Cook-Scheel (lower panels) cases. However, we have attempted to identify similar field lines by ensuring they pass through the same Kerr-Schild spatial coordinate locations on selected surfaces. (The color of the lines and horizon are similar to Figure 8.5)

cilitate a more appropriate comparison, we observe that the Boyer-Lindquist azimuthal coordinate singularity depicted in Figure 8.4 causes the tendex and vortex lines in Boyer-Lindquist slicing to wind in  $\phi$  direction when close to horizon. This feature is clearly visible in Figure 8.7 (c) and (d), where we display the tendex and vortex lines in Kerr-Schild spatial coordinates.

Based on our comparison of Kerr-Schild and Cook-Scheel slicings (Figure 8.6), and our analysis of the ubiquity of azimuthal spiraling lines in horizon-penetrating slices (Appendix 8.C), we conjecture that horizon-penetrating slicings of any black-hole spacetime will generically share the same qualitative and semi-quantitative structures of tendex and vortex lines. This conjecture is of key importance for our use of tendex and vortex lines to extract intuition into the dynamical processes observed in numerical simulations. More specifically:

Numerical spacetimes have dynamically chosen slicings, and the primary commonality from simulation to simulation is that the time slicing must be horizon penetrating, to prevent coordinate singularities from arising on the numerical grid near the horizon. Our conjecture implies that, regardless of the precise slicing used in a simulation, we expect the tendex and vortex lines to faithfully reveal the underlying physical processes. We will build more support for this conjecture in Paper III, by comparing the final stages of a numerical black-hole merger with a perturbed Kerr black hole, using very different slicing prescriptions.

We conclude this section with a digression from its slicing-dependence focus:

When we compare the  $a/M = 0.875$  black hole of Figure 8.6 with the  $a/M = 0.95$  hole of Figure 8.5, the most striking difference is in the tendex lines very near the horizon. The value  $a/M = 0.875$  is only slightly above the critical spin  $a/M = \sqrt{3}/2 = 0.8660$  at which the horizon's poles acquire negative scalar curvature. Correspondingly, for  $a/M = 0.875$ , the blue tendex lines that connect the two poles emerge from a smaller region at the poles than for  $a/M = 0.95$ , and they hug the horizon more tightly as they travel from one pole to the other; and the red, radial tendex lines near the poles suffer much smaller deflections than for  $a/M = 0.95$  as they descend into the horizon (see insets).

## 8.7 Conclusion

Using vortex and tendex lines and their vorticities and tendicities, we have visualized the spacetime curvature of stationary black holes. Stationary black-hole spacetimes are a simple arena in which to learn about the properties of these visualization tools in regions of strong spacetime curvature. From the features of the vortex and tendex lines and their vorticities and tendicities that we describe below, we have gained an understanding of these visualization tools and made an important stride toward our larger goal of using these tools to identify geometrodynamical properties of strongly curved spacetimes—particularly those in the merger of binary black holes.

Black hole spacetimes have an event horizon (a feature that was absent in our study of weakly gravitating systems in Paper I). To understand our visualization tools on the horizon, we defined and discussed the *horizon tendicity* and *horizon vorticity* of stationary black holes. The horizon tendicity and vorticity are directly proportional to the intrinsic and extrinsic curvature scalars of a two-dimensional horizon. As a result, the average value of the horizon tendicity must be negative, and the horizon vorticity must average to zero. Any region of large vorticity on the horizon (a horizon vortex), therefore, must be accompanied by an equivalent vortex of the opposite sign, but there is not an analogous constraint for horizon tendexes.

Outside the horizon, we also visualized the tendex lines and vortex lines, the tendicities and vorticities, and the regions of large tendicity (*tendexes*) and large vorticity (*vortexes*) for Schwarzschild and Kerr black holes (the latter both slowly and rapidly spinning). In particular, we investigated how the vortex and tendex lines of Kerr black holes changed when they were drawn in different time slices and with different spatial coordinates—within the set of those time slices that smoothly pass through the horizon and spatial coordinates that are everywhere regular. We found our visualizations are quite similar between two commonly used, though rather different, horizon-penetrating time functions: Kerr-Schild and Cook-Scheel. The spatial-coordinate dependence was also mild, and was easily understandable in terms of the relation between the different coordinate systems. Because the coordinate systems used in numerical simulations of black holes are also horizon penetrating, this suggests that the vortex and tendex lines will not be very different, even though the dynamical coordinates of the simulation may be.

This study is a foundation for future work on computing the tendexes and vortexes of black-hole spacetimes. A recent work by Dennison and Baumgarte [4]—in which the authors calculated the tendex and vortex fields of approximate initial data representing non-spinning, boosted black holes, and also black-hole binaries—will also be helpful for understanding binaries. In addition, our investigations of the slicing and coordinate dependence of tendexes and vortexes is complemented by another recent study of Dennison and Baumgarte [33], where expressions are given for computing curvature invariants in terms of the vorticities, tendicities, and the eigenvector fields which give the tendex and vortex lines. These expressions will likely be of use in future analytic and numerical studies of tendexes and vortexes.

In a companion paper (Paper III), we turn to perturbed black holes. We aim to deepen our understanding of tendex and vortex lines in these well-understood situations and to see what new insights we can draw from these spacetimes by using vortex and tendex lines. Ultimately, we will apply these visualization techniques and our intuition from simpler analytical spacetimes to study numerical simulations of strongly curved and dynamic spacetimes and their geometrodynamics. In Paper IV, we will do just this, focusing on binary-black-hole mergers.

## Acknowledgements

We thank Jeandrew Brink and Jeff Kaplan for helpful discussions. We would like to thank Mark Scheel for helpful discussions and for version control assistance, and Béla Szilágyi for his help on numerical grid construction. A.Z. would also like to thank the National Institute for Theoretical Physics of South Africa for hosting him during a portion of this work. Some calculations have been performed using the Spectral Einstein Code (SpEC) [7] on the Caltech computer cluster ZWICKY. This research was supported by NSF grants PHY-0960291, PHY-1068881 and CAREER grant PHY-0956189 at Caltech, by NSF grants PHY-0969111 and PHY-1005426 at Cornell, by NASA grant NNX09AF97G at Caltech, by NASA grant NNX09AF96G at Cornell, and by the Sherman Fairchild Foundation at Caltech and Cornell, the Brinson Foundation at Caltech, and the David and Barbara Groce fund at Caltech.

## 8.A Kerr Black Hole in Boyer-Lindquist Slicing and Coordinates

For a rapidly rotating Kerr black hole in Boyer-Lindquist (BL) coordinates  $\{t, r, \theta, \phi\}$ , the metric is given by Eq. (8.28) above. A “BL observer”, who moves orthogonally to the slices of constant BL time  $t$ , has a 4-velocity  $\vec{u}$  and orthonormal tetrad given by

$$\begin{aligned}\vec{u} &= \sqrt{\frac{A}{\Sigma\Delta}} \left( \partial_t - \frac{2Mar}{A} \partial_\phi \right), & \vec{e}_{\hat{r}} &= \sqrt{\frac{\Delta}{\Sigma}} \partial_r, \\ \vec{e}_{\hat{\theta}} &= \frac{1}{\sqrt{\Sigma}} \partial_\theta, & \vec{e}_{\hat{\phi}} &= \sqrt{\frac{\Sigma}{A}} \frac{1}{\sin\theta} \partial_\phi.\end{aligned}\tag{8.39}$$

This tetrad is also often called the locally non-rotating frame [34, 35]. In this orthonormal basis, the tidal and frame-drag fields are given by (cf. Eqs. (6.8a-6.9d) of [36])

$$\mathcal{E}_{\hat{a}\hat{b}} = \begin{pmatrix} -Q_e \frac{2+\xi}{1-\xi} & \mu Q_m & 0 \\ * & Q_e \frac{1+2\xi}{1-\xi} & 0 \\ * & * & Q_e \end{pmatrix},\tag{8.40a}$$

$$\mathcal{B}_{\hat{a}\hat{b}} = \begin{pmatrix} -Q_m \frac{2+\xi}{1-\xi} & -\mu Q_e & 0 \\ * & Q_m \frac{1+2\xi}{1-\xi} & 0 \\ * & * & Q_m \end{pmatrix},\tag{8.40b}$$

with entries denoted by \* fixed by the symmetry of the tensors, and where

$$Q_e = \frac{Mr(r^2 - 3a^2 \cos^2 \theta)}{\Sigma^3},\tag{8.40c}$$

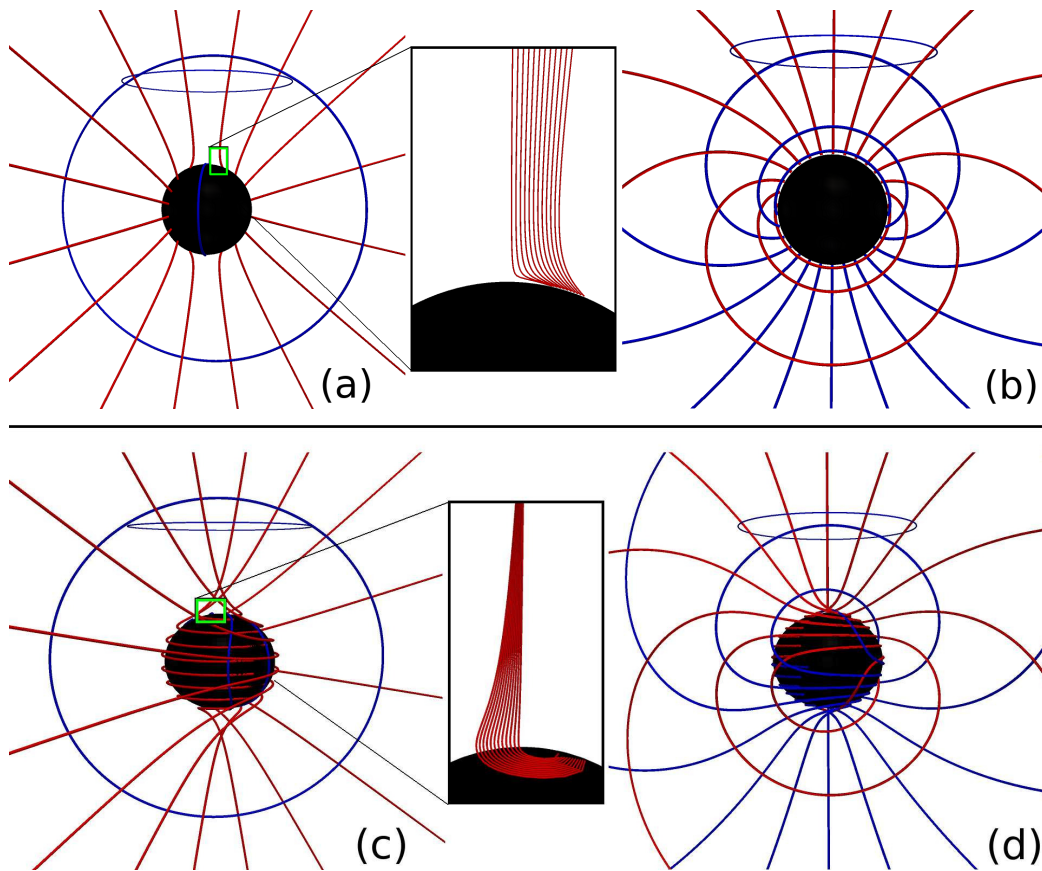


Figure 8.7: (a) Tendex lines for a Kerr black hole with  $a/M = 0.875$  on a slice of constant Boyer-Lindquist time  $t$ , plotted in *Boyer-Lindquist spatial coordinates*. The lines with positive tendicity are colored blue and negative are colored red. (b) Vortex lines for this same black hole, slicing and coordinates, with lines of positive vorticity colored blue and negative colored red. (c) and (d) Tendex and vortex lines for the same black hole and same Boyer-Lindquist slicing, but drawn in the *Kerr-Schild spatial coordinates*. (The color of the lines and horizon are similar to Figure 8.5)

$$Q_m = \frac{Ma \cos \theta (3r^2 - a^2 \cos^2 \theta)}{\Sigma^3}, \quad (8.40d)$$

$$\xi = \frac{\Delta a^2 \sin^2 \theta}{(r^2 + a^2)^2}, \quad (8.40e)$$

$$\mu = \frac{3a\sqrt{\Delta}(r^2 + a^2) \sin \theta}{A} = \frac{3\sqrt{\xi}}{1 - \xi}. \quad (8.40f)$$

The functions  $Q_e$  and  $Q_m$  are related to the real and imaginary parts of the complex Weyl scalar  $\Psi_2$  calculated using the Kinnersley null tetrad by  $\Psi_2 = -Q_e + iQ_m$ . Note that there is a duality between the electric and the magnetic curvature tensors: namely, by replacing  $Q_e \rightarrow Q_m$  and  $Q_m \rightarrow -Q_e$ , the tensor transforms as  $\mathcal{E}_{\hat{a}\hat{b}} \rightarrow \mathcal{B}_{\hat{a}\hat{b}}$ .

The block diagonal forms of  $\mathcal{E}_{\hat{a}\hat{b}}$  and  $\mathcal{B}_{\hat{a}\hat{b}}$  imply that one of the eigenvectors for each will be  $\vec{e}_\phi$ . When integrated, this gives toroidal tendex and vortex lines (i.e., lines that are azimuthal, closed circles). The other two sets of lines for each tensor are poloidal (i.e., they lie in slices of constant  $\phi$ ).

More specifically, the eigenvectors of the tidal field are

$$\vec{V}_r^\mathcal{E} = \frac{(\lambda_r^\mathcal{E} - \mathcal{E}_{\hat{\theta}\hat{\theta}})\vec{e}_{\hat{r}} + \mathcal{E}_{\hat{r}\hat{\theta}}\vec{e}_{\hat{\theta}}}{\sqrt{(\lambda_r^\mathcal{E} - \mathcal{E}_{\hat{\theta}\hat{\theta}})^2 + (\mathcal{E}_{\hat{r}\hat{\theta}})^2}}, \quad \vec{V}_\theta^\mathcal{E} = \frac{(\lambda_\theta^\mathcal{E} - \mathcal{E}_{\hat{\theta}\hat{\theta}})\vec{e}_{\hat{r}} + \mathcal{E}_{\hat{r}\hat{\theta}}\vec{e}_{\hat{\theta}}}{\sqrt{(\lambda_\theta^\mathcal{E} - \mathcal{E}_{\hat{\theta}\hat{\theta}})^2 + (\mathcal{E}_{\hat{r}\hat{\theta}})^2}}, \quad \vec{V}_\phi^\mathcal{E} = \vec{e}_{\hat{\phi}}. \quad (8.41)$$

The labeling of these eigenvectors is such that, as  $a \rightarrow 0$ , they limit to the corresponding eigenvectors (8.18) of a Schwarzschild black hole. The tendicities (eigenvalues) associated with these three eigenvectors, which appear in the above formulas, are

$$\lambda_r^\mathcal{E} = -\frac{Q_e}{2} - \sqrt{\left(\frac{3Q_e}{2}\right)^2 \left(\frac{1+\xi}{1-\xi}\right)^2 + \mu^2 Q_m^2}, \quad \lambda_\theta^\mathcal{E} = -\frac{Q_e}{2} + \sqrt{\left(\frac{3Q_e}{2}\right)^2 \left(\frac{1+\xi}{1-\xi}\right)^2 + \mu^2 Q_m^2},$$

$$\lambda_\phi^\mathcal{E} = Q_e. \quad (8.42)$$

The eigenvectors of the frame-drag field are

$$\vec{V}_\pm^\mathcal{B} = \frac{(\lambda_\pm^\mathcal{B} - \mathcal{B}_{\hat{\theta}\hat{\theta}})\vec{e}_{\hat{r}} + \mathcal{B}_{\hat{r}\hat{\theta}}\vec{e}_{\hat{\theta}}}{\sqrt{(\lambda_\pm^\mathcal{B} - \mathcal{B}_{\hat{\theta}\hat{\theta}})^2 + (\mathcal{B}_{\hat{r}\hat{\theta}})^2}}, \quad \vec{V}_\phi^\mathcal{B} = \vec{e}_{\hat{\phi}}. \quad (8.43)$$

Here the labeling  $+$  and  $-$  of the poloidal eigenvectors corresponds to the signs of their eigenvalues (vorticities). The eigenvalues are

$$\lambda_\pm^\mathcal{B} = -\frac{Q_m}{2} \pm \sqrt{\left(\frac{3Q_m}{2}\right)^2 \left(\frac{1+\xi}{1-\xi}\right)^2 + \mu^2 Q_e^2}, \quad \lambda_\phi^\mathcal{B} = Q_m. \quad (8.44)$$

The tendex and vortex lines tangent to the eigenvectors (8.41) and (8.43) are shown in Figure 8.7 for a rapidly rotating black hole,  $a/M = 0.875$ . The lines with positive eigenvalues (tendicity or vorticity) are colored blue, and those with negative eigenvalues are colored red. Far from the black hole, the tendex lines resemble those of a Schwarzschild black hole, and the vortex lines resemble those of a slowly spinning hole. However, near the horizon the behavior is quite different. The nearly radial tendex lines in the inset of Figure 8.7 are bent sharply as they near the horizon, because of the black hole's spin.

Before closing this appendix, we describe the behavior of the eigenvalues near the poles. From Eqs. (8.42), we see that as  $\theta \rightarrow 0$  and  $\theta \rightarrow \pi$ ,  $\lambda_\theta^\mathcal{E} \rightarrow \lambda_\phi^\mathcal{E}$ . Along the polar axis, therefore, the poloidal and axial eigenvectors of  $\mathcal{E}_{\hat{a}\hat{b}}$  become degenerate, and any vector in the plane spanned by these directions is also an eigenvector at the axis. Meanwhile, for  $\mathcal{B}_{\hat{a}\hat{b}}$ , Eqs. (8.44) show that as  $\theta \rightarrow 0$ ,  $\lambda_+^\mathcal{B} \rightarrow \lambda_\phi^\mathcal{B}$ , and as  $\theta \rightarrow \pi$ ,  $\lambda_-^\mathcal{B} \rightarrow \lambda_\phi^\mathcal{B}$ . Once again there is a degenerate plane spanned by two eigenvectors at the polar axis. In Paper III, in which we study the tendex and vortex lines of perturbed Kerr black holes, the degenerate regions have a strong influence on the perturbed tendex and vortex lines (see Appendix F of Paper III).

## 8.B Kerr Black Hole in Kerr-Schild Slicing and Ingoing-Kerr Coordinates

In ingoing-Kerr coordinates  $\{\tilde{t}, r, \theta, \tilde{\phi}\}$  [Eqs. (8.29) and (8.32)], the Kerr metric takes the form (see, e.g., Chapter 33 of [27], though we use the Kerr-Schild time  $\tilde{t}$  [29, 30], or Eq. (D.4) of [37])

$$\begin{aligned}
ds^2 = & - \left(1 - \frac{2Mr}{\Sigma}\right) d\tilde{t}^2 + \frac{4Mr}{\Sigma} dr d\tilde{t} - \frac{4Mar \sin^2 \theta}{\Sigma} d\tilde{t} d\tilde{\phi} + H^2 dr^2 + \Sigma d\theta^2 - 2aH \sin^2 \theta dr d\tilde{\phi} \\
& + \frac{A \sin^2 \theta}{\Sigma} d\tilde{\phi}^2, \\
H^2 = & 1 + \frac{2Mr}{\Sigma},
\end{aligned} \tag{8.45}$$

where  $\Sigma$  and  $A$  are defined in Eq. (8.28). The 4-velocities of ingoing-Kerr observers, who move orthogonally to slices of constant  $\tilde{t}$ , and the orthonormal tetrads they carry, are given by

$$\begin{aligned}
\bar{u} &= H \partial_{\tilde{t}} - \frac{2Mr}{H\Sigma} \partial_r, & \bar{e}_{\hat{r}} &= \frac{\sqrt{A}}{H\Sigma} \partial_r + \frac{aH}{\sqrt{A}} \partial_{\tilde{\phi}}, \\
\bar{e}_{\hat{\theta}} &= \frac{1}{\sqrt{\Sigma}} \partial_{\theta}, & \bar{e}_{\hat{\phi}} &= \sqrt{\frac{\Sigma}{A}} \frac{1}{\sin \theta} \partial_{\tilde{\phi}}
\end{aligned} \tag{8.46}$$

(see, e.g., [38] or [37]).

The components of the tidal field in this orthonormal basis are

$$\mathcal{E}_{\hat{a}\hat{b}} = \begin{pmatrix} -Q_e \frac{2+\xi}{1-\xi} & Q_m \frac{3a(r^2+a^2) \sin \theta}{H\sqrt{A}\Sigma} & Q_e \frac{6aMr(r^2+a^2) \sin \theta}{HA\sqrt{\Sigma}} \\ * & Q_e \left(1 + \frac{3a^2 \sin^2 \theta}{H^2\Sigma}\right) & -Q_m \frac{6a^2Mr \sin^2 \theta}{H^2\Sigma\sqrt{A}} \\ * & * & Q_e \frac{2+\xi}{1-\xi} - Q_e \left(1 + \frac{3a^2 \sin^2 \theta}{H^2\Sigma}\right) \end{pmatrix}, \tag{8.47}$$

where  $Q_e$ ,  $Q_m$ , and  $\xi$  are defined in Eqs. (8.40c), (8.40d), and (8.40e). Just as in Boyer-Lindquist slicing and coordinates (Appendix 8.A), so also here, the components  $\mathcal{B}_{\hat{a}\hat{b}}$  of the frame-drag field can be deduced from  $\mathcal{E}_{\hat{a}\hat{b}}$  by the duality relation

$$\mathcal{B}_{\hat{a}\hat{b}} = \mathcal{E}_{\hat{a}\hat{b}}|_{Q_e \rightarrow Q_m, Q_m \rightarrow -Q_e}. \tag{8.48}$$

The eigenvalues of the tidal field (8.47), i.e. the tendicities, and their corresponding eigenvectors are

$$\begin{aligned}
\lambda_r^{\mathcal{E}} &= -\frac{3\zeta}{2H^2\Sigma} - \frac{Q_e}{2}, & \lambda_{\theta}^{\mathcal{E}} &= \frac{3\zeta}{2H^2\Sigma} - \frac{Q_e}{2}, & \lambda_{\phi}^{\mathcal{E}} &= Q_e; \\
\zeta^2 &= Q_e^2 (H^2\Sigma)^2 + \frac{(2Ma \sin \theta)^2 F}{\Sigma^3}, & F &= r^2 + 2Mr + a^2; \\
\vec{V}_r^{\mathcal{E}} &= \frac{1}{v_r} \left( H\sqrt{\Sigma}(r^2 + a^2) \bar{e}_{\hat{r}} + \frac{\sqrt{A}}{2Q_m a \sin \theta} [Q_e(F + a^2 \sin^2 \theta) - \zeta] \bar{e}_{\hat{\theta}} - 2Mar \sin \theta \bar{e}_{\hat{\phi}} \right),
\end{aligned} \tag{8.49}$$

$$\begin{aligned}\vec{V}_\theta^\mathcal{E} &= \frac{1}{v_\theta} \left( H\sqrt{\Sigma}(r^2 + a^2)\vec{e}_{\hat{r}} + \frac{\sqrt{A}}{2Q_m a \sin\theta} [Q_e(F + a^2 \sin^2\theta) + \zeta] \vec{e}_{\hat{\theta}} - 2Mar \sin\theta \vec{e}_{\hat{\phi}} \right), \\ \vec{V}_\phi^\mathcal{E} &= \frac{1}{v_{\hat{\phi}}} \left( 2Mar \sin\theta \vec{e}_{\hat{r}} + H\sqrt{\Sigma}(r^2 + a^2)\vec{e}_{\hat{\phi}} \right).\end{aligned}\quad (8.50)$$

Here the quantities  $v_r$ ,  $v_\theta$ , and  $v_{\hat{\phi}}$  are the norms of the vectors in large parentheses (which give the eigenvectors  $\vec{V}^\mathcal{E}$  unit norms). As for Boyer-Lindquist slicing, our  $r$ ,  $\theta$ ,  $\phi$  labels for the eigenvectors and eigenvalues are such that as  $a \rightarrow 0$ , they limit to the corresponding Schwarzschild quantities in Eddington-Finkelstein slicing. Note that although the expressions for  $\vec{V}_r^\mathcal{E}$  and  $\vec{V}_\theta^\mathcal{E}$  appear nearly identical, the coefficient of the term in front of  $\vec{e}_{\hat{\theta}}$  for  $\vec{V}_r^\mathcal{E}$  includes  $-\zeta$ , and that in front of  $\vec{e}_{\hat{\theta}}$  for  $\vec{V}_\theta^\mathcal{E}$  includes  $+\zeta$ . This seemingly small difference determines whether the eigenvectors are predominantly radial or poloidal. Note also that the limit  $a \rightarrow 0$  must be taken carefully with the vectors written in this form in order to recover the eigenvectors of a Schwarzschild hole.

As for Boyer-Lindquist slicing, so also here, the eigenvectors and eigenvalues (vorticities) for  $\mathcal{B}_{\hat{a}\hat{b}}$  can be derived from those for  $\mathcal{E}_{\hat{a}\hat{b}}$  using the Kerr duality relations:

$$\{\vec{V}_-^\mathcal{B}, \vec{V}_+^\mathcal{B}, \vec{V}_\phi^\mathcal{B}\} = \{\vec{V}_r^\mathcal{E}, \vec{V}_\theta^\mathcal{E}, \vec{V}_\phi^\mathcal{E}\}|_{Q_e \rightarrow Q_m, Q_m \rightarrow -Q_e}, \quad (8.51)$$

$$\{\lambda_-^\mathcal{B}, \lambda_+^\mathcal{B}, \lambda_\phi^\mathcal{B}\} = \{\lambda_r^\mathcal{E}, \lambda_\theta^\mathcal{E}, \lambda_\phi^\mathcal{E}\}|_{Q_e \rightarrow Q_m, Q_m \rightarrow -Q_e}. \quad (8.52)$$

As in the case of Boyer-Lindquist slicing, so also for Kerr-Schild slicing, the transverse (nonradial) eigenvectors are degenerate on the polar axis. This can be seen, for example, from the form of  $\mathcal{E}_{\hat{a}\hat{b}}$  in Eq. (8.47), or from the corresponding eigenvalues in Eqs. (8.49): as  $\sin\theta \rightarrow 0$ , the matrix becomes diagonal with two equal eigenvalues,  $\lambda_\theta$  and  $\lambda_\phi$ . This is an inevitable consequence of axisymmetry.

## 8.C Spiraling Axial Vortex and Tendex Lines for Kerr Black Holes in Horizon-Penetrating Slices

In Figures 8.5, 8.6, and 8.7, the azimuthal tendex and vortex lines of a Kerr black hole in horizon-avoiding Boyer-Lindquist slices are closed circles, while those in horizon-penetrating Kerr-Schild and Cook-Scheel slices are outward spirals. In this section, we argue that outward spirals are common to a wide class of horizon-penetrating slices, including ingoing-Kerr and Cook-Scheel slicings.

The class of time slices that we will investigate are those that differ from Boyer-Lindquist slices,  $t$ , by a function of Boyer-Lindquist  $r$ ,

$$t' = t + f(r). \quad (8.53)$$

For example, both ingoing Kerr and Cook-Scheel times fall into this category. By computing the normal to a slice of constant  $t'$  [when expressed in terms of the locally non-rotating frame of Eq.

(8.39)] we find that

$$\vec{u}' = \sqrt{\frac{g^{tt}}{g^{t't'}}} \left( \vec{u} + \sqrt{\frac{g^{rr}}{g^{tt}}} \frac{df(r)}{dr} \vec{e}_{\hat{r}} \right). \quad (8.54)$$

Here  $g^{tt}$  and  $g^{rr}$  are the contravariant components of the metric in Boyer-Lindquist coordinates, and  $g^{t't'}$  are those in coordinates that use  $t'$  instead. Defining

$$\gamma = \sqrt{\frac{g^{tt}}{g^{t't'}}}, \quad v = \sqrt{\frac{g^{rr}}{g^{tt}}} \frac{df(r)}{dr}, \quad (8.55)$$

we can see that the above transformation has the form of a set of local Lorentz transformations between the locally non-rotating frame and the new frame, and that  $\gamma^2 = 1/(1-v^2)$ . This implies that we can express the timelike normal and the new radial vector as

$$\vec{u}' = \gamma(\vec{u} + v\vec{e}_{\hat{r}}), \quad \vec{e}'_{\hat{r}} = \gamma(v\vec{u} + \vec{e}_{\hat{r}}), \quad (8.56)$$

and that we need not change the vectors  $\vec{e}_{\hat{\theta}}$  and  $\vec{e}_{\hat{\phi}}$  in making this transformation.

From the expressions for how the tidal and frame-drag fields transform under changes of slicing (see Appendix B of [28]), we find that we can compute the new components of the tidal field in the transformed slicing and tetrad from the tidal and frame-drag fields in the Boyer-Lindquist slicing and tetrad [Eq. (8.40a) and (8.40b)]. For a change in slicing corresponding to a radial boost, these general transformation laws simplify to

$$\mathcal{E}'_{\hat{r}'\hat{r}'} = \mathcal{E}_{\hat{r}\hat{r}}^{\text{BL}}, \quad (8.57a)$$

$$\mathcal{E}'_{\hat{r}'\hat{A}'} = \gamma(\mathcal{E}_{\hat{r}\hat{A}}^{\text{BL}} - v\epsilon_{\hat{A}\hat{r}\hat{C}}\mathcal{B}_{\hat{C}\hat{r}}^{\text{BL}}), \quad (8.57b)$$

$$\mathcal{E}'_{\hat{A}'\hat{B}'} = \gamma^2[(1+v^2)\mathcal{E}_{\hat{A}\hat{B}}^{\text{BL}} + v^2\mathcal{E}_{\hat{r}\hat{r}}^{\text{BL}}\delta_{\hat{A}\hat{B}} - 2v\epsilon_{\hat{r}\hat{C}(\hat{A}}\mathcal{B}_{\hat{B})\hat{C}}^{\text{BL}}], \quad (8.57c)$$

where  $\hat{A}$ ,  $\hat{B}$ , and  $\hat{C} = \hat{\theta}$  and  $\hat{\phi}$ , and where repeated lowered index  $\hat{C}$  is summed over its two values. To understand how  $\mathcal{B}$  is transformed, we use the duality  $\mathcal{E} \rightarrow \mathcal{B}$  and  $\mathcal{B} \rightarrow -\mathcal{E}$  in the transformation laws (8.57a)–(8.57c).

By substituting the explicit expressions for the Boyer-Lindquist slicing and tetrad tidal fields and the definition of  $\mu$  in Eq. (8.40f), we see

$$\mathcal{E}'_{\hat{a}'\hat{b}'} = \begin{pmatrix} -\left(\frac{2+\xi}{1-\xi}\right) Q_e & \gamma\left(\frac{3\sqrt{\xi}}{1-\xi}\right) Q_m & \gamma v\left(\frac{3\sqrt{\xi}}{1-\xi}\right) Q_e \\ * & \gamma^2\left(\frac{1+2\xi}{1-\xi} - v^2\right) Q_e & -\gamma^2 v\left(\frac{3\xi}{1-\xi}\right) Q_m \\ * & * & \gamma^2\left(1 - v^2\frac{1+2\xi}{1-\xi}\right) Q_e \end{pmatrix}. \quad (8.58)$$

In calculating  $\mathcal{B}$ , we could again use the duality in Eq. (8.48).

To compute the tendex lines and the tendicity, we express Eq. (8.58) in a new basis given by

$$\vec{e}_{\hat{r}''} = \frac{1}{\sqrt{1 + \gamma^2 v^2 \xi}} (\vec{e}_{\hat{r}'} - \gamma v \sqrt{\xi} \vec{e}_{\hat{\phi}}), \quad (8.59a)$$

$$\vec{e}_{\hat{\phi}''} = \frac{1}{\sqrt{1 + \gamma^2 v^2 \xi}} (\gamma v \sqrt{\xi} \vec{e}_{\hat{r}'} + \vec{e}_{\hat{\phi}}), \quad (8.59b)$$

and where  $\vec{e}_{\hat{\theta}}$  is again unchanged. In this basis, the tidal field becomes block diagonal

$$\mathcal{E}_{\hat{a}''\hat{b}''} = \begin{pmatrix} \gamma^2 \left( 2v^2 - \frac{2+\xi}{1-\xi} \right) Q_e & \frac{3\gamma\sqrt{\xi(1+\gamma^2 v^2 \xi)}}{1-\xi} Q_m & 0 \\ * & \gamma^2 \left( \frac{1+2\xi}{1-\xi} - v^2 \right) Q_e & 0 \\ * & * & Q_e \end{pmatrix}. \quad (8.60)$$

We then see that the tendicities are

$$\lambda_{r''} = -\frac{Q_e}{2} - \frac{3}{2(1-\xi)} \sqrt{[(1 + \gamma^2 v^2 \xi) + \gamma^2 \xi]^2 Q_e^2 + 4\gamma^2 \xi (1 + \gamma^2 v^2 \xi) Q_m^2}, \quad (8.61a)$$

$$\lambda_{\theta''} = -\frac{Q_e}{2} + \frac{3}{2(1-\xi)} \sqrt{[(1 + \gamma^2 v^2 \xi) + \gamma^2 \xi]^2 Q_e^2 + 4\gamma^2 \xi (1 + \gamma^2 v^2 \xi) Q_m^2}, \quad (8.61b)$$

$$\lambda_{\phi''} = Q_e, \quad (8.61c)$$

and the corresponding vectors have an identical form to those in Eq. (8.41), when one replaces the components of the tidal field, the tendicities, and the unit vectors there with the equivalent (primed) quantities in Eqs. (8.59)–(8.61):

$$\vec{V}_{r''} = \frac{(\lambda_{r''} - \mathcal{E}_{\hat{r}''\hat{\theta}''})\vec{e}_{\hat{r}''} + \mathcal{E}_{\hat{r}''\hat{\theta}''}\vec{e}_{\hat{\theta}''}}{\sqrt{(\lambda_{r''} - \mathcal{E}_{\hat{r}''\hat{\theta}''})^2 + (\mathcal{E}_{\hat{r}''\hat{\theta}''})^2}}, \quad (8.62a)$$

$$\vec{V}_{\theta''} = \frac{(\lambda_{\theta''} - \mathcal{E}_{\hat{\theta}''\hat{\theta}''})\vec{e}_{\hat{r}''} + \mathcal{E}_{\hat{\theta}''\hat{\theta}''}\vec{e}_{\hat{\theta}''}}{\sqrt{(\lambda_{\theta''} - \mathcal{E}_{\hat{\theta}''\hat{\theta}''})^2 + (\mathcal{E}_{\hat{\theta}''\hat{\theta}''})^2}}, \quad (8.62b)$$

$$\vec{V}_{\phi''} = \vec{e}_{\hat{\phi}''}. \quad (8.62c)$$

From the expressions for the eigenvectors, we can explain several features of the tendex lines in Figures 8.5, 8.6, and 8.7. When  $v = 0$  [i.e., when  $f(r) = 0$  and the slicing is given by the horizon-avoiding, Boyer-Lindquist time], the azimuthal lines formed closed loops, and the radial and polar lines live within a plane of constant  $\phi$ . For all other slicings in this family [i.e.,  $v \neq 0$  and  $f(r) \neq 0$ ], the azimuthal lines pick up a small radial component, and they will spiral outward on a cone of constant  $\theta$  with a pitch angle whose tangent is proportional to  $\gamma v \sqrt{\xi}$ ; the radial and polar lines will also wind slightly in the azimuthal direction (an effect that is more difficult to see in Figures 8.5 and 8.6). By duality, an identical result holds for the azimuthal vortex lines of  $\mathcal{B}$ , and an analogous behavior holds for the poloidal vortex lines (in Boyer-Lindquist slicing, they remain in planes of constant  $\phi$ , but in horizon-penetrating slicings, they twist azimuthally).

For this class of slices, the azimuthal eigenvector of the tidal field changes linearly in the velocity of the boost, but the tendicity along the corresponding tendex line is unchanged. The other eigenvectors also change linearly in the velocity, but their tendicities are quadratic in  $v$ ; therefore, for small changes in the slicing, the tendicities change more weakly. This result is reminiscent of a similar qualitative result for perturbations of black holes in the next paper of this series: the tendex lines appear to be more slicing dependent than their corresponding tendicities.

In the relatively general class of slicings investigated here, we showed that the generic behavior of the azimuthal lines in horizon-penetrating slices is to spiral outward radially (and the other lines must also wind azimuthally as well). This, however, is not the most general set of slicings that still respect the symmetries of the Kerr spacetime [e.g., those of the form  $t' = t + g(r, \theta)$  are]. These slicings will have a  $\theta$  component to their boost velocities, and (based on the argument for slowly spinning black holes in Section 8.5.3), the azimuthal vortex lines will also wind in the polar direction. A more generic behavior, therefore, would be azimuthal lines that no longer wind on cones of constant  $\theta$ . Because we were not aware of any simple analytical slicings of this form, we did not investigate here; however, we suspect that this more general behavior of the lines may appear in numerical simulations.

Before concluding, we note that by choosing

$$\gamma = \sqrt{\frac{A}{H^2 \Delta \Sigma}}, \quad v = \frac{2Mr}{\sqrt{A}}, \quad (8.63)$$

we can recover the results given in Appendix 8.B for the tidal field (and by duality, the frame-drag field). Similarly, if we choose

$$\gamma = \sqrt{\frac{A(r - r_-)}{\Delta[(r - r_-)\Sigma + 2M(r^2 + r_+ r + r_+^2 + a^2)]}}, \quad v = \frac{r_+^2 + a^2}{\sqrt{A}}, \quad (8.64)$$

then we can use Eq. (8.58) to calculate the tidal and frame-drag fields in time-harmonic Cook-Scheel slicing (and its associated tetrad). The expressions were not as simple as those in Appendix 8.B, and for this reason, we do not give them here. Because the velocity in Cook-Scheel slicing falls off more rapidly in radius than that in ingoing-Kerr slicing, the azimuthal lines should have a tighter spiral (a feature that we observe in Figure 8.6).

## Bibliography

- [1] R. Owen, J. Brink, Y. Chen, J. D. Kaplan, G. Lovelace, K. D. Matthews, D. A. Nichols, M. A. Scheel, F. Zhang, A. Zimmerman, et al., Phys. Rev. Lett. **106**, 151101 (2011).
- [2] D. A. Nichols, R. Owen, F. Zhang, A. Zimmerman, J. Brink, Y. Chen, J. Kaplan, G. Lovelace,

- K. D. Matthews, M. A. Scheel, et al., Phys. Rev. D. **84**, 124914 (2011), 1108.5486.
- [3] A. Zimmerman, D. A. Nichols, and F. Zhang, Phys. Rev. D **84**, 044037 (2011).
- [4] K. A. Dennison and T. W. Baumgarte, Phys.Rev. **D86**, 084051 (2012), 1207.2431.
- [5] J. M. Bowen and J. W. York, Jr., Phys. Rev. D **21**, 2047 (1980).
- [6] H. Stephani, D. Kramer, M. MacCallum, C. Hoenselaers, and E. Herlt, *Exact Solutions of Einstein's Field Equations* (Cambridge University Press, Cambridge, UK, 2003).
- [7] <http://www.black-holes.org/SpEC.html>.
- [8] E. Newman and R. Penrose, J. Math. Phys. **3**, 566 (1962).
- [9] R. Penrose and W. Rindler, *Spinors and Space-time, Volume 1* (Cambridge University Press, Cambridge, 1992).
- [10] T. Damour, in *Proceedings of the Second Marcel Grossman Meeting on General Relativity*, edited by R. Ruffini (North-Holland Publishing Company, Amsterdam, 1982), pp. 587–606.
- [11] J. D. Brown and J. W. York, Phys. Rev. D **47**, 1407 (1993).
- [12] A. Ashtekar, C. Beetle, and J. Lewandowski, Phys. Rev. D **64**, 044016 (2001), gr-qc/0103026.
- [13] A. Ashtekar and B. Krishnan, Phys. Rev. D **68**, 104030 (2003).
- [14] O. Dreyer, B. Krishnan, D. Shoemaker, and E. Schnetter, Phys. Rev. D **67**, 024018 (2003).
- [15] G. B. Cook and B. F. Whiting, Phys. Rev. D **76**, 041501(R) (2007).
- [16] R. Owen, Ph.D. thesis, California Institute of Technology (2007), URL <http://resolver.caltech.edu/CaltechETD:etd-05252007-143511>.
- [17] G. Lovelace, R. Owen, H. P. Pfeiffer, and T. Chu, Phys. Rev. D **78**, 084017 (2008).
- [18] P. Anninos, D. Bernstein, S. R. Brandt, D. Hobill, E. Seidel, and L. Smarr, Phys. Rev. D **50**, 3801 (1994).
- [19] S. R. Brandt and E. Seidel, Phys. Rev. D **52**, 870 (1995).
- [20] M. Alcubierre, B. Brügmann, P. Diener, F. Guzmán, I. Hawke, S. Hawley, F. Herrmann, M. Koppitz, D. Pollney, E. Seidel, et al., Phys. Rev. D **72**, 044004 (2005).
- [21] T. Chu, H. P. Pfeiffer, and M. A. Scheel, Phys. Rev. D **80**, 124051 (2009), 0909.1313.
- [22] A. Ashtekar, J. Engle, T. Pawłowski, and C. V. D. Broeck, Class. Quantum Grav. **21**, 2549 (2004).

- [23] E. Schnetter, B. Krishnan, and F. Beyer, Phys. Rev. D **74**, 024028 (2006), [gr-qc/0604015](#).
- [24] R. Owen, Phys. Rev. D **80**, 084012 (2009).
- [25] N. Vasset, J. Novak, and J. L. Jaramillo, Phys. Rev. D **79**, 124010 (2009).
- [26] M. Jasiulek, Class. Quantum Grav. **26**, 254008 (2009).
- [27] C. W. Misner, K. S. Thorne, and J. A. Wheeler, *Gravitation* (Freeman, New York, New York, 1973).
- [28] R. Maartens, Phys. Rev. D **58**, 124006 (1998), [arXiv:astro-ph/9808235](#).
- [29] R. P. Kerr, Physical Review Letters **11**, 237 (1963).
- [30] R. H. Boyer and R. W. Lindquist, Journal of Mathematical Physics **8**, 265 (1967).
- [31] G. B. Cook and M. A. Scheel, Phys. Rev. D **56**, 4775 (1997).
- [32] L. Smarr, Phys. Rev. D **7**, 289 (1973).
- [33] K. A. Dennison and T. W. Baumgarte (2012), [arXiv:gr-qc/1208.1218](#).
- [34] J. M. Bardeen, Astrophys. J. **162**, 71 (1970).
- [35] J. M. Bardeen, W. H. Press, and S. A. Teukolsky, Astrophys. J. **178**, 347 (1972).
- [36] K. S. Thorne, R. H. Price, and D. A. MacDonald, *Black Holes: The Membrane Paradigm* (Yale University Press, New Haven and London, 1986).
- [37] E. Gourgoulhon and J. L. Jaramillo, Phys. Rep. **423**, 159 (2006), [gr-qc/0503113](#).
- [38] A. R. King, J. P. Lasota, and W. Kundt, Phys. Rev. D **12**, 3037 (1975).

## Chapter 9

# Visualizing Spacetime Curvature via Frame-Drag Vortexes and Tidal Tendexes III. Quasinormal Pulsations of Schwarzschild and Kerr Black Holes

In recent papers, we and colleagues have introduced a way to visualize the full vacuum Riemann curvature tensor using *frame-drag vortex lines and their vorticities*, and *tidal tendex lines and their tendicities*. We have also introduced the concepts of *horizon vortexes and tendexes* and *3-D vortexes and tendexes* (regions on or outside the horizon where vorticities or tendicities are large). In this paper, using these concepts, we discover a number of previously unknown features of quasinormal modes of Schwarzschild and Kerr black holes. These modes can be classified by a radial quantum number  $n$ , spheroidal harmonic orders  $(l, m)$ , and parity, which can be *electric*  $[(-1)^l]$  or *magnetic*  $[(-1)^{l+1}]$ . Among our discoveries are these: (i) There is a near duality between modes of the same  $(n, l, m)$ : a duality in which the tendex and vortex structures of electric-parity modes are interchanged with the vortex and tendex structures (respectively) of magnetic-parity modes. (ii) This near duality is perfect for the modes' complex eigenfrequencies (which are well known to be identical) and perfect on the horizon; it is slightly broken in the equatorial plane of a non-spinning hole, and the breaking becomes greater out of the equatorial plane, and greater as the hole is spun up; but even out of the plane for fast-spinning holes, the duality is surprisingly good. (iii) Electric-parity modes can be regarded as generated by 3-D tendexes that stick radially out of the horizon. As these "longitudinal," near-zone tendexes rotate or oscillate, they generate longitudinal-transverse near-zone vortexes and tendexes, and outgoing and ingoing grav-

itational waves. The ingoing waves act back on the longitudinal tendexes, driving them to slide off the horizon, which results in decay of the mode's strength. (iv) By duality, magnetic-parity modes are driven in this same manner by longitudinal, near-zone vortexes that stick out of the horizon. (v) When visualized, the 3-D vortexes and tendexes of a  $(l, m) = (2, 2)$  mode, and also a  $(2, 1)$  mode, spiral outward and backward like water from a whirling sprinkler, becoming outgoing gravitational waves. By contrast, a  $(2, 2)$  mode superposed on a  $(2, -2)$  mode has oscillating horizon vortexes or tendexes that eject 3-dimensional vortexes and tendexes, which propagate outward becoming gravitational waves; and so does a  $(2, 0)$  mode. (vi) For magnetic-parity modes of a Schwarzschild black hole, the perturbative frame-drag field, and hence also the perturbative vortexes and vortex lines, are strictly gauge invariant (unaffected by infinitesimal magnetic-parity changes of time slicing and spatial coordinates). (vii) We have computed the vortex and tendex structures of electric-parity modes of Schwarzschild in two very different gauges and find essentially no discernible differences in their pictorial visualizations. (viii) We have compared the vortex lines, from a numerical-relativity simulation of a black hole binary in its final ringdown stage, with the vortex lines of a  $(2, 2)$  electric-parity mode of a Kerr black hole with the same spin ( $a/M = 0.945$ ) and find remarkably good agreement.

---

Originally published as D. A. Nichols, A. Zimmerman, Y. Chen, G. Lovelace, K. D. Matthews, R. Owen, F. Zhang, and K. S. Thorne, *Phys. Rev. D* **86**, 104028 (2012).  
Copyright 2012 by the American Physical Society.

## 9.1 Motivations, Foundations and Overview

### 9.1.1 Motivations

This is the third in a series of papers that introduce a new set of tools for visualizing the Weyl curvature tensor (which, in vacuum, is the same as the Riemann tensor), and that develop, explore, and exploit these tools.

We gave a brief overview of these new tools and their applications in an initial Physical Review Letter [1]. Our principal motivation for these tools was described in that Letter, and in greater detail in Section I of our first long, pedagogical paper [2] (Paper I). In brief: we are motivated by the quest to understand *the nonlinear dynamics of curved spacetime* (what John Wheeler has called *geometrodynamics*).

The most promising venue, today, for probing geometrodynamics is numerical simulations of the collisions and mergers of binary black holes [3]. Our new tools provide powerful ways to visualize the results of those simulations. As a byproduct, our visualizations may motivate new ways to compute

the gravitational waveforms emitted in black-hole mergers—waveforms that are needed as templates in LIGO’s searches for and interpretation of those waves.

We will apply our tools to black-hole binaries in Paper IV of this series. But first, in Papers I–III, we are applying our tools to analytically understood spacetimes, with two goals: (i) to gain intuition into the relationships between our tools’ visual pictures of the vacuum Riemann tensor and the analytics, and (ii) to gain substantial new insights into phenomena that were long thought to be well understood. Specifically, in Paper I [2], after introducing our tools, we applied them to weak-gravity situations (“linearized theory”); in Paper II [4], we applied them to stationary (Schwarzschild and Kerr) black holes; and here in Paper III we will apply them to weak perturbations (quasinormal modes) of stationary black holes.

### 9.1.2 Our New Tools, In Brief

In this section, we briefly summarize our new tools. For details, see Sections II, III, and IV of Paper I [2], and Sections II and III of Paper II [4].

When spacetime is foliated by a family of spacelike hypersurfaces (surfaces on which some time function  $t$  is constant), the electromagnetic field tensor  $F_{\mu\nu}$  splits up into an electric field  $E_{\hat{i}} = F_{\hat{i}0}$  and a magnetic field  $B_{\hat{i}} = \frac{1}{2}\epsilon_{\hat{i}\hat{j}\hat{k}}F_{\hat{j}\hat{k}}$ , which are 3-vector fields living in the spacelike hypersurfaces. Here the indexes are components in proper reference frames (orthonormal tetrads) of observers who move orthogonally to the hypersurfaces, and  $\epsilon_{\hat{i}\hat{j}\hat{k}}$  is the Levi-Civita tensor in those hypersurfaces.

Similarly, the Weyl (and vacuum Riemann) tensor  $C_{\mu\nu\lambda\rho}$  splits up into: (i) a *tidal field*  $\mathcal{E}_{\hat{i}\hat{j}} = C_{\hat{i}0\hat{j}0}$ , which produces the tidal gravitational accelerations that appear, e.g., in the equation of geodesic deviation,  $\Delta a_{\hat{j}} = -\mathcal{E}_{\hat{j}\hat{k}}\Delta x^{\hat{k}}$  [Eq. (3.3) of Paper I]; and (ii) a *frame-drag field*  $\mathcal{B}_{\hat{i}\hat{j}} = \frac{1}{2}\epsilon_{\hat{i}\hat{p}\hat{q}}C_{\hat{j}0\hat{p}\hat{q}}$ , which produces differential frame-dragging (differential precession of gyroscopes),  $\Delta\Omega_{\hat{j}} = \mathcal{B}_{\hat{j}\hat{k}}\Delta x^{\hat{k}}$  [Eq. (3.11) of Paper I].

We visualize the tidal field  $\mathcal{E}$  by the integral curves of its three eigenvector fields, which we call *tendex lines*, and also by the eigenvalue of each tendex line, which we call the *tendicity* of the line and we depict using colors. Similarly, we visualize the frame-drag field  $\mathcal{B}$  by frame-drag *vortex lines* (integral curves of its three eigenvector fields) and their *vorticities* (eigenvalues, color coded). See Figures 9.2 and 9.3 below for examples. Tendex and vortex lines are analogs of electric and magnetic field lines. Whereas through each point in space there pass just one electric and one magnetic field line, through each point pass three orthogonal tendex lines and three orthogonal vortex lines, which identify the three principal axes of  $\mathcal{E}$  and  $\mathcal{B}$ .

A person whose body is oriented along a tendex line gets stretched or squeezed with a relative head-to-foot gravitational acceleration that is equal to the person’s height times the line’s tendicity (depicted blue [dark gray] in our figures for squeezing [positive tendicity] and red [light gray] for stretching [negative tendicity]). Similarly, if the person’s body is oriented along a vortex line, a

gyroscope at her feet precesses around her body axis, relative to inertial frames at her head, with an angular velocity equal to her height times the line's vorticity (depicted blue [dark gray] for clockwise precession [positive vorticity] and red [light gray] for counterclockwise [negative vorticity]).

We color code the horizon of a black hole by the normal-normal component of the tidal field,  $\mathcal{E}_{NN}$ , to which we give the name *horizon tendicity*, and also by the normal-normal component of the frame-drag field,  $\mathcal{B}_{NN}$ , the *horizon vorticity*; see, e.g., Figure 9.9 below. These quantities are boost-invariant along the normal direction  $\mathbf{N}$  to the horizon in the foliation's hypersurfaces.

A person hanging radially above the horizon or falling into it experiences head-to-foot squeezing (relative acceleration) equal to the horizon tendicity times the person's height, and a differential head-to-foot precession of gyroscopes around the person's body axis with an angular velocity equal to the horizon vorticity times the person's height.

For any black hole, static or dynamic, the horizon tendicity  $\mathcal{E}_{NN}$  and vorticity  $\mathcal{B}_{NN}$  are related to the horizon's Newman-Penrose Weyl scalar  $\Psi_2$ , and its scalar intrinsic curvature  $\mathcal{R}$  and scalar extrinsic curvature  $\mathcal{X}$  by

$$\mathcal{E}_{NN} + i\mathcal{B}_{NN} = 2\Psi_2 = -\frac{1}{2}(\mathcal{R} + i\mathcal{X}) + 2(\mu\rho - \lambda\sigma); \quad (9.1)$$

[5], and Section III of [4]. Here  $\rho$ ,  $\sigma$ ,  $\mu$ ,  $\lambda$  are spin coefficients related to the expansion and shear of the null vectors  $\vec{l}$  and  $\vec{n}$  used in the Newman-Penrose formalism [with  $(\vec{l} + \vec{n})/\sqrt{2} = \vec{u}$  the normal to the foliation's hypersurfaces,  $(\vec{l} - \vec{n})/\sqrt{2} = \vec{N}$  the normal to the horizon in the foliation's hypersurfaces, and  $\vec{e}_2 = (\vec{m} + \vec{m}^*)/\sqrt{2}$  and  $\vec{e}_3 = (\vec{m} - \vec{m}^*)/(i\sqrt{2})$  tangent to the instantaneous horizon in the foliation's hypersurfaces]. For stationary black holes,  $\rho$  and  $\sigma$  vanish, and  $\mathcal{E}_{NN} = -\frac{1}{2}\mathcal{R}$  and  $\mathcal{B}_{NN} = -\frac{1}{2}\mathcal{X}$ .

For perturbations of Schwarzschild black holes, it is possible to adjust the slicing at first order in the perturbation, and adjust the associated null tetrad, so as to make the spin coefficient terms in Eq. (9.1) vanish at first order in the perturbation; whence  $\mathcal{E}_{NN} = -\frac{1}{2}\mathcal{R}$  and  $\mathcal{B}_{NN} = -\frac{1}{2}\mathcal{X}$ . For perturbations of the Kerr spacetime, however, this is not possible. See Appendix 9.E for details. Following a calculation by Hartle [6], we show in this appendix that for Kerr one can achieve  $\mathcal{R} + i\mathcal{X} = -4(\Psi_2 + \lambda^{(0)}\sigma^{(1)})$  on the horizon, accurate through first order. Here, and throughout this paper, the superscripts  $^{(i)}$  (or subscripts  $_{(i)}$ ) indicate orders in the perturbation.

For the dynamical black holes described in [1] and for the weakly perturbed holes in this paper, we found that the spin terms in Eq. (9.1) are numerically small compared to the other terms, so  $\mathcal{E}_{NN} \simeq -\frac{1}{2}\mathcal{R}$  and  $\mathcal{B}_{NN} \simeq -\frac{1}{2}\mathcal{X}$ . In addition, in a recent study of the tendexes and vortexes of approximate black hole initial data, Dennison and Baumgarte [7] found that these spin terms vanish to a high order in the small velocities of their black holes, giving further evidence that these terms are typically negligible.

Because  $\mathcal{X}$  is the 2-dimensional curl of a 2-dimensional vector (the Hájíček field) [8], its integral over the black hole's 2D horizon vanishes; and by virtue of the Gauss-Bonnet theorem, the horizon integral of  $\mathcal{R}$  is equal to  $8\pi$ . Correspondingly, for fully dynamical black holes as well as weakly perturbed black holes, the horizon integrals of  $\mathcal{E}_{NN}$  and  $B_{NN}$  have the approximate values [1]

$$\int_{\mathcal{H}} \mathcal{B}_{NN} \simeq 0, \quad \int_{\mathcal{H}} \mathcal{E}_{NN} \simeq -4\pi. \quad (9.2)$$

### 9.1.3 Overview of This Paper's Results

#### 9.1.3.1 Slicing, Coordinates and Gauges

Throughout this paper, we use slices of constant Kerr-Schild time  $\tilde{t}$  (which penetrate smoothly through the horizon) to decompose the Weyl tensor into its tidal and frame-drag fields; and we express our quasinormal perturbations, on the slices of constant  $\tilde{t}$ , in Kerr-Schild spatial coordinates (Sections 9.2.1 and 9.2.2, and also Paper II [4]). In the zero-spin (Schwarzschild) limit, the Kerr-Schild slices become slices of constant ingoing Eddington-Finkelstein time  $\tilde{t}$  and the spatial coordinates become those of Schwarzschild. Our choice of Kerr-Schild is dictated by these coordinates' resemblance to the coordinates that are typically used in numerical-relativity simulations of binary black holes, at late times, when the merged hole is settling down into its final Kerr-black-hole state; see, e.g., Figure 9.15 below.

For a perturbed black hole, the slices and coordinates get modified at perturbative order in ways that depend on the *gauge* used to describe the perturbations (i.e., the slicing and spatial coordinates at perturbative order); see Section 9.2.3.

For spinning black holes, we perform all our computations in ingoing radiation gauge (Section 9.2.1 and Appendix 9.C). For non-spinning (Schwarzschild) black holes, we explore gauge dependence by working with two gauges that appear to be quite different: ingoing radiation gauge (Appendix 9.C), and Regge-Wheeler gauge (Appendix 9.A). Remarkably, for each mode we have explored, the field-line visualizations that we have carried out in these two gauges look nearly the same to the human eye; visually we see little gauge dependence. We discuss this and the differences in the gauges, in considerable detail, in Section 9.2.3 and Appendix 9.D.

For a Schwarzschild black hole, we have explored somewhat generally the influence of perturbative slicing changes and perturbative coordinate changes on the tidal and frame-drag fields, and on their tendex and vortex lines, and tendicities and vorticities (Section 9.2.3). We find that the tendicities and vorticities are less affected by perturbative slicing changes, than the shapes of the tendex and vortex lines. We also find that while coordinate changes affect the shapes of the tendex and vortex lines, the tendicity and vorticity along a line is unchanged, and that in the wave zone a perturbative change in coordinates affects the tendicity and vorticity at a higher order than the

effect of gravitational radiation.

For this reason, in this paper we pay considerable attention to vorticity and tendicity contours, as well as to the shapes of vortex and tendex lines.

### 9.1.3.2 Classification of Quasinormal Modes

As is well known, the quasinormal-mode, complex eigenfrequencies of Schwarzschild and Kerr black holes can be characterized by three integers: a poloidal quantum number  $l = 2, 3, \dots$ , an azimuthal quantum number  $m = -l, -l + 1, \dots + l$ , and a radial quantum number  $n$ . For each  $\{n, l, m\}$  and its eigenfrequency  $\omega_{nlm}$ , there are actually two different quasinormal modes (a two-fold degeneracy). Of course, any linear combination of these two modes is also a mode. We focus on those linear combinations of modes that have *definite parity* (Appendix 9.C).

We define a tensor field to have positive parity if it is unchanged under reflections through the origin, and negative parity if it changes sign. A quasinormal mode of order  $(n, l, m)$  is said to have *electric parity* [or *magnetic parity*] if the parity of its metric perturbation is  $(-1)^l$  [or  $(-1)^{l+1}$ ]. The parity of the tidal-field perturbation is the same as that of the metric perturbation, but that of the frame-drag field is opposite. In much of the literature the phrase “even parity” is used in place of “electric parity”, and “odd parity” in place of “magnetic parity”; we avoid those phrases because of possible confusion with positive parity and negative parity.

In this paper, we focus primarily on the most slowly damped ( $n = 0$ ) quadrupolar ( $l = 2$ ) modes, for various azimuthal quantum numbers  $m$  and for electric- and magnetic-parity. Since we discuss exclusively the  $n = 0$  modes, we will suppress the  $n$  index and abbreviate mode numbers as  $(l, m)$ .

### 9.1.3.3 The Duality of Magnetic-Parity and Electric-Parity Modes

In vacuum, the exact Bianchi identities for the Riemann tensor become, under a slicing-induced split of spacetime into space plus time, a set of Maxwell-like equations for the exact tidal field and frame-drag field [Eqs. (2.15) of Paper I [2] in a local Lorentz frame; Eqs. (2.13) and (2.4) of Paper I in general]. These Maxwell-like equations exhibit an exact duality: If one takes any solution to them and transforms  $\mathcal{E} \rightarrow \mathcal{B}$ ,  $\mathcal{B} \rightarrow -\mathcal{E}$ , they continue to be satisfied (Section II B 1 of Paper I [2]).

This duality, however, is broken by the spacetime geometry of a stationary black hole. A Schwarzschild black hole has a monopolar tidal field  $\mathcal{E}$  and vanishing frame-drag field  $\mathcal{B}$ ; and a Kerr black hole has a monopolar component to its tidal field (as defined by a spherical-harmonic analysis at large radii or at the horizon), but only dipolar and higher-order components to its frame-drag field.

When a Schwarzschild or Kerr black hole is perturbed, there is a near duality between its electric-parity mode and its magnetic-parity mode of the same  $(l, m)$ ; but the duality is not exact. The unperturbed hole’s duality breaking induces (surprisingly weak) duality-breaking imprints in the

quasinormal modes. We explore this duality breaking in considerable detail in this paper (Sections 9.2, 9.3.1, 9.3.2.3, and 9.3.3.2, and Appendices 9.C and 9.E.2).

If one tries to see the duality between electric-parity and magnetic-parity modes, visually, in pictures of the perturbed hole's tendex and vortex lines, the duality is hidden by the dominant background tidal field and (for a spinning hole) the background frame-drag field. To see the duality clearly, we must draw pictures of tendex and vortex lines for the perturbative parts  $\delta\mathcal{E}$  and  $\delta\mathcal{B}$  of the tidal and frame-drag fields, with the unperturbed fields subtracted off. We draw many such pictures in this paper.

We have made extensive comparisons of the least damped ( $n = 0$ ) electric-parity and magnetic-parity modes with ( $l = 2, m = 2$ ). These two (2, 2) modes (for any chosen black-hole mass  $M$  and spin parameter  $a$ ) have identically the same complex eigenfrequency, i.e., they are degenerate (as has long been known and as we discussed above). This frequency degeneracy is an unbroken duality.

Pictures of the perturbative vortex and tendex lines and their color-coded vorticities and tendicities show a strong but not perfect duality: For a non-spinning hole, the perturbative vortex lines and their vorticities for the magnetic-parity mode (e.g., Figure 9.2) look almost the same as the perturbative tendex lines and their tendicities for the electric-parity mode (Figure 9.12); and similarly for the other pair of lines and eigenvalues. As the hole's spin is increased, the duality becomes weaker (the corresponding field lines and eigenvalues begin to differ noticeably); but even for very high spins, the duality is strikingly strong; see bottom row of Figure 9.12 below. The duality remains perfect on the horizon in ingoing radiation gauge for any spin, no matter how fast (Section 9.3.1 and Appendix 9.E), and there is a sense in which it also remains perfect on the horizon of Schwarzschild in Regge-Wheeler gauge (last paragraph of Appendix 9.A.5).

#### 9.1.3.4 Digression: Electromagnetic Perturbations of a Schwarzschild Black Hole

As a prelude to discussing the physical character of the gravitational modes of a black hole, we shall discuss electromagnetic (EM) modes, i.e., quasinormal modes of the EM field around a black hole. The properties of EM modes that we shall describe can be derived from Maxwell's equations in the Schwarzschild and Kerr spacetimes, but we shall not give the derivations.

Because the unperturbed hole has no EM field and the vacuum Maxwell equations exhibit a perfect duality (they are unchanged when  $\mathbf{E} \rightarrow \mathbf{B}$  and  $\mathbf{B} \rightarrow -\mathbf{E}$ ), the EM modes exhibit perfect duality. For any magnetic-parity EM mode, the magnetic field pierces the horizon, so its normal component  $B_N$  is nonzero, while  $E_N$  vanishes. By duality, an electric-parity EM mode must have  $E_N \neq 0$  and  $B_N = 0$ . For a magnetic-parity mode, the near-zone magnetic fields that stick out of the horizon can be thought of as the source of the mode's emitted EM waves. We make this claim more precise by focusing on the fundamental ( $n = 0$ ), magnetic-parity,  $l = 1, m = 1$  mode:

Figure 9.2 shows magnetic field lines for this (1,1) mode, on the left (a) in the hole's equatorial

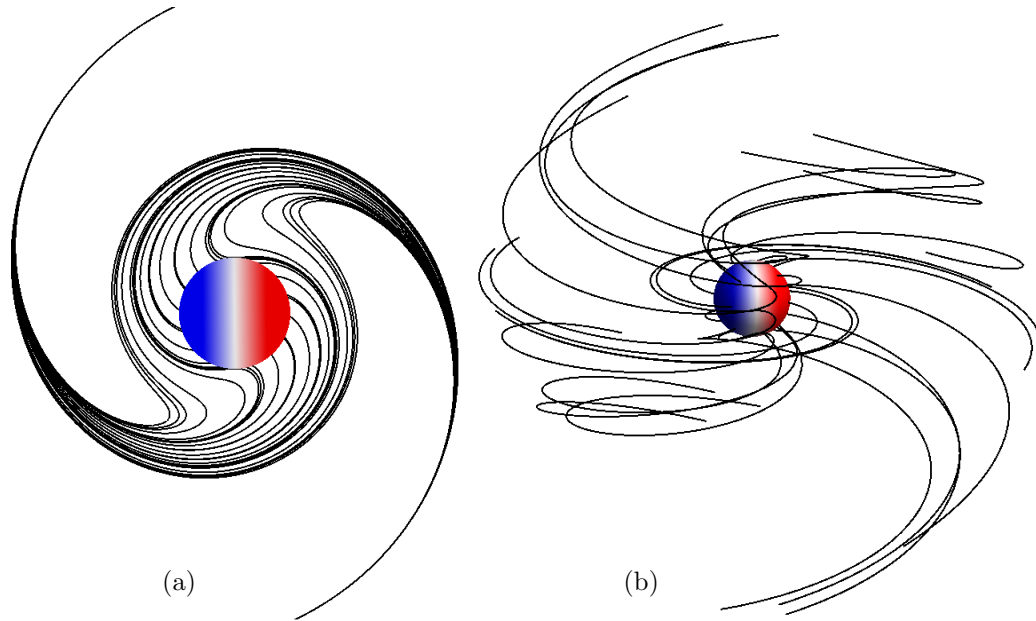


Figure 9.1: (a) Some magnetic field lines in the equatorial plane for the  $(1, 1)$  quasinormal mode of the electromagnetic field around a Schwarzschild black hole, with Eddington-Finkelstein slicing. The horizon is color coded by the sign of the normal component of the magnetic field. The configuration rotates counterclockwise in time. (b) Some magnetic field lines for this same quasinormal mode, in 3 dimensions.

plane, and on the right (b) in 3 dimensions with the equatorial plane horizontal. On the left, we see a bundle of magnetic field lines that thread through the horizon and rotate counterclockwise. As they rotate, the field lines spiral outward and backward, like water streams from a whirling sprinkler, becoming the magnetic-field component of an outgoing electromagnetic wave. The electric field lines for this mode (not shown) are closed circles that represent the electric part of electromagnetic waves traveling outward at radii  $r \gg 2M$  and inward at radii  $r \simeq 2M$ . This mode's waves, we claim, are generated by the near-zone, rotating magnetic field lines that thread the hole (Figure 9.1a). An analogy will make this clear.

Consider a rotating (angular velocity  $\sigma$ ), perfectly conducting sphere in which is anchored a magnetic field with the same dipolar normal component  $B_N \propto \Re[Y^{11}(\theta, \phi)e^{-i\sigma t}]$  as the horizon's  $B_N$  for the  $(1,1)$  quasinormal mode (the red [light gray] and blue [dark gray] coloring on the horizon in Figure 9.1). At some initial moment of time, lay down outside the conducting sphere, a magnetic-field configuration that (i) has this  $B_N$  at the sphere, (ii) satisfies the constraint equation  $\nabla \cdot \mathbf{B} = 0$ , (iii) resembles the field of Figure 9.1 in the near zone, i.e., at  $r \lesssim \lambda = c/\sigma$  and at larger radii has some arbitrary form that is unimportant; and (iv) (for simplicity) specify a vanishing initial electric field. Evolve these initial fields forward in time using the dynamical Maxwell equations. It should be obvious that the near-zone, rotating magnetic field will not change much. However, as it rotates, via Maxwell's dynamical equations it will generate an electric field, and those two fields, interacting,

will give rise to the outgoing electromagnetic waves of a  $l = 1$ ,  $m = 1$  magnetic dipole. Clearly, the ultimate source of the waves is the rotating, near-zone magnetic field that is anchored in the sphere. (Alternatively, one can regard the ultimate source as the electric currents in the sphere, that maintain the near-zone magnetic field.)

Now return to the magnetized black hole of Figure 9.1, and pose a similar evolutionary scenario: At some initial moment of time, lay down a magnetic-field configuration that (i) has the same normal component at the horizon as the (1,1) mode, (ii) satisfies the constraint equation  $\nabla \cdot \mathbf{B} = 0$ , and (iii) resembles the field of Figure 9.1 in the near zone. In this case, the field is not firmly anchored in the central body (the black hole), so we must also specify its time derivative to make sure it is rotating at the same rate as the (1,1) quasinormal mode. This means (by a dynamical Maxwell equation) that we will also be giving a nonvanishing electric field that resembles, in the near zone, that of the (1,1) mode and in particular does not thread the horizon. Now evolve this configuration forward in time. It will settle down, rather quickly, into the (1,1) mode, with outgoing waves in the wave zone, and ingoing waves at the horizon. This is because the (1,1) mode is the most slowly damped quasinormal mode that has significant overlap with the initial data.

As for the electrically conducting, magnetized sphere, so also here, the emitted waves are produced by the rotation of the near-zone magnetic field. But here, by contrast with there, the emitted waves act back on the near-zone magnetic field, causing the field lines to gradually slide off the horizon, resulting in a decay of the field strength at a rate given by the imaginary part of the mode's complex frequency.

This back-action can be understood in greater depth by splitting the electric and magnetic fields, *near the horizon*, into their *longitudinal* (radial) and *transverse* pieces. The longitudinal magnetic field is  $B_N$  and it extends radially outward for a short distance; the tangential magnetic field is a 2-vector  $\mathbf{B}^T$  parallel to the horizon; and similarly the electric field has  $E_N = 0$ , and so is purely transverse. The tangential fields actually only look like ingoing waves to observers who, like the horizon, move outward at (almost) the speed of light: the observers of a Schwarzschild time slicing. As one learns in the Membrane Paradigm for black holes (Sections III.B.4 and III.C.2 of [9]), such observers can map all the physics of the event horizon onto a *stretched horizon*—a spacelike 2-surface of constant lapse function  $\alpha = \sqrt{1 - 2M/r} \ll 1$  very close in spacetime to the event horizon. On the stretched horizon, these observers see  $\mathbf{E}^T = \mathbf{N} \times \mathbf{B}^T$  (ingoing-wave condition), and the tangential magnetic field acts back on the longitudinal field via

$$\frac{\partial B_N}{\partial t} + {}^{(2)}\nabla \cdot (\alpha \mathbf{B}^T) = 0. \quad (9.3)$$

Here  ${}^{(2)}\nabla \cdot (\alpha \mathbf{B}^T)$  is the 2-dimensional divergence in the stretched horizon, and the lapse function in this equation compensates for the fact that the Schwarzschild observers see a tangential field that

diverges as  $1/\alpha$  near the horizon, due to their approach to the speed of light.

Equation (9.3) is a conservation law for magnetic field lines on the stretched horizon. The density (number per unit area) of field lines crossing the stretched horizon is  $B_N$ , up to a multiplicative constant; the flux of field lines (number moving through unit length of some line in the stretched horizon per unit time) is  $\mathbf{B}^T$ , up to the same multiplicative constant; and Eq. (9.3) says that the time derivative of the density plus the divergence of the flux vanishes: the standard form for a conservation law.

*The longitudinal magnetic field  $B_N(\theta, \phi)$  is laid down as an initial condition (satisfying the magnetic constraint condition). As it rotates, it generates the ingoing-wave near-horizon transverse fields embodied in  $\mathbf{E}^T$  and  $\mathbf{B}^T$  (and also the outgoing electromagnetic waves far from the hole); and the divergence of  $\alpha\mathbf{B}^T$ , via Eq. (9.3), then acts back on the longitudinal field that produced it, pushing the field lines away from the centers of the blue (dark gray) and red (light gray) spots on the stretched horizon toward the white ring. Upon reaching the white ring, each field line in the red region attaches onto a field line from the blue region and slips out of the horizon. Presumably, the field line then travels outward away from the black hole and soon becomes part of the outgoing gravitational waves. The gradual loss of field lines in this way is responsible for the mode's exponential decay.*

### 9.1.3.5 The Physical Character of Magnetic-Parity and Electric-Parity Modes

For a Schwarzschild black hole, the physical character of the gravitational modes is very similar to that of the electromagnetic modes:

*Just as a magnetic-parity EM mode has nonzero  $B_N$  and vanishing  $E_N$ , so similarly: for a Schwarzschild black hole, the **magnetic-parity** modes of any  $(l, m)$  have nonzero (solely perturbative) horizon vorticity  $\delta\mathcal{B}_{NN} = \mathcal{B}_{NN}$ , and vanishing perturbative horizon tendicity  $\delta\mathcal{E}_{NN} = 0$ ; and correspondingly, from the horizon there emerge nearly normal vortex lines that are fully perturbative and no nearly normal, perturbative tendex lines.*

Just as in the EM case the near-zone magnetic fields that emerge from the horizon are the source of the emitted electromagnetic waves, so also in the gravitational case, *for a magnetic-parity mode, the emerging, near-zone, vortex lines and their vorticities can be thought of as the source of the emitted magnetic-parity gravitational waves* (see the next subsection). In this sense, magnetic-parity modes can be thought of as fundamentally frame-drag in their physical origin. Figure 9.2 below depicts a (2, 2) example. We will discuss this example in Section 9.1.3.6.

For a Schwarzschild black hole, *the **electric-parity** modes of any  $(l, m)$  have nonzero perturbative horizon tendicity  $\delta\mathcal{E}_{NN} \neq 0$ , and vanishing horizon vorticity  $\delta\mathcal{B}_{NN} = \mathcal{B}_{NN} = 0$ ; and correspondingly, from the horizon there emerge nearly normal perturbative tendex lines and no nearly normal vortex lines.* The emerging, near-zone, perturbative tendex lines can be thought of as the source of the mode's emitted electric-parity gravitational waves. In this sense, electric-parity modes can be

thought of as fundamentally tidal in their physical origin.

There is a close analogy, here, to the tidal and frame-drag fields of dynamical multipoles in linearized theory (Paper I [2]): Electric-parity (mass) multipoles have a tidal field that rises more rapidly, as one approaches the origin, than the frame-drag field, so these electric-parity multipoles are fundamentally tidal in physical origin. By contrast, for magnetic-parity (current) multipoles it is the frame-drag field that grows most rapidly as one approaches the origin, so they are fundamentally frame-drag in physical origin.

When a black hole is spun up, the horizon vorticities of its electric-parity modes become nonzero, and the horizon tendicities of its magnetic-parity modes acquire nonzero perturbations. However, these spin-induced effects leave the modes still predominantly tidal near the horizon for electric-parity modes, and predominantly frame-drag near the horizon for magnetic-parity modes (Section 9.3).

### 9.1.3.6 The (2, 2) Magnetic-Parity Mode of a Schwarzschild Hole

In this and the next several subsections, we summarize much of what we have learned about specific  $n = 0, l = 2$  modes (the least-damped quadrupolar modes), for various  $m$ . We shall focus primarily on magnetic-parity modes, since at the level of this discussion the properties of electric-parity modes are the same, after a duality transformation  $\delta\mathcal{E} \rightarrow \delta\mathcal{B}$ ,  $\delta\mathcal{B} \rightarrow -\delta\mathcal{E}$ .

It is a remarkable fact that, for a magnetic-parity mode of a Schwarzschild black hole, all gauges share the same slicing, and the mode's frame-drag field is unaffected by perturbative changes of spatial coordinates; therefore, the frame-drag field is fully gauge invariant. See Section 9.2.3. This means that Figures 9.2–9.8 are fully gauge invariant.

We begin with the (2, 2) magnetic-parity mode of a Schwarzschild black hole. Figure 9.2 depicts the negative-vorticity vortex lines (red) and contours of their vorticity (white and purple [dark gray]), in the hole's equatorial plane. Orthogonal to the red (solid) vortex lines (but not shown) are positive-vorticity vortex lines that also lie in the equatorial plane. Vortex lines of the third family pass orthogonally through the equatorial plane. The entire configuration rotates counterclockwise, as indicated by the thick dashed arrow. The dotted lines, at radii  $r = \lambda$  and  $r = \pi\lambda$  (where  $\lambda$  is the emitted waves' reduced wavelength), mark the approximate outer edge of the near zone, and the approximate inner edge of the wave zone.

Just as the near-zone electromagnetic (1,1) perturbations are dominated by radial field lines that thread the black hole and have a dipolar distribution of field strength, so here the *near-zone gravitational perturbations* are dominated by (i) the radial vortex lines that thread the hole and have a quadrupolar distribution of their horizon vorticity  $\mathcal{B}_{NN} = \delta\mathcal{B}_{NN}$ , and also by (ii) a transverse, isotropic frame-drag field  $\mathcal{B}_{\hat{\theta}\hat{\theta}} = \mathcal{B}_{\hat{\phi}\hat{\phi}} = -\frac{1}{2}\delta\mathcal{B}_{NN}$  that is tied to  $\mathcal{B}_{NN}$  in such a way as to guarantee that this dominant part of  $\mathcal{B}$  is traceless.

This full structure, the normal-normal field and its accompanying isotropic transverse field, makes

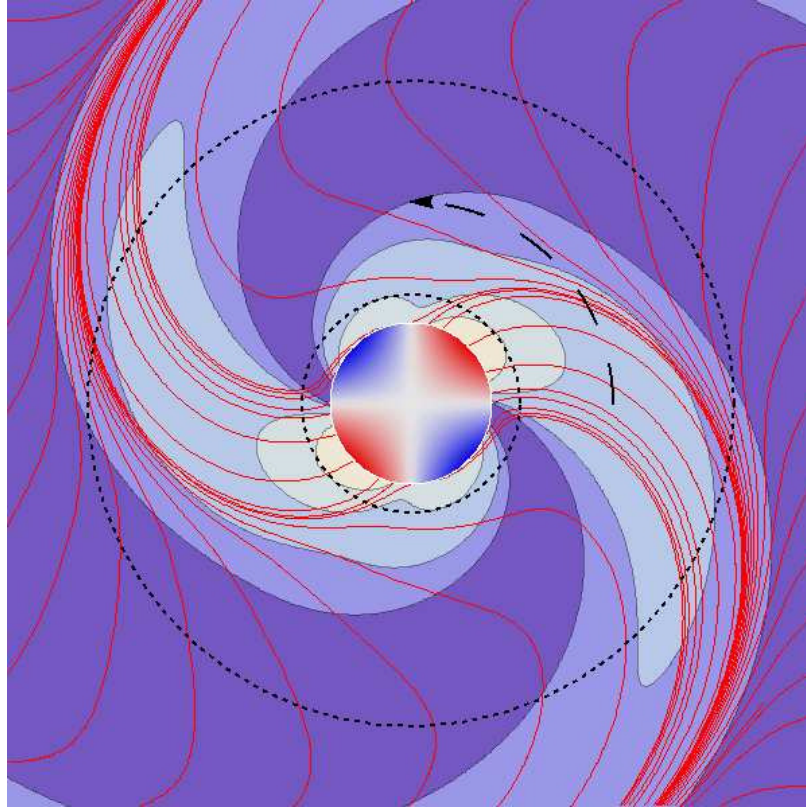


Figure 9.2: Some vortex lines (solid, red lines) and contours of vorticity (shaded regions) in the equatorial plane for the  $(2, 2)$  *magnetic-parity* quasinormal mode of a non-rotating, Schwarzschild black hole, with complex eigenfrequency  $\omega = (0.37367 - 0.08896i)/M$  where  $M$  is the hole's mass. The horizon (central circle) is color coded by the horizon vorticity  $\mathcal{B}_{NN}$  as seen by someone looking down on the black hole; this vorticity is entirely perturbative. The thick, solid red curves are one set of vortex lines in the equatorial plane—the set with negative vorticity. These lines include some that emerge from the horizon in the negative-vorticity (red) regions, and some that never reach the horizon. The other, positive-vorticity, equatorial vortex lines are orthogonal to the ones shown, and are identical to those shown but rotated through 90 degrees around the hole so some of them emerge from the horizon in the positive-vorticity (blue) regions. The contours represent the vorticity of the red (negative-vorticity) vortex lines, with largest magnitude of vorticity white and smallest purple (dark gray); the contours mark where the vorticity has fallen to 50%, 25%, 10%, and 5% of the maximum value attained at the center of the horizon vortex. The two dotted circles are drawn at Schwarzschild radii  $r = \lambda$  and  $r = \pi\lambda = \lambda/2$ . They mark the approximate outer edge of the near zone and the approximate inner edge of the wave zone. The arrow marks the direction of rotation of the perturbation.

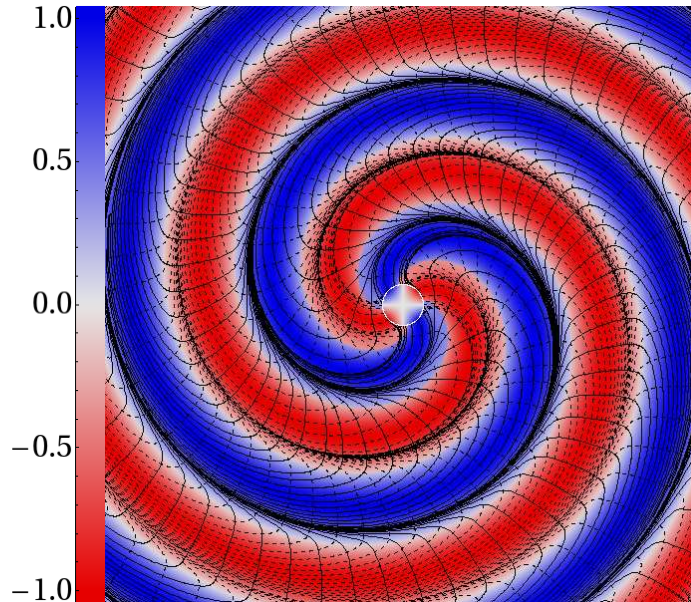


Figure 9.3: The vortex lines (solid black for clockwise; dashed black for counterclockwise) and color-coded vorticities in the equatorial plane for the same magnetic-parity (2, 2) mode as in Figure 9.2. This figure differs from Figure 9.2 in ways designed to give information about the emitted gravitational waves: (i) It extends rather far out into the wave zone. (ii) It shows the angular structure of the vorticity for the dominant vortex lines in each region of the equatorial plane. More specifically: the color at each point represents the vorticity of the equatorial vortex line there which has the largest magnitude of vorticity, with radial variations of vorticity normalized away (so the linear color code on the left indicates vorticity relative to the maximum at any given radius). The regions of large positive vorticity (blue [dark gray]) are *clockwise vortexes*; those of large negative vorticity (red [light gray]) are *counterclockwise vortexes*.

up the *longitudinal, nonradiative frame-drag field*  $\mathcal{B}^L$  near the horizon. (As we shall discuss below, this longitudinal structure is responsible for generating the mode's gravitational waves, and all of the rest of its fields.) Somewhat smaller are (i) the longitudinal-transverse components of  $\mathcal{B}$  ( $\mathcal{B}_{\hat{r}\hat{\theta}}$  and  $\mathcal{B}_{\hat{r}\hat{\phi}}$ ), which together make up the *longitudinal-transverse* part of the frame-drag field, a 2-vector  $\mathcal{B}^{LT}$  parallel to the horizon, and give the horizon-piercing vortex lines small non-normal components; and (ii) transverse-traceless components  $\mathcal{B}_{\hat{\theta}\hat{\theta}} = -\mathcal{B}_{\hat{\phi}\hat{\phi}}$ , which make up the *transverse-traceless* part of the frame-drag field, a 2-tensor  $\mathcal{B}^{TT}$  parallel to the horizon, and are ingoing gravitational waves as seen by Schwarzschild observers. (This decomposition into L, LT, and TT parts is useful only near the horizon and in the wave zone, where there are preferred longitudinal directions associated with wave propagation.)

As the near-zone, longitudinal frame-drag field  $\mathcal{B}^L$  rotates, it generates a near-zone longitudinal-transverse (LT) perturbative frame-drag field  $\mathcal{B}^{LT}$  via  $\mathcal{B}$ 's propagation equation (the wave equation for the Riemann tensor), and it generates a LT tidal field  $\delta\mathcal{E}^{LT}$  via the Maxwell-like Bianchi identity which says, in a local Lorentz frame (for simplicity),  $\partial\mathcal{E}/\partial t = (\nabla \times \mathcal{B})^S$ , where the superscript S means "symmetrize" [Eq. (2.15) of Paper I]. These three fields,  $\mathcal{B}^L$ ,  $\mathcal{B}^{LT}$ , and  $\delta\mathcal{E}^{LT}$  together maintain

each other during the rotation via this Maxwell-like Bianchi identity and its (local-Lorentz-frame) dual  $\partial\mathcal{B}/\partial t = -(\nabla \times \mathcal{E})^S$ . They also generate the transverse-traceless parts of both fields,  $\mathcal{B}^{\text{TT}}$  and  $\delta\mathcal{E}^{\text{TT}}$ , which become the outgoing gravitational waves in the wave zone and ingoing gravitational waves at the horizon.

In the equatorial plane, this outgoing-wave generation process, described in terms of vortex and tendex structures, is quite pretty, and is analogous to the (1,1) magnetic-field mode of Figure 9.1 and Section 9.1.3.4: As one moves outward into the induction zone and then the wave zone, the equatorial vortex lines bend backward into outgoing spirals (Figure 9.2) and gradually acquire accompanying tendex lines. The result, locally, in the wave zone, is the standard pattern of transverse, orthogonal red and blue vortex lines; and (turned by 45 degrees to them) transverse, orthogonal red and blue tendex lines, that together represent plane gravitational waves (Figure 7 of Paper I).

It is instructive to focus attention on regions of space with large magnitude of vorticity. We call these regions *vortexes*. Figure 9.3 shows that the equatorial frame-drag field consists of four outspiraling vortexes, two red ([light gray] counterclockwise) and two blue ([dark gray] clockwise).

The solid black lines in the figure are clockwise vortex lines. In the clockwise vortexes of the wave zone, they have the large magnitude of vorticity that is depicted as blue (dark gray), and they are nearly transverse to the radial wave-propagation direction; so they represent crests of outgoing waves. In the counterclockwise vortexes (red [light gray] regions), these clockwise vortex lines have very small magnitude of vorticity and are traveling roughly radially, leaping through a red vortex (a wave trough) from one blue vortex (wave crest) to the next. These clockwise vortex lines accumulate at the outer edges of the clockwise (blue) vortexes.

The dashed black lines are counterclockwise vortex lines, which are related to the red (light gray), counterclockwise vortexes in the same way as the solid clockwise vortex lines are related to the blue (dark gray), clockwise vortexes.

Outside the equatorial plane, this mode also represents outgoing gravitational waves, once one gets into the wave zone. We depict the strengths of those waves in Figure 9.4. The blue (dark gray) regions are locations where one vortex line has vorticity at least 85% of the maximum at that radius; in this sense, they are clockwise vortexes. In the near zone, two (blue) clockwise vortexes emerge radially from the horizon parallel to the plane of the picture, and two (red) counterclockwise vortexes emerge radially toward and away from us. These are 3-dimensional versions of the four vortexes emerging from the horizon in the equatorial plane of Figure 9.3. In the wave zone, the “85%” vortexes are concentrated in the polar regions, because this mode emits its gravitational waves predominantly along the poles. The waves are somewhat weaker in the equatorial plane, so although there are spiraling vortexes in and near that plane (Figure 9.3), they do not show up at the 85% level of Figure 9.4. The off-white, spiral-arm structures in the equatorial plane represent the four regions where the wave strength is passing through a minimum.

## Magnetic

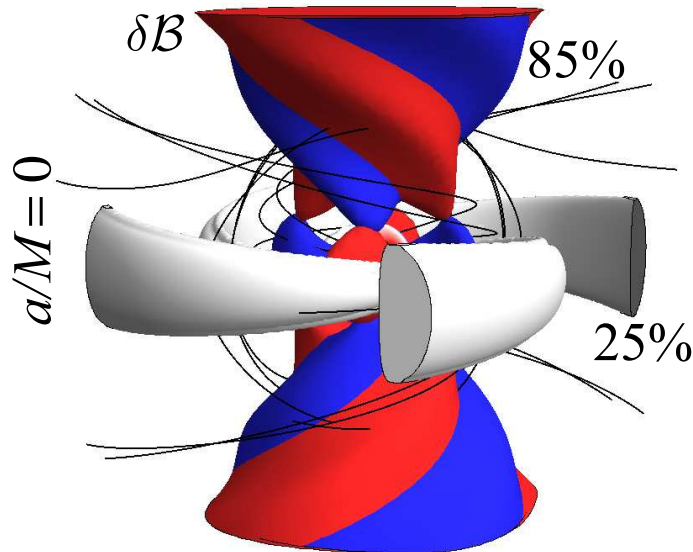


Figure 9.4: Some 3-dimensional clockwise vortex lines (shown black) and regions of large vorticity (vortexes, shown blue [dark gray] and red [light gray]) and small vorticity (shown off-white), for the same magnetic-parity mode of a Schwarzschild black hole as in Figures 9.2 and 9.3. More specifically: the inner sphere is the horizon, color coded by its vorticity. The blue region is a clockwise vortex in which one vortex line has vorticity at least 85% of the maximum value at that radius, and similarly for the counterclockwise red region. The four off-white regions are locations where no vortex line has magnitude of vorticity in excess of 25% of the maximum at that radius.

Turn attention from the wave zone to the horizon. There the ingoing waves, embodied in  $\mathbf{B}^{\text{TT}}$  and  $\delta\mathcal{E}^{\text{TT}}$  (which were generated in the near and transition zones by rotation of  $\mathbf{B}^{\text{L}}$ ), act back on  $\mathbf{B}^{\text{L}}$ , causing its vortex lines to gradually slide off the horizon and thereby producing the mode's exponential decay.

Just as this process in the electromagnetic case is associated with the differential conservation law (9.3) for magnetic field lines threading the horizon,  $\partial B_N/\partial t + {}^{(2)}\nabla \cdot (\alpha\mathbf{B}^{\text{T}})$ , so also here it is associated with an analogous (approximate) conservation law and an accompanying driving equation, Eqs. (9.111) of Appendix 9.E:

$$\mathbf{D}\Psi_2^{(1)} + (\delta^* + 2\pi - 2\alpha)\Psi_1 = 0, \quad (9.4a)$$

$$(\mathbf{D} - 2\epsilon)\Psi_1 = (\delta^* + \pi - 4\alpha)\Psi_0. \quad (9.4b)$$

Here the notation is that of Newman and Penrose:  $\mathbf{D}$  is a time derivative on the horizon,  $\Psi_2^{(1)}$  is the mode's  $\delta\mathcal{E}^{\text{L}} + i\mathcal{B}^{\text{L}}$  (equivalently  $\delta\mathcal{E}_{NN} + i\mathcal{B}_{NN}$  in disguise), with  $\delta\mathcal{E}^{\text{L}}$  and  $\delta\mathcal{E}_{NN}$  vanishing for our mode;  $\Psi_1$  is the LT field  $\delta\mathcal{E}^{\text{LT}} + i\delta\mathcal{B}^{\text{LT}}$  (as measured by Schwarzschild observers) in disguise;  $\Psi_0$  is the ingoing-wave  $\delta\mathcal{E}^{\text{TT}} + i\delta\mathcal{B}^{\text{TT}}$  (as measured by Schwarzschild observers) in disguise;  $\delta^*$  is a

divergence in disguise; and  $\epsilon$ ,  $\pi$  and  $\alpha$  are NP spin coefficients. Equation (9.4b) says that the ingoing waves embodied in  $\delta\mathcal{E}^{\text{TT}} + i\mathcal{B}^{\text{TT}}$  drive the evolution of the quantity  $\Psi_1$ , and Equation (9.4a) is an approximate differential conservation law in which this  $\Psi_1$  plays the role of the flux of longitudinal vortex lines (number crossing a unit length per unit time) and  $\Psi_2$  (i.e.,  $\mathcal{B}_{NN}$ ) is the density of longitudinal vortex lines. This differential conservation law says that the time derivative of the vortex-line density plus the divergence of the vortex-line flux is equal to some spin-coefficient terms that, we believe, are generally small. (By integrating this approximate conservation law over the horizon  $\mathcal{H}$ , we see that  $\int_{\mathcal{H}} B_{NN} dA$  must be nearly conserved, in accord with Eq. (9.2) above, which tells us that the horizon integral is nearly zero. In both cases, the integral conservation law (9.2) and the differential conservation law (9.4a), it is numerically small spin coefficients that slightly spoil the conservation. In Eq. (9.28), for a magnetic-parity mode of Schwarzschild and Eddington-Finkelstein slicing, we make this conservation law completely concrete and find that in this case it is precise; there are no small spin coefficients to spoil it.

Returning to the evolution of the (2,2) magnetic-parity mode: The ingoing waves, via Eqs. (9.4), push the longitudinal vortex lines away from the centers of the horizon vortexes toward their edges (toward the white horizon regions in Figures 9.2 and 9.3). At the edges, clockwise vortex lines from the blue (dark gray) horizon vortex and counterclockwise from the red (light gray) horizon vortex meet and annihilate each other, leading to decay of the longitudinal part of the field and thence the entire mode.

We expect to explore this evolutionary process in greater detail and with greater precision in future work.

Turn, next, to spinning black holes. In this case, the (2, 2) magnetic-parity mode has qualitatively the same character as for a non-spinning black hole. The principal change is due to the spin raising the mode's eigenfrequency, and the near zone thereby essentially disappearing, so the perturbed vortex lines that emerge from the horizon have a significant back-spiral-induced tilt to them already at the horizon. See Figure 9.12 below.

### 9.1.3.7 The (2,1) Magnetic-Parity Mode of a Schwarzschild Hole

For the (2,1) magnetic-parity mode of a Schwarzschild black hole, there are two horizon vortexes in the hole's northern hemisphere (one counterclockwise, the other clockwise), and two in the southern hemisphere. From these emerge the longitudinal part of the frame-drag field, in the form of four 3D vortexes (Figure 9.5).

These four vortexes actually form two spiral arms, each of which contains vortex lines of both signs (clockwise and counterclockwise). The surface of each arm is color coded by the sign of the vorticity that is largest in magnitude in that region of the arm. This dominant vorticity flips sign when one passes through the equatorial plane—from positive (i.e., blue [dark gray]; clockwise) on

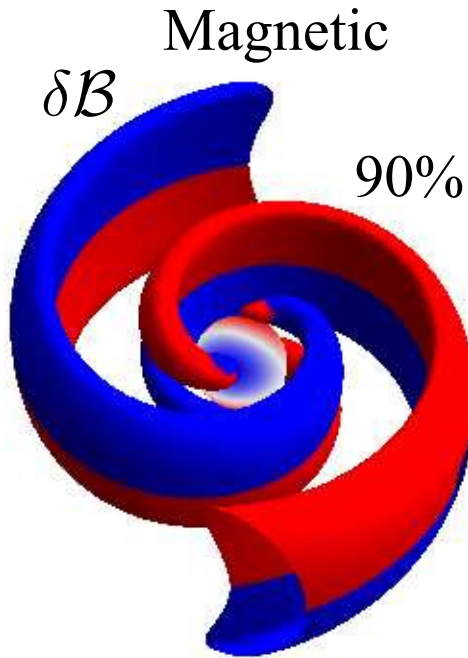


Figure 9.5: Three-dimensional vortices for the magnetic-parity, (2,1) mode of a Schwarzschild black hole. The colored surfaces enclose the region where, for each radius, the vorticity of at least one vortex line exceeds 90% of the maximum for that radius. In the blue and red (dark and light gray) regions, the clockwise and counterclockwise vortex lines, respectively, have the larger vorticity.

one side of the equator to negative (i.e., red [light gray]; clockwise) on the other side. The reason for this switch is that for  $m = 1$  the  $e^{im\phi}$  angular dependence means reflection antisymmetry through the polar axis, which combined with the positive parity of the  $l = 2$  frame-drag field implies reflection antisymmetry through the equatorial plane. The (2,2) mode of the previous section, by contrast, was reflection symmetric through both the polar axis and the equatorial plane.

By contrast with the (2,2) mode, whose region of largest vorticity switched from equatorial in the near zone to polar in the wave zone (Figure 9.3), for this (2,1) mode, the region of largest vorticity remains equatorial in the wave zone. In other words, this mode's gravitational waves are stronger in near-equator directions than in near-polar directions. (Recall that in the wave zone, the vortices are accompanied by tendexes with tendicities equal in magnitude to the vorticities at each event, so we can discuss the gravitational-wave strengths without examining the tidal field.)

Close scrutiny of the near-horizon region of Figure 9.5 reveals a surprising feature: Within the 90% vortices (colored surfaces), the sign of the largest vorticity switches as one moves from the near zone into the transition zone—which occurs not very far from the horizon; see the inner dashed circle in Figure 9.2 above). This appears to be due to the following: The near-zone vortices are

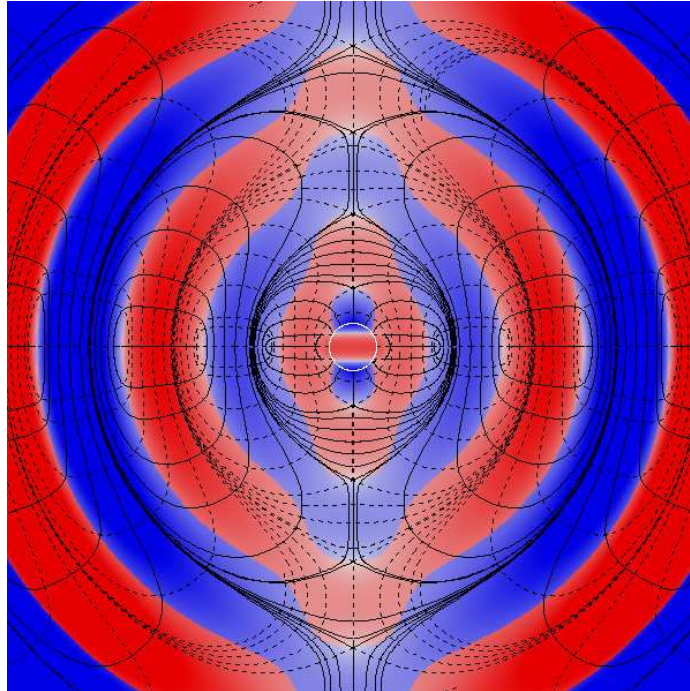


Figure 9.6: Vortex lines and vorticities for magnetic-parity (2,0) mode of Schwarzschild in a surface  $\mathcal{S}_\phi$  of constant  $\phi$ . The line and coloring conventions are the same as in Figure 9.3 (solid lines for clockwise, dashed for counterclockwise; color shows vorticity of the vortex line with largest magnitude of vorticity, with radial variations removed and intensity of color as in the key on right edge of Figure 9.3). The central circle is the horizon, color coded by the horizon vorticity.

dominated by the longitudinal part of the frame-drag field  $\delta\mathcal{B}^L$ , which generates all the other fields including  $\delta\mathcal{B}^{LT}$  via its rotation [see discussion of the (2,2) mode above]. The longitudinal-transverse field  $\delta\mathcal{B}^{LT}$  is strong throughout the near zone and comes to dominate over  $\delta\mathcal{B}^L$  as one moves into the transition zone. Its largest vorticity has opposite sign from that of  $\delta\mathcal{B}^L$ , causing the flip of the dominant vorticity and thence the color switch as one moves into the transition zone. (Note that a similar switch in the sign of the strongest vorticity occurs for the magnetic-parity (2,2) mode vortices illustrated in Figure 9.4, although there the transition occurs farther out, at the edge of the wave zone.)

In Sections 9.5.1 and 9.5.2, we explore in considerable detail this magnetic-parity (2,1) mode and also its near dual, the electric-parity (2,1) mode, focusing especially on the shapes of their vortices.

### 9.1.3.8 The (2,0) Magnetic-Parity Mode of a Schwarzschild Hole

The (2,0) magnetic-parity mode has very different dynamical behavior from that of the (2,1) and (2,2) modes. Because of its axisymmetry, this mode cannot be generated by longitudinal, near-zone vortices that rotate around the polar axis, and its waves cannot consist of outspiraling, intertwined vortex and tendex lines.

Instead, this mode is generated by longitudinal, near-zone vortexes that oscillate, and its waves are made up of intertwined vortex lines and tendex lines that wrap around deformed tori. These gravitational-wave tori resemble smoke rings and travel outward at the speed of light. More specifically:

Because of axisymmetry, the (2,0) magnetic-parity mode has one family of vortex lines that are azimuthal circles of constant  $r$  and  $\theta$ , and two families that lie in surfaces  $\mathcal{S}_\phi$  of constant  $\phi$ . Figure 9.6 is a plot in one of these  $\mathcal{S}_\phi$  surfaces. (The plot for any other  $\phi$  will be identical to this, by axisymmetry.) This plot shows the vortex lines that lie in  $\mathcal{S}_\phi$ , and by color coding at each point, the vorticity of the strongest of those lines.

Notice that, at this phase of oscillation, there are clockwise (solid) vortex lines sticking nearly radially out of the horizon's polar regions and counterclockwise (dashed) vortex lines sticking nearly radially out of the horizon's equatorial region. A half cycle later the poles will be red (light gray) and equator blue (dark gray). These near-zone vortex lines are predominantly the longitudinal part of the frame-drag field  $\delta\mathcal{B}^L$ , which we can regard as working hand in hand with the near-zone, longitudinal-transverse tidal field  $\delta\mathcal{E}^{LT}$  to generate the other fields.

As we shall see in Section 9.5.3 (and in more convincing detail for a different oscillatory mode in Section 9.4.3), the dynamics of the oscillations are these: Near-zone energy<sup>1</sup> oscillates back and forth between the near-zone  $\delta\mathcal{B}^L$ , and the near-zone  $\delta\mathcal{B}^{LT}$  and  $\delta\mathcal{E}^{LT}$ . As  $\delta\mathcal{B}^L$  decays, its vortex lines slide off the hole and (we presume) form closed loops, lying in  $\mathcal{S}_\phi$ , which encircle outgoing deformed tori of perturbed tendex lines that become the transverse-traceless gravitational waves. Only part of the energy in  $\delta\mathcal{B}^L$  goes into the outgoing waves. Some goes into the TT ingoing waves, and the rest (a substantial fraction of the total energy) goes into  $\delta\mathcal{B}^{LT}$  and  $\delta\mathcal{E}^{LT}$ , which then use it to regenerate  $\delta\mathcal{B}^L$ , with its horizon-penetrating vortex lines switched in sign (color), leading to the next half cycle of oscillation.

The vortex lines that encircle the gravitational-wave tori are clearly visible in Figure 9.6. Each solid (clockwise) line is tangential (it points nearly in the  $\theta$  direction) when it is near the crest

---

<sup>1</sup>We use the term *energy* in a generalized and descriptive sense here and elsewhere in this paper. We note, however, that with a suitable (nonunique) definition of local energy, we can make these notions more precise. For example, the totally symmetric, traceless Bel-Robinson tensor serves as one possible basis for this. In vacuum it is  $T_{\mu\nu\rho\sigma} = 1/2(C_{\mu\alpha\nu\beta}C_\rho{}^\alpha{}_\sigma{}^\beta + C_{\mu\alpha\nu\beta}^*C_\rho{}^\alpha{}_\sigma{}^\beta)$  with  $*$  denoting the Hodge dual, and it is completely symmetric and obeys the *differential* conservation law  $\nabla_\mu T^\mu{}_{\nu\rho\sigma} = 0$ . Given a unit timelike slicing vector  $\vec{u}$  we conveniently have  $W(\vec{u}) = T_{\mu\nu\rho\sigma}u^\mu u^\nu u^\rho u^\sigma = 1/2(E_{ij}E^{ij} + B_{ij}B^{ij}) \geq 0$  as a positive-definite *superenergy* built from the squares of the tidal and frame-drag fields in a given slice (see the reprint of Bel's excellent paper [10] for motivation and definition, e.g., Penrose and Rindler [5] for the spinor representation of the Bel-Robinson tensor, and e.g., [11] for its relation to notions of quasilocal energy). As another example, magnetic-parity modes of Schwarzschild are describable by the Regge-Wheeler function  $Q(r_*, t)$  which satisfies the Sturm-Liouville equation  $Q_{,r_*r_*} - Q_{,tt} - \mathcal{V}(r_*)Q = 0$  [Eq. (9.33) but with the  $e^{-i\omega t}$  time dependence absorbed into  $Q$ ]. The *integral* conservation law associated with this Sturm-Liouville equation is  $\partial/\partial t \int_a^b (Q_{,r_*}^2 + Q_{,t}^2 + \mathcal{V}Q^2) dr_* = 2Q_{,r_*}Q_{,t}|_a^b$ . The quantity inside the integral can be regarded as an energy density, and the quantity on the right hand side an energy flux. For the (2,  $m$ ) magnetic-parity mode, Eqs. (9.40a) and (9.40d) express  $Q$  in terms of the time derivative of the longitudinal part of  $\delta\mathcal{B}$  with its angular dependence  $Y^{2m}$  removed:  $Q = (r^3/12)\partial\delta\mathcal{B}_{\hat{r}\hat{r}}/\partial t$ . Other expressions in Eqs. (9.40) and (9.54) relate  $Q_{,r_*}$  to the LT parts of  $\delta\mathcal{B}$  and  $\delta\mathcal{E}$ . This could be the foundation for a second way to make more precise the notion of energy fed back and forth between the various parts of  $\delta\mathcal{B}$  and  $\delta\mathcal{E}$ .

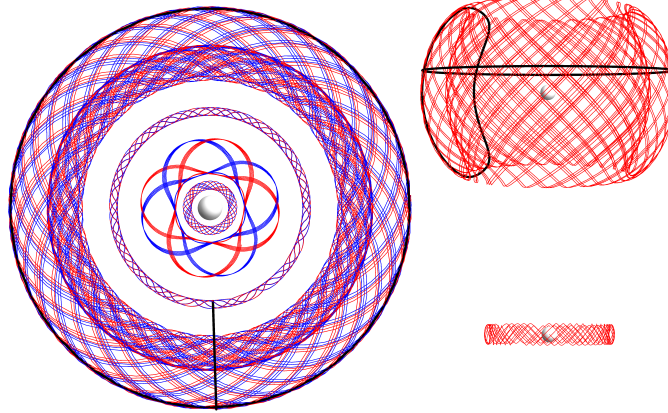


Figure 9.7: Positive-tendicity (blue) and negative-tendicity (red) perturbative tendex lines of a  $(2, 0)$  magnetic-parity perturbation of a Schwarzschild black hole. These lines spiral around deformed tori of progressively larger diameter. The viewpoint is looking down onto the equatorial plane from the positive symmetry axis. *Upper right inset:* The negative tendex line spiraling around the outermost torus, viewed in cross section from the equatorial plane. *Lower right inset:* The negative tendex line spiraling around the small torus third from the center, viewed in cross section from the equatorial plane. Also shown, in black in the main drawing and the large inset, are two of this mode's vortex lines, one from Figure 9.6 wrapping around the outermost torus in a  $\mathcal{S}_\phi$  plane; the other an azimuthal circle wrapping around that torus in the  $\phi$  direction. This figure was actually drawn depicting vortex lines of the electric-parity mode discussed in Section 9.5.4; but by duality (which is excellent in the wave zone), it also represents the tendexes of the magnetic-parity mode discussed in this section.

(the maximum-vorticity surface) of a blue (dark gray), lens-shaped gravitational-wave vortex. As it nears the north or south pole, it swings radially outward becoming very weak (low vorticity) and travels across the red trough of the wave, until it nears the next blue crest. There it swings into the transverse,  $\theta$  direction and travels toward the other pole, near which it swings back through the red trough and joins onto itself in the original blue crest.

Each dashed (counterclockwise) closed vortex line behaves in this same manner, but with its transverse portions lying near red (light gray) troughs (surfaces of most negative vorticity). Near the red troughs, there are blue azimuthal vortex lines (not shown) that encircle the hole in the  $\phi$  direction, and near the blue crests, there are red azimuthal lines.

Figure 9.7 sheds further light on these gravitational-wave tori. It shows in three dimensions some of the perturbative tendex lines for the  $(2,0)$  magnetic-parity mode that we are discussing. (For this mode, two families of perturbative tendex lines, one red [counterclockwise] and the other blue [clockwise], have nonzero tendicity and the third family has vanishing tendicity.) As is required by the structure of a gravitational wave (transverse tendex lines rotated by 45 degrees relative to transverse vortex lines), these perturbative tendex lines wind around tori with pitch angles of 45 degrees; one family winds clockwise and the other counterclockwise, and at each point the two lines have the same magnitude of vorticity.

A close examination of Figure 9.7 reveals that the tori around which the perturbative tendex

lines wrap are half as thick as the tori around which the vortex lines wrap. Each tendex-line torus in Figure 9.7 is centered on a single node of the gravitational-wave field; the thick red torus in the upper right panel reaches roughly from one crest of the wave to an adjacent trough. By contrast, each vortex-line torus (Figure 9.6 and black poloidal curves in Figure 9.7) reach from crest to crest or trough to trough and thus encompass two gravitational-wave nodes.

Each node in the wave zone has a family of nested tendex-line tori centered on it. The four tendex-line tori shown in Figure 9.7 are taken from four successive families, centered on four successive nodes. The second thin torus is from near the center of one nested family; it tightly hugs a node and therefore has near vanishing tendicity. The two thick tori are from the outer reaches of their nested families.

For further details of the  $(2,0)$  modes, see Sections 9.5.3 and 9.5.4 below.

### 9.1.3.9 The Superposed $(2, 2)$ and $(2, -2)$ Magnetic-Parity Mode of a Schwarzschild Hole

As we have seen, the magnetic-parity,  $(2, 2)$  mode of a Schwarzschild black hole represents vortexes that rotate counterclockwise around the hole, spiraling outward and backward (Figures 9.2, 9.3 and 9.4 above). If we change the sign of the azimuthal quantum number to  $m = -2$ , the vortexes rotate in the opposite direction, and spiral in the opposite direction. If we superpose these two modes (which, for Schwarzschild, have the same eigenfrequency), then, naturally, we get a non-rotating, oscillatory mode—whose dynamics are similar to those of the  $(2,0)$  mode of the last subsection. See Section 9.4 for details.

Figure 9.8 is a snapshot of the two families of vortex lines that lie in this mode's equatorial plane. The plane is colored by the vorticity of the dashed vortex lines; they are predominantly counterclockwise (red), though in some regions they are clockwise (blue).

The red (light gray) regions form *interleaved rings* around the black hole, that expand outward at the speed of light, along with their dashed vortex lines. These rings are not tori in three dimensions because [by contrast with the  $(2, 0)$  mode] the frame drag field grows stronger as one moves up to the polar regions, rather than weakening. As the mode oscillates, the longitudinal near-zone frame-drag field  $\mathcal{B}^L$ , which drives the mode, generates new interleaved rings, one after another and sends them outward.

During the oscillations, there are phases at which the longitudinal field  $\mathcal{B}^L$  threading the hole goes to zero, and so the hole has vanishing horizon vorticity. The near-zone oscillation energy, at these phases, is locked up in the near-zone, longitudinal-transverse fields  $\mathcal{B}^{LT}$  and  $\delta\mathcal{E}^{LT}$ , which, via the Maxwell-like Bianchi identities (and the propagation equation that they imply), then feed energy into the longitudinal near-zone frame-drag field  $\mathcal{B}^L$ , thereby generating new horizon-threading vortex lines, which will give rise to the next ejected interleaved ring.

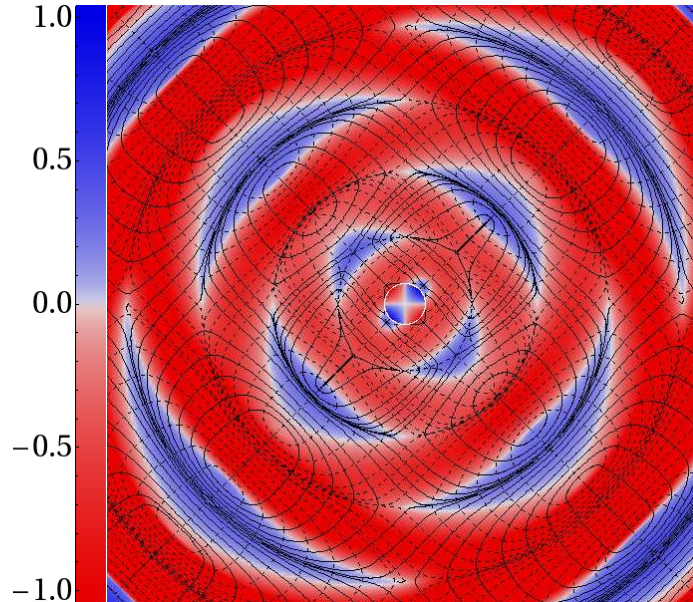


Figure 9.8: Equatorial vortex structure of the superposed  $(2,2)$  and  $(2,-2)$ , magnetic-parity, fundamental modes of a Schwarzschild black hole. The colors encode the vorticity of the dashed vortex lines. The vorticity of the solid lines is not shown, but can be inferred from the fact that under a  $90^\circ$  rotation, the dashed lines map into solid and the solid into dashed.

We explore these dynamics in greater detail in Section 9.4.3.

#### 9.1.4 This Paper's Organization

The remainder of this paper is organized as follows: In Section 9.2, we introduce the time slicing and coordinates used throughout this paper for the background Schwarzschild and Kerr spacetimes, we introduce the two gauges that we use for Schwarzschild perturbations (Regge-Wheeler-Zerilli and ingoing radiation gauges) and the one gauge (ingoing radiation) we use for Kerr, we discuss how our various results are affected by changes of gauge, and we discuss how we perform our computations. In Sections 9.3, 9.4, and 9.5, we present full details of our results for the fundamental (most slowly damped) quadrupolar modes of Schwarzschild and Kerr:  $(2,2)$  modes in Section 9.3; superposed  $(2,2)$  and  $(2,-2)$  modes in Section 9.4, and both  $(2,1)$  and  $(2,0)$  modes in Section 9.5. In Section 9.3.4, we compare vortex lines computed in a numerical-relativity simulation of a binary black hole at a late time, when the merged hole is ringing down, with the vortex lines from this paper for the relevant quasinormal mode; we obtain good agreement. In Section 9.6, we make a few concluding remarks. And in six appendices, we present mathematical details that underlie a number of this paper's computations and results.

## 9.2 Slicings, Gauges and Computational Methods

When calculating the tidal and frame-drag fields of perturbed black-hole spacetimes, we must choose a slicing and also spatial coordinates on each slice, for both the background spacetime and at first order in the perturbations (“perturbative order”). The perturbative-order choices of slicing and spatial coordinates are together called the chosen *gauge*. We will always use the same choice of background slicing and coordinates in this study, but we will use different choices for our gauge.

This section describes the choices we make, how they influence the vortex and tendex lines and their vorticities and tendicities (which together we call the “vortex and tendex structures”), and a few details of how, having made our choices, we compute the perturbative frame-drag and tidal fields and the vortex and tendex structures. Most of the mathematical details are left to later sections and especially appendices.

In Section 9.2.1, we describe our choices of slicing and spatial coordinates. In Section 9.2.2, we sketch how we calculate the perturbative frame-drag and tidal fields and visualize their vortex and tendex structures. In Section 9.2.3, we explore how those structures change under changes of gauge, i.e., changes of the perturbative slicing and perturbative spatial coordinates.

### 9.2.1 Slicing, Spatial Coordinates, and Gauge

Throughout this paper, for the background (unperturbed) Kerr spacetime, we use slices of constant Kerr-Schild (KS) time  $\tilde{t}$ , which is related to the more familiar Boyer-Lindquist time by

$$\tilde{t} = t + r_* - r, \quad \text{where} \quad \frac{dr_*}{dr} = \frac{r^2 + a^2}{\Delta} \quad (9.5)$$

(Eq. (6.2) of Paper II [4]). Here  $t$  and  $r$  are the Boyer-Lindquist time and radial coordinates,  $a$  is the black hole’s spin parameter (angular momentum per unit mass), and  $\Delta \equiv r^2 - 2Mr + a^2$ , with  $M$  the black-hole mass. Our slices of constant  $\tilde{t}$  penetrate the horizon smoothly, by contrast with slices of constant  $t$ , which are singular at the horizon. In the Schwarzschild limit  $a \rightarrow 0$ ,  $t$  and  $r$  become Schwarzschild’s time and radial coordinates, and  $\tilde{t}$  becomes ingoing Eddington-Finkelstein time,  $\tilde{t} = t + 2M \ln|r/2M - 1|$ .

On a constant- $\tilde{t}$  slice in the background Kerr spacetime, we use Cartesian-like KS (Kerr-Schild) spatial coordinates, when visualizing vortex and tendex structures; but in many of our intermediary computations, we use Boyer-Lindquist spatial coordinates  $\{r, \theta, \phi\}$  (which become Schwarzschild as  $a \rightarrow 0$ ). The two sets of coordinates are related by

$$x + iy = (r + ia)e^{i\tilde{\phi}} \sin \theta, \quad z = r \cos \theta, \quad (9.6)$$

[Eq. (6.7) of Paper II]. Here

$$\tilde{\phi} = \phi + \int_r^\infty \frac{a}{\Delta} dr \quad (9.7)$$

[Eq. (6.5) of Paper II] is an angular coordinate that, unlike  $\phi$ , is well behaved at the horizon. In the Schwarzschild limit, the KS  $\{x, y, z\}$  coordinates become the quasi-Cartesian  $\{x, y, z\}$  associated with Eddington-Finkelstein (EF) spherical coordinates  $\{r, \theta, \phi\}$ .

Our figures (e.g., 9.2–9.8 above) are drawn as though the KS  $\{x, y, z\}$  were Cartesian coordinates in flat spacetime—i.e., in the Schwarzschild limit, as though the EF  $\{r, \theta, \phi\}$  were spherical polar coordinates in flat spacetime.

We denote by  $g_{\mu\nu}^{(0)}$  the background metric in KS spacetime coordinates [Eq. (6.8) of Paper II] (or EF spacetime coordinates in the Schwarzschild limit). When the black hole is perturbed, the metric acquires a perturbation  $h_{\mu\nu}$  whose actual form depends on one’s choice of gauge—i.e., one’s choice of slicing and spatial coordinates at perturbative order.

For Schwarzschild black holes, we use two different gauges, as a way to assess the gauge dependence of our results: (i) *Regge-Wheeler-Zerilli (RWZ) gauge*, in which  $h_{\mu\nu}$  is a function of two scalars ( $Q$  for magnetic parity and  $Z$  for electric parity) that obey separable wave equations in the Schwarzschild spacetime and that have spin-weight zero (see Appendix 9.A for a review of this formalism), and (ii) *ingoing radiation (IR) gauge*, in which  $h_{\mu\nu}$  is computed from the Weyl scalar  $\Psi_0$  (or  $\Psi_4$ ) that obeys the separable Bardeen-Press equation. The method used to compute the metric perturbation from  $\Psi_0$  is often called *the Chrzanowski-Cohen-Kegeles (CCK) procedure of metric reconstruction* (see Appendix 9.C).

In Appendix 9.D, we exhibit explicitly the relationship between the RWZ and IR gauges, for electric- and magnetic-parity perturbations. The magnetic-parity perturbations have different perturbative spatial coordinates, but the same slicing. (In fact, *all* gauges related by a magnetic-parity gauge transform have identically the same slicing for magnetic-parity perturbations of Schwarzschild [although the same is not true for Kerr]; see Section 9.2.3). For electric-parity perturbations, the two gauges have different slicings and spatial coordinates.

For all the perturbations that we visualize in this paper, the tendexes and vortexes show quite weak gauge dependence. See, e.g., Section 9.3, where we present results from both gauges. The results in Sections 9.4 and 9.5 are all computed in RWZ gauge.

For Kerr black holes, there is no gauge analogous to RWZ; but the IR gauge and the CCK procedure that underlies it are readily extended from Schwarzschild to Kerr. In this extension, one constructs the metric perturbation from solutions to the Teukolsky equation (see Appendix 9.B) for the perturbations to the Weyl scalars  $\Psi_0$  and  $\Psi_4$ , in an identical way to that for a Schwarzschild black hole described above. Our results in this paper for Kerr black holes, therefore, come solely from the IR gauge.

## 9.2.2 Sketch of Computational Methods

This section describes a few important aspects of how we calculate the tidal and frame-drag fields, and their vortex and tendex structures which are visualized and discussed in Sections 9.3, 9.4, and 9.5.

We find it convenient to solve the eigenvalue problem in an orthonormal basis (orthonormal tetrad) given by the four-velocities of the Kerr-Schild (KS) or Eddington-Finkelstein (EF) observers, and a spatial triad,  $\vec{e}_{\hat{a}}$ , carried by these observers.

The background EF tetrad for the Schwarzschild spacetime, expressed in terms of Schwarzschild coordinates, is

$$\begin{aligned}\vec{u}^{(0)} &= \frac{1}{\sqrt{1+2M/r}} \left( \frac{1}{\alpha^2} \frac{\partial}{\partial t} - \frac{2M}{r} \frac{\partial}{\partial r} \right), & \vec{e}_{\hat{r}}^{(0)} &= \frac{1}{\sqrt{1+2M/r}} \left( \frac{\partial}{\partial r} - \frac{2M}{\alpha^2 r} \frac{\partial}{\partial t} \right), \\ \vec{e}_{\hat{\theta}}^{(0)} &= \frac{1}{r} \frac{\partial}{\partial \theta}, & \vec{e}_{\hat{\phi}}^{(0)} &= \frac{1}{r \sin \theta} \frac{\partial}{\partial \phi}\end{aligned}\quad (9.8)$$

[cf. Eqs. (4.4) of Paper II, which, however, are written in terms of the EF coordinate basis rather than Schwarzschild]. The background orthonormal tetrad for KS observers (in ingoing Kerr coordinates  $\{\tilde{t}, r, \theta, \tilde{\phi}\}$ ; see Paper II, Section VI C) is

$$\begin{aligned}\vec{u}^{(0)} &= H \partial_{\tilde{t}} - \frac{2Mr}{H\Sigma} \partial_r, & \vec{e}_{\hat{r}}^{(0)} &= \frac{\sqrt{A}}{H\Sigma} \partial_r + \frac{aH}{\sqrt{A}} \partial_{\tilde{\phi}}, \\ \vec{e}_{\hat{\theta}}^{(0)} &= \frac{1}{\sqrt{\Sigma}} \partial_{\theta}, & \vec{e}_{\hat{\phi}}^{(0)} &= \sqrt{\frac{\Sigma}{A}} \frac{1}{\sin \theta} \partial_{\tilde{\phi}},\end{aligned}\quad (9.9a)$$

where we have defined

$$\Sigma = r^2 + a^2 \cos^2 \theta, \quad H = 1 + \frac{2Mr}{\Sigma}, \quad A = (r^2 + a^2)^2 - a^2(r^2 - 2Mr + a^2) \sin^2 \theta \quad (9.9b)$$

[see Eq. (B2) of Paper II].

When the black hole is perturbed, the tetrad  $\{\vec{u}^{(0)}, \vec{e}_{\hat{r}}^{(0)}, \vec{e}_{\hat{\theta}}^{(0)}, \vec{e}_{\hat{\phi}}^{(0)}\}$  acquires perturbative corrections that keep it orthonormal with respect to the metric  $g_{\mu\nu} = g_{\mu\nu}^{(0)} + h_{\mu\nu}$ . We choose the perturbative corrections to the observers' 4-velocity so as to keep it orthogonal to the space slices, i.e., so as to keep  $\vec{u} = -\alpha \vec{\nabla} \tilde{t}$ . (Here  $\alpha = d\tau/d\tilde{t}$ , differentiating along the observer's world line, is the observer's lapse function.) A straightforward calculation using the perturbed metric gives the following contravariant components of this  $\vec{u}$ :

$$u^\mu = u_{(0)}^\mu + u_{(1)}^\mu, \quad u_{(1)}^\mu = -\frac{1}{2} h_{\hat{0}\hat{0}} u_{(0)}^\mu - h^{\mu\nu} u_{\nu}^{(0)}, \quad (9.10)$$

where  $h_{\hat{0}\hat{0}} = h_{\mu\nu} u_{(0)}^\mu u_{(0)}^\nu$ , and  $u_{(0)}^\mu$  is the four-velocity of the background observers.

We choose the perturbative corrections to the spatial triad  $\{\vec{e}_{\hat{i}}\}$  so the radial vector stays orthogonal to surfaces of constant  $r$  in slices of constant  $\tilde{t}$ , the  $\hat{\theta}$  direction continues to run orthogonal to curves of constant  $\theta$  in surfaces of constant  $r$  and  $\tilde{t}$ , and the  $\hat{\phi}$  vector changes only in its normalization.

When written in terms of the unperturbed tetrad and projections of the metric perturbation into the unperturbed tetrad, the perturbation to the tetrad then takes the form

$$\vec{u}_{(1)} = \frac{1}{2}h_{\hat{0}\hat{0}}\vec{u}_{(0)} - h_{\hat{0}\hat{i}}\vec{e}_{\hat{i}}^{(0)}, \quad \vec{e}_{\hat{r}}^{(1)} = -\frac{1}{2}h_{\hat{r}\hat{r}}\vec{e}_{\hat{r}}^{(0)} - h_{\hat{r}\hat{A}}\vec{e}_{\hat{A}}^{(0)}, \quad (9.11a)$$

$$\vec{e}_{\hat{\theta}}^{(1)} = -\frac{1}{2}h_{\hat{\theta}\hat{\theta}}\vec{e}_{\hat{\theta}}^{(0)} - h_{\hat{\theta}\hat{\phi}}\vec{e}_{\hat{\phi}}^{(0)}, \quad \vec{e}_{\hat{\phi}}^{(1)} = -\frac{1}{2}h_{\hat{\phi}\hat{\phi}}\vec{e}_{\hat{\phi}}^{(0)}, \quad (9.11b)$$

where  $\hat{i}$  is summed over  $\hat{r}$ ,  $\hat{\theta}$ , and  $\hat{\phi}$ , and  $\hat{A}$  is summed over only  $\hat{\theta}$  and  $\hat{\phi}$ .

In Appendices 9.A (RWZ gauge) and 9.C (IR gauge), we give the details of how we compute the components

$$\mathcal{E}_{\hat{i}\hat{j}} = \mathcal{E}_{\hat{i}\hat{j}}^{(0)} + \mathcal{E}_{\hat{i}\hat{j}}^{(1)}, \quad \mathcal{B}_{\hat{i}\hat{j}} = \mathcal{B}_{\hat{i}\hat{j}}^{(0)} + \mathcal{B}_{\hat{i}\hat{j}}^{(1)} \quad (9.12)$$

of the tidal and frame-drag field in this perturbed tetrad. The background portions  $\mathcal{E}_{\hat{i}\hat{j}}^{(0)}$  and  $\mathcal{B}_{\hat{i}\hat{j}}^{(0)}$  are the stationary fields of the unperturbed black hole, which were computed and visualized in Paper II. The perturbative pieces,  $\mathcal{E}_{\hat{i}\hat{j}}^{(1)}$  and  $\mathcal{B}_{\hat{i}\hat{j}}^{(1)}$  are the time-dependent, perturbative parts, which carry the information about the quasinormal modes, their geometrodynamics, and their gravitational radiation.

As part of computing the perturbative  $\mathcal{E}_{\hat{i}\hat{j}}^{(1)} \equiv \delta\mathcal{E}_{\hat{i}\hat{j}}$  and  $\mathcal{B}_{\hat{i}\hat{j}}^{(1)} \equiv \delta\mathcal{B}_{\hat{i}\hat{j}}$  for a chosen quasinormal mode of a Kerr black hole, we have to solve for the mode's Weyl-scalar eigenfunctions  $\Psi_0^{(1)}$  and  $\Psi_4^{(1)}$  and eigenfrequency  $\omega$ . To compute the frequencies, we have used, throughout this paper, Emanuele Berti's elegant computer code [12], which is discussed in [13] and is an implementation of Leaver's method [14]. To compute the eigenfunctions, we have used our own independent code (which also uses the same procedure as that of Berti). In Appendix 9.C, we describe how we extract the definite-parity (electric or magnetic) eigenfunctions from the non-definite-parity functions.

To best visualize each mode's geometrodynamics and generation of gravitational waves in Sections 9.3, 9.4, and 9.5, we usually plot the tendex and vortex structures of the perturbative fields  $\mathcal{E}_{\hat{i}\hat{j}}^{(1)}$  and  $\mathcal{B}_{\hat{i}\hat{j}}^{(1)}$ . However, when we compare our results with numerical-relativity simulations, it is necessary to compute the tendex and vortex structures of the full tidal and frame-drag fields (background plus perturbation), because of the difficulty of unambiguously removing a stationary background field from the numerical simulations. As one can see in Figures 9.15 and 9.26, in this case much of the detail of the geometrodynamics and wave generation is hidden behind the large background field.

In either case, the tendex and vortex structure of the perturbative fields or the full fields, we compute the field lines and their eigenvalues in the obvious way: At selected points on a slice, we

numerically solve the eigenvalue problem

$$\mathcal{E}_{i\hat{j}}V_{\hat{j}} = \lambda V_{\hat{i}} \quad (9.13)$$

for the three eigenvalues  $\lambda$  and unit-normed eigenvectors  $V_{\hat{i}}$  of  $\mathcal{E}_{i\hat{j}}$ , and similarly for  $\mathcal{B}_{i\hat{j}}$ ; and we then compute the integral curve (tendex or vortex line) of each eigenvector field by evaluating its coordinate components  $V^j$  in the desired coordinate system (KS or EF) and then numerically integrating the equation

$$\frac{dx^j}{ds} = V^j, \quad (9.14)$$

where  $s$  is the proper distance along the integral curve.

### 9.2.3 Gauge Changes: Their Influence on Tidal and Frame-Drag Fields and Field Lines

For perturbations of black holes, a perturbative gauge change is a change of the spacetime coordinates,  $x^{\alpha'} = x^\alpha + \xi^\alpha$ , that induces changes of the metric that are of the same order as the metric perturbation; when dealing with definite parity perturbation, we split the generator of the transform  $\xi^\alpha$  into definite electric- and magnetic-parity components. The gauge change has two parts: A change of slicing generated by  $\xi^0$ , and a change of spatial coordinates

$$\tilde{t}' = \tilde{t} + \xi^0 \quad x^{j'} = x^j + \xi^j. \quad (9.15)$$

Here all quantities are to be evaluated at the same event,  $\mathcal{P}$ , in spacetime.

Because  $\xi^0$  is a scalar under rotations in the Schwarzschild spacetime—and all scalar fields in Schwarzschild have electric parity—for a magnetic-parity  $\xi^\alpha$ ,  $\xi^0$  vanishes, and *the slicings for magnetic-parity quasinormal modes of Schwarzschild are unique. For these modes, all gauges share the same slicing* (see Appendix 9.D).<sup>2</sup>

<sup>2</sup>In the Kerr spacetime, however, there are magnetic-parity changes of slicing, because  $\xi^0$  no longer behaves as a scalar under rotations. To understand this more clearly, consider, as a concrete example, a vector in Boyer-Lindquist coordinates with covariant components  $\xi_\mu = (0, 0, X_\theta^{lm}, X_\phi^{lm})f(r)e^{-i\omega t}$ , where  $X_A^{lm}$  are the components of a magnetic-parity vector spherical harmonic [see Eq. (9.86a)]. This vector's contravariant components are  $\xi^\mu = (g^{t\phi}X_\phi^{lm}, 0, g^{\theta\theta}X_\theta^{lm}, g^{\phi\phi}X_\phi^{lm})f(r)e^{-i\omega t}$ , where  $g^{t\phi}$ ,  $g^{\theta\theta}$ , and  $g^{\phi\phi}$  are the contravariant components of the Kerr metric (which have positive parity). The vector  $\xi^\mu$ , has magnetic parity and a nonvanishing component  $\xi^0$ ; therefore, it is an example of a magnetic-parity gauge-change generator in the Kerr spacetime that changes the slicing.

### 9.2.3.1 Influence of a Perturbative Slicing Change

For (electric-parity) changes of slicing, the new observers, whose world lines are orthogonal to the new slices,  $\tilde{t}' = \text{const}$ , move at velocity

$$\Delta \mathbf{v} = -\alpha \nabla \xi^0 \quad (9.16)$$

with respect the old observers, whose world lines are orthogonal to the old slices  $\tilde{t} = \text{const}$ ). Here  $\nabla$  is the gradient in the slice of constant  $\tilde{t}$ , and  $\alpha = (d\tau/d\tilde{t})$  is the lapse function, evaluated along the observer's worldline. In other words,  $\Delta \mathbf{v}$  is the velocity of the boost that leads from an old observer's local reference frame to a new observer's local reference frame. Just as in electromagnetic theory, this boost produces a change in the observed electric and magnetic fields for small  $\Delta \mathbf{v}$  given by  $\Delta \mathbf{B} = \Delta \mathbf{v} \times \mathbf{E}$  and  $\Delta E = -\Delta \mathbf{v} \times B$ , so also it produces a change in the observed tidal and frame-drag fields given by

$$\Delta \mathbf{B} = (\Delta \mathbf{v} \times \mathbf{E})^S, \quad \Delta \mathbf{E} = -(\Delta \mathbf{v} \times \mathbf{B})^S \quad (9.17)$$

(e.g., Eqs. (A12) and (A13) of [15], expanded to linear order in the boost velocity). Here the superscript S means symmetrize.

### 9.2.3.2 Example: Perturbative Slicing Change for Schwarzschild Black Hole

For a Schwarzschild black hole, because the unperturbed frame-drag field vanishes,  $\Delta \mathbf{E}$  is second order in the perturbation and thus negligible, so *the tidal field is invariant under a slicing change*. By contrast, the (fully perturbative) frame-drag field *can* be altered by a slicing change;  $\Delta \mathbf{B} = (\Delta \mathbf{v} \times \mathbf{E})^S$  is nonzero at first order.

Since the unperturbed tidal field is isotropic in the transverse  $(\theta, \phi)$  plane, the radial part of  $\Delta \mathbf{v}$  produces a vanishing  $\Delta \mathbf{B}$ . The transverse part of  $\Delta \mathbf{v}$ , by contrast, produces a radial-transverse  $\Delta \mathbf{B}$  (at first-order in the perturbation). In other words, *a perturbative slicing change in Schwarzschild gives rise to a vanishing  $\Delta \mathbf{E}$  and an electric-parity  $\Delta \mathbf{B}$  whose only nonzero components are*

$$\Delta \mathcal{B}_{\hat{r}\hat{\theta}} = \Delta \mathcal{B}_{\hat{\theta}\hat{r}} \quad \text{and} \quad \Delta \mathcal{B}_{\hat{r}\hat{\phi}} = \Delta \mathcal{B}_{\hat{\phi}\hat{r}}. \quad (9.18)$$

For a Schwarzschild black hole that is physically unperturbed, the first-order frame-drag field is just this radial-transverse  $\Delta \mathbf{B}$ , and its gauge-generated vortex lines make 45 degree angles to the radial direction.

### 9.2.3.3 Influence of a Perturbative Change of Spatial Coordinates

Because  $\mathcal{E}$  and  $\mathcal{B}$  are tensors that live in a slice of constant  $\tilde{t}$ , the perturbative change of spatial coordinates, which is confined to that slice, produces changes in components that are given by the standard tensorial transformation law,  $\mathcal{E}_{i'j'}(x^{k'}[\mathcal{P}]) = \mathcal{E}_{pq}(x^k[\mathcal{P}])(\partial x^q/\partial x^{i'})(\partial x^p/\partial x^{j'})$ . To first order in the gauge-change generators  $x^k$ , this gives rise to the following perturbative change in the tidal field

$$\Delta\mathcal{E}_{ij} = -\mathcal{E}_{ij,k}\xi^k - \mathcal{E}_{ik}\xi^k{}_{,j} - \mathcal{E}_{jk}\xi^k{}_{,i} - \mathcal{E}_{ij|k}\xi^k - \mathcal{E}_{ik}\xi^k{}_{|j} - \mathcal{E}_{jk}\xi^k{}_{|i}, \quad (9.19)$$

and similarly for the frame-drag field  $\mathcal{B}$ . Here the subscript  $|$  denotes covariant derivative with respect to the background metric, in the slice of constant  $\tilde{t}$ . The two expressions in Eq. (9.19) are equal because the connection coefficients all cancel.

The brute-force way to compute the influence of a spatial coordinate change  $x^{j'} = x^j + \xi^j$  on the coordinate shape  $x^j(s)$  of a tendex line (or vortex line) is to (i) solve the eigenequation to compute the influence of  $\Delta\mathcal{E}_{ij}$  [Eq. (9.19)] on the line's eigenvector, and then (ii) compute the integral curve of the altered eigenvector field.

Far simpler than this brute-force approach is to note that the tendex line, written as location  $\mathcal{P}(s)$  in the slice of constant  $\tilde{t}$  as a function of spatial distance  $s$  along the curve, is unaffected by the coordinate change. Therefore, if the old coordinate description of the tendex line is  $x^j(s) = x^j[\mathcal{P}(s)]$ , then the new coordinate description is  $x^{j'}(s) = x^j[\mathcal{P}(s)] + \xi^j[\mathcal{P}(s)]$ ; i.e.,  $x^{j'}(s) = x^j(s) + \xi^j[x^j(s)]$ . In other words, *as seen in the new (primed) coordinate system, the tendex line appears to have been moved from its old coordinate location, along the vector field  $\xi^j$ , from its tail to its tip; and similarly for any vortex line.*

### 9.2.3.4 Example: Perturbative Spatial Coordinate Change for a Schwarzschild Black Hole

*Because the frame-drag field of a perturbed Schwarzschild black hole is entirely perturbative, it is unaffected by a spatial coordinate change. This, together with  $\Delta\mathcal{B} = 0$  for magnetic-parity modes implies that the frame-drag field of any magnetic-parity mode of Schwarzschild is fully gauge invariant!*

By contrast, a spatial coordinate change (of any parity) mixes some of the background tidal field into the perturbation, altering the coordinate locations of the tendex lines.

As an example, consider an electric-parity (2,2) mode of a Schwarzschild black hole. In RWZ gauge and in the wave zone, the tidal field is given by

$$\mathcal{E}_{\hat{\phi}\hat{\phi}} = \frac{M}{r^3} + \frac{A}{r} \cos[2(\phi - \phi_o) - \omega(t - r_*)],$$

$$\begin{aligned}
\mathcal{E}_{\hat{\theta}\hat{\theta}} &= \frac{M}{r^3} - \frac{A}{r} \cos[2(\phi - \phi_o) - \omega(t - r_*)] \\
\mathcal{E}_{\hat{r}\hat{\phi}} &= \frac{2A}{\omega r^2} \cos[2(\phi - \phi_o) - \omega(t - r_*)] , \\
\mathcal{E}_{\hat{r}\hat{r}} &= -\frac{2M}{r^3} + \mathcal{O}\left(\frac{A}{\omega^2 r^3}\right) ,
\end{aligned} \tag{9.20}$$

where  $A$  is the wave amplitude.

Focus on radii large enough to be in the wave zone, but small enough that the wave's tidal field is a small perturbation of the Schwarzschild tidal field. Then the equation for the shape of the nearly circular tendex lines that lie in the equatorial plane, at first order in the wave's amplitude, is

$$\frac{1}{r} \frac{dr}{d\phi} = \frac{\mathcal{E}_{\hat{r}\hat{\phi}}}{(\mathcal{E}_{\hat{\phi}\hat{\phi}} - \mathcal{E}_{\hat{r}\hat{r}})} = \frac{2rA}{3M\omega} \cos[2(\phi - \phi_o) - \omega(t - r_*)] \tag{9.21}$$

(an equation that can be derived using the standard perturbation theory of eigenvector equations). Solving for  $r(\phi)$  using perturbation theory, we obtain for the tendex line's coordinate location

$$\begin{aligned}
r(\phi, t) &= r_o + \rho(\phi, r_o, t) , \\
\rho(\phi, r_o, t) &\equiv r_o \frac{Ar_o}{3M\omega} \sin[2(\phi - \phi_o) - \omega(t - r_{o*})] .
\end{aligned} \tag{9.22}$$

Here  $r_o$  is the radius that the chosen field line has when  $\phi = \phi_o$ . Notice that the field line undergoes a quadrupolar oscillation, in and out, as it circles around the black hole, and it is closed—i.e., it is an ellipse centered on the hole. The ellipticity is caused by the gravitational wave. As time passes, the ellipse rotates with angular velocity  $d\phi/dt = \omega/2$ , and the phasing of successive ellipses at larger and larger radii  $r_o$  is delayed by an amount corresponding to speed-of-light radial propagation.

Now, consider an unperturbed Schwarzschild black hole. We can produce this same pattern of elliptical oscillations of the equatorial-plane tendex lines, in the absence of any gravitational waves, by simply changing our radial coordinate: Introduce the new coordinate

$$r' = r + \xi^r, \quad \text{where} \quad \xi^r = \rho(\phi, r, t) , \tag{9.23}$$

with  $\rho$  the function defined in Eq. (9.22). In Schwarzschild coordinates, the equatorial tendex lines are the circles  $r = r_o = \text{constant}$ . In the new coordinate system, those tendex lines will have precisely the same shape as that induced by our gravitational wave [Eq. (9.22)]:  $r' = r_o + \rho(\phi, r_o, t)$ . Of course, a careful measurement of the radius of curvature of one of these tendex lines will show it to be constant as one follows it around the black hole (rather than oscillating), whereas the radius of curvature of the wave-influenced tendex line will oscillate. In fact, if we follow along with the tendex line and measure the tendicity *along* the line, we find that the tendicity of the line is unchanged by the change in coordinates. To be explicit, consider the tendicity, which we denote  $\lambda_\phi$ , along one of

the lines  $r = r_o$ . Enacting the coordinate transform on the tendicity but continuing to evaluate it along the perturbed line, we have the identity

$$\lambda_\phi(r)|_{r=r_o} = \lambda_\phi(r' - \xi^r)|_{r'=r_o+\rho} = \lambda_\phi(r_o + \rho - \rho) = \lambda_\phi(r_o). \quad (9.24)$$

Nevertheless, if one just casually looks at the Schwarzschild tendex lines in the new, primed, coordinate system, one will see a gravitational-wave pattern.

The situation is a bit more subtle for the perturbed black hole. In this case, the tendex lines are given by Eq. (9.22), and we can change their ellipticity by again changing radial coordinates, say to

$$r' = r + \alpha\rho(\phi, r, t). \quad (9.25)$$

The radial oscillations  $\Delta r'$  of the elliptical tendex lines in the new  $(r', \phi, t)$  coordinate system will have amplitudes  $1 + \alpha$  times larger than in the original  $(r, \phi, t)$  coordinates, and in the presence of the gravitational waves it may not be easy to figure out how much of this amplitude is due to the physical gravitational waves and how much due to rippling of the coordinates.

On the other hand, the tendicities of these tendex lines are unaffected by rippling of the coordinates. They remain equal to  $\lambda_\phi = \mathcal{E}_{\hat{\phi}\hat{\phi}} = M/r^3 + (A/r) \cos[2(\phi - \phi_o) - \omega(t - r_*)] = M/(r')^3 + (A/r') \cos[2(\phi - \phi_o) - \omega(t - r'_*)]$  at leading order, which oscillates along each closed line by the amount  $\Delta\mathcal{E}_{\hat{\phi}\hat{\phi}} = (A/r) \cos[2(\phi - \phi_o) - \omega(t - r_*)]$  that is precisely equal to the gravitational-wave contribution to the tendicity. Note that in this example, even without evaluating the tendicity along the perturbed lines to cancel the coordinate change, the change in the tendicity due to the coordinate change enters at a higher order than the contribution from the gravitational wave.

*Therefore, in this example, the tendicity and correspondingly the structures of tendexes capture the gravitational waves cleanly, whereas the tendex-line shapes do not do so; the lines get modified by spatial coordinate changes.* This is why we pay significant attention to tendexes and also vortexes in this paper, rather than focusing solely or primarily on tendex and vortex lines.

### 9.3 (2, 2) Quasinormal Modes of Schwarzschild and Kerr Black Holes

In Section 9.1.3.6, we described the most important features of the fundamental, (2,2) quasinormal modes of Schwarzschild black holes. In this section, we shall explore these modes in much greater detail and shall extend our results to the (2,2) modes of rapidly spinning Kerr black holes. For binary-black-hole mergers, these are the dominant modes in the late stages of the merged hole's final ringdown (see, e.g., [16]).

### 9.3.1 Horizon Vorticity and Tendicity

We can compute the horizon tendicity  $\mathcal{E}_{NN}$  and vorticity  $\mathcal{B}_{NN}$  [or equivalently  $\Psi_2 = \frac{1}{2}(\mathcal{E}_{NN} + i\mathcal{B}_{NN})$ ] using two methods: first, we can directly evaluate them from the metric perturbations, and second, we can calculate them, via Eq. (9.114) in the form (9.116), from the ingoing-wave curvature perturbation  $\Psi_0$ , which obeys the Teukolsky equation (Appendix 9.B). For perturbations of Schwarzschild black holes, both methods produce simple analytical expressions for the horizon quantities; they both show that the quantities are proportional to a time-dependent phase times a scalar spherical harmonic,  $e^{-i\omega t}Y_{lm}$  [see, e.g., Eq. (9.121)]. For Kerr holes, the simplest formal expression for the horizon quantities is Eq. (9.116), and there is no very simple analytical formula. Nevertheless, from these calculations one can show that there is an exact duality between  $\mathcal{E}_{NN}$  and  $\mathcal{B}_{NN}$  in ingoing radiation gauge for quasinormal modes with the same order parameters  $(n, l, m)$  but opposite parity, for both Schwarzschild and Kerr black holes; see Appendix 9.E.2. For Schwarzschild black holes in RWZ gauge, there is also a duality for the horizon quantities, although it is complicated by a perturbation to the position of the horizon in this gauge; see Appendices 9.A.4 and 9.A.5 for further discussion.

In Figure 9.9, we show  $\delta E_{NN}$  and  $\delta B_{NN}$  for the  $(2, 2)$  modes with both parities, of a Schwarzschild black hole (upper row) and a rapidly rotating Kerr black hole (bottom row).

The duality is explicit in the labels at the top: the patterns are identically the same for  $\delta E_{NN}$  (tendexes) of electric-parity modes and  $\delta B_{NN}$  (vortexes) of magnetic-parity modes [left column]; and also identically the same when the parities are switched [right column] The color coding is similar to Figure 9.3 above (left-hand scale). The red (light gray) regions are stretching tendexes or counterclockwise vortexes (negative eigenvalues); the blue (dark gray), squeezing tendexes or clockwise vortexes (positive eigenvalues).

For the Schwarzschild hole, the electric-parity tendex pattern and magnetic-parity vortex pattern (upper left) is that of the spherical harmonic  $Y^{22}(\theta, \phi)$ , and the perturbative electric-parity vorticity and magnetic-parity tendicity vanish (upper right).

For the rapidly spinning Kerr hole, the electric-parity tendexes and magnetic-parity vortexes (lower left) are concentrated more tightly around the plane of reflection symmetry than they are for the Schwarzschild hole, and are twisted; but their patterns are still predominantly  $Y^{22}$ . And also for Kerr, the (perturbative) electric-parity vorticity and magnetic-parity tendicity have become nonzero (lower right), they appear to be predominantly  $Y^{32}(\theta, \phi)$  in shape, they are much less concentrated near the equator and somewhat weaker than the electric-parity tendicity and magnetic-parity vorticity (lower left).

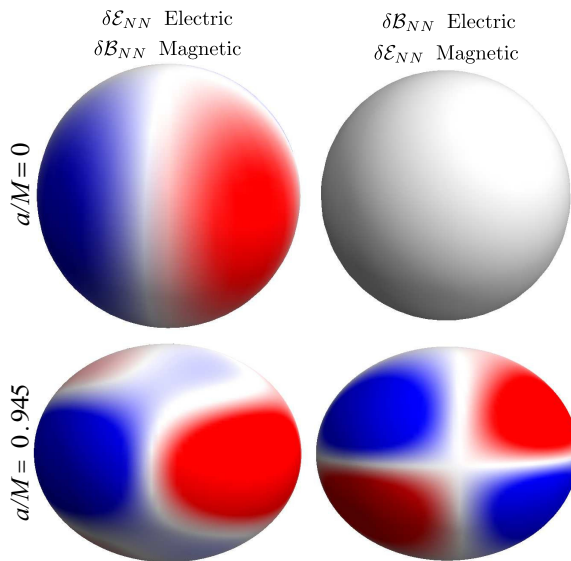


Figure 9.9: Perturbative horizon tendencies  $\delta E_{NN}$  and vorticities  $\delta B_{NN}$  for the  $(2, 2)$  quasinormal modes with electric and magnetic parities (see column labels at the top). The top row is for a Schwarzschild black hole,  $a = 0$ ; the bottom for a rapidly spinning Kerr black hole,  $a/M = 0.945$ . The color intensity is proportional to the magnitude of the tendency or vorticity, with blue (dark gray) for positive and red (light gray) for negative. For discussion, see Section 9.3.1 of the text.

### 9.3.2 Equatorial-Plane Vortex and Tendex Lines, and Vortexes and Tendexes

As for the weak-field, radiative sources of Paper I, so also here, the equatorial plane is an informative and simple region in which to study the generation of gravitational waves.

For the  $(2, 2)$  modes that we are studying, the  $\delta \mathcal{E}_{jk}$  of an electric-parity perturbation and the  $\delta \mathcal{B}_{jk}$  for magnetic parity are symmetric about the equatorial plane. This restricts two sets of field lines (tendex lines for electric-parity  $\delta \mathcal{E}_{jk}$ ; vortex lines for magnetic-parity  $\delta \mathcal{B}_{jk}$ ) to lie in the plane and forces the third to be normal to the plane. By contrast, the electric-parity  $\delta \mathcal{B}_{jk}$  and magnetic-parity  $\delta \mathcal{E}_{jk}$  are reflection antisymmetric. This requires that two sets of field lines cross the equatorial plane at  $45^\circ$  angles, with equal and opposite eigenvalues (tendencies or vorticities), and forces the third set to lie in the plane and have zero eigenvalue (which makes them have less physical interest).

In this section, we shall focus on the in-plane field lines and their vorticities and tendencies.

#### 9.3.2.1 Magnetic-Parity Perturbations of Schwarzschild Black Holes

In Section 9.1.3.6 and Figures 9.2 and 9.3, we discussed some equatorial-plane properties of the magnetic-parity  $(2, 2)$  mode. Here we shall explore these and other properties more deeply. Recall that for the magnetic-parity mode, the frame-drag field, and hence also the vortex lines and their vorticities, are fully gauge invariant.

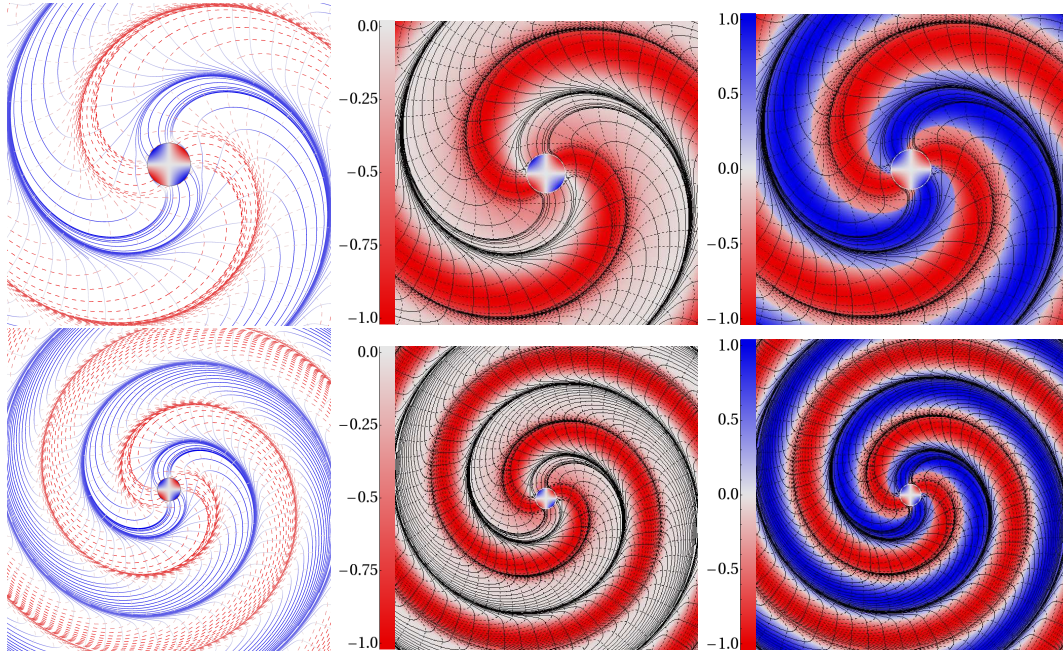


Figure 9.10: Three representations of the vortex lines and vortexes in the equatorial plane of a Schwarzschild black hole perturbed by a magnetic-parity  $(2, 2)$  quasinormal mode. The bottom panels span a region  $56M$  on each side, and the top panels are a zoom-in of the lower panels,  $30M$  on each side. All panels show positive-vorticity lines as solid and negative-vorticity lines as dashed. In all panels, blue (dark gray) corresponds to positive and red (light gray) to negative; the intensity of the color indicates the strength of the vorticity at that point normalized by the maximum of the vorticity at that radius (darker shading indicates a larger strength and lighter, weaker). Similarly, in all panels, the central circle surrounded by a narrow white line is the horizon colored by its vorticity as described above. *Left column*: Vortex lines colored and shaded by their scaled vorticity. *Middle column*: Negative vorticity coloring the plane with black vortex lines. *Right column*: Vorticity with the larger absolute value coloring the plane and black vortex lines. For discussion of this figure, see Section 9.3.2.1.

In Figure 9.10, we show six different depictions of the vortex lines and their vorticities in the equatorial plane, each designed to highlight particular issues. See the caption for details of what is depicted.

The radial variation of vorticity is not shown in this figure, only the angular variation. The vorticity actually passes through a large range of values as a function of radius: from the horizon to roughly  $r = 4M \simeq 1.5\lambda$  (roughly the outer edge of the near zone), the vorticity rapidly decreases; between  $r \simeq 4M$  and  $12M$  (roughly the extent of the transition zone), it falls off as  $1/r$ ; and at  $r \gtrsim 12M$  (the wave zone), it grows exponentially due to the damping of the quasinormal mode as time passes. (The wave field at larger radii was emitted earlier when the mode was stronger.) In the figure, we have removed these radial variations in order to highlight the angular variations.

By comparing the left panels of Figure 9.10 with Fig 9 of Section VI D of Paper I, we see a strong resemblance between the vortex lines of our  $(2, 2)$ , magnetic-parity perturbation of a Schwarzschild black hole, and those of a rotating current quadrupole in linearized theory. As in linearized theory,

when the radial (or, synonymously, longitudinal) vortex lines in the near zone rotate, the effects of time retardation cause the lines, in the transition and wave zones, to collect around four backward-spiraling regions of strong vorticity (the vortexes) and to acquire perturbative tendex lines as they become transverse-traceless gravitational waves. The most important difference is that, for the black-hole perturbations, the positive vortex lines emerge from the blue, clockwise horizon vortexes and spiral outward (and the negative vortex lines emerge from the counterclockwise horizon vortexes) rather than emerging from a near-zone current quadrupole.

Although the left panels of Figure 9.10 highlight most clearly the comparison with figures in Paper I, the middle and right panels more clearly show the relationship between the vortex lines (in black) and the vorticities, throughout the equatorial plane. In the middle panels (which show only the negative vorticity), the negative vortex lines that emerge longitudinally from the horizon stay in the center of their vortex in the near zone, and then collect onto the outer edge of the vortex in the transition and wave zones. Interestingly, near the horizon, there are also two weaker regions of negative vorticity between the two counterclockwise vortexes, regions associated with the tangential negative vortex lines that pass through this region without attaching to the horizon (and that presumably represent radiation traveling into the horizon).

In the right panels of Figure 9.10 (which show the in-plane vorticity with the larger absolute value), a clockwise vortex that extends radially from the horizon takes the place of the weaker region of counterclockwise vorticity. From these panels, it is most evident that the vortexes and vortex lines of opposite signs are identical, though rotated by  $90^\circ$ . These panels also highlight that there are four spirals of nearly zero vorticity that separate the vortexes in the wave zone, which the spiraling vortex lines approach. All three vorticities nearly vanish at these spirals; in the limit of infinite radius, they become vanishing points for the radiation, which must exist for topological reasons [17].

### 9.3.2.2 Gauge Dependence of Electric-Parity Tendexes for a Schwarzschild Black Hole

In this subsection, we explore the gauge dependence of the (2,2) modes for a Schwarzschild black hole. In Section 9.2.3, we showed that for magnetic-parity modes, all gauges share the same slicing. Therefore, to maximize any gauge dependence that there might be, we focus on the electric-parity (2,2) mode.

Because the frame-drag field of the unperturbed Schwarzschild black hole vanishes, this mode's perturbative frame-drag field will be unaffected by perturbative changes of the spatial coordinates. Therefore, we focus on the perturbative tidal field  $\delta\mathcal{E}$  of the electric-parity mode, which is sensitive to *both* perturbative slicing changes and perturbative spatial coordinate changes.

In Figure 9.11, we plot this field's perturbative equatorial tendexes and tendex lines for the electric-parity (2,2) mode in RWZ gauge (left panel) and IR gauge (right panel)—which differ, for

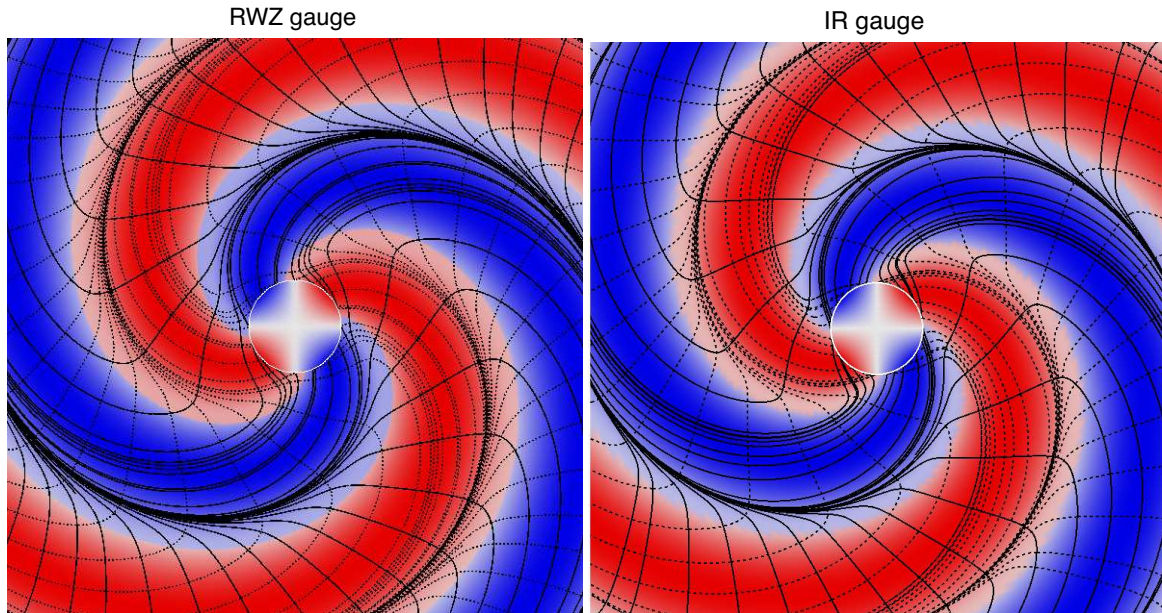


Figure 9.11: The equatorial-plane, electric-parity tendexes and tendex lines of a  $(2, 2)$  perturbation of a Schwarzschild black hole in RWZ gauge (left panel) and IR gauge (right panel). The conventions for the lines, the coloring and the shading are identical to those in the right panels of Figure 9.10.

this mode, in both slicing and spatial coordinates. The tendex lines for the two gauges were seeded at the same coordinate points, so all the differences between the panels can be attributed to the gauge differences.

The two panels are almost identical. Therefore, these maximally sensitive tendexes and tendex lines are remarkably unaffected by switching from one gauge to the other. The primary differences are that (i) the tendex lines of IR gauge tend to be pulled closer to the horizon very near the horizon as compared to RWZ gauge (ii) the lines falling onto the attracting spiral are bunched even more tightly in IR gauge than in RWZ gauge; however, more lines reach the spiral in RWZ gauge in this figure, and (iii) the four tendex spirals wind more tightly in IR gauge, which is most easily seen by comparing the lower right and upper left corners of the two panels.

One subtlety that must be remarked upon is that the central circle colored by the normal-normal component of the tidal field (surface tendicity) in the RWZ gauge (left panel of Figure 9.11) is simply the surface  $r = 2M$ , and not the true event horizon. The location of the event horizon is affected by the perturbations in a gauge-dependent manner, as discussed by Vega, Poisson, and Massey [18]. We rely on the results of this article in the brief discussion that follows. In RWZ gauge, the horizon is at  $r_H = 2M + \delta r(\tilde{t}, \theta, \phi)$ , where the function  $\delta r$  can be solved for by ensuring that the vector tangent to the perturbed generators (in our case,  $l^\mu = \partial x^\mu / \partial \tilde{t}$ ) remains null [18]. We give an expression for  $\delta r$  in Appendix 9.A.5. There we also discuss the correction to the horizon tendicity in RWZ gauge. One key result is that the horizon tendicity has the same angular distribution in RWZ gauge as in

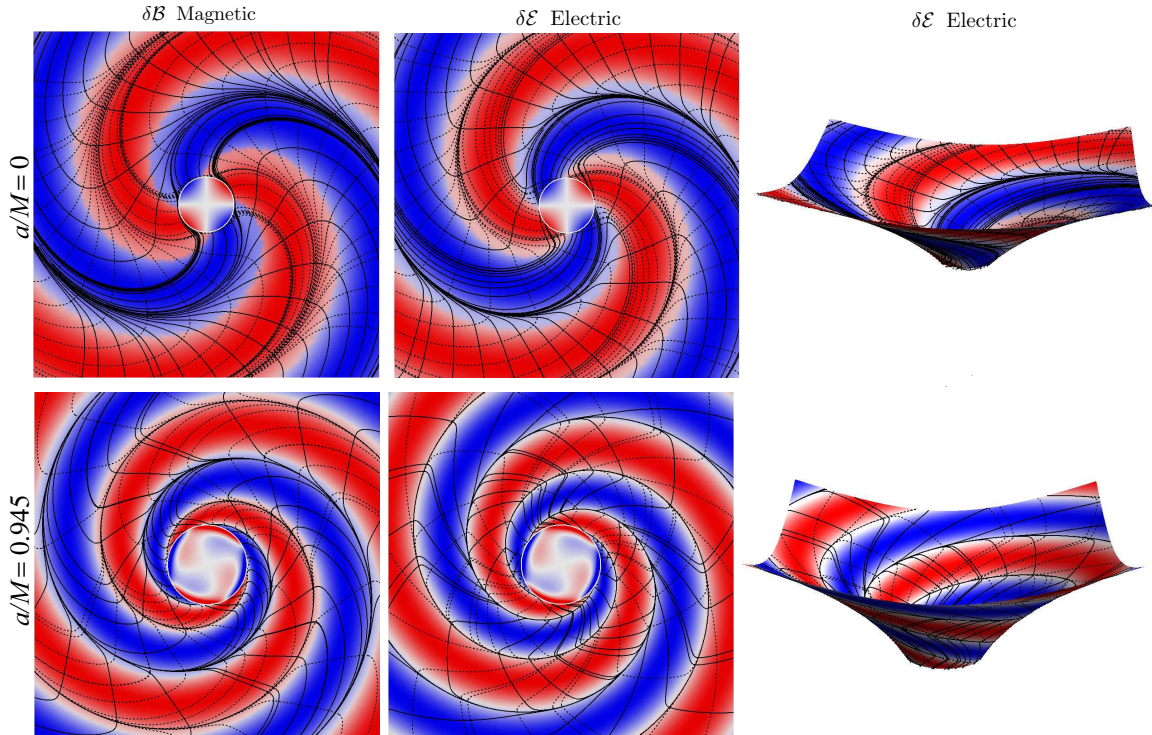


Figure 9.12: Vortexes and tendexes and their field lines in the equatorial plane for  $(2, 2)$  modes of Schwarzschild and Kerr black holes. The lines, the coloring and the shading are identical to those in the right panels of Figure 9.10. The upper row is for a Schwarzschild black hole ( $a = 0$ ); the lower row, for a rapidly spinning Kerr black hole ( $a = 0.945$ ); see labels on the left. The left column shows the vortex lines and vorticities for magnetic parity (which are gauge invariant for the perturbations of a Schwarzschild hole); the middle and right columns show the tendex lines and tendicities for the electric-parity mode in IR gauge; see labels at the top. In the right column, the equatorial plane is isometrically embedded in three-dimensional Euclidean space. The top panels are  $24M$  across; the bottom,  $14M$ . This figure elucidates duality and the influence of black-hole spin; see the discussion in Section 9.3.2.3.

IR gauge (given by the  $Y^{22}$  spherical harmonic), so that the normal-normal tendicity on the horizon and on the surface at  $r = 2M$  differ only by an amplitude and phase in RWZ gauge. Meanwhile, in IR gauge the horizon remains at  $r_H = 2M$  and so the colored central circle is in fact the horizon, colored by its horizon tendicity.

However, the bulk tendexes and tendex lines are determined completely independently of these horizon considerations, and so Figure 9.11 provides an accurate comparison of them in the two gauges.

### 9.3.2.3 Duality and Influence of Spin in the Equatorial Plane

In this subsection, we use Figure 9.12 to explore duality and the influence of spin, for the fundamental  $(2, 2)$  mode.

By comparing the left and center panels in the top row of Figure 9.12, we see *visually* the

near duality between the electric- and magnetic-parity modes for a Schwarzschild hole. This near duality is explored *mathematically* in Appendix 9.C. Specifically, the vortexes and their lines for the magnetic-parity mode (left) are nearly identical to the tendexes and their lines for the electric-parity mode. The only small differences appear in the size of the nearly zero-vorticity (or tendicity) regions, and the curvatures of the lines.

For the fast-spinning Kerr black hole (the bottom left and center panels of Figure 9.12), the near duality is still obvious, especially in the colored vortexes and tendexes; but it is less strong than for Schwarzschild, especially in the field lines. The vortex lines (on the left) continue to look like those of a Schwarzschild black hole, but the tendex lines (in the middle) curve in the opposite direction, which makes some lines reach out from the horizon and connect back to it instead of spiraling away from the horizon.

By comparing the top and bottom panels in the left and center columns of Figure 9.12, we see the influence of the background black hole's spin on the dynamics of the perturbative vortexes and tendexes. For fast Kerr (bottom), the vortexes and tendexes near the horizon look more transverse (less radial) than for Schwarzschild, because the size of the near zone is much smaller. (The frequency of the waves is nearly twice that for a perturbed Schwarzschild hole.) The higher frequency also explains why the spirals of the vortexes and tendexes are tighter.

In the isometric embedding diagrams in the right column of Figure 9.12, we see that proper radial distance in the near zone is somewhat larger than it appears in the flat, planar drawing. Taking this into account, we conclude that, aside from a few small differences, the qualitative ways in which waves are generated for fast Kerr and for Schwarzschild are the same: two pairs of vortexes or tendexes emerge longitudinally from horizon vortexes, and twist into backward spirals that eventually form the transverse-traceless gravitational waves.

#### 9.3.2.4 Vortexes of Electric-Parity Mode, and Perturbative Tendexes of Magnetic-Parity Mode for a Schwarzschild Black Hole

In Figure 9.13, we visualize the vortexes of the electric-parity  $(2, 2)$  mode of a Schwarzschild hole. (By near duality, the perturbative tendexes of the magnetic-parity mode must look nearly the same.)

As noted at the beginning of Section 9.3.2, reflection antisymmetry of the frame-drag field for this electric-parity mode dictates that through each point in the plane there will pass one zero-vorticity vortex line lying in the plane, and two vortex lines with equal and opposite vorticities that pass through the plane at 45 degree angles and are orthogonal to each other and to the zero-vorticity line. The vorticity plotted in Figure 9.13 is that of the counterclockwise, 45 degree line. For the clockwise line, the vorticity pattern is identically the same, but blue instead of red.

There are again four regions of strong vorticity (four vortexes), which spiral outward from the horizon, becoming gravitational waves. In this case, the four regions look identical, whereas for the

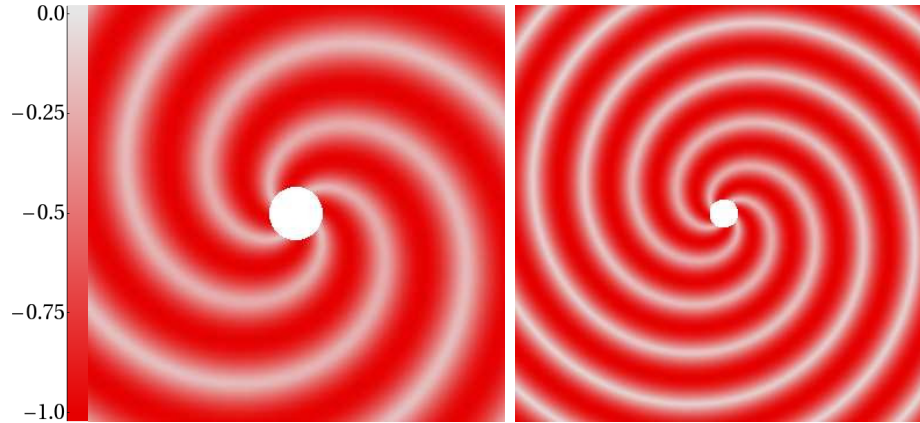


Figure 9.13: For an electric-parity  $(2,2)$  mode of a Schwarzschild black hole: the vorticity of the counterclockwise vortex lines that pass through the equatorial plane at a 45 degree angle. The clockwise vortex lines that pass through the plane have equal and opposite vorticity. By near duality, this figure also depicts the perturbative tendex structure for the magnetic-parity  $(2,2)$  mode. The conventions for coloring and shading are the same as in Figure 9.10. Because the horizon vorticity is exactly zero for this mode, the horizon is shown as a white disk. The left panel, a region  $30M$  across, is a zoom in of the right panel, which is  $56M$  across.

tendexes of this same electric-parity mode (middle column of Figure 9.12) there is an alternation between blue and red. There is actually an alternation here, too, though it does not show in the figure: The relative tilt of the lines (in the sense of the  $\phi$  direction) rotates, such that in one tendex, the red tendex lines pass through the plane with a forward 45 degree tilt on average, and in the next tendex, with a backward 45 degree tilt; and conversely for the blue tendex lines.

### 9.3.3 Three-Dimensional Vortexes and Tendexes

In this section, we shall explore the 3-dimensional vortexes and tendexes of the  $(2,2)$  modes of Schwarzschild and Kerr black holes, which are depicted in Figure 9.14. In the first subsection, we shall focus on what this figure tells us about the generation of gravitational waves, and in the second, what it tells us about duality.

#### 9.3.3.1 Physical Description of Gravitational-Wave Generation

In Section 9.1.3.6 of the Introduction, we summarized in great detail what we have learned about gravitational-wave generation from our vortex and tendex studies. There we focused on the  $(2,2)$  magnetic-parity mode, and among other things we scrutinized the upper left panel of Figure 9.14 (which we reproduced as Figure 9.4). Here, instead, we shall focus on the  $(2,2)$  electric-parity mode as depicted in the right half of Figure 9.14.

We begin with the perturbative tendexes of the electric-parity,  $(2,2)$  mode of a Schwarzschild black hole (third panel on top row of Figure 9.14). The 3-D tendexes emerge from the horizon as

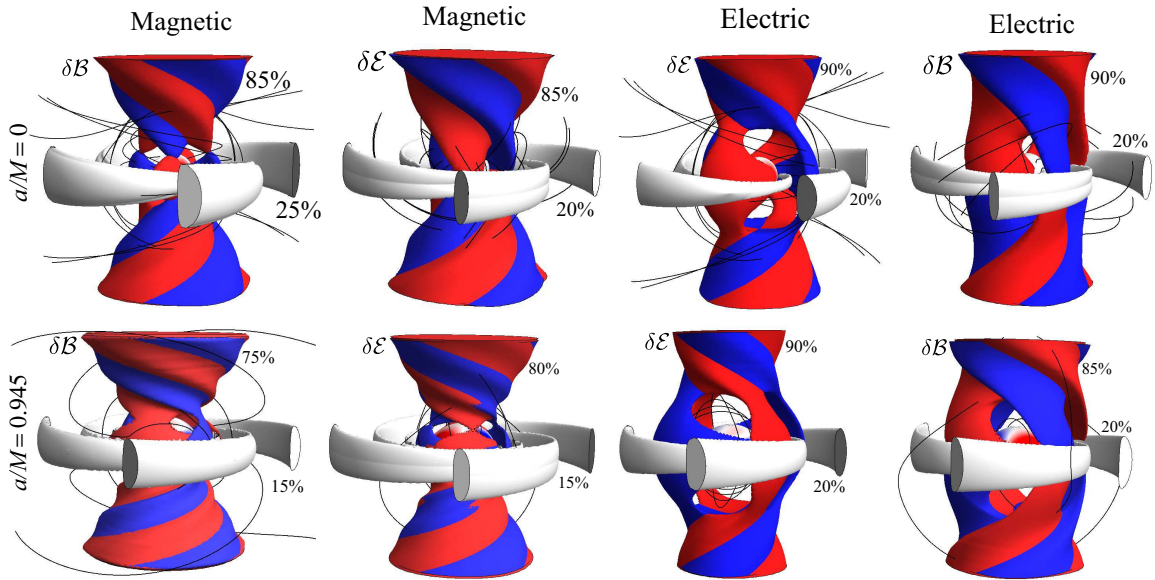


Figure 9.14: Three-dimensional vortices and tendexes of the same four modes as are shown in Figure 9.12. As there, so here, the top row is for a Schwarzschild black hole, and the bottom for fast-spin Kerr,  $a = 0.945$ ; the left two columns (one in Figure 9.12) are for a magnetic-parity (2,2) mode (with the vortices in IR coordinates), and the right two columns (one in Figure 9.12) are for electric parity in IR gauge. For each parity, the first column shows structures of the field that generates the waves ( $\delta B$  for magnetic parity;  $\delta E$  for electric parity) and the second column shows structures of the other field (not included in the equatorial-plane drawings of Figure 9.12). In each panel, the colored surfaces show the outer faces of vortices (for  $\delta B$ ) or tendexes (for  $\delta E$ ), defined as the locations, for a given radius, where the largest-in-magnitude eigenvalue of the field being plotted ( $\delta B$  or  $\delta E$ ) has dropped to a certain percentage (90, 85, 80 or 75) of its maximum for that radius; that percentage is shown alongside the colored surfaces. As in previous figures, the surface is red (light gray) if that largest-in-magnitude eigenvalue is negative and blue (dark gray) if positive. The off-white regions are surfaces where the largest-in-magnitude eigenvalue has dropped to 15%, 20% or 25% of the maximum at that radius. In each panel the black lines are a few of the vortex lines (for  $\delta B$  panels) or tendex lines (for  $\delta E$  panels) that become transverse when they reach large radii, and thereby produce the tidal or frame-drag force of an emitted gravitational wave. For discussion of this figure, see Section 9.3.3.

four deformed-cylinder structures, two red (light gray) and two blue (dark gray). These are the extensions into the third dimension of the four near-zone, equatorial-plane tendexes of the center panel in Figure 9.12 above. As we enter the transition zone, the four 3D tendexes lengthen vertically (parallel to the poles), and then as we enter the wave zone, they spiral upward and downward around the poles; they have become gravitational waves. They are concentrated near the poles because the (2,2)-mode gravitational waves are significantly stronger in polar directions than in the equator.

In this panel, we also see black tendex lines that emerge from the horizon and spiral upward and downward alongside the polar-spiraling tendexes, becoming nearly transverse at large radii—part of the outgoing gravitational waves. Of course, there are similar tendex lines, not shown, inside the spiraling tendexes. In addition, we also see tendex lines in the inner part of the wave zone that are approximately polar circles; these are also part of the outgoing waves.

The top rightmost panel depicts the vortexes associated with this electric-parity mode. The horizon vorticity vanishes, so the horizon is white. The vortexes near the horizon are dominated by the longitudinal-transverse part of the frame-drag field  $\mathcal{B}^{LT}$ , which interacts with  $\delta\mathcal{E}^L$  and  $\delta\mathcal{E}^{LT}$  to maintain their joint near-zone structure as they rotate (cf. the description of the dual magnetic-parity mode in Section 9.1.3.6). However, of course, there is also a  $\mathcal{B}^{TT}$  associated with the ingoing gravitational waves. At large radii, in the outgoing-wave zone, the vortexes, like the tendexes of the third panel top row, spiral upward and downward around the polar axis; they have joined with the tendexes to form the full gravitational-wave structure.

For insight into how (we think) the near-zone tendexes of this electric-parity mode, extending radially out of the horizon, generate these outgoing gravitational waves, and how the ingoing waves, that they also generate, act back on them and drive their gradual decay, see the description of this mode's dual in Section 9.1.3.6.

For the rapid-spin Kerr black hole, the tendex and vortex structures (last two panels of second row of Figure 9.14) are quite similar to those for the Schwarzschild black hole. The detailed differences are similar to those in the equatorial plane (see discussion in Section 9.3.2.3 above): smaller near zone and tighter spiraling for the tendexes because of the higher eigenfrequency; nonvanishing horizon vorticity with a predominantly  $Y^{32}(\theta, \phi)$  angular structure. In the near zone, the 3D vortexes seem to have acquired a longitudinal (radial) part, emerging from the  $Y^{32}$  horizon vortexes (though this is largely hidden behind the off-white structures). Thus, for a Kerr black hole, one might intuitively describe the generation of gravitational waves as being produced by a superposition of near-zone tendexes that induce vortexes by their motions, and near-zone vortexes that induce tendexes by their motions. However, because the near-zone vortexes are weaker than the tendexes, the tendexes still play the dominant role for gravitational-wave generation in this electric-parity mode.

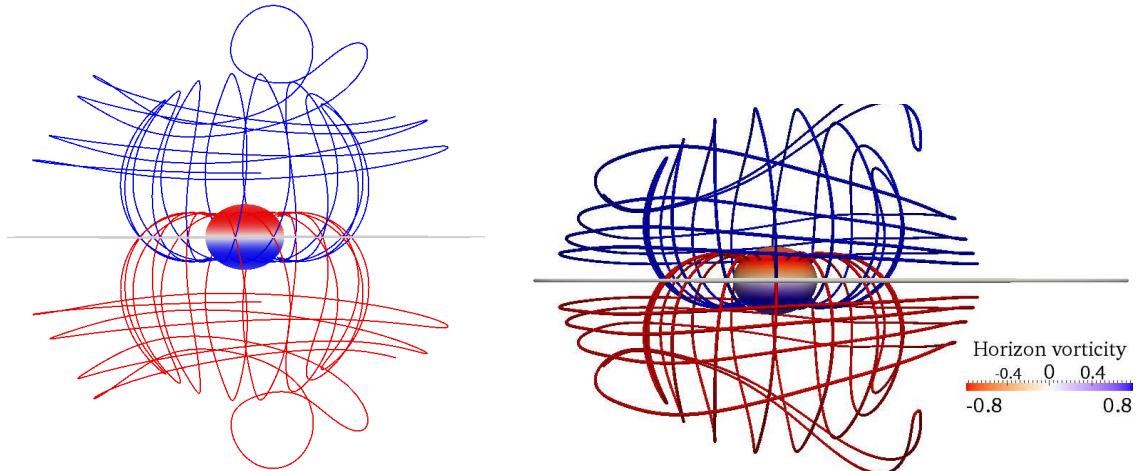


Figure 9.15: *Left:* Vortex lines of a  $a/M = 0.945$  Kerr black hole perturbed by an electric-parity  $(2, 2)$  quasinormal-mode in IR gauge. *Right:* Vortex lines from a  $a/M = 0.945$  ringing down Kerr black hole obtained from a numerical simulation [19] of two identical merging black holes with spins of magnitude 0.97 aligned parallel to the orbital angular momentum. In the simulation, we chose a late enough time that the common apparent horizon is essentially that of a single, perturbed black hole, and we computed the vortex lines using methods summarized in Reference [1].

### 9.3.3.2 Approximate Duality

By comparing the magnetic-parity left half of Figure 9.14 with the electric-parity right half, we can visually assess the degree to which there is a duality between the modes in three dimensions. For the perturbations of Schwarzschild black holes (top row), the most notable difference between the magnetic- and electric-parity perturbations is that the transition between the longitudinal near-zone and spiraling wave-zone vortexes of the magnetic-parity perturbation is more abrupt, and happens closer to the horizon than it does in the electric-parity perturbations. The reason for this is encoded in Eqs. (9.89), (9.90), and (9.91), but we do not have a simple physical explanation for why this occurs. This difference is magnified for perturbations of the rapidly rotating Kerr black hole (bottom row). Thus, the small breaking of duality quantified in Appendix 9.C for Schwarzschild black holes seems to be more pronounced in three-dimensions than in two, and stronger for rapidly rotating black holes than for non-rotating ones.

Nevertheless, the qualitative picture of wave generation by longitudinal near-zone tendexes and vortexes is essentially dual for perturbations of the two parities.

### 9.3.4 Comparing Vortex Lines of a Perturbed Kerr Black Hole and a Binary-Black-Hole-Merger Remnant

As a conclusion to this section and a prelude to future work, in Figure 9.15 we compare the vortex lines found using our analytic methods to those found in a numerical ringdown of a fast-spinning

Kerr black hole.

More specifically, we compare an electric-parity,  $(2, 2)$  quasinormal-mode perturbation of a Kerr black hole with dimensionless spin  $a/M = 0.945$ , to a ringing-down Kerr black hole of the same spin formed in a numerical simulation [19] of the merger of two equal-mass black holes with equal spins of magnitude 0.97 aligned with the orbital angular momentum. (Note that because of the symmetry of this configuration, during the ringdown there is no magnetic-parity  $(2, 2)$  mode excited.)

For both the analytical and numerical calculations, the vortex lines are those of the full frame-drag tensor  $\mathcal{B}_{i\hat{j}} = \mathcal{B}_{i\hat{j}}^{(0)} + \mathcal{B}_{i\hat{j}}^{(1)}$ , including the background part  $\mathcal{B}_{i\hat{j}}^{(0)}$  and the perturbation  $\mathcal{B}_{i\hat{j}}^{(1)} \equiv \delta\mathcal{B}_{i\hat{j}}$  (as in Appendix 9.F). This makes the lines look quite different from those for just  $\delta\mathcal{B}_{i\hat{j}}$  depicted in Figures 9.12 and 9.14.

Near the equator, the vortex lines in both panels look like those of an unperturbed Kerr black hole (see Paper II). Closer to the axis of rotation, the background vortex lines become degenerate, and the perturbations break the degeneracy by picking the principal axes of the perturbative field. Correspondingly, near the rotation axis and at large enough radii to be in or near the wave zone, the vortex lines resemble those of transverse-traceless gravitational waves, which are emitted symmetrically above and below the hole.

Although the vortex lines from these similar physical situations were computed using very different methods and gauge conditions, the results are remarkably similar (see Figure 9.15). This gives us confidence that our analytical methods can guide our understanding of the vortexes and tendexes in the late stages of numerical simulations.

## 9.4 Superposed $(2, 2)$ and $(2, -2)$ Quasinormal Modes of Schwarzschild

### 9.4.1 Magnetic-Parity Superposed Modes

In Section 9.1.3.9, we summarized the properties of the quasinormal mode of Schwarzschild that is obtained by superposing the magnetic-parity  $(2, 2)$  and  $(2, -2)$  modes. Here we give details. The vortex lines and vorticities for this superposed mode are depicted in Figure 9.16 using the three types of visualizations in Figure 9.10.

The left column of Figure 9.16 shows the two families of vortex lines that lie in the equatorial plane, color coded by their vorticities. The solid-line family has predominantly positive (clockwise) vorticity, but in some regions its vorticity becomes weakly negative (counterclockwise). The dashed-line family has predominantly negative vorticity, but in some regions it is weakly positive. A rotation around the hole by angle  $\pi/2$  maps each family into the other.

In the center column of Figure 9.16, the vortex lines are drawn black and the equatorial plane

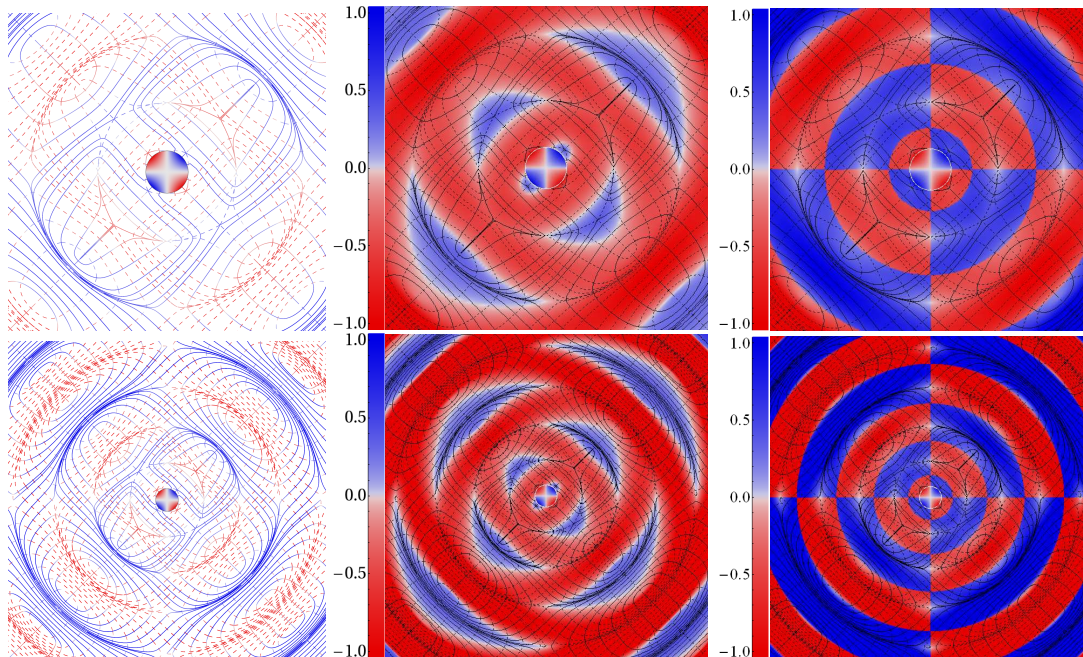


Figure 9.16: The vorticities and vortex lines in the equatorial plane of a Schwarzschild black hole, for the fundamental magnetic-parity  $(2, 2)$  mode superposed on the fundamental magnetic-parity  $(2, -2)$  mode, depicted using the same three visualization techniques as in Figure 9.10. Here, however, we do not scale the vorticity by any function, but the numbers on the vorticity scale on the left of the panels are equal to  $\sqrt{\text{vorticity} \times r}$  (where  $r$  is radius), in units of the maximum value of this quantity, which occurs on the horizon at  $\phi = 3\pi/4$  and  $\phi = 7\pi/4$ . The top panels cover a region  $30M$  across, and the bottom panels are a zoom-out of the upper panels,  $56M$  across. The central circle in all panels is the horizon as viewed from the polar axis, colored by its vorticity. *Left column:* The two families of vortex lines (one shown dashed, the other solid) with each line colored, at each point, by the sign of its vorticity (blue [dark gray] for positive, i.e., clockwise; red [light gray] for negative, i.e., counterclockwise), and each line has an intensity proportional to the magnitude of its vorticity. *Center column:* The same vortex lines are colored black, and the equatorial plane is colored by the vorticity of the dashed family of lines. *Right column:* The same as the center column, but the equatorial plane is colored by the vorticity with the larger magnitude.

is colored by the vorticity of the dashed lines. To deduce the coloring for the solid lines, just rotate the colored plane (but not the lines) by  $\pi/2$  and interchange red (light gray) and blue (dark gray). By contrast with most previous figures, the radial variation of the vorticity is not scaled out of this figure; so in the wave zone (roughly, the outer half of right panel) the coloring oscillates radially, in color and intensity, in the manner of a gravitational wave. At large radii, there is also a growth of intensity (and saturation of the color scale) due to the waves emitted earlier having larger amplitude.

In the right column of Figure 9.16, the vortex lines are again drawn black, and the equatorial plane is now colored by the larger of the two vorticities in amplitude.

Together, the columns of Figure 9.16 provide the following picture: For each family of lines, the equatorial-plane vortices form interleaved rings (dashed lines and red [light gray] vortices for center column). Most of the family's vortex lines form closed, distorted ellipses that, when tangential, lie

in a single vortex (red for dashed lines), and when more nearly radial, travel from one vortex to another. In the wave zone, these line and vortex structures grow longer tangentially as they propagate outward, and they maintain fixed radial thickness. When one looks at both families simultaneously, focusing on the strongest at each point (right column), one sees vortexes of alternating red and blue vorticity (light and dark gray). The angular oscillations are those of a quadrupolar structure; the radial oscillations are those of a propagating wave.

In the near zone, the vortex lines have rather sharp, right angled features associated with the quadrupolar nature of the near-zone perturbation; this is to be compared to the oscillating current quadrupole in linearized gravity (Paper I, Section VI, Figure 15). There are multiple singular points in the lines: degenerate points where the lines cross with sharp bends, and where both families of vortex lines take on the same eigenvalue. (The third eigenvalue, that of the lines perpendicular to the plane, must then be minus twice the vorticity of these lines, in order for the sum of the eigenvalues to vanish).

We shall discuss the dynamics of these vortex lines and vortexes in Section 9.4.3 below, after first gaining insight into the electric-parity superposed mode (whose vortexes will teach us about this magnetic-parity mode's tendencies through the near duality).

### 9.4.2 Electric-Parity Superposed Mode

For the mode constructed by superposing electric-parity (2,2) and (2,-2) modes of Schwarzschild, as for the electric-parity (2,2) mode itself (Section 9.3.2.4), symmetry considerations dictate that: (i) one family of vortex lines lies in the equatorial plane and has vanishing vorticity, (ii) two families pass through the equatorial plane at  $45^\circ$  angles, with equal and opposite vorticities, and (iii) the horizon vorticity vanishes.

In Figure 9.17 [analog of Figure 9.13 for the (2,2) electric-parity mode], we show the vorticity of the family of counterclockwise vortex lines, as they pass through the equatorial plane.

In the near zone of this figure, we see again a distinct quadrupolar structure, with four lobes of strong vorticity present near the horizon (four near-zone vortexes). Beyond these near-zone lobes, there is a ring of vanishing vorticity, followed by an annulus where the cast-off vortexes of a previous cycle have begun to deform into an annulus of stronger vorticity. In the wave zone, the vortexes have transitioned into outward traveling transverse waves, with regions of vanishing vorticity between the crests and troughs of each wave. The waves are strongest along the diagonals, though in the near zone the (LT) frame-drag field is strongest in the up, down, left and right directions.

By (near) duality, the tendencies of the magnetic-parity superposed mode will have the same form as these electric-parity-mode vortexes. Accordingly, in the next section, we will use this figure to elucidate the magnetic-parity mode's dynamics — and by duality, also the dynamics of this electric-parity mode.

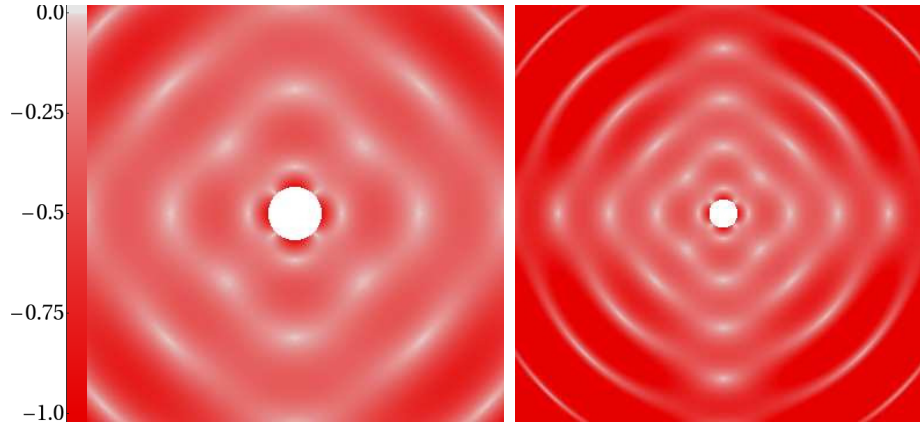


Figure 9.17: For the electric-parity, superposed (2,2) and (2,-2) fundamental modes of Schwarzschild: the vorticity of the counterclockwise vortex lines that pass through the equatorial plane at  $45^\circ$  angles. By near duality, this figure also depicts the perturbative tendex structure for the magnetic-parity superposed mode. The intensity scale of the red color (left edge of figure) is the same as that in the center column of Figure 9.16. The left panel, a region  $30M$  across, is a zoom-in of the right panel, which is  $56M$  across. This figure is the superposed-mode analog of Figure 9.13.

### 9.4.3 Dynamics of the Magnetic-Parity Superposed Mode

We now turn to the dynamics of the magnetic-parity superposed mode, which we studied in Section 9.4.1

In Figure 9.18 for this mode we show, in the equatorial plane, the time evolution of (i) the vortex lines and their vorticities near the black hole (top row), and (ii) on a larger scale that extends into the wave zone, the mode's vortexes (middle row) and perturbative tendexes (bottom row). The four panels in the top row are stills from a movie at [20]. To be absolutely clear, the vortexes and tendexes are those of the same magnetic-parity mode. As in the center column of Figure 9.16, the top and middle rows show only one family of vortexes, that for the dashed vortex lines which have predominantly negative vorticity; and as in Figure 9.17, the bottom row shows only the tendicity of the negative-tendicity perturbative tendexes that pass through the equatorial plane at  $45^\circ$ . Time  $t = 0$  (left panels of Figure 9.18) is chosen at a moment when the horizon vorticity is maximum, whereas Figures 9.16 and 9.17 are snapshots at the slightly earlier time  $\sigma t \approx -\pi/3$  (which gives nearly the same vortex structures as the fourth column, after a rotation by  $\pi/2$ ).

In interpreting Figure 9.18, especially the top row, we emphasize that there is no unique way of following a single vortex or tendex line in time. The same is true of electric and magnetic field lines in Maxwell's theory (cf. [21]). While we hope to elucidate this issue in future work, here, in constructing the panels in the top row of Figure 9.18, we have simply started the integration of the vortex lines from the same points at each time step, *making no attempt to identify and follow individual lines from moment to moment*. Correspondingly, in order to interpret Figure 9.18 and gain insight into the dynamics of the superposed mode, instead of trying to follow individual lines,

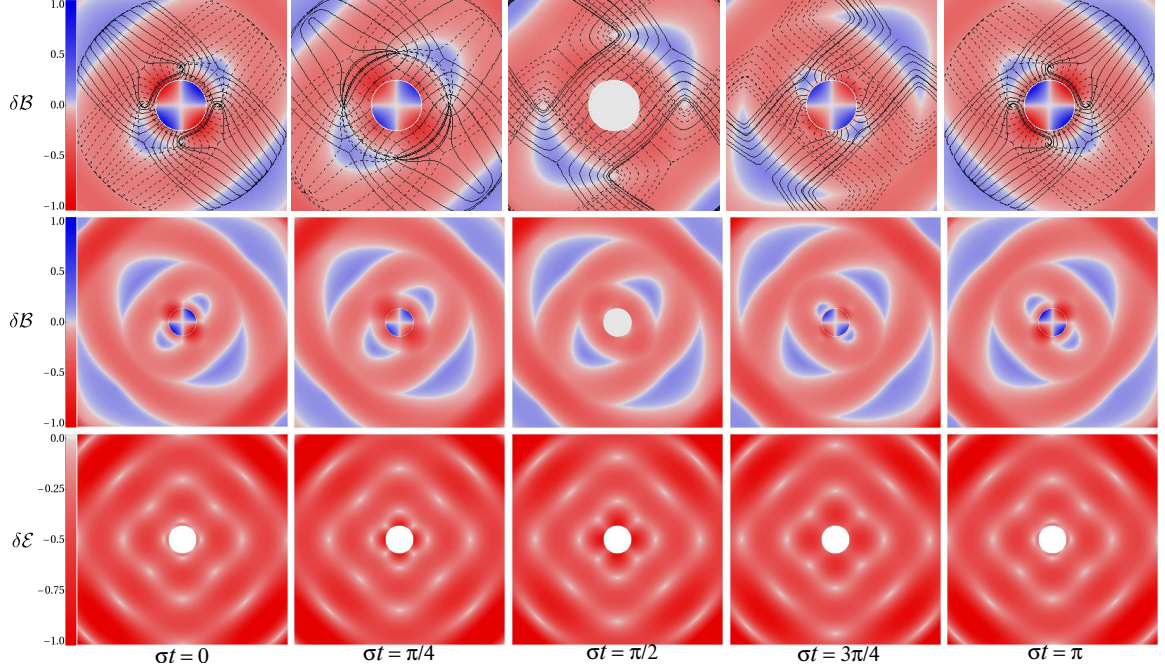


Figure 9.18: Time evolution of the equatorial vortices (top and middle rows) and equatorial perturbative tendexes (bottom row) for the superposed  $(2, 2)$  and  $(2, -2)$  magnetic-parity mode of Schwarzschild in RWZ gauge. The color scale is the same as the center column of Figure 9.16, and the gravitational-wave-induced exponential decay of the vorticity and tendicity has been removed. *Top row:* Equatorial vortex lines and their vorticity plotted in a region near the horizon ( $16M$  across) followed over time  $t$ . The real part of the eigenfrequency is denoted  $\sigma$ , so the successive panels, left to right, cover half a cycle of the mode's oscillation. *Middle row:* The vorticity of the equatorial vortex lines in the near, intermediate and beginning of wave zone ( $30M$  across) at the same time steps as the top row. *Bottom row:* Tendicity of the counterclockwise tendex lines passing through the equatorial plane (which is dual to the left panel of Figure 9.17), plotted at the same time steps as the top row.

we will focus on the lines' evolving shapes, and the structures of the vortices and tendexes and the equations governing their evolution on the horizon.

As a foundation for understanding the near-zone dynamics depicted in this figure, we write down explicit expressions for the longitudinal and longitudinal-transverse parts of the frame-drag and tidal fields *on the horizon*:

$$\mathcal{B}_{\hat{r}\hat{r}} = \Re \left[ \frac{3}{2i\omega M^3} e^{-i\omega(\hat{t}+2M)} \right] \mathcal{Y}(\theta, \phi), \quad (9.26a)$$

$$\mathcal{B}_{\hat{r}\hat{A}} = \Re \left[ \frac{1}{2\sqrt{2}M^2} (1 - \beta) e^{-i\omega(\hat{t}+2M)} \right] D_{\hat{A}} \mathcal{Y}, \quad (9.26b)$$

$$\delta E_{\hat{r}\hat{A}} = \Re \left[ \frac{1}{2\sqrt{2}M^2} (1 + \beta) e^{-i\omega(\hat{t}+2M)} \right] \left( -\epsilon_{\hat{A}}^{\hat{B}} D_{\hat{A}} \right) \mathcal{Y}, \quad (9.26c)$$

where

$$\beta \equiv \frac{3}{2i\omega M(1 - 4i\omega M)}. \quad (9.26d)$$

Here the normalization is that of Appendix 9.A,  $\omega = (0.37367 - 0.08896i)/M$  is the mode's eigenfrequency,  $\epsilon_{\hat{A}}^{\hat{B}}$  is the Levi-Civita tensor on the horizon,

$$\mathcal{Y} \equiv Y^{22} + Y^{2-2} = \sqrt{15/8\pi} \sin^2 \theta \cos 2\phi \quad (9.26e)$$

is this mode's scalar spherical harmonic, and  $D_{\hat{A}}$  is the covariant derivative on the unit 2-sphere (related to the covariant derivative on the horizon by  $D_{\hat{A}} = 2M\nabla_{\hat{A}}$ ). [Equations (9.26) follow from Eqs. (9.40), (9.41), (9.54) of Appendix 9.A, the vector-spherical-harmonic definitions (9.82a) and (9.86a), and definition (9.5) of the EF time coordinate.]

Equations (9.26) are the fields measured by Eddington-Finkelstein observers. The conservation law (9.4a) for longitudinal field lines threading the horizon (which we shall need below) involves, by contrast, the LT frame-drag field measured by Schwarzschild observers on the “stretched horizon” (very close to the event horizon). Since the Schwarzschild observers move outward with velocity  $\mathbf{v} = (2M/r)\mathbf{N} \simeq \mathbf{N}$  with respect to the EF observers, and with  $\gamma \equiv 1/\sqrt{1-v^2} \simeq 1/(\sqrt{2}\alpha)$ , the field they measure is  $\mathcal{B}_{\text{Sch}}^{\text{LT}} = \gamma(\mathcal{B}^{\text{LT}} - \mathbf{N} \times \delta\mathcal{E}^{\text{LT}})$ . This field diverges as  $1/\alpha$  as the stretched horizon is pushed toward the event horizon; to remove that divergence, in the Membrane Paradigm [9]) we renormalize by multiplying with  $\alpha$ :

$$\mathcal{B}_{\hat{r}\hat{A}}^{\text{H}} \equiv \alpha\mathcal{B}_{\text{Sch}}^{\text{LT}} = \alpha\gamma(\mathcal{B}^{\text{LT}} - \mathbf{N} \times \delta\mathcal{E}^{\text{LT}}) = \Re \left[ \frac{1}{4M^2} e^{-i\omega(\tilde{t}+2M)} \right] D_{\hat{A}}\mathcal{Y}. \quad (9.27)$$

The second line is obtained by inserting the EF fields (9.26a) and (9.26b), and  $\gamma = 1/\sqrt{2}\alpha$ , into the first line. The conservation law for longitudinal vortex lines threading the horizon (actually, one of the Maxwell-like Bianchi identities in disguise) says that

$$\partial\mathcal{B}_{NN}/\partial\tilde{t} + \nabla_{\hat{A}}(-\mathcal{B}_{\hat{r}\hat{A}}^{\text{H}}) = 0; \quad (9.28)$$

cf. Eq. (9.4a) and subsequent discussion. (In this Schwarzschild-perturbation-theory case, there are no small spin-coefficient terms to spoil the perfection of the conservation law.) The vortex-line density and flux expressions (9.26a) and (9.27) do, indeed, satisfy this conservation law, by virtue of the fact that the 2-dimensional Laplacian acting on the quadrupolar spherical harmonic  $\mathcal{Y}$  gives  $D_{\hat{A}}D^{\hat{A}}\mathcal{Y} = -6\mathcal{Y}$ .

Equations (9.26) and (9.28) tell us the following: (i) On and near the horizon, the LT fields  $\mathcal{B}^{\text{LT}}$  [Eq. (9.26b)] and  $\delta\mathcal{E}^{\text{LT}}$  [Eq. (9.26c)], and also  $\mathcal{B}_{\hat{r}\hat{A}}^{\text{H}}$  [Eq. (9.27)], all oscillate approximately out of

phase with the longitudinal field  $\mathcal{B}^L$  [Eq. (9.26a)].<sup>3</sup> Therefore, near-zone energy is fed back and forth between the L and LT fields as the black hole pulsates.

(ii) The conservation law (9.28) says that, if we regard  $\mathcal{B}_{NN}$  as the density of vortex lines of  $\mathcal{B}^L$  threading the horizon, and  $-\mathcal{B}_{\hat{r}\hat{A}}^H$  as the flux of vortex lines (number crossing a unit length in the horizon per unit time), then these horizon-threading vortex lines of  $\mathcal{B}^L$  are conserved during the pulsation. More specifically:

(iii) As the mode evolves in Figure 9.18 from  $\sigma t = 0$  to  $\sigma t = \pi$ , the conserved vortex lines are pushed away from the center of each horizon vortex toward its white edges, and there the conserved lines from the red region (counterclockwise) annihilate with the conserved lines from the blue region (clockwise). The pushing is embodied in the vortex-line flux  $-\mathcal{B}_{\hat{r}\hat{A}}^H$ , which grows stronger during this evolution.

(iv) As the mode evolves further from  $\sigma t = \pi/2$  to  $\sigma t = \pi$ , conserved vortex lines of  $\mathcal{B}^L$  are created in pairs (one clockwise, the other counterclockwise) at the white edges of the horizon vortexes, and move inward toward the center of each vortex.

Turn, now, from the conserved vortex lines of  $\mathcal{B}^L$  piercing the horizon to the 3D vortex lines outside the horizon, depicted in the top row of Figure 9.18. Because these are lines of the full 3D frame-drag field  $\mathcal{B}$  and not its longitudinal part  $\mathcal{B}^L$ , they do not obey a conservation law and there is no unique way of following individual lines from one panel to the next. However, their evolving shapes teach us much about the geometrodynamics of this superposed mode:

At time  $\sigma t = 0$  (upper left panel), the horizon-piercing vortex lines of the full frame-drag field  $\mathcal{B}$  are almost perfectly radial, with clockwise (solid) tendex lines emerging from the two blue horizon tendexes, and counterclockwise (dashed) tendex lines emerging from the two red horizon tendexes. As time passes, the horizon piercing lines become less radial and the horizon vorticity decreases ( $\sigma t = \pi/4$ ) until the lines' angles to the horizon are almost all near  $45^\circ$  and the horizon vorticity vanishes ( $\sigma t = \pi/2$ ). Note that the lines that lie precisely on the diagonals, and which contact the horizon radially in the middle panel ( $\sigma t = \pi/2$ ), have zero vorticity where they strike the horizon. This latter fact allows them to have a more radial angle of intersection than almost all other lines. The near-horizon frame-drag field has evolved at this time from being predominantly longitudinal,  $\mathcal{B}^L$ , to being predominantly longitudinal-transverse,  $\mathcal{B}^{LT}$ , but with some small admixture of transverse-traceless ingoing waves,  $\mathcal{B}^{TT}$ . As time moves onward from  $\sigma t = \pi/2$  to  $\sigma t = \pi$ , the vortex lines in the outer part of each panel reach around on the horizon and attach to a quadrant on the side rather than directly below themselves—a quadrant that has newly acquired the color corresponding to the lines' own vorticity (blue for solid lines, red for dashed lines).

<sup>3</sup>The longitudinal-transverse frame-drag field  $\mathcal{B}^{LT}$  lags approximately  $1.04 \approx \pi/3$  radians behind  $\mathcal{B}_{NN}$  on the horizon, while the LT component of the tidal field,  $\mathcal{E}^{LT}$ , lags approximately  $1.21 \approx 2\pi/5$  radians behind  $\mathcal{B}_{NN}$ . Most importantly for interpreting Figure 9.18, the two nonzero tendicities of the tidal field are (in the equatorial plane)  $\pm \sqrt{\mathcal{E}_{\hat{r}\hat{\theta}}^2 + \mathcal{E}_{\hat{\theta}\hat{\phi}}^2}$ , and on the horizon they lag nearly  $\pi/2$  radians behind  $\mathcal{B}_{NN}$ ; the damping of the perturbation adds slightly to the phase lag, so that it is actually  $\pi/2 + \arctan[\Im(\omega)/\Re(\omega)] \simeq \pi/2 + 0.234$  out of phase with  $\mathcal{B}_{NN}$ .

At  $\sigma t = 0$  (upper left panel), the near-horizon, nearly circular vortex lines in each quadrant represent, predominantly, the transverse-isotropic part of  $\mathcal{B}^L$  and keep it trace free. As time passes and  $\mathcal{B}^L$  decreases, we can regard these lines as traveling outward, forming the distorted ellipses which become gravitational waves in the far zone. The manner in which these circular vortex lines are restored each cycle appears to be as follows: As discussed above, as the horizon vorticity oscillates through zero, formerly longitudinal lines are pushed away from their respective vortices and become first more longitudinal-transverse, and then attach to a different quadrant of the horizon; meanwhile the  $\mathcal{B}^L$  is being regenerated with opposite sign in each quadrant, which requires new transverse-isotropic lines of opposite vorticity. These lines run tangent to the horizon, hugging it while they cross through a vortex of strong opposite vorticity. At each edge of the vortex these isotropic-transverse lines link up with predominantly radial lines which have the same sign of vorticity (it appears that it is the degenerate points at these edges that allow for such a reconnection). This deforms the highly distorted, nearly circular arcs, which then lift off the horizon and propagate away as the cycle progresses.

This entire evolution is being driven by the oscillatory turn-off and turn-on of the longitudinal part of the frame-drag field  $\mathcal{B}^L$ .

Turn attention to the evolution of the mode's equatorial vortices (middle row) and tendexes (bottom row). In accord with our discussion above of the evolution of the horizon fields, Eqs. (9.26), these panels reveal (see below) that the vortices and tendexes oscillate out of phase with each other. Near-zone energy (see footnote 1 in Section 9.1.3.8) gets fed back and forth between vortices and tendexes in an oscillatory manner (though during this feeding, some of it leaks out into the transition zone and thence into gravitational waves). This oscillatory feeding enables the near-zone perturbative tendexes to store half of the oscillation energy (while the LT vortices store the other half) when the longitudinal frame-drag field  $\mathcal{B}^L$  is temporarily zero; and then use that energy to regenerate  $\mathcal{B}^L$ .

The evidence for this near-zone feeding, in Figure 9.18, is the following: (i) The near-horizon vortices are strongest along the diagonals, while the regions of strong near-zone tendicity always occur along the vertical and horizontal directions. Thus, the vortices and tendexes tend to occupy different regions, with a  $\pi/4$  rotation between the patterns [as one should expect from the angular dependences in Eqs. (9.26a) and (9.26c)]. (ii) There is a  $\simeq \pi/2$  phase difference in the time evolution of the vortices and tendexes. At those times when the horizon vorticity and near-horizon vortices are strongest, the near-horizon tendexes are weak. As the horizon oscillates through zero vorticity, the tendexes are reaching their maximum strength.

A careful study of the phases of these time behaviors reveals that the dynamics are not precisely  $\pi/2$  out of phase, as can be seen clearly in the first panel in the bottom row of Figure 9.18: though the horizon vorticity is at its maximum, the tendicities have just oscillated through zero in this

region and are beginning to regenerate. As mentioned in footnote 3 above, this additional phase lag is due to the mode's damping, and in radians its magnitude is  $\arctan[\Im(\omega)/\Re(\omega)] \simeq 0.234$ .

The  $\pi/4$  differences in spatial phase and  $\simeq \pi/2$  differences in temporal phase are lost as the frame-drag and tidal fields travel outward through the intermediate zone and into the wave zone; an inspection of the outer edges of the time series plots shows bands of strong tendicity and vorticity *in phase* in time and space, propagating outward in synch. This must be the case, since for plane waves in linearized gravity, the vortex and tendex lines are in phase temporally and spatially (though the lines are rotated by  $\pi/4$  with respect to each other at each event; see Paper I, Sec VI A).

By scrutinizing the middle and bottom rows of Figure 9.18, (which extend from the near zone through the intermediate zone and into the inner parts of the wave zone), one can see visually how the oscillatory feeding of energy between near-zone vortexes and tendexes gives rise to outgoing vortexes and tendexes that represent gravitational waves.

## 9.5 (2, 1) and (2, 0) Quasinormal Modes of Schwarzschild

In this section we will complete our study of the quadrupolar perturbations of Schwarzschild black holes. Specifically, we will explore the vortex and tendex structures and the dynamics of the (2, 1) and (2, 0) magnetic- and electric-parity perturbations of a Schwarzschild hole, in RWZ gauge.

### 9.5.1 Vortexes of (2, 1) Magnetic-Parity Mode and Perturbative Tendexes of (2, 1) Electric-Parity Mode

In Section 9.1.3.7, we summarized the most important properties of the (2,1) magnetic-parity mode of a Schwarzschild black hole. In this subsection and the next, we shall give additional details about this mode and its electric-parity dual. We begin with the vortex structure for magnetic parity.

The horizon vorticity of the magnetic-parity (2,1) mode has an angular dependence given by the spherical harmonic  $Y^{21}(\theta, \phi)$  (of course). We display this horizon vorticity in the left panel of Figure 9.19. There are four horizon vortexes, two of each sign, and vanishing horizon vorticity all along the equator.

As we noted in Section 9.1.3.7, this mode's symmetry dictates that the frame-drag field be reflection antisymmetric through the equatorial plane. As for the electric-parity (2,2) frame drag field, which also has this property (second paragraph of Section 9.3.2; also Section 9.3.2.4 and Figure 9.13), this implies that one family of vortex lines lies in the equatorial plane with vanishing vorticity, and two cross through that plane at  $45^\circ$  with equal and opposite vorticities. The negative vorticities of the crossing lines are plotted in the middle panel of Figure 9.19, along with the projected horizon vorticity, as if the horizon were viewed from above. The positive-vorticity pattern of the

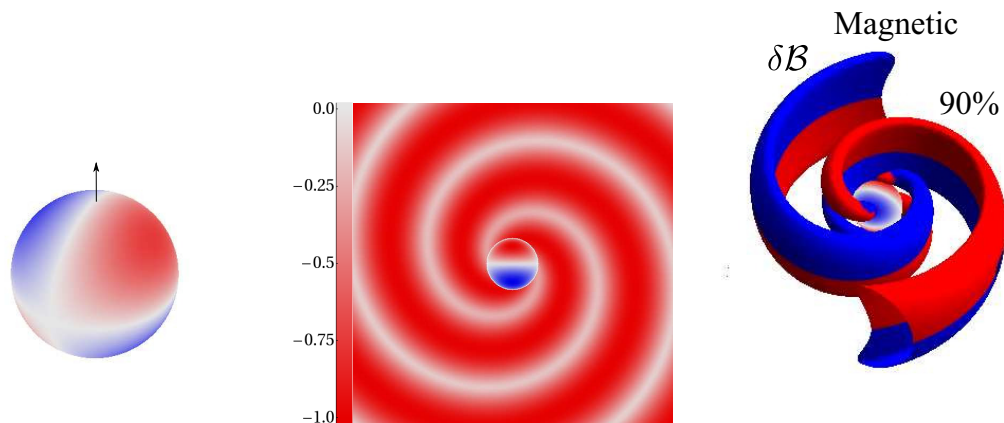


Figure 9.19: The  $(2, 1)$  magnetic-parity horizon vorticity and vortices. *Left panel:* The horizon vorticity for the  $(2, 1)$  magnetic-parity perturbation of Schwarzschild, colored as in Figure 9.9. There are four horizon vortices, two clockwise (blue [dark gray]) and two counterclockwise (red [light gray]). The horizon vorticity vanishes at the equator and the poles. *Middle panel:* Vorticity of the counterclockwise vortex lines passing through the equatorial plane, colored and normalized as in the middle and right hand columns of Figure 9.10 and plotted in a region  $24M$  across. The (blue [dark gray]) vorticity of the clockwise vortex lines has precisely this same pattern, because the two families of lines pass through the equatorial plane with the same magnitude of vorticity at each point. *Right panel:* Three dimensional vortices colored and labeled as in Figure 9.14. By near duality, this figure also represents (to good accuracy) the tendicity and tendex structure of the  $(2,1)$  electric-parity mode.

other family of crossing lines is identical to this negative-vorticity pattern, since at each point the two lines have the same vorticity magnitude.

The fact that there are just two spiraling vortices in this figure, by contrast with four for the  $(2,2)$  modes, is guaranteed by the modes' azimuthal orders,  $m = 1$  here and  $m = 2$  for  $(2,2)$ .

The vortex structure outside the equatorial plane, depicted in the right panel of Figure 9.19, was discussed in Section 9.1.3.7. The two red (light gray), 3D vortices are the same ones depicted in the middle panel. They actually extend across the equatorial plane (via the  $45^\circ$  vortex lines) into the region occupied by the blue (dark gray) vortices; but we do not see them there in the 3D drawing because the blue vortices have larger vorticity and we have chosen to show at each point only the largest-vorticity vortex.

### 9.5.2 Vortices of $(2, 1)$ Electric-Parity Mode and Perturbative Tendexes of $(2, 1)$ Magnetic-Parity Mode

Turn, next, to the vortex lines and vortex structure of the  $(2,1)$  electric-parity mode. [By near duality, the perturbative tendex lines and tendex structure of the  $(2,1)$  magnetic-parity mode will be the same.]

For this mode, with the parity reversed from the previous section, the frame-drag field is sym-

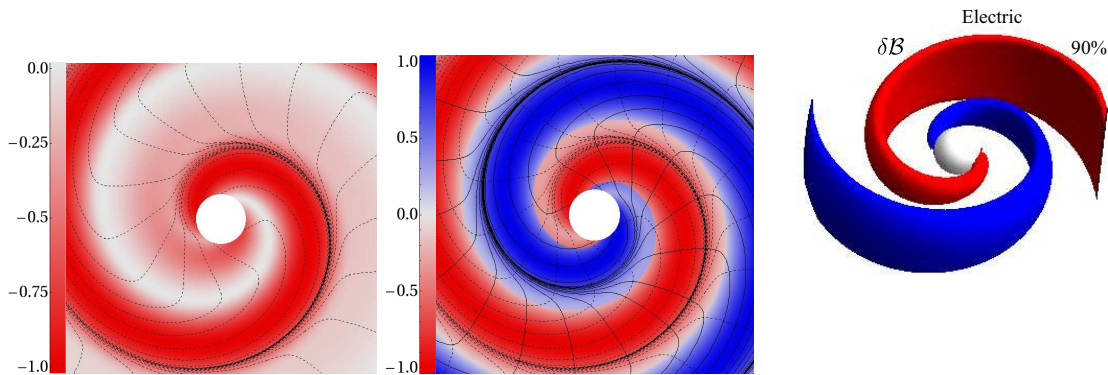


Figure 9.20: The  $(2, 1)$  electric-parity vortex lines, vorticities and vortices in the equatorial plane. For this mode the horizon's vorticity vanishes, so the horizon is plotted as a white disk or sphere. *Left panel:* Counterclockwise vortex lines (dashed) and their vorticity (red [light gray] color) normalized as in Figure 9.10, and plotted in a region  $24M$  across. *Middle panel:* Both clockwise (solid) and counterclockwise (dashed) vortex lines, and the vorticity (color) of the line with the larger magnitude of vorticity, in a region  $24M$  across. *Right Panel:* Three-dimensional vortices colored and labeled as in Figure 9.14. By near duality, this figure also represents to good accuracy the perturbative tendex lines, tendicities and tendexes for the magnetic-parity  $(2, 1)$  mode.

metric under reflection through the equatorial plane rather than antisymmetric. Therefore, there are two sets of vortex lines that remain in the equatorial plane, with the third set normal to it. In this sense the vortices' structures are analogous to those of the magnetic-parity,  $(2, 2)$  mode; and in fact they are strikingly similar, aside from having two arms rather than four.

We show the vortices and vortex lines in Figure 9.20. The left and middle panels of Figure 9.20 show the lines that remain in the equatorial plane, along with color-intensity plots depicting the lines' vorticities.

The left panel of Figure 9.20 shows the counterclockwise lines and their vorticities. As in the case of the  $(2, 2)$  mode, we see a spiraling region of strong vorticity which contacts the horizon, and an accompanying spiral of low vorticity. At the horizon, the frame-drag field is primarily longitudinal-transverse, and correspondingly its vortex lines enter the horizon at a (nearly)  $45^\circ$  angle. As for the  $(2, 2)$  mode, there is a limiting spiral that all the outspiraling vortex lines approach, near the edge of the vortex.

There is also a small region of strong vorticity near the horizon which forms a second spiral, opposite the primary spiral, although it quickly becomes weak; this second vortex coincides with the region of strong positive vorticity, as we see in the middle panel of Figure 9.20, and we think its existence is due to the frame-drag field at the horizon being primarily longitudinal-transverse. It also should be compared to the similar regions of strong negative vorticity near the positive horizon vortices of the magnetic-parity  $(2, 2)$  mode in Figure 9.10.

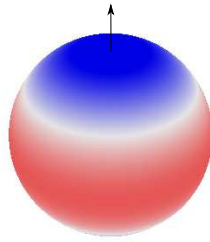


Figure 9.21: The horizon vorticities ( $\delta\mathcal{B}_{NN}$ ) of the quadrupolar,  $(2,0)$ , magnetic-parity mode. As in Figure 9.9, the color intensity is proportional to the magnitude of the vorticity with blue (dark gray) for positive and red (light gray) for negative. The arrow points along the polar axis. The vorticity oscillates sinusoidally in time, causing  $\delta\mathcal{B}_{NN}$  first to vanish and then to change sign.

In the middle panel, we plot both the counterclockwise (dashed) and clockwise (solid) vortex lines, and we color each point by the vorticity that is strongest. We see two strong vortexes spiraling out to form gravitational waves, and we see that under a rotation through  $180^\circ$  the clockwise and counterclockwise vortex lines map into each other.

Finally, in the right panel of Figure 9.20, we show the vortexes in three dimensions using the same conventions as in Figure 9.14: the red (light gray) and blue (dark gray) surfaces are the locations where the vorticity of largest magnitude has fallen to 90% of its maximum at each radius. By contrast with the  $(2,1)$  magnetic-parity mode, where the 3D vortexes are antisymmetric through the equator (and so they flip colors; see Figure 9.19), here they are symmetric and so have the same color above and below the equatorial plane.

By duality, for the  $(2,1)$  magnetic-parity mode, with its antisymmetric 3D vortexes (Figure 9.19), the 3D perturbative tendexes are symmetric through the equatorial plane and have the form shown in this right panel of Figure 9.20.

### 9.5.3 Vortexes of $(2,0)$ Magnetic-Parity Mode and Perturbative Tendexes of $(2,0)$ Electric-Parity Mode

In Section 9.1.3.8, we described in detail the dynamics of the axisymmetric  $(2,0)$  magnetic-parity mode of Schwarzschild and the gravitational waves it emits—waves in which the vortex and tendex lines wrap around deformed tori. In this section and the next, we shall discuss some other details of this mode and its dual, the  $(2,0)$  electric-parity mode.

In Figure 9.21, we show the horizon vorticity for this magnetic-parity mode. Of course, it is proportional to the scalar spherical harmonic  $Y^{20}(\theta, \phi)$ . At this moment of time, there are clockwise vortexes (blue [dark gray]) in the northern and southern hemispheres, and a band-shaped counterclockwise vortex (red [light gray]) in the equatorial region. As time passes, the horizon

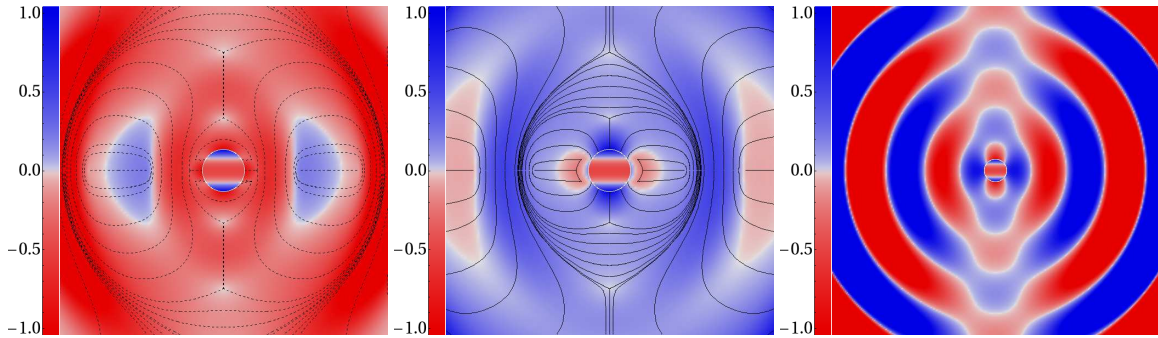


Figure 9.22: *Left and middle panels:* Near- and transition-zone vortex lines and their vorticities in an  $\mathcal{S}_\phi$  plane of constant  $\phi$ , for the axisymmetric (2,0) magnetic-parity mode of Schwarzschild in the near and transition zones ( $30M$  across). *Left panel:* The predominantly counterclockwise family of vortex lines. *Middle panel:* The predominantly clockwise family of vortex lines. *Right panel:* Vorticity of the axial lines normal to an  $\mathcal{S}_\phi$  plane, in near and wave zones ( $56M$  across). The color intensity in each panel gives the vorticity of the lines, scaled as in Figure 9.16.

vorticity oscillates, with red vortexes becoming blue and blue becoming red in each half cycle, while also decaying exponentially. The cause of these oscillations, as we discussed in Section 9.1.3.8, is exchange of energy between  $\delta\mathcal{B}^L$  (whose normal-normal component is the horizon vorticity) and  $\delta\mathcal{E}^{LT}$  (which we will visualize in the next section).

As we discussed in Section 9.1.3.8, symmetries dictate that this mode has two families of vortex lines lying in planes  $\mathcal{S}_\phi$  of constant  $\phi$  and a third family consisting of azimuthal circles of constant  $r$  and  $\theta$ . In Figure 9.6, we explored in detail the wave-zone wrap-around-torus shapes of the  $\mathcal{S}_\phi$  vortex lines, and their vorticity patterns. In the near zone, the line shapes and vorticities are somewhat more complex. We elucidate them in Figure 9.22, where, to make the figure more understandable and preserve some features lost in Figure 9.6, we show the two families of vortex lines in separate panels, left and center.

As for the superposed (2, 2) and (2, -2) perturbations of Section 9.4, each family takes on both positive and negative vorticities, but is predominantly one or the other. And unlike the (2,2) mode and the superposed mode, the (2,0) line families do not map into each other after a  $90^\circ$  rotation; rather, they have distinct patterns (as one might expect, since their plane is  $\mathcal{S}_\phi$  rather than the equatorial plane). On the other hand, because of this mode's oscillating nature, the predominantly positive lines are the same as the predominantly negative lines a half-cycle previous (with signs reversed). For this reason, we illustrate the two families at the same moment in time, the moment when the horizon vorticity reaches a maximum with blue (dark gray) near the poles and red (light gray) near the equator.

One striking feature of Figure 9.22 is a set of isolated points where six lines meet, three from each family (three in each panel). These are nodes (zeros) of the frame-drag field, as one can see from the fact that the coloring there is white. These are also points where, dynamically, the field

lines can reconnect, changing their topologies.

Let us focus on the near-horizon, predominantly negative vortex lines (dashed lines) in the left panel of Figure 9.22. The lines that emerge from the counterclockwise horizon vortex in the equatorial region loop over the north or south pole of the black hole, and reconnect to the opposite side of that horizon vortex. We think that, as the mode oscillates, these lines will merge at the equator then slide off the horizon and form closed loops surrounding the hole, of the sort that we see in the outer parts of the lenticular blue (dark gray) region of the center panel, and these will then expand and deform and reconnect to form the set of wrap-around-deformed-torus lines of the left panel, which lie in the outer part of the transition zone and are becoming outgoing gravitational waves.

Next focus on the near-horizon, predominantly positive vortex lines (solid lines) in the middle panel of Figure 9.22. The lines, that emerge from the clockwise horizon vortex in the north polar region, swing around the equator and descend into the south polar horizon vortex. We think that, as the oscillation proceeds, these lines will slide off the horizon and immediately form closed loops that wrap around deformed tori, which expand to become like those near the left and right edges of the left panel (outer part of transition zone), and then continue their expansion, becoming the gravitational-wave wrap-around-torus lines whose inner parts are at the left and right edges of the right panel.

Notice, in the middle panel near the equator, two regions of weakly negative (pink [light gray]) vorticity, and their near-zone lines that appear to have just disconnected from the horizon but are mostly radially directed. And notice similarly the pink regions near the left and right edges of this panel, again with vortex lines that are traveling roughly radially. These pink regions are actually toroidal, because of the rotation symmetry around the vertical axis. In the outer transition zone and the wave zone, they are the regions in which this family's wrap-around-torus, gravitational-wave vortex lines are crossing over from one clockwise vortex (wave crest) to another. This feature of crossover lines with weakly reversed vorticity appears to be a robust feature of oscillatory modes. For other examples, see the weakly blue regions in the left panel, and see the superposed (2,2) and (2,-2) mode in Figure 9.16, where the dashed vortex lines, with predominantly counterclockwise (red [light gray]) vorticity, become weakly blue (darker gray) in the crossover regions.

The right panel of Fig 9.22 shows the vorticity of the axial lines (constant  $r, \theta$  circles) in both near zone and wave zone. Near the horizon, these lines are largely part of the transverse, isotropic piece of the longitudinal field  $\delta\mathcal{B}^L$ ; they have opposite color to the horizon vortexes at the horizon, as they must, in order to keep  $\delta\mathcal{B}^L$  trace-free. Near the horizon, these lines also contain a smaller component of the ingoing-wave transverse-traceless field  $\delta\mathcal{B}^{TT}$ . In the wave zone, they are fully outgoing-wave  $\delta\mathcal{B}^{TT}$ .

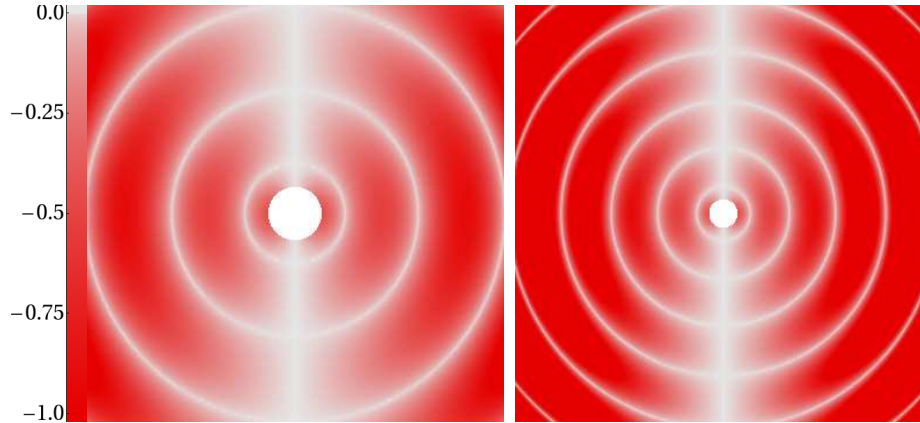


Figure 9.23: For the (2,0) electric-parity mode of Schwarzschild in RWZ gauge: the vorticity of the counterclockwise vortex lines that pass through the plane  $\mathcal{S}_\phi$  of constant  $\phi$ . The color intensity (scale on left) is scaled as in Figure 9.16. *Left panel:* 30M across, showing the near and intermediate zones and beginning of the wave zone. *Right panel:* 56M across.

#### 9.5.4 Vortex Lines of (2,0) Electric-Parity Mode and Perturbative Tendex Lines of (2,0) Magnetic-Parity Mode

For the (2,0) electric-parity mode of Schwarzschild in RWZ gauge, the only nonzero components of the frame-drag field are  $\delta\mathcal{B}_{\hat{r}\hat{\phi}}$  and  $\delta\mathcal{B}_{\hat{\theta}\hat{\phi}}$ . Near the horizon, where decomposition into longitudinal, longitudinal-transverse, and transverse-traceless parts is meaningful,  $\delta\mathcal{B}^L$  vanishes (and hence the horizon vorticity vanishes),  $\delta\mathcal{B}_{\hat{r}\hat{\phi}}$  is the sole component of  $\delta\mathcal{B}^{LT}$ , and  $\delta\mathcal{B}_{\hat{\theta}\hat{\phi}}$  is the sole component of  $\delta\mathcal{B}^{TT}$ .

By (near) duality, the same is true for the (2,0) magnetic-parity mode of the last subsection, with  $\delta\mathcal{B}$  replaced by  $\delta\mathcal{E}$ .

Because the only nonzero components are  $\delta\mathcal{B}_{\hat{r}\hat{\phi}}$  and  $\delta\mathcal{B}_{\hat{\theta}\hat{\phi}}$  and because of the axisymmetry, there is a family of zero-vorticity vortex lines which lie in a plane  $\mathcal{S}_\phi$  of constant  $\phi$ , and the other two sets of vortex lines have equal and opposite vorticity and pass through  $\mathcal{S}_\phi$  at 45 degree angles. In Figure 9.23, we show in  $\mathcal{S}_\phi$  the vorticity of the counterclockwise lines that pass through it. A plot for the clockwise lines would be identical, but with blue changed into red.

Notice the remarkable absence of structure in the near zone. All we see is toroidal vortexes separated by circular null surfaces and a polar null line. (Recall the axisymmetry around the vertical polar axis). The absence of structure is presumably due to the fact that this mode is sourced by the longitudinal perturbative tendex field, and not by this frame-drag field (though its longitudinal-transverse part plays a key role of periodically storing near-zone energy during the oscillations; cf. the discussion of the dual mode below). The vorticity vanishes along the polar axis because of axisymmetry and the fact that the radial-radial part of the frame-drag field vanishes.

For greater insight into this frame-drag field, we show in the left panel of Figure 9.24 several of

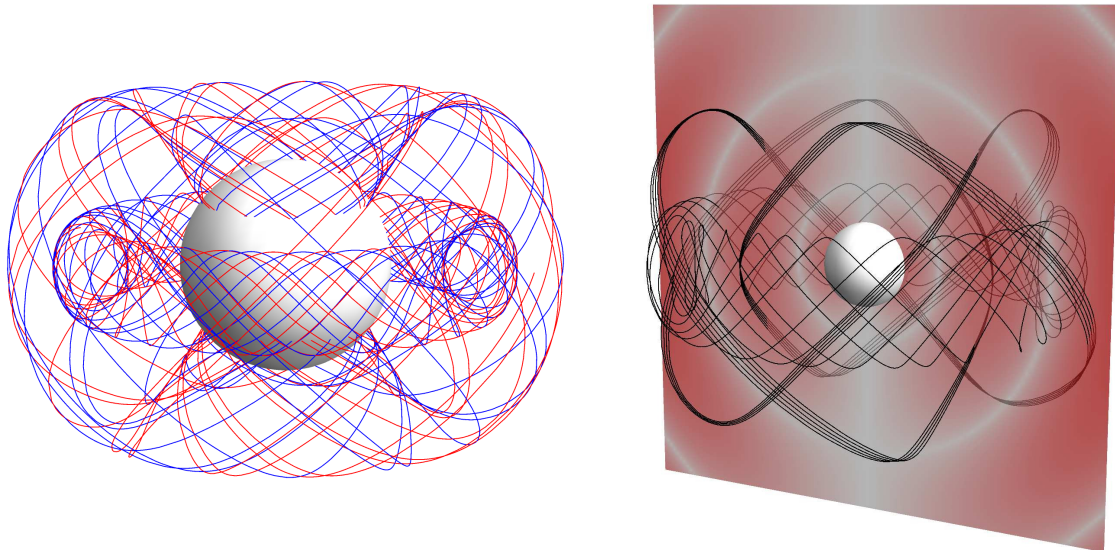


Figure 9.24: Vortex lines for the  $(2,0)$  electric-parity mode of Schwarzschild in RWZ gauge. *Left panel:* Two vortex lines of each sign in the near zone and innermost part of transition zone. The positive (blue lines) and negative (red) lines are identical but wind their tori in opposite directions. *Right panel:* Two counterclockwise vortex lines in the transition zone, with the vorticity shown in a semitransparent slice  $\mathcal{S}_\phi$  of constant  $\phi$  as a density plot. The vortex lines are plotted in black rather than red in this panel to aid the eye.

its three-dimensional vortex lines in the near zone and innermost part of the transition zone. These vortex lines wind densely around axisymmetric deformed tori.

Note that the large torus is attached to the horizon. Its vortex lines intersect the horizon at the approximately  $45^\circ$  angles characteristic of the longitudinal-transverse part of the field, which is these lines' dominant component.

For the dual, magnetic-parity  $(2,0)$  mode, this torus depicts the perturbative tendex lines of the near zone, and those lines predominantly belong to the longitudinal-transverse part of the tidal field,  $\delta\mathcal{E}^{\text{LT}}$ . This is the part that stores the mode's near-zone oscillation energy when  $\delta\mathcal{B}^{\text{L}}$  is passing through zero and its perturbative vortex lines are detached from the horizon (see the discussion of this mode's dynamics in Section 9.1.3.8). Immediately after this snapshot, these tendex lines'  $\delta\mathcal{E}^{\text{LT}}$  begin to regenerate the near-horizon longitudinal frame-drag field  $\delta\mathcal{B}^{\text{L}}$  and its horizon vorticity. As it does so, these tendex lines and their torus (presumably) detach from the horizon and expand outward into the transition then wave zone, becoming the tendex-line component of a gravitational-wave torus like those displayed in Figure 9.7 above.

The small torus in the left panel of Figure 9.24 encircles the equatorial point on the innermost node of the field (innermost white circle in Figure 9.23). It is also the innermost torus shown in Figure 9.7 above.

In the right-hand panel of Figure 9.24, for the  $(2,0)$  electric-parity mode we show two counter-

clockwise vortex lines in the transition zone. By chance, the larger of the selected lines nearly forms closed orbits, and so even after wrapping its torus four times it appears as a thin ribbon. While it is difficult to tell with this nearly closed line, extended integration reveals that it does wrap a (deformed) torus.

Notice that both lines (both tori) in the right panel straddle the second null of the frame-drag field (second-from-center white circle in Figure 9.23).

## 9.6 Conclusions

Although the theory of black-hole quasinormal modes is roughly half a century old, most past studies of them have focused on their mathematical properties, their eigenfrequencies and emitted gravitational waves, and their excitation by various physical processes. Aside from a geometric-optics interpretation of high-frequency modes (see, e.g., [22–24]), little was known, before this paper, about their geometrodynamical properties—e.g., the structure and dynamics of their spacetime curvature in the near zone and transition zone, and how the near-zone curvature generates gravitational waves.

In this paper we have used our new vortex and tendex tools to explore, in depth, the geometrodynamics of the quadrupolar modes for Schwarzschild and Kerr black holes. Most importantly, we have discovered that:

(i) There is a near duality between electric-parity modes and magnetic-parity modes, in which tendexes get mapped into vortexes and vortexes into tendexes.

(ii) The electric-parity  $(l, m) = (2, 2)$  and  $(2, 1)$  modes are generated by near-zone, longitudinal vortexes that extend out of the horizon and rotate (four tendexes for  $m = 2$ ; two for  $m = 1$ ). The vortexes' rotation generates outgoing and ingoing gravitational waves; the ingoing waves act back on the longitudinal vortexes, gradually pushing them off the horizon, which results in the mode's exponential attenuation.

(iv) By (near) duality, the electric-parity  $(2, 2)$  and  $(2, 1)$  modes are generated and attenuated in the same way, but with near-zone, longitudinal tendexes rather than vortexes playing the central role.

(v) The magnetic-parity  $(2, 0)$  mode and superposed  $(2, 2)$  &  $(2, -2)$  mode are generated by near-zone, longitudinal vortexes that extend out of the horizon and oscillate between clockwise and counterclockwise vorticity. In these oscillations, energy is fed back and forth between the longitudinal vortexes and longitudinal-transverse, near-zone tendexes that do not penetrate the horizon. In each oscillation, as the horizon vorticity passes through zero, the longitudinal vortex lines slide off the horizon and reconnect to form toroidal vortexes that travel outward, becoming gravitational waves; and the near-zone tendexes then regenerate the longitudinal vortexes (with reversed vorticity), thereby triggering the next half cycle of oscillation.

(vi) The electric-parity (2,0) mode and superposed (2,2) & (2,-2) mode exhibit these same geometrodynamics, but with the roles of the vortexes and tendexes reversed.

In future papers, these quasinormal-mode insights will be a foundation as we explore the geometrodynamics of merging binary black holes using numerical simulations.

While all analytic approximations fail near the time of merger, black-hole perturbation theory does approximate a binary-black-hole spacetime well in some epochs: the merged hole during its ringdown, each tidally deformed hole during inspiral, and each perturbed hole during the initial relaxation that causes spurious “junk” gravitational radiation. Before exploring the fully nonlinear vortex and tendex structures in simulations, we are likely first to compare numerical vortex and tendex structures during these epochs with the corresponding perturbative results (as in Figure 9.15). Such comparisons will allow us to determine to what degree the insights we have gained from our perturbative studies can also be applied to numerical simulations—particularly the relative insensitivity of vortexes and tendexes to changes in gauge and slicing.

Building on these comparisons, our future work will then include initial explorations of the fully nonlinear geometrodynamics of the warped spacetimes present in binary-black-hole simulations. For example, Kamaretsos, Hannam, and Sathyaprakash [25] have recently observed relationships between the properties (masses and spins) of the initial holes in a binary-black-hole merger and the particular quasinormal modes that are excited in the remnant (modes which generate the ringdown portion of the gravitational waves). By examining the vortex and tendex structures of a variety of binary-black-hole mergers, we hope to gain insight into the origin of such relationships. Also, following Dennison and Baumgarte’s recent exploration [7] of the vortex and tendex structures in approximate, perturbative initial data, we intend to explore the vortex and tendex structures of constraint-satisfying binary-black-hole initial data, which could give insight into the initial perturbations (and the corresponding spurious “junk” gravitational radiation) that appear in all currently used, binary-black-hole initial-data schemes.

Ultimately, we plan to use vortexes and tendexes to explore the geometrodynamics of binary-black-hole spacetimes throughout the entire simulated inspiral, merger, and ringdown. We expect that these tools will provide insights into the behavior of these spacetimes and perhaps also motivate new ways of constructing phenomenological waveform templates for use in gravitational-wave data analysis.

## Acknowledgments

We thank John Belcher, Jeandrew Brink, and Richard Price for helpful discussions. We thank Jeff Kaplan for helpful discussions and web assistance. We thank Mark Scheel for helpful discussions and for version control assistance. A.Z. would also like to thank the National Institute for Theoretical

Physics of South Africa for hosting him during a portion of this work. Some calculations in this paper were performed using the Spectral Einstein Code (SpEC) [26]. This research was supported by NSF grants PHY-0960291, PHY-1068881 and CAREER grant PHY-0956189 at Caltech, by NSF grants PHY-0969111 and PHY-1005426 at Cornell, by NASA grant NNX09AF97G at Caltech, by NASA grant NNX09AF96G at Cornell, and by the Sherman Fairchild Foundation at Caltech and Cornell, the Brinson Foundation at Caltech, and the David and Barbara Groce fund at Caltech.

## 9.A Quasinormal Modes of a Schwarzschild Black Hole in Regge-Wheeler Gauge

In this appendix, we review the Regge-Wheeler-Zerilli (RWZ) formalism for black-hole perturbations, and we discuss the calculations that underlie the results reported in Sections 9.3, 9.4, and 9.5 for quadrupolar perturbations of non-spinning black holes in the RWZ gauge.

### 9.A.1 Regge-Wheeler-Zerilli Formalism

Here we review the equations governing quasinormal modes for a non-rotating black hole in the Regge-Wheeler-Zerilli gauge [27, 28].<sup>4</sup> We write the metric in Schwarzschild coordinates with a small perturbation  $h_{\mu\nu}$ ,

$$ds^2 = -\alpha^2 dt^2 + \frac{dr^2}{\alpha^2} + r^2(d\theta^2 + \sin^2\theta d\phi^2) + h_{\mu\nu} dx^\mu dx^\nu, \quad \alpha^2 = 1 - 2M/r. \quad (9.29)$$

The components of  $h_{\mu\nu}$  obey separable differential equations, and importantly  $h_{\mu\nu}$  can be split into definite-parity perturbations (electric and magnetic) which do not couple to each other.

For magnetic-parity perturbations, the only nonzero components of  $h_{\mu\nu}$  in Regge-Wheeler gauge are

$$h_{tA} = h_0(r)e^{-i\omega t} X_A^{lm}(\theta, \phi), \quad h_{rA} = h_1(r)e^{-i\omega t} X_A^{lm}(\theta, \phi). \quad (9.30)$$

Here  $\omega$  is the mode's complex QNM eigenfrequency, and  $X_A^{lm}$  is the magnetic-parity vector spherical harmonic on the unit two-sphere,

$$X_\theta^{lm} = -\csc\theta Y^{lm}_{,\phi}, \quad X_\phi^{lm} = \sin\theta Y^{lm}_{,\theta}, \quad (9.31)$$

with  $Y^{lm}(\theta, \phi)$  denoting the scalar spherical harmonics. Regge and Wheeler [27, 29] showed that the radial parts of the metric perturbation,  $h_0(r)$  and  $h_1(r)$ , can be expressed in terms of a single

---

<sup>4</sup>There are many errors in the original paper of Regge and Wheeler [27], most of which were corrected by Edelman and Vishveshwara [29]. We use the corrected equations without further comment.

scalar radial eigenfunction  $Q(r)$  as

$$h_0 = -\frac{\alpha^2}{i\omega}(rQ)_{,r}, \quad h_1 = \frac{rQ}{\alpha^2}, \quad (9.32)$$

which satisfies the eigenequation

$$Q_{,r_*r_*} + \omega^2 Q = \mathcal{V}_Q(r)Q, \quad \mathcal{V}_Q(r) = \alpha^2 \left( \frac{l(l+1)}{r^2} - \frac{6M}{r^3} \right). \quad (9.33)$$

Here  $r_*$  is the tortoise coordinate

$$dr_* = \frac{dr}{\alpha^2}, \quad r_* = r + 2M \ln(\alpha^2 r/2M), \quad (9.34)$$

which goes to  $+\infty$  far from the hole and  $-\infty$  at the hole's horizon. This eigenequation must be solved subject to the boundary conditions of outgoing waves at infinity,  $Q \sim e^{i\omega r_*}$  as  $r_* \rightarrow +\infty$ , and ingoing waves at the horizon,  $Q \sim e^{-i\omega r_*}$  as  $r_* \rightarrow -\infty$ .

For electric-parity modes, the nonzero components of  $h_{\mu\nu}$  in RWZ gauge are [28]

$$\begin{aligned} h_{tt} &= \alpha^2 H_0(r) e^{-i\omega t} Y^{lm}, & h_{rr} &= \frac{H_0(r)}{\alpha^2} e^{-i\omega t} Y^{lm}, \\ h_{tr} &= H_1(r) e^{-i\omega t} Y^{lm}, & h_{AB} &= r^2 \Omega_{AB} K(r) e^{-i\omega t} Y^{lm}. \end{aligned} \quad (9.35)$$

Here  $\Omega_{AB}$  denotes the metric on the unit 2-sphere. We can write the metric perturbation functions in terms of the Zerilli function  $Z(r)$  as<sup>5</sup>

$$\begin{aligned} K &= \left[ \frac{\lambda(\lambda+1)r^2 + 3\lambda Mr + 6M^2}{r^2(\lambda r + 3M)} \right] Z + \alpha Z_{,r}, \\ H_1 &= -i\omega \left[ \frac{\lambda r^2 - 3\lambda Mr - 3M^2}{(r-2M)(\lambda r + 3M)} \right] Z - i\omega r Z_{,r}, \\ H_0 &= \left[ \frac{\lambda r(r-2M) - \omega^2 r^4 + M(r-3M)}{(r-2M)(\lambda r + 3M)} \right] K + \left[ \frac{(\lambda+1)M - \omega^2 r^3}{i\omega r(\lambda r + 3M)} \right] H_1. \end{aligned} \quad (9.36)$$

Here we have used Zerilli's notation

$$\lambda = \frac{1}{2}(l-1)(l+2). \quad (9.37)$$

The Zerilli function satisfies the eigenequation

$$Z_{,r_*r_*} + \omega^2 Z = \mathcal{V}_z(r)Z, \quad (9.38)$$

---

<sup>5</sup>In  $H_1$  we have corrected a term in the numerator of the fraction: the last term,  $-3M^2$ , was incorrectly written as  $-3M$  by Zerilli, an error that should be obvious on dimensional grounds.

where

$$\mathcal{V}_z(r) = \alpha^2 \left[ \frac{2\lambda^2(\lambda+1)r^3 + 6\lambda^2Mr^2 + 18\lambda M^2r + 18M^3}{r^3(\lambda r + 3M)^2} \right]. \quad (9.39)$$

The slices of constant Schwarzschild time  $t$  do not intersect the black hole's horizon, so in performing our 3+1 split, we use slices of constant Eddington-Finkelstein time  $\tilde{t} = t + 2M \ln(r/2M - 1)$ . Written in Schwarzschild coordinates, the perturbed tetrad for the EF observers is given by Eqs. (9.8) and (9.11). For any chosen mode, we compute the frame-drag and tidal fields by (i) computing, from the metric-perturbation components  $h_{\mu\nu}$ , the perturbation  $\delta R_{\alpha\beta\gamma\delta}$  to the Riemann tensor (same as Weyl) in Schwarzschild coordinates; (ii) projecting the total Riemann tensor  $R_{\alpha\beta\gamma\delta} = R_{\alpha\beta\gamma\delta}^{(0)} + \delta R_{\alpha\beta\gamma\delta}$  (where  $R_{\alpha\beta\gamma\delta}^{(0)}$  is the unperturbed Riemann tensor) onto the perturbed EF tetrad; (iii) reading off  $\mathcal{E}_{\hat{a}\hat{b}} = R_{\hat{a}\hat{0}\hat{b}\hat{0}}$  and  $\mathcal{B}_{\hat{a}\hat{b}} = \frac{1}{2}\epsilon_{\hat{a}\hat{p}\hat{q}}R_{\hat{p}\hat{q}\hat{0}\hat{b}}$  and splitting them into their unperturbed and perturbed parts.

### 9.A.2 Magnetic-Parity $(2, m)$ Mode: Frame-Drag Field

We first focus on the  $(2, m)$  quadrupolar modes for magnetic-parity perturbations. Carrying out the above computation, expressing the answer for the frame-drag field in terms of the Regge-Wheeler function  $Q(r)$  and the electric-parity scalar, vector, and tensor harmonics (see discussion in Appendix 9.C.3), and simplifying using Eq. (9.33), we obtain:

$$\mathcal{B}_{\hat{r}\hat{r}}^{(1)} = \Re [B_{1(m)} e^{-i\omega t} Y^{2m}] , \quad (9.40a)$$

$$\mathcal{B}_{\hat{r}\hat{A}}^{(1)} = \Re [B_{2(m)} e^{-i\omega t} Y_A^{2m}] , \quad (9.40b)$$

$$\mathcal{B}_{\hat{A}\hat{B}}^{(1)} = \Re \left[ \left( -\frac{1}{2} B_{1(m)} \delta_{\hat{A}\hat{B}} Y^{2m} + B_{3(m)} Y_{\hat{A}\hat{B}}^{2m} \right) e^{-i\omega t} \right] , \quad (9.40c)$$

$$B_{1(m)}(r) = -\frac{12Q}{i\omega r^3} , \quad (9.40d)$$

$$B_{2(m)}(r) = -\frac{4iM\omega Q + 2\alpha^2 r Q'}{i\omega r^3 \alpha^2 \sqrt{1 + 2M/r}} , \quad (9.40e)$$

$$B_{3(m)}(r) = -\frac{1}{i\omega r^5 \alpha^4 (r + 2M)} \left( [3\alpha^2(r - M)(r^2 + 4M^2) + 4iM\omega r^2(r - 3M) - r^3\omega^2(r^2 + 4M^2)] Q + r\alpha^2 [(r - 3M)(r^2 + 4M^2) + 4iM\omega r^3] Q' \right) , \quad (9.40f)$$

where a prime denotes a derivative with respect to  $r$ ,  $Y_A^{lm}$  and  $Y_{AB}^{lm}$  are given by Eqs. (9.83), and  $\delta_{\hat{A}\hat{B}}$  is the Kronecker delta.

We have solved the Regge-Wheeler equation (9.33) numerically for the most slowly damped, quadrupolar normal mode. When the numerical solution is inserted into the above expressions for

$\mathcal{B}_{\hat{a}\hat{b}}^{(1)}$ , numerical errors cause problems with delicate cancellations in the transverse-traceless and radial-transverse components near the horizon. To deal with this, we have derived the following asymptotic formula for  $Q(r)$  near the horizon,  $r_*/M \ll -1$ :

$$Q = Y^{-2iM\omega} \left[ 1 + \frac{3Y}{(1-4iM\omega)e} + \frac{9iM\omega Y^2}{(1-4iM\omega)(1-2iM\omega)e^2} - \frac{3(1+12iM\omega+40M^2\omega^2)Y^3}{2(1-4iM\omega)(1-2Mi\omega)(3-4iM\omega)e^3} + O(Y^4) \right] \quad (9.41)$$

where  $Y = e^{r_*/2M}$ . Inserting this into Eqs. (9.40), we find, of course, that all components of  $\mathcal{B}_{\hat{a}\hat{b}}$  are finite at the horizon.

Using Eqs. (9.40) for the frame-drag field, our analytic formula (9.41) for  $Q(r)$  near the horizon, and our numerical solution for  $Q(r)$  at larger radii, and the (2,2) harmonics, we compute the vortex lines and their vorticities for the fundamental (2,2) quasinormal mode. We illustrate them in Figures 9.2, 9.3, 9.4 and 9.10.

For our superposition of the (2,2) and (2,-2) modes we can simply sum the (2,2) and (2,-2) harmonics in the above expressions. We plot the vortex lines for the resulting frame-drag field in Figures 9.8, 9.16, and the top row of Figure 9.18. We use the (2,1) harmonics for generating the vortexes of the magnetic-parity, (2,1) perturbations that are illustrated in Figure 9.19. Finally, we use the (2,0) harmonics to produce the vortexes and vortex lines of the (2,0) magnetic-parity perturbation. We note that  $Y_{\hat{\phi}}^{20} = Y_{\hat{\theta}\hat{\phi}}^{20} = 0$  for this mode. This means that  $\mathcal{B}_{\hat{a}\hat{b}}^{(1)}$  is block-diagonal, and the vortex lines split into a pair of lines which remains in a slice of constant  $\phi$  and a single, axial line that runs in circles of constant  $(r, \theta)$ . In a slice of constant  $\phi$ , we illustrate the two sets of vortex lines in the slice and their vorticity together in Figure 9.6 and separately in the left and middle panels of Figure 9.22. We also plot the vorticity of the axial lines in a slice in the right panel of Figure 9.22.

### 9.A.3 Electric-Parity (2, $m$ ) Modes: Frame-Drag Field

Carrying out the calculation described at the end of Section 9.A.1 using the electric-parity metric perturbation (9.35), expressing the result in terms of the Zerilli function  $Z$  with the aid of Eqs. (9.36), and simplifying using Zerilli's differential equation (9.38), we obtain for the frame-drag field of a (2,  $m$ ) electric-parity perturbation

$$\mathcal{B}_{\hat{r}\hat{r}}^{(1)} = 0, \quad (9.42a)$$

$$\mathcal{B}_{\hat{r}\hat{A}}^{(1)} = \Re [B_{1(e)} e^{-i\omega t} X_{\hat{A}}^{2m}], \quad (9.42b)$$

$$\mathcal{B}_{\hat{A}\hat{B}}^{(1)} = \Re [B_{2(e)} e^{-i\omega t} X_{\hat{A}\hat{B}}^{2m}], \quad (9.42c)$$

where

$$B_{1(e)} = \frac{[6M^2\alpha^2 - i\omega r^2(2r + 3M)] Z - 2Mr\alpha^2(2r + 3M)Z'}{2r^5\alpha^2\sqrt{1 + 2M/r}}, \quad (9.42d)$$

$$B_{2(e)} = \frac{1}{2r^4\alpha^4(2r + 3M)(r + 2M)} \left( [-12M\alpha^2(M^2 + 4r\beta_1) - i\omega(r^2 + 4M^2)\beta_2 + 4M\omega^2r^3(2r + 3M)] Z - r\alpha^2 [4M\beta_2 + i\omega r(2r + 3M)(r^2 + 4M^2)] Z' \right). \quad (9.42e)$$

Here a prime denotes a derivative with respect to  $r$ , and  $X_A^{lm}$  and  $X_{AB}^{lm}$  are the magnetic-parity vector and tensor spherical harmonics given by Eqs. (9.86) (see discussion in Appendix 9.C.3). We have defined here for convenience the functions

$$\beta_1 = \frac{r^2 + Mr + M^2}{2r + 3M}, \quad \beta_2 = (2r^2 - 6Mr - 3M^2). \quad (9.42f)$$

We note again that the horizon vorticity,  $\mathcal{B}_{NN}^{(1)}$ , vanishes. With this  $\mathcal{B}_{\hat{a}\hat{b}}^{(1)}$  we can again compute the eigenvector fields and eigenvalues for the perturbed spacetime, and from them compute the vortex lines. We use these expressions to calculate the vortex lines and their vorticities generated by electric-parity perturbations. In order to compute the vortex lines for these modes, once again we expand  $Z$  around the horizon in terms of  $Y = e^{r^*/2M}$  up to  $O(Y^3)$ . We use this series to match to a numerical solution of the Zerilli equation subject to ingoing-wave boundary conditions. Because the Zerilli potential  $\mathcal{V}_z$  is more complicated than the Regge-Wheeler potential  $\mathcal{V}_Q$ , the coefficients of the expansion of  $Z$  in powers of  $Y$  are lengthy, but easily computed using algebraic computing software such as Mathematica. For this reason, we do not give the coefficients here.

For an electric-parity  $(2, 2)$  perturbation, the only set of vortex lines that are confined to the equatorial plane have vanishing vorticity (and are of less physical interest). Instead, we used the above frame-drag field to compute, and then plot in Figure 9.13, the vorticity of one of the sets of vortex lines that pass through the equatorial plane at a 45 degree angle: the set with negative vorticity. Just as with the magnetic-parity modes, we superpose a  $(2, 2)$  perturbation with a  $(2, -2)$  perturbation by a simple sum of the harmonics. The vorticity of these lines passing through the equatorial plane (the analog of Figure 9.13) is plotted in Figure 9.17.

For the vortex lines of the  $(2, 1)$  mode, there is a reflection symmetry about the equatorial plane, which implies that there are two sets of vortex lines confined to the plane, with a third normal to it. We illustrate the vortex lines and 3D vortexes of this mode in Figure 9.20. Finally, when we use the  $(2, 0)$  harmonics, we note that  $X_{\hat{\theta}}^{20} = X_{\hat{\theta}\hat{\theta}}^{20} = X_{\hat{\phi}\hat{\phi}}^{20} = 0$ . While this means that the frame drag field is simple, it is not block-diagonal and its nonzero vortex lines pass through all three dimensions. There is a single set of axial vortex lines with zero vorticity, and two sets with equal and opposite

vorticity that wind around deformed tori. We illustrate the vorticity in a slice of constant  $\phi$  for the negative lines in Figure 9.23. In addition, we illustrate some 3D vortex lines in Figures 9.7 and 9.24.

#### 9.A.4 Electric-Parity (2, 2) Mode: Tidal Field

To help understand the slicing dependence of our results, we compare fields generated by electric-parity perturbations, because the slicings are identical for all magnetic-parity perturbations. In particular, we focused on the perturbed tidal field for the electric-parity, (2, 2) mode. Carrying out the calculation of this mode as above when using the electric-parity metric perturbation (9.35), we obtain

$$\mathcal{E}_{\hat{r}\hat{r}}^{(1)} = \Re [E_{1(e)} e^{-i\omega t} Y^{22}] \quad (9.43a)$$

$$\mathcal{E}_{\hat{r}\hat{A}}^{(1)} = \Re [E_{2(e)} e^{-i\omega t} Y_{\hat{A}}^{22}] , \quad (9.43b)$$

$$\mathcal{E}_{\hat{A}\hat{B}}^{(1)} = \Re \left[ \left( -\frac{1}{2} E_{1(e)} \delta_{\hat{A}\hat{B}} Y^{22} + E_{3(e)} Y_{\hat{A}\hat{B}}^{22} \right) e^{-i\omega t} \right] , \quad (9.43c)$$

$$E_{1(e)}(r) = -\frac{3\mathcal{Z}}{2r^3} , \quad (9.43d)$$

$$E_{2(e)}(r) = \frac{[3M\alpha^2 - 2iM\omega(2r + 3M)] Z - \alpha^2 r(2r + 3M)Z'}{2r^4 \alpha^2 \sqrt{1 + 2M/r}} , \quad (9.43e)$$

$$E_{3(e)}(r) = \frac{1}{2r^4 \alpha^4 (r + 2M)} \left( \left[ -\frac{3\alpha^2(3M^3 + 6M^2r + 4Mr^2 + 4r^3)(4M + r\alpha^2)}{(2r + 3M)^2} + \frac{4iM\omega r(3M^2 + 6Mr - 2r^2)}{(2r + 3M)} + \omega^2 r^3(4M + r\alpha^4) \right] Z + \alpha^2 r \left[ \frac{(3M^2 + 6Mr - 2r^2)(4M + r\alpha^2)}{2r + 3M} - 4iM\omega r^2 \right] Z' \right) , \quad (9.43f)$$

where  $\mathcal{Z}$  is a function which obeys the same Regge-Wheeler equation (9.33) as  $Q$  and can be built from the Zerilli function  $Z$  as, (see, e.g., Ch. 4, Eq. (156) of [30])

$$\mathcal{Z} = \left[ \frac{\lambda^2(\lambda + 1)}{3M} + \frac{3M\alpha^2}{r(\lambda r + 3M)} \right] Z - \frac{Z_{,r_*}}{\lambda} , \quad (9.44)$$

for integers  $l \geq 2$ . This implies there is an exact duality between  $\mathcal{E}_{\hat{r}\hat{r}}$  for electric-parity perturbations and  $\mathcal{B}_{\hat{r}\hat{r}}$  magnetic-parity perturbations [in fact for any  $(l, m)$  mode] in RWZ gauge. This follows from the facts that these radial-radial components have the same time, radial, and angular dependence (but not necessarily the same amplitude and phase). However, we can fix the relative normalization of the Regge-Wheeler function  $Q$  and Zerilli function  $Z$  such that  $Q = -\omega\mathcal{Z}/8$ , in which case we

have for Eqs. (9.40d) and (9.43a)

$$B_{1(m)}(r) = iE_{1(e)}(r). \quad (9.45)$$

Substituting  $\mathcal{Z}$  into Eqs. (9.43b)—(9.43c) does not illustrate the near-duality of the other components of  $\mathcal{E}^{(1)}$  and  $\mathcal{B}^{(1)}$  in an obvious manner, so we leave these equations in terms of  $Z$ .

As we discuss in the next section, however, the exact duality of  $\mathcal{E}_{\hat{r}\hat{r}}^{(1)}$  and  $\mathcal{B}_{\hat{r}\hat{r}}^{(1)}$  does not immediately correspond to an exact duality of the horizon tendicity and vorticity. This happens because in RWZ gauge, the electric-parity perturbations deform the horizon, which changes the horizon tendicity.

For the electric-parity, (2, 2) perturbation, the tidal field is symmetric about the equatorial plane, and there are two sets of tendex lines that remain in the equatorial plane (just as the vortex lines of the (2, 2) magnetic-parity mode did). The tendex lines are illustrated in the left-hand panel of Figure 9.11.

### 9.A.5 Perturbed Horizon and Horizon Tendicity for Electric-Parity Modes

We discuss here the correction to the position of the horizon and its influence on the perturbed horizon tendicity for the electric-parity (2, 2) modes. First, we calculate the correction to the horizon position  $\delta r$  using the same procedure as that of Vega, Poisson, and Massey [18]. The horizon generators,  $\vec{l}$ , for the perturbed spacetime are given by

$$l^\mu = \frac{\partial x^\mu}{\partial \tilde{t}} = (1 + \delta\dot{t}, \delta\dot{r}, \delta\dot{\theta}, \delta\dot{\phi}), \quad (9.46)$$

where an overdot represents a derivative with respect to  $\tilde{t}$ . The functions  $\delta\theta$  and  $\delta\phi$  change the location of individual generators, but do not alter the shape of the surface defined by the instantaneous horizon. We will not treat them here, but they are described in [18]. By requiring that the generators remain null to first order in the perturbation, we find

$$\delta r - 4M\delta\dot{r} = 2Mh_{ll}. \quad (9.47)$$

For IR gauge,  $h_{ll} = 0$  and the only physical solution of Eq. (9.47) is  $\delta r = 0$ . Magnetic-parity RWZ perturbations also have  $h_{ll} = 0$ , and, therefore, the coordinate location of the horizon does not change in this gauge either. For electric-parity perturbations in RWZ gauge, we use the fact that  $h_{ll} = h_{\tilde{t}\tilde{t}}$  on the horizon to solve for the perturbation to the horizon's shape. For a general electric-parity perturbation of indexes  $(l, m)$ , Eqs. (9.35) allow us to write

$$\delta r = \Re \left[ \frac{e^{-2iM\omega}}{\kappa + i\omega} e^{-i\omega\tilde{t}} Y_{lm} \lim_{r \rightarrow 2M} \left( \frac{H_1 - H_0}{r - 2M} e^{i\omega r^*} \right) \right], \quad (9.48)$$

where  $\kappa = (4M)^{-1}$  is the horizon's unperturbed surface gravity. We evaluate these quantities on the horizon using the near-horizon expansion of the Zerilli function  $Z$ , and they are finite.

The perturbation to the position of the horizon corrects the perturbative horizon tendicity in two ways: First, the background horizon tendicity  $\mathcal{E}_{\hat{r}\hat{r}}^{(0)}$ , when evaluated at  $r = 2M + \delta r$ , becomes, through first order in  $\delta r$ ,

$$\mathcal{E}_{\hat{r}\hat{r}}^{(0)}(r = r_H) = -\frac{1}{4M^2} + \frac{3}{8M^3}\delta r. \quad (9.49)$$

Next, we recall that  $\vec{e}_{\hat{r}} = \vec{e}_{\hat{r}}^{(0)} + \vec{e}_{\hat{r}}^{(1)}$  is normal to surfaces of constant  $r$  through perturbative order. Now that the horizon's surface is deformed, however, the normal to the horizon  $\vec{N}$  is no longer precisely the same as  $\vec{e}_{\hat{r}}$ . It receives a correction such that

$$N^\mu = \frac{1}{N}\gamma^{\mu\nu}\nabla_\nu(r + \delta r) = e_{\hat{r}}^{(0)\mu} + e_{\hat{r}}^{(1)\mu} + \delta N^\mu - \left(\delta N_\nu e_{\hat{r}}^{(0)\nu}\right) e_{\hat{r}}^{(0)\mu}, \quad (9.50)$$

where  $N = N^{(0)} + N^{(1)}$  is a normalization factor and  $\delta N^\mu = (\gamma_{(0)}^{\mu\nu}\nabla_\nu\delta r)/N^{(0)}$  deforms  $\vec{N}$  away from  $\vec{e}_{\hat{r}}$ . Note that the leading-order normal remains  $\vec{N}^{(0)} = \vec{e}_{\hat{r}}^{(0)}$ . The deformation of the horizon normal produces additional modifications to the horizon tendicity,

$$\mathcal{E}_{NN} = \mathcal{E}_{\mu\nu}(2M + \delta r)N^\mu N^\nu = \mathcal{E}_{\hat{r}\hat{r}}^{(0)} + \mathcal{E}_{\hat{r}\hat{r}}^{(1)} + \frac{3}{8M^3}\delta r + 2\mathcal{E}_{\hat{r}\mu}^{(0)}\delta N^\mu - 2\mathcal{E}_{\hat{r}\hat{r}}^{(0)}\delta N_\nu e_{\hat{r}}^{(0)\nu}, \quad (9.51)$$

where, as usual,  $\mathcal{E}_{\hat{r}\hat{r}}^{(1)}$  includes the effects of both the perturbation to the tidal field and to  $\vec{e}_{\hat{r}}^{(1)}$  (and where all quantities are evaluated at the unperturbed horizon position  $r = 2M$ ). The new contributions [the last three terms on the right-hand side of Eq. (9.51)] come from the displacement of the position of the horizon  $\delta r$  and the deformation to the normal  $\delta\vec{N}$ .

In RWZ gauge, the  $(\tilde{t}, r)$  components of  $\delta\vec{N}$  vanish, although  $\delta\vec{N}$  does have angular components; this means that the deformation to the normal to the horizon  $\delta\vec{N}$  does not affect the horizon tendicity in RWZ gauge. [To show this, note first that when the deformation to the normal has no  $(\tilde{t}, r)$  components  $\delta N_\nu e_{\hat{r}}^{(0)\nu} = 0$ . Then observe that the (projected) spatial tidal field  $\mathcal{E}_{\alpha\beta}^{(0)}$  is diagonal and that  $\delta\vec{N}$  has only angular components; therefore, the term  $\mathcal{E}_{\hat{r}\mu}^{(0)}\delta N^\mu = 0$  and all terms involving  $\delta\vec{N}$  in Eq. (9.51) vanish as well.] Only the shifted coordinate location of the horizon, changes the horizon tendicity, and we find

$$\mathcal{E}_{NN}^{(1)} = \mathcal{E}_{\hat{r}\hat{r}}^{(1)} + \frac{3}{8M^3}\delta r. \quad (9.52)$$

From Eq. (9.48), we see that the angular distribution of  $\mathcal{E}_{NN}^{(1)}$  in RWZ gauge is the same as in IR gauge [it is  $Y^{22}(\theta, \phi)$ ].

With the angular dependence of the horizon tendicity well understood, let us focus on the ampli-

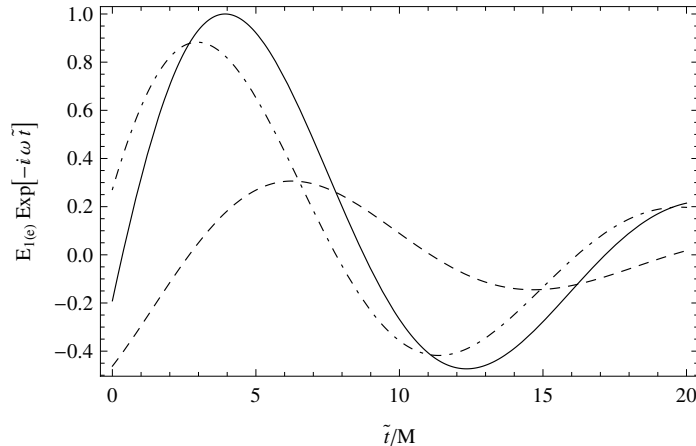


Figure 9.25: Plot illustrating the contributions to the amplitude  $E_{1(e)}e^{-i\omega\tilde{t}}$  [Eq. (9.53)] of the perturbed horizon tendicity  $\mathcal{E}_{NN}^{(1)}$ , in RWZ gauge for the electric-parity, (2,2) perturbation. Plotted against  $\tilde{t}$  are the amplitude contributions from  $\mathcal{E}_{\hat{r}\hat{r}}^{(1)}$  (dashed line), and from the perturbative shift of the horizon generators [dot-dashed line; see Eqs. (9.49) and (9.52)]. The time-dependent amplitude of the total perturbed horizon tendicity is the solid line.

tude and time dependence of the horizon tendicity. Using a notation analogous to that in Eq. (9.43a), we write the horizon tendicity in the form

$$\mathcal{E}_{NN}^{(1)} = E_{1(e)}(r = 2M)e^{-i\omega\tilde{t}}Y^{22}, \quad (9.53)$$

for some amplitude  $E_{1(e)}$  [we can do this because both terms in Eq. (9.52) have the same time dependence]. This amplitude has two contributions: one from the amplitude (and phase) of  $\mathcal{E}_{\hat{r}\hat{r}}^{(1)}$ , and the other from the correction to the radial perturbation of the generators [second term on the right hand side of Eq. (9.52)]. We plot these contributions to  $E_{1(e)}e^{-i\omega\tilde{t}}$  of Eq. (9.53) in Figure 9.25, as a function of  $\tilde{t}$  and normalized by the maximum of the (perturbed) horizon tendicity. We also plot the amplitude of total perturbation to the horizon tendicity,  $E_{1(e)}e^{-i\omega\tilde{t}}$  (the sum of the two contributions). The two contributions are of roughly the same magnitude, but are out of phase. The influence of the change in horizon position (dot-dashed line) is slightly larger than  $\mathcal{E}_{\hat{r}\hat{r}}^{(1)}$  (dashed line).

That  $\mathcal{E}_{NN}^{(1)}$  differs from  $\mathcal{E}_{\hat{r}\hat{r}}^{(1)}$  only by an amplitude and phase means that, in some sense, the duality between the horizon tendicity and vorticity (which is exact in IR gauge) is still intact; however, they are no longer related by the simple phase shift of  $i$ . In fact, we could choose a different normalization between the Regge-Wheeler function  $Q$  and the Zerilli function  $Z$  than we did in Appendix 9.A.4 to restore this duality relation, but this would only hold for the horizon tendicity and vorticity [and the duality in Eq. (9.45) would be more complicated, with a complex amplitude replacing the factor of  $i$ ].

### 9.A.6 Magnetic-Parity, Superposed (2, 2) and (2, -2) Modes: Tidal Field

In order to understand better the dynamics and interaction of the tendexes and vortexes, we compute the perturbations to the tidal field that must accompany the frame-drag field of a magnetic-parity perturbation for the superposed (2, 2) and (2, -2) modes. These tidal perturbations are much like the frame-drag perturbations of an electric-parity metric perturbation, as expected by the near-duality. Their odd parity ensures that they must be reflection antisymmetric about the equatorial plane. If we consider the tendex lines of  $\mathcal{E}^{(1)}$  alone, there must be a zero tendicity set of tendex lines in the plane, and two sets which pass through the plane at  $45^\circ$  with equal and opposite tendicity. We are also assured that  $\mathcal{E}_{NN}^{(1)} = 0$ . From the calculation described at the beginning of Section 9.A.1 above, we obtain:

$$\mathcal{E}_{\hat{r}\hat{r}}^{(1)} = 0, \quad (9.54a)$$

$$\mathcal{E}_{\hat{r}\hat{A}}^{(1)} = \Re \left[ E_{1(m)} e^{-i\omega t} \left( X_{\hat{A}}^{22} + X_{\hat{A}}^{2-2} \right) \right], \quad (9.54b)$$

$$\mathcal{E}_{\hat{A}\hat{B}}^{(1)} = \Re \left[ E_{2(m)} e^{-i\omega t} \left( X_{\hat{A}\hat{B}}^{22} + X_{\hat{A}\hat{B}}^{2-2} \right) \right], \quad (9.54c)$$

$$E_{1(m)} = \frac{2i\omega r Q + 4M\alpha^2 Q'}{i\omega r^3 \alpha^2 \sqrt{1 + 2M/r}}, \quad (9.54d)$$

$$E_{2(m)} = \frac{[6M\alpha^2(\alpha^2 + 1) + i\omega(r^2 - 3Mr - 2M^2 + 6M^2\alpha^2) - 4M\omega^2 r^2] Q}{i\omega r^4 \alpha^4 (1 + 2M/r)} + \frac{\alpha^2 [-12M^2 + 4r(M + iM^2\omega) + i\omega r^3] Q'}{i\omega r^4 \alpha^4 (1 + 2M/r)}. \quad (9.54e)$$

We illustrate the tendicity of the predominantly negative tendex lines in the equatorial plane in the time series of Figure 9.18 (bottom row), which shows the evolution over a half period of oscillation of the metric perturbation.

## 9.B Teukolsky's Equation and Black-Hole Perturbations in the Newman-Penrose Formalism

The results in this appendix appear in many places in the literature (see, for example, Teukolsky's paper [31]). We summarize them here because we will need them in Appendices 9.C and 9.E.

Teukolsky's equation relies on the Newman-Penrose (NP) formalism using Kinnersley's tetrad, which is the principal complex null tetrad in the Schwarzschild and Kerr spacetimes. For Kerr, in the Boyer-Lindquist coordinate basis  $\{\partial_t, \partial_r, \partial_\theta, \partial_\phi\}$  [Eq. (6.1) of Paper II], this tetrad's contravariant

components are given by

$$\begin{aligned}
l^\mu &= \frac{1}{\Delta}(r^2 + a^2, \Delta, 0, a), \\
n^\mu &= \frac{1}{2\Sigma}(r^2 + a^2, -\Delta, 0, a), \\
m^\mu &= \frac{1}{\sqrt{2}(r + ia \cos \theta)}(ia \sin \theta, 0, 1, i \csc \theta),
\end{aligned} \tag{9.55}$$

with the final leg given by  $\vec{m}^*$ , the complex conjugate of  $\vec{m}$ . Here

$$\Delta = r^2 + 2Mr + a^2, \quad \Sigma = r^2 + a^2 \cos^2 \theta. \tag{9.56}$$

When  $a$  is taken to zero, we recover the Kinnersley tetrad for Schwarzschild spacetime in the Schwarzschild coordinate basis [Eq. (4.1) of Paper II]. The Teukolsky equation also requires the NP spin coefficients, certain contractions of covariant derivatives of the tetrad above given by Eq. (4.1a) of [32] (though with the opposite signs because of differing metric-signature conventions). The nonzero spin coefficients in this tetrad are

$$\begin{aligned}
\rho &= -\frac{1}{r - ia \cos \theta}, & \pi &= \frac{ia}{\sqrt{2}}\rho^2 \sin \theta, \\
\beta &= -\frac{1}{2\sqrt{2}}\rho^* \cot \theta, & \alpha &= \pi - \beta^*, \\
\mu &= \frac{\rho^* \Delta}{2\Sigma}, & \gamma &= \mu + \frac{r - M}{2\Sigma}, \\
\tau &= -\frac{ia}{\sqrt{2}\Sigma} \sin \theta.
\end{aligned} \tag{9.57}$$

The Weyl scalars  $\Psi_0$  and  $\Psi_4$  are defined in terms of the Weyl tensor by  $\Psi_0 = C_{\mu\nu\rho\sigma}l^\mu m^\nu l^\rho m^\sigma$  and  $\Psi_4 = C_{\mu\nu\rho\sigma}n^\mu m^{*\nu} n^\rho m^{*\sigma}$ . These both vanish in the background when using the Kinnersley tetrad, and are gauge invariant at first order in the perturbation theory [31], consequently. At that perturbative order, they satisfy decoupled, linear, second-order partial-differential equations. Teukolsky's big breakthrough [31] was to show that, when those equations are re-expressed in terms of

$$\psi_2 \equiv \Psi_0 \quad \text{and} \quad \psi_{-2} \equiv \rho^{-4}\Psi_4, \tag{9.58}$$

they take on a unified form (the *Teukolsky equation*) that depends on the spin-weight  $s = +2$  for  $\psi_2$  and  $s = -2$  for  $\psi_{-2}$ , and that is separable; i.e., it has a solution of the form  $\psi_s^{lm\omega} = {}_sR_{lm\omega}(r){}_sS_{lm\omega}(\theta)e^{i(m\phi - \omega t)}$ . The Teukolsky equation implies for the radial function  ${}_sR_{lm\omega}$  the fol-

lowing ordinary differential equation (in vacuum)

$$0 = \Delta^{-s} \frac{d}{dr} \left( \Delta^{s+1} \frac{d {}_s R_{lm\omega}}{dr} \right) + \left( \frac{K^2 - 2is(r-M)K}{\Delta} + 4is\omega r + 2am\omega - a^2\omega^2 - {}_s A_{lm} \right) {}_s R_{lm\omega}, \quad (9.59)$$

where  ${}_s A_{lm}$  is a separation constant that is a function of  $a\omega$  [i.e.,  ${}_s A_{lm} = {}_s A_{lm}(a\omega)$ ], and  $K \equiv (r^2 + a^2)\omega - am$ . The radial function has the symmetries  ${}_s R_{lm\omega} = (-1)^m {}_s R_{l-m-\omega^*}$ . The angular function,  ${}_s S_{lm\omega}(\theta)$ , (called the spin-weighted spheroidal harmonic) satisfies the ordinary differential equation (in vacuum)

$$\begin{aligned} & \csc \theta \frac{d}{d\theta} \left( \sin \theta \frac{d {}_s S_{lm\omega}}{d\theta} \right) \\ & + (a^2\omega^2 \cos^2 \theta - m^2 \csc^2 \theta - 2a\omega s \cos \theta - 2ms \cot \theta \csc \theta - s^2 \cot^2 \theta + s + {}_s A_{lm}) {}_s S_{lm\omega} = 0. \end{aligned} \quad (9.60)$$

This angular function has the symmetries  ${}_s S_{lm\omega}(\pi - \theta) = (-1)^{(m+l)} {}_s S_{lm\omega}(\theta)$  and  ${}_s S_{lm\omega}^*(\theta) = (-1)^{m+s} {}_s S_{l-m-\omega^*}(\theta)$ , where we are using a phase convention such that the angular functions agree with the usual convention for spin-weighted spherical harmonics in the limit that spin parameter,  $a$ , goes to zero.

It is often useful, in working with the perturbation equations, to change variables from the separation constants  ${}_s A_{lm}$  to Chandrasekhar's [30]

$${}_s \lambda_{lm} \equiv {}_s A_{lm} + s + |s| - 2am\omega + a^2\omega^2, \quad (9.61)$$

which are the same for positive and negative spin weights,  $\pm s$ .

## 9.C The Chrzanowski-Cohen-Kegeles Procedure and the Ingoing-Radiation-Gauge Metric

In this appendix, we will review the formalism used for computing the ingoing-radiation-gauge (IR gauge) metric, using what is known as the Chrzanowski-Cohen-Kegeles (CCK) procedure. We will also connect the CCK procedure to Chrzanowski's original calculation of definite-parity harmonics, which we find useful for our calculations.

Although Chrzanowski conjectured that “the conceptual benefits of having found the perturbed Kerr metric potentials surpass the usefulness of these potentials for doing future computations” [33], the procedure he helped to formulate has found several applications in the past few years. Lousto and Whiting [34] revisited Chrzanowski's construction and found explicit expressions for computing the Hertz potential corresponding to specific perturbations of the Weyl curvature scalars  $\Psi_0$  and  $\Psi_4$  in

the Schwarzschild spacetime. Ori then derived a similar result for Kerr black holes, using a frequency-domain calculation [35]. Yunes and Gonzalez were the first to explicitly compute the metric of a perturbed Kerr black hole from the Hertz potential [36], and Keidl, Friedman, and Wiseman were the first to use the procedure to calculate the metric perturbation from a static point particle in the Schwarzschild spacetime [37]. More recently, Keidl, Shah, and their collaborators articulated a formalism for computing the gravitational self-force of a point particle in the Schwarzschild or Kerr spacetimes using the metric constructed from a Hertz potential [38]. They were then able to compute the conservative piece of the self-force from this metric perturbation in the Schwarzschild spacetime [39]. In the first article [38], they gave a concise summary of constructing metric perturbations from a Hertz potential, and they called this process the Chrzanowski-Cohen-Kegeles (CCK) procedure or formalism (names we will also adopt).

In the first part of this appendix, we will review the CCK formalism in a similar manner to how Keidl summarized it in [38]. While the metric we ultimately compute in this paper is nearly identical to that described by Chrzanowski [33], we find it helpful to put Chrzanowski's original calculation into the context of the more recent work on the CCK procedure. Furthermore, we review the CCK procedure here, rather than simply referring the interested reader to [38], because there are several differences between our calculation and that set forth in [38]: we use a metric of the opposite signature, we calculate the metric corresponding to quasinormal modes with complex frequencies, we construct the metric in a different radiation gauge, and (like Chrzanowski's original calculation) we are interested in metric perturbations of definite parities.

Because the CCK formalism relies heavily on the Newman-Penrose formalism and Teukolsky's equation for perturbations of Weyl curvature scalars, we review these in Appendix 9.B. In the second part of this appendix, we will describe how to use the CCK procedure to compute definite-parity metric perturbations corresponding to quasinormal modes. In the third part of this appendix, we compute the metric perturbations in a notation in which they can be compared more easily with those of the RWZ formalism (a calculation originally performed by [33]), and we also give explicit analytical expressions for the tidal and frame-drag fields for  $(2, 2)$  perturbations, which highlight a near duality between the perturbative pieces of these fields for perturbations of opposite parities. In the final part, we summarize how we numerically calculate the IR gauge metric perturbations that we use in the visualizations in Figures 9.4, 9.12, 9.14, 9.15, and 9.26.

### 9.C.1 The CCK Procedure

The purpose of the CCK procedure is to construct a metric perturbation,  $h_{\mu\nu}$ , from a given solution to Teukolsky's equation, either  $\psi_2 = \Psi_0$  or  $\psi_{-2} = \rho^{-4}\Psi_4$  (see Appendix 9.B for a summary of the Teukolsky formalism). As part of the calculation, it is necessary to relate the solutions of the Teukolsky equation to a Hertz potential from which the metric perturbation is directly constructed

[see Eq. (9.66) for the general relationship, Eq. (9.72) for the relationship for the radial functions for their harmonics, and Eq. (9.78) for the relationship of the radial functions of definite-parity perturbations].

The CCK procedure can construct a metric in either ingoing-radiation (IR) gauge,

$$h_{\mu\nu}l^\nu = 0, \quad h_{\mu\nu}g_{(0)}^{\mu\nu} = 0, \quad (9.62)$$

or outgoing-radiation gauge

$$h_{\mu\nu}n^\nu = 0, \quad h_{\mu\nu}g_{(0)}^{\mu\nu} = 0, \quad (9.63)$$

for Schwarzschild and Kerr black holes. Here  $l^\nu$  and  $n^\nu$  are two vectors of a Newman-Penrose null tetrad [for our calculations, we will use the Kinnersley tetrad, Eq. (9.55)], and  $g_{(0)}^{\mu\nu}$  is the background Schwarzschild or Kerr metric. Because our goal is to compute vacuum perturbations of Kerr that are regular on the future event horizon, we will construct the metric perturbation in IR gauge, and we will be able to compute it by algebraically inverting a differential relationship between the harmonics of the Hertz potential and those of  $\psi_{-2}$  [the result is in Eq. (9.72)].

The Hertz potential is tensor with the same symmetries as the Riemann tensor, whose double coordinate divergence is a harmonic coordinate metric. Stewart [40] showed that in Type D spacetimes, there is sufficient gauge freedom that one can represent the independent degrees of freedom of the perturbative part of the Hertz potential as a single complex scalar; furthermore, if one applies a coordinate transformation from harmonic gauge into IR gauge, the Hertz potential, which we will denote by  $\Psi_H$ , is a solution of the vacuum Teukolsky equation for scalars of spin weight  $s = -2$  (the same as  $\psi_{-2}$ ). One can then construct a metric perturbation from the Hertz potential by applying several differential operators to  $\Psi_H$ ,

$$\begin{aligned} h_{\mu\nu} = & \{-l_\mu l_\nu (\delta + \alpha^* + 3\beta - \tau)(\delta + 4\beta + 3\tau) - m_\mu m_\nu (\mathbf{D} - \rho + 3\epsilon - \epsilon^*)(\mathbf{D} + 3\rho + 4\epsilon) \\ & + l_{(\mu} m_{\nu)} [(\mathbf{D} + \rho^* - \rho + \epsilon^* + 3\epsilon)(\delta + 4\beta + 3\tau) + (\delta + 3\beta - \alpha^* - \pi^* - \tau)(\mathbf{D} + 3\rho + 4\epsilon)]\} \Psi_H \\ & + \text{c.c.} \end{aligned} \quad (9.64)$$

(see, e.g., Eqs. (93) and (94) of [37]). The differential operators are defined by  $\mathbf{D} = l^\mu \nabla_\mu$  and  $\delta = m^\mu \nabla_\mu$ . The last term in Eq. (9.64), denoted by ‘‘c.c.,’’ means to take the complex conjugate of the entire expression, so that the metric perturbation is real.

When computing perturbations of black holes, it is helpful to be able to relate a given Hertz potential  $\Psi_H$  to a specific perturbation of the Weyl scalar  $\Psi_4$ . It is possible to do this by computing the components of the perturbative Riemann tensor from the metric perturbations (9.64) that correspond to the Weyl scalar

$$\Psi_4 = C_{\alpha\beta\mu\nu} n^\alpha m^{*\beta} n^\mu m^{*\nu}. \quad (9.65)$$

The result can be expressed compactly as

$$\psi_{-2} = \frac{1}{8} (\mathcal{L}^{\dagger 4} \Psi_H^* - 12M \partial_t \Psi_H) \quad (9.66)$$

[see, e.g., Table I of the paper by Keidl [38], where our  $\mathcal{L}^\dagger$  is their  $\tilde{\mathcal{L}}$ ]. We have used the shorthand that  $\mathcal{L}^{\dagger 4} = \mathcal{L}_{-1}^\dagger \mathcal{L}_0^\dagger \mathcal{L}_1^\dagger \mathcal{L}_2^\dagger$  where

$$\mathcal{L}_s^\dagger = -(\partial_\theta + s \cot \theta - i \csc \theta \partial_\phi) + ia \sin \theta \partial_t. \quad (9.67)$$

In general, solving for the Hertz potential  $\Psi_H$  that corresponds to a perturbed Weyl scalar  $\Psi_4$  involves inverting the fourth-order partial differential equation (9.66); however, when  $\Psi_H$  and  $\psi_{-2}$  are expanded in harmonics in the frequency domain, it is possible to perform the inversion algebraically.

The algebraic inversion can be completed by expanding  $\psi_{-2}$  in harmonics,

$$\psi_{-2} = \sum_{lm\omega} \psi_{-2}^{(lm\omega)} = \sum_{lm\omega} {}_{-2}R_{lm\omega}(r) {}_{-2}S_{lm\omega}(\theta) e^{i(m\phi - \omega t)}, \quad (9.68)$$

where  ${}_{-2}R_{lm\omega}(r)$  and  ${}_{-2}S_{lm\omega}(\theta)$  satisfy Eqs. (9.59) and (9.60). In the IR gauge, the Hertz potential is a solution to the Teukolsky equation with spin  $s = -2$ ; consequently, it can also be expanded in the same harmonics

$$\Psi_H = \sum_{lm\omega} \Psi_H^{(lm\omega)} = \sum_{lm\omega} {}_{-2}X_{lm\omega}(r) {}_{-2}S_{lm\omega}(\theta) e^{i(m\phi - \omega t)}. \quad (9.69)$$

The radial function of the Hertz potential's harmonics  ${}_{-2}X_{lm\omega}(r)$  also satisfies the vacuum Teukolsky radial equation, but because it is not the same radial function as in the harmonics of  $\psi_{-2}$ , we denote it with a different function. The radial functions of the harmonics of  $\Psi_H$  and  $\psi_{-2}$  can be related by substituting Eqs. (9.68) and (9.69) into Eq. (9.66) and using the Teukolsky-Starobinsky identity

$$\mathcal{L}^{\dagger 4} {}_{-2}S_{lm\omega} = D {}_{-2}S_{lm\omega} \quad (9.70)$$

(Eq. (59) of Ch. 9 of [30], after noting that our  $\mathcal{L}_s^\dagger$  is equivalent to  $-\mathcal{L}_s$  there), and the identity

$${}_{-2}S_{lm\omega}^* = (-1)^m {}_{-2}S_{l-m-\omega^*}. \quad (9.71)$$

Then, it is necessary to equate the full radial function for a given angular and time harmonic of the Hertz potential to the radial functions  ${}_{-2}R_{lm\omega}$  of  $\psi_{-2}$ . After this relationship is inverted, the individual radial harmonics of the Hertz potential can be written as

$${}_{-2}X_{lm\omega} = 8 \frac{(-1)^m D^* {}_{-2}R_{l-m-\omega^*}^* - 12iM\omega {}_{-2}R_{lm\omega}}{D^{*2} + 144M^2\omega^2}. \quad (9.72)$$

The constant  $D^* \equiv D_{lm\omega}^* = D_{l-m-\omega^*}$  is defined by

$$D^2 = \lambda^2(\lambda + 2)^2 - 8\lambda(5\lambda + 6)(a^2\omega^2 - am\omega) + 96\lambda a^2\omega^2 + 144(a^2\omega^2 - am\omega)^2, \quad (9.73)$$

where  $\lambda$  is the separation constant (9.61) used by Chandrasekhar [30] (a choice of the separation constant that is the same for both the angular and the radial equations). Although the Teukolsky-Starobinsky identities are usually derived assuming real frequencies, they have been shown to hold for complex frequencies as well (for a recent derivation, see [41]).

The general description of the CCK formalism is now complete: (i) For a vacuum perturbation of  $\Psi_4$ , we can find the Hertz potential  $\Psi_H$  that corresponds to this perturbation by expanding  $\Psi_H$  in harmonics [Eq. (9.69)], and expressing the radial functions of this expansion in terms of those of  $\psi_{-2} = \rho^{-4}\Psi_4$  via Eq. (9.72). (ii) From the resulting  $\Psi_H$ , we can then compute the metric perturbations via Eq. (9.64).

Next, we will show that if we choose the radial function of the Hertz potential to correspond to a perturbation of  $\psi_{-2}$  with definite parity, then the result of this calculation is equivalent to Chrzanowski's original calculation of definite-parity metric perturbations [33].

### 9.C.2 Definite-Parity Harmonics and Chrzanowski's Calculation

Let us now connect this CCK procedure with Chrzanowski's original calculation of metric perturbations of definite parities. We shall begin by showing that, if the perturbations have definite parity (electric or magnetic), then the Hertz potential must itself transform as  $\Psi_H \rightarrow \pm(-1)^l \Psi_H^*$  under parity (the plus and minus correspond to electric- and magnetic-parity perturbations, respectively), and its radial harmonics must satisfy  ${}_2X_{l-m-\omega^*}^* = \pm(-1)^m {}_2X_{lm\omega}$ . In turn, this implies that the radial harmonics of  $\psi_{-2}$  must satisfy the same relationship  ${}_2R_{l-m-\omega^*}^* = \pm(-1)^m {}_2R_{lm\omega}$ .

To deduce these relationships, we discuss the parity of the terms that appear in Eq. (9.64). The Newman-Penrose tetrad and spin coefficients of the background spacetime transform in several different ways under parity:  $\vec{l}$  and  $\vec{n}$  have positive parity, and  $\vec{m}$  does not have a definite parity,  $\vec{m} \rightarrow -\vec{m}^*$ . Similarly, the differential operator  $\mathbf{D} = l^\mu \nabla_\mu$  has positive parity, and  $\delta = m^\mu \nabla_\mu$  again does not have a definite parity,  $\delta \rightarrow -\delta^*$ . Three of the nonzero spin coefficients map to their complex conjugates under parity ( $\rho \rightarrow \rho^*$ ,  $\mu \rightarrow \mu^*$ , and  $\gamma \rightarrow \gamma^*$ ), and the remaining four spin coefficients become minus their complex conjugates under parity ( $\alpha \rightarrow -\alpha^*$ ,  $\beta \rightarrow -\beta^*$ ,  $\pi \rightarrow -\pi^*$ , and  $\tau \rightarrow -\tau^*$ ). These relationships hold true for both Schwarzschild and Kerr, although in the former case, the spin coefficients are real and, therefore, have definite parity.

When applying a parity transformation to the perturbative metric tensor,  $h_{\mu\nu} dx^\mu dx^\nu$ , where  $h_{\mu\nu}$  is given by Eq. (9.64), we can show that the tensor differential operator in Eq. (9.64) becomes its complex conjugate by using the parity transformations for the spin coefficients, NP tetrad, and

differential operators above. As a result, the metric perturbation will have either electric or magnetic parity when the Hertz potential transforms as

$$\Psi_H \rightarrow \pm(-1)^l \Psi_H^* \quad (9.74)$$

under parity. The plus sign corresponds to an electric-parity perturbation, and the minus sign describes a magnetic-parity perturbation. The condition this implies on the harmonics is also quite simple, and we can determine it by applying a parity transformation to the Hertz potential expanded in harmonics [Eq. (9.69)] and equating it to its complex conjugate. Then using the properties of the Teukolsky angular functions

$${}_s S_{lm\omega}(\pi - \theta) = (-1)^{m+l} {}_{-s} S_{lm\omega}(\theta), \quad {}_s S_{lm\omega}^*(\theta) = (-1)^{m+s} {}_{-s} S_{l-m-\omega^*}(\theta), \quad (9.75)$$

(see Appendix 9.B) and equating the radial function of each time and angular harmonic, we obtain the following condition on its radial functions,

$${}_{-2} X_{l-m-\omega^*}^* = \pm(-1)^m {}_{-2} X_{lm\omega}. \quad (9.76)$$

Similarly by substituting Eq. (9.72) into the expression above, we find an analogous relationship for the radial function of the Weyl scalar  $\psi_{-2}$ ,

$${}_{-2} R_{l-m-\omega^*}^* = \pm(-1)^m {}_{-2} R_{lm\omega}. \quad (9.77)$$

For these definite-parity perturbations, the relationship between the radial functions of the Hertz potential and  $\psi_{-2}$ , Eq. (9.72) also simplifies,

$${}_{-2} X_{lm\omega} = \pm 8(D^* \pm 12iM\omega)^{-1} {}_{-2} R_{lm\omega}; \quad (9.78)$$

namely, for definite-parity perturbations, the radial functions of  $\psi_{-2}$  and  $\Psi_H$  differ by only a complex constant. Because Eq. (9.78) shows that the two radial functions  ${}_{-2} X_{lm\omega}$  and  ${}_{-2} R_{lm\omega}$  differ only by a constant multiple, we will express both  $\Psi_H$  and  $\psi_{-2}$  in terms of the radial function of  $\psi_{-2}$ ,  ${}_{-2} R_{lm\omega}$ , for simplicity.

In the next part (and also for all other IR gauge calculations in this paper), we will compute a metric perturbation that corresponds to a perturbation of  $\psi_{-2}$  of the form

$$\begin{aligned} \psi_{-2} = & \pm \frac{1}{8} (D^* \pm 12iM\omega) {}_{-2} R_{lm\omega} e^{i(m\phi - \omega t)} {}_{-2} S_{lm\omega} \\ & + \frac{1}{8} (-1)^m (D \mp 12iM\omega^*) {}_{-2} R_{lm\omega}^* e^{-i(m\phi - \omega^* t)} {}_{-2} S_{l-m-\omega^*}. \end{aligned} \quad (9.79)$$

The corresponding Hertz potential is

$$\Psi_H = {}_{-2}R_{lm\omega} e^{i(m\phi - \omega t)} {}_{-2}S_{lm\omega} \pm (-1)^m {}_{-2}R_{lm\omega}^* e^{-i(m\phi - \omega^* t)} {}_{-2}S_{l-m-\omega^*} . \quad (9.80)$$

We choose the prefactors on the modes of  $\psi_{-2}$  so as to make the Hertz potential (and, therefore, the metric) as simple as possible. Furthermore, this choice gives the same definite-parity metric as that of Chrzanowski (when we take the real part of his expressions).

### 9.C.3 Definite-Parity CCK Metric Perturbations and Tidal and Frame- Drag Fields for Schwarzschild Black Holes

In the first two parts of this section, we will calculate electric- and magnetic-parity perturbations of Schwarzschild black holes in IR gauge. Because Chrzanowski performed this calculation in Table III of reference [33], and our results agree with his, we do not go into great detail describing the calculations; instead, we aim show the results here so as to be able to compare with the RWZ formalism in Appendix 9.A. In the third part, we will compute the tidal and frame-drag fields corresponding to these metric perturbations and show a near duality of the tidal and frame-drag fields of opposite parity perturbations for the (2, 2) mode.

#### 9.C.3.1 Electric-Parity Metric Perturbations

We begin this part by comparing the metric produced by the CCK procedure to that of the RWZ formalism. We will write the RWZ metric using the covariant notation described by Martel and Poisson [42]. Martel and Poisson write the electric-parity perturbations as

$$h_{ab}^{(e)} = \sum_{lm} h_{ab}^{lm} Y^{lm} , \quad (9.81a)$$

$$h_{aB}^{(e)} = \sum_{lm} j_a^{lm} Y_B^{lm} , \quad (9.81b)$$

$$h_{AB}^{(e)} = r^2 \sum_{lm} (K^{lm} \Omega_{AB} Y^{lm} + G^{lm} Y_{AB}^{lm}) , \quad (9.81c)$$

where the lowercase indexes run over the radial and time coordinates (e.g.,  $a, b = t, r$ ), and uppercase indexes run over the angular coordinates as before,  $A, B = \theta, \phi$ . The angular functions  $Y^{lm}$  are scalar spherical harmonics,  $Y_B^{lm}$  are the electric-parity Regge-Wheeler harmonics, and  $Y_{AB}^{lm}$  are transverse-traceless, electric-parity tensor harmonics; the term  $\Omega_{AB}$  is the metric on a 2-sphere. The vector and tensor harmonics are defined by

$$Y_A^{lm} = D_A Y^{lm} , \quad (9.82a)$$

$$Y_{AB}^{lm} = \left[ D_A D_B + \frac{1}{2} l(l+1) \Omega_{AB} \right] Y^{lm}, \quad (9.82b)$$

where  $D_A$  is the covariant derivative on a 2-sphere.

Because the Schwarzschild spacetime is spherically symmetric, we can see, intuitively, that the CCK metric, Eq. (9.64), corresponding to an electric-parity quasinormal-mode perturbation [the plus sign in Eq. (9.80)] will have a relatively simple form. The angular operators acting on the Hertz potential in Eq. (9.64) become the spin-weight raising and lowering operators, and the angular functions become the spin-weighted spherical harmonics; furthermore, and when the spin-weighted harmonics are combined with the appropriate factors of  $\bar{m}$  and  $\bar{m}^*$  the angular functions become proportional to the scalar, vector, and tensor harmonics described above. When performing the calculation, we will need to use the following identities, which can be found, for example, by adapting Eqs. (2.22a) and (2.38e) in the review by Thorne [43] to the notation used here,

$$Y_A^{lm} = \sqrt{\frac{l(l+1)}{2}} (-{}_1Y_{lm} m_A - {}_1Y_{lm} m_A^*), \quad (9.83a)$$

$$Y_{AB}^{lm} = \frac{\sqrt{D}}{2} (-{}_2Y_{lm} m_A m_B + {}_2Y_{lm} m_A^* m_B^*). \quad (9.83b)$$

The Teukolsky-Starobinsky constant for spin-weighted spherical harmonics is  $D = (l+2)!/(l-2)!$ .

We can then find that the metric coefficients are given by

$$h_{tt}^{(e)} = -\alpha^2 h_{tr}^{(e)} = \alpha^4 h_{rr}^{(e)} = -\frac{2\sqrt{D}}{r^2} \Re[-{}_2R_{lm} e^{-i\omega t} Y^{lm}], \quad (9.84a)$$

$$h_{tA}^{(e)} = -\alpha^2 h_{rA}^{(e)} = \frac{\sqrt{D}}{2l(l+1)\alpha^2} \Re \left\{ \left[ \frac{d}{dr_*} {}_2R_{lm} - \left( i\omega + \frac{2\alpha^2}{r} \right) {}_2R_{lm} \right] Y_A^{lm} e^{-i\omega t} \right\}, \quad (9.84b)$$

$$h_{AB}^{(e)} = \frac{2}{\sqrt{D}\alpha^4} \Re \left\{ \left[ (i\omega r^2 - M) \frac{d}{dr_*} {}_2R_{lm} - \left[ \frac{1}{2} \mu^2 \alpha^2 - i\omega(-3r + 7M) - r^2 \omega^2 \right] {}_2R_{lm} \right] Y_{AB}^{lm} e^{-i\omega t} \right\}. \quad (9.84c)$$

In the last equation we have used the radial Teukolsky equation to eliminate the second-derivative term, and we have defined  $\mu^2 = (l-1)(l+2)$  [which is also equal to  $l(l+1) - s(s+1)$  for  $s = -2$ ].

There are a few noteworthy differences between the IR gauge electric-parity perturbations, and the electric-parity RWZ-gauge metric. The CCK metric has a strictly angular part of the perturbation which is proportional to the transverse-traceless harmonics, and the trace portion of the angular block vanishes; conversely, the angular block of the RWZ metric perturbation has a trace part, but no transverse-traceless perturbation. The  $h_{tr}^{(e)}$  part of the metric perturbation also has a simpler relationship with the  $h_{tt}^{(e)}$  and  $h_{rr}^{(e)}$  components in IR gauge than in RWZ gauge; one reason for this is that the IR gauge metric has electric-parity vector perturbations, whereas the RWZ metric sets these to zero. Finally, the IR gauge metric is finite on the future event horizon for ingoing radiation. One can see this by noting that both  ${}_2R_{lm}$  and  $d{}_2R_{lm}/dr_*$  scale as  $\alpha^4 e^{-i\omega r_*}$  near the

horizon, which will cancel any negative powers of  $\alpha^2$  in the expressions for the metric coefficients. The same is not as manifest for the RWZ perturbations (see Appendix 9.A for more details on the RWZ formalism).

### 9.C.3.2 Magnetic-Parity Metric Perturbations

The magnetic-parity perturbations are given by

$$h_{ab}^{(m)} = 0, \quad (9.85a)$$

$$h_{aB}^{(m)} = \sum_{lm} h_a^{lm} X_B^{lm}, \quad (9.85b)$$

$$h_{AB}^{(m)} = \sum_{lm} h_2^{lm} X_{AB}^{lm}, \quad (9.85c)$$

where the magnetic-parity harmonics are defined by

$$X_A^{lm} = -\epsilon_A^B D_B Y^{lm}, \quad (9.86a)$$

$$X_{AB}^{lm} = -\frac{1}{2}(\epsilon_A^C D_B + \epsilon_B^C D_A) D_C Y^{lm}, \quad (9.86b)$$

and  $\epsilon_{AB}$  is the Levi-Civita tensor on a unit 2-sphere. As in the previous part, we can compute the CCK metric (9.64), which is relatively simple for a Schwarzschild black hole. The reason for the simplification is the same, but we will need the following two identities that relate the spin-weighted spherical harmonics to magnetic-parity vector and tensor harmonics

$$X_A^{lm} = -i\sqrt{\frac{l(l+1)}{2}}(-{}_1Y_{lm}m_A + {}_1Y_{lm}m_A^*), \quad (9.87a)$$

$$X_{AB}^{lm} = -i\frac{\sqrt{D}}{2}(-{}_2Y_{lm}m_A m_B - {}_2Y_{lm}m_A^* m_B^*). \quad (9.87b)$$

These relationships can be found in Eqs. (2.22b) and (2.38f) of [43]. The magnetic-parity metric perturbations have the same radial and time dependence as the electric-parity perturbations for the vector and tensor parts,

$$\alpha^2 h_{rA}^{(m)} = -h_{tA}^{(m)} = \frac{\sqrt{D}}{2l(l+1)\alpha^2} \Im \left\{ \left[ \frac{d}{dr_*} {}_{-2}R_{lm} - \left( i\omega + \frac{2\alpha^2}{r} \right) {}_{-2}R_{lm} \right] X_A^{lm} e^{-i\omega t} \right\}. \quad (9.88a)$$

$$h_{AB}^{(m)} = -\frac{2}{\sqrt{D}\alpha^4} \Im \left\{ \left[ (i\omega r^2 - M) \frac{d}{dr_*} {}_{-2}R_{lm} - \left[ \frac{1}{2}\mu^2\alpha^2 - i\omega(-3r + 7M) - r^2\omega^2 \right] {}_{-2}R_{lm} \right] X_{AB}^{lm} e^{-i\omega t} \right\}. \quad (9.88b)$$

Because they have the same radial dependence as the electric-parity metric, the magnetic-parity perturbations will also be well-behaved on the future event horizon.

The major difference between the RWZ formalism's magnetic-parity metric and the IR gauge

metric is that in IR gauge, the transverse-traceless metric perturbation is no longer required to be zero.

### 9.C.3.3 Tidal and Frame-Drag Fields of the (2,2) Mode

In this part, we calculate the tidal and frame-drag fields for a (2, 2) mode in IR gauge of both electric and magnetic parities. We find an interesting near duality between the tidal and frame-drag fields of opposite-parity perturbations that we noted in Sections 9.1.3.3, 9.3.2.3 and 9.3.3.2.

We compute the tidal and frame-drag fields from the metric by evaluating the components of the Weyl tensor and its dual in the tetrad (9.8) including the perturbative corrections to the tetrad (9.11a)–(9.11b). We find that for an electric-parity mode, the tidal and frame-drag fields can be written as

$$\mathcal{E}_{\hat{r}\hat{r}}^{(1,e)} = 2\Re[E_{\text{I}(e)}(r)Y^{22}e^{-i\omega t}], \quad (9.89a)$$

$$\mathcal{E}_{\hat{r}\hat{A}}^{(1,e)} = 2\Re[E_{\text{II}(e)}(r)Y_{\hat{A}}^{22}e^{-i\omega t}], \quad (9.89b)$$

$$\mathcal{E}_{\hat{A}\hat{B}}^{(1,e)} = 2\Re\left[\left(-\frac{1}{2}E_{\text{I}(e)}(r)\delta_{\hat{A}\hat{B}}Y^{22} + E_{\text{II}(e)}(r)Y_{\hat{A}\hat{B}}^{22}\right)e^{-i\omega t}\right], \quad (9.89c)$$

$$\mathcal{B}_{\hat{r}\hat{r}}^{(1,e)} = 0, \quad (9.89d)$$

$$\mathcal{B}_{\hat{r}\hat{A}}^{(1,e)} = 2\Re[B_{\text{I}(e)}(r)X_{\hat{A}}^{22}e^{-i\omega t}], \quad (9.89e)$$

$$\mathcal{B}_{\hat{A}\hat{B}}^{(1,e)} = 2\Re[B_{\text{II}(e)}(r)X_{\hat{A}\hat{B}}^{22}e^{-i\omega t}]. \quad (9.89f)$$

The symbol  $\delta_{\hat{A}\hat{B}}$  is the Kronecker delta function, and the traceless property of  $\mathcal{E}$  requires that the radial function in front of the Kronecker delta must be minus one-half that of  $\mathcal{E}_{\hat{r}\hat{r}}^{(1)}$  [i.e.,  $-(1/2)E_{\text{I}(e)}(r)$ ].

For the magnetic-parity perturbation, the frame-drag and tidal fields are

$$\mathcal{B}_{\hat{r}\hat{r}}^{(1,m)} = 2\Re[B_{\text{I}(m)}(r)Y^{22}e^{-i\omega t}], \quad (9.90a)$$

$$\mathcal{B}_{\hat{r}\hat{A}}^{(1,m)} = 2\Re[B_{\text{II}(m)}(r)Y_{\hat{A}}^{22}e^{-i\omega t}], \quad (9.90b)$$

$$\mathcal{B}_{\hat{A}\hat{B}}^{(1,m)} = 2\Re\left[\left(-\frac{1}{2}B_{\text{I}(m)}(r)\delta_{\hat{A}\hat{B}}Y^{22} + B_{\text{III}(m)}(r)Y_{\hat{A}\hat{B}}^{22}\right)e^{-i\omega t}\right], \quad (9.90c)$$

$$\mathcal{E}_{\hat{r}\hat{r}}^{(1,m)} = 0, \quad (9.90d)$$

$$\mathcal{E}_{\hat{r}\hat{A}}^{(1,m)} = 2\Re[E_{\text{I}(m)}(r)X_{\hat{A}}^{22}e^{-i\omega t}], \quad (9.90e)$$

$$\mathcal{E}_{\hat{A}\hat{B}}^{(1,m)} = 2\Re[E_{\text{II}(m)}(r)X_{\hat{A}\hat{B}}^{22}e^{-i\omega t}]. \quad (9.90f)$$

Interestingly, the radial functions of the tidal and frame-drag fields of the opposite-parity perturbations are nearly identical

$$B_{\text{I}(m)}(r) = iE_{\text{I}(e)}(r) \quad (9.91a)$$

$$B_{\text{II(m)}}(r) = iE_{\text{II(e)}}(r) - i \frac{M\sqrt{3(r+2M)}}{r^5\alpha^4\sqrt{2r}} \left[ -(2\alpha^2 + i\omega r) {}_{-2}R_{22} + r \frac{d}{dr_*} {}_{-2}R_{22} \right], \quad (9.91b)$$

$$B_{\text{III(m)}}(r) = iE_{\text{III(e)}}(r) + \frac{\sqrt{3(r+2M)}}{r^5\alpha^4\sqrt{2}} M\omega {}_{-2}R_{22}, \quad (9.91c)$$

$$E_{\text{I(m)}}(r) = -iB_{\text{I(e)}}(r) + i \frac{M\sqrt{3(r+2M)}}{r^5\alpha^4\sqrt{2r}} \left[ -(2\alpha^2 + i\omega r) {}_{-2}R_{22} + r \frac{d}{dr_*} {}_{-2}R_{22} \right], \quad (9.91d)$$

$$E_{\text{II(m)}}(r) = -iB_{\text{II(e)}}(r) - \frac{\sqrt{3(r+2M)}}{r^5\alpha^4\sqrt{2}} M\omega {}_{-2}R_{22}. \quad (9.91e)$$

In fact, there is an exact duality of the radial-radial components, which implies that the horizon vorticity of a magnetic-parity perturbation is the same as the horizon tendicity of an electric-parity perturbation. For completeness, we list the expressions for the radial functions for the electric-parity perturbations, which are lengthy, but will be needed in the next appendix.

$$E_{\text{I(e)}}(r) = - \frac{2\sqrt{6}}{r^6\alpha^4} \left\{ r^2(r-3M+i\omega r^2) \frac{d}{dr_*} {}_{-2}R_{22} + [-5r^2 + 16Mr - 12M^2 - i\omega r^2(4r-9M) + r^4\omega^2] {}_{-2}R_{22} \right\}, \quad (9.92a)$$

$$E_{\text{II(e)}}(r) = \frac{1}{r^6\sqrt{6r(r+2M)}\alpha^4} \left\{ r^2[3r^2 + 6M^2 + i\omega r^2(r-3M) + r^4\omega^2] \frac{d}{dr_*} {}_{-2}R_{22} + [(-9r^3 + 18Mr^2 - 12M^2r + 24M^3) - i\omega r^2(8r^2 - 16Mr + 18M^2) + 2\omega^2 r^4(4r-9M) + ir^6\omega^3] {}_{-2}R_{22} \right\}, \quad (9.92b)$$

$$E_{\text{III(e)}}(r) = \frac{1}{r^5(r+2M)\alpha^4\sqrt{6}} \left\{ ir^2\omega(-2r^2 + 3Mr + 3M^2 + r^4\omega^2) \frac{d}{dr_*} {}_{-2}R_{22} + [6(r^2 + 4M^2) + i\omega(4r^3 - 11Mr^2 + 12M^2r + 12M^3) - \omega^2 r^2(4r^2 - 4Mr - 9M^2) - 3i\omega^3 r^5\alpha^2 + r^6\omega^4] {}_{-2}R_{22} \right\}, \quad (9.92c)$$

$$B_{\text{I(e)}}(r) = \frac{\sqrt{2}}{r^5\sqrt{3r(r+2M)}\alpha^4} \left\{ r^2[9M - i\omega r(r-3M) + r^3\omega^2] \frac{d}{dr_*} {}_{-2}R_{22} + [-24Mr\alpha^2 + i\omega r(12M^2 - 25Mr + 5r^2) - \omega^2 r^3(4r-9M) - ir^5\omega^3] {}_{-2}R_{22} \right\}, \quad (9.92d)$$

$$B_{\text{II(e)}}(r) = \frac{1}{r^4(r+2M)\alpha^4\sqrt{6}} \left\{ i\omega r(-2r^2 + 3Mr + 3M^2 + r^4\omega^2) \frac{d}{dr_*} {}_{-2}R_{22} + [-24M + 2i\omega r(2r-7M) + \omega^2 r(-4r^2 + 4Mr + 9M^2) - 3i\omega^3 r^4\alpha^2 + r^5\omega^4] {}_{-2}R_{22} \right\}. \quad (9.92e)$$

From these expressions, it is clear that the tidal and frame drag-fields are regular on the horizon, because, as noted above  ${}_{-2}R_{lm}$  and  $d {}_{-2}R_{lm}/dr_*$  scale as  $\alpha^4 e^{-i\omega r_*}$  near the horizon; consequently, they will cancel the corresponding powers of  $\alpha$  in the denominators of these functions.

### 9.C.4 Analytical and Numerical Methods for Computing Metric Perturbations and Tidal and Frame-Drag Fields in IR Gauge

The procedures for calculating the metric perturbations and their tidal and frame-drag fields are identical for Schwarzschild and Kerr black holes; however, because the analytical expressions for the Newman-Penrose quantities, the angular Teukolsky function, and the metric derived from these mathematical objects are significantly simpler for Schwarzschild black holes, the amount of work we can perform analytically differs for rotating and non-rotating black holes. Even for Schwarzschild black holes, however, we will not be able to compute all aspects of the metric perturbation analytically. We calculate the the least-damped  $l = 2$ ,  $m = 2$  quasinormal-mode frequencies for both Schwarzschild and Kerr black holes using the Mathematica notebook associated with [13], an implementation of Leaver's method [14]. Similarly, we compute the radial Teukolsky functions  ${}_{-2}R_{lm\omega}$  corresponding to a quasinormal-mode solution for both Schwarzschild and Kerr black holes numerically. We compute it in two ways, which give comparable results: we solve the boundary-value problem for a quasinormal mode solution to the radial Teukolsky equation, Eq. (9.59), using a shooting method, and we compare the result with a series solution given by Leaver [14] (as is also done in the notebook of [13]). For Kerr black holes, the numerical solution requires the angular eigenvalue,  ${}_sA_{lm}$  associated with the quasinormal mode frequency, which we again compute from the implementation of Leaver's method in [13].

The most significant difference between the calculations of quasinormal modes of Schwarzschild and Kerr black holes arises from differences in the Teukolsky angular function, and the angular operators used in computing the metric (9.64). First, the spin-weighted spheroidal harmonics in the expression for the Hertz potential, Eq. (9.80), reduce to spin-weighted spherical harmonics for Schwarzschild black holes. Second, the angular operators in Eq. (9.64) reduce to spin-weight lowering operators, in the non-spinning limit. As a result, the metric perturbation can be expressed, analytically, in terms of electric- or magnetic-parity scalar, vector, and tensor spherical harmonics of a single  $l$ , for Schwarzschild black holes. For perturbations of Kerr black holes, there are not these additional simplifications. First, we must calculate the spin-weighted spheroidal harmonics numerically, which we do using a series solution put forward by Leaver [14] (the same method as that implemented in [13]). Second, the angular operators are no longer the spin-weight lowering operators. The metric perturbation computed from these functions, therefore, is not nearly as simple as that of the Schwarzschild limit. In fact, for our calculations with spinning black holes, we find it easier to work with a numerical fit to the analytical expression for the metric.

Once we calculate the metric perturbation, we construct the perturbation to the Weyl tensor in the same way for both rotating and non-rotating black holes. We can then calculate the tetrad components of the tidal field,  $\mathcal{E}_{\hat{a}\hat{b}}$ , and frame-drag field,  $\mathcal{B}_{\hat{a}\hat{b}}$ , using the background tetrad in Eq.

(9.8 for Schwarzschild holes or Eq. (9.9a) for Kerr holes and its perturbative corrections in Eqs. (9.11a)–(9.11b). From these fields, we can solve the eigenvalue problem and compute tendex and vortex lines, and their corresponding tendicities and vorticities.

## 9.D Relationship Between Regge-Wheeler-Zerilli and Ingoing-Radiation Gauges

In this appendix, we construct generators of infinitesimal coordinate transformations between RWZ and IR gauges, for both magnetic- and electric-parity perturbations of Schwarzschild black holes.

### 9.D.1 Magnetic-Parity Gauge Transformation

In this part, we compute the gauge-change generator that transforms the magnetic-parity metric in IR gauge to the same metric in Regge-Wheeler gauge. We show, as noted in Section 9.2.3, that this infinitesimal magnetic-parity coordinate transformation does not change the time function that specifies the slicing (into surfaces of constant  $\tilde{t}$ ). In addition, perturbative changes of the spatial coordinates will not alter the coordinate (or tetrad) components of the frame-drag field; therefore, the fields in both gauges will be equal.

The calculation that shows these facts is relatively straightforward. Regge and Wheeler showed in Eq. (17) of [27] that, beginning in any gauge, it is possible to remove the transverse-traceless part of the magnetic-parity metric perturbation [Eq. (9.85c) in the notation used in Appendix 9.C.3] by an infinitesimal coordinate transformation of the form

$$\vec{\xi}^{(m)} = -\frac{1}{2} \sum_{lm} h_2^{lm}(0, 0, \mathbf{X}^{lm}), \quad (9.93)$$

where  $\mathbf{X}^{lm}$  is a magnetic-parity, vector spherical harmonic. This follows from the fact that the perturbation to the metric transforms under this change of coordinates by

$$h_{\mu\nu} \rightarrow h_{\mu\nu} + 2\xi_{(\mu|\nu)}, \quad (9.94)$$

(where  $|$  denotes a covariant derivative with respect to the background metric, and parenthesis around the indexes means the expression is symmetrized) and from the definition of the magnetic-parity, transverse-traceless tensor harmonics (9.86b). The result can also be found from Eqs. (5.5) and (5.6) of [42].

For a multipolar perturbation with indexes  $(l, m)$  in IR gauge, the function  $-\frac{1}{2} \sum_{lm} h_2^{lm}/2$  is given by the radial function in Eq. (9.88b) multiplied by  $e^{-i\omega t}$ , and the full coordinate transformation

vector is therefore

$$\xi_t^{(m)} = \xi_r^{(m)} = 0, \quad (9.95a)$$

$$\xi_A^{(m)} = \frac{1}{\sqrt{D}\alpha^4} \Im \left\{ \left[ (i\omega r^2 - M) \frac{d}{dr_*} {}_{-2}R_{lm} - \left[ \frac{1}{2}\mu^2\alpha^2 - i\omega(-3r + 7M) - r^2\omega^2 \right] {}_{-2}R_{lm} \right] X_A^{lm} e^{-i\omega t} \right\}. \quad (9.95b)$$

A short calculation can verify that  $h_{tA}$  and  $h_{rA}$  are the only nonzero components of the metric after this transformation (the same as in RWZ gauge) and they are given by

$$h_{tA} = \Im \left\{ \frac{1}{\sqrt{l(l+1)D}r\alpha^4} \left[ \left[ -\frac{1}{2}\mu^2 r\alpha^2 + (iM\omega + r^2\omega^2) \right] \frac{d}{dr_*} {}_{-2}R_{lm} + \left[ \alpha^2(\alpha^2 + i\omega r) - \omega^2 r(3r - 7M) - i\omega^3 r^3 \right] {}_{-2}R_{lm} \right] X_A^{lm} e^{-i\omega t} \right\}, \quad (9.96a)$$

$$h_{rA} = \Im \left\{ \frac{-i\omega}{\sqrt{l(l+1)D}\alpha^6} \left[ (r - 3M + i\omega r^2) \frac{d}{dr_*} {}_{-2}R_{lm} + \left[ -\alpha^2(\frac{1}{2}\mu^2 + 3\alpha^2) - i\omega(4r - 9M) + \omega^2 r^2 \right] {}_{-2}R_{lm} \right] X_A^{lm} e^{-i\omega t} \right\}. \quad (9.96b)$$

It is not immediately apparent, however, that this gauge is RWZ gauge, because it is expressed in terms of the radial function of  $\psi_{-2}$ , ( ${}_{-2}R_{lm}$ ), rather than the Regge-Wheeler function  $Q$ .

To show that this transformation did bring the metric into Regge-Wheeler gauge, it is necessary to use the relationship between  $Q$  and  ${}_{-2}R_{lm}$  given in, e.g., Eq. (319) of Ch. 4 of [30]<sup>6</sup>

$$Q = \frac{-2i\omega}{r\alpha^4(D - 12iM\omega)} \left\{ (r - 3M + i\omega r^2) \frac{d}{dr_*} {}_{-2}R_{lm} + \left[ -\alpha^2(\frac{1}{2}\mu^2 + 3\alpha^2) - i\omega(4r - 9M) + r^2\omega^2 \right] {}_{-2}R_{lm} \right\}. \quad (9.97)$$

After substituting this relationship into Eqs. (9.32) and (9.30) and taking its imaginary part—so that the RWZ metric is real and is expressed in terms of  ${}_{-2}R_{lm}$ —it becomes apparent that the transformation brings the IR gauge metric into RWZ gauge.

Because the gauge change from IR to RWZ is generated by a strictly spatial  $\vec{\xi}^{(m)}$  and because  $\mathcal{B}$  is a strictly first-order quantity for perturbations of Schwarzschild holes, the frame-drag analog of Eq. (9.19) guarantees that the frame-drag field must be identically the same in the two gauges:

$$\mathcal{B}_{\hat{i}\hat{j}}^{\text{IRG}} = \mathcal{B}_{\hat{i}\hat{j}}^{\text{RW}}. \quad (9.98)$$

<sup>6</sup>Aside from several differences in notation (the radial function used by Chandrasekhar,  $Z^{(-)}$ , is related to the Regge-Wheeler function by  $Q = i\omega Z^{(-)}$ , and his radial function for the Teukolsky equation,  $Y_{-2}$  is related to that of this paper by  ${}_{-2}R_{lm} = r^3 Y_{-2}$ ), there is one additional subtle point about using this equation. This equation is expressed as a relationship between  $Y_{+2}$  (proportional to the radial function of  $\Psi_0$ ) and  $Z^{(-)}$ . Because the time dependence of  $\Psi_0$  is given by  $e^{+i\sigma t}$  in [30], then the  $Y_{+2}$  there is equivalent to  $Y_{+2}^*$  of  $\Psi_0$  with a time dependence given by  $e^{-i\omega t}$ . In addition, because  $Y_{-2}$  satisfies the same equation as  $Y_{+2}^*$ , then this equation is valid for  $Y_{-2}$  when  $\sigma$  is replaced by  $\omega$ .

This can be confirmed explicitly for the (2,2) mode by substituting Eq. (9.97) into the tetrad components of the RWZ frame-drag field in Eqs. (9.40a)–(9.40f) and finding that they are identical to the IR gauge frame-drag field of Eqs. (9.90), (9.91), and (9.92).

When thought of as abstract tensors without reference to any coordinate system, it is also the case that the tidal fields are equal,

$$\boldsymbol{\mathcal{E}}^{\text{IRG}} = \boldsymbol{\mathcal{E}}^{\text{RW}}. \quad (9.99)$$

Because there is a background tidal field, perturbative differences in the coordinates enter into the components of the tidal field and the components are no longer equal; see Eq. (9.19). Therefore, visualizations of the tendex lines or tendicity in the two coordinate systems (when the coordinates are drawn as though they were flat) look different.

## 9.D.2 Electric-Parity Gauge Transformation

In this part, we construct an infinitesimal generator of an electric-parity coordinate transformation that brings the electric-parity IR gauge to RWZ gauge. The transformation changes the time function (and hence how we define the slicing) in addition to the spatial coordinates. This implies that neither the frame-drag fields nor the coordinate components of the tidal field will equal in the two gauges (but the tidal field written without coordinates will be); see Eqs. (9.18) and (9.19), respectively.

The gauge-change generator that connects the two gauges is somewhat more complex for the electric-parity perturbations than it was for the magnetic-parity ones. The transformation can be found by using Eq. (19) of [27] or Eqs. (4.6)–(4.9) of [42]. The general approach to find the transformation is to use  $\xi_A^{(e)}$  to remove the transverse-traceless part of the IRG metric, and then use  $\xi_t^{(e)}$  and  $\xi_r^{(e)}$  to annul the transverse metric coefficients. After a short calculation, it is possible to express the generator as

$$\begin{aligned} \xi_t^{(e)} = & \frac{1}{2\mu^2 r^2 \alpha^4} \Re \left\{ \left[ -r^2 [\mu^3 \alpha^2 - 4i\omega(M - r^2\omega)] \frac{d}{dr_*} {}_{-2}R_{lm} \right. \right. \\ & \left. \left. + [\mu^3 r \alpha^4 + i\omega r^2 \mu^2 \alpha^2 (\mu - 2) - 4rM\omega^2 r^2 (3r - 7M) - 4i\omega^3 r^4] {}_{-2}R_{lm} \right] Y^{lm} e^{-i\omega t} \right\} \quad (9.100a) \end{aligned}$$

$$\begin{aligned} \xi_r^{(e)} = & \frac{1}{2\mu^2 r^3 \alpha^6} \Re \left\{ \left[ r^3 [\alpha^2 \mu^2 (\mu + 2) + 4i\omega(r - 3M) - 4r^2 \omega^2] \frac{d}{dr_*} {}_{-2}R_{lm} \right. \right. \\ & + \{-r\mu^2 \alpha^2 (\mu + 2)(2r\alpha^2 + ir^2\omega) - 2r^2(\mu + 2) - 2i\omega r[(\mu^2 + \mu - 2)r^2 + 2Mr(\mu - 8) + 24M^2] \\ & \left. \left. + 4\omega^2 r^3 (4r - 9M) + 4i\omega^3 r^5\} {}_{-2}R_{lm} \right] Y^{lm} e^{-i\omega t} \right\} \quad (9.100b) \end{aligned}$$

$$\begin{aligned} \xi_A^{(e)} = & \frac{-1}{\sqrt{D}\alpha^4} \Re \left\{ \left[ (i\omega r^2 - M) \frac{d}{dr_*} {}_{-2}R_{lm} - [\frac{1}{2}\mu^2 \alpha^2 - i\omega(-3r + 7M) - r^2 \omega^2] {}_{-2}R_{lm} \right] Y_A^{lm} e^{-i\omega t} \right\}, \quad (9.100c) \end{aligned}$$

where we used Eq. (9.59) to reduce second-order radial derivatives to first-order ones.

To confirm that this gauge-change generator does bring the IR-gauge metric to the RWZ metric, we again use the relation between the Zerilli function and the radial Teukolsky function encoded in Eq. (319) of Ch. 4 of [30]:

$$Z = \frac{1}{r^2 \alpha^4 (D + 12iM\omega)(\mu^2 r + 6M)} \left\{ 2r [i\omega r^2 (\mu^2 r + 6M) + (\mu^2 r^2 - 3\mu^2 Mr - 6M^2)] \frac{d}{dr_*} {}_{-2}R_{lm} + \{ \alpha^2 (\mu^2 r + 6M)^2 + 2(3\alpha^2 + i\omega r) [\mu^2 r^2 - 3\mu^2 Mr - 6M^2 + i\omega r^2 (\mu^2 r + 6M)] \} {}_{-2}R_{lm} \right\}. \quad (9.101)$$

This allows us to confirm that the IR metric was brought to RWZ gauge through the transformation vector  $\vec{\xi}^{(e)}$ .

With this expression, we can also compare the frame-drag fields in the two gauges for the (2, 2) mode. By expressing the radial functions for the frame-drag field of a (2, 2), electric-parity mode in RWZ gauge [ $B_{1(e)}(r)$  and  $B_{2(e)}(r)$  of Eqs. (9.42d) and (9.42e)] in terms of the radial Teukolsky function  ${}_{-2}R_{22}$ , we find

$$B_{1(e)}(r) = B_{I(e)}(r) + \frac{\sqrt{3}}{2r^5 \alpha^4 \sqrt{2r(r+2M)}} \left\{ [-4r\alpha^2 - 2i\omega(2r^2 - 5Mr + 6M^2) + 3r^2\omega^2(r - 3M) + ir^4\omega^3] {}_{-2}R_{22} - r^2\alpha^2(r^2\omega^2 + 3iM\omega - 2) \frac{d}{dr_*} {}_{-2}R_{22} \right\}, \quad (9.102a)$$

$$B_{2(e)}(r) = B_{II(e)}(r), \quad (9.102b)$$

where  $B_{I(e)}(r)$  and  $B_{II(e)}(r)$  are the equivalent radial functions of the IR-gauge frame-drag field in Eqs. (9.92). Because the functions  $B_{1(e)}(r)$  and  $B_{I(e)}(r)$  determine the radial dependence of the transverse part of the frame-drag field (and  $B_{2(e)}(r)$  and  $B_{II(e)}(r)$  do the same for the transverse-traceless part), we see a particular illustration of the result of Eq. (9.18) of Section 9.2.3.2: namely, a change in slicing from an electric-parity gauge change will induce a change in the longitudinal-transverse components of the frame-drag field (but not the longitudinal or transverse-traceless parts).

## 9.E Horizon Tendicity and Vorticity Calculated from the Weyl Scalar $\Psi_0$

In this appendix, we modify a calculation by Hartle [6] to compute the horizon tendicity and vorticity by applying differential operators of the background spacetime to a perturbation of  $\Psi_0 \equiv \psi_2$  (where  $\psi_2$  satisfies Teukolsky's equation; see Appendix 9.B). Using this result, we derive the duality between the horizon vorticity and tendicity of opposite-parity perturbation mentioned in Section 9.3.1, for both Schwarzschild and Kerr black holes. We also relate the horizon quantities to the complex curvature and show that they are proportional for Schwarzschild holes and differ only by the product

of spin coefficients  $\lambda^{(0)}\sigma^{(1)}$  for Kerr holes. This proves these claims made in Section 9.1.2.

### 9.E.1 Constructing a Hypersurface-Orthogonal Tetrad on the Horizon

As in Hartle's calculation, we must work in a NP tetrad in which the null vector  $\vec{l}$  is tangent to the horizon,  $\vec{n}$  is normal to the horizon, and  $\vec{m}$  and its complex conjugate lie in the instantaneous horizon (constant  $v = \tilde{t} + r$  for Hartle, though we will use constant  $\tilde{t}$ ). This NP tetrad must also satisfy additional constraints

$$\vec{u} = \frac{1}{\sqrt{2}}(\vec{l} + \vec{n}), \quad \vec{N} = \frac{1}{\sqrt{2}}(\vec{l} - \vec{n}), \quad \vec{m} = \frac{1}{\sqrt{2}}(\vec{e}_2 + i\vec{e}_3), \quad (9.103a)$$

[with the associated non-null tetrad given by Eqs. (9.9a) and (9.11)], which ensure that the slicing vector  $\vec{u}$  associated with this NP tetrad is hypersurface-orthogonal on the horizon and the spatial basis vectors are tied to our coordinate system in the desired way.

To describe the unperturbed NP tetrad, it is useful to first construct Hartle's tetrad, which can be obtained from Kinnersley's tetrad (9.55), by a boost followed by a null rotation about  $\vec{l}$  (also called class III and I transformations, respectively):

$$\vec{l}_H = \frac{\Delta}{2(r^2 + a^2)} \vec{l}_K, \quad (9.104a)$$

$$\vec{m}_H = \vec{m}_K - \frac{ia \sin \theta}{\sqrt{2}(r + ia \cos \theta)} \vec{l}_H, \quad (9.104b)$$

$$\vec{n}_H = \frac{2(r^2 + a^2)}{\Delta} \vec{n}_K + \frac{ia \sin \theta}{\sqrt{2}(r + ia \cos \theta)} \vec{m}_K - \frac{ia \sin \theta}{\sqrt{2}(r + ia \cos \theta)} \vec{m}_K^* + \frac{a^2 \sin^2 \theta}{2\Sigma} \vec{l}_H. \quad (9.104c)$$

The quantities  $\Delta$  and  $\Sigma$  are defined in Eq. (9.56). Then, we can construct an unperturbed tetrad from Hartle's tetrad using the following spin-boost transformation (also called class III):

$$\vec{l}_{(0)} = N_l \vec{l}_H, \quad \vec{m}_{(0)} = e^{i\Theta} \vec{m}_H, \quad \vec{n}_{(0)} = N_l^{-1} \vec{n}_H, \quad (9.105a)$$

where

$$N_l = \sqrt{\frac{\Sigma + 2Mr}{2\Sigma}}, \quad e^{i\Theta} = \frac{r + ia \cos \theta}{\sqrt{\Sigma}}. \quad (9.105b)$$

One can verify that the resulting orthonormal tetrad

$$\vec{u}^{(0)} = \frac{1}{\sqrt{2}}(\vec{l}_{(0)} + \vec{n}_{(0)}), \quad \vec{N}^{(0)} \equiv \vec{e}_r^{(0)} = \frac{1}{\sqrt{2}}(\vec{l}_{(0)} - \vec{n}_{(0)}), \quad (9.106a)$$

$$\vec{e}_\theta^{(0)} = \frac{1}{\sqrt{2}}(\vec{m}_{(0)} + \vec{m}_{(0)}^*), \quad \vec{e}_\phi^{(0)} = \frac{1}{i\sqrt{2}}(\vec{m}_{(0)} - \vec{m}_{(0)}^*), \quad (9.106b)$$

is exactly the ingoing-Kerr tetrad (9.9a), when evaluated on the horizon, though away from the horizon it is not.

For the NP null tetrad to correspond, on the horizon, to the hypersurface-orthogonal  $\{\vec{u}, \vec{e}_{\hat{r}}, \vec{e}_{\hat{\theta}}, \vec{e}_{\hat{\phi}}\}$  of Eqs. (9.9a) and (9.11) via Eqs. (9.103), we must choose the perturbative corrections to the tetrad to satisfy

$$\vec{l}_{(1)} = \frac{1}{2\sqrt{2}}[(h_{\hat{0}\hat{0}}\vec{u}_{(0)} - h_{\hat{r}\hat{r}}\vec{e}_{\hat{r}}^{(0)}) - 2h_{\hat{0}\hat{i}}\vec{e}_{(0)}^{\hat{i}} - 2h_{\hat{r}\hat{A}}\vec{e}_{(0)}^{\hat{A}}], \quad (9.107a)$$

$$\vec{n}_{(1)} = \frac{1}{2\sqrt{2}}[(h_{\hat{0}\hat{0}}\vec{u}_{(0)} + h_{\hat{r}\hat{r}}\vec{e}_{\hat{r}}^{(0)}) - 2h_{\hat{0}\hat{i}}\vec{e}_{(0)}^{\hat{i}} + 2h_{\hat{r}\hat{A}}\vec{e}_{(0)}^{\hat{A}}], \quad (9.107b)$$

$$\vec{m}_{(1)} = -\frac{1}{2\sqrt{2}}[(h_{\hat{\theta}\hat{\theta}}\vec{e}_{\hat{\theta}}^{(0)} + ih_{\hat{\phi}\hat{\phi}}\vec{e}_{\hat{\phi}}^{(0)}) + 2h_{\hat{\theta}\hat{\phi}}\vec{e}_{\hat{\phi}}^{(0)}]. \quad (9.107c)$$

Because  $\vec{e}_{\hat{r}}$  is normal to surfaces of constant  $r$  in slices of constant  $\tilde{t}$  through perturbative order, we will need to choose our gauge so that the coordinate position of the horizon does not move from the constant value  $r = r_+$ . Although Poisson [44] has shown that there are a wide class of gauges that satisfy this property (horizon-locking gauges), for our calculation, we find it convenient to work in an ingoing radiation gauge based on the unperturbed tetrad vector  $\vec{l}_{(0)}$ ,

$$h_{\mu\nu}l_{(0)}^\nu = 0, \quad g^{\mu\nu}h_{\mu\nu} = 0. \quad (9.108)$$

On the horizon, these gauge conditions imply that

$$h_{\hat{0}\hat{0}} = h_{\hat{r}\hat{r}} = -h_{\hat{0}\hat{r}}, \quad (9.109a)$$

and that the null vector  $\vec{l}$  undergoes a perturbative boost,

$$\vec{l}_{(1)} = \frac{1}{2}h_{\hat{0}\hat{0}}\vec{l}_{(0)}. \quad (9.109b)$$

[To derive this, one should split  $-2h_{\hat{0}\hat{i}}\vec{e}_{(0)}^{\hat{i}}$  into a sum of two terms  $-2(h_{\hat{0}\hat{r}}\vec{e}_{(0)}^{\hat{r}} + h_{\hat{0}\hat{A}}\vec{e}_{(0)}^{\hat{A}})$  and use the relation in Eq. (9.103).] In addition to keeping the horizon at a constant coordinate position  $r = r_+$  (see [44]), using this gauge condition allows us to calculate the perturbation to  $\Psi_2$  in a much simpler way, as we describe in the next subsection.

### 9.E.2 Computing the Horizon Tendicity and Vorticity from $\Psi_0$

Although the explicit expressions for spin coefficients in this tetrad are somewhat lengthy (and, as a result, we do not give them here), through a direct calculation we can verify that on the horizon

$$\rho_{(0)} = \sigma_{(0)} = \kappa_{(0)} = 0, \quad \epsilon_{(0)} \in \mathbb{R}. \quad (9.110a)$$

Moreover, because in this ingoing radiation gauge the perturbation to the vector  $\vec{l}$  can be obtained by applying a boost (Class III) transformation to the tetrad, the perturbed value of  $\kappa$  will also vanish,

$$\kappa_{(1)} = 0. \quad (9.110b)$$

From Eq. (310a) of Ch. 1 of [30] (which describes the components of the Riemann tensor in the Newman-Penrose formalism), we see that the perturbation to the spin-coefficient  $\rho$  satisfies an equation

$$\mathbf{D}_{(0)}\rho_{(1)} = 2\epsilon_{(0)}\rho_{(1)},$$

where  $\epsilon_{(0)} > 0$ . If  $\rho_{(1)}$  is not zero, then the separated solution to this equation,  $\rho_{(1)} = f(r, \theta)e^{-i(\omega\bar{t} - m\bar{\phi})}$ , implies the constraint that  $2\epsilon_{(0)} + iN_l(\omega - m\omega_+) = 0$  [here  $\omega_+ = a/(2Mr_+)$  is the horizon angular velocity]. This condition is not satisfied for constant frequencies  $\omega$ , so the perturbation to the spin coefficient must vanish:

$$\rho_{(1)} = 0. \quad (9.110c)$$

From these conditions on the spin coefficients, and the fact that  $\Psi_0^{(0)} = \Psi_1^{(0)} = 0$ , we can write the Bianchi identities (see, e.g., Eqs. (321a) and (321b) of Ch. 1 of [30]) as

$$(\mathbf{D} - 2\epsilon)\Psi_1 = (\delta^* + \pi - 4\alpha)\Psi_0, \quad (9.111a)$$

$$\mathbf{D}\Psi_2^{(1)} = (\delta^* + 2\pi - 2\alpha)\Psi_1, \quad (9.111b)$$

where we have dropped the superscripts indicating perturbative orders on all differential operators and spin coefficients (because they are all background quantities) and the Weyl scalars  $\Psi_0$  and  $\Psi_1$  (because they are strictly perturbative quantities). Note that we do not need the term of the form  $\mathbf{D}_{(1)}\Psi_2^{(0)}$ , because on the horizon the differential operator  $\mathbf{D}_{(1)}$  contains only time and azimuthal-angle derivatives, but the background Weyl scalar  $\Psi_2^{(0)}$  is only a function of  $r$  and  $\theta$ .

By applying the differential operator  $(D - 2\epsilon)$  to the second Bianchi identity and using the identity (valid on the horizon) that  $\delta^*\mathbf{D} - \mathbf{D}\delta^* = (\alpha + \beta^* - \pi)\mathbf{D}$ , we find that

$$(\mathbf{D} - 2\epsilon)\mathbf{D}\Psi_2^{(1)} = [\delta^* + 3(\pi - \alpha) - \beta^*](\delta^* + \pi - 4\alpha)\Psi_0 - (\mathbf{D} - 2\epsilon)(\lambda\Psi_0). \quad (9.112)$$

Using Geroch-Held-Penrose [45] notation, and the equation for a component of the Riemann tensor (Eq. (310g) of Ch. 1 of [30]) restricted to the horizon

$$\mathbf{D}\lambda - \delta^*\pi = -2\epsilon\lambda + \pi(\pi + \alpha - \beta^*), \quad (9.113)$$

we find that

$$\mathfrak{D}\Psi_2^{(1)} = (\delta'\delta' + 4\pi\delta' + 2\pi^2 - \lambda\mathfrak{D})\Psi_0. \quad (9.114)$$

Note that the  $\Psi_0$  here is related to that which satisfies Teukolsky's equation in the Kinnersley tetrad by

$$\Psi_0 = \frac{N_l^2 e^{2i\Theta} \Delta^2}{(r^2 + a^2)^2} \Psi_0^K \equiv A\Psi_0^K. \quad (9.115)$$

Starting from a modal solution for the Kinnersley  $\Psi_0$  (denoted by  $\Psi_{0lm\omega}^K$ ), then we see that the corresponding perturbation to  $\Psi_2$  is given by

$$\Psi_{2lm\omega}^{(1)} = \frac{\delta'\delta' + 4\pi\delta' + 2\pi^2 + \lambda(iN_l\Omega + 4\epsilon)}{N_l\Omega(2i\epsilon - N_l\Omega)} (A\Psi_{0lm\omega}^K), \quad (9.116)$$

where  $\Omega = \omega - m\omega_+$ , and where we have used the fact that  $\mathbf{D} = N_l(\partial_{\bar{t}} + \omega_+\partial_{\bar{\phi}})$  on the horizon.

A Weyl scalar,  $\Psi_0$ , formed from the superposition of modes  $\Psi_{0lm\omega}^K \pm (-1)^m \Psi_{0l-m-\omega^*}^K$ , with radial functions that obey  ${}_2R_{l-m-\omega^*} = \pm(-1)^m {}_2R_{lm\omega}^*$ , transforms under parity as  $\Psi_0 \rightarrow \pm(-1)^l \Psi_0^*$ . The perturbation of  $\Psi_2$  formed from superimposing Eq. (9.116) for the individual modes of  $\Psi_0^K$  above also transforms under parity as  $\Psi_2 \rightarrow \pm(-1)^l \Psi_2^*$ . Using the relation  $2\Psi_2 = \mathcal{E}_{NN} + i\mathcal{B}_{NN}$  and taking the real and imaginary parts of  $\Psi_2$ , it becomes clear that  $\mathcal{E}_{NN}$  and  $\mathcal{B}_{NN}$  have definite parity. Moreover, it is not difficult to see that  $\mathcal{E}_{NN}$  of an electric-parity mode is equal to  $i\mathcal{B}_{NN}$  of a magnetic-parity mode of  $i\Psi_{0lm\omega}^K$ , and  $\mathcal{E}_{NN}$  of a magnetic-parity mode is  $-i\mathcal{B}_{NN}$  of an electric-parity mode of  $i\Psi_{0lm\omega}^K$ .

*This demonstrates a perfect duality between electric-parity modes and magnetic-parity modes, on the horizon of a Kerr black hole.*

### 9.E.3 Relationship Between $\Psi_2$ and the Complex Curvature

As a final part of this appendix, we discuss how the relationship between the complex curvature and  $\Psi_2$ ,

$$\frac{1}{4}(\mathcal{R} + i\mathcal{X}) = -\Psi_2 + \mu\rho - \lambda\sigma, \quad (9.117)$$

simplifies for perturbations of Schwarzschild and Kerr black holes in the tetrad and gauge discussed in the sections of this appendix above. First, we note that the spin coefficient  $\lambda$  has as its unperturbed value on the horizon

$$\lambda_{(0)} = -\frac{Mr_+\omega_+^2 \sin^2\theta e^{-2i\Theta}}{N_l(r - ia \cos\theta)^3} [4Mr_+ + (r_+ - M)(r_+ - ia \cos\theta)], \quad (9.118)$$

where we have made use of the fact that on the horizon  $r_+^2 + a^2 = 2Mr_+$ . For a Schwarzschild black hole  $\omega_+$  vanishes, and, therefore, the background values of all four spin coefficients  $\mu$ ,  $\rho$ ,  $\lambda$ , and  $\sigma$

all vanish. Through first-order in perturbation theory, therefore,

$$\mathcal{R} = -2\mathcal{E}_{NN}, \quad \mathcal{X} = -2\mathcal{B}_{NN}. \quad (9.119)$$

[We briefly digress here to note that for Schwarzschild black hole, the spin coefficient  $\pi$  also vanishes, and Eq. (9.114) reduces to

$$\mathfrak{b}\mathfrak{b}\Psi_2^{(1)} = \delta'\delta'\Psi_0. \quad (9.120)$$

For a modal solution, Eq. (9.116) also simplifies to

$$\Psi_{2lm\omega}^{(1)} = \frac{4M\sqrt{2D}\alpha^4}{\omega(i - 4M\omega\sqrt{2})} {}_2R_{lm} Y_{lm} e^{-i\omega t}, \quad (9.121)$$

where  $\alpha^2 = 1 - 2M/r$ ,  $D = (l+2)!/(l-2)!$ ,  $\omega = \Omega$  (because  $\omega_+ = 0$ ), and the radial function of  $\psi_2$ ,  ${}_2R_{lm}$ , is evaluated at the horizon  $r = 2M$ . We have also used the fact that  $\epsilon = 1/(8M)$  in this tetrad. Because the spin coefficients vanish in Eq. (9.117) for this perturbed Schwarzschild hole, the above expression is equivalent to minus one quarter of the complex curvature.]

For a Kerr black hole  $\lambda_{(0)} \neq 0$ , and we must compute the perturbation to  $\sigma$ . It satisfies the differential equation

$$(\mathbf{D} - 2\epsilon)\sigma_{(1)} = \Psi_0 \quad (9.122)$$

[Eq. (310b) of Ch. 1 of [30] specialized to our tetrad and gauge]. For a modal solution of  $\sigma_{(1)}$ , we can solve this to find

$$\sigma_{(1)} = -\frac{\Psi_0}{iN_l\Omega + 2\epsilon}, \quad (9.123)$$

which implies that the perturbation to  $\sigma$  does not vanish. Thus, for a Kerr black hole,

$$\frac{1}{4}(\mathcal{R}_{(1)} + i\mathcal{X}_{(1)}) = -\Psi_2^{(1)} - \lambda_{(0)}\sigma_{(1)}, \quad (9.124)$$

so the horizon tendicity and vorticity are no longer exactly equal to the horizon's intrinsic and extrinsic scalar curvatures.

## 9.F Vortex and Tendex Lines of (2, 2) Perturbations of Schwarzschild and Kerr Black Holes with the Background Frame-Drag and Tidal Fields

In this appendix, we show the tendex and vortex lines of Schwarzschild and Kerr black holes when we plot a small (2, 2) perturbation of either electric or magnetic parity on top of the background

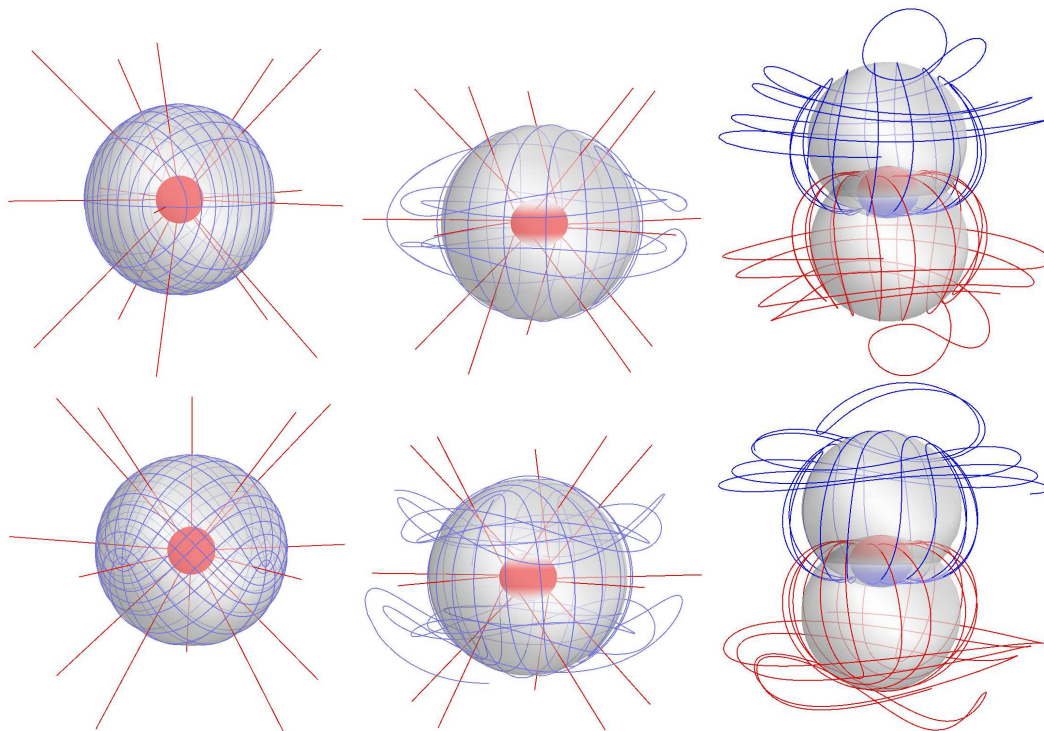


Figure 9.26: Tendex and vortex lines of Schwarzschild and Kerr black holes (of spin  $a/M = 0.945$ ) perturbed by a  $(2, 2)$  mode of either electric or magnetic parity, without removing the background tidal or frame-drag fields. The tendex lines and vortex lines are colored by the signs of their respective tendicities and vorticities (blue [dark gray] for positive and red [light gray] for negative). The horizons are colored and shaded by their vorticities or tendicities, and the transparent spheres have no physical significance, but they help to add perspective to the figures. The top panels are electric-parity perturbations and the bottom panels are magnetic-parity ones. *Left column:* Tendex lines of Schwarzschild black holes. *Middle column:* Tendex lines of Kerr black holes. *Right column:* Vortex lines of Kerr black holes.

tidal or frame-drag fields in Figure 9.26. Specifically, we plot the vortex and tendex lines of

$$\mathcal{E} = \mathcal{E}^{(0)} + \epsilon \mathcal{E}^{(1)}, \quad \mathcal{B} = \mathcal{B}^{(0)} + \epsilon \mathcal{B}^{(1)}, \quad (9.125)$$

where  $\mathcal{E}^{(0)}$  and  $\mathcal{B}^{(0)}$  are the stationary, unperturbed background fields (visualized in Paper II),  $\mathcal{E}^{(1)}$  and  $\mathcal{B}^{(1)}$  are the perturbations (visualized by themselves in Figure 9.14), and  $\epsilon$  is a constant that sets the scale of the perturbation. To describe the strength of the perturbation, we will compare the perturbative horizon tendicity or vorticity to the background tendicity (for Schwarzschild holes) and the tendicity or vorticity (for Kerr black holes). For the Schwarzschild black holes in Figure 9.26, we chose  $\mathcal{E}_{NN}^{(1)}/\mathcal{E}_{NN}^{(0)} \approx 2 \times 10^{-4}$  for the electric-parity perturbations and  $\mathcal{B}_{NN}^{(1)}/\mathcal{E}_{NN}^{(0)} \approx 2 \times 10^{-4}$  for the magnetic-parity perturbations. For electric-parity perturbations of Kerr holes, we chose  $\mathcal{E}_{NN}^{(1)}/\mathcal{E}_{NN}^{(0)} \approx 3.5 \times 10^{-3}$  and  $\mathcal{B}_{NN}^{(1)}/\mathcal{B}_{NN}^{(0)} \approx 3 \times 10^{-3}$ , and for the magnetic-parity perturbations the ratios we selected were  $\mathcal{E}_{NN}^{(1)}/\mathcal{E}_{NN}^{(0)} \approx 2.5 \times 10^{-3}$  and  $\mathcal{B}_{NN}^{(1)}/\mathcal{B}_{NN}^{(0)} \approx 5 \times 10^{-3}$ . We anticipate that these images may be useful for comparing with the results of numerical-relativity simulations, for which it is more difficult to separate a spacetime into a stationary background and dynamical perturbations.

In the top panels of Figure 9.26 are electric-parity perturbations, and the bottom panels are magnetic-parity perturbations. The left column of images are tendex lines of Schwarzschild black holes, the center column are tendex lines of Kerr black holes of spin  $a/M = 0.945$ , and the right column are the corresponding vortex lines of the perturbed Kerr black holes. The lines are colored by the sign of their tendicity or vorticity (blue [dark gray] for positive and red [light gray] for negative) and the horizons are colored by their tendicity or vorticity. The transparent spheres are placed in the figures to help guide the eye, and do not indicate any feature of the vortexes or tendexes.

In these figures, we must choose an amplitude for the perturbation (described in the first paragraph above). For the all the black holes, we make the perturbation sufficiently small that one cannot see the effect of the perturbation in either the horizon tendicity, or the red (light gray) radial tendex lines. For the Kerr holes, we also require that the amplitude of the perturbation is less than the difference of the tendicities of the two non-radial tendex lines at the equatorial plane and around the radius at which the angular lines reach closest to the horizon. With this choice, the angular tendex lines will retain some features of the unperturbed lines before they become more distorted by the perturbation in the regions near the poles.

First, we will describe the tendex lines of the Schwarzschild black holes. An unperturbed Schwarzschild black hole is spherically symmetric, the tendicity on a sphere of constant radius is constant, and, therefore, any direction tangent to the sphere is a valid tendex line. For a weakly perturbed Schwarzschild black hole, although the perturbation may be small, the perturbation restricted to a sphere of constant  $r$  completely determines the variation in the tendicity, and, furthermore, it will determine the directions of the tendex lines. This is analogous to degenerate perturbation the-

ory in quantum mechanics, in which the eigenstates of the perturbing Hamiltonian restricted to the subspace spanned by the degenerate eigenstates are treated as the unperturbed states within the degenerate subspace. In directions that are not degenerate, however, its effects are negligible.

We can now use these facts about degeneracy to understand the tendex lines in the angular direction. The tidal field in the strictly angular directions, Eq. (9.89c) will determine the structure of the tendex lines on the sphere. The angular dependence is determined by the transverse-traceless, electric-parity tensor harmonic (for the top-left panel), because the trace term in Eq. (9.89c) is proportional to the identity and will not lift the degeneracy of the tendex lines. We would expect, therefore, that the tendex lines in the angular direction would resemble those of transverse-traceless,  $l = 2$ ,  $m = 2$ , gravitational waves generated by a time-dependent mass quadrupole. These were shown in [2, 17], and the pattern of the lines is nearly identical. The tendicity along the lines is quite different from those of a gravitational wave, because for the perturbed Schwarzschild black hole, the tendicity is primarily determined by the constant unperturbed value on the sphere. Nevertheless, the tendex lines on the sphere show a striking similarity to those of gravitational waves at infinity.

For the magnetic-parity perturbation (the bottom-left panel), the tendex lines are determined by an  $l = 2$ ,  $m = 2$ , magnetic-parity tensor harmonic; consequently, we would expect that the lines would resemble those of transverse-traceless gravitational waves at infinity, produced by a time-dependent, current-quadrupole source. Those lines were shown in [17], and they appear identical. Once more, though, the value of the tendicity along the lines is set by the background Schwarzschild black hole for the lines in bottom-left panel of Figure 9.26 (unlike the tendicity of the lines studied in [17]).

The degeneracy between the angular tendex and vortex lines can also be used to explain the tendex and vortex lines in the middle and right columns of Figure 9.26, respectively. For both the tendex and vortex lines, when the lines are near the equatorial plane ( $\theta = \pi/2$ ) they resemble the unperturbed lines, but as they head toward the poles, they begin to become perturbed. This happens because the perturbation is small compared to the difference in the eigenvalues near the equatorial plane, and the perturbations have little effect on the tendex or vortex lines. Near the poles, however, the background vorticities and tendicities in the angular directions become degenerate (see the discussion at the end of Appendices A and B of Paper II), and the perturbation restricted to the degenerate subspace controls the lines' directions. In the vicinity of the poles, the degenerate subspace is a plane parallel to the equatorial plane, and the perturbative tendex lines must form a regular grid around these points. When we combine this observation with the parity of the perturbation, we see that the lines at the opposite poles must be either parallel or orthogonal. Thus, these few simple constraints combine to explain the relatively simple pattern of the vortex and tendex lines of the perturbation plus the background frame-drag and tidal fields.

## Bibliography

- [1] R. Owen, J. Brink, Y. Chen, J. D. Kaplan, G. Lovelace, K. D. Matthews, D. A. Nichols, M. A. Scheel, F. Zhang, A. Zimmerman, et al., *Phys. Rev. Lett.* **106**, 151101 (2011).
- [2] D. A. Nichols, R. Owen, F. Zhang, A. Zimmerman, J. Brink, Y. Chen, J. Kaplan, G. Lovelace, K. D. Matthews, M. A. Scheel, et al., *Phys. Rev. D.* **84**, 124914 (2011), 1108.5486.
- [3] J. Centrella, J. G. Baker, B. J. Kelly, and J. R. van Meter, *Rev. Mod. Phys.* **82**, 3069 (2010).
- [4] F. Zhang, A. Zimmerman, D. A. Nichols, Y. Chen, G. Lovelace, K. D. Matthews, R. Owen, and K. S. Thorne, submitted to *Phys. Rev. D* (2012).
- [5] R. Penrose and W. Rindler, *Spinors and Space-time, Volume 1* (Cambridge University Press, Cambridge, 1992).
- [6] J. Hartle, *Phys. Rev. D* **9**, 2749 (1974).
- [7] K. A. Dennison and T. W. Baumgarte (2012), [arXiv:gr-qc/1207.2431](https://arxiv.org/abs/gr-qc/1207.2431).
- [8] T. Damour, in *Proceedings of the Second Marcel Grossman Meeting on General Relativity*, edited by R. Ruffini (North-Holland Publishing Company, Amsterdam, 1982), pp. 587–606.
- [9] K. S. Thorne, R. H. Price, and D. A. MacDonald, *Black Holes: The Membrane Paradigm* (Yale University Press, New Haven and London, 1986).
- [10] L. Bel, *General Relativity and Gravitation* **32**, 2047 (2000).
- [11] J. D. Brown, S. R. Lau, and J. W. York, *Phys. Rev. D* **59**, 064028 (1999).
- [12] <http://www.phy.olemiss.edu/~berti/qnms.html>.
- [13] E. Berti, V. Cardoso, and A. O. Starinets, *Classical and Quantum Gravity* **26**, 163001 (2009), 0905.2975.
- [14] E. W. Leaver, *Proc. R. Soc. Lond. A* **402**, 285 (1985).
- [15] R. Maartens, T. Gebbie, and G. F. Ellis, *Phys. Rev. D* **59**, 083506 (1999), [astro-ph/9808163](https://arxiv.org/abs/astro-ph/9808163).
- [16] J. D. Schnittman, A. Buonanno, J. R. van Meter, J. G. Baker, W. D. Boggs, J. Centrella, B. J. Kelly, and S. T. McWilliams, *Phys. Rev. D* **77**, 044031 (2008).
- [17] A. Zimmerman, D. A. Nichols, and F. Zhang, *Phys. Rev. D* **84**, 044037 (2011).
- [18] I. Vega, E. Poisson, and R. Massey, *Class. Quant. Grav.* **28**, 175006 (2011), 1106.0510.

- [19] G. Lovelace, M. Boyle, M. A. Scheel, and B. Szilágyi, *Class. Quant. Grav.* **29**, 045003 (2012), [arXiv:1110.2229](#).
- [20] <http://www.black-holes.org/oscillateQuadVortex.html>.
- [21] J. W. Belcher and S. Olbert, *Am. J. Phys.* **71**, 220 (2003).
- [22] V. Ferrari and B. Mashhoon, *Phys. Rev. D* **30**, 295 (1984).
- [23] S. R. Dolan, *Phys. Rev. D* **82**, 104003 (2010).
- [24] H. Yang, D. A. Nichols, F. Zhang, A. Zimmerman, Z. Zhang, and Y. Chen (2012), [arXiv:1207.4253](#).
- [25] I. Kamaretsos, M. Hannam, and B. Sathyaprakash (2012), [1207.0399](#).
- [26] <http://www.black-holes.org/SpEC.html>.
- [27] T. Regge and J. A. Wheeler, *Phys. Rev.* **108**, 1063 (1957).
- [28] F. J. Zerilli, *Phys. Rev. D* **2**, 2141 (1970).
- [29] L. A. Edelman and C. V. Vishveshwara, *Phys. Rev. D* **1**, 3514 (1970).
- [30] S. Chandrasekhar, *The Mathematical Theory of Black Holes* (Oxford University Press, Oxford, 1983).
- [31] S. Teukolsky, *Astrophys. J.* **185**, 635 (1973).
- [32] E. Newman and R. Penrose, *J. Math. Phys.* **3**, 566 (1962).
- [33] P. L. Chrzanowski, *Phys. Rev. D* **11**, 2042 (1975).
- [34] C. O. Lousto and B. F. Whiting, *Phys. Rev. D* **66**, 024026 (2002).
- [35] A. Ori, *Phys. Rev. D* **67**, 124010 (2003).
- [36] N. Yunes and J. Gonzalez, *Phys. Rev. D* **73**, 024010 (2006).
- [37] T. S. Keidl, J. L. Friedman, and A. G. Wiseman, *Phys. Rev. D* **75**, 124009 (2007).
- [38] T. S. Keidl, A. G. Shah, J. L. Friedman, D.-H. Kim, and L. R. Price, *Phys. Rev. D* **82**, 124012 (2010).
- [39] A. G. Shah, T. S. Keidl, J. L. Friedman, D.-H. Kim, and L. R. Price, *Phys. Rev. D* **83**, 064018 (2011).
- [40] J. M. Stewart, *Proc. R. Soc. Lond. A* **367**, 527 (1979).

- [41] P. P. Fiziev, Phys. Rev. D **80**, 124001 (2009).
- [42] K. Martel and E. Poisson, Phys. Rev. D **71**, 104003 (2005).
- [43] K. S. Thorne, Rev. Mod. Phys. **52**, 299 (1980).
- [44] E. Poisson, Phys. Rev. D **70**, 084044 (2004).
- [45] R. Geroch, A. Held, and R. Penrose, J. Math. Phys. **14**, 874 (1973).